U.PORTO
FEUP FACULDADE DE ENGENHARIA
UNIVERSIDADE DO PORTO

PhD Thesis

Multi-Scale Modelling and Analysis of Multi-Phase Solids Using Second-Order Computational Homogenisation at Finite Strains with Parallel Computing

Igor André Rodrigues Lopes

Supervisor:
Prof. Francisco Manuel Andrade Pires

Doctoral Program in Mechanical Engineering

Thesis submitted to Faculdade de Engenharia da Universidade do Porto in partial fulfilment of the requirements for the degree of Doctor of Philosophy in Mechanical Engineering

Porto, 2019

CM2S

Computational Multi-Scale
Modeling of Solids and Structures

Multi-Scale Modelling and Analysis of Multi-Phase Solids Using Second-Order Computational Homogenisation at Finite Strains with Parallel Computing

Igor André Rodrigues Lopes

Abstract

Multi-scale models based on computational homogenisation have become a valuable tool to model and analyse materials with complex microstructures, providing a link between the macroscopic behaviour and the underlying microstructural phenomena. This constitutive approach is general and can naturally account for finite strains and dissipative mechanisms. Three different types of multi-scale formulations are addressed in this thesis: (i) the standard first-order homogenisation scheme, (ii) second-order homogenisation-based models where the macro-scale is modelled as a second-order continuum, while the micro-scale is described by the classical first-order continuum mechanics and (iii) a fully second-order homogenisation multi-scale formulation, where the material behaviour is modelled with a second-order continuum at both scales. The *method of multi-scale virtual power* is employed to derive the formulations introduced, guaranteeing a variationally consistent scale transition.

Due to the assumption of the uniformity of the macroscopic deformation gradient in the RVE, the standard first-order homogenisation scheme enables only linear deformation modes to be modelled at the micro-scale, and the response remains valid as long as the *scales separation principle* is respected, i.e., when the RVE length is much smaller than the macro-scale deformation wavelength. This fact limits the application of this kind of models, that cannot be employed, for instance, in the modelling of deformations involving high curvatures or localised strains. Second-order homogenisation-based models enlarge the domain of applicability of multi-scale models for situations with higher strain gradients and allow the analysis of loadings like bending or torsion at the micro-scale. Moreover, it is observed that second-order homogenisation models are able to capture second-order effects due to the geometrical non-linearity of the microstructure. This type of formulations recovers the benefits of strain gradient models, since a second-order continuum theory is used to describe the macro-scale behaviour and therefore the homogenised response results in a second-order constitutive law. The discretisation of the resulting macro-scale problem requires C^1 continuous elements. Although 2D mixed elements are well established and available in the literature, a 3D hexahedral mixed element is proposed here.

A second-order homogenisation model is formulated, by introducing a modified definition of the homogenised second gradient, and the corresponding numerical implementation with the Lagrange multiplier method is presented. The relative merits of this alternative model are compared with other formulations available in the literature. Besides providing more consistent results, the use of Lagrange multipliers enables the establishment of relations with physical quantities such as homogenised stresses, which is conveniently used to obtain the consistent tangents in a straightforward fashion. It is fundamental to enforce volumetric constraints at the micro-scale, even though this raises some issues when modelling voids.

The fact that the homogenised response converges with an increasing RVE size, observed for first-order homogenisation models, does not hold for second-order homogenisation schemes, since the RVE length is a parameter that influences the second-order response. After demonstrating numerically that second-order homogenisation models are insensitive to the micro-constituents size, the concept of generalised RVE size is introduced, allowing to decouple the RVE length and the RVE size in the numerical model, and including an appropriate number of constituents in a RVE with a fixed RVE length. Several numerical examples show that the scales separation limit for first-order

homogenisation models depends on the magnitude of the macroscopic strains, in addition to the RVE length and the macroscopic second gradient. Based on these observations, an adaptive framework for analysis with second-order homogenisation models is proposed. Aiming to include size effects due to the micro-constituents size, a fully second-order homogenisation model is formulated at finite strains.

Finally, in order to minimise the computational burden associated with FE^2 simulations, a mixed parallel strategy that combines a master-slave algorithm with dynamic scheduling and a non-conforming macro-domain decomposition method with an adaptive distribution of working CPUs is proposed to deal with highly non-linear problems.

Keywords: Multi-scale modelling, Computational homogenisation, Heterogeneous materials, Second-order continuum, Finite element method, Finite strains, Lagrange multiplier method, Method of multi-scale virtual power, Parallel computing.

Modelação e Análise Multi-Escala de Sólidos Multi-Fásicos Usando Homogeneização Computacional de Segunda Ordem com Deformações Finitas e Computação Paralela

Igor André Rodrigues Lopes

Sumário

Os modelos multi-escala baseados em homogeneização computacional têm-se revelado uma ferramenta de relevo para a análise e modelação de materiais com microestruturas complexas, estabelecendo uma ligação entre o comportamento macroscópico e os fenómenos microestruturais subjacentes. Esta abordagem constitutiva apresenta um carácter genérico, possibilitando a inclusão de deformações finitas e mecanismos dissipativos de um modo natural. Nesta tese são abordados três tipos de formulações multi-escala: (i) a formulação tradicional de homogeneização de primeira ordem, (ii) modelos baseados em homogeneização de segunda ordem em que a macro-escala é modelada como um meio contínuo de segunda ordem, enquanto a micro-escala é descrita pela mecânica clássica dos meios contínuos de primeira ordem e (iii) uma formulação multi-escala baseada em homogeneização completamente em segunda ordem, onde o comportamento do material é modelado através de uma teoria dos meios contínuos de segunda ordem em ambas as escalas. É utilizado o *método da potência virtual multi-escala* para derivar as formulações apresentadas, garantindo assim uma transição de escalas variacionalmente consistente.

Dado que para os modelos tradicionais de primeira ordem se assume que o gradiente de deformação macroscópico é uniforme no Elemento de Volume Representativo (EVR), estes apenas permitem modelar modos de deformação lineares na micro-escala, e a resposta obtida só é válida quando o *princípio da separação de escalas* é verificado, ou seja, quando o comprimento do EVR é muito inferior ao comprimento característico das deformações macroscópicas. Este facto limita a aplicação deste tipo de modelos, que não podem ser utilizados na modelação de deformações localizadas ou na presença de grandes curvaturas, por exemplo. Os modelos baseados em homogeneização de segunda ordem ampliam o domínio de aplicabilidade dos modelos multi-escala para situações em que se observam gradientes de deformações mais elevados, permitindo a análise de solicitações como flexão ou torção à micro-escala. Para além disto, verifica-se que os modelos com homogeneização de segunda ordem têm a capacidade de prever efeitos de segunda ordem devidos à não-linearidade geométrica da microestrutura. Este tipo de formulações apresenta as vantagens dos modelos baseados no gradiente das deformações, uma vez que comportamento à macro-escala é descrito através de uma teoria para meios contínuos de segunda ordem e, consequentemente, a resposta homogeneizada resulta numa lei constitutiva de segunda ordem. A resolução do problema de elementos finitos resultante à macro-escala requer a utilização de elementos com continuidade C^1. Existem elementos mistos 2D bem estabelecidos na literatura para este tipo de problemas. Apesar disso, é proposto nesta tese um elemento misto hexaédrico para problemas 3D.

É efectuada a formulação de um modelo de homogeneização computacional de segunda ordem com base numa definição modificada do segundo gradiente homogeneizado, e a sua implementação numérica é apresentada utilizando o método dos multiplicadores de Lagrange. Este modelo alternativo é comparado com outras formulações disponíveis na literatura. Para além de permitir obter resultados mais consistentes, a utilização de multiplicadores de Lagrange neste modelo permite estabelecer relações com quantidades físicas, como as tensões homogeneizadas, o que é conveniente para o cálculo directo das tangentes consistentes. É fundamental impor restrições volumétricas na micro-escala, apesar de se levantarem questões quanto à sua aplicação em microestruturas com vazios.

O facto observado em modelos baseados em homogeneização de primeira ordem, em que

a resposta homogeneizada converge com o aumento do tamanho do EVR, não se verifica para homogeneização de segunda ordem, uma vez que o comprimento do EVR funciona como um parâmetro que influencia a resposta de segunda ordem. Após demonstrar numericamente que os modelos baseados em homogeneização de segunda ordem são insensíveis ao tamanho dos micro-constituintes, é introduzido o conceito de tamanho do EVR generalizado, que permite desacoplar o tamanho do EVR e o comprimento do EVR no modelo numérico, e incluir um número adequado de constituintes num EVR com um determinado comprimento. Vários exemplos numéricos mostram que o limite da separação de escalas para a homogeneização de primeira ordem depende não só do comprimento do EVR e do segundo gradiente macroscópico, mas também da magnitude das deformações macroscópicas. Com base nestes resultados, é proposto um algoritmo adaptativo para a análise com homogeneização computacional de segunda ordem. Com o objectivo de incorporar efeitos de escala devidos ao tamanho dos micro-constituintes, é formulado um modelo de homogeneização completamente de segunda ordem com grandes deformações.

Finalmente, com intuito de minimizar o esforço computacional associado às simulações multi-escala acopladas (FE^2), é proposta uma estratégia mista de computação paralela para a resolução de problemas não-lineares, que combina um algoritmo *master-slave* incluindo alocação dinâmica de processadores com um método não-conforme de decomposição de domínios à macro-escala, onde a distribuição de recursos é realizada de forma adaptativa.

Palavras-chave: Modelação multi-escala, Homogeneização computacional, Materiais heterogéneos, Meios contínuos de segunda ordem, Método dos elementos finitos, Deformações finitas, Método dos multiplicadores de Lagrange, Método da potência virtual multi-escala, Computação paralela.

Agradecimentos

A minha primeira palavra de gratidão vai para o Professor Francisco Pires, pela oportunidade proporcionada há já dez anos de começar a trabalhar na temática da Mecânica Computacional, e pela motivação transmitida através do entusiasmo com que aborda cada temática.

Os dias de trabalho teriam sido bem mais solitários, e menos animados, sem o convívio e a colaboração com os membros do CM2S, que contribuíram também para o desenvolvimento de outras competências. As conversas com o Fernando, amigo e companheiro neste desafio, que têm posto à prova a minha cultura geral e os meus conhecimentos de geopolítica e numismática, permitiram-me abstrair da Mecânica Computacional. A tarefa de encontrar e resolver os bugs iniciais e as longas horas dedicadas à construção do cluster *Atlanticus* com o Rodrigo foram extremamente desafiantes. O meu sentido de estética e organização não seria o mesmo sem a interacção com o Rodrigo e o Bernardo. Os estudos desenvolvidos com materiais policristalinos só foram possíveis com a enriquecedora colaboração do Miguel e do Daniel. Agradeço ao Fábio Reis pelas dicas e ideias deixadas para o desenvolvimento dos programas de análise multi-escala, e pelo cuidado em acompanhar este percurso. A disponibilidade da Carla Monteiro para ajudar com todas as questões burocráticas que surgiram foi essencial para conseguir manter o foco no desenvolvimento deste trabalho.

O rumo do trabalho desenvolvido foi clarificado graças às conversas sobre dobradiças flexíveis que tive com o Pedro Mimoso.

Aos amigos que me têm acompanhado nestes tempos, obrigado por todos os momentos de descontração que me proporcionaram. Um agradecimento especial para a Marieta, pelas suas palavras que tiveram um papel decisivo no sucesso desta caminhada.

Finalmente, agradeço à minha família pela paciência e por todo o apoio prestado. Uma palavra especial para os meus pais, por proporcionarem os meios para o meu percurso académico e crescimento pessoal. À Diana, minha mulher, obrigado por, com a nossa filha Ariana, seres sempre a minha maior fonte de motivação e inspiração.

O trabalho desenvolvido nesta tese foi financiado pela Fundação para a Ciência e a Tecnologia através da bolsa de doutoramento com a referência SFRH/BD/100093/2014.

Contents

List of Symbols

Acronyms and abbreviations

b.c. Boundary condition

CMSP Coupled Multi-Scale Problem

CPU Central Processing Unit (processor)

DNS Direct Numerical Simulation

dof Degree of freedom

FEM Finite Element Method

FETI Finite element tearing and interconnecting

MMVP Method of Multi-Scale Virtual Power

MPI Message Passing Interface

MSP Micro-Scale Problem

RAM Random Access Memory

RVE Representative Volume Element

General Convention

$(\bullet)_0$ Variable defined in the reference configuration

$(\bullet)_\mu$ Micro-scale variable

$\mathbf{a}, \mathbf{A}$ Higher-order tensors

$\boldsymbol{A}$ Second-order tensors

$\boldsymbol{a}$ Vectors

$\mathbf{a}, \mathbf{A}$ Finite elements related arrays (vectors and matrices)

$\mathscr{A}$ Spaces, generic functions

a, A Scalar values

Variables

$\mathbf{A}$ Material tangent modulus in matrix format

$\mathbf{a}$ Spatial tangent modulus in matrix format

$\mathbf{A}_G$	Consistent tangent $\mathbf{A}_G$ in matrix format
$\mathbf{A}$	Material tangent modulus $\partial \boldsymbol{P}/\partial \boldsymbol{F}$
$\mathbf{a}$	Spatial tangent modulus
$\mathbf{A}_G$	Consistent tangent $\partial \boldsymbol{P}/\partial \mathbf{G}$
$\boldsymbol{\beta}$	Microscopic set of internal variables
$\boldsymbol{\lambda}$	Lagrange multiplier vector
$\boldsymbol{\sigma}$	Cauchy stress tensor
$\boldsymbol{\tau}$	Kirchhoff stress tensor
$\boldsymbol{\theta}$	Macroscopic set of internal variables
$\boldsymbol{\alpha}$	Micro-scale dependency matrix
$\boldsymbol{\lambda}$	Nodal Lagrange multiplier vector
$\boldsymbol{\varphi}$	Deformation mapping function
$\boldsymbol{\xi}$	Coordinates in element natural space
$\boldsymbol{B}$	Left Cauchy-Green strain tensor
$\boldsymbol{b}$	External volume force vector in the current configuration
$\boldsymbol{C}$	Right Cauchy-Green strain tensor
$\boldsymbol{E}, \boldsymbol{\varepsilon}$	Strain tensors
$\boldsymbol{e}_i^*$	Eulerian principal directions
$\boldsymbol{e}_i$	Lagrangian principal directions
$\boldsymbol{F}$	Deformation gradient
$\boldsymbol{g}$	Gap function
$\boldsymbol{I}$	Second-order identity tensor
$\boldsymbol{J}$	Second-order moment of volume, Jacobian matrix
$\boldsymbol{N}$	Unit outward normal vector in the reference configuration
$\boldsymbol{n}$	Unit outward normal vector in the current configuration
$\boldsymbol{P}$	First Piola-Kirchhoff stress tensor
$\boldsymbol{R}$	Rotation tensor
$\boldsymbol{R}_0$	Double traction tensor in the reference configuration
$\boldsymbol{r}_0$	Double tractions in the reference configuration
$\boldsymbol{S}$	Second Piola-Kirchhoff stress tensor
$\boldsymbol{s}$	Deviatoric stress tensor

$\boldsymbol{s}_0$ External line forces in the reference configuration

$\boldsymbol{t}$ External traction vector in the current configuration

$\boldsymbol{U}$ Right stretch tensor

$\boldsymbol{u}$ Displacement vector

$\boldsymbol{V}$ Left stretch tensor

$\boldsymbol{v}$ Velocity vector

$\boldsymbol{X}$ Macroscopic material coordinate

$\boldsymbol{x}$ Macroscopic spatial coordinate

$\boldsymbol{Y}$ Microscopic material coordinate

$\boldsymbol{y}$ Microscopic spatial coordinate

G Second gradient of the displacements

$\Delta\mathbf{u}$ Nodal iterative displacement vector

$\tilde{\boldsymbol{u}}$ Displacement fluctuation vector

$\tilde{\mathbf{u}}$ Nodal displacement fluctuation vector

ϵ_{tol} Convergence tolerance

$\hat{\boldsymbol{F}}$ Relaxed deformation gradient

$\hat{\mathbf{F}}$ Nodal vector with the relaxed deformation gradient

$\hat{\mathbf{G}}$ Relaxed second gradient in vector format

$\mathbf{H}$ Consistent tangent H in matrix format

$\mathbf{H}_F$ Consistent tangent H_F in matrix format

H Consistent tangent $\partial\mathsf{Q}/\partial\mathsf{G}$

H_F Consistent tangent $\partial\mathsf{Q}/\partial\boldsymbol{F}$

Q Higher-order stress tensor

$\boldsymbol{L}$ Lagrange multiplier enforcing the first-order minimal constraint

M Lagrange multiplier enforcing the second-order minimal constraint

$\{\mathbf{I}\}$ Identity tensor in vector format

$\mathbf{A}^m$,$\mathbf{A}^{nm}$,$\mathbf{D}^{nm}$ Mortar matrices

$\mathbf{B}$ Discrete symmetric gradient operator matrix

$\mathbf{b}$ External volume force nodal vector

$\mathbf{C}$ Constraint matrix

$\mathbf{D}$ Coordinates matrix

$\mathbf{F}$	Deformation gradient in vector format
$\mathbf{f}^{ext}$	Nodal external force vector
$\mathbf{f}^{int}$	Nodal internal force vector
$\mathbf{G}$	Discrete gradient operator matrix
$\mathbf{I}$	Identity matrix
$\mathbf{k}$	Stiffness sub-matrix
$\mathbf{K}_e$	Element stiffness matrix
$\mathbf{K}_T$	Global tangent stiffness matrix
$\mathbf{L}$	Lagrange multiplier $\boldsymbol{L}$ in vector format
$\mathbf{M}$	Lagrange multiplier M in vector format
$\mathbf{N}, \mathbf{N}^u$	Shape function matrix
$\mathbf{N}^\lambda$	Lagrange multiplier interpolation function matrix
$\mathbf{N}^F$	Relaxed deformation gradient interpolation function matrix
$\mathbf{P}$	First Piola-Kirchhoff stress tensor in vector format
$\mathbf{Q}$	Higher-order stress in vector format
$\mathbf{r}$	Nodal residual vector
$\mathbf{T}$	Transformation matrix
$\mathbf{t}$	External traction nodal vector
$\mathbf{u}$	Nodal displacement vector
$\mathbf{V}$	Second-order coordinates matrix
$\mathbf{W}$	Mortar constraint matrix
$\mathcal{V}$	Space of admissible virtual displacements
μ, λ	Lamé parameters
ν	Poisson's ratio
Ω	Domain
Ω^d	Discretised domain
$\partial\Omega, \Gamma$	Domain boundary
ρ	Mass density
σ_y	Yield stress
σ_{y0}	Initial yield stress
$\boldsymbol{\sigma}$	Vector representation of $\boldsymbol{\sigma}$

$\delta \boldsymbol{u}$ Virtual displacements vector

$\delta \mathbf{u}$ Nodal virtual displacements vector

E Young's modulus, Parallel efficiency

f Void volume fraction

G Shear modulus

H Hardening modulus

J Determinant of the deformation gradient (Jacobian of deformation)

J_p Determinant of the Jacobian of the transformation mapping

K Bulk modulus

l Characteristic length

l_{RVE} RVE length

M_i Mortar Lagrange multipliers interpolation functions related to the node i

N_i^{λ} Lagrange multiplier interpolation functions related to the node i

N_i^F, H_i^F Relaxed deformation gradient interpolation functions related to the node i

n_e Number of elements

N_i, N_i^u, H_i Shape functions related to the node i

n_n Number of nodes

n_p Number of points

p Hydrostatic pressure

S Speedup

s_{RVE} RVE size

t Time variable

V Volume

W_0 Elastic strain energy function per unit reference volume

w_p Gaussian quadrature weight value

Operators

$(\bullet)^S$ Symmetric of $(\bullet)$: $(\bullet)^S = 1/2(\bullet + \bullet^T)$

$(\bullet)^T$ Transpose of $(\bullet)$: $\boldsymbol{A}^T = A_{ji}\boldsymbol{e}_i \otimes \boldsymbol{e}_j$, $\mathbf{A}^T = A_{ikj}\boldsymbol{e}_i \otimes \boldsymbol{e}_j \otimes \boldsymbol{e}_k$

$(\bullet)^{-1}$ Inverse of $(\bullet)$

: Double contraction: $\boldsymbol{A} : \boldsymbol{B} = A_{ij}B_{ij}$, $\mathbf{A} : \boldsymbol{B} = \mathsf{A}_{ijk}B_{jk}\boldsymbol{e}_k$

$\cdot$ Single contraction, dot product: $\boldsymbol{A} \cdot \boldsymbol{v} = A_{ij}v_j\boldsymbol{e}_i$, $\boldsymbol{A} \cdot \boldsymbol{B} = A_{ij}B_{jk}\boldsymbol{e}_i \otimes \boldsymbol{e}_k$, $\mathbf{A} \cdot \boldsymbol{v} = \mathsf{A}_{ijk}v_k\boldsymbol{e}_i \otimes \boldsymbol{e}_j$

δ_{ij} Kronecker delta

$\mathrm{div}(\bullet)$ Divergence of $(\bullet)$

$\mathrm{div}^n(\bullet)$ Normal divergence of $(\bullet)$

$\mathrm{div}^t(\bullet)$ Tangential divergence of $(\bullet)$

$\mathrm{div}_X(\bullet)$ Material divergence of $(\bullet)$ (macro-scale)

$\mathrm{div}_x(\bullet)$ Spatial divergence of $(\bullet)$ (macro-scale)

$\mathrm{div}_Y(\bullet)$ Material divergence of $(\bullet)$ (micro-scale)

$\mathrm{div}_y(\bullet)$ Spatial divergence of $(\bullet)$ (micro-scale)

$\dot{(\bullet)}$ Temporal derivative $\partial \bullet / \partial t$

$\nabla(\bullet)$ Gradient of $(\bullet)$

$\nabla^s(\bullet)$ Symmetric gradient of $(\bullet)$

$\nabla^t(\bullet)$ Tangential gradient of $(\bullet)$: $\nabla^t(\bullet) = \nabla(\bullet) \cdot (\boldsymbol{I} - \boldsymbol{N} \otimes \boldsymbol{N})$

$\nabla_X(\bullet)$ Material gradient of $(\bullet)$ (macro-scale)

$\nabla_x(\bullet)$ Spatial gradient of $(\bullet)$ (macro-scale)

$\nabla_Y(\bullet)$ Material gradient of $(\bullet)$ (micro-scale)

$\nabla_y(\bullet)$ Spatial gradient of $(\bullet)$ (micro-scale)

$\|\bullet\|$ Norm or jump of $(\bullet)$

$\otimes$ Tensor Product

$\partial(\bullet)/\partial(*)$ Partial derivative of $(\bullet)$ with respect to $(*)$

$\vdots$ Triple contraction: $\mathbf{A}\vdots\mathbf{B} = \mathsf{A}_{ijk}\mathsf{B}_{ijk}$

$D_0(\bullet)$ Normal gradient of $(\bullet)$: $D_0(\bullet) = \nabla(\bullet) \cdot \boldsymbol{N}$

$\mathrm{tr}(\bullet)$ Trace of $(\bullet)$

Chapter 1

Introduction

1.1 Context

Multi-scale modelling of materials is becoming one of the key approaches for the structural analysis and design of engineering materials and structures. Indeed, the goal of multi-scale models is to relate the large-scale behaviour of materials and structures with their underlying heterogeneous microstructure by continuous interchange of information between scales. Therefore, they can provide not only a deeper physical insight into the material behaviour but also offer the possibility to tailor new materials by manipulating their microstructure via numerical simulations. Nevertheless, the solution of realistic problems with these modelling approaches is extremely challenging due to the computational complexity involved in solving problems at two (or more) scales.

Multi-scale models can be categorised into (Matouš et al., 2017): (i) concurrent methods, where there is no separation of scales and therefore different parts of a problem domain are modeled with distinct scales (Lloberas-Valls et al., 2012a,b), (ii) hierarchical methods, where the length scales of micro and macro problems are sufficiently separate (Feyel and Chaboche, 2000, Kouznetsova et al., 2001) and consequently different scales are hierarchically coupled in the same portion of the domain, and (iii) hybrid methods, which have a hybrid coupling scheme between scales (Miehe and Bayreuther, 2007, Plews and Duarte, 2015). The work developed in this thesis focus on hierarchical computational homogenisation-based multi-scale models, where the macroscopic stress and deformation measures are defined as volume averages of their microscopic counterparts over a Representative Volume Element (RVE). The RVE is a confined model of the heterogeneous microstructure which incorporates all statistically relevant microstructural features and where the behaviour of the different constituents and phases is typically modelled by continuum constitutive models following the formalism of thermodynamics with internal variables (see Figure 1.1). This spatial multi-scale technique has emerged as a very effective way to describe complex microstructural geometries, arbitrary constitutive material behaviour and microstructural evolution. It is based on the nested solution of two coupled problems, one at a macro-scale and other at the micro-scale, where a micro-scale computation is conducted over the statistically RVE.

1.2 Modelling heterogeneous materials

The effort to develop constitutive laws for materials that are heterogeneous at small scales emerged with the need to characterise the behaviour of composites. Therefore most of the seminal work concerning homogenisation of heterogeneous media response is related to the determination of the homogenised elastic properties of composite materials. Several analytical models have been proposed, such as the simple Taylor model (rule of mixtures), models based on the effective medium approximation (Eshelby, 1957) or the self-consistent approach (Hill, 1965). Reviews on modelling heterogeneous composites may be found in Hashin (1983), or more recently in Kanouté et al. (2009).

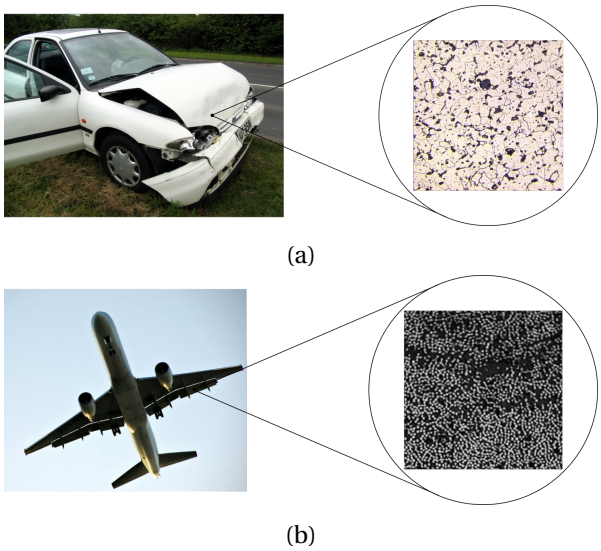

(a)

(b)

Figure 1.1: Representative Volume Elements for (a) steel and (b) carbon fibre composites.

The models based on the analysis of RVEs appeared as a tool to overcome the limitations of analytical models, where only relatively simple constituents shapes and distributions can be treated. Indeed, Representative Volume Element-based techniques provide a more general analysis tool, which allows to model microstructures without geometrical restrictions, and to introduce models of any mechanism and phenomena at the RVE level.

1.3 Multi-scale models based on computational homogenisation

Pioneering contributions towards the development of multi-scale models based on computational homogenisation performed with RVEs were presented during the 1990s and beginning of 2000s. Guedes and Kikuchi (1990) presented a numerical scheme where the macroscopic elastic properties of composite structures are obtained from finite element analyses of RVEs, through an asymptotic homogenisation procedure, and then used in the macroscopic finite element model. A postprocessing procedure is also included, aiming to recover the microstructural distribution of stress and strain fields. A similar strategy is proposed by Ghosh et al. (1995), where the asymptotic homogenisation theory is combined with Voronoi cell finite element method to obtain the global mechanical behaviour. Smit et al. (1998) introduces a multi-level finite element model, where a unique discretised RVE is attached to each macroscopic integration point. Macroscopic stresses are obtained by computational homogenisation, after the solution of the RVE equilibrium, that is subjected to the macroscopic deformation history, under periodicity conditions. This coupled multi-scale implementation, with distinct meshes at micro and macro-level, is suitable for large deformation analyses and complex constitutive behaviour at micro-scale. Important contributions are also made by Miehe and Koch (2002), Miehe et al. (1999a,b), namely in what refers to the macro-problem linearisation of both small and finite strain frameworks, and the tangent modulus needed in the standard Newton-Raphson iterative scheme. Other coupled multi-scale implementations that established this method as a relevant simulation tool are presented by Feyel and Chaboche (2000), which introduces the designation FE^2, and Kouznetsova et al. (2001).

The definition of the RVE model plays a major role on the representativeness of the homogenised results. The homogenisation convergence in terms of RVE size and applied boundary condition (see Figure 1.2) is studied by Terada et al. (2000). A numerical method for the quantitative determination of RVE size, based on statistical considerations is proposed by Kanit et al. (2003).

In addition to coupled multi-level simulations, homogenisation-based multi-scale models are

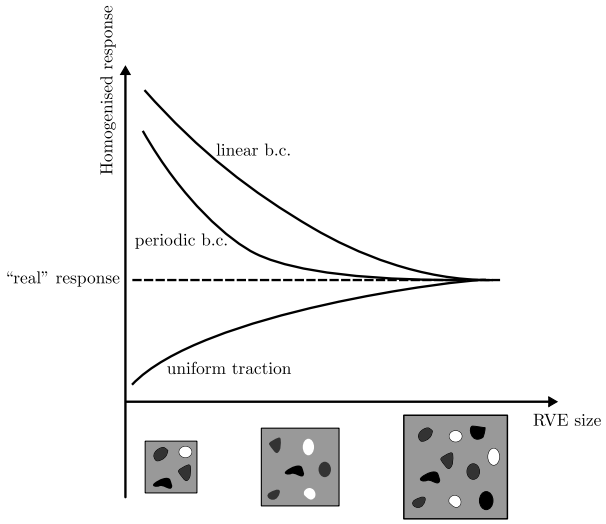

Figure 1.2: Schematic illustration of the convergence of the homogenised response with an increasing RVE size, depending on the applied boundary condition, observed in first-order homogenisation schemes.

also employed to perform micro-mechanical studies, aiming to assess or improve existing constitutive models, calibrate parameters or develop new laws. This is conceptually equivalent to study a single point at the macro-scale, hence a unique RVE is considered. Several authors have used this approach. For instance, Pellegrino et al. (1999) developed a small-strain homogenised constitutive relation for periodic composite materials, with elasto-plastic constituents. Giusti et al. (2009) and Fritzen et al. (2012) applied homogenisation-based results to investigate the macroscopic yielding behaviour of porous metals, and assess Gurson and GTN models (Gurson, 1977, Tvergaard and Needleman, 1984). Brünig et al. (2013) performed a damage model parameter calibration based on RVE simulations. More recently, reduced order models are being obtained through exhaustive analysis of the RVE behaviour under distinct loading conditions, whose results are somehow stored in libraries, and can later be used as a constitutive law in macro-scale analysis (Fritzen and Leuschner, 2015, Fritzen et al., 2014, Hernández et al., 2014) or employed in data-driven based design schemes (Bessa et al., 2017). In fact, an interesting application of multi-scale models is related to the design of materials with a pre-defined behaviour, through manipulation of its microstructure. Topology optimisation techniques may be applied to RVEs, aiming to obtain a desired macroscopic response. Some contributions to this field have been presented by Rodrigues et al. (2002), Giusti (2009), de Souza Neto et al. (2010), Amstutz et al. (2010), Coelho et al. (2011), Kato et al. (2014), Xia and Breitkopf (2014) and Ferrer et al. (2016).

In fact, the main advantage of computational homogenisation is its generality (Kouznetsova, 2002, Reis, 2014):

- it is not necessary to define *apriori* formats for macroscopic constitutive response, in both stress and tangent modulus, as it naturally arises from the homogenisation procedure;
- large deformations can be simply incorporated with suitable finite element implementations;
- no restrictions are imposed in what refers to microstructural geometry and topology, as well as to micro-constitutive descriptions;
- besides the finite element method, any numerical method may be used to solve problems at distinct scales.

Three different types of multi-scale formulations based on computational homogenisation are addressed in this thesis: (i) the standard first-order homogenisation scheme, (ii) second-order ho-

mogenisation based models where the macro-scale is modelled as a second-order continuum, while the micro-scale is described by the classical first-order continuum mechanics and (iii) a fully second-order homogenisation multi-scale formulation, where the material behaviour is modelled with a second-order continuum at both scales.

1.3.1 Developments on first-order computational homogenisation

The majority of the contributions in the field of multi-scale models are related to first-order computational homogenisation based models, where the deformation measure that is passed from the macro to the micro-scale depends on the first gradient of the macro-displacement field. As this technique became well established, it has been employed in many particular applications, such as non-conventional materials. For instance, the dissipative behaviour of natural wood has been analysed by (Saavedra Flores et al., 2011). Furthermore, several improvements have been introduced in multi-scale formulations in order to include additional phenomena.

A complete variational foundation for multi-scale constitutive theories of solids based on computational homogenisation is introduced by de Souza Neto and Feijóo (2006, 2010). It has been recently extended to a general framework by Blanco et al. (2016a), where the Principle of Multi-scale Virtual Power is introduced as an extension of the Hill-Mandel Principle. de Souza Neto et al. (2015) have employed this framework for the inclusion of inertia and body force effects in the multi-scale theory. The inclusion of micro-inertia effects allows to model and design locally resonant acoustic metamaterials (Roca et al., 2018, Sridhar et al., 2016).

The multi-scale analysis of damage and fracture has been subject of intensive research. The lack of objectivity of the solution may arise from either the macroscale or microscale domains. As localisation occurs, the separation of scales is intrinsically violated. This has triggered an interesting discussion about the applicability of first-order homogenisation schemes and the existence of a RVE (Gitman et al., 2007).

Massart (2003) addressed the issue of damage localisation on masonry. Gitman et al. (2007) studied the existence and size determination of RVEs under distinct regimes, concluding that representativeness is lost when softening occurs. In order to overcome this issue, Gitman et al. (2008) introduced a coupled-volume strategy for quasi-brittle materials. Nguyen et al. (2010) have shown that with an alternative homogenisation procedure, where the averaging procedure is carried out on the damaged zone, a RVE can be defined for concrete-like materials undergoing softening. A multiscale failure model for concrete was later proposed (Nguyen et al., 2012b). In these works, a gradient enhanced damage model is used at the microscale to overcome mesh dependency. Fish et al. (2012) have proposed a multiscale model for heterogeneous materials (at small strains) that combines reduced-order homogenisation with an integral non-local formulation. Reis (2014), Reis et al. (2018) introduced an integral non-local formulation to regularise the solution of the RVE problem for ductile heterogeneous materials at finite strains.

With regard to the modelling of fracture across scales, Sánchez et al. (2013) and Toro et al. (2014) proposed the Failure-Oriented Multi-Scale Formulation (FOMF), where a cohesive crack (traction-separation kinematics) is nucleated at the macro-scale when the acoustic tensor becomes singular. This model is generalised by Toro et al. (2016a,b), based on the variational foundations proposed by Blanco et al. (2016a). More contributions to this subject are given by Bosco et al. (2014, 2015), Coenen et al. (2012a,b), Nguyen et al. (2012a), Oliver et al. (2015).

1.3.2 Second-order computational homogenisation

The concept of second-order computational homogenisation was firstly introduced by Kouznetsova et al. (2002), Kouznetsova (2002), Kouznetsova et al. (2004b). It consists on passing the second gradient of the displacements from the macro to micro-scale, in addition to the first-order strain measure (the deformation gradient in the case of finite strains). While the micro-scale is still being

modelled by a first-order continuum, the macro-scale must be considered a second-order continuum. An important advantage of using this kind of approach is that a second-order constitutive law is obtained at the macro-scale without the need to formulate its underlying equations, since it comes naturally from the homogenisation process and standard first-order consitutive laws can be used at the RVE level. Moreover, while first-order homogenisation is insensitive to the RVE absolute length, in a second-order scheme the RVE absolute length is related with the homogenised non-local response. The scale separation principle is relaxed with this formulation, since a linear variation of the macro-deformation is assumed in the RVE, whereas the RVE must be small enough in a first-order approach so that the macro-deformation can be considered constant within it. The relaxation of the scale separation principle makes second-order homogenisation models suitable for the analysis of very small structures like micro-beams subjected to bending (Figure 1.3). In spite of being able to analyse moderate localisation at the macro-scale, second-order models cannot be used to model strong localisation or fracture, that is not consistent with the assumption of linear variation of the macro-strain.

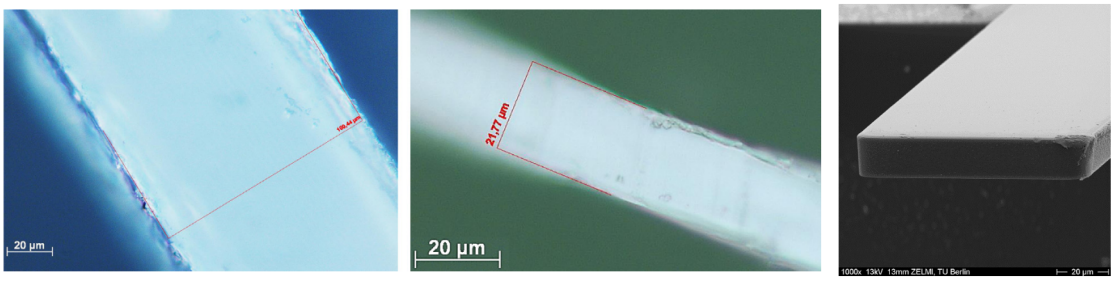

(a) (b)

Figure 1.3: Examples of micro-beams made of (a) epoxy and (b) the polymer SU-8 (Liebold and Müller, 2016).

In contrast to first-order homogenisation, where the homogenised response converges as the RVE size increases (see Figure 1.2), the 2nd-order homogenised response does not, since it depends on the RVE length, which obviously increases as the RVE size increases to capture more constituents. Therefore, the RVE size must be chosen to be representative, and with an appropriate length to correctly characterise the characteristic length at the macro-scale. Kouznetsova et al. (2004a) found that the response of a homogeneous elastic RVE under small strain can be linked to a Mindlin-like full gradient model, where the macro-characteristic length is proportional to the RVE length. The optimal RVE size is defined by these authors as the minimum RVE size that is still representative of important microscopic mechanisms (Geers et al., 2010, Kouznetsova et al., 2004a).

In addition to the advantages referred, it should be highlighted that whereas first-order homogenisation models enable only linear deformation modes to be prescribed at the micro-scale, due to the assumption of the uniformity of the macroscopic strain in the RVE, second-order homogenisation schemes include the effect of quadratic deformation modes, like bending and torsion, in the RVE. This is critical for the modelling of multi-phase materials undergoing deformations involving high curvatures and strain gradients, where phenomena like phase transformation and debonding between fibres and matrix should be analysed in detail to achieve a realistic description of the material behaviour. As a matter of fact, self-deployable structures used for space applications, for instance in micro-satellites, are currently employing tape spring hinges that may be based on composite tubes (Mallikarachchi, 2011, Yee and Pellegrino, 2005) or shape memory alloys (Jeong et al., 2014). This kind of hinges undergoes high curvatures during the folding process (Figure 1.4), requiring special attention in its design so that the desired behaviour is actually observed during deployment. Second-order homogenisation may be useful for the structural analysis of these devices as well as for the design of new solutions for these applications. This subject is rel-

evant in the Portuguese context, since a micro-satellite launch pad is being implemented in Açores (Governo da República Portuguesa, 2019, Governo dos Açores, 2016)).

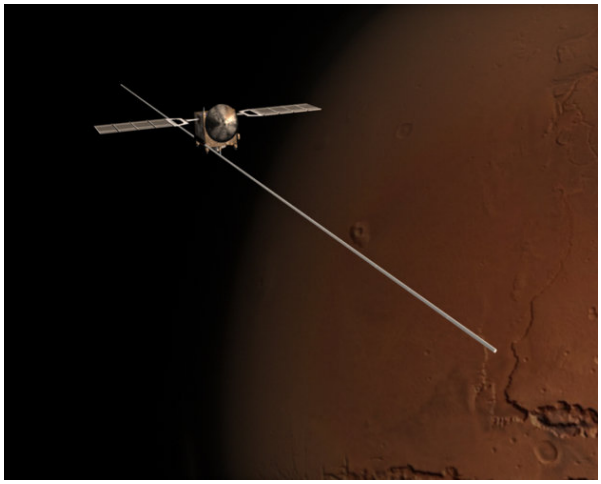

(a)

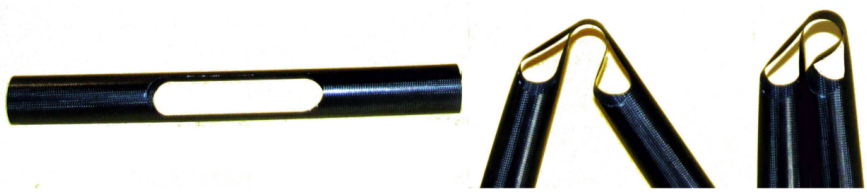

(b)

Figure 1.4: (a) Illustration of the deployed MARSIS antenna boom (European Space Agency, 2005) and (b) detail of the folding process of a composite tube hinge (Mallikarachchi, 2011).

Despite the advantages and promising applications of second-order homogenisation models, related research is not extensively found in the literature. In addition to Kouznetsova's formulation, which has been extended to other classical micro-scale boundary conditions by Kaczmarczyk et al. (2008) and employed by Nguyen et al. (2013) in the modelling of cellular materials, Luscher (2010) proposed a formulation where the micro-constraints are obtained through orthogonality conditions. This author refers that in a scale transition where a second-order continuum is employed at the macro-scale and a first-order description at the micro-scale, the micro-constraints result on a constant body force in the RVE domain, since a volumetric constraint arises along with the boundary conditions. Recently, Blanco et al. (2016b) proposed a second-order multi-scale formulation which also accounts for inertia and body forces at both scales, based on the Principle of Multi-scale Virtual Power (Blanco et al., 2016a), which results on micro-constraints that are different from either Kouznetsova and Luscher models. Nevertheless, neither implementation details nor results have been presented. Lesičar (2015), Lesičar et al. (2017) introduced a homogenisation framework for small strain where second-order continuum is employed at both scales.

In this work, a critical and detailed comparison of the second-order computational homogenisation models available in the literature, where the micro-scale behaviour is described by the classical first-order continuum theory, is performed. The model proposed by Blanco et al. (2016b) is particularised for the case where inertia and body forces are absent, such that a fair comparison can be made. An alternative formulation is derived following the *Method of Multi-Scale Virtual Power*, by modifying the definition of the homogenised second gradient. In spite of resulting in micro-scale constraints similar to the ones presented by Luscher (2010), this formulation allows a

deeper insight on the physical meaning of their reactive nature. The computational treatment of multi-scale models that link the classical continuum at the RVE level to a macro-strain gradient theory is presented in detail.

Several numerical examples are used to assess the differences obtained between different models and understand the features related with second-order homogenisation. The impact of micro-scale constraints in the consistency of the results is studied, and it is possible to conclude that volumetric constraints are fundamental in this kind of multi-scale models, where the RVE is modelled with a first-order continuum theory. In addition, the consequences of this fact in the particular case of RVEs containing voids in its microstructure are analysed. The isolated influence of the RVE length and the micro-constituents size is evaluated numerically, for a composite and a polycrystalline microstructure, where the parameters that limit applicability of first-order homogenisation schemes are identified. Based on the results obtained from the numerical examples, an adaptive framework is proposed for second-order homogenisation analyses. A three-dimensional finite element is formulated to deal with the second-gradient problem arising at the macro-scale. FE^2 simulations are performed with the models based on the *Principle of Multi-Scale Virtual Power*, demonstrating that the linearisation of the equilibrium equations and the strategy for computation of the consistent tangents leads to quadratic convergence rates in the Newton-Raphson schemes at both scales.

Finally, a variationally consistent fully second-order homogenisation model is formulated at finite strains, where a second-order continuum theory is employed to describe the micro-scale behaviour, aiming to include micro-constituents size effects in the multi-scale response. The finite element implementation of the resulting micro-scale equilibrium problem is described in detail. Numerical examples involving either micro-scale and multi-scale simulations are introduced to assess the influence of the RVE length and the micro-scale characteristic length on the obtained response. The capability of this model to capture size effects due to the size of micro-constituents is demonstrated.

1.4 Speedup FE^2 simulations

Despite the significant advances that have been made to enrich multi-scale analysis capabilities over the last years, the multiplicative character of the algorithmic complexity and the corresponding computational cost continues to be one the main obstacles to its widespread application. Several strategies have been proposed to minimise this drawback, such as parallel computing (Feyel and Chaboche, 2000, Kouznetsova, 2002), selective usage of multi-scale modelling (Ghosh et al., 2001) and sub-incrementation schemes (Reis and Andrade Pires, 2013, Somer et al., 2009). More recently, reduced-order models have been employed to minimise both computing time and memory requirements (Fritzen and Leuschner, 2015, Fritzen et al., 2014, Hernández et al., 2014) and have gained significant acceptance within the computational mechanics community. Nevertheless, in order to obtain results from a full multi-scale analysis without any simplifications, parallel computing seems to be the most suitable strategy to accelerate simulations.

Different approaches for the parallelisation of multi-scale analyses can be found in the literature. Feyel and Chaboche (2000) employed the finite element tearing and interconnecting (FETI) domain decomposition method at the macro-scale to parallelise the multi-scale analysis of a SiC/Ti composite material. Kuramae et al. (2010) use a domain partition technique for dynamic explicit multi-scale simulations, with a dynamic workload-balancing algorithm for elasto-plastic analyses. Recently, Balzani et al. (2016) employed a FETI-DP domain decomposition technique to parallelise the solution of multi-scale simulations at the RVE level. Good scalability results are obtained for hyperelastic micro-constituents. In this framework, the number of available processors is much higher than the number of RVEs, which is not common. Mosby and Matouš (2015) proposed a hierarchically parallel implementation for the multi-scale modelling of heterogeneous cohesive layers. The macroscopic domain is decomposed with a traditional domain decomposition method.

Micro-scale computations are performed in parallel by micro-servers and each micro-server has several cores, so that domain decomposition is also applied to RVEs. A noteworthy scalability is observed with regard to the number of micro-servers, which may be extended up to hundreds of micro-servers (Mosby and Matouš, 2016).

On the other hand, the so-called master-slaves approaches naturally fit to multi-scale solution algorithms. In this case, each independent finite element problem at the micro-scale can be solved in parallel by a slave process, while the master process controls the macroscopic problem (Belytschko and Song, 2010, Kouznetsova, 2002, Matsui et al., 2004, Nguyen et al., 2012b). Within this framework, Matsui et al. (2004) proposed a semi-dynamic workload balance algorithm to improve the parallel efficiency when elasto-plastic models are used in the RVE. Rahul and De (2010) suggested an alternative to the standard master-slave approach, in the context of explicit multi-scale models, where a coarser granularity is adopted for the distribution of parallel work concerning micro-scale computations. A low communication overhead is achieved due to a matrix-free approach, which allows for a good scalability up to hundreds of processors.

In the present thesis, a mixed parallel strategy for the solution of multi-scale analyses at finite strains, with possibly path dependent constitutive behaviour at the micro-scale, is presented. It combines a non-conforming macro-domain decomposition method in the first parallelisation level, with a master-slave approach employed within each subdomain, for the second level. In the master-slave scheme introduced here, instead of distributing parallel work by macro-Gauss points, the basic task which is performed in parallel is the analysis of a macroscopic element. This includes the solution of the micro-scale equilibrium problem together with the homogenisation of the stress and tangent modulus for all Gauss points of the element. In addition, the element contributions for the internal force vector and tangent stiffness matrix are also computed. Therefore, the amount of work done in parallel is increased, and the number of communications is reduced. Dynamic scheduling is adopted for the distribution of macro-elements among available central processing units (CPUs), in order to minimise idling time. The performance of a stand-alone implementation of the proposed master-salve scheme is analysed. Its main drawback is related to memory requirements of the computer running the master process, that may become prohibitive as the multi-scale problem size increases, due to the underlying microscopic data.

The combination of the master-slave scheme with a macroscopic domain decomposition alleviates memory requirements through distribution of data among different machines. The resulting equilibrium problem is solved with an algorithm based on the FETI method (Farhat and Roux, 1991), that does not require iterative solvers as long as there are non-floating subdomains. The mortar method (Wohlmuth, 2001) is employed to deal with non-conforming meshes. Besides allowing an easier mesh generation for complex geometries, the possibility of employing a non-conforming mesh at the macro-scale may be used to reduce the computational cost, decreasing the number of macroscopic elements in certain zones, while maintaining an adequate refinement where it is needed. In order to equilibrate the workload distribution in this mixed parallel strategy, the number of slave CPUs working on each subdomain is adaptively defined according to the computational demand. This parallel strategy, which is implemented through the Message Passing Interface (MPI) standard, allows to run hierarchical multi-scale simulations in computers with either shared or distributed-memory architectures, from a multi-processor workstation to a *Beowulf* cluster, within a reasonable time, and minimising hardware limitations.

The efficiency of the solution of micro-scale problems cannot be disregarded. A comparison between the performance of the condensation method Reis (2014), Reis and Andrade Pires (2013, 2014) and the Lagrange multipliers method to enforce micro-constraints is undertaken.

1.5 Computational framework

The numerical implementations and simulations described throughout this document are carried out within the in-house finite element program Links (Figure 1.5), that has been developed in the CM2S research group over the last years. This program is written in Fortran, and allows the mechanical analysis of solids using implicit algorithms, at both small and large strains, the micro-scale analysis based on RVEs and FE^2 simulations at large strains. It is the result of merging three independent finite element programs: (i) Hyplas (de Souza Neto et al., 2008), (ii) MSP and (iii) CMSP (Reis, 2014).

Figure 1.5: Links logo.

1.6 Thesis layout

This thesis is divided in different chapters according to the subjects addressed. In addition to the list of symbols provided in the beginning of the document, the meaning of each variable employed is defined appropriately in the text.

The fundamental concepts related to the classical first-order description of solids kinematics of deformation and mechanical equilibrium are presented in Chapter 2, along with the main ingredients for the discretisation and solution in the context of the finite element method.

Multi-scale models based on first-order computational homogenisation are introduced in Chapter 3. The *Method of Multi-Scale Virtual Power* is employed to formulate the homogenisation scheme. The micro-scale constraints are enforced in the numerical problem with the condensation method and the Lagrange multiplier method, being observed that the latter performs better in micro-scale and FE^2 simulations.

A full gradient formulation for second-order continuum at large strains is presented in Chapter 4, along with a description of the numerical solution of the resulting equilibrium problem with mixed finite elements. While well established 2D finite elements are adopted for bi-dimensional problems, a hexahedral mixed finite element is proposed to deal with 3D simulations. Numerical examples are used to test the finite element implementation by comparison with analytical solutions.

In Chapter 5, second-order homogenisation-based models, where a first-order continuum is employed at the micro-scale, are presented. In the first place, the formulation proposed by Blanco et al. (2016b) is particularised for the quasi-static case, in the absence of external body forces. Thereafter, an alternative model is formulated, also based on the *Method of Multi-Scale Virtual Power*, based on a modified definition of the homogenised second gradient. The numerical solution of the micro-scale equilibrium problems, with finite elements and the Lagrange multiplier method, is described and a strategy that enables the straightforward computation of the consistent tangents is devised. In addition, in order to clarify the impact of the assumptions made with distinct formulations available in the literature, Kouznetsova and Luscher's models are also introduced, and a critical comparison of the resulting micro-scale constraints is performed.

The impact of employing different formulations in the results of micro-scale simulations is assessed in Chapter 6, along with the effect of geometrical non-linearities and the influence of the

macroscopic second gradient. The influence of the RVE length and the micro-constituents size is analysed separately. Micro-scale simulations accounting for the macroscopic first and second gradient of displacements are conducted over polycrystalline RVEs. In addition, fully coupled FE^2 simulations are also performed. Based on the results obtained, an adaptive framework for second-order homogenisation is proposed.

A fully second-order homogenisation scheme for solids undergoing finite strains is formulated in Chapter 7, aiming to introduce the effect of micro-constituents size in the multi-scale response. In this case, a second gradient continuum theory is considered at the micro-scale. Several numerical examples are introduced to verify the implementation and understand the main features of this approach.

A mixed parallel strategy that combines a master-slave algorithm with a mortar-based macro-domain decomposition method is presented in Chapter 8. Several numerical applications show that this strategy is able to reduce the computational burden associated with FE^2 simulations, with regard to computation time and memory requirements, even when problems with a high degree of non-linearity are analysed.

Additional topics are provided in Appendices A to D, in order to provide more detail of main subjects and maintain this document self-contained.

1.7 Contributions

The main contributions of the present thesis are summarised in what follows:

- a second-order homogenisation-based model is formulated at finite strains, based on an alternative definition of the homogenised second gradient. This model provides consistent results, and its Lagrange multiplier version allows a deeper insight in the meaning of the resulting micro-scale constraints;
- a fully second-order homogenisation-based model, where the micro-scale is modelled with a second-order continuum theory, is formulated at finite strains and a numerical solution based on mixed finite elements is proposed;
- an adaptive framework is presented for the second-order homogenisation, where the concept of generalised RVE size is introduced and the magnitude of the first-order strain is also taken into account in the definition of the scale separation limit;
- a hexahedral mixed finite element is proposed to deal with 3D second-order continuum equilibrium problems;
- a critical comparison of the different formulations for second-order homogenisation available in the literature is performed;
- a mixed parallel strategy is proposed to minimise the computational burden of FE^2 simulations (Rodrigues Lopes et al., 2018);
- the computational performance of the condensation method and the Lagrange multiplier method, used to enforce micro-scale constraints, are compared, being concluded that the latter is more efficient.

Chapter 2

Mechanics of first-order continuum

Fundamental concepts related to the analysis and mechanical equilibrium of solids described by a 1^{st}-order continuum, undergoing large deformation, are introduced in this chapter. In addition, the *Finite Element Method*, which is the most popular numerical tool for structural analysis, is briefly introduced along with the main ingredients for its implementation.

2.1 Kinematics of deformation

2.1.1 Motion

Consider a tri-dimensional body, whose undeformed domain is defined by Ω and its boundary $\partial\Omega$, which is subjected to a deformation defined by a smooth function $\boldsymbol{\varphi}$, as represented in Figure 2.1.

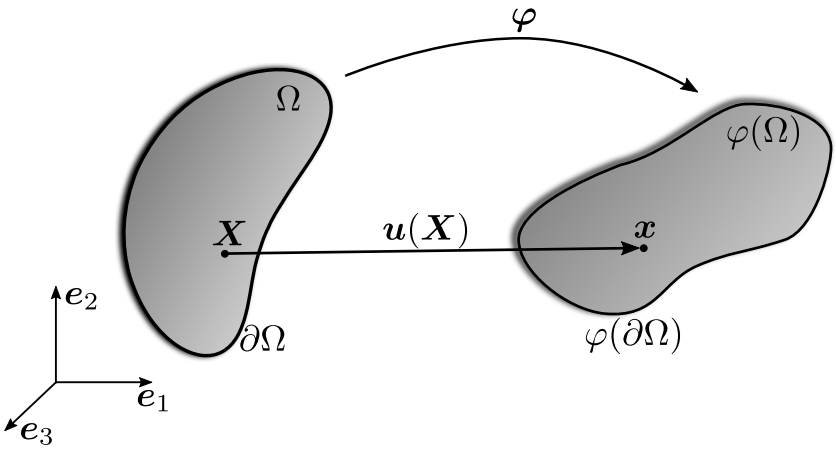

Figure 2.1: Deformation of a body.

A material particle that in the reference (undeformed) configuration has coordinate $\boldsymbol{X}$, after the deformation map defined by $\boldsymbol{\varphi}$, at time t, occupies the position $\boldsymbol{x}$:

$$\boldsymbol{x}(t) = \boldsymbol{\varphi}(\boldsymbol{X}, t). \tag{2.1}$$

The displacement of this material particle is then:

$$\boldsymbol{u}(\boldsymbol{X}, t) = \boldsymbol{\varphi}(\boldsymbol{X}, t) - \boldsymbol{X}. \tag{2.2}$$

Thus, the current position can be given by:

$$\boldsymbol{x}(t) = \boldsymbol{X} + \boldsymbol{u}(\boldsymbol{X}, t). \tag{2.3}$$

Considering the inverse of the mapping function $\boldsymbol{\varphi}^{-1}$, the reference position is recovered from the current position by:

$$\boldsymbol{X} = \boldsymbol{\varphi}^{-1}(\boldsymbol{x}) = \boldsymbol{x} - \boldsymbol{u}(\boldsymbol{\varphi}^{-1}(\boldsymbol{x}, t), t). \tag{2.4}$$

2.1.2 Material and spatial descriptions

The material description (or Lagrangian description) of motion is related to the description of the deformation with reference to the undeformed configuration, i.e., focusing on a material particle defined by $\boldsymbol{X}$. On the other hand, if the kinematic variables are expressed in the deformed configuration, looking to a point in space defined by $\boldsymbol{x}$, a spatial description (or Eulerian description) is considered.

For the sake of completeness, consider the velocity field. In the material description, it is given by:

$$\boldsymbol{v}\boldsymbol{X}, t) = \dot{\boldsymbol{u}}(\boldsymbol{X}, t) = \frac{\partial \boldsymbol{\varphi}(\boldsymbol{X}, t)}{\partial t}, \tag{2.5}$$

and represents the velocity of the material particle $\boldsymbol{X}$. Considering now a spatial description, the spatial velocity is expressed as:

$$\boldsymbol{v}(\boldsymbol{x}, t) = \dot{\boldsymbol{u}}(\boldsymbol{\varphi}^{-1}(\boldsymbol{x}, t), t), \tag{2.6}$$

which represents the velocity of the material particle that occupies the point $\boldsymbol{x}$ at time t.

The same thought is applied when distinguishing material and spatial gradients. Consider a generic field α, that can be represented in both material or spatial reference:

$$\alpha_m(\boldsymbol{X}, t) = \alpha(\boldsymbol{\varphi}(\boldsymbol{X}, t), t), \tag{2.7}$$

$$\alpha_s(\boldsymbol{x}, t) = \alpha(\boldsymbol{\varphi}^{-1}(\boldsymbol{x}, t), t). \tag{2.8}$$

The material gradient is obtained as the derivative of the material field with respect to $\boldsymbol{X}$, as expressed by

$$\nabla_X \alpha = \frac{\partial}{\partial \boldsymbol{X}} \alpha_m(\boldsymbol{X}, t), \tag{2.9}$$

and the spatial gradient is the derivative of the spatial field with respect to $\boldsymbol{x}$:

$$\nabla_x \alpha = \frac{\partial}{\partial \boldsymbol{x}} \alpha_s(\boldsymbol{x}, t). \tag{2.10}$$

The divergence can also be computed in the material or spatial version. In the case of the divergence of a tensor field $\boldsymbol{A}$:

$$\mathrm{div}_X(\boldsymbol{A})_i = \frac{\partial A_{ij}}{\partial X_j}, \tag{2.11}$$

$$\mathrm{div}_x(\boldsymbol{A})_i = \frac{\partial A_{ij}}{\partial x_j}. \tag{2.12}$$

2.1.3 Deformation gradient

The deformation gradient is a second-order tensor that relates the distance between two neighbour particles $\boldsymbol{X}$ and $\boldsymbol{X} + d\boldsymbol{X}$ with the distance between the positions they occupy after body deformation $\boldsymbol{x}$ and $\boldsymbol{x} + d\boldsymbol{x}$. It is expressed by:

$$\boldsymbol{F}(\boldsymbol{X}, t) = \nabla_X \boldsymbol{\varphi}(\boldsymbol{X}, t) = \frac{d\boldsymbol{x}}{d\boldsymbol{X}}. \tag{2.13}$$

Taking into account Expression (2.3), it can be rewritten as

$$\boldsymbol{F} = \boldsymbol{I} + \nabla_X \boldsymbol{u}. \tag{2.14}$$

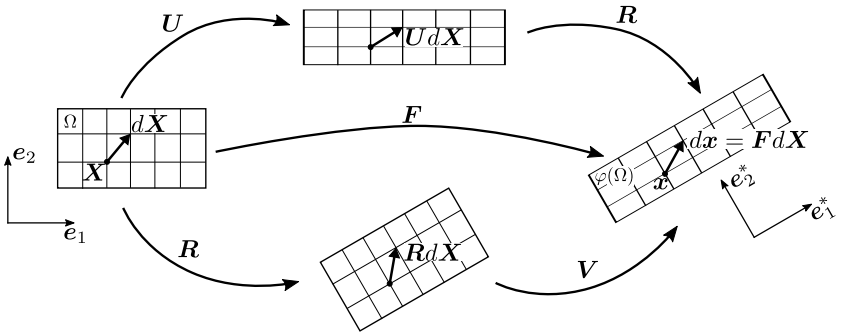

Figure 2.2: Representation of left and right *polar decomposition* of the deformation gradient.

It may also be represented according to a spatial description:

$$\boldsymbol{F}(\boldsymbol{x},t) = \left[\nabla_x \boldsymbol{\varphi}^{-1}(\boldsymbol{x},t)\right]^{-1} = \left[\boldsymbol{I} - \nabla_x \boldsymbol{u}\right]^{-1}. \tag{2.15}$$

Considering an infinitesimal volume dV in the undeformed body, the change in volume is given through the determinant of the deformation gradient, such that the deformed volume is:

$$dv = JdV, \tag{2.16}$$

where $J = \det \boldsymbol{F}$. In the case of an isochoric (volume preserving) deformation, $J = 1$.

The deformation can be split into isochoric and volumetric components, and so can be the deformation gradient:

$$\boldsymbol{F} = \boldsymbol{F}_v \boldsymbol{F}_{iso}, \tag{2.17}$$

where the volumetric component of $\boldsymbol{F}$ is:

$$\boldsymbol{F}_v = J^{\frac{1}{3}} \boldsymbol{I}, \tag{2.18}$$

and the isochoric component is expressed by:

$$\boldsymbol{F}_{iso} = J^{-\frac{1}{3}} \boldsymbol{F}. \tag{2.19}$$

Polar decomposition

The deformation gradient may be decomposed into one tensor that is related to a rotation and another that defines the stretches. This is called *polar decomposition*, and is expressed as:

$$\boldsymbol{F} = \boldsymbol{R}\boldsymbol{U} = \boldsymbol{V}\boldsymbol{R}, \tag{2.20}$$

where there are unique tensors $\boldsymbol{R}$, $\boldsymbol{U}$ and $\boldsymbol{V}$ that satisfy these equalities.

The rotation tensor $\boldsymbol{R}$ is proper orthogonal:

$$\boldsymbol{R}\boldsymbol{R}^T = \boldsymbol{I}, \quad \det \boldsymbol{R} = 1, \tag{2.21}$$

and the right stretch tensor $\boldsymbol{U}$ and the left stretch tensor $\boldsymbol{V}$ are symmetric positive definite tensors.

Note that in the right polar decomposition $\boldsymbol{F} = \boldsymbol{R}\boldsymbol{U}$, in first place the stretches are mapped by $\boldsymbol{U}$ and then the rotation, whereas considering the left polar decomposition $\boldsymbol{F} = \boldsymbol{V}\boldsymbol{R}$, the rotation is mapped before the stretches, as shown in Figure 2.2.

Considering the spectral decomposition of the stretch tensors:

$$\boldsymbol{U} = \sum_{i=1}^{3} \lambda_i \boldsymbol{e}_i \otimes \boldsymbol{e}_i, \quad \boldsymbol{V} = \sum_{i=1}^{3} \lambda_i \boldsymbol{e}_i^* \otimes \boldsymbol{e}_i^*, \tag{2.22}$$

the eigenvalues λ_i shared by both tensors are the principal stretches, and the eigenvectors define the Lagrangian ($\boldsymbol{e}_i$) and Eulerian ($\boldsymbol{e}_i^*$) principal directions, that are related through:

$$\boldsymbol{e}_i^* = \boldsymbol{R}\boldsymbol{e}_i. \tag{2.23}$$

2.1.4 Strain measures

Several tensors have been proposed to describe the strain in a solid. Nevertheless, all of them derive from the concept of deformation gradient.

The right and left Cauchy-Green strain tensors are defined taking into account the respective stretch tensors:

$$\boldsymbol{C} = \boldsymbol{U}^2 = \boldsymbol{F}^T \boldsymbol{F}, \tag{2.24}$$

$$\boldsymbol{B} = \boldsymbol{V}^2 = \boldsymbol{F}\boldsymbol{F}^T. \tag{2.25}$$

From the right stretch tensor, the family of Lagrangian strain tensors is defined:

$$\boldsymbol{E}^{(m)} = \begin{cases} \frac{1}{m}\left(\boldsymbol{U}^m - \boldsymbol{I}\right) & m \neq 0 \\ \ln(\boldsymbol{U}) & m = 0 \end{cases}, \tag{2.26}$$

where the Green-Lagrange tensor belongs:

$$\boldsymbol{E}^{(2)} = \frac{1}{2}\left(\boldsymbol{C} - \boldsymbol{I}\right). \tag{2.27}$$

Similarly, with the left stretch tensor, the family of Eulerian strain tensors is expressed by:

$$\boldsymbol{\varepsilon}^{(m)} = \begin{cases} \frac{1}{m}\left(\boldsymbol{V}^m - \boldsymbol{I}\right) & m \neq 0 \\ \ln(\boldsymbol{V}) & m = 0 \end{cases}. \tag{2.28}$$

In the case of infinitesimal deformations, reference and deformed configuration coincide, and the tensors of both families can be approximated by the infinitesimal strain tensor:

$$\boldsymbol{\varepsilon} = \nabla^s \boldsymbol{u} = \frac{1}{2}\left[\nabla \boldsymbol{u} + (\nabla \boldsymbol{u})^T\right]. \tag{2.29}$$

Within a large strain spatial formulation, the Eulerian logarithmic strain tensor is usually employed as a strain measure, which allows to re-use constitutive models developed for small strains.

2.2 Forces and stress measures

The deformation of a body is a consequence of the application of forces that may be *surface forces* or *body forces*. Body forces or volume forces are measured in force per unit volume, and typical examples are gravitational or magnetic forces. Surface forces are applied on the boundary of the body and transmitted across its interior, where the material interacts with its adjacent parts. This leads to the concept of *stress*, which units are force per unit area. Several stress tensors measures are presented next.

2.2.1 Cauchy stress tensor

The Cauchy stress tensor $\boldsymbol{\sigma}$ is a spatial description of the stresses since it refers to the deformed domain. It is defined by:

$$\boldsymbol{t}(\boldsymbol{n}, t) = \boldsymbol{\sigma} \cdot \boldsymbol{n}, \tag{2.30}$$

where $\boldsymbol{n}$ is the unit outward vector normal to the considered surface of the deformed body, and $\boldsymbol{t}$ is the resulting surface traction.

This symmetric stress tensor can be split into an hydrostatic and deviatoric component as follows:

$$\boldsymbol{\sigma} = \boldsymbol{s} + p\boldsymbol{I}, \tag{2.31}$$

where the hydrostatic pressure is:

$$p = \frac{1}{3}\operatorname{tr}\boldsymbol{\sigma}, \tag{2.32}$$

and $\boldsymbol{s}$ denotes the deviatoric stress tensor.

2.2.2 First Piola-Kirchhoff stress tensor

The material counterpart of the Cauchy stress tensor is the First Piola-Kirchhoff stress tensor $\boldsymbol{P}$, which is related to the former by:

$$\boldsymbol{P} = J\boldsymbol{\sigma}\boldsymbol{F}^{-T}. \tag{2.33}$$

Unlike the Cauchy tensor, $\boldsymbol{P}$ is not necessarily symmetric.

2.2.3 Second Piola-Kirchhoff stress tensor

An alternative stress measure is provided by the Second Piola-Kirchhoff stress tensor, that is the conjugate of the Green-Lagrange strain tensor (Equation (2.27)). This stress tensor is related to the First Piola-Kirchhoff stress through:

$$\boldsymbol{S} = \boldsymbol{F}^{-1} \cdot \boldsymbol{P}. \tag{2.34}$$

2.2.4 Kirchhoff stress tensor

Another stress tensor that is often used, especially in the context of finite deformations, is the Kirchhoff stress tensor, simply obtained as:

$$\boldsymbol{\tau} = J\boldsymbol{\sigma}. \tag{2.35}$$

2.3 Fundamental conservation principles

The mechanical behaviour of continuum media complies with several fundamental laws. Besides the thermodynamic principles (de Souza Neto et al., 2008), that are not stated here, the *conservation of mass* and the *momentum balance principle* govern the deformation of a body.

2.3.1 Conservation of mass

The conservation of mass principle postulates that:

$$\dot{\rho} + \rho \operatorname{div}_x \dot{\boldsymbol{u}} = 0, \tag{2.36}$$

where ρ denotes the density of the solid.

2.3.2 Momentum balance

The momentum balance principle may be expressed either in the spatial or material description of motion. In the spatial description, the following equations are stated:

$$\begin{cases} \operatorname{div}_x \boldsymbol{\sigma} + \boldsymbol{b} = \rho \ddot{\boldsymbol{u}} & \text{in } \varphi(\Omega) \\ \boldsymbol{t} = \boldsymbol{\sigma} \cdot \boldsymbol{n} & \text{on } \varphi(\partial\Omega) \end{cases}, \tag{2.37}$$

where $\boldsymbol{b}$ represents the volume forces in the deformed solid and $\boldsymbol{t}$ the traction vector field on its boundary, with normal outward unit vector $\boldsymbol{n}$.

Under a material formulation, this principle is defined by:

$$\begin{cases} \operatorname{div}_X \boldsymbol{P} + \boldsymbol{b}_0 = \rho_0 \ddot{\boldsymbol{u}} & \text{in } \Omega \\ \boldsymbol{t}_0 = \boldsymbol{P} \cdot \boldsymbol{N} & \text{on } \partial\Omega \end{cases}, \tag{2.38}$$

with $\boldsymbol{b}_0$ denoting the volume force in the reference configuration,

$$\boldsymbol{b}_0 = J\boldsymbol{b}, \tag{2.39}$$

ρ_0 reference density,

$$\rho_0 = J\rho, \tag{2.40}$$

and $\boldsymbol{t}_0$ represents the traction vector field on the undeformed boundary, with normal outward unit vector $\boldsymbol{N}$.

In both cases, these equations define the *Strong Equilibrium Equations*, where local values of the fields and their derivatives are related.

2.4 Weak equilibrium equations

From the numerical point of view it is not desirable to solve the problem in a point-wise fashion, with the strong equilibrium equations. It is preferable to solve the problem in an average sense, which gives rise to the Integral or *Weak Equilibrium Equations*. This formulation is the basis of the finite element methods in mechanical analysis, and may be obtained by applying the *Virtual Work Principle*.

Considering a quasi-static deformation, the spatial version of the weak equilibrium is stated by:

$$\int_{\varphi(\Omega)} [\boldsymbol{\sigma} : \nabla_x \delta\boldsymbol{u} - \boldsymbol{b} \cdot \delta\boldsymbol{u}]\, dV - \int_{\varphi(\partial\Omega)} \boldsymbol{t} \cdot \delta\boldsymbol{u} dA = 0, \quad \forall \delta\boldsymbol{u} \in \mathcal{V} \tag{2.41}$$

where $\delta\boldsymbol{u}$ denotes the virtual displacements belonging to the space of admissible virtual displacements $\mathcal{V}$.

The quasi-static material version is expressed as:

$$\int_{\Omega} [\boldsymbol{P} : \nabla_X \delta\boldsymbol{u} - \boldsymbol{b}_0 \cdot \delta\boldsymbol{u}]\, dV - \int_{\partial\Omega} \boldsymbol{t}_0 \cdot \delta\boldsymbol{u} dA = 0, \quad \forall \delta\boldsymbol{u} \in \mathcal{V}. \tag{2.42}$$

The strong form of the equilibrium problem can be recovered from the weak equations through variational calculus.

2.5 Finite element method

The Finite Element Method is probably the most widespread numerical method to predict the mechanical behaviour of a solid, in both scientific and industrial environments. The weak equilibrium equation and a discretisation of the spatial domain are the bases of this method.

2.5.1 Domain spatial discretisation

The spatial domain refers to the solid under analysis. It is divided into a finite number of subdomains n_e called elements, such that the set of all element domains defines the discretised solid domain Ω^d:

$$\Omega \approx \Omega^d = \bigcup_{e=1}^{n_e} \Omega^e. \tag{2.43}$$

Each element is defined by a number of nodes n_n, that are specific points where the interest variables, usually displacements, are evaluated. All fields (displacement, stress, ...) are interpolated inside the element, from their nodal values, through shape functions, as exemplified in Equation (2.44) for a generic vectorial field $\boldsymbol{a}(\boldsymbol{x})$. In this case, $\mathbf{a}_i$ denotes the nodal value and $N_i^e(\boldsymbol{x})$ the shape function value related to each node, evaluated at a point $\boldsymbol{x}$ inside the element.

$$\boldsymbol{a}(\boldsymbol{x}) = \sum_{i=1}^{n_n} N_i^e(\boldsymbol{x})\mathbf{a}_i, \quad \boldsymbol{x} \in \Omega^e. \tag{2.44}$$

Considering the whole discretised domain Ω^d, the global shape function related to each node of several elements can be defined, considering that outside the element it is zero-valued. Thus, the approximation is given by:

$$\boldsymbol{a}(\boldsymbol{x}) = \sum_{i=1}^{n_p} N_i(\boldsymbol{x})\mathbf{a}_i, \quad \boldsymbol{x} \in \Omega^d, \tag{2.45}$$

where n_p is the total number of nodes in the discretised domain, that is lower than $n_n \times n_e$ since adjacent elements share nodes.

Storing all nodal values in a vector $\mathbf{a}$:

$$\mathbf{a} = \begin{Bmatrix} \mathbf{a}_1 \\ \mathbf{a}_2 \\ \vdots \\ \mathbf{a}_{n_p} \end{Bmatrix}, \tag{2.46}$$

and the shape functions in a matrix $\mathbf{N}(\boldsymbol{x})$:

$$\mathbf{N}(\boldsymbol{x}) = \left[\begin{array}{cc|cc|c|cc} N_1(\boldsymbol{x}) & 0 & N_2(\boldsymbol{x}) & 0 & \cdots & N_{n_p}(\boldsymbol{x}) & 0 \\ 0 & N_1(\boldsymbol{x}) & 0 & N_2(\boldsymbol{x}) & & 0 & N_{n_p}(\boldsymbol{x}) \end{array}\right], \tag{2.47}$$

then the vectorial field in a point $\boldsymbol{x}$ can be expressed as:

$$\boldsymbol{a}(\boldsymbol{x}) = \mathbf{N}(\boldsymbol{x})\mathbf{a}. \tag{2.48}$$

In Expression (2.47), a 2-dimensional field was assumed. In the case of a 3D field, the shape function matrix would assume dimension $3 \times 3n_p$.

Discrete gradient operators are defined from the shape function derivatives, namely the discrete symmetric gradient operator $\mathbf{G}^g$ and its symmetric counterpart $\mathbf{B}^g$, which for 2D are expressed by:

$$\mathbf{B}^g = \left[\begin{array}{cc|cc|c|cc} \frac{\partial N_1}{\partial x} & 0 & \frac{\partial N_2}{\partial x} & 0 & \cdots & \frac{\partial N_{n_p}}{\partial x} & 0 \\ 0 & \frac{\partial N_1}{\partial y} & 0 & \frac{\partial N_2}{\partial y} & & 0 & \frac{\partial N_{n_p}}{\partial y} \\ \frac{\partial N_1}{\partial y} & \frac{\partial N_1}{\partial x} & \frac{\partial N_2}{\partial y} & \frac{\partial N_2}{\partial x} & & \frac{\partial N_{n_p}}{\partial y} & \frac{\partial N_{n_p}}{\partial x} \end{array}\right], \tag{2.49}$$

$$\mathbf{G}^g = \left[\begin{array}{cc|cc|c|cc} \frac{\partial N_1}{\partial x} & 0 & \frac{\partial N_2}{\partial x} & 0 & \cdots & \frac{\partial N_{n_p}}{\partial x} & 0 \\ 0 & \frac{\partial N_1}{\partial x} & 0 & \frac{\partial N_2}{\partial x} & & 0 & \frac{\partial N_{n_p}}{\partial x} \\ \frac{\partial N_1}{\partial y} & 0 & \frac{\partial N_2}{\partial y} & 0 & & \frac{\partial N_{n_p}}{\partial y} & 0 \\ 0 & \frac{\partial N_1}{\partial y} & 0 & \frac{\partial N_2}{\partial y} & & 0 & \frac{\partial N_{n_p}}{\partial y} \end{array}\right]. \tag{2.50}$$

2.5.2 Discretisation of the equilibrium equation

With the domain discretisation presented above, the discretised version of the spatial weak equilibrium equation (Expression (2.41)) is given by:

$$\left\{\int_{\varphi(\Omega^d)} \left[(\mathbf{B}^g)^T\boldsymbol{\sigma} - \mathbf{N}^T\mathbf{b}\right] dV - \int_{\varphi(\partial\Omega^d)} \mathbf{N}^T\mathbf{t}\, dA\right\}^T \cdot \delta\mathbf{u} = 0, \quad \forall\delta\mathbf{u} \in \mathcal{V}^d, \tag{2.51}$$

where $\mathcal{V}^d$ represents the discretised virtual displacement space, and $\boldsymbol{\sigma}$ is the vector representation of $\boldsymbol{\sigma}$. A finite strain framework is considered in the present equations. According to the virtual work

principle, the above equation must be satisfied for all admissible virtual displacements, thus it can be rewritten as:

$$\mathbf{f}^{int} - \mathbf{f}^{ext} = \mathbf{0}, \tag{2.52}$$

with the internal and external forces given by:

$$\mathbf{f}^{int} = \int_{\varphi(\Omega^d)} (\mathbf{B}^g)^T \boldsymbol{\sigma} dV, \tag{2.53}$$

$$\mathbf{f}^{ext} = \int_{\varphi(\Omega^d)} \mathbf{N}^T \mathbf{b} dV + \int_{\varphi(\partial\Omega^d)} \mathbf{N}^T \mathbf{t} dA. \tag{2.54}$$

One of the biggest advantages of this approach is that it can be naturally implemented in a numerical framework, analysing element by element. Elemental force vectors are obtained by integration over the element domain:

$$\mathbf{f}_e^{int} = \int_{\varphi(\Omega^e)} (\mathbf{B}^e)^T \boldsymbol{\sigma} dV, \tag{2.55}$$

$$\mathbf{f}_e^{ext} = \int_{\varphi(\Omega^e)} (\mathbf{N}^e)^T \mathbf{b} dV + \int_{\varphi(\partial\Omega^e)} (\mathbf{N}^e)^T \mathbf{t} dA, \tag{2.56}$$

and then are assembled into the global force vectors:

$$\mathbf{f}^{int} = \mathop{\mathsf{A}}_{e=1}^{n_{el}} \mathbf{f}_e^{int}, \tag{2.57}$$

$$\mathbf{f}^{ext} = \mathop{\mathsf{A}}_{e=1}^{n_{el}} \mathbf{f}_e^{ext}. \tag{2.58}$$

2.5.3 Time discretisation

The constitutive response of materials is usually dependent on its history, i.e., on the path of the loading they were subjected to. This can be introduced in the description of the material behaviour through internal variables $\boldsymbol{\theta}$ in the constitutive relations, that store information about the intrinsic material state. In what refers to the finite element method application, in order to obtain a solution that accounts for this path-dependence, the load must be applied in a finite number of increments, corresponding to distinct instants of a pseudo-time interval. The constitutive stress response at increment $n+1$ is then obtained considering the current deformation state and the internal variables of the previous increment:

$$\boldsymbol{\sigma}_{n+1} = \hat{\boldsymbol{\sigma}}(\boldsymbol{F}_{n+1}, \boldsymbol{\theta}_n), \tag{2.59}$$

where $\hat{\boldsymbol{\sigma}}(\boldsymbol{F}_{n+1}, \boldsymbol{\theta}_n)$ is the incremental constitutive functional.

Note that in the case of infinitesimal deformations, the current deformation state is defined by the infinitesimal strain tensor (2.29), thus:

$$\boldsymbol{\sigma}_{n+1} = \hat{\boldsymbol{\sigma}}(\boldsymbol{\varepsilon}_{n+1}, \boldsymbol{\theta}_n). \tag{2.60}$$

With this at hand, the incremental boundary value problem is stated as follows:

Problem 2.1. *Given the set of internal variables $\boldsymbol{\theta}_n$ and the displacement field obtained in the previous increment, knowing the current applied forces $\boldsymbol{b}_{n+1}$ and $\boldsymbol{t}_{n+1}$, find $\boldsymbol{u}_{n+1}$ that satisfies (2.61) for all $\delta\boldsymbol{u} \in \mathcal{V}$.*

$$\int_{\varphi(\Omega)} [\hat{\boldsymbol{\sigma}}(\boldsymbol{F}_{n+1}, \boldsymbol{\theta}_n) : \nabla_x \delta\boldsymbol{u} - \boldsymbol{b}_{n+1} \cdot \delta\boldsymbol{u}] \, dV - \int_{\varphi(\partial\Omega)} \boldsymbol{t}_{n+1} \cdot \delta\boldsymbol{u} dA = 0, \forall \, \delta\boldsymbol{u} \in \mathcal{V}. \tag{2.61}$$

2.5.4 Incremental finite element solution

Applying a finite element discretisation to the incremental problem, Expression (2.61), the equilibrium equation can be expressed as:

$$\mathbf{r}(\mathbf{u}_{n+1}) = \mathbf{f}^{int}(\mathbf{u}_{n+1}) - \mathbf{f}^{ext}_{n+1} = \mathbf{0}, \tag{2.62}$$

where the unknown is the nodal vector displacement $\mathbf{u}_{n+1}$ such that the residual $\mathbf{r}$ vanishes. The internal and external force vectors are assembled from their elemental counterparts:

$$\mathbf{f}^{int}_{e,n+1} = \int_{\varphi(\Omega^e)} (\mathbf{B}^e)^T \hat{\boldsymbol{\sigma}}(\boldsymbol{F}_{n+1}, \boldsymbol{\theta}_n) dV, \tag{2.63}$$

$$\mathbf{f}^{ext}_{e,n+1} = \int_{\varphi(\Omega^e)} (\mathbf{N}^e)^T \mathbf{b}_{n+1} dV + \int_{\varphi(\partial\Omega^e)} (\mathbf{N}^e)^T \mathbf{t}_{n+1} dA. \tag{2.64}$$

Equation (2.62) is non-linear due to the possibly non-linear material behaviour or to geometrical non-linearities. The iterative Newton-Raphson scheme is used to solve this equation, since its quadratic convergence rate allows to obtain a relatively efficient and robust method. In each iteration, the linearised version of Expression (2.62) is solved. To obtain the linearised version of the discretised incremental equilibrium equation, the linearised virtual work, Expression (A.19), is discretised, which results in:

$$\left\{\int_{\varphi(\Omega^d)} (\mathbf{G}^g)^T \mathbf{a} \mathbf{G}^g dV\right\} \Delta\mathbf{u} \cdot \delta\mathbf{u} = \\ -\left\{\int_{\varphi(\Omega^d)} \left[(\mathbf{B}^g)^T \boldsymbol{\sigma} - (\mathbf{N}^g)^T \mathbf{b}\right] dV - \int_{\varphi(\partial\Omega^d)} (\mathbf{N}^g)^T \mathbf{t} dA\right\} \cdot \delta\mathbf{u}, \ \forall \delta\mathbf{u} \in \mathcal{V}^d. \tag{2.65}$$

Since this equality must be satisfied for any admissible virtual displacement vector $\delta\mathbf{u}$, then it can be rewritten as:

$$\left\{\int_{\varphi(\Omega^d)} (\mathbf{G}^g)^T \mathbf{a} \mathbf{G}^g dV\right\} \Delta\mathbf{u} = -\left\{\int_{\varphi(\Omega^d)} \left[(\mathbf{B}^g)^T \boldsymbol{\sigma} - (\mathbf{N}^g)^T \mathbf{b}\right] dV - \int_{\varphi(\partial\Omega^d)} (\mathbf{N}^g)^T \mathbf{t} dA\right\}, \tag{2.66}$$

where the matrix representation of the spatial tangent modulus (see Expression (A.18)) and the stress tensor are given by $\mathbf{a}$ and $\boldsymbol{\sigma}$.

For the increment $n+1$, the initial guess for the displacement field is assumed to be the last converged value, $\mathbf{u}^{(0)}_{n+1} = \mathbf{u}_n$, and within an iteration (j) it is updated as follows:

$$\mathbf{u}^{(j)}_{n+1} = \mathbf{u}^{(j-1)}_{n+1} + \Delta\mathbf{u}^{(j)}, \tag{2.67}$$

where $\Delta\mathbf{u}^{(j)}$ is obtained solving the linear system of equations:

$$\mathbf{K}^{(j-1)}_T \Delta\mathbf{u}^{(j)} = -\mathbf{r}(\mathbf{u}^{(j-1)}_{n+1}). \tag{2.68}$$

$\mathbf{K}^{(j-1)}_T$ represents the global tangent stiffness matrix, which is computed as:

$$\mathbf{K}^{(j-1)}_T = \int_{\varphi(\Omega^d)} (\mathbf{G}^g)^T \mathbf{a} \mathbf{G}^g dV = \left.\frac{\partial \mathbf{r}}{\partial \mathbf{u}_{n+1}}\right|_{\mathbf{u}^{(j-1)}_{n+1}}. \tag{2.69}$$

Following the same approach for the nodal force vectors, the global stiffness matrix is assembled from its elemental counterparts:

$$\mathbf{K}_T = \bigwedge_{e=1}^{n_{el}} \mathbf{K}_e. \tag{2.70}$$

The iterative procedure is stopped for the iteration (m) if the following convergence criteria is verified:

$$\left|\frac{\mathbf{r}^{(m)}}{\mathbf{f}^{ext}_{n+1}}\right| \leq \epsilon_{tol}, \tag{2.71}$$

with the convergence tolerance being a sufficiently small value ϵ_{tol}. The solution for Problem 2.1 is then $\mathbf{u}_{n+1} = \mathbf{u}^{(m)}_{n+1}$.

2.5.5 Gaussian quadrature

It is noteworthy to mention that all integrations are computed using Gaussian quadrature. For the sake of completeness, this method is described here. The integral of a generic quantity $\boldsymbol{a}$ may be computed as the sum over a finite number of n_p integration points:

$$\int_{\Omega} \boldsymbol{a}(\boldsymbol{x})\, dV = \sum_{p=1}^{n_p} \boldsymbol{a}(\boldsymbol{\xi}_p)\, w_p J_p. \tag{2.72}$$

The integration points $\boldsymbol{\xi}_p$ are define *apriori* in the natural space, as well as the corresponding weight w_p. These values are well known for the usual finite element types. The scalar value J_p is the determinant of the Jacobian for the mapping from physical to natural space. The number of integration points to use depends on the degree of non-linearity of the field $\boldsymbol{a}$.

Chapter 3

Multi-scale models based on first-order computational homogenisation

A multi-scale formulation for quasi-static problems, where the constitutive behaviour at each macro-point is determined through 1st-order computational homogenisation of the underlying RVE response, is presented in this chapter. It is based on the variational multi-scale theory introduced by de Souza Neto and co-workers (Blanco et al., 2016a, de Souza Neto and Feijóo, 2006, 2010, de Souza Neto et al., 2015).

3.1 Homogenised constitutive response

Within the context of multi-scale modelling based on computational homogenization, the influence of the underlying material microstructure is explicitly accounted for in the macroscopic constitutive response through the analysis of Representative Volume Elements (RVEs). For *Coupled Multi-scale Finite Element Analysis* (FE^2), the solution of two nested boundary value problems, corresponding to the coupled macro and micro-scale, is required. The macro-scale problem is solved with the standard finite element framework, where the only difference lies on the constitutive description. A RVE is attached to each macro-integration point and the constitutive response is determined through the solution of the RVE equilibrium problem, which is driven by the macroscopic deformation gradient. When the RVE equilibrium state is found, the macroscopic stress tensor is obtained by homogenization of the microscopic counterparts, along with the homogenised consistent tangent modulus. This process, schematically represented in Figure 3.1, can be seen as the constitutive functional $\hat{\boldsymbol{\sigma}}$ of Equation (2.59), where the internal variables $\boldsymbol{\theta}$ are defined by the RVE state.

Here, finite element discretization and analysis is employed at both scales. However, it is possible to use distinct numerical methods for the solution of either the macro and micro-problems.

3.2 Scale transition theory

Let us consider a solid defined by the macro-domain Ω, with a characteristic length L, and an infinitesimal spatial point $\boldsymbol{x} \in \Omega$ at the macro-scale. The underlying microstructure is modelled by a RVE of size s_{RVE}, where the characteristic length of the micro-constituents is denoted by l. A generic infinitesimal spatial point at the RVE domain Ω_μ is denoted by $\boldsymbol{y}$ and a generic material point by $\boldsymbol{Y}$.

Several definitions have been proposed for a Representative Volume Element in the literature over the years. A review can be found in the work of Gitman et al. (2007). The main idea is that a RVE must be large enough such that it is representative of all microstructural heterogeneities, i.e. $l << s_{RVE}$, but should be much smaller than the macroscopic structure, such that the *Scale Separation Principle* applies ($s_{RVE} << L$). In this case, a RVE may be identified with a generic infinitesimal point

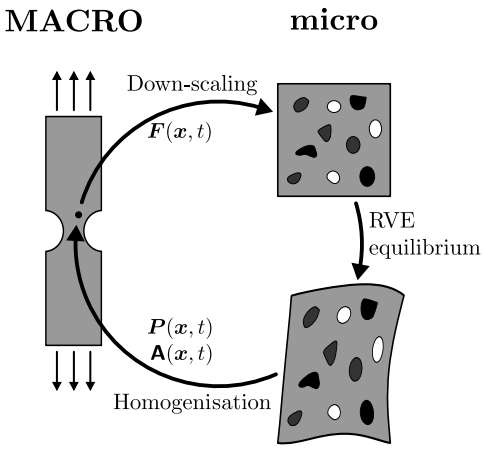

Figure 3.1: Schematic representation of a coupled multi-scale finite element analysis.

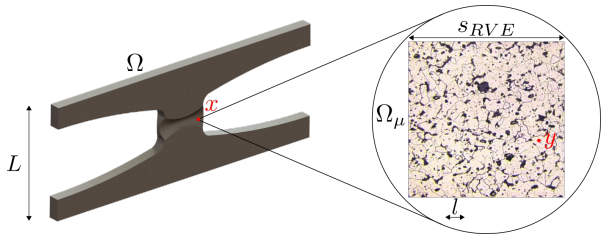

Figure 3.2: RVE definition and *scale separation principle*.

$\boldsymbol{x}$ at the macro-scale, as represented in Figure 3.2. Terada et al. (2000) and Kanit et al. (2003) among others have made several studies on the representativeness and size determination of a RVE.

The formulation of the multi-scale problem is presented in the next section. The *Method of multi-scale virtual power* (Blanco et al., 2016a) is employed to derive the formulation, guaranteeing it is variationally consistent across the scales.

3.2.1 Multi-scale kinematics

The kinematic insertion and kinematic homogenisation definitions are the basic ingredients needed to develop the multi-scale formulation within the *Method of multi-scale virtual power* context. These procedures relate the kinematic descriptors from both scales.

Kinematic insertion

This procedure defines how macro-scale kinematical quantities contribute to the micro-scale kinematics. The macroscopic deformation gradient is enforced to the RVE, which generates a microscopic displacement field. It can be expressed as the sum of its linear part, that depends directly on the prescribed deformation gradient, and the displacement fluctuation $\tilde{\boldsymbol{u}}$:

$$\boldsymbol{u}(\boldsymbol{Y},t) = [\boldsymbol{F}(\boldsymbol{X},t) - \boldsymbol{I}] \cdot \boldsymbol{Y} + \tilde{\boldsymbol{u}}(\boldsymbol{Y},t). \tag{3.1}$$

Note that the unknown of the micro-scale equilibrium problem is in fact the fluctuation field, since the linear displacement is prescribed.

Kinematic homogenisation

The kinematic homogenisation procedure establishes how micro-scale kinematical quantities are averaged in some sense to be related to the corresponding macro-scale counterparts. The macro-

scopic deformation gradient, that drives the micro-scale deformation, is obtained as an average of the microscopic deformation gradient field over the undeformed RVE domain Ω_μ:

$$\begin{aligned}\boldsymbol{F}(\boldsymbol{X},t) &= \frac{1}{V_\mu}\int_{\Omega_\mu}\boldsymbol{F}(\boldsymbol{Y},t)\,dV \\ &= \boldsymbol{I}+\frac{1}{V_\mu}\int_{\Omega_\mu}\nabla_Y\boldsymbol{u}(\boldsymbol{Y},t)\,dV.\end{aligned} \tag{3.2}$$

The scalar V_μ denotes the RVE undeformed volume, $\boldsymbol{I}$ is the second-order identity tensor and ∇_Y is the material gradient with respect to the micro-scale.

Kinematic admissibility

The constraints defining the kinematic admissibility are a result of the compatibilisation between the kinematic insertion and kinematic homogenisation definitions. Introducing the definition of Expression (3.1) into Expression (3.2), the following equation is obtained after some manipulation:

$$\boldsymbol{F}(\boldsymbol{X},t) = \boldsymbol{F}(\boldsymbol{X},t)+\frac{1}{V_\mu}\int_{\Omega_\mu}\nabla_Y\tilde{\boldsymbol{u}}(\boldsymbol{Y},t)\,dV. \tag{3.3}$$

Thus, the *minimal kinematic admissible constraint* is given by

$$\int_{\Omega_\mu}\nabla_Y\tilde{\boldsymbol{u}}(\boldsymbol{Y},t)\,dV = \boldsymbol{0}, \tag{3.4}$$

which can be written as the boundary constraint of Equation (3.5), where $\boldsymbol{N}$ denotes the outward unit reference vector:

$$\int_{\partial\Omega_\mu}\tilde{\boldsymbol{u}}(\boldsymbol{Y},t)\otimes\boldsymbol{N}\,dA = \boldsymbol{0}. \tag{3.5}$$

The space of admissible displacement fluctuations is therefore defined by:

$$\tilde{\mathcal{K}} \equiv \left\{\tilde{\boldsymbol{u}},\ \text{sufficiently regular}\middle|\int_{\partial\Omega_\mu}\tilde{\boldsymbol{u}}\otimes\boldsymbol{N}\,dA=\boldsymbol{0}\right\}. \tag{3.6}$$

The application of this constraint yields the so-called uniform traction boundary condition. Additional constraints may be introduced, as detailed in Section 3.2.4.

3.2.2 Hill-Mandel Principle

The classical *Hill-Mandel Principle* establishes the energetic equivalence between the two coupled scales, stating that the macroscopic stress power must be equal to the average of its microscopic counterpart over the RVE. In the framework of the *Method of multi-scale virtual power*, for the standard 1$^{\text{st}}$-order homogenisation formulation, the *Hill-Mandel Principle* is equivalent to the *Principle of multi-scale virtual power*, which establishes the equivalence of the virtual power across the scales:

$$\boldsymbol{P}(\boldsymbol{X},t):\delta\boldsymbol{F}(\boldsymbol{X},t) = \frac{1}{V_\mu}\int_{\Omega_\mu}\boldsymbol{P}(\boldsymbol{Y},t):\delta\boldsymbol{F}(\boldsymbol{Y},t)\,dV. \tag{3.7}$$

This must be satisfied for any virtual deformation gradient at the macro-scale $\delta\boldsymbol{F}(\boldsymbol{X},t)$ and for any virtual deformation gradient at the micro-scale $\delta\boldsymbol{F}(\boldsymbol{Y},t)$.

For the sake of compactness, the arguments $(\boldsymbol{Y},t)$ and $(\boldsymbol{X},t)$ are dropped in what follows, and the subscript $(\bullet)_\mu$ is employed to identify the micro-scale variables.

Taking into account the deformation gradient definition (Equation (2.14)) and the micro-scale displacement field (Equation (3.1)), the microscopic deformation gradient is expressed by:

$$\boldsymbol{F}_\mu = \boldsymbol{I}+\nabla_Y\boldsymbol{u}_\mu = \boldsymbol{F}+\nabla_Y\tilde{\boldsymbol{u}}. \tag{3.8}$$

Therefore the *Principle of multi-scale virtual power* may be rewritten as

$$\boldsymbol{P} : \delta \boldsymbol{F} = \frac{1}{V_\mu} \int_{\Omega_\mu} \boldsymbol{P}_\mu : [\delta \boldsymbol{F} + \nabla_Y \delta \tilde{\boldsymbol{u}}] \, dV, \tag{3.9}$$

for any admissible virtual deformation gradient at the macro-scale $\delta \boldsymbol{F}$ and any admissible virtual displacement fluctuation at the micro-scale $\delta \tilde{\boldsymbol{u}}$.

3.2.3 Micro-scale equilibrium problem

The micro-scale equilibrium equation can be determined as a consequence of the *Principle of multi-scale virtual power*, assuming that $\delta \boldsymbol{F} = \boldsymbol{0}$, which results in

$$\int_{\Omega_\mu} \boldsymbol{P}_\mu : \nabla_Y \delta \tilde{\boldsymbol{u}} dV = 0, \quad \forall \, \delta \tilde{\boldsymbol{u}} \in \tilde{\mathcal{V}}, \tag{3.10}$$

or, in a spatial description:

$$\int_{\varphi(\Omega_\mu)} \boldsymbol{\sigma}_\mu : \nabla_y \delta \tilde{\boldsymbol{u}} dV = 0, \quad \forall \, \delta \tilde{\boldsymbol{u}} \in \tilde{\mathcal{V}}, \tag{3.11}$$

where the virtual displacement fluctuation $\delta \tilde{\boldsymbol{u}}$ belongs to the space of admissible displacement fluctuations $\tilde{\mathcal{V}} \equiv \tilde{\mathcal{K}}$. The goal is to find the displacement fluctuation field $\tilde{\boldsymbol{u}}$ that satisfies the equilibrium equation.

Looking at a general virtual work equation (material version):

$$\int_{\Omega_\mu} \left[\boldsymbol{P}_\mu : \nabla_Y \delta \tilde{\boldsymbol{u}} - \boldsymbol{b}_{\mu 0} \cdot \delta \tilde{\boldsymbol{u}} \right] dV - \int_{\partial \Omega_\mu} \boldsymbol{t}_{\mu 0} \cdot \delta \tilde{\boldsymbol{u}} dA = 0, \forall \, \delta \tilde{\boldsymbol{u}} \in \tilde{\mathcal{V}}, \tag{3.12}$$

it is possible to conclude that a consequence of the Hill-Mandel principle is that external traction forces and body forces do not produce work:

$$\int_{\Omega_\mu} \boldsymbol{b}_{\mu 0} \cdot \delta \tilde{\boldsymbol{u}} dV = 0, \quad \forall \delta \tilde{\boldsymbol{u}} \in \tilde{\mathcal{V}}, \tag{3.13}$$

$$\int_{\partial \Omega_\mu} \boldsymbol{t}_{\mu 0} \cdot \delta \tilde{\boldsymbol{u}} dA = 0, \quad \forall \delta \tilde{\boldsymbol{u}} \in \tilde{\mathcal{V}}. \tag{3.14}$$

In a quasi-static framework and in the absence of body forces ($\boldsymbol{b}_{\mu 0} = \boldsymbol{0}$), which is the case considered here, this means that external forces $\boldsymbol{t}_{\mu 0}$ are reactions arising from the enforcement of the boundary conditions. Therefore, the strong form of the micro-equilibrium equation can be stated by

$$\operatorname{div}_Y \boldsymbol{P}_\mu = \boldsymbol{0}, \quad \text{in } \Omega_\mu \tag{3.15}$$

$$\boldsymbol{t}_{\mu 0} = \boldsymbol{P}_\mu \cdot \boldsymbol{N}, \quad \text{on } \partial \Omega_\mu. \tag{3.16}$$

The micro-scale equilibrium problem defined by Equation (3.11) is solved independently for each RVE, with the finite element method, using the iterative Newton-Raphson scheme. Even though the macro and micro systems of equations are not solved monolithically, the incremental strategy must be consistent between both scales. This subject is discussed in Section 3.3.1.

The constitutive behaviour of micro-constituents is modelled by conventional internal variable-based dissipative constitutive equations. A finite strain approach is assumed at micro-level, where materials may be path dependent. Thus, the micro-constitutive functional is driven by the microscopic deformation gradient and microscopic internal variables $\boldsymbol{\beta}$:

$$\boldsymbol{\sigma}_{\mu,n+1}(\boldsymbol{y}) = \hat{\boldsymbol{\sigma}}(\boldsymbol{F}_{\mu,n+1}(\boldsymbol{y}), \boldsymbol{\beta}_n(\boldsymbol{y})). \tag{3.17}$$

3.2.4 Micro-scale boundary conditions

Uniform traction boundary condition

The minimal kinematic constraint given by Equation (3.5) is the minimal boundary condition that satisfies the compatibility between the macroscopic deformation gradient and the micro-scale displacement field. It yields a uniform traction on the RVE boundary which is driven by the homogenised Piola-Kirchhoff:

$$\boldsymbol{t}_{\mu 0} = \boldsymbol{P}_{\mu} \cdot \boldsymbol{N} = \boldsymbol{P} \cdot \boldsymbol{N}. \tag{3.18}$$

This constraint results in the most compliant homogenised response.

Periodic boundary condition

The periodic boundary condition enforces similar fluctuations on opposite sides of the RVE, such that the microstructure may be seen as a pattern of repeated RVEs. Splitting the RVE boundary sides in a positive part $\partial\Omega_{\mu}^{+}$, with outward unit vector denoted by $\boldsymbol{N}^{+}$, and their opposite counterparts as negative $\partial\Omega_{\mu}^{-}$, with unit outward $\boldsymbol{N}^{-} = -\boldsymbol{N}^{+}$ such that:

$$\partial\Omega_{\mu} = \partial\Omega_{\mu}^{+} \cup \partial\Omega_{\mu}^{-}, \tag{3.19}$$

this boundary condition is stated by:

$$\tilde{\boldsymbol{u}}(\boldsymbol{Y}^{+}, t) = \tilde{\boldsymbol{u}}(\boldsymbol{Y}^{-}, t), \tag{3.20}$$

where $\boldsymbol{Y}^{+} \in \partial\Omega_{\mu}^{+}$ and $\boldsymbol{Y}^{-} \in \partial\Omega_{\mu}^{-}$ are corresponding points on the opposite sides.

The periodic boundary condition is the most popular micro-constraint due to the fact that the resulting homogenised properties converge faster to their real values as the RVE size increases (Kanit et al., 2003, Terada et al., 2000). In fact, the uniform traction condition provides a lower bound for the homogenised response, the linear boundary condition returns an upper bound, and the macro-response obtained with the periodic constraint lies between both.

Linear boundary condition

This condition defines that on the boundary of the RVE, the displacement field is coincident with the imposed linear displacement, i.e, the displacement fluctuation field is null on the boundary:

$$\tilde{\boldsymbol{u}}(\boldsymbol{Y}) = \boldsymbol{0}, \ \forall \boldsymbol{Y} \in \partial\Omega_{\mu}. \tag{3.21}$$

The conditions introduced by Expressions (3.5) and (3.14) are automatically satisfied, and Expression (3.13) is verified in the absence of body forces and accelerations.

Taylor condition

The trivial solution $\tilde{\boldsymbol{u}} = \boldsymbol{0}$ over the entire domain is the simplest condition respecting the minimal kinematic admissible fluctuations. In this case, the microscopic displacement field is the linear displacement enforced by the macroscopic deformation gradient. This constraint is known as Taylor condition, which is equivalent to the rule of mixtures commonly used to obtain the homogenised properties of composites. This constraint overestimates the stiffness of heterogeneous materials, providing a response even stiffer than the linear boundary condition.

3.2.5 Homogenised stress tensor

When the micro-equilibrium is found, the macroscopic stress can be determined by homogenization. This procedure is also a consequence of the *Principle of Multi-Scale Virtual Power*, when $\delta\bar{\boldsymbol{u}} = \mathbf{0}$ is assumed. The macroscopic *First Piola-Kirchhoff* tensor is obtained as a volume averaging of its microscopic counterpart:

$$\boldsymbol{P} = \frac{1}{V_\mu}\int_{\Omega_\mu} \boldsymbol{P}_\mu dV. \tag{3.22}$$

Developing the above right hand side through integration by parts:

$$\int_{\Omega_\mu} \boldsymbol{P}_\mu dV = \int_{\Omega_\mu} \boldsymbol{P}_\mu \cdot \nabla_Y \boldsymbol{Y}\, dV = \int_{\partial\Omega_\mu} \boldsymbol{P}_\mu \cdot \boldsymbol{N} \otimes \boldsymbol{Y}\, dA - \int_{\Omega_\mu} \mathrm{div}_Y\, \boldsymbol{P}_\mu \otimes \boldsymbol{Y}\, dV. \tag{3.23}$$

Introducing the strong form of the equilibrium problem allows to re-write Equation (3.22) in terms of a boundary integral as

$$\boldsymbol{P} = \frac{1}{V_\mu}\int_{\partial\Omega_\mu} \boldsymbol{t}_{\mu 0} \otimes \boldsymbol{Y}\, dV = \frac{1}{V_\mu}\int_{\varphi(\partial\Omega_\mu)} \boldsymbol{t}_\mu \otimes \boldsymbol{Y}\, dV. \tag{3.24}$$

The Cauchy stress tensor, which is the stress measure used at the macro-scale, is obtained through the relation:

$$\boldsymbol{\sigma} = \frac{1}{\det \boldsymbol{F}} \boldsymbol{P}\boldsymbol{F}^T. \tag{3.25}$$

3.3 Numerical solution of the multi-scale equilibrium problem

The finite element method is employed to solve the equilibrium problems arising at both scales. While the macro-scale problem is treated as a standard finite element problem (see Section 2.5), additional numerical treatment is applied at the micro-scale, to deal with the nature of the micro-constraints. In fact, the only difference between a standard finite element simulation and the macro-scale problem lies on the determination of the constitutive behaviour at the macroscopic integration points, which is obtained by stress homogenisation from the underlying RVE, and the computation of the homogenised consistent tangent operator.

3.3.1 Large-strain and path dependent framework

In the present contribution, a large strain formulation is assumed at both scales, with possibly path dependent constitutive models describing the micro-constituents behaviour. Consequently, the macroscopic constitutive response is also path dependent. The macro-level constitutive functional in Expression (2.59) represents the micro-scale analysis and stress homogenization procedure. The macro-internal variables $\boldsymbol{\theta}$ can be interpreted as the underlying RVE state. This state is characterized by the microscopic internal variables $\boldsymbol{\beta}$, the microscopic geometry defined by the RVE updated coordinates $\boldsymbol{y}$, and the micro-stress field $\boldsymbol{\sigma}_\mu(\boldsymbol{y})$.

The RVE state must be stored during the iterative solution of the macroscopic problem, so that the state update can be performed within each incremental step, taking into account the load history. Moreover, incrementation at both scales must be consistent. Sub-incrementation strategies have been proposed in order to improve the robustness of the RVE iterative solution and reduce the computational time for multi-scale analysis, while keeping the consistency between incremental schemes at both scales (Reis and Andrade Pires, 2013, Somer et al., 2009). A schematic representation of the multi-scale analysis involving large strains at both scales is shown in Figure 3.3, where the incremental consistency between scales and the importance of the RVE state are highlighted.

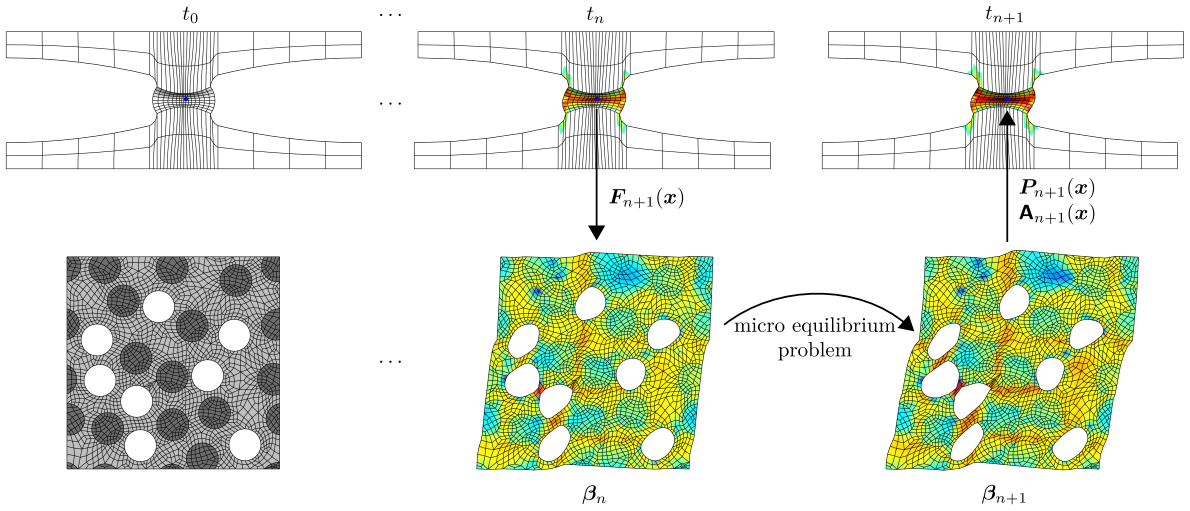

Figure 3.3: Schematic representation of a coupled multi-scale finite element analysis at large strains with path dependent descriptions.

3.3.2 Finite element discretisation

The finite element discretisation of the weak equilibrium Equation (3.11) results in:

$$\delta\tilde{\mathbf{u}}^T \cdot \mathbf{f}^{int}(\tilde{\mathbf{u}}) = 0, \quad \forall \delta\tilde{\mathbf{u}} \in \tilde{\mathcal{V}}^d, \tag{3.26}$$

where the internal force vector is given by:

$$\mathbf{f}^{int}(\tilde{\mathbf{u}}) = \int_{\varphi(\Omega_\mu)} (\mathbf{B}^g)^T \hat{\boldsymbol{\sigma}}(\boldsymbol{F}_{n+1}(\boldsymbol{y}), \boldsymbol{\beta}_n(\boldsymbol{y}))\, dV. \tag{3.27}$$

Since Equation (3.26) must be satisfied for any admissible virtual displacement vector $\delta\tilde{\mathbf{u}}$, the equilibrium equation can be simply stated as:

$$\mathbf{f}^{int}(\tilde{\mathbf{u}}) = \mathbf{0}. \tag{3.28}$$

Therefore, the residual vector coincides with the internal force vector, and no external forces are included in this formulation, since the boundary conditions are already taken into account in the admissible virtual displacements set $\tilde{\mathcal{V}}^d$. This non-linear problem is solved with the Newton-Raphson's method. A schematic representation of the solution of the micro-scale equilibrium problem is presented in Figure 3.4.

Condensation method

The condensation method is used in order to embed the micro-constraints into the process of finding the displacement fluctuation field (Reis, 2014, Reis and Andrade Pires, 2013, 2014). Without loss of generality, the degrees of freedom (*dof*) are split into distinct groups, according to the position of the corresponding node on the RVE finite element model:

(i) interior *dof*, related to nodes in the interior of the RVE;

(f) free *dof* on RVE boundary;

(d) dependent *dof*, defined on RVE boundary, whose displacement fluctuation depends on free counterparts;

(p) prescribed *dof*, on the boundary of the RVE, where null displacement fluctuation is defined, in order to avoid rigid body motion.

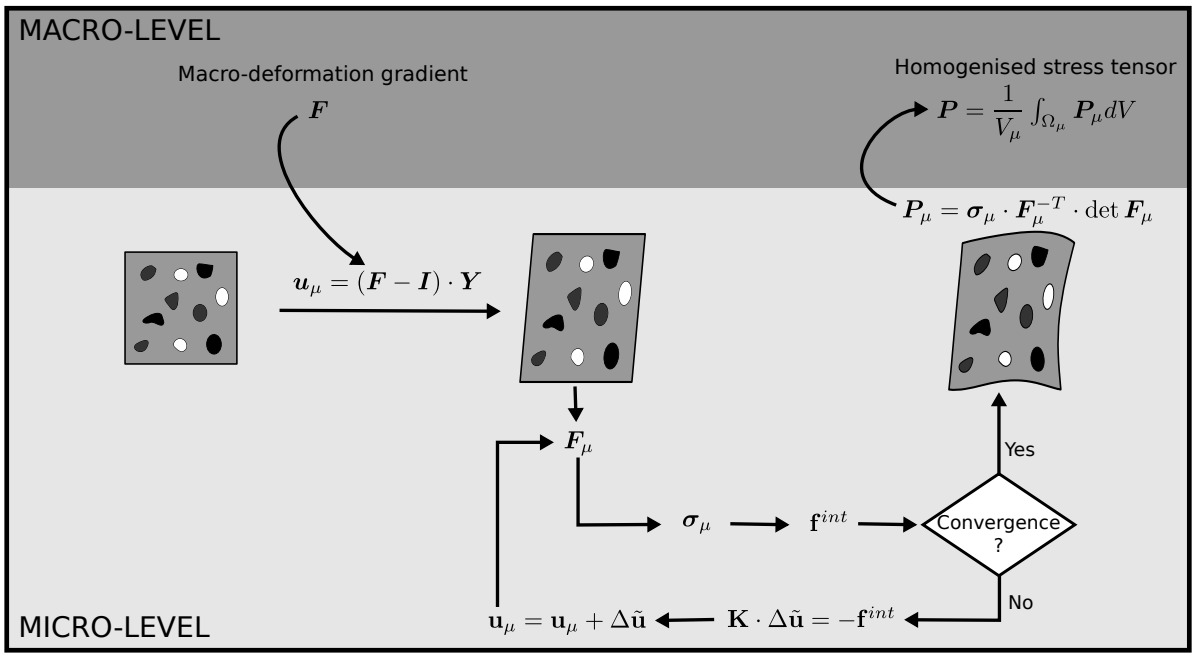

Figure 3.4: Schematic representation of the insertion, micro-scale equilibrium solution and stress homogenisation procedures.

The displacement fluctuation, virtual displacement and internal force vectors are re-arranged according to these groups:

$$\tilde{\mathbf{u}} = \begin{Bmatrix} \tilde{\mathbf{u}}^i \\ \tilde{\mathbf{u}}^f \\ \tilde{\mathbf{u}}^d \\ \tilde{\mathbf{u}}^p \end{Bmatrix}, \quad \delta\tilde{\mathbf{u}} = \begin{Bmatrix} \delta\tilde{\mathbf{u}}^i \\ \delta\tilde{\mathbf{u}}^f \\ \delta\tilde{\mathbf{u}}^d \\ \delta\tilde{\mathbf{u}}^p \end{Bmatrix}, \quad \mathbf{f}^{int} = \begin{Bmatrix} \mathbf{f}^i \\ \mathbf{f}^f \\ \mathbf{f}^d \\ \mathbf{f}^p \end{Bmatrix}, \tag{3.29}$$

and so is the linearised version of Expression (3.26), needed for the Newton-Raphson's scheme:

$$\begin{Bmatrix} \delta\tilde{\mathbf{u}}^i \\ \delta\tilde{\mathbf{u}}^f \\ \delta\tilde{\mathbf{u}}^d \\ \delta\tilde{\mathbf{u}}^p \end{Bmatrix}^T \left\{ \begin{bmatrix} \mathbf{k}^{ii} & \mathbf{k}^{if} & \mathbf{k}^{id} & \mathbf{k}^{ip} \\ \mathbf{k}^{fi} & \mathbf{k}^{ff} & \mathbf{k}^{fd} & \mathbf{k}^{fp} \\ \mathbf{k}^{di} & \mathbf{k}^{df} & \mathbf{k}^{dd} & \mathbf{k}^{dp} \\ \mathbf{k}^{pi} & \mathbf{k}^{pf} & \mathbf{k}^{pd} & \mathbf{k}^{pp} \end{bmatrix} \begin{Bmatrix} \Delta\tilde{\mathbf{u}}^i \\ \Delta\tilde{\mathbf{u}}^f \\ \Delta\tilde{\mathbf{u}}^d \\ \Delta\tilde{\mathbf{u}}^p \end{Bmatrix} + \begin{Bmatrix} \mathbf{f}^i \\ \mathbf{f}^f \\ \mathbf{f}^d \\ \mathbf{f}^p \end{Bmatrix} \right\} = 0. \tag{3.30}$$

Here, the concept of stiffness matrix and iterative solution, which is introduced in Section 2.5, is recalled.

Boundary conditions are introduced on the present problem by choosing suitable dependent and prescribed boundary *dof*, and a relation between dependent and free displacement fluctuation, which in general is defined by a dependency matrix $\boldsymbol{\alpha}$ through:

$$\tilde{\mathbf{u}}^d = \boldsymbol{\alpha}\tilde{\mathbf{u}}^f. \tag{3.31}$$

With this relation at hand, together with the fact that $\tilde{\mathbf{u}}^p = \mathbf{0}$, Expression (3.30) is condensed. In the first place, all contributions from prescribed *dof* are eliminated, since $\tilde{\mathbf{u}}^p$ is not an unknown anymore. In the second place, considering the above relation, that is also valid to relate $\delta\tilde{\mathbf{u}}^d$ and $\delta\tilde{\mathbf{u}}^f$, the linearised virtual work is rewritten as:

$$\begin{Bmatrix} \delta\tilde{\mathbf{u}}^i \\ \delta\tilde{\mathbf{u}}^f \\ \boldsymbol{\alpha}\delta\tilde{\mathbf{u}}^f \end{Bmatrix}^T \left\{ \begin{bmatrix} \mathbf{k}^{ii} & \mathbf{k}^{if} & \mathbf{k}^{id} \\ \mathbf{k}^{fi} & \mathbf{k}^{ff} & \mathbf{k}^{fd} \\ \mathbf{k}^{di} & \mathbf{k}^{df} & \mathbf{k}^{dd} \end{bmatrix} \begin{Bmatrix} \Delta\tilde{\mathbf{u}}^i \\ \Delta\tilde{\mathbf{u}}^f \\ \boldsymbol{\alpha}\Delta\tilde{\mathbf{u}}^f \end{Bmatrix} + \begin{Bmatrix} \mathbf{f}^i \\ \mathbf{f}^f \\ \mathbf{f}^d \end{Bmatrix} \right\}. \tag{3.32}$$

Applying condensation to the $\Delta\tilde{\mathbf{u}}$ vector, the unknown part $\tilde{\mathbf{u}}^d$ is removed from the equation:

$$\left\{\begin{array}{c}\delta\tilde{\mathbf{u}}^i\\ \delta\tilde{\mathbf{u}}^f\\ \boldsymbol{\alpha}\delta\tilde{\mathbf{u}}^f\end{array}\right\}^T \left\{\left[\begin{array}{c|c}\mathbf{k}^{ii} & \mathbf{k}^{if}+\mathbf{k}^{id}\boldsymbol{\alpha}\\ \hline \mathbf{k}^{fi} & \mathbf{k}^{ff}+\mathbf{k}^{fd}\boldsymbol{\alpha}\\ \hline \mathbf{k}^{di} & \mathbf{k}^{df}+\mathbf{k}^{dd}\boldsymbol{\alpha}\end{array}\right]\left\{\begin{array}{c}\Delta\tilde{\mathbf{u}}^i\\ \Delta\tilde{\mathbf{u}}^f\end{array}\right\}+\left\{\begin{array}{c}\mathbf{f}^i\\ \mathbf{f}^f\\ \mathbf{f}^d\end{array}\right\}\right\}=0. \tag{3.33}$$

Finally, the same procedure is applied to the virtual displacement vector, which results in:

$$\left\{\begin{array}{c}\delta\tilde{\mathbf{u}}^i\\ \delta\tilde{\mathbf{u}}^f\end{array}\right\}^T \left\{\left[\begin{array}{c|c}\mathbf{k}^{ii} & \mathbf{k}^{if}+\mathbf{k}^{id}\boldsymbol{\alpha}\\ \hline \mathbf{k}^{fi}+\boldsymbol{\alpha}^T\mathbf{k}^{di} & \mathbf{k}^{ff}+\mathbf{k}^{fd}\boldsymbol{\alpha}+\boldsymbol{\alpha}^T\mathbf{k}^{df}+\boldsymbol{\alpha}^T\mathbf{k}^{dd}\boldsymbol{\alpha}\end{array}\right]\left\{\begin{array}{c}\Delta\tilde{\mathbf{u}}^i\\ \Delta\tilde{\mathbf{u}}^f\end{array}\right\}+\left\{\begin{array}{c}\mathbf{f}^i\\ \mathbf{f}^f+\boldsymbol{\alpha}^T\mathbf{f}^d\end{array}\right\}\right\}=0. \tag{3.34}$$

Since the above equality must hold for any set of virtual displacements, the equilibrium problem falls into the iterative solution of the condensed system of equations:

$$\left[\begin{array}{c|c}\mathbf{k}^{ii} & \mathbf{k}^{if}+\mathbf{k}^{id}\boldsymbol{\alpha}\\ \hline \mathbf{k}^{fi}+\boldsymbol{\alpha}^T\mathbf{k}^{di} & \mathbf{k}^{ff}+\mathbf{k}^{fd}\boldsymbol{\alpha}+\boldsymbol{\alpha}^T\mathbf{k}^{df}+\boldsymbol{\alpha}^T\mathbf{k}^{dd}\boldsymbol{\alpha}\end{array}\right]\left\{\begin{array}{c}\Delta\tilde{\mathbf{u}}^i\\ \Delta\tilde{\mathbf{u}}^f\end{array}\right\}=-\left\{\begin{array}{c}\mathbf{f}^i\\ \mathbf{f}^f+\boldsymbol{\alpha}^T\mathbf{f}^d\end{array}\right\}. \tag{3.35}$$

The dependent component $\Delta\tilde{\mathbf{u}}^d$ is recovered through Expression (3.31), and the solution is updated in each iteration by:

$$\tilde{\mathbf{u}}_{n+1}^{(j+1)}=\tilde{\mathbf{u}}_{n+1}^{(j)}+\Delta\tilde{\mathbf{u}}. \tag{3.36}$$

3.3.3 Micro-scale boundary conditions

The linear system of equations for the micro-scale Newton-Raphson's scheme presented in Equation (3.35) is particularised for each boundary condition presented in Section 3.2.4 (linear, periodic and uniform traction) in what follows.

Linear boundary condition

Within the linear boundary condition, a null fluctuation is imposed on the entire RVE boundary. Therefore all boundary *dof* are prescribed and only the interior fluctuations $\tilde{\mathbf{u}}^i$ are unknown. This results in:

$$\mathbf{k}^{ii}\Delta\tilde{\mathbf{u}}^i=-\mathbf{f}^i. \tag{3.37}$$

This constraint naturally avoids rigid body motion.

Periodic boundary condition

A standard implementation of the periodic boundary condition requires the mesh to be conform on opposite faces of the RVE, i.e., for each node on the negative boundary (free), there is a node with corresponding coordinates on the opposite face (dependent). With a suitable sorting of vectors $\tilde{\mathbf{u}}^f=\tilde{\mathbf{u}}^-$ and $\tilde{\mathbf{u}}^d=\tilde{\mathbf{u}}^+$, this direct relation leads to a dependency matrix that simply corresponds to the identity matrix $\boldsymbol{\alpha}\equiv\mathbf{I}$ and the system of equation is simplified to:

$$\left[\begin{array}{c|c}\mathbf{k}^{ii} & \mathbf{k}^{i+}+\mathbf{k}^{i-}\\ \hline \mathbf{k}^{+i}+\mathbf{k}^{-i} & \mathbf{k}^{++}+\mathbf{k}^{+-}+\mathbf{k}^{-+}+\mathbf{k}^{--}\end{array}\right]\left\{\begin{array}{c}\Delta\tilde{\mathbf{u}}^i\\ \Delta\tilde{\mathbf{u}}^-\end{array}\right\}=-\left\{\begin{array}{c}\mathbf{f}^i\\ \boldsymbol{f}^++\boldsymbol{f}^-\end{array}\right\}. \tag{3.38}$$

In order to use non-conform finite element meshes, the mortar periodic boundary condition (Reis, 2014, Reis and Andrade Pires, 2014) is employed. In this case, the general Expression (3.35) is used, where the dependency matrix α is computed from the so-called mortar matrices (see Appendix B).

In both implementations, RVE corners are prescribed in order to avoid rigid body motion.

Uniform traction boundary condition

Similarly to the mortar periodic constraint, the general linear system of equations of Expression (3.35) is employed for the uniform traction boundary condition. The dependency matrix is obtained from the discretised version of Equation (3.5), which, taking into account the decomposition presented in Expression (3.29), is defined as:

$$\left[\begin{array}{cc} \mathbf{C}^f & \mathbf{C}^d \end{array}\right] \left\{\begin{array}{c} \tilde{\mathbf{u}}^f \\ \tilde{\mathbf{u}}^d \end{array}\right\} = \mathbf{0}. \tag{3.39}$$

The constraint matrices $\mathbf{C}^*$ are assembled from their element counterparts, given by

$$\mathbf{C}_L = \left[\begin{array}{c:c:c} \left(\int H_1 N_1 dA\right)\mathbf{I} & \left(\int H_2 N_1 dA\right)\mathbf{I} & \cdots \\ \left(\int H_1 N_2 dA\right)\mathbf{I} & \left(\int H_2 N_2 dA\right)\mathbf{I} & \cdots \\ \left(\int H_1 N_3 dA\right)\mathbf{I} & \left(\int H_2 N_3 dA\right)\mathbf{I} & \cdots \end{array}\right] \tag{3.40}$$

for 3D problems and, for 2D RVEs:

$$\mathbf{C}_L = \left[\begin{array}{c:c:c} \left(\int H_1 N_1 dA\right)\mathbf{I} & \left(\int H_2 N_1 dA\right)\mathbf{I} & \cdots \\ \left(\int H_1 N_2 dA\right)\mathbf{I} & \left(\int H_2 N_2 dA\right)\mathbf{I} & \cdots \end{array}\right]. \tag{3.41}$$

In the above definition, integrals are computed over element surfaces which intersect RVE boundaries, N_i denotes the i-th component of the outward unit vector $\boldsymbol{N}$ related to the corresponding surface in the reference configuration and H_i represents the value of the i-th shape function.

With straightforward manipulation of (3.39), the following relation between dependent and free boundary nodes arises:

$$\tilde{\mathbf{u}}^d = -\left[\mathbf{C}^d\right]^{-1} \mathbf{C}^f \tilde{\mathbf{u}}^f. \tag{3.42}$$

Therefore, the dependency matrix is defined by:

$$\boldsymbol{\alpha} = -\left[\mathbf{C}^d\right]^{-1} \mathbf{C}^f. \tag{3.43}$$

This matrix is determined during the initialisation of the problem, remaining unchanged during the simulation.

Only one node has to be prescribed, in order to avoid rigid body translation, since rigid body rotation is naturally constrained by Equation (3.5), as shown next. If a displacement fluctuation field results in a rigid rotation about a point $\boldsymbol{Q}$, defined by the rotation tensor $\boldsymbol{R}$, then it may be defined as

$$\tilde{\boldsymbol{u}} = \boldsymbol{Q} + \boldsymbol{R} \cdot (\boldsymbol{Y} - \boldsymbol{Q}) - \boldsymbol{Y}, \tag{3.44}$$

Introducing this definition into Equation (3.5) yields:

$$\int_{\partial\Omega_\mu} (\boldsymbol{Q} \otimes \boldsymbol{N} + \boldsymbol{R} \cdot \boldsymbol{Y} \otimes \boldsymbol{N} - \boldsymbol{R} \cdot \boldsymbol{Q} \otimes \boldsymbol{N} - \boldsymbol{Y} \otimes \boldsymbol{N})\, dA = \mathbf{0}. \tag{3.45}$$

Since $\boldsymbol{Q}$ and $\boldsymbol{R}$ are constant and $\int_{\partial\Omega_\mu} \boldsymbol{N}\, dA = \boldsymbol{0}$, the first and third terms of the above left-hand-side vanish, resulting in

$$\int_{\partial\Omega_\mu} (\boldsymbol{R}\cdot\boldsymbol{Y}\otimes\boldsymbol{N} - \boldsymbol{Y}\otimes\boldsymbol{N})\, dA = \boldsymbol{0} \Leftrightarrow \boldsymbol{R} = \boldsymbol{I}. \tag{3.46}$$

Therefore, the only possible rigid rotation tensor under the minimal kinematic constraint is the identity tensor, which is the absence of rotation indeed.

The choice of dependent *dof* must be carefully performed so that $\mathbf{C}^d$ can be inverted. Due to the matrix size, four dependent *dof* must be defined for 2D models, and nine dependent *dof* are chosen for the 3D case. Therefore, two dependent nodes suffice in 2D, and three in 3D. In the 3D RVE models, where 6-noded triangular (*tri 6*) elements may arise at the boundary, the dependent nodes cannot coincide with the triangle vertices, since the integration of the corresponding shape function on the boundary is null (see Appendix C), and the matrix $\mathbf{C}^d$ becomes singular.

3.3.4 Homogenised stress tensor

When the solution of the RVE equilibrium problem is found, the macroscopic stress is obtained by homogenisation, through Equation (3.22). In a discretised domain, this integration is performed over the volume with Gaussian quadrature rules. A more efficient stress homogenisation can be performed through discretisation of Expression (3.24), where a boundary integral is performed instead. Therefore, the homogenised stress tensor may be computed in vector form as:

$$\mathbf{P} = \frac{1}{V_\mu}\mathbf{D}_b\mathbf{f}_b^{int}, \tag{3.47}$$

where $\mathbf{f}_b^{int}$ contains internal nodal forces at boundary nodes, and $\mathbf{D}_b$ is a suitable matrix with boundary reference nodal coordinates:

$$\mathbf{D}_b = \begin{bmatrix}\mathbf{D}_1 & \mathbf{D}_2 & \dots & \mathbf{D}_{n_b}\end{bmatrix}, \tag{3.48}$$

where n_b denotes the number of nodes on the RVE boundary, and the nodal contributions are given by

$$\mathbf{D}_i = \begin{bmatrix} Y_1\cdot\mathbf{I} \\ Y_2\cdot\mathbf{I} \\ Y_3\cdot\mathbf{I} \end{bmatrix}_i. \tag{3.49}$$

3.3.5 Homogenised consistent tangent modulus

In the context of the Newton-Raphson iterative scheme at the macro-scale problem, the tangent modulus consistent with the state update must be determined. Since in the presented multi-scale framework the homogenised stress in each Gauss point is obtained through the solution of the corresponding RVE equilibrium problem, followed by homogenisation of the first Piola-Kirchhoff tensor, the material tangent modulus:

$$\mathbf{A} = \frac{\partial \boldsymbol{P}}{\partial \boldsymbol{F}} \tag{3.50}$$

has to be computed. In the work of Miehe et al. (1999b) and Feyel and Chaboche (2000) a finite difference approximation is employed to obtain this derivative. However, this is not a robust strategy, since it implies the solution of extra RVE problems, which inevitably increases the computing time of this kind of problems.

Looking at the homogenised stress tensor definition introduced by Expression (3.47), the condensation method can be used to determine the homogenised tangent modulus (Kouznetsova,

2002, Miehe and Koch, 2002, Reis, 2014). Taking into account the vector format employed to store either the homogenised Piola-Kirchhoff stress tensor and the macroscopic deformation gradient:

$$\mathbf{P} = \begin{Bmatrix} P_{11} \\ P_{21} \\ P_{31} \\ P_{12} \\ P_{22} \\ P_{32} \\ P_{13} \\ P_{23} \\ P_{33} \end{Bmatrix}, \quad \mathbf{F} = \begin{Bmatrix} F_{11} \\ F_{21} \\ F_{31} \\ F_{12} \\ F_{22} \\ F_{32} \\ F_{13} \\ F_{23} \\ F_{33} \end{Bmatrix}, \tag{3.51}$$

the material tangent modulus matrix is obtained as:

$$\mathbf{A} = \frac{1}{V_\mu} \mathbf{D}^b \frac{\partial \mathbf{f}^b}{\partial \mathbf{F}}, \tag{3.52}$$

which is developed by the application of the chain rule, as follows

$$\mathbf{A} = \frac{1}{V_\mu} \mathbf{D}^b \frac{\partial \mathbf{f}^b}{\partial \mathbf{u}} \frac{\partial \mathbf{u}}{\partial \mathbf{F}}. \tag{3.53}$$

The discretised displacement field may be split in groups according to the respective nodes position in the RVE, as shown in Section 3.3.2. Introducing this division in the above expression results in:

$$\mathbf{A} = \frac{1}{V_\mu} \mathbf{D}_b \left[\frac{\partial \mathbf{f}^b}{\partial \mathbf{u}^i} \frac{\partial \mathbf{u}^i}{\partial \mathbf{F}} + \frac{\partial \mathbf{f}^b}{\partial \mathbf{u}^f} \frac{\partial \mathbf{u}^f}{\partial \mathbf{F}} + \frac{\partial \mathbf{f}^b}{\partial \mathbf{u}^d} \frac{\partial \mathbf{u}^d}{\partial \mathbf{F}} + \frac{\partial \mathbf{f}^b}{\partial \mathbf{u}^p} \frac{\partial \mathbf{u}^p}{\partial \mathbf{F}} \right]. \tag{3.54}$$

The derivatives of internal forces in relation to displacements correspond to the respective stiffness components:

$$\frac{\partial \mathbf{f}^b}{\partial \mathbf{u}^i} = \mathbf{k}^{bi} \tag{3.55}$$

$$\frac{\partial \mathbf{f}^b}{\partial \mathbf{u}^f} = \mathbf{k}^{bf} \tag{3.56}$$

$$\frac{\partial \mathbf{f}^b}{\partial \mathbf{u}^d} = \mathbf{k}^{bd} \tag{3.57}$$

$$\frac{\partial \mathbf{f}^b}{\partial \mathbf{u}^p} = \mathbf{k}^{bp}. \tag{3.58}$$

Recalling Expression (3.1), where the displacement field is decomposed in the linear component and fluctuation, it is possible to write its discretised version as

$$\mathbf{u} = \mathbf{D}^T (\mathbf{F} - \mathbf{I}) + \tilde{\mathbf{u}}. \tag{3.59}$$

Consequently, derivatives of displacements with respect to the macroscopic deformation gradient are given by:

$$\frac{\partial \mathbf{u}^{(\bullet)}}{\partial \boldsymbol{F}} = \mathbf{D}^{(\bullet),T} + \frac{\partial \tilde{\mathbf{u}}^{(\bullet)}}{\partial \boldsymbol{F}}. \tag{3.60}$$

It is noteworthy that for prescribed nodes $\tilde{\mathbf{u}}^p = \mathbf{0}$, hence the derivative $\partial \tilde{\mathbf{u}}^p / \partial \boldsymbol{F}$ is null.

With the above definitions, Expression (3.54) is rewritten as:

$$\mathbf{A} = \frac{1}{V_\mu}\mathbf{D}^b \left(\begin{bmatrix} \mathbf{k}^{bi} & \mathbf{k}^{bf} & \mathbf{k}^{bd} \end{bmatrix} \begin{bmatrix} \dfrac{\partial \tilde{\mathbf{u}}^i}{\partial \mathbf{F}} \\ \dfrac{\partial \tilde{\mathbf{u}}^f}{\partial \mathbf{F}} \\ \dfrac{\partial \tilde{\mathbf{u}}^d}{\partial \mathbf{F}} \end{bmatrix} + \left[\mathbf{K}^B\right] \left[\mathbf{D}^{total}\right]^T \right), \tag{3.61}$$

where $\left[\mathbf{K}^B\right]$ is the stiffness matrix referring to all boundary degrees of freedom, with a suitable sorting:

$$\left[\mathbf{K}^B\right] = \begin{bmatrix} \mathbf{k}^{bi} & \mathbf{k}^{bf} & \mathbf{k}^{bd} & \mathbf{k}^{bp} \end{bmatrix} = \begin{bmatrix} \mathbf{k}^{fi} & \mathbf{k}^{ff} & \mathbf{k}^{fd} & \mathbf{k}^{fp} \\ \mathbf{k}^{di} & \mathbf{k}^{df} & \mathbf{k}^{dd} & \mathbf{k}^{dp} \\ \mathbf{k}^{pi} & \mathbf{k}^{pf} & \mathbf{k}^{pd} & \mathbf{k}^{pp} \end{bmatrix}, \tag{3.62}$$

and $\left[\mathbf{D}^{total}\right]$ is the assemblage of the coordinate matrices, introduced by Expression (3.49), for all nodes in the micro-scale mesh:

$$\left[\mathbf{D}^{total}\right] = \begin{bmatrix} \mathbf{D}^i & \mathbf{D}^f & \mathbf{D}^d & \mathbf{D}^p \end{bmatrix}. \tag{3.63}$$

Finally, considering the condensation procedure presented in Section 3.3.2, the above expression is simplified to

$$\mathbf{A} = \frac{1}{V_\mu}\mathbf{D}_b \left(\left[\begin{array}{c|c} \mathbf{k}^{bi} & \mathbf{k}^{bf} + \mathbf{k}^{bd}\boldsymbol{\alpha} \end{array}\right] \begin{bmatrix} \dfrac{\partial \tilde{\mathbf{u}}^i}{\partial \mathbf{F}} \\ \dfrac{\partial \tilde{\mathbf{u}}^f}{\partial \mathbf{F}} \end{bmatrix} + \left[\mathbf{K}^B\right] \left[\mathbf{D}^{total}\right]^T \right). \tag{3.64}$$

The derivatives of the displacement fluctuations with respect to the deformation gradient have to be determined to complete the definition of the material tangent modulus. Starting from the fact that when RVE equilibrium is attained:

$$\begin{bmatrix} \dfrac{\partial \mathbf{f}^i}{\partial \mathbf{F}} \\ \dfrac{\partial \mathbf{f}^f}{\partial \mathbf{F}} + \boldsymbol{\alpha}^T \dfrac{\partial \mathbf{f}^d}{\partial \mathbf{F}} \end{bmatrix} = \mathbf{0}, \tag{3.65}$$

with an expansion and mathematical treatment of this expression, following a strategy similar to the applied above, it results the following equation:

$$\left[\begin{array}{c:c} \mathbf{k}^{ii} & \mathbf{k}^{if} + \mathbf{k}^{id}\boldsymbol{\alpha} \\ \hdashline \mathbf{k}^{fi} + \boldsymbol{\alpha}^T\mathbf{k}^{di} & \mathbf{k}^{ff} + \mathbf{k}^{fd}\boldsymbol{\alpha} + \boldsymbol{\alpha}^T\mathbf{k}^{df} + \boldsymbol{\alpha}^T\mathbf{k}^{dd}\boldsymbol{\alpha} \end{array}\right] \begin{bmatrix} \dfrac{\partial \tilde{\mathbf{u}}^i}{\partial \mathbf{F}} \\ \dfrac{\partial \tilde{\mathbf{u}}^f}{\partial \mathbf{F}} \end{bmatrix} + \begin{bmatrix} \mathbf{K}^I \\ \mathbf{K}^F + \boldsymbol{\alpha}^T\mathbf{K}^D \end{bmatrix} \left[\mathbf{D}_{total}\right]^T = \mathbf{0}, \tag{3.66}$$

where

$$\left[\mathbf{K}^\bullet\right] = \begin{bmatrix} \mathbf{k}^{\bullet i} & \mathbf{k}^{\bullet f} & \mathbf{k}^{\bullet d} & \mathbf{k}^{\bullet p} \end{bmatrix}. \tag{3.67}$$

Then, these derivatives can be obtained from the matrix Equation (3.66). Note that in practice, the matrix that results from $\left[\mathbf{K}^I\right]\left[\mathbf{D}^{total}\right]^T$ has 4 columns in 2D problems, or 9 in the 3D case.

Finally, as the current finite element implementation is based on a spatial description, the spatial tangent modulus has to be computed, which is easily calculated from its material counterpart through the relation introduced in Expression (A.16).

3.4 Lagrange multipliers formulation for the uniform traction condition

A multi-scale formulation where the minimal constraint is enforced by Lagrange multipliers is introduced in this section. This kind of formulation allows to identify the reactive nature of the boundary conditions through the analysis of the role of the Lagrange multipliers. The numerical solution of the resulting constrained problem, where the Lagrange multipliers are included as an unknown, leads to an alternative to the condensation method to impose the boundary condition in the linear system of equations.

3.4.1 Principle of multi-scale virtual power

The *method of multi-scale virtual power* is employed to develop the multi-scale formulation. Within the present formulation, the minimal kinematic constraint (Equation (3.5)) is enforced by including the Lagrange multiplier $\boldsymbol{L}$, which is a second-order tensor, in the *principle of multi-scale virtual power* statement:

$$\begin{aligned}\boldsymbol{P}:\delta\boldsymbol{F} = \frac{1}{V_\mu}\Bigg[&\int_{\Omega_\mu}\boldsymbol{P}_\mu:(\delta\boldsymbol{F}+\nabla_Y\delta\tilde{\boldsymbol{u}})\,dV \\ &-\delta\boldsymbol{L}:\left(\int_{\partial\Omega_\mu}\tilde{\boldsymbol{u}}\otimes\boldsymbol{N}dA\right)-\boldsymbol{L}:\left(\int_{\partial\Omega_\mu}\delta\tilde{\boldsymbol{u}}\otimes\boldsymbol{N}dA\right)\Bigg],\quad\forall\,(\delta\boldsymbol{F},\delta\tilde{\boldsymbol{u}},\delta\boldsymbol{L})\,.\end{aligned} \tag{3.68}$$

3.4.2 Micro-scale equilibrium problem

The micro-scale weak equilibrium equation is obtained by setting $\delta\boldsymbol{F}=\boldsymbol{0}$ in Equation (3.68). Therefore, the micro-problem consists in finding the fluctuation field $\tilde{\boldsymbol{u}}$ and the Lagrange multiplier $\boldsymbol{L}$ such that:

$$\int_{\Omega_\mu}\boldsymbol{P}_\mu:\nabla_Y\delta\tilde{\boldsymbol{u}}dV-\delta\boldsymbol{L}:\left(\int_{\partial\Omega_\mu}\tilde{\boldsymbol{u}}\otimes\boldsymbol{N}dA\right)-\boldsymbol{L}:\left(\int_{\partial\Omega_\mu}\delta\tilde{\boldsymbol{u}}\otimes\boldsymbol{N}dA\right)=0. \tag{3.69}$$

The strong form of the equilibrium problem is determined by setting $\delta\boldsymbol{L}=\boldsymbol{0}$ in Equation (3.69), which including the equivalence between Expressions (3.4) and (3.5) results in the following

$$\int_{\Omega_\mu}\left(\boldsymbol{P}_\mu-\boldsymbol{L}\right):\nabla_Y\delta\tilde{\boldsymbol{u}}dV=0. \tag{3.70}$$

Integrating by parts, and taking into account that $\boldsymbol{L}$ is constant on the RVE domain, the above expression is elaborated to

$$\begin{aligned}&\int_{\partial\Omega_\mu}\left(\left[\boldsymbol{P}_\mu-\boldsymbol{L}\right]\cdot\boldsymbol{N}\right)\cdot\delta\tilde{\boldsymbol{u}}dA-\int_{\Omega_\mu}\operatorname{div}\left[\boldsymbol{P}_\mu-\boldsymbol{L}\right]\cdot\delta\tilde{\boldsymbol{u}}dV= \\ &\int_{\partial\Omega_\mu}\left(\left[\boldsymbol{P}_\mu-\boldsymbol{L}\right]\cdot\boldsymbol{N}\right)\cdot\delta\tilde{\boldsymbol{u}}dA-\int_{\Omega_\mu}\operatorname{div}\boldsymbol{P}_\mu\cdot\delta\tilde{\boldsymbol{u}}dV=0\end{aligned} \tag{3.71}$$

Since this holds for any $\delta\tilde{\boldsymbol{u}}$, then the equations stating the strong equilibrium are expressed by

$$\boldsymbol{P}_\mu\cdot\boldsymbol{N}=\boldsymbol{L}\cdot\boldsymbol{N},\quad\text{on }\partial\Omega_\mu, \tag{3.72}$$

$$\operatorname{div}\boldsymbol{P}_\mu=\boldsymbol{0},\quad\text{in }\Omega_\mu. \tag{3.73}$$

Looking at Equation (3.72), it becomes clear that the Lagrange multiplier is directly related to the external traction on the RVE boundary,

$$\boldsymbol{t}_{\mu 0}=\boldsymbol{L}\cdot\boldsymbol{N}. \tag{3.74}$$

In addition, since the Lagrange multiplier $\boldsymbol{L}$ is constant on the RVE boundary, it is shown that the minimal constraint expressed by Equation (3.5) results in a uniform traction on the boundary.

3.4.3 Homogenised stress tensor

The expression for the homogenised Piola-Kirchhoff is obtained from the *principle of multi-scale virtual power* by defining $\delta \boldsymbol{L} = \boldsymbol{0}$ and $\delta \tilde{\boldsymbol{u}} = \boldsymbol{0}$ in Equation (3.68), which yields:

$$\boldsymbol{P} : \delta \boldsymbol{F} = \frac{1}{V_\mu} \int_{\Omega_\mu} \boldsymbol{P}_\mu : \delta \boldsymbol{F} dV \Rightarrow \boldsymbol{P} = \frac{1}{V_\mu} \int_{\Omega_\mu} \boldsymbol{P}_\mu dV. \tag{3.75}$$

The above expression may be developed through integration by parts of the right-hand side:

$$\begin{aligned}
&\int_{\Omega_\mu} \boldsymbol{P}_\mu dV = \int_{\Omega_\mu} \boldsymbol{P}_\mu \cdot \nabla_Y \boldsymbol{Y} dV \\
\Rightarrow &\int_{\Omega_\mu} P_{ij} \frac{\partial Y_k}{\partial Y_j} dV = \int_{\Omega_\mu} \frac{\left(\partial P_{ij} Y_k\right)}{\partial Y_j} dV - \int_{\Omega_\mu} \frac{\partial P_{ij}}{\partial Y_j} Y_k dV \\
\Leftrightarrow &\int_{\Omega_\mu} P_{ij} \frac{\partial Y_k}{\partial Y_j} dV = \int_{\partial\Omega_\mu} P_{ij} N_j Y_k dA - \int_{\Omega_\mu} \frac{\partial P_{ij}}{\partial Y_j} Y_k dV \\
\Rightarrow &\int_{\Omega_\mu} \boldsymbol{P}_\mu dV = \int_{\partial\Omega_\mu} \boldsymbol{P}_\mu \cdot \boldsymbol{N} \otimes \boldsymbol{Y} dA - \int_{\Omega_\mu} \mathrm{div}_Y \boldsymbol{P}_\mu \otimes \boldsymbol{Y} dV.
\end{aligned} \tag{3.76}$$

Therefore the homogenised Piola-Kirchhoff stress tensor is rewritten as

$$\boldsymbol{P} = \frac{1}{V_\mu} \left[\int_{\partial\Omega_\mu} \boldsymbol{P}_\mu \cdot \boldsymbol{N} \otimes \boldsymbol{Y} dA - \int_{\Omega_\mu} \mathrm{div}_Y \boldsymbol{P}_\mu \otimes \boldsymbol{Y} dV \right]. \tag{3.77}$$

In view of the strong form of the micro-problem, the second term of the above is null and the homogenised stress $\boldsymbol{P}$ can be expressed as:

$$\boldsymbol{P} = \frac{1}{V_\mu} \int_{\partial\Omega_\mu} \boldsymbol{L} \cdot \boldsymbol{N} \otimes \boldsymbol{Y} dA. \tag{3.78}$$

Developing this expression as follows:

$$P_{ik} = \frac{1}{V_\mu} \int_{\partial\Omega_\mu} L_{ij} N_j Y_k dA = \frac{1}{V_\mu} L_{ij} \int_{\partial\Omega_\mu} N_j Y_k dA \tag{3.79}$$

$$= \frac{1}{V_\mu} L_{ij} \int_{\Omega_\mu} \frac{\partial Y_k}{\partial Y_j} dV = \frac{1}{V_\mu} L_{ij} \int_{\Omega_\mu} \delta_{kj} dV = L_{ik}, \tag{3.80}$$

it is proved that the Lagrange multiplier $\boldsymbol{L}$ equals the homogenised Piola-Kirchhoff stress tensor $\boldsymbol{P}$:

$$\boldsymbol{L} = \boldsymbol{P}. \tag{3.81}$$

3.4.4 Numerical solution of the micro-equilibrium problem

Similarly to the approach for the condensation method (see Section 3.3.2), the RVE degrees of freedom are split into interior, free and prescribed *dof*, where the last two groups belong to the RVE boundary. The displacement fluctuation, virtual displacement and internal force vectors are written as:

$$\tilde{\mathbf{u}} = \begin{Bmatrix} \tilde{\mathbf{u}}^i \\ \tilde{\mathbf{u}}^f \\ \tilde{\mathbf{u}}^p \end{Bmatrix}, \quad \delta\tilde{\mathbf{u}} = \begin{Bmatrix} \delta\tilde{\mathbf{u}}^i \\ \delta\tilde{\mathbf{u}}^f \\ \delta\tilde{\mathbf{u}}^p \end{Bmatrix}, \quad \mathbf{f}^{int} = \begin{Bmatrix} \mathbf{f}^i \\ \mathbf{f}^f \\ \mathbf{f}^p \end{Bmatrix}, \tag{3.82}$$

where $\tilde{\mathbf{u}}^p = \delta\tilde{\mathbf{u}}^p = \mathbf{0}$. The Lagrange multiplier vector is denoted by $\boldsymbol{\lambda}_L$. The discretised version of the minimal kinematic constraint is defined by a suitable constraint matrix $\mathbf{C}_L$ (see Section 3.3.3), such that

$$\mathbf{C}_L \cdot \tilde{\mathbf{u}} = \mathbf{0} \Leftrightarrow \begin{bmatrix} \mathbf{0} & \mathbf{C}^f \end{bmatrix} \cdot \begin{Bmatrix} \tilde{\mathbf{u}}^i \\ \tilde{\mathbf{u}}^f \end{Bmatrix} = \mathbf{0}. \tag{3.83}$$

Therefore, the finite element discretised version of Equation (3.69) is written as

$$\delta\tilde{\mathbf{u}}^T \cdot \mathbf{f}^{int} - \delta\boldsymbol{\lambda}_L^T \cdot (\mathbf{C}_L \cdot \tilde{\mathbf{u}}) - \delta\tilde{\mathbf{u}}^T \cdot \left(\mathbf{C}_L^T \cdot \boldsymbol{\lambda}_L\right) = 0. \tag{3.84}$$

Since this must hold for any $\delta\tilde{\mathbf{u}}$ and $\delta\boldsymbol{\lambda}_L$, then the residual vector defining the discretised problem is expressed by

$$\mathbf{r} = \begin{Bmatrix} \mathbf{f}^{int} - \mathbf{C}_L^T \cdot \boldsymbol{\lambda}_L \\ \mathbf{C}_L \cdot \tilde{\mathbf{u}} \end{Bmatrix} = \mathbf{0}. \tag{3.85}$$

After linearisation, the resulting linear system of equations is defined as

$$\begin{bmatrix} \mathbf{k}^{ii} & \mathbf{k}^{if} & \mathbf{0} \\ \mathbf{k}^{fi} & \mathbf{k}^{ff} & -\mathbf{C}^f \\ \mathbf{0} & \mathbf{C}^f & \mathbf{0} \end{bmatrix} \begin{Bmatrix} \Delta\tilde{\mathbf{u}}^i \\ \Delta\tilde{\mathbf{u}}^f \\ \Delta\boldsymbol{\lambda} \end{Bmatrix} = - \begin{Bmatrix} \mathbf{f}^i \\ \mathbf{f}^f - \mathbf{C}^{f,T} \cdot \boldsymbol{\lambda}_L \\ \mathbf{C}^f \cdot \tilde{\mathbf{u}}^f \end{Bmatrix}. \tag{3.86}$$

3.4.5 Homogenised consistent tangent modulus

At the micro-scale equilibrium solution, the derivative of the residual vector with regard to the macro-deformation gradient is null:

$$\frac{\partial}{\partial \mathbf{F}} \begin{Bmatrix} \mathbf{f}^i \\ \mathbf{f}^f - \mathbf{C}^{f,T} \cdot \boldsymbol{\lambda}_L \\ \mathbf{C}^f \cdot \tilde{\mathbf{u}}^f \end{Bmatrix} = \begin{bmatrix} \dfrac{\partial \mathbf{f}^i}{\partial \mathbf{F}} \\ \dfrac{\partial \mathbf{f}^f}{\partial \mathbf{F}} - \mathbf{C}^{f,T} \cdot \dfrac{\partial \boldsymbol{\lambda}_L}{\partial \mathbf{F}} \\ \mathbf{C}^f \cdot \dfrac{\partial \tilde{\mathbf{u}}^f}{\partial \mathbf{F}} \end{bmatrix} = \mathbf{0}. \tag{3.87}$$

The derivatives $\partial \mathbf{f}^\bullet / \partial \mathbf{F}$ are developed as (see Section 3.3.5)

$$\begin{aligned} \frac{\partial \mathbf{f}^\bullet}{\partial \mathbf{F}} &= \frac{\partial \mathbf{f}^\bullet}{\partial \mathbf{u}^i} \frac{\partial \mathbf{u}^i}{\partial \mathbf{F}} + \frac{\partial \mathbf{f}^\bullet}{\partial \mathbf{u}^f} \frac{\partial \mathbf{u}^f}{\partial \mathbf{F}} + \frac{\partial \mathbf{f}^\bullet}{\partial \mathbf{u}^p} \frac{\partial \mathbf{u}^p}{\partial \mathbf{F}} \\ &= \mathbf{k}^{\bullet i} \cdot \left(\mathbf{D}^{i,T} + \frac{\partial \tilde{\mathbf{u}}^i}{\partial \mathbf{F}} \right) + \mathbf{k}^{\bullet f} \cdot \left(\mathbf{D}^{f,T} + \frac{\partial \tilde{\mathbf{u}}^f}{\partial \mathbf{F}} \right) + \mathbf{k}^{\bullet p} \cdot \mathbf{D}^{p,T}, \end{aligned} \tag{3.88}$$

while the derivatives $\partial\tilde{\mathbf{u}}/\partial\mathbf{F}$ and $\partial\boldsymbol{\lambda}_L/\partial\mathbf{F}$ are unknown. Therefore, Expression (3.87) can be rearranged in the following linear system of equations with multiple right-hand-sides:

$$\begin{bmatrix} \mathbf{k}^{ii} & \mathbf{k}^{if} & \mathbf{0} \\ \mathbf{k}^{fi} & \mathbf{k}^{ff} & -\mathbf{C}^{f,T} \\ \mathbf{0} & \mathbf{C}^f & \mathbf{0} \end{bmatrix} \cdot \begin{bmatrix} \dfrac{\partial \tilde{\mathbf{u}}^i}{\partial \mathbf{F}} \\ \dfrac{\partial \tilde{\mathbf{u}}^f}{\partial \mathbf{F}} \\ \dfrac{\partial \boldsymbol{\lambda}_L}{\partial \mathbf{F}} \end{bmatrix} = - \begin{bmatrix} \mathbf{k}^{ii} & \mathbf{k}^{if} & \mathbf{k}^{ip} \\ \mathbf{k}^{fi} & \mathbf{k}^{ff} & \mathbf{k}^{fp} \\ \mathbf{0} & \mathbf{0} & \mathbf{0} \end{bmatrix} \cdot \begin{bmatrix} \mathbf{D}^i & \mathbf{D}^f & \mathbf{D}^p \end{bmatrix}^T. \tag{3.89}$$

Since the Lagrange multiplier vector $\boldsymbol{\lambda}_L$ is coincident with the homogenised Piola-Kirchoff stress vector $\mathbf{P}$, then the material tangent modulus is obtained from the solution of this system of equations:

$$\mathbf{A} = \frac{\partial \mathbf{P}}{\partial \mathbf{F}} = \frac{\partial \boldsymbol{\lambda}_L}{\partial \mathbf{F}}. \tag{3.90}$$

3.5 A comparison between the condensation method and the Lagrange multiplier method

The numerical solution of the micro-scale equilibrium with the condensation method is described in Section 3.3. In spite of being able to reduce the number of unknowns in the linear system of

equations, a pre-processing of the tangent matrix, involving several matrix multiplications, is required in the case of the mortar periodic and uniform traction boundary conditions, due to the concept of dependency matrix (c.f. Equation (3.35)). Alternatively, the Lagrange multiplier method can be directly applied to the solution of the constrained micro-equilibrium problem, as presented in Section 3.4 for the uniform traction condition. The Lagrange multiplier formulation for the mortar periodic condition is introduced in Appendix B.4. This strategy is often avoided in the literature due to the increase of the number of unknowns on the linear system of equations and the resulting saddle point structure of the tangent matrix (Kouznetsova, 2002, Nguyen et al., 2016, Reis and Andrade Pires, 2014). It must be remarked that two direct linear solvers (MA41 (HSL, 2013) and Intel Pardiso (Intel, 2018)) have been tested for the solution of the system of equations resulting from the Lagrange multiplier method, and both are able to deal correctly with the tangent matrix saddle point structure.

The performance of both strategies is assessed in this section, for micro-scale analyses with RVE models requiring distinct computational efforts and for a coupled FE^2 simulation. All the simulations are performed on the same computer, which has a processor Intel i7-3770k (4 physical cores, 3.50 GHz) and 16 GB RAM. The Intel Pardiso direct solver (Intel, 2018) is employed in all simulations.

3.5.1 Micro-scale simulations

Aiming to compare the performance of the condensation method with the Lagrange multiplier method, in terms of computational time and memory requirements, under different conditions, four microstructures involving distinct mesh sizes and constitutive models are analysed.

RVE with elastic constituents

In the first place, the RVE model for a composite shown in Figure 3.5 is analysed. Both the matrix and rigid inclusions are described by linear elastic laws with the properties presented in Table 3.1. The mesh is composed by 896 8-noded quadrilateral elements with reduced integration, resulting in 2793 nodes, which requires a relatively low computational cost. A vertical traction macro-deformation gradient is prescribed in 10 increments:

$$\boldsymbol{F} = \begin{bmatrix} 1.0 & 0.0 \\ 0.0 & 1.2 \end{bmatrix}. \tag{3.91}$$

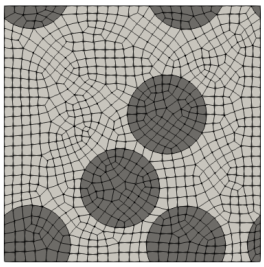

Figure 3.5: RVE model for a composite with elastic constituents. Mesh with 896 elements and 2793 nodes.

RVE with elasto-plastic matrix

A more complex microstructure is considered in this example, where voids are included, in addition to a larger number of inclusions. Two different meshes are employed, where the model is discretised

Table 3.1: Material properties for the constituents of the RVE shown in Figure 3.5.

	Matrix	Inclusions
Young modulus (E) [GPa]	72.4	400.0
Poisson ratio (ν)	0.3	0.3

by 8-noded quadrilateral elements, as shown in Figure 3.6. The von Mises elasto-plastic constitutive law is used to model the matrix, while the inclusions are elastic, with the material properties defined in Table 3.2. The following macro-deformation gradient is enforced in 50 increments:

$$\boldsymbol{F} = \begin{bmatrix} 1.0 & 0.01 \\ 0.01 & 1.0 \end{bmatrix}. \tag{3.92}$$

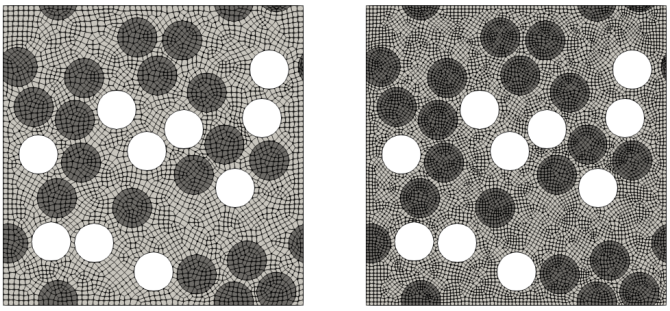

(a) Mesh 1 - 3763 elements, 11756 nodes (b) Mesh 2 - 7765 elements, 23968 nodes

Figure 3.6: Meshes used for the RVE with elasto-plastic matrix, elastic inclusions and voids.

Table 3.2: Material properties for the constituents of the RVE shown in Figure 3.6.

	Matrix	Inclusions
Young modulus (E) [GPa]	30.0	74.0
Poisson ratio (ν)	0.3	0.2
Yielding stress (σ_{y0}) [MPa]	93.0	
Hardening modulus (H) [MPa]	100.0	

3D RVE with a spherical void

The three dimensional RVE model presented in Figure 3.7 describes a material with a microstructure that consists of spherical voids in a von Mises elasto-plastic matrix, with 2% void volume fraction. The mesh contains 1864 20-noded hexahedral elements, with reduced integration, resulting in 8726 nodes. The material properties are summarised in Table 3.3. The macroscopic deformation gradient enforced is defined by:

$$\boldsymbol{F} = \begin{bmatrix} 1.0052 & 0.000 & 0.006 \\ 0.000 & 1.0052 & 0.000 \\ 0.000 & 0.000 & 1.0052 \end{bmatrix}, \tag{3.93}$$

and prescribed in 10 increments.

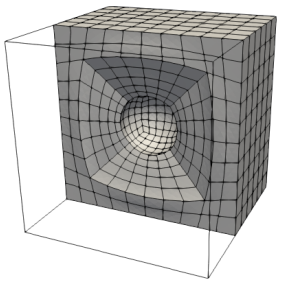

Figure 3.7: Clipping of the finite element model for the RVE with a spherical void occupying 2% of the volume (1864 elements, 8726 nodes).

Table 3.3: Material properties for the RVE shown in Figure 3.7.

Young modulus (E) [GPa]	210.0
Poisson ratio (ν)	0.3
Yielding stress (σ_{y0}) [MPa]	240.0
Hardening modulus (H) [MPa]	100.0
Void volume fraction (f)	2%

Results

The contour plots of the equivalent strain and equivalent Cauchy stress on the deformed meshes are shown in Figures 3.8 to 3.10. It is important to remark that the results obtained with both strategies coincide.

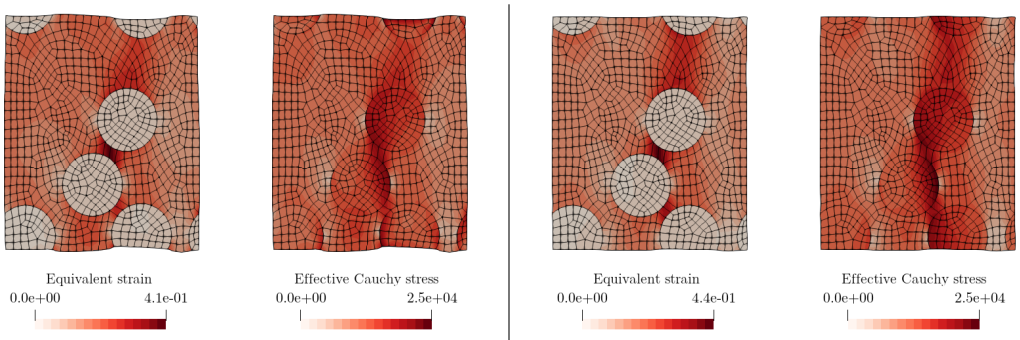

(a) Uniform traction (b) Mortar periodic

Figure 3.8: Contour plots of the equivalent strain (left) and equivalent stress [MPa] (right) in the RVE with elastic constituents.

In what refers to the computational performance of each method, the time elapsed in the linear solver for a typical iteration, the time for that iteration and the total simulation time are summarised in Tables 3.4 to 3.6, along with the speedup S obtained with the Lagrange multiplier implementation:

$$S = \frac{t_{condensation}}{t_{Lagrangemult.}}. \tag{3.94}$$

Additionaly, the memory usage peak observed in each case is listed in the Table 3.7.

In the simulations presented here, significant speedups are achieved by employing the Lagrange multiplier implementation, despite increasing the number of unknowns in the system of equations. Regarding the uniform traction boundary condition, most of the speedup is achieved due to a sig-

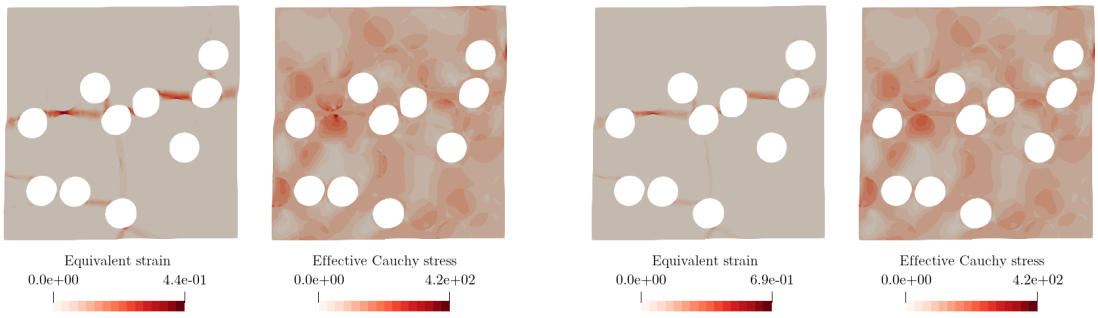

(a) Uniform traction, Mesh 1

(b) Uniform traction, Mesh 2

(c) Mortar periodic, Mesh 1

(d) Mortar periodic, Mesh 2

Figure 3.9: Contour plots of the equivalent strain (left) and equivalent stress [MPa] (right) on the RVE with voids and inclusions. Mesh is omitted for the sake of clarity.

nificant reduction in the direct solver time. As shown in Table 3.8, the number of non-zeros on the tangent matrix is strongly affected by the implementation. The condensation method leads to a much larger number of non-zeros due to the manipulation of the stiffness sub-matrices, which are multiplied by the dependency matrix (Equation (3.35)), resulting in blocks with dense sub-matrices. Obviously, this requires additional effort in the solution of the linear system of equations.

For the mortar periodic condition, the sparsity of the tangent matrix is not affected significantly. The solver time also remains similar, despite the important increase in the number of unknowns. In this case, most of the time spent in the condensation implementation is in the manipulation of the tangent matrix, requiring several matrix multiplications, which is obviated with the Lagrange multiplier implementation. This process is also observed with the uniform traction condition, but is not so critical due to the smaller dimensions of the dependency matrix and condensation related sub-matrices.

This last observation also explains the reduction in the memory requirements (see Table 3.7), since the allocation of the condensation related sub-matrices is not needed within the Lagrange multiplier implementation.

In summary, in spite of increasing the number of unknowns and changing the structure of the tangent matrix, the use of the Lagrange multiplier method to enforce micro-scale constraint shows a much superior computational performance, regarding either computing time and memory requirements.

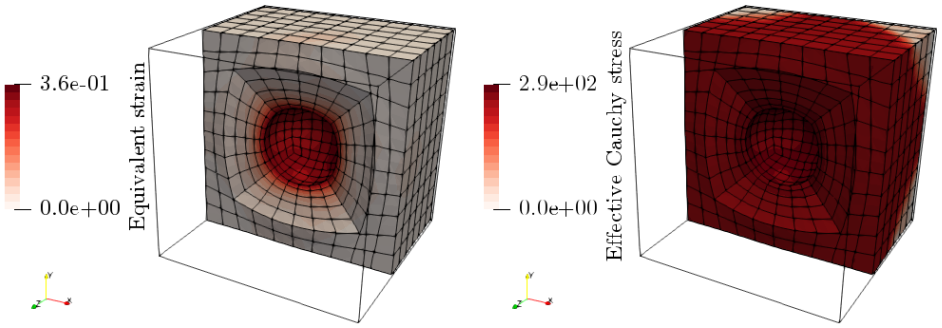

Figure 3.10: Contour plots of the equivalent strain (left) and equivalent stress [MPa] (right) on the 3D RVE with spherical void (uniform traction).

Table 3.4: Computational time comparison for the RVE with elastic inclusions.

		Time (s)		Speedup
		Cond.	L.M.	
Uniform traction	solver	0.071	0.043	1.65
	iteration	0.101	0.061	1.66
	total	3.53	2.35	1.50
Mortar periodic	solver	0.058	0.069	0.84
	iteration	0.129	0.095	1.36
	total	3.85	2.85	1.35

Table 3.5: Computational time comparison for the RVE with voids and inclusions.

	Mesh 1				Mesh 2			
	Time (s)			Speedup	Time (s)			Speedup
		Cond.	L.M.			Cond.	L.M.	
Uniform traction	solver	0.521	0.200	2.61	solver	1.89	0.606	3.12
	iteration	0.763	0.278	2.74	iteration	1.25	0.442	2.83
	total	253.6	88.6	2.66	total	677.6	226.6	2.99
Mortar periodic	solver	0.250	0.222	1.13	solver	0.563	0.523	1.08
	iteration	1.11	0.304	3.65	iteration	3.99	0.685	5.82
	total	312.3	89.6	3.49	total	1391	247.5	5.62

Table 3.6: Computational time comparison for the 3D RVE with spherical void.

		Time (s)		Speedup
		Cond.	L.M.	
Uniform traction	solver	24.2	4.3	5.63
	iteration	25.7	4.6	5.59
	total	1952	369.8	5.28

Table 3.7: Memory peak observed for each case with both implementations (in MB), along with the fraction of memory needed by the Lagrange multiplier method comparing with the condensation method.

			Cond.	L.M.	%
Elastic composite (Figure 3.5)		U. Traction	57.1	36	63.0
		Mortar P.	82.5	39.5	47.9
Voids and inclusions (Figure 3.6)	Mesh 1	U. Traction	307	120.4	39.2
		Mortar P.	400.6	133.2	33.3
	Mesh 2	U. Traction	770.7	247.1	32.1
		Mortar P.	1013.7	286.4	28.3
Spherical void (Figure 3.7)		U. Traction	3973.1	904.6	22.8

Table 3.8: Comparison of the sparsity of the resulting tangent matrix. The values represent the percentage of non-zero values in the tangent matrix.

			Cond.	L.M.
Elastic composite (Figure 3.5)		U. Traction	1.1%	0.55%
		Mortar P.	0.63%	0.52%
Voids and inclusions (Figure 3.6)	Mesh 1	U. Traction	0.29%	0.13%
		Mortar P.	0.14%	0.13%
	Mesh 2	U. Traction	0.15%	0.06%
		Mortar P.	0.07%	0.06%
Spherical void (Figure 3.7)		U. Traction	4.9%	0.60%

3.5.2 FE^2 simulation

The impact of the speedup obtained by employing Lagrange multipliers to the micro-scale solution in a coupled scale FE^2 simulation is assessed in this section.

The 2D beam model represented in Figure 3.11 is subjected to a bending rotation of 120°, employing the RVE presented in Figure 3.5, with the material properties from Table 3.1, to model its underlying microstructure. The macro-scale finite element model contains 200 8-noded quadrilateral elements, with reduced integration, resulting in 709 nodes and a total of 800 RVEs to be analysed. The rotation is applied in 30 increments. This simulation is performed in parallel, with the master-slave scheme proposed on Section 8.1, using 4 slave processors.

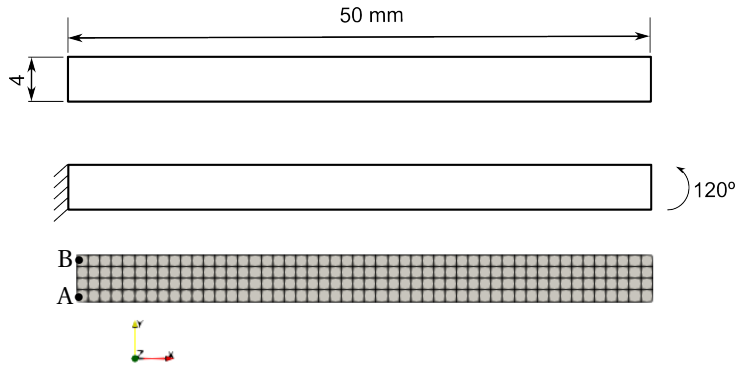

Figure 3.11: Geometry and finite element model for the beam subjected to a bending rotation. Points A and B identify the positions of RVEs analysed in the results.

Results

The contour plots of the equivalent strain and effective Cauchy stress are shown in Figures 3.12 and 3.13 for the macro-scale model and two RVEs in the positions A and B defined in Figure 3.11.

The performance of both implementations in terms of elapsed time per macro-scale iteration and total simulation time is compared on Table 3.9.

As expected, the Lagrange multiplier implementation allows to solve the problem faster than with the condensation method. The speedup obtained in the coupled simulation is even superior to the corresponding micro-scale simulation (see Table 3.4). This is explained by the additional time gained in the computation of the homogenised consistent tangent operator.

Table 3.9: Comparison of the time elapsed for a macro-iteration and total simulation time for the FE^2 simulation of the bending beam.

		Time (s)		Speedup
		Cond.	L.M.	
Uniform traction	iteration	153.7	57.5	2.67
	total	20650	7407	2.79
Mortar periodic	iteration	129.3	67.6	1.91
	total	17670	8425	2.10

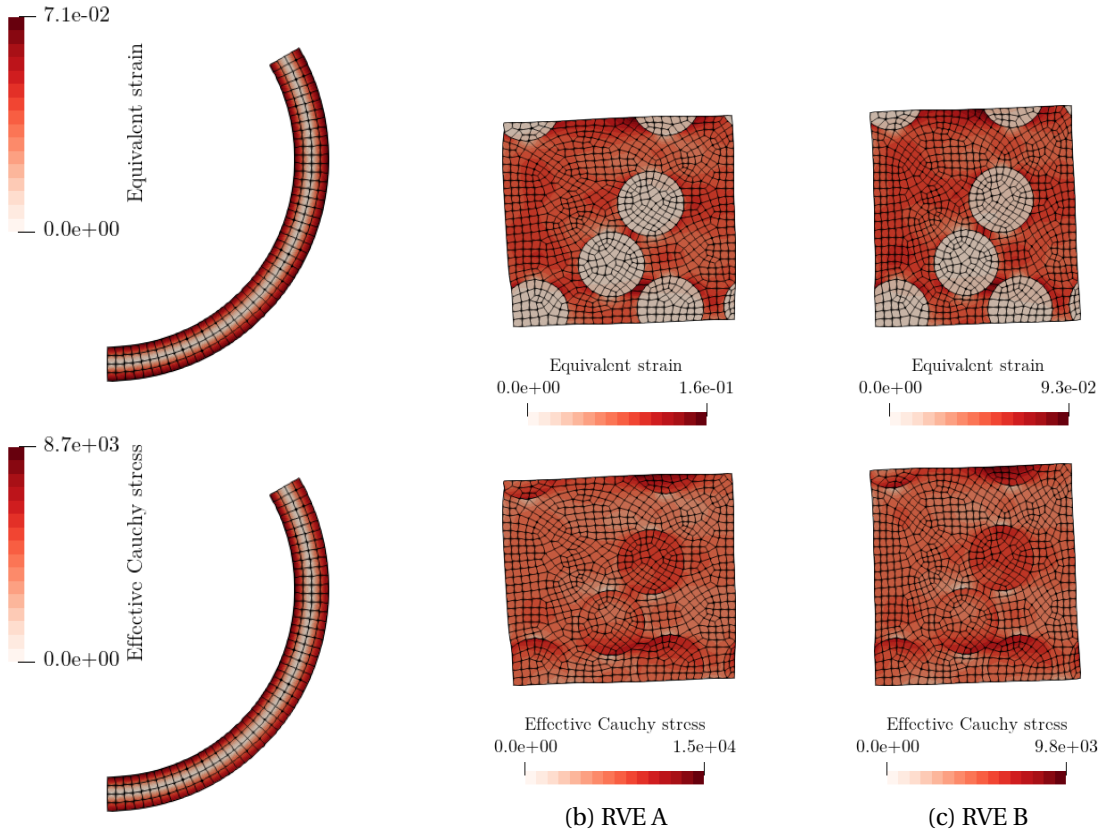

(a) Macro-scale

(b) RVE A

(c) RVE B

Figure 3.12: Contour plots of the equivalent strain (top) and equivalent stress [MPa] (bottom) for the FE^2 simulation of the bending beam, with uniform traction condition at the micro-scale.

3.6 Conclusions

The *method of multi-scale virtual power* is employed to introduce a multi-scale formulation based on first-order computational homogenisation in this chapter. Two different approaches are presented to enforce the micro-scale boundary conditions (uniform traction and mortar periodic) in the resulting finite element equilibrium problem: (i) the condensation method and (ii) the Lagrange multiplier method. The Lagrange multiplier-based formulation for the uniform traction condition allows to clearly identify the reactive nature related to minimal constraint. In spite of leading to a linear system of equations with a greater number of unknowns, the Lagrange multiplier implementation requires less computational effort, regarding either computing time and memory requirements, to solve the micro-scale problem. In a FE^2 framework, the Lagrange multiplier method also enables a more efficient computation of the consistent tangents. These time and memory savings are of utmost importance in FE^2 simulations, since most of computational time is spent in the solution of the RVE problems.

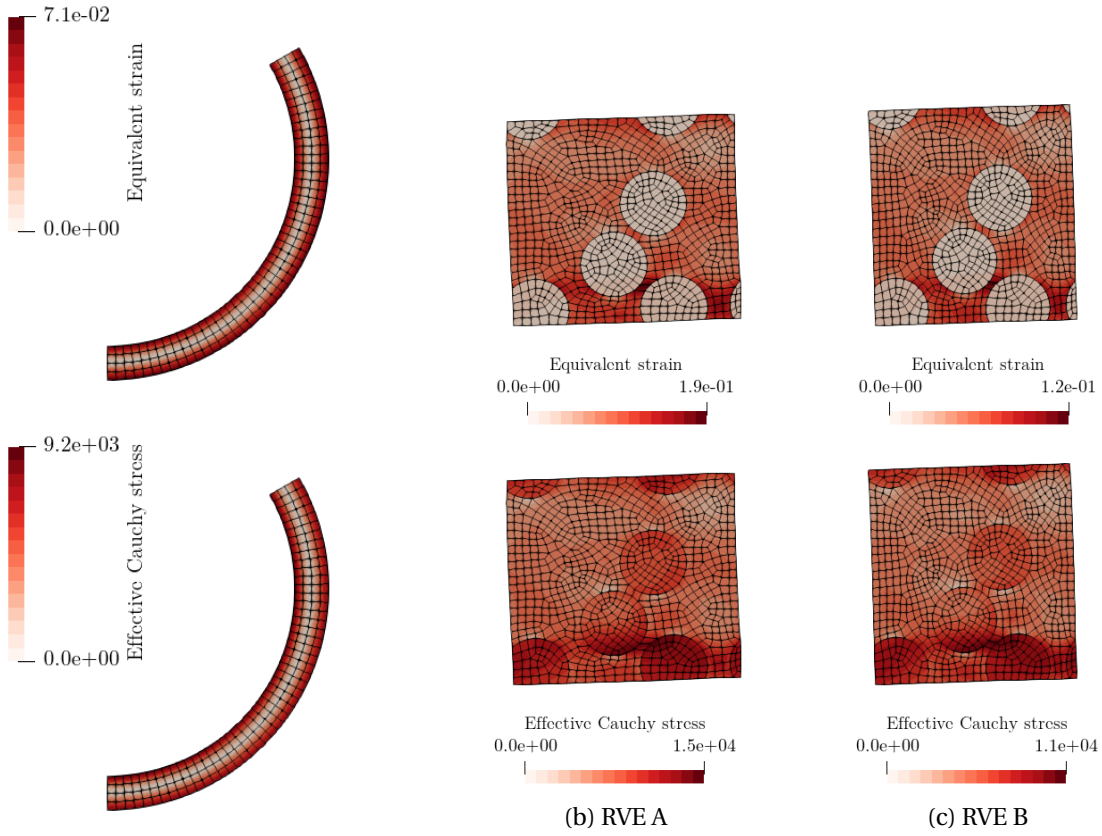

(a) Macro-scale

(b) RVE A

(c) RVE B

Figure 3.13: Contour plots of the equivalent strain (top) and equivalent stress [MPa] (bottom) for the FE^2 simulation of the bending beam, with mortar periodic condition at the micro-scale.

Chapter 4

Mechanics of second-order continuum

The mechanical behaviour of solids is usually described by classical 1^{st}-order continuum theories (also known as Cauchy continuum), as presented in Section 2, which are the so-called local approaches in the sense that the constitutive response at a given point is a function of the strain (based on the displacement gradient) and state variables at that point. This lies on the assumption that the underlying micro-structural mechanisms driving the material response occur at a spatial scale much smaller than the structural scale, and a uniform strain field undergoes on the micro-structural region dictating the response for a given point at the macro-scale. Classical 1^{st}-order theories are not appropriate to model situations where this assumption is violated, i.e., when the deformation field wavelength at the structural level approaches the material characteristic length, related to the material micro-structural length scale.

For instance, 1^{st}-order theories are unable to model strain localisation properly, due to the loss of ellipticity of the governing equilibrium equations. Consequently, the boundary value problem becomes ill-posed and the associated finite element solution becomes dependent of the spatial discretisation (Bažant and Lin, 1988, Bažant and Pijaudier-Cabot, 1988, Bazant and Jirásek, 2002, Jirásek, 1998, Jirásek and Rolshoven, 2003). Non-local approaches have been developed within the framework of 1^{st}-order continuum aiming to minimize the mesh dependence pathology (Andrade et al., 2009, 2011, 2014, Jirásek and Patzák, 2002, Pijaudier-Cabot and Bazant, 1987, Reis et al., 2018). The basic idea is to include a characteristic length and make the behaviour at a given point depend on the neighbouring points which are closer than the defined length. Some authors employ gradient-based formulations for damage and plasticity (De Borst and Mühlhaus, 1992, Peerlings et al., 1996, 2001), where gradients of the state variables are incorporated in the constitutive equations.

Second-order continuum theories, which include the second gradient of the displacement field in the kinematical description, are intrinsically non-local, naturally incorporating the material characteristic length, in spite of maintaining the local character of the constitutive laws. Size effects can also be captured within the framework of second-order continuum models for solids behaviour. Higher-order theories have arisen from the pioneering works of Cosserat and Cosserat (1909), Mindlin (1964), Mindlin and Eshel (1968), Toupin (1964). In fact, most of the applications focus on guaranteeing mesh independence (Matsushima et al., 2002) and capture size effects (Fleck et al., 1994). A comprehensive review on general higher-order theories is provided by Bertram (2017).

In the context of the present thesis, a second-order continuum description is of utmost importance in order to achieve an enhanced description of micro-structural phenomena through a second-order homogenisation framework. In this sense, in order for the micro-scale kinematics to be enriched taking into account the second gradient of the macro displacements in a consistent fashion, the macro-scale must be properly modelled by a second-order continuum model.

Therefore, a full gradient formulation for 2^{nd}-order continuum at large strains is presented in this chapter, along with the numerical solution through the finite element method. A well estab-

lished 2D finite element is adopted and a 3D hexahedral element is proposed. Numerical examples are used to assess the finite element implementation, where a relatively simple second-order constitutive law is considered.

4.1 Second gradient of displacements

Consider a 2nd-order continuum body occupying the domain Ω in the reference configuration, which is subjected to external body forces $\boldsymbol{b}_0$, external boundary tractions $\boldsymbol{t}_0$ and double tractions $\boldsymbol{r}_0$ on part of its boundary $\partial\Omega^N$, and line forces $\boldsymbol{s}_0$ on Γ^N (Figure 4.1). In addition to the deformation gradient $\boldsymbol{F}$, the material constitutive behaviour of this body is also driven by the second gradient of the displacement field $\mathbf{G}$, which can be seen as the gradient of the displacement gradient:

$$\mathbf{G} = \nabla_X \boldsymbol{F} = \nabla_X (\nabla_X \boldsymbol{u}) \Rightarrow G_{ijk} = \frac{\partial u_i}{\partial X_j \partial X_k}. \tag{4.1}$$

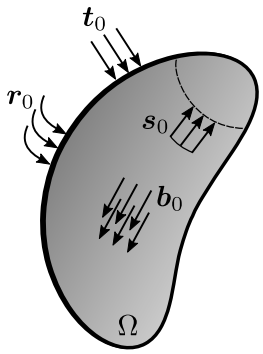

Figure 4.1: Schematic representation of a 2nd-order continuum body subjected to external actions.

While the 1st Piola-Kirchhoff is dual to the deformation gradient, the higher-order stress denoted by $\mathbf{Q}$ is the conjugate quantity of the second displacements gradient.

A physical interpretation of the 2nd-gradient $\mathbf{G}$ and its dual stress $\mathbf{Q}$ is found in the contribution of Polizzoto (2016). Basically, when the second-gradient is considered in the solid deformation kinematics, the infinitesimal volume element associated with a given point undergoes second-order deformation modes, which are accounted for in the strain energy density function. This is illustrated in Figure 4.2.

4.2 Weak equilibrium equation

Based on the work of Kouznetsova (2002), a variational approach is employed to determine the weak equilibrium equation. All the formulation is developed in the material configuration.

The *Virtual Work Principle* states that the internal virtual work, that accounts for in the contribution of the higher-order stress and the second gradient, must equal the variation of the external work, where the contribution of the double tractions $\boldsymbol{r}_0$, which are dual to the normal displacements gradient $D_0\delta\boldsymbol{u} = \nabla_X \delta\boldsymbol{u} \cdot \boldsymbol{N}$, is also included. Therefore the weak equilibrium equation yields:

$$\int_\Omega \left(\boldsymbol{P} : \delta\boldsymbol{F} + \mathbf{Q} \vdots \delta\mathbf{G} \right) dV = \int_\Omega \boldsymbol{b}_0 \cdot \delta\boldsymbol{u} dV + \int_{\partial\Omega^N} \boldsymbol{t}_0 \cdot \delta\boldsymbol{u} dA + \int_{\partial\Omega^N} \boldsymbol{r}_0 \cdot D_0\delta\boldsymbol{u} dA + \int_{\Gamma^N} \boldsymbol{s}_0 \cdot \delta\boldsymbol{u} dA, \tag{4.2}$$

where $\boldsymbol{b}_0$ denotes the external body forces, $\boldsymbol{t}_0$ the external boundary tractions, $\boldsymbol{r}_0$ the external double tractions on the boundary and $\boldsymbol{s}_0$ represents the external line forces.

(a) undeformed (b) 1st-order modes (c) 2nd-order modes

Figure 4.2: Representation of typical 1st-order and 2nd-order deformation modes, associated with conventional strains and the second gradient of displacements.

4.3 Strong equilibrium

The strong form of the equilibrium problem is determined from its weak version in this section. The left-hand-side of Equation (4.2) is developed by performing integration by parts. The first term results in

$$\int_\Omega \boldsymbol{P} : \delta \boldsymbol{F} dV = \int_\Omega \boldsymbol{P} : \nabla_X \delta \boldsymbol{u} dV = \int_{\partial\Omega} (\boldsymbol{P} \cdot \boldsymbol{N}) \cdot \delta \boldsymbol{u} dA - \int_\Omega \operatorname{div} \boldsymbol{P} \cdot \delta \boldsymbol{u} dV. \tag{4.3}$$

The term related to the second gradient yields:

$$\begin{aligned} \int_\Omega \mathbf{Q} \vdots \delta \mathbf{G} dV &= \int_\Omega \mathbf{Q} \vdots \nabla_X \nabla_X \delta \boldsymbol{u} dV \\ &= \int_{\partial\Omega} (\mathbf{Q} \cdot \boldsymbol{N}) : \nabla_X \delta \boldsymbol{u} dA - \int_{\partial\Omega} \operatorname{div} \mathbf{Q} \cdot \boldsymbol{N} \cdot \delta \boldsymbol{u} dA + \int_\Omega \operatorname{div} (\operatorname{div} \mathbf{Q}) \cdot \delta \boldsymbol{u} dV. \end{aligned} \tag{4.4}$$

This result can be better understood by analysing the following step-by-step deduction:

$$\begin{aligned} \int_\Omega \mathbf{Q} \vdots \nabla_X \nabla_X \delta \boldsymbol{u} dV \Rightarrow & \int_\Omega Q_{ijk} \frac{\partial^2 \delta u_i}{\partial X_j \partial X_k} \\ &= \int_\Omega \left[\frac{\partial}{\partial X_k} \left(Q_{ijk} \frac{\partial \delta u_i}{\partial X_j} \right) - \frac{\partial Q_{ijk}}{\partial X_k} \frac{\partial \delta u_i}{\partial X_j} \right] dV \\ &= \int_{\partial\Omega} Q_{ijk} \frac{\partial \delta u_i}{\partial X_j} N_k dA - \int_\Omega \frac{\partial Q_{ijk}}{\partial X_k} \frac{\partial \delta u_i}{\partial X_j} dV \\ &= \int_{\partial\Omega} Q_{ijk} \frac{\partial \delta u_i}{\partial X_j} N_k dA - \int_\Omega \left[\frac{\partial}{\partial X_j} \left(\frac{\partial Q_{ijk}}{\partial X_k} \delta u_i \right) - \frac{\partial}{\partial X_j} \left(\frac{\partial Q_{ijk}}{\partial X_k} \right) \delta u_i \right] dV \\ &= \int_{\partial\Omega} Q_{ijk} \frac{\partial \delta u_i}{\partial X_j} N_k dA - \int_{\partial\Omega} \frac{\partial Q_{ijk}}{\partial X_k} \delta u_i N_j dA + \int_\Omega \frac{\partial}{\partial X_j} \left(\frac{\partial Q_{ijk}}{\partial X_k} \right) \delta u_i dV \\ &\Rightarrow \int_{\partial\Omega} (\mathbf{Q} \cdot \boldsymbol{N}) : \nabla_X \delta \boldsymbol{u} dA - \int_{\partial\Omega} \operatorname{div} \mathbf{Q} \cdot \boldsymbol{N} \cdot \delta \boldsymbol{u} dA + \int_\Omega \operatorname{div} (\operatorname{div} \mathbf{Q}) \cdot \delta \boldsymbol{u} dV. \end{aligned} \tag{4.5}$$

The gradient $\nabla_X \delta \boldsymbol{u}$ is not independent from $\delta \boldsymbol{u}$, and must be decomposed into its normal and surface components before proceeding (Blanco et al., 2016b, Brand, 1947, Kouznetsova, 2002,

Lesičar, 2015, Luscher, 2010):

$$\begin{aligned}\nabla_X \delta\boldsymbol{u} &= \nabla_X^t \delta\boldsymbol{u} + D_0\delta\boldsymbol{u}\otimes\boldsymbol{N}\\ &= \nabla_X\delta\boldsymbol{u}\cdot(\boldsymbol{I}-\boldsymbol{N}\otimes\boldsymbol{N}) + \nabla_X\delta\boldsymbol{u}\cdot\boldsymbol{N}\otimes\boldsymbol{N}.\end{aligned} \tag{4.6}$$

As a consequence, the same decomposition can be applied to the divergence operator:

$$\operatorname{div}\delta\boldsymbol{u} = \operatorname{div}^t\delta\boldsymbol{u} + \operatorname{div}^n\delta\boldsymbol{u}, \tag{4.7}$$

where $\operatorname{div}\delta\boldsymbol{u} = \nabla_X\delta\boldsymbol{u}:\boldsymbol{I}$, $\operatorname{div}^t\delta\boldsymbol{u} = \nabla_X^t\delta\boldsymbol{u}:\boldsymbol{I}$ and $\operatorname{div}^n\delta\boldsymbol{u} = (D_0\delta\boldsymbol{u}\otimes\boldsymbol{N}):\boldsymbol{I}$.

Therefore, the term $(\mathbf{Q}\cdot\boldsymbol{N}):\nabla_X\delta\boldsymbol{u}$ is developed according to this decomposition. Assuming that $\boldsymbol{A} = \mathbf{Q}\cdot\boldsymbol{N}$, for the sake of simplification, then

$$\boldsymbol{A}:\nabla_X\delta\boldsymbol{u} = \boldsymbol{A}:\nabla_X^t\delta\boldsymbol{u} + \boldsymbol{A}:(D_0\delta\boldsymbol{u}\otimes\boldsymbol{N}). \tag{4.8}$$

The second term of the right-hand-side may be simply rewritten by

$$\boldsymbol{A}:(D_0\delta\boldsymbol{u}\otimes\boldsymbol{N}) = D_0\delta\boldsymbol{u}\cdot\boldsymbol{A}\cdot\boldsymbol{N}. \tag{4.9}$$

Regarding the first term, it is developed as follows:

$$\begin{aligned}\boldsymbol{A}:\nabla_X^t\delta\boldsymbol{u} = \boldsymbol{A}:[\nabla_X\delta\boldsymbol{u}\cdot(\boldsymbol{I}-\boldsymbol{N}\otimes\boldsymbol{N})] &= A_{ij}\frac{\partial u_i}{\partial X_k}\left(\delta_{kj}-N_kN_j\right)\boldsymbol{e}_i\otimes\boldsymbol{e}_j\\ &= A_{ij}\frac{\partial u_i}{\partial X_k}\left(\delta_{kj}-N_kN_j\right)\boldsymbol{e}_i\otimes\boldsymbol{e}_j\\ &= \frac{\partial\left(u_iA_{ij}\right)}{\partial X_k}\left(\delta_{kj}-N_kN_j\right) - u_i\frac{\partial A_{ij}}{\partial X_k}\left(\delta_{kj}-N_kN_j\right)\boldsymbol{e}_i\otimes\boldsymbol{e}_j\\ \Leftrightarrow\ \boldsymbol{A}:\nabla_X^t\delta\boldsymbol{u} &= \operatorname{div}^t(\delta\boldsymbol{u}\cdot\boldsymbol{A}) - \delta\boldsymbol{u}\cdot\operatorname{div}^t\boldsymbol{A}.\end{aligned} \tag{4.10}$$

According to Brand (1947)

$$\int_{\partial\Omega}\operatorname{div}^t(\delta\boldsymbol{u}\cdot\boldsymbol{A})\,dA = \int_{\partial\Omega}\operatorname{div}^t(\boldsymbol{N})\,\boldsymbol{N}\cdot(\delta\boldsymbol{u}\cdot\boldsymbol{A})\,dA + \oint_{\partial\Gamma}\boldsymbol{m}\cdot(\delta\boldsymbol{u}\cdot\boldsymbol{A})\,dL, \tag{4.11}$$

where $\boldsymbol{m}$ denotes the external unit vector normal to the closed boundary curve Γ and tangent to the surface, obtained as $\boldsymbol{m} = \boldsymbol{\tau}\times\boldsymbol{N}$, with $\boldsymbol{\tau}$ denoting the unit vector tangent to the curve. The last term vanishes in the presence of a surface $\partial\Omega$ without the presence of edges or corners. If the surface has n_e edges, then the line integral can be expressed as (Kouznetsova, 2002)

$$\oint_{\Gamma}\boldsymbol{m}\cdot(\delta\boldsymbol{u}\cdot\boldsymbol{A})\,dL = \sum_{i=1}^{n_e}\oint_{\Gamma^i}\|\boldsymbol{m}\cdot(\delta\boldsymbol{u}\cdot\boldsymbol{A})\|\,dL. \tag{4.12}$$

Therefore, the integral

$$\begin{aligned}\int_{\partial\Omega}(\mathbf{Q}\cdot\boldsymbol{N}):\nabla_X\delta\boldsymbol{u}dA = &\int_{\partial\Omega}\operatorname{div}^t(\boldsymbol{N})\left((\mathbf{Q}\cdot\boldsymbol{N})\cdot\boldsymbol{N}\right)\cdot\delta\boldsymbol{u}dA -\\ &\int_{\partial\Omega}\operatorname{div}^t(\mathbf{Q}\cdot\boldsymbol{N})\cdot\delta\boldsymbol{u}dA + \sum_{i=1}^{n_e}\oint_{\Gamma^i}\|(\mathbf{Q}\cdot\boldsymbol{N})\cdot\boldsymbol{m}\|\cdot\delta\boldsymbol{u}dL +\\ &\int_{\partial\Omega}(\mathbf{Q}\cdot\boldsymbol{N})\cdot\boldsymbol{N}\cdot D_0\delta\boldsymbol{u}dA.\end{aligned} \tag{4.13}$$

Finally, including the above developments, Equation (4.2) is rewritten as

$$\begin{aligned}&\int_{\Omega}\left[\operatorname{div}(\operatorname{div}\mathbf{Q}) - \operatorname{div}\boldsymbol{P}\right]\cdot\delta\boldsymbol{u}dV +\\ &\int_{\partial\Omega^N}\left[\boldsymbol{P}\cdot\boldsymbol{N} - \operatorname{div}\mathbf{Q}\cdot\boldsymbol{N} + \operatorname{div}^t\boldsymbol{N}\,(\mathbf{Q}\cdot\boldsymbol{N})\cdot\boldsymbol{N} - \operatorname{div}^t(\mathbf{Q}\cdot\boldsymbol{N})\right]\cdot\delta\boldsymbol{u}dA +\\ &\int_{\partial\Omega}(\mathbf{Q}\cdot\boldsymbol{N})\cdot\boldsymbol{N}\cdot D_0\delta\boldsymbol{u}dA + \sum_{i=1}^{n_e}\oint_{\Gamma^i}\|(\mathbf{Q}\cdot\boldsymbol{N})\cdot\boldsymbol{m}\|\cdot\delta\boldsymbol{u}dL\\ &= \int_{\Omega}\boldsymbol{b}_0\cdot\delta\boldsymbol{u}dV + \int_{\partial\Omega^N}\boldsymbol{t}_0\cdot\delta\boldsymbol{u}dA + \int_{\partial\Omega^N}\boldsymbol{r}_0\cdot D_0\delta\boldsymbol{u}dA + \int_{\Gamma^N}\boldsymbol{s}_0\cdot\delta\boldsymbol{u}dA.\end{aligned} \tag{4.14}$$

By standard variational arguments, since Equation (4.14) must be satisfied for any admissible displacement variation $\delta \boldsymbol{u}$, the strong form of the equilibrium problem is expressed by the following set of equations:

$$\boldsymbol{b}_0 = \operatorname{div}(\operatorname{div}\mathbf{Q}) - \operatorname{div}\boldsymbol{P}, \qquad \text{in } \Omega \tag{4.15}$$

$$\boldsymbol{t}_0 = \boldsymbol{P}\cdot\boldsymbol{N} - \operatorname{div}\mathbf{Q}\cdot\boldsymbol{N} + \operatorname{div}^t \boldsymbol{N}\,(\mathbf{Q}\cdot\boldsymbol{N})\cdot\boldsymbol{N} - \operatorname{div}^t(\mathbf{Q}\cdot\boldsymbol{N}), \qquad \text{on } \partial\Omega \tag{4.16}$$

$$\boldsymbol{r}_0 = (\mathbf{Q}\cdot\boldsymbol{N})\cdot\boldsymbol{N}, \qquad \text{on } \partial\Omega \tag{4.17}$$

$$\boldsymbol{s}_0 = \|(\mathbf{Q}\cdot\boldsymbol{N})\cdot\boldsymbol{m}\|, \qquad \text{on } \Gamma \tag{4.18}$$

4.4 Finite element solution for the second-order equilibrium problem

One difficulty associated with the application of the finite element method is related to the fact that conventional elements are not suitable to solve the discretised version of Equation (4.2), since in this case C^1 continuity of the displacements field must be guaranteed, i.e., the first derivative of the displacements must be continuous throughout the discretised domain, and standard finite elements are only C^0 continuous.

Research has been made regarding the development of C^1 continuous elements. Petera and Pittman (1994) proposed a family of bi-dimensional C^1 continuous elements where the shape functions are not explicitly defined, and the degrees of freedom are the displacements, the first and the mixed second derivatives. Zervos et al. (2009) compares the elements proposed by Petera and Pittman (1994) with penalty based elements in the framework of gradient elasticity, concluding that C^1 continuous elements show a robust performance and the results obtained have a better quality. Papanicolopulos et al. (2009) presented a hexahedral C^1 continuous element, based on the work of Petera and Pittman (1994). Lesičar et al. (2016) employs a triangular C^1 finite element in multi-scale analysis with 2^{nd}-order gradient, where the nodal degrees of freedom are the displacements and their first and second Cartesian derivatives. The main disadvantage of this kind of elements is the number of integration points required. Triangular elements require 13 integration points (Lesičar et al., 2016, Zervos et al., 2009), the hexahedral from Papanicolopulos et al. (2009) requires 27, and the quadrilateral element requires 9 Gauss points (Zervos et al., 2009). In view of a multi-scale homogenisation based framework, where a RVE problem must be solved at each macro-integration point, the computational effort arising from C^1 continuous elements at the macro-scale becomes prohibitive.

In the context of a 2^{nd}-order multi-scale scheme, Nguyen and Noels (2014), Nguyen et al. (2013) employed the discontinuous-Galerkin method to allow the use of standard C^0 elements. Continuity of the fields across finite elements is weakly enforced by the introduction of a numerical flux at the elements interface. However, this leads to the need of integrating terms with the homogenised stresses on both sides of each element interface, which represents a significant amount of additional integration points.

Alternatively, mixed formulations, where the continuity of the displacements first derivative is accomplished through Lagrange multipliers, are available (Kwon and Lee, 2017, Matsushima et al., 2002, Shu et al., 1999, Zybell et al., 2012). Kouznetsova et al. (Kouznetsova, 2002, Kouznetsova et al., 2004b) analysed several 2D mixed elements, concluding that the quadrilateral element presented by Matsushima et al. (2002) is stable and provides accurate results employing a reduced integration scheme. This element has also been successfully used by Luscher (2010). The major drawback of this kind of finite elements is related to the increased number of degrees of freedom. However, in a multi-scale context most of the solution time is spent in the micro-scale analysis, which is mainly driven by the number of macro-scale Gauss points, and the computational cost of the macro-scale problem is negligible. Therefore, this approach is employed here to solve the second-order equilibrium problem with the finite element method. The mixed formulation is presented in what follows and more details on the employed mixed elements are given in Section 4.4.2.

4.4.1 Mixed formulation

The continuity of the first derivative of the displacements field is guaranteed in the solution of Equation (4.2) through a mixed formulation where Lagrange multipliers enforce the continuity of the deformation gradient. In addition to the displacements $\boldsymbol{u}$, a deformation gradient field $\hat{\boldsymbol{F}}$ is introduced as a problem unknown, which is interpolated with C^0 functions after discretisation. Thus the deformation gradient field $\hat{\boldsymbol{F}}$ is continuous over the discretised body. The compatibility between $\hat{\boldsymbol{F}}$ and the deformation gradient computed from the displacement field $\boldsymbol{F} = \boldsymbol{I} + \nabla_X \boldsymbol{u}$ is enforced by the Lagrange multipliers $\boldsymbol{\lambda}$. Including the compatibility term in the equilibrium Equation (4.2), and neglecting external line forces $\boldsymbol{s_0}$, results in

$$\int_\Omega \left(\boldsymbol{P} : \delta \boldsymbol{F} + \mathbf{Q} \vdots \nabla_X \delta \hat{\boldsymbol{F}} - \delta \left[\boldsymbol{\lambda} : \left(\boldsymbol{F} - \hat{\boldsymbol{F}} \right) \right] \right) dV = \int_\Omega \boldsymbol{b_0} \cdot \delta \boldsymbol{u} dV + \int_{\partial\Omega} \boldsymbol{t_0} \cdot \delta \boldsymbol{u} dA + \int_{\partial\Omega} \boldsymbol{R_0} : \delta \hat{\boldsymbol{F}} dA, \quad (4.19)$$

where $\boldsymbol{R}_0$ denotes the double traction tensor $\boldsymbol{R}_0 = \boldsymbol{r}_0 \otimes \boldsymbol{N}$.

Remark 1. *According to Kouznetsova (2002), assuming that the deformation gradient compatibility is satisfied in a weak sense in the domain, the contribution of the external surfaces integral can be neglected. This assumption has already been included in Equation (4.19).*

4.4.2 Mixed finite elements

The finite element method is used to discretise the problem, and the displacements $\boldsymbol{u}$, the deformation gradient $\hat{\boldsymbol{F}}$ and the Lagrange multipliers $\boldsymbol{\lambda}$ are interpolated from the corresponding nodal values through independently defined interpolation functions:

$$\boldsymbol{u} = \sum_{k=1}^{n_{nu}} N_k^u \boldsymbol{u}_k = \mathbf{N}^u \mathbf{u}, \quad (4.20)$$

$$\hat{\boldsymbol{F}} = \sum_{k=1}^{n_{nF}} N_k^F \hat{\boldsymbol{F}}_k = \mathbf{N}^F \hat{\mathbf{F}}, \quad (4.21)$$

$$\boldsymbol{\lambda} = \sum_{k=1}^{n_\lambda} N_k^\lambda \boldsymbol{\lambda} = \mathbf{N}^\lambda \boldsymbol{\lambda}. \quad (4.22)$$

In the above interpolation relations, $\mathbf{N}^u$ is the shape function matrix for displacements and coordinates, $\mathbf{N}^F$ is the matrix for deformation gradient and $\mathbf{N}^\lambda$ for the Lagrange multipliers, while $\mathbf{u}$, $\hat{\mathbf{F}}$ and $\boldsymbol{\lambda}$ denote the respective nodal vectors.

2D mixed element

Kouznetsova (2002) has analysed the performance of several 2D mixed finite elements for the solution of a 2nd-order equilibrium problem. The element referred as Q8F4L1, presented by Matsushima et al. (2002) and represented in Figure 4.3, shows the best balance between computational cost and accuracy. It employs 8 nodes for displacements and geometry interpolation, with quadratic shape functions, a bi-linear interpolation for the deformation gradient, with 4 nodes, and constant Lagrange multiplier field in the element domain, resulting in a total of 36 degrees of freedom. A 2×2 Gauss integration scheme is enough for this element. This element has also been used by Luscher (2010) and performed very well when compared with a triangular C^1 element (Lesičar, 2015).

This element has been implemented in the *in-house* finite element program LINKS as a superimposition of a *quad 8* element for displacements and geometry interpolation with a *quad 4* element for relaxed deformation gradients, with a constant Lagrange multiplier field to enforce the compatibility.

Moreover, for the sake of comparison and aiming to assess the mixed elements implementation strategy, the Q9F9L4 element (70 degrees of freedom per element) has also been implemented. This element requires a 3×3 integration scheme for the stress terms and 2×2 Gauss points for the Lagrange multiplier related terms, since the Lagrange multipliers are defined on the 4 Gauss points (Shu et al., 1999).

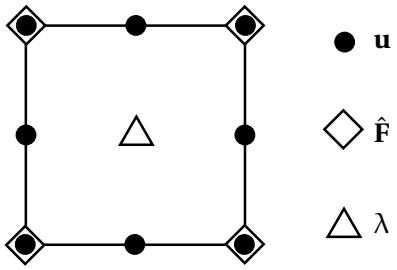

Figure 4.3: Mixed finite element Q8F4L1 used for 2D 2^{nd}-order analysis.

3D mixed element

In this section, a mixed 3D element is devised to deal with 2^{nd}-order equilibrium problems. Zervos (2008) proposed several 2D and 3D elements to be used in a gradient elasticity context, where a penalty parameter is employed, instead of a Lagrange multiplier. Zybell et al. (2012) proposed a mixed 3D element, based on the 27-noded hexahedron, and Kwon and Lee (2017) studied elements of the same type in the framework of a modified couple stress theory. However, this type of element carries a large number of degrees of freedom.

A mixed element based on the 20-noded hexahedron is proposed here, as an extension of the 2D Q8F4L1 mixed element. The H20F8L1 element uses quadratic shape functions (20 nodes) to interpolate the displacements and geometry, 8 corner nodes are used for a linear interpolation of the deformation gradient, and a constant Lagrange multiplier field is considered. It is represented in Figure 4.4.

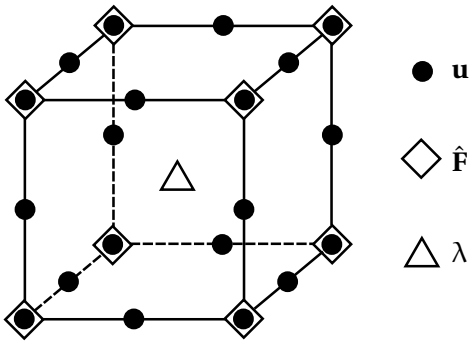

Figure 4.4: Mixed finite element H20F8L1 used for 3D 2^{nd}-order analysis.

To the author knowledge, this type of element has not been used before to solve this type of equilibrium problems.

4.4.3 Discretisation of the equilibrium equation

The discretised version of weak equilibrium equation (4.19) is obtained by incorporating the definitions of Equations (4.20-4.22), and taking into account that $\delta \boldsymbol{F} = \nabla_X \delta \boldsymbol{u}$. This process is performed step by step in what follows, for the sake of clarity.

Discretisation of the terms related to the displacement variation

Discretisation of the 1st Piola-Kirchhoff stress term is similar to the classical continuum case, yielding:

$$\int_{\Omega} \boldsymbol{P} : \nabla_X \delta \boldsymbol{u} dV \Rightarrow \int_{\Omega^d} \mathbf{P}^T \left(\mathbf{G}^u \delta \mathbf{u} \right) dV = \delta \mathbf{u}^T \int_{\Omega^d} (\mathbf{G}^u)^T \mathbf{P} dV, \tag{4.23}$$

where $\mathbf{P}$ is the first Piolla-Kirchhoff stress tensor in vector format, and the matrix $\mathbf{G}^u$ is the discrete gradient operator, containing derivatives of the displacement related shape functions.

The term including the Lagrange multiplier results in:

$$\int_{\Omega} \boldsymbol{\lambda} : \nabla_X \delta \boldsymbol{u} dV \Rightarrow \delta \mathbf{u}^T \int_{\Omega^d} (\mathbf{G}^u)^T \mathbf{N}^{\lambda} dV \boldsymbol{\lambda}. \tag{4.24}$$

Discretised standard external forces terms are expressed as:

$$\int_{\Omega} \boldsymbol{b}_0 \cdot \delta \boldsymbol{u} dV + \int_{\partial\Omega} \boldsymbol{t}_0 \cdot \delta \boldsymbol{u} dA \Rightarrow \delta \mathbf{u}^T \left[\int_{\Omega^d} (\mathbf{N}^u)^T \mathbf{b}_0 dV + \int_{\partial\Omega^d} (\mathbf{N}^u)^T \mathbf{t}_0 dA \right]. \tag{4.25}$$

Discretisation of the terms related to the relaxed deformation gradient variation

The term including the higher-order stress is discretised as

$$\int_{\Omega} \mathbf{Q} \vdots \nabla_X \delta \hat{\boldsymbol{F}} \Rightarrow \delta \hat{\mathbf{F}}^T \int_{\Omega^d} (\mathbf{G}^F)^T \mathbf{Q} dV, \tag{4.26}$$

where $\mathbf{Q}$ is the higher order stress tensor $\mathbf{Q}$ stored in vector format and $\mathbf{G}^F$ is the appropriate discrete gradient operator, containing derivatives of the deformation gradient related shape functions.

The Lagrange multiplier term results in

$$\int_{\Omega} \boldsymbol{\lambda} : \delta \hat{\boldsymbol{F}} dV \Rightarrow \delta \hat{\mathbf{F}}^T \int_{\Omega^d} \left(\mathbf{N}^F \right)^T \mathbf{N}^{\lambda} dV \boldsymbol{\lambda}, \tag{4.27}$$

and the external double traction term in

$$\int_{\partial\Omega} \boldsymbol{R}_0 : \delta \hat{\boldsymbol{F}} dA \Rightarrow \delta \hat{\mathbf{F}}^T \int_{\partial\Omega^d} \left(\mathbf{N}^F \right)^T \mathbf{R}_0 dA, \tag{4.28}$$

where $\mathbf{R}_0$ denotes the double traction tensor $\boldsymbol{R}_0$ in vector format.

Discretisation of the terms related to the Lagrange multipliers variation

The discretised version of the term containing the relaxed deformation gradient is given by:

$$\int_{\Omega} \delta \boldsymbol{\lambda} : \hat{\boldsymbol{F}} dV \Rightarrow \delta \boldsymbol{\lambda}^T \int_{\Omega^d} \left(\mathbf{N}^{\lambda} \right)^T \mathbf{N}^F dV \hat{\mathbf{F}}. \tag{4.29}$$

In what concerns the term with the deformation gradient computed from the displacements field, looking at Equation (2.13), it results in

$$\int_{\Omega} \delta \boldsymbol{\lambda} : \boldsymbol{F} dV = \int_{\Omega} \delta \boldsymbol{\lambda} : \nabla_X \boldsymbol{x} dV \Rightarrow \delta \boldsymbol{\lambda}^T \int_{\Omega^d} \left(\mathbf{N}^{\lambda} \right)^T \mathbf{G}^u dV \mathbf{x}, \tag{4.30}$$

where $\mathbf{x}$ denotes the vector of current nodal coordinates.

4.4.4 Numerical solution

Introducing the discretised terms of Equations (4.23-4.30) into the weak equilibrium Equation (4.19) results in

$$\begin{aligned}
&\delta\mathbf{u}^T\left\{\int_{\Omega^d}(\mathbf{G}^u)^T\mathbf{P}dV-\int_{\Omega^d}(\mathbf{G}^u)^T\mathbf{N}^\lambda dV\boldsymbol{\lambda}-\int_{\Omega^d}(\mathbf{N}^u)^T\mathbf{b}_0dV-\int_{\partial\Omega^d}(\mathbf{N}^u)^T\mathbf{t}_0dA\right\}\\
&+\delta\hat{\mathbf{F}}^T\left\{\int_{\Omega^d}(\mathbf{G}^F)^T\mathbf{Q}dV+\int_{\Omega^d}\left(\mathbf{N}^F\right)^T\mathbf{N}^\lambda dV\boldsymbol{\lambda}-\int_{\partial\Omega^d}\left(\mathbf{N}^F\right)^T\mathbf{R}_0dA\right\}\\
&+\delta\boldsymbol{\lambda}^T\left\{\int_{\Omega^d}-\left(\mathbf{N}^\lambda\right)^T\mathbf{G}^udV\mathbf{x}+\int_{\Omega^d}\left(\mathbf{N}^\lambda\right)^T\mathbf{N}^FdV\hat{\mathbf{F}}\right\}=0
\end{aligned}\tag{4.31}$$

Since this discretised equilibrium equation must hold for any variation $\delta\mathbf{u}$, $\delta\hat{\mathbf{F}}$ and $\delta\boldsymbol{\lambda}$, the problem consists in finding the nodal vectors $\mathbf{u}$, $\hat{\mathbf{F}}$ and $\boldsymbol{\lambda}$ such that:

$$\begin{Bmatrix}\mathbf{r}^u\\ \mathbf{r}^F\\ \mathbf{r}^\lambda\end{Bmatrix}=\mathbf{0},\tag{4.32}$$

where the residual vectors are defined by:

$$\mathbf{r}^u=\int_{\Omega^d}(\mathbf{G}^u)^T\mathbf{P}dV-\int_{\Omega^d}(\mathbf{G}^u)^T\mathbf{N}^\lambda dV\boldsymbol{\lambda}-\int_{\Omega^d}(\mathbf{N}^u)^T\mathbf{b}_0dV-\int_{\partial\Omega^d}(\mathbf{N}^u)^T\mathbf{t}_0dA,\tag{4.33}$$

$$\mathbf{r}^F=\int_{\Omega^d}(\mathbf{G}^F)^T\mathbf{Q}dV+\int_{\Omega^d}\left(\mathbf{N}^F\right)^T\mathbf{N}^\lambda dV\boldsymbol{\lambda}-\int_{\partial\Omega^d}\left(\mathbf{N}^F\right)^T\mathbf{R}_0dA,\tag{4.34}$$

$$\mathbf{r}^\lambda=\int_{\Omega^d}\left(\mathbf{N}^\lambda\right)^T\mathbf{N}^FdV\hat{\mathbf{F}}-\int_{\Omega^d}\left(\mathbf{N}^\lambda\right)^T\mathbf{G}^udV\mathbf{x}.\tag{4.35}$$

It is important to highlight that the gradient operators definition must be consistent with the vector form employed. For example, since second-order tensors are stored in a major-column sorting:

$$\mathbf{P}_i=\begin{Bmatrix}P_{11}\\P_{21}\\P_{12}\\P_{22}\end{Bmatrix}_i,\quad \mathbf{F}_i=\begin{Bmatrix}F_{11}\\F_{21}\\F_{12}\\F_{22}\end{Bmatrix}_i,\tag{4.36}$$

and the displacements gradient operator must be consistent with $\mathbf{F}=\mathbf{G}^u\mathbf{x}=\mathbf{I}+\mathbf{G}^u\mathbf{u}$, then it is defined as

$$\mathbf{G}^u=\begin{bmatrix}\cdots & \dfrac{\partial N_i^u}{\partial X_1} & 0 & \cdots\\ \cdots & 0 & \dfrac{\partial N_i^u}{\partial X_1} & \cdots\\ \cdots & \dfrac{\partial N_i^u}{\partial X_2} & 0 & \cdots\\ \cdots & 0 & \dfrac{\partial N_i^u}{\partial X_1} & \cdots\end{bmatrix}.\tag{4.37}$$

Third-order tensors are stored in vector format as:

$$\mathbf{Q}_i=\begin{Bmatrix}Q_{111}\\Q_{211}\\Q_{121}\\Q_{221}\\Q_{112}\\Q_{212}\\Q_{122}\\Q_{222}\end{Bmatrix}_i,\quad \hat{\mathbf{G}}_i=\begin{Bmatrix}\hat{G}_{111}\\\hat{G}_{211}\\\hat{G}_{121}\\\hat{G}_{221}\\\hat{G}_{112}\\\hat{G}_{212}\\\hat{G}_{122}\\\hat{G}_{222}\end{Bmatrix}_i.\tag{4.38}$$

The second-order gradient $\hat{\mathbf{G}}$ is symmetric in the last two indices, $\hat{G}_{ijk} = \hat{G}_{ikj}$, due to its definition (see Equation (4.1)). In order to guarantee this symmetry in the current finite element formulation, it is obtained by

$$\hat{G}_{ijk} = \frac{1}{2}\left(\frac{\partial \hat{F}_{ij}}{\partial X_k} + \frac{\partial \hat{F}_{ik}}{\partial X_j}\right). \tag{4.39}$$

The gradient operator $\mathbf{G}^F$ must be suitably defined, since $\hat{\mathbf{G}} = \mathbf{G}^F \hat{\mathbf{F}}$, thus

$$\mathbf{G}^F = \left[\begin{array}{c|cccc|c}
\dots & \frac{\partial N_i^F}{\partial X_1} & 0 & 0 & 0 & \dots \\
\dots & 0 & \frac{\partial N_i^F}{\partial X_1} & 0 & 0 & \dots \\
\dots & \frac{1}{2}\frac{\partial N_i^F}{\partial X_2} & 0 & \frac{1}{2}\frac{\partial N_i^F}{\partial X_1} & 0 & \dots \\
\dots & 0 & \frac{1}{2}\frac{\partial N_i^F}{\partial X_2} & 0 & \frac{1}{2}\frac{\partial N_i^F}{\partial X_1} & \dots \\
\dots & \frac{1}{2}\frac{\partial N_i^F}{\partial X_2} & 0 & \frac{1}{2}\frac{\partial N_i^F}{\partial X_1} & 0 & \dots \\
\dots & 0 & \frac{1}{2}\frac{\partial N_i^F}{\partial X_2} & 0 & \frac{1}{2}\frac{\partial N_i^F}{\partial X_1} & \dots \\
\dots & 0 & 0 & \frac{\partial N_i^F}{\partial X_2} & 0 & \dots \\
\dots & 0 & 0 & 0 & \frac{\partial N_i^F}{\partial X_2} & \dots
\end{array}\right]. \tag{4.40}$$

These operators have been defined for 2D in the above, but can be derived for 3D analogously.

4.4.5 Linearisation

In order to solve the non-linear equation (4.32), the Newton-Raphson method is employed, resulting in an iterative procedure, where at an iteration $(k+1)$ the linear system of equations

$$[\mathbf{K}]^{(k)} \Delta\bar{\mathbf{u}}^{(k+1)} = -\bar{\mathbf{r}}^{(k)}, \tag{4.41}$$

which can be expressed in its expanded version as

$$\begin{bmatrix} \mathbf{K}^{uu} & \mathbf{K}^{uF} & \mathbf{K}^{u\lambda} \\ \mathbf{K}^{Fu} & \mathbf{K}^{FF} & \mathbf{K}^{F\lambda} \\ \mathbf{K}^{\lambda u} & \mathbf{K}^{\lambda F} & \mathbf{K}^{\lambda\lambda} \end{bmatrix}^{(k)} \begin{Bmatrix} \Delta\mathbf{u} \\ \Delta\hat{\mathbf{F}} \\ \Delta\boldsymbol{\lambda} \end{Bmatrix}^{(k+1)} = -\begin{Bmatrix} \mathbf{r}^u \\ \mathbf{r}^F \\ \mathbf{r}^\lambda \end{Bmatrix}^{(k)}. \tag{4.42}$$

Once the solution is found, the unknown variables are updated through

$$\begin{Bmatrix} \mathbf{u} \\ \hat{\mathbf{F}} \\ \boldsymbol{\lambda} \end{Bmatrix}^{(k+1)} = \begin{Bmatrix} \mathbf{u} \\ \hat{\mathbf{F}} \\ \boldsymbol{\lambda} \end{Bmatrix}^{(k)} + \begin{Bmatrix} \Delta\mathbf{u} \\ \Delta\hat{\mathbf{F}} \\ \Delta\boldsymbol{\lambda} \end{Bmatrix}^{(k+1)}. \tag{4.43}$$

The stiffness matrices are obtained through linearisation of the residual vectors with respect to the unknown vector, as shown in what follows.

First residual vector

Linearisation of the first residual vector yields:

$$\Delta\mathbf{r}^u = \frac{\partial \mathbf{r}^u}{\partial \mathbf{u}}\Delta\mathbf{u} + \frac{\partial \mathbf{r}^u}{\partial \hat{\boldsymbol{F}}}\Delta\hat{\boldsymbol{F}} + \frac{\partial \mathbf{r}^u}{\partial \boldsymbol{\lambda}}\Delta\boldsymbol{\lambda}. \tag{4.44}$$

The related stiffness matrices are determined in the following:

$$\mathbf{K}^{uu} = \frac{\partial \mathbf{r}^u}{\partial \mathbf{u}} = \int_{\Omega^d} \left[\mathbf{G}^u\right]^T \frac{\partial \mathbf{P}}{\partial \mathbf{F}} \frac{\partial \mathbf{F}}{\partial \mathbf{u}} dV = \int_{\Omega^d} \left[\mathbf{G}^u\right]^T [\mathbf{A}] \left[\mathbf{G}^u\right] dV, \tag{4.45}$$

$$\mathbf{K}^{uF} = \frac{\partial \mathbf{r}^u}{\partial \hat{\mathbf{F}}} = \int_{\Omega^d} \left[\mathbf{G}^u\right]^T \frac{\partial \mathbf{P}}{\partial \hat{\mathbf{G}}} \frac{\partial \hat{\mathbf{G}}}{\partial \hat{\mathbf{F}}} dV = \int_{\Omega^d} \left[\mathbf{G}^u\right]^T [\mathbf{A}_G] \left[\mathbf{G}^F\right] dV, \tag{4.46}$$

$$\mathbf{K}^{u\lambda} = \frac{\partial \mathbf{r}^u}{\partial \boldsymbol{\lambda}} = -\int_{\Omega^d} \left[\mathbf{G}^u\right]^T \left[\mathbf{N}^\lambda\right] dV, \tag{4.47}$$

where $\mathbf{A}$ and $\mathbf{A}^G$ denote the first Piola-Kirchhoff tangent matrices, defined by

$$\mathbf{A} = \frac{\partial \mathbf{P}}{\partial \mathbf{F}}, \tag{4.48}$$

$$\mathbf{A}_G = \frac{\partial \mathbf{P}}{\partial \hat{\mathbf{G}}}. \tag{4.49}$$

Second residual vector

Similarly, linearisation of the second residual vector results in

$$\Delta \mathbf{r}^F = \frac{\partial \mathbf{r}^F}{\partial \mathbf{u}} \Delta \mathbf{u} + \frac{\partial \mathbf{r}^F}{\partial \hat{\boldsymbol{F}}} \Delta \hat{\boldsymbol{F}} + \frac{\partial \mathbf{r}^F}{\partial \boldsymbol{\lambda}} \Delta \boldsymbol{\lambda}. \tag{4.50}$$

The stiffness matrices are obtained through

$$\mathbf{K}^{Fu} = \frac{\partial \mathbf{r}^F}{\partial \mathbf{u}} = \int_{\Omega^d} \left[\mathbf{G}^F\right]^T \frac{\partial \mathbf{Q}}{\partial \mathbf{F}} \frac{\partial \mathbf{F}}{\partial \mathbf{u}} dV = \int_{\Omega^d} \left[\mathbf{G}^F\right]^T [\mathbf{H}_F] \left[\mathbf{G}^u\right] dV, \tag{4.51}$$

$$\mathbf{K}^{FF} = \frac{\partial \mathbf{r}^F}{\partial \hat{\mathbf{F}}} = \int_{\Omega^d} \left[\mathbf{G}^F\right]^T \frac{\partial \mathbf{Q}}{\partial \hat{\mathbf{G}}} \frac{\partial \hat{\mathbf{G}}}{\partial \hat{\mathbf{F}}} dV = \int_{\Omega^d} \left[\mathbf{G}^F\right]^T [\mathbf{H}] \left[\mathbf{G}^F\right] dV, \tag{4.52}$$

$$\mathbf{K}^{F\lambda} = \frac{\partial \mathbf{r}^F}{\partial \boldsymbol{\lambda}} = \int_{\Omega^d} \left[\mathbf{N}^F\right]^T \left[\mathbf{N}^\lambda\right] dV, \tag{4.53}$$

where $\mathbf{H}$ and $\mathbf{H}_F$ denote the higher-order stress tangent matrices, defined by

$$\mathbf{H}_F = \frac{\partial \mathbf{Q}}{\partial \mathbf{F}}, \tag{4.54}$$

$$\mathbf{H} = \frac{\partial \mathbf{Q}}{\partial \hat{\mathbf{G}}}. \tag{4.55}$$

Third residual vector

Finally, the third residual vector is linearised as follows

$$\Delta \mathbf{r}^\lambda = \frac{\partial \mathbf{r}^\lambda}{\partial \mathbf{u}} \Delta \mathbf{u} + \frac{\partial \mathbf{r}^\lambda}{\partial \hat{\boldsymbol{F}}} \Delta \hat{\boldsymbol{F}} + \frac{\partial \mathbf{r}^\lambda}{\partial \boldsymbol{\lambda}} \Delta \boldsymbol{\lambda}, \tag{4.56}$$

resulting in the definition of the tangent matrices:

$$\mathbf{K}^{\lambda u} = \frac{\partial \mathbf{r}^\lambda}{\partial \mathbf{u}} = \frac{\partial \mathbf{r}^\lambda}{\partial \mathbf{x}} \frac{\partial \mathbf{x}}{\partial \mathbf{u}} = -\int_{\Omega} \left[\mathbf{N}^\lambda\right]^T \left[\mathbf{G}^u\right] dV, \tag{4.57}$$

$$\mathbf{K}^{\lambda F} = \frac{\partial \mathbf{r}^\lambda}{\partial \hat{\mathbf{F}}} = \int_{\Omega} \left[\mathbf{N}^\lambda\right]^T \left[\mathbf{N}^F\right] dV, \tag{4.58}$$

$$\mathbf{K}^{\lambda\lambda} = \frac{\partial \mathbf{r}^\lambda}{\partial \boldsymbol{\lambda}} = [\mathbf{0}]. \tag{4.59}$$

4.5 Mindlin elastic constitutive model

One of the main drawbacks in the use of 2nd-order models consists of the need to develop new constitutive equations, since conventional constitutive models cannot be directly applied with higher-order continuum theories. Second-order constitutive laws must establish a relation between the first Piola-Kirchhoff stress $\boldsymbol{P}$ and the higher-order stress $\mathbf{Q}$ with the 1st and 2nd displacement gradients ($\boldsymbol{F}$ and $\mathbf{G}$).

Aiming to assess the mixed finite element implementation at a relatively low computational cost, a simple constitutive model is introduced in this section. This model has been used by other authors. In particular, Kouznetsova (2002) and Luscher (2010) employed simplified energy functions based on the proposal of Mindlin (1964) to derive a 2nd-order constitutive model, the so-called Mindlin elastic constitutive model.

4.5.1 Energy function

The linear elastic 2nd-order constitutive model is obtained from the following elastic strain energy function per unit reference volume (Luscher, 2010):

$$\begin{aligned} W_0 = &\frac{1}{2}\lambda E_{ii}E_{jj} + \mu E_{ij}E_{ij} \\ &+ a_1 G_{jij}G_{kik} + a_2 G_{kii}G_{jkj} + a_3 G_{kii}G_{kjj} + a_4 G_{kij}G_{kij} + a_5 G_{kij}G_{ijk}. \end{aligned} \tag{4.60}$$

The 1st-order deformation contribution is driven by the Green-Lagrange strain tensor $\boldsymbol{E}$, defined in Expression (2.27), and the the Lamé parameters denoted by λ and μ. The 2nd-order contribution is included through the 2nd displacements gradient $\mathbf{G}$, where all the variables a_i assume the value $a_i = 0.5\mu l^2$, $i = 1,5$, with l denoting the material characteristic length, which is a model parameter.

4.5.2 First Piola-Kirchhoff stress

The first Piola-Kirchhoff stress tensor is obtained through:

$$\boldsymbol{P} = \frac{\partial W_0}{\partial \boldsymbol{F}} = \frac{\partial W_0}{\partial \boldsymbol{E}} \cdot \frac{\partial \boldsymbol{E}}{\partial \boldsymbol{F}} \Rightarrow P_{ij} = \frac{\partial W_0}{\partial E_{ab}} \cdot \frac{\partial E_{ab}}{\partial F_{ij}}. \tag{4.61}$$

The derivative of the energy function with regard to the Green-Lagrange strain tensor results in:

$$\frac{\partial W_0}{\partial E_{ab}} = 2\mu E_{ab} + \lambda E_{kk}\delta_{ab} = S_{ab} \Rightarrow \frac{\partial W_0}{\partial \boldsymbol{E}} = \boldsymbol{S} = 2\mu \boldsymbol{E} + \lambda \operatorname{tr}(\boldsymbol{E}) \cdot \boldsymbol{I}, \tag{4.62}$$

which is the definition of the second Piola-Kirchhoff stress tensor $\boldsymbol{S}$.

The derivative of $\boldsymbol{E}$ with regard to the deformation gradient $\boldsymbol{F}$ yields:

$$\frac{\partial E_{ab}}{\partial F_{ij}} = \frac{1}{2}\left(F_{ib}\delta_{ja} + F_{ia}\delta_{jb}\right). \tag{4.63}$$

Due to the symmetry of $\boldsymbol{S}$, the first Piola-Kirchhoff stress tensor is finally obtained as

$$\boldsymbol{P} = \boldsymbol{F} \cdot \boldsymbol{S}. \tag{4.64}$$

4.5.3 Higher-order stress tensor

The higher-order stress tensor is obtained by differentiation of the strain energy function with regard to the 2nd-order gradient, which results in:

$$\begin{aligned} \mathbf{Q} = \frac{\partial W_0}{\partial \mathbf{G}} \Rightarrow Q_{ijk} = &2a_1\delta_{ik}G_{ljl} + a_2\left(\delta_{jk}G_{lil} + \delta_{ik}G_{jll}\right) + 2a_3\delta_{jk}G_{ill} \\ &+ 2a_4 G_{ijk} + a_5\left(G_{jki} + G_{kij}\right). \end{aligned} \tag{4.65}$$

4.5.4 Tangent modulus

The derivatives of the stresses with regard to $\boldsymbol{F}$ and $\mathbf{G}$ must be defined, in order to determine the tangent modulus needed for the numerical solution through the Newton-Raphson method, where the global tangent matrices are required (see Sections 4.4.4 and 4.4.5).

The derivative of the first Piola-Kirchhoff stress with regard to the deformation gradient results in

$$\mathbf{A} = \frac{\partial \boldsymbol{P}}{\partial \boldsymbol{F}} \Rightarrow \mathsf{A}_{ijkl} = \frac{\partial P_{ij}}{\partial F_{kl}} = \delta_{ik} S_{lj} + F_{in} \frac{\partial S_{nj}}{\partial F_{kl}}. \tag{4.66}$$

The derivative of the second Piola-Kirchhoff with regard to the deformation gradient is obtained by applying the chain rule:

$$\frac{\partial \boldsymbol{S}}{\partial \boldsymbol{F}} = \frac{\partial \boldsymbol{S}}{\partial \boldsymbol{E}} : \frac{\partial \boldsymbol{E}}{\partial \boldsymbol{F}} = \mathbf{C} : \mathbf{H}, \tag{4.67}$$

where

$$\mathsf{C}_{ijkl} = \frac{\partial S_{ij}}{\partial E_{kl}} = \lambda \delta_{ij} \delta_{kl} + 2\mu \delta_{ik} \delta_{kl}, \tag{4.68}$$

and

$$\mathsf{H}_{ijkl} = \frac{\partial E_{ij}}{\partial F_{kl}} = \frac{1}{2} \left(\delta_{il} F_{kj} + \delta_{jl} F_{ki} \right). \tag{4.69}$$

The first Piola-Kirchhoff stress does not depend on the second gradient of the displacements, thus:

$$\mathbf{A}_G = \frac{\partial \boldsymbol{P}}{\partial \mathbf{G}} = \mathbf{0}. \tag{4.70}$$

Similarly, the higher-order stress tensor is independent from the deformation gradient, therefore

$$\mathbf{H}_F = \frac{\partial \mathbf{Q}}{\partial \boldsymbol{F}} = \mathbf{0}. \tag{4.71}$$

Finally, the derivative of the higher-order stress with regard to $\mathbf{G}$ is expressed in index notation by

$$\begin{aligned} \mathsf{H}_{ijklmn} = \frac{\partial Q_{ijk}}{\partial G_{lmn}} =& 2a_1 \delta_{ik} \delta_{ln} \delta_{jm} + a_2 \left(\delta_{jk} \delta_{ln} \delta_{im} + \delta_{ik} \delta_{mn} \delta_{lj} \right) + 2a_3 \delta_{jk} \delta_{li} \delta_{mn} + \\ & 2a_4 \delta_{il} \delta_{jm} \delta_{kn} + a_5 \left(\delta_{jl} \delta_{km} \delta_{in} + \delta_{kl} \delta_{im} \delta_{jn} \right). \end{aligned} \tag{4.72}$$

All these tangents are represented in their matrix form $\mathbf{A}$, $\mathbf{A}_G$, $\mathbf{H}_F$ and $\mathbf{H}$ in Equations (4.45), (4.46), (4.51) and (4.52).

4.6 Numerical results

The implementation of the mixed finite element solution is assessed in this section through the solution of several numerical examples. In the first place, the mixed elements Q8F4L1 and H20F8L1 are tested with a linear and quadratic patch tests. Thereafter, distinct classical problems are modelled with 2D and 3D meshes, and the numerical solution is obtained with different values of the material characteristic length. When available, the results are compared with analytical solutions. The 2D results obtained with the Q8F4L1 element are also compared with the Q9F9L4 element, and an equivalence between the 3D and the 2D results is devised, in order to validate the H20F8L1 element. The material elastic properties are $E = 5294$ MPa and $\nu = 0.32$ for all examples, corresponding to the shear modulus of $G = 2000$ MPa and bulk modulus of $K = 5000$ MPa.

4.6.1 Linear Patch test

2D

The patch test used by Kouznetsova (2002) and Luscher (2010) is also employed here to assess the implementation of the mixed quadrilateral element. This patch test consists in prescribing the boundary nodal degrees of freedom of the patch represented in Figure 4.5 according to a displacement field corresponding to a linear polynomial, and checking if the linear displacement field and constant deformation gradient and strain is recovered in the interior of the mesh.

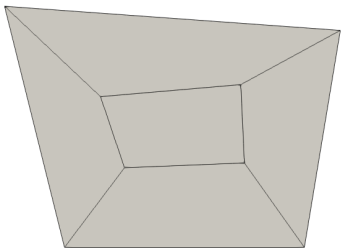

Figure 4.5: Patch test discretisation for Q8F4L1 elements.

A displacement field corresponding to the following deformation gradient

$$\boldsymbol{F} = \begin{bmatrix} 1.0 & 0.5 \\ 0.5 & 1.0 \end{bmatrix} \tag{4.73}$$

is prescribed on the mesh boundary nodes, along with the relaxed deformation gradient. The correct reproduction of constant strain due to constant deformation gradient and linear displacement field in the interior nodes is verified, as shown in Figure 4.6. The results are independent of the material characteristic length, which was tested with the following values $l = 0.01, 0.1, 1.0, 10$ mm. Constant first Piola-Kirchhoff stress and null second-gradient and higher-order stresses are also observed, which is consistent with the expected results.

3D

The finite element mesh for the 3D patch test consists of a cubic block of material of side $L = 1$ mm, discretised with eight H20F4L1 elements, as shown in Figure 4.7. The central node is deviated from

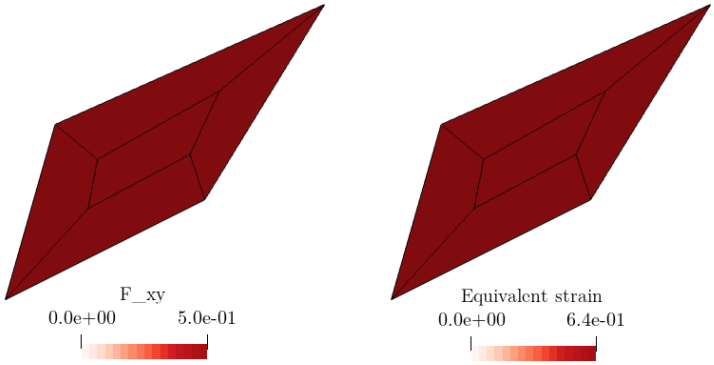

Figure 4.6: Contour plots of F_{12} and the equivalent strain in the interior of the linear patch test for the Q8F4L1 element.

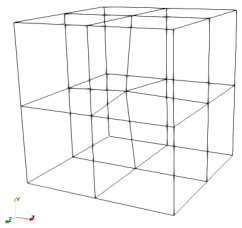

Figure 4.7: Patch test discretisation for H20F8L1 elements.

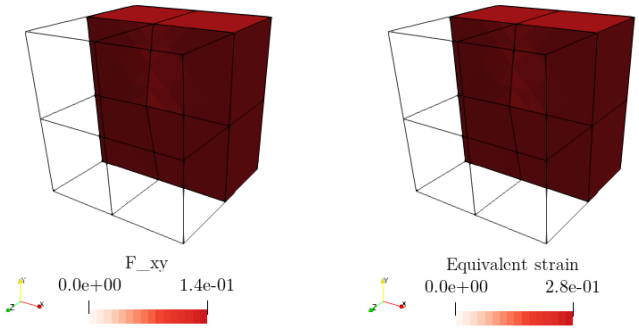

Figure 4.8: Contour plots of F_{12} and the equivalent strain in the interior of the patch test.

the geometric center in order to induce some distortion in the elements. Similar patch tests have been used by Papanicolopulos et al. (2009) and Zybell et al. (2012).

The boundary nodes are prescribed according to the following deformation gradient:

$$\boldsymbol{F} = \begin{bmatrix} 1.12 & 0.14 & 0.16 \\ 0.11 & 1.13 & 0.15 \\ 0.21 & 0.22 & 1.23 \end{bmatrix}. \tag{4.74}$$

As expected, a constant deformation state with linear displacement field is recovered in the interior of the patch domain (see Figure 4.8).

4.6.2 Quadratic patch test

2D

In addition to the standard linear patch test, the current element must also satisfy a quadratic patch test where it should be able to capture the linear variation of the deformation gradient field and a constant 2^{nd} gradient (Kouznetsova, 2002, Lesičar, 2015).

The following quadratic displacement field, also employed by (Lesičar, 2015) to validate a C^1 element, is considered in this case:

$$\begin{aligned} u_1 &= 0.12X_1 + 0.14X_2 + 0.16X_1^2 + 0.18X_1X_2 + 0.20X_2^2, \\ u_2 &= 0.11X_1 + 0.13X_2 + 0.15X_1^2 + 0.10X_1X_2 + 0.21X_2^2. \end{aligned} \tag{4.75}$$

As referred by Kouznetsova (2002), an appropriate body force field must be included in order to satisfy Equation (4.15). Here, the displacement field is enforced in the whole patch test domain and the deformation gradient values are enforced only at the boundary, being expected that a linear relaxed deformation gradient field is recovered in the interior nodes.

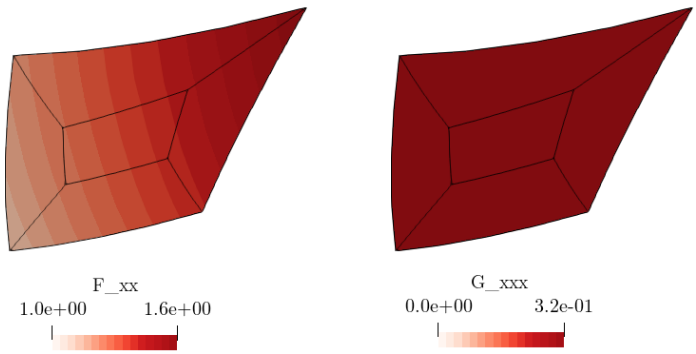

Figure 4.9: Contour plots of F_{11} and G_{111} on the quadratic patch test deformed mesh.

Figure 4.9 shows the distribution of F_{11} and G_{111}, confirming that the expected results are obtained.

The quadratic patch test is repeated with a simpler displacement field:

$$\begin{aligned} u_1 &= 0.50 X_2^2, \\ u_2 &= 0, \end{aligned} \tag{4.76}$$

which yields $F_{12} = X_2$ and $G_{122} = 1\ \text{mm}^{-1}$. Again, the displacement field is enforced over the domain and the deformation gradient on the boundary. The expected fields of deformation gradient and 2$^{\text{nd}}$ gradient are recovered in the interior nodes, as shown in Figure 4.10.

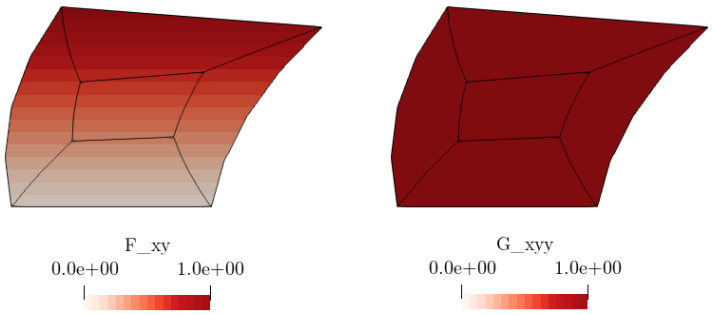

Figure 4.10: Contour plots of F_{12} and G_{122} on the quadratic patch test deformed mesh.

These patch tests have been checked for different values of the material characteristic length.

3D

The 3D patch mesh represented in Figure 4.7 is subjected separately to two quadratic displacement fields. In the first case, the displacement field is defined by $u_1 = 0.5X_2^2$, leading to $F_{12} = X_2$ and $G_{122} = 1.0\ \text{mm}^{-1}$. In the second situation, it is defined as $u_1 = X_2 X_3$, resulting in $F_{12} = X_3$, $F_{13} = X_2$ and $G_{123} = 1.0\ \text{mm}^{-1}$. In both cases, due to the difficulties in guaranteeing the compatibility without including body forces, the displacement field is enforced on all nodes and the deformation gradient is imposed on the boundaries. It is expected that the solution recovers a linear variation of the deformation on the interior of the patch, resulting in a constant second gradient coincident with the imposed displacement field.

The quadratic patch test is verified in both cases, as shown in Figures 4.11 and 4.12, for distinct values of the material characteristic length.

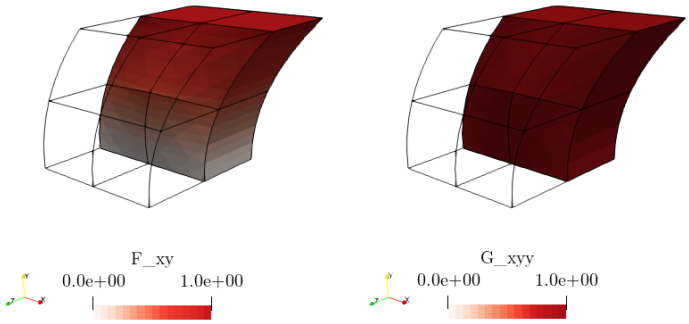

Figure 4.11: Contour plots of F_{12} and G_{122} on the interior of the deformed mesh of the first quadratic patch test.

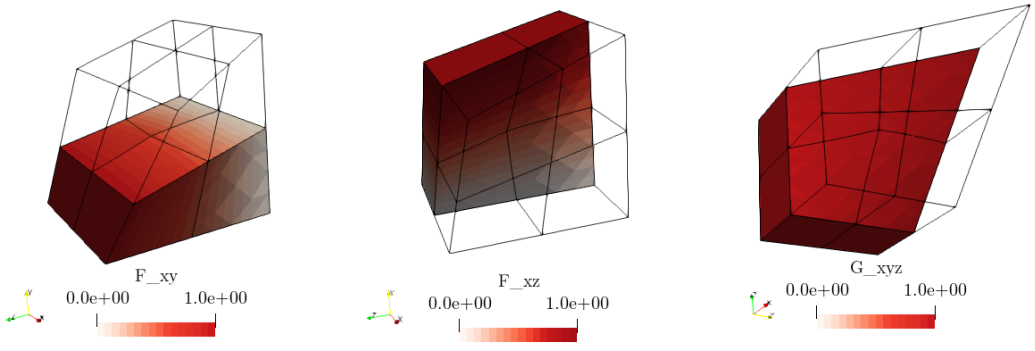

Figure 4.12: Contour plots of F_{12}, F_{13} and G_{123} on the interior of the deformed mesh of the second quadratic patch test.

4.6.3 Boundary shear layer

2D

The boundary shear layer problem is a classical example where second-order effects play an important role, and the influence of the material characteristic length is evident. It considers a material layer with infinite length in the directions x_1 and x_3 and height h, which is fixed on the bottom and subjected to a horizontal displacement on the top surface. Null deformation is enforced at both surfaces. This problem is represented in Figure 4.13. Due to the infinite length in x_1 and x_3, the 2D finite element model assumes plain strain, and only a vertical strip of elements is used in the discretisation, with periodicity imposed on the degrees of freedom of both left and right sides. The results only vary on x_2.

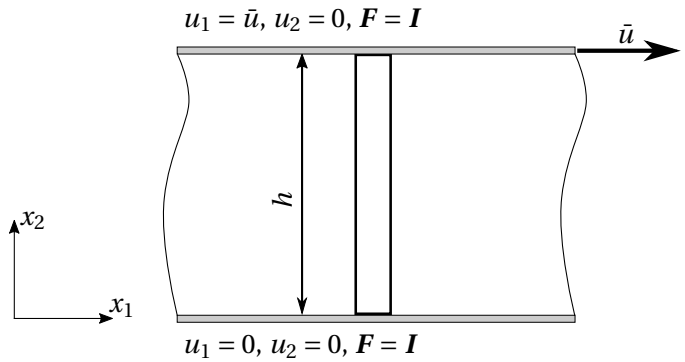

Figure 4.13: Schematic representation of the boundary shear layer problem.

As reported by Luscher (2010) and Kouznetsova (2002), the analytical expression for the value of the deformation gradient component F_{12} along x_2 is given by

$$F_{12} = \bar{u} \cdot \frac{\sinh\left(\frac{x_2}{\hat{l}}\right) - \sinh\left(\frac{h}{\hat{l}}\right) + \sinh\left(\frac{h - x_2}{\hat{l}}\right)}{2\hat{l}\left(\cosh\left(\frac{h}{\hat{l}}\right) - 1\right) - h\sinh\left(\frac{h}{\hat{l}}\right)}, \tag{4.77}$$

where $\hat{l} = \sqrt{2}l$, and l denotes the material length scale parameter.

This problem has been solved with both Q8F4L1 and Q9F9L4 mixed finite elements, employing three different discretisations. The height of the layer is $h = 1$ mm, and a displacement $\bar{u} = 0.03$ was applied. Both the numerical and analytical results are plotted in Figure 4.14.

In general, the results obtained with both elements follow the expected solution. The distribution of F_{12} is better captured with the Q9F9L4 element, which is explained by the greater number of nodes for its discretisation.

The numerical results diverge from the analytical solution when the material characteristic length assumes the smallest value ($l = 0.01$ mm). This is more significant in the region close to the surfaces with the Q8F4L1 element, where an oscillation is obtained in the response. It is also observed with the Q9F9L4 for the coarser discretisations. For very small values of l, the solution would approach the standard 1$^{\text{st}}$ order solution, where F_{12} is constant throughout the layer. However, since the constraint $F_{12} = 0$ is enforced at the surfaces, a sharp evolution is obtained, which is hard to capture without a very fine mesh. Indeed, in order to obtain good approximations, the size of the element should be smaller than the material characteristic length (Kouznetsova, 2002). As the value of l increases, the variation of F_{12} becomes smoother and the numerical results capture the analytical response accurately with both elements.

3D

A 3D finite element model is employed to solve the boundary shear layer problem using H20F8L1 elements. Since the layer is infinite in x_1 and x_3, only one strip of elements is used to discretise along the height, with periodicity constraints in these two directions. The distribution of the deformation gradient component F_{12} in x_2 is plotted in Figure 4.15, for different material characteristic lengths and discretisations.

The results obtained with the 3D model of the boundary shear layer are coincident with the 2D counterparts obtained with the Q8F4L1 element. This is consistent with the fact that the H20F8L1 element is an extension of the Q8F4L1 element.

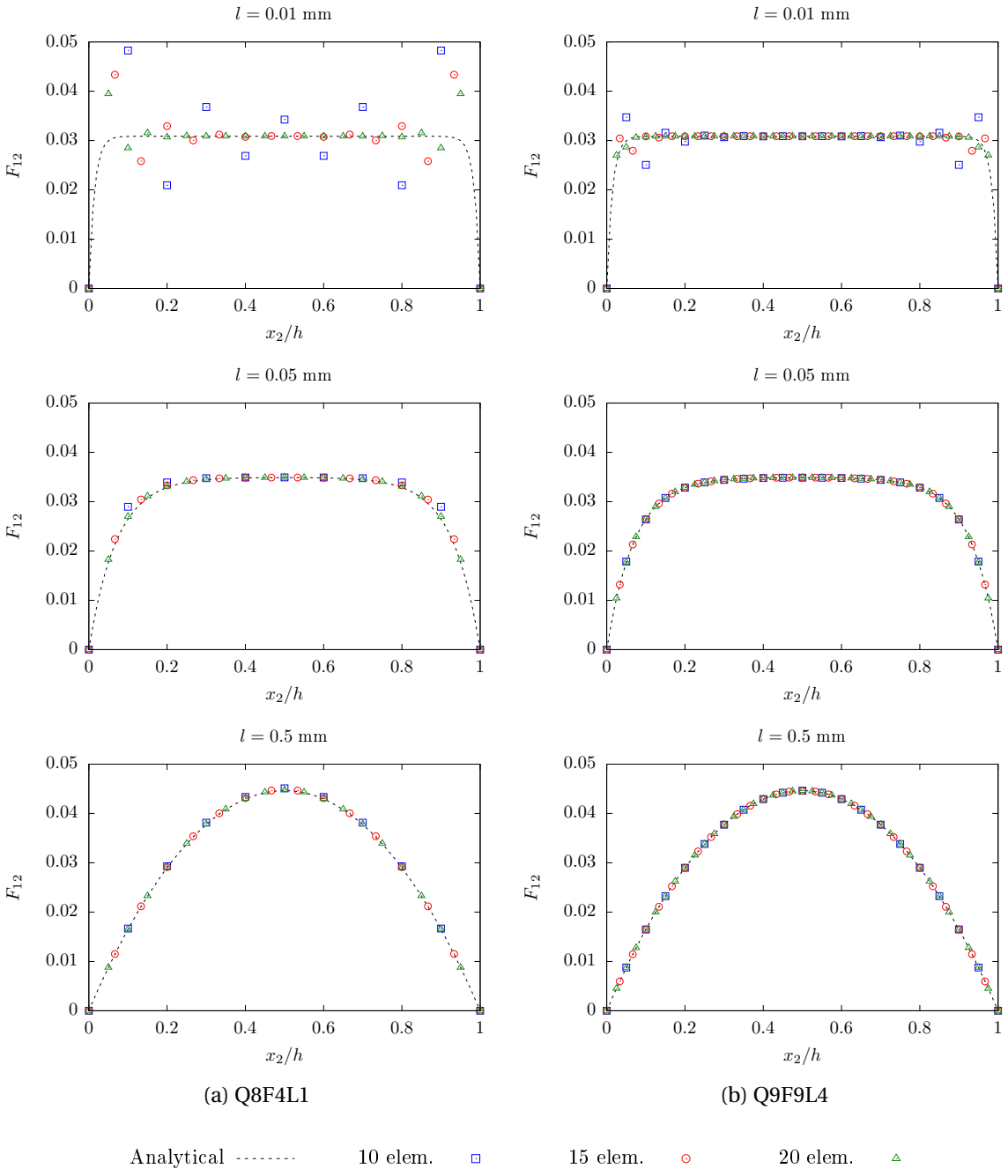

(a) Q8F4L1 (b) Q9F9L4

Figure 4.14: Numerical and analytical results for the deformation gradient component F_{12}, in the 2D boundary shear layer problem.

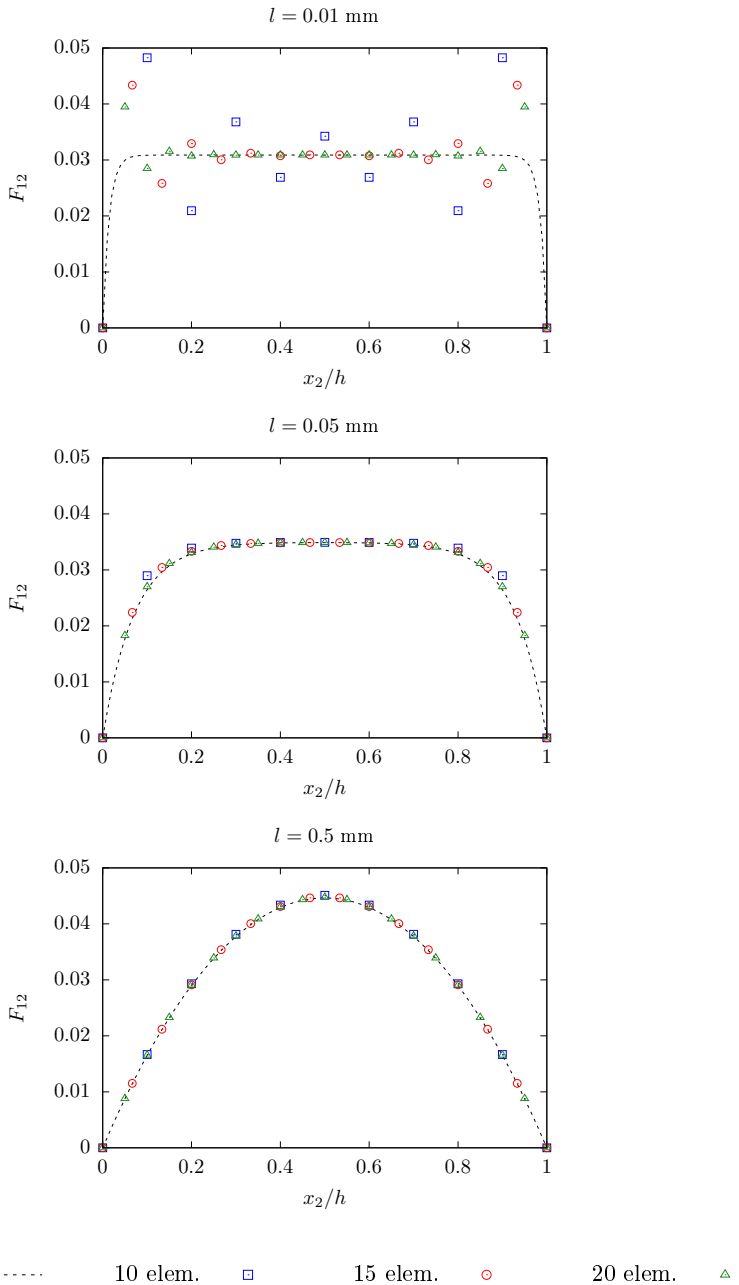

Figure 4.15: Numerical and analytical results for the deformation gradient component F_{12}, in the 3D boundary shear layer problem.

4.6.4 Stress concentration factor in a solid with a cylindrical hole

The influence of the material characteristic length on the stress concentration factor is analysed in this example. An infinite solid with a cylindrical hole is subjected to remote uniform traction. This example has been analysed by Shu et al. (1999) in a couple-stress framework. In that case it is observed that the stress concentration factor increases and approaches the value of 3 as the material characteristic length decreases.

A 2D model of this problem is employed here, where a block of material with size $L = 20$ mm containing a centred hole with radius $r = 1$ mm is subjected to remote tension $\sigma_{22} = 1$ MPa (Figure 4.16). Due to the symmetries, only a quarter of the domain is discretised with Q8F4L1 elements, with the appropriate boundary conditions: $u_1 = 0$ on the vertical symmetry axis, $u_2 = 0$ on the horizontal counterpart, and $F_{12} = F_{21} = 0$ on both.

The contour plot of the resulting stress field is shown in Figure 4.17 for different values of the material characteristic length. The evolution of the stress concentration factor with l is plotted in Figure 4.18.

As expected, an increasing value of the material characteristic length leads to a decrease of the stress concentration factor. The stress concentration value tends to 3 in the limiting case of $l \approx 0$, which is consistent with linear theories.

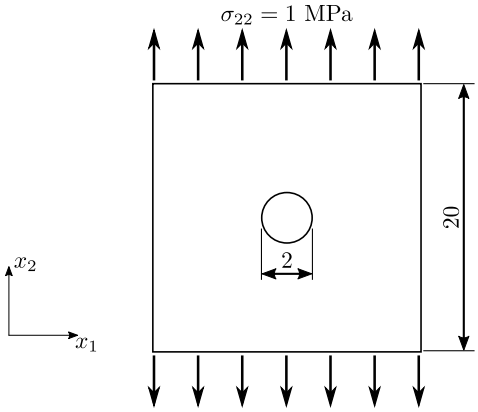

Figure 4.16: Geometry and dimensions for the model of a solid with a cylindrical hole.

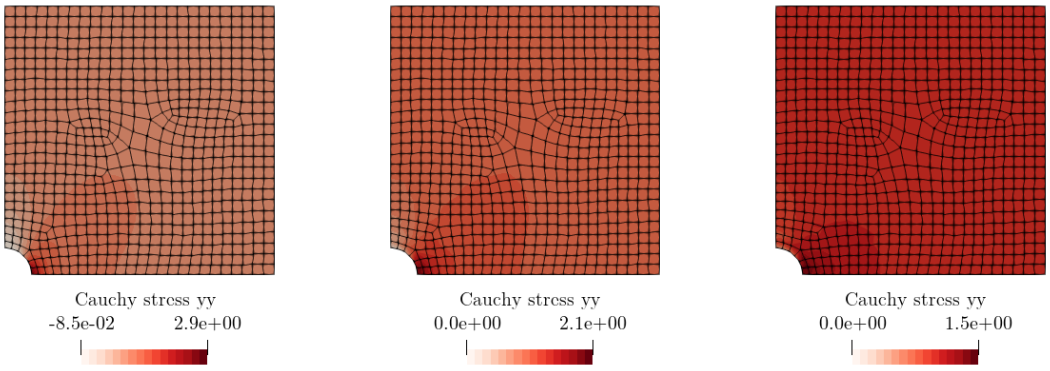

(a) $l = 0.1$ mm (b) $l = 0.5$ mm (c) $l = 1$ mm

Figure 4.17: Contour plot of the Cauchy stress σ_{22} on the solid with cylindrical hole.

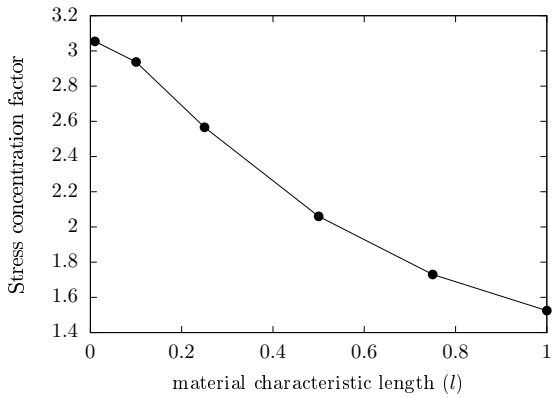

Figure 4.18: Evolution of the stress concentration factor with the material characteristic length.

4.6.5 Cantilever beam

2D

The classical problem of bending of a cantilever beam is analysed. A 2D beam with dimensions 50×10 mm, in plane strain state, is clamped on the left border ($\boldsymbol{u} = \boldsymbol{0}$, $\boldsymbol{F} = \boldsymbol{I}$) and a vertical load $t = 1$ MPa is applied on the right face (Figure 4.19). It is discretised with 80 Q8F4L1 elements, as shown in Figure 4.20. The vertical displacement throughout the beam mid plane is plotted in Figure 4.21a, for different values of the material characteristic length.

It is clearly observed that an increasing characteristic length provides additional stiffness to the beam, resulting in a smaller deflection. This is in agreement with the results presented by Kwon and Lee (2017) for a similar study employing a 3D model. Q9F9L4 elements are also employed, and the solution coincides with the obtained with Q8F4L1 elements.

3D

A 3D beam with dimensions $50 \times 10 \times 10$ mm is clamped on the left border ($\boldsymbol{u} = \boldsymbol{0}$, $\boldsymbol{F} = \boldsymbol{I}$) and a vertical load $t = 1$ MPa is applied on the right face. It is discretised with 320 H20F8L1 elements. The vertical deflection obtained over the mid of the side face is plotted in Figure 4.21b, for different values of the material characteristic length. The deformed meshes are shown in Figure 4.22. Similarly to the 2D case, the results are coherent with the work of Kwon and Lee (2017), being observed that an increasing characteristic length provides additional stiffness to the beam, resulting in a smaller deflection.

Moreover, comparing the distributions of the 1$^{\text{st}}$-order stress with the higher-order stress in Figure 4.22, it is possible to conclude that the higher-order stresses become dominant as the value of l increases, and the conventional 1$^{\text{st}}$-order stress loses its importance.

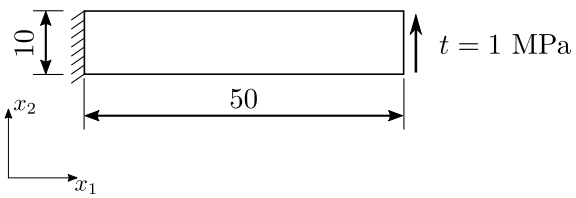

Figure 4.19: Geometry and dimensions of the cantilever beam.

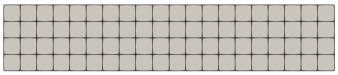

Figure 4.20: Mesh used to discretise the 2D cantilever beam.

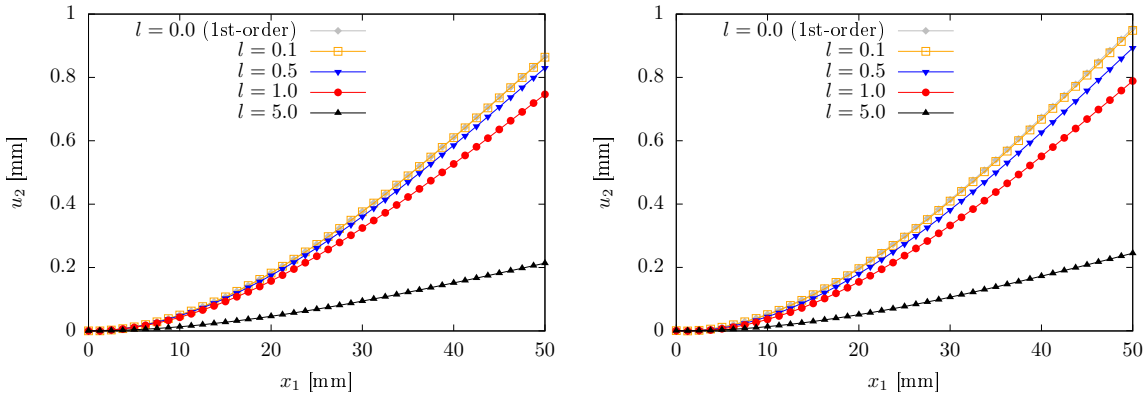

(a) 2D (b) 3D

Figure 4.21: Vertical displacement on the beam mid plane for different values of the material characteristic length.

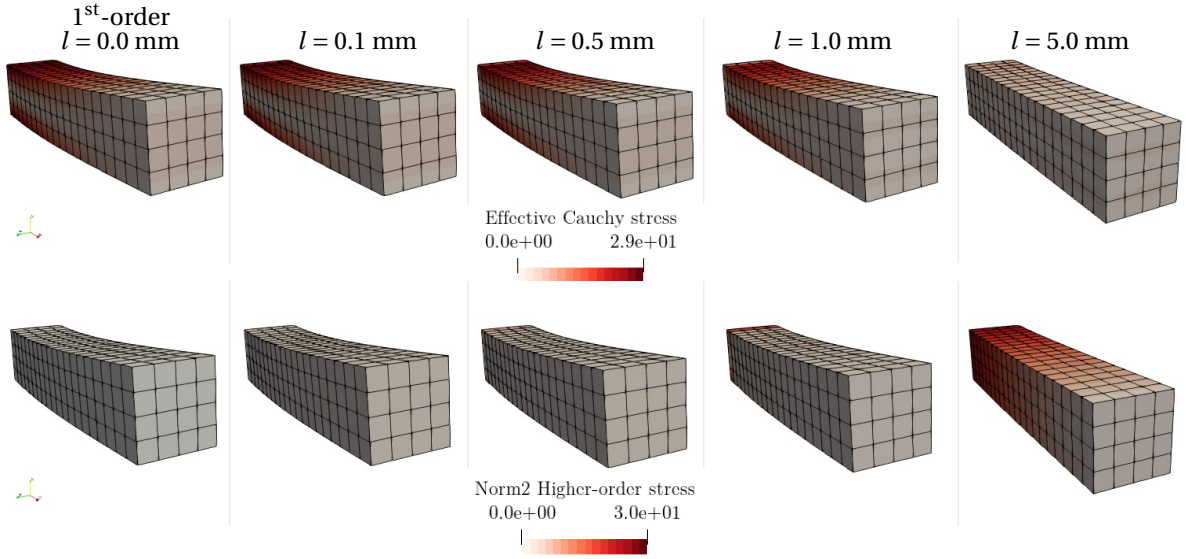

Figure 4.22: Contour plot of the equivalent stress (top) and norm of the higher-order stress tensor $\mathbf{Q}$ (bottom) on the deformed mesh, for different values of the characteristic length.

4.6.6 Thick hollow cylinder

2D

A thick hollow cylinder subjected to external radial pressure is analysed in this section. The internal and external radius are $r_i = 0.05$ mm and $r_e = 0.5$ mm, respectively. Plane strain condition is assumed. External pressure $\sigma_r = 1$ MPa is applied. Only a quarter of the domain is discretised with Q8F4L1 elements, as shown in Figure 4.23, due to symmetries. Appropriate boundary conditions are applied: $u_1 = 0$ and $F_{21} = 0$ on the vertical symmetry axis, and $u_2 = 0$ and $F_{12} = 0$ on the horizontal counterpart. Zervos et al. (2009) analyses this example in a small strain framework and provides analytical solutions for the radial displacement and deformation.

Both the horizontal displacement and deformation obtained numerically on the bottom face are plotted in Figure 4.24a, for different values of the material characteristic length, against their analytical solution.

It is observed that for the case of $l = 0.01$ mm, the same analysed by Zervos et al. (2009), both numerical and analytical solutions agree very well. In the remaining cases, the solutions diverge in the region near the internal surface of the hollow cylinder. This is particularly significant when looking at the strain measures. Nonetheless, a good solution is obtained in general.

This problem is also solved numerically with Q9F9L4 elements. The results are shown in Figure 4.24b, being similar to the results obtained with Q8F4L1 elements.

3D

The problem of the thick hollow cylinder under external radial pressure is now analysed with a 3D model. The thickness of the 3D model is $t = 0.05$ mm, and periodicity constraints are enforced along this direction in order to recover the plane strain state. Only a quarter of the domain is discretised with H20F8L1 elements (see Figure 4.25), employing the appropriate boundary conditions: $u_1 = 0$ and $F_{21} = 0$ on the plane $x = 0$, $u_2 = 0$ and $F_{12} = 0$ on $y = 0$ and $F_{33} = 1$ and $F_{13} = F_{31} = F_{23} = F_{32} = 0$ on both symmetry planes.

The numerical results are plotted along with the analytical solutions in Figure 4.24c. The results are very similar to the ones obtained with the 2D model with Q8F4L1 elements.

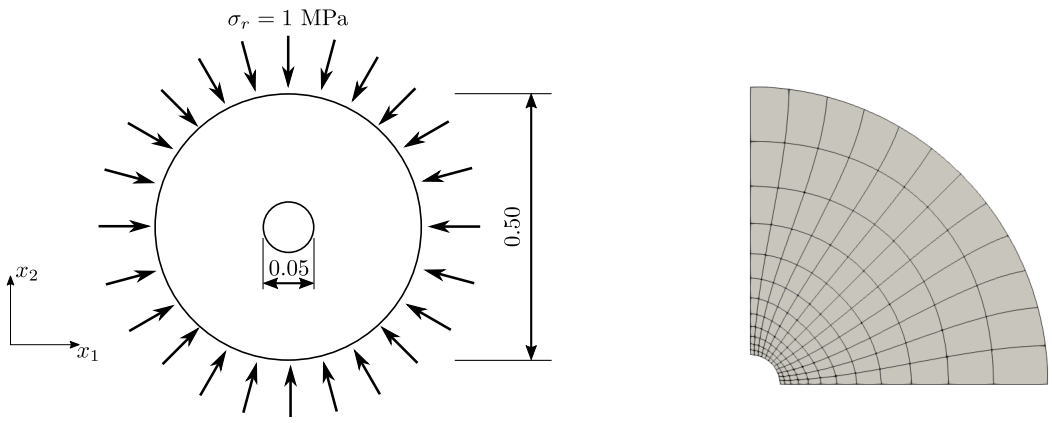

Figure 4.23: Geometry and finite element model used for the thick hollow cylinder.

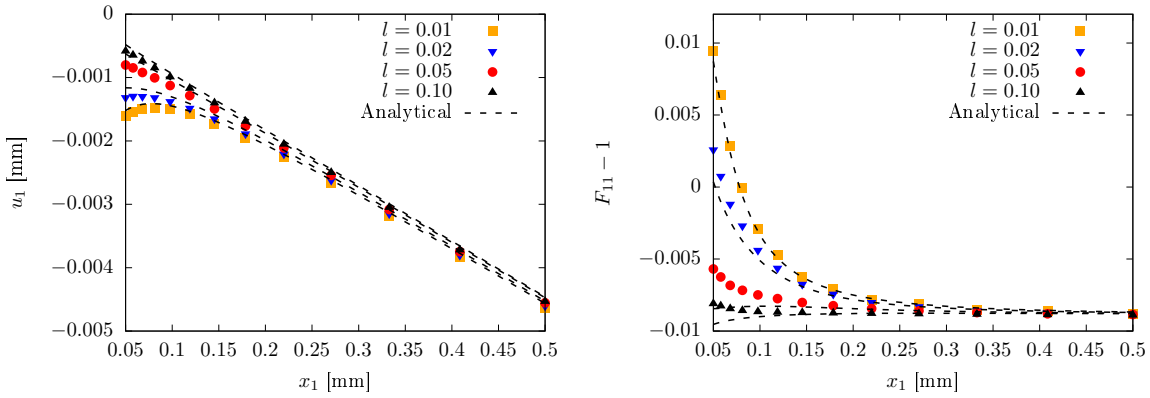

(a) Q8F4L1

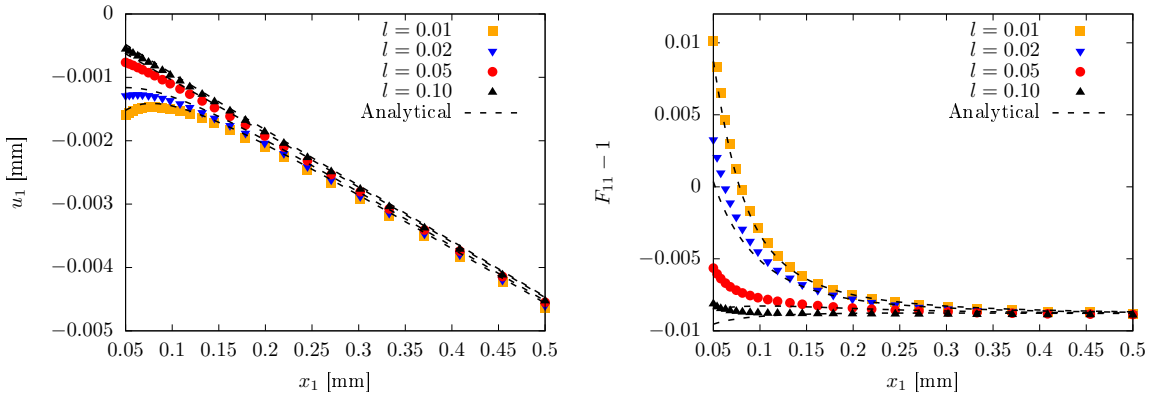

(b) Q9F9L4

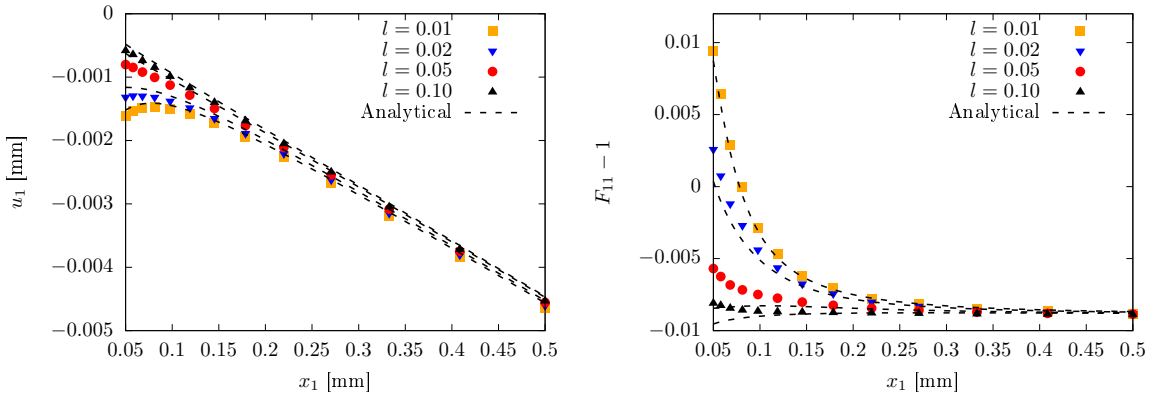

(c) H20F8L1

Figure 4.24: Comparison of numerical and analytical solutions for the radial displacement (left) and deformation (right) on the thick hollow cylinder, with different values of the material characteristic length and distinct elements.

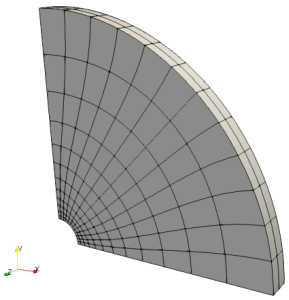

Figure 4.25: Mesh used for the thick hollow cylinder 3D model.

4.7 Conclusions

A 2nd-order continuum theory is presented in this chapter along with the corresponding finite element solution through a mixed formulation. The finite element implementation is assessed through several numerical examples, where the Q8F4L1 element, adopted here for 2D analysis, is employed, and the results compared with the Q9F9L4 element. Additionally, the H20F8L1 3D mixed element is proposed as an extension of the Q8F4L1 element. Results from the examples where 2D and 3D models can be directly compared show the equivalence between these elements. Moreover, comparisons with analytical solutions indicate that the mixed elements adopted here provide good approximations.

Chapter 5

Multi-Scale Models based on second-order computational homogenisation

Multi-scale models based on 2^{nd}-order computational homogenisation are an extension of the conventional 1^{st}-order homogenisation-based models, where the scale transition of kinematic variables is enriched with more information from the macro-scale. The macro-scale is described by a 2^{nd}-order continuum theory where the second gradient of the displacements is accounted for in the strain energy density function in addition to the deformation gradient (see Chapter 4). Therefore both tensors are inserted into the micro-scale, that is still modelled by a 1^{st}-order continuum model. As a consequence, the macroscopic higher-order stress is determined by homogenisation along with the 1^{st} Piola-Kirchhoff stress tensor. In a FE^2 framework, the corresponding consistent tangents must also be computed. This scheme is illustrated in Figure 5.1.

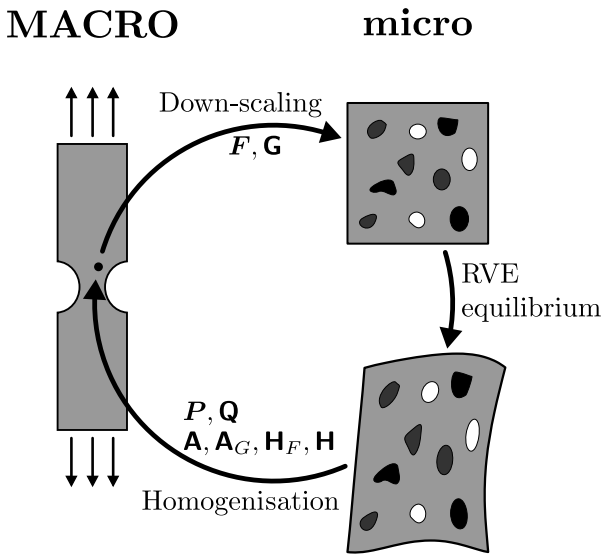

Figure 5.1: Schematic representation of a coupled multi-scale finite element analysis based on 2^{nd}-order homogenisation.

This approach has been proposed by Kouznetsova et al. (2002), Kouznetsova (2002), Kouznetsova et al. (2004b). The advantages of 2^{nd}-order continuum models described in Chapter 4 are recovered at the macro-scale with multi-scale models based on 2^{nd}-order homogenisation. Namely, the natural introduction of a material characteristic length, which is related to the chosen RVE length

(Kouznetsova et al., 2004a), provides mesh regularisation when softening occurs at the macro-scale and incorporates the influence of the absolute size of the microstructure. Being pointed as a difficulty, the development of 2^{nd}-order constitutive laws is obviated by this strategy, since the higher-order behaviour is naturally obtained by homogenisation of a micro-scale behaviour described by conventional constitutive equations. In addition, the *Scale Separation Principle* is relaxed when a 2^{nd}-order homogenisation framework is employed. While in a 1^{st}-order setting the RVE must be much smaller than the structural length, so that the assumption of constant deformation remains valid, a linear variation of the micro-deformation gradient is deemed in 2^{nd}-order homogenisation, allowing to use RVEs that are not that small, or cases where the macro-scale loadings or deformations wavelength is close to the RVE length. Ameen et al. (2018) analyses the scale separation limits with higher-order asymptotic homogenisation schemes, showing that a 2^{nd}-order scheme has a wider validity range than a 1^{st}-order scheme. Furthermore, second-order deformation modes including bending and twisting can be analysed at the micro-scale, permitting to unveil and analyse microstructural phenomena that cannot be captured with conventional multi-scale models.

In the sequence of the pioneering work of Kouznetsova, Kaczmarczyk et al. (2008, 2010) extended the formulation to other classical micro-scale boundary conditions. Lesičar (2015), Lesičar et al. (2016), Nguyen and Noels (2014), Nguyen et al. (2013) have followed this formulation. Luscher (2010) presented a formulation based on orthogonality conditions that results in different micro-scale constraints, thus yielding a distinct 2^{nd}-order homogenisation-based model. This author argues that a micro-scale volumetric constraint, resulting in a reactive constant body force, must be considered to correctly define the scale transitions between a 2^{nd}-order and a 1^{st}-order continuum. More recently, Blanco et al. (2016b) developed a formulation for a 2^{nd}-order multi-scale model also accounting for inertia and body forces at both scales, based on the *Principle of Multi-scale Virtual Power* (Blanco et al., 2016a). The resulting model differs from Kouznetsova and Luscher models. Nevertheless, neither implementation details nor numerical results have been reported. Marty et al. (2016) designed an experimental framework to analyse the performance of different higher-order homogenisation schemes describing the micro-scale behaviour.

Despite the advantages of 2^{nd}-order homogenisation models, only a few contributions address this kind of multi-scale models, the majority of which considering a small strain framework. Moreover, a critical comparison of the three main formulations found in the literature (Blanco et al., 2016b, Kouznetsova, 2002, Luscher, 2010) is lacking.

The formulation proposed by Blanco et al. (2016b) is particularised for the quasi-static case, in the absence of external body forces, and its finite element solution is described in detail in this chapter. An alternative formulation, also based on the *Method of Multi-Scale Virtual Power*, is developed and implemented. In addition, in order to clarify the impact of the assumptions made in distinct formulations available in the literature, Kouznetsova and Luscher's models are also introduced.

5.1 A quasi-static formulation based on the method of multi-scale virtual power

The 2^{nd}-order homogenisation multi-scale model proposed by Blanco et al. (2016b) is particularised here for the case where inertia and external body forces are not considered. It is based on the *Method of the Multi-Scale Virtual Power*, that allows to develop a variationally consistent multi-scale model, deriving naturally the micro-scale equilibrium problem, along with its kinematic constraints, and the homogenised stresses from the postulation of kinematic insertion and kinematic homogenisation. The formulation presented here is defined as symmetric due to the definition of the homogenised second gradient (more details in Section 5.1.1).

5.1.1 Multi-scale kinematics

Kinematic insertion

Kinematic insertion consists of the expression that defines the micro-scale displacement as a function of the macro-scale quantities. Blanco et al. (2016b) proposes the following formulae:

$$\boldsymbol{u}_\mu = \boldsymbol{u}_M + (\boldsymbol{F} - \boldsymbol{I})\,\boldsymbol{Y} + \frac{1}{2}\mathbf{G} : (\boldsymbol{Y} \otimes \boldsymbol{Y} - \boldsymbol{J}) + \tilde{\boldsymbol{u}}, \tag{5.1}$$

where $\boldsymbol{Y}$ denotes the vector of RVE reference coordinates, $\tilde{\boldsymbol{u}}$ the micro displacement fluctuation field and $\boldsymbol{J}$ the second-order moment of volume tensor:

$$\boldsymbol{J} = \frac{1}{V_\mu}\int_{\Omega_\mu} \boldsymbol{Y} \otimes \boldsymbol{Y}\, d\Omega_\mu. \tag{5.2}$$

Comparing Equation (5.1) with the insertion operator employed by Kouznetsova (2002) and Luscher (2010), the term $-\frac{1}{2}\mathbf{G} : \boldsymbol{J}$ is added, which results in a rigid body movement. Although this term is required for a correct characterisation of the external power per volume unit in the formulation of Blanco et al. (2016b), it may be disregarded when inertia and body forces are not included. In fact, it is easily observed that it results in a rigid body movement at the micro-scale. Therefore, since the absence of inertia and external body forces is assumed here, the kinematic insertion operator employed here is defined by:

$$\boldsymbol{u}_\mu = \boldsymbol{u}_M + (\boldsymbol{F} - \boldsymbol{I})\,\boldsymbol{Y} + \frac{1}{2}\mathbf{G} : (\boldsymbol{Y} \otimes \boldsymbol{Y}) + \tilde{\boldsymbol{u}}. \tag{5.3}$$

Without loss of generality, it is conveniently assumed that the origin of the micro coordinate system is located at the geometric center of the RVE, such that

$$\int_{\Omega_\mu} \boldsymbol{Y}\, d\Omega_\mu = \mathbf{0}. \tag{5.4}$$

Kinematic homogenisation

This procedure defines how micro-scale kinematical quantities are averaged in some sense to produce the macroscopic counterparts.

Like in a 1st-order homogenisation scheme, the macro-deformation gradient is obtained through volume averaging of its micro counterpart:

$$\boldsymbol{F} = \frac{1}{V_\mu}\int_{\Omega_\mu} \boldsymbol{F}_\mu\, d\Omega_\mu \Leftrightarrow \nabla \boldsymbol{u}_M = \frac{1}{V_\mu}\int_{\Omega_\mu} \nabla_Y \boldsymbol{u}_\mu\, d\Omega_\mu. \tag{5.5}$$

Since the problem at the micro-scale is still a 1st-order problem, the homogenised second-order gradient cannot be defined as the volume averaging its micro-scale counterpart. Following the proposal of Blanco et al. (2016b), it is defined as:

$$\mathbf{G} = \frac{1}{V_\mu}\int_{\Omega_\mu} \left[\left(\nabla_Y \boldsymbol{u}_\mu \otimes \boldsymbol{Y}\right) \cdot \boldsymbol{J}^{-1}\right]^S d\Omega_\mu. \tag{5.6}$$

The symmetry operator guarantees that the second gradient $\mathbf{G}$ is symmetric in the last two indices, as required by its definition (see Equation (4.1)).

Kinematic admissibility

The compatibility between kinematic insertion and kinematic homogenisation is ensured through constraints imposed at the RVE level. At this stage, it is convenient to derive the micro-scale displacement gradient, which is obtained from Equation (5.3) as

$$\nabla_Y \boldsymbol{u}_\mu = \frac{\partial \boldsymbol{u}_\mu}{\partial \boldsymbol{Y}} = (\boldsymbol{F} - \boldsymbol{I}) + \mathbf{G} \cdot \boldsymbol{Y} + \nabla_Y \tilde{\boldsymbol{u}}. \tag{5.7}$$

Inserting this definition into Equation (5.5), considering also Equation (5.4), results in:

$$\boldsymbol{F} = \boldsymbol{F} + \frac{1}{V_\mu}\mathbf{G} \cdot \int_{\Omega_\mu} \boldsymbol{Y}\, dV + \frac{1}{V_\mu}\int_{\Omega_\mu} \nabla_Y \tilde{\boldsymbol{u}} dV \Leftrightarrow \int_{\Omega_\mu} \nabla_Y \tilde{\boldsymbol{u}} dV = \mathbf{0}, \tag{5.8}$$

which can be expressed as a boundary integral

$$\int_{\partial\Omega_\mu} \tilde{\boldsymbol{u}} \otimes \boldsymbol{N} dA = \mathbf{0}, \tag{5.9}$$

where $\boldsymbol{N}$ denotes the outward reference unit vector. This is the minimal kinematic constraint arising also from 1$^{\text{st}}$-order homogenisation schemes, usually known as uniform traction boundary condition.

Likewise, inserting Equation (5.7) into (5.6) leads to

$$\mathbf{G} = \frac{1}{V_\mu}\int_{\Omega_\mu} \left[((\boldsymbol{F} - \boldsymbol{I}) \otimes \boldsymbol{Y}) \cdot \boldsymbol{J}^{-1}\right]^S dV + \frac{1}{V_\mu}\int_{\Omega_\mu} \left[(\mathbf{G} \cdot \boldsymbol{Y} \otimes \boldsymbol{Y}) \cdot \boldsymbol{J}^{-1}\right]^S dV + \frac{1}{V_\mu}\int_{\Omega_\mu} \left[(\nabla_Y \tilde{\boldsymbol{u}} \otimes \boldsymbol{Y}) \cdot \boldsymbol{J}^{-1}\right]^S dV. \tag{5.10}$$

Including the definition of the second-order moment of volume (Equation (5.2)) and Equation (5.4), the above equation is simplified to

$$\int_{\Omega_\mu} \left[(\nabla_Y \tilde{\boldsymbol{u}} \otimes \boldsymbol{Y}) \cdot \boldsymbol{J}^{-1}\right]^S dV = \mathbf{0}. \tag{5.11}$$

This volumetric constraint may be split into a volumetric and a boundary integral component. The left hand side is written in index notation as:

$$\int_{\Omega_\mu} \left[\nabla_Y \tilde{\boldsymbol{u}} \otimes \left(\boldsymbol{Y} \cdot \boldsymbol{J}^{-1}\right)\right]^S dV \Rightarrow \mathrm{sym}_{jk}\left[\int_{\Omega_\mu} \frac{\partial \tilde{u}_i}{\partial Y_j} J^{-1}_{kl} Y_l dV\right]. \tag{5.12}$$

Assuming $v_k = J^{-1}_{kl} Y_l$, and employing the rule of the product derivative:

$$\frac{\partial \tilde{u}_i}{\partial Y_j} v_k = \frac{\partial \tilde{u}_i v_k}{\partial Y_j} - \frac{\partial v_k}{\partial Y_j}\tilde{u}_i, \tag{5.13}$$

Equation (5.12) is further developed as follows

$$\mathrm{sym}_{jk}\left[\int_{\Omega_\mu} \frac{\partial \tilde{u}_i}{\partial Y_j} J^{-1}_{kl} Y_l dV\right] = \mathrm{sym}_{jk}\left[\int_{\Omega_\mu} \frac{\partial \tilde{u}_i v_k}{\partial Y_j} - \frac{\partial v_k}{\partial Y_j}\tilde{u}_i dV\right]. \tag{5.14}$$

As a consequence of the divergence theorem, the first term of the above right hand side is transformed into a boundary integral:

$$\int_{\Omega_\mu} \frac{\partial \tilde{u}_i v_k}{\partial Y_j} dV = \int_{\partial\Omega_\mu} \tilde{u}_i v_k N_j dA. \tag{5.15}$$

Therefore, taking into account that $\boldsymbol{J}^{-1}$ is symmetric and constant on the RVE domain, Equation (5.11) is finally expressed by:

$$\mathrm{sym}_{jk}\left[\int_{\partial\Omega_\mu} \tilde{u}_i N_j J^{-1}_{kl} Y_l dA - \int_{\Omega_\mu} \tilde{u}_i J^{-1}_{kj} dV\right] = 0 \Leftrightarrow$$
$$\int_{\partial\Omega_\mu} \left[(\tilde{\boldsymbol{u}} \otimes \boldsymbol{N} \otimes \boldsymbol{Y}) \cdot \boldsymbol{J}^{-1}\right]^S dA - \int_{\Omega_\mu} \tilde{\boldsymbol{u}} dV \otimes \boldsymbol{J}^{-1} = \mathbf{0}. \tag{5.16}$$

5.1.2 Principle of multi-scale virtual power

The Lagrange multiplier method has proven to be an efficient strategy to enforce micro-scale constraints (see Section 3.5). In addition, Lagrange multipliers are useful to understand the reactive nature of kinematic constraints (Blanco et al., 2016b). Therefore a formulation based on the Lagrange multiplier method is employed here.

The *Principle of Multi-scale Virtual Power* is employed to ensure the conservation of the virtual power in the scale transition, as a generalisation of the Hill-Mandel Principle. In this case, it states that

$$\begin{aligned}\boldsymbol{P}:\delta\boldsymbol{F}+\mathbf{Q}\vdots\delta\mathbf{G}=\frac{1}{V_\mu}\Bigg[&\int_{\Omega_\mu}\boldsymbol{P}_\mu:(\delta\boldsymbol{F}+\delta\mathbf{G}\cdot\boldsymbol{Y}+\nabla_Y\delta\tilde{\boldsymbol{u}})\,dV\\&-\delta\boldsymbol{L}:\left(\int_{\partial\Omega_\mu}\tilde{\boldsymbol{u}}\otimes\boldsymbol{N}dA\right)-\boldsymbol{L}:\left(\int_{\partial\Omega_\mu}\delta\tilde{\boldsymbol{u}}\otimes\boldsymbol{N}dA\right)\\&-\delta\mathbf{M}\vdots\left(\int_{\Omega_\mu}\left[(\nabla_Y\tilde{\boldsymbol{u}}\otimes\boldsymbol{Y})\cdot\boldsymbol{J}^{-1}\right]^S dV\right)\\&-\mathbf{M}\vdots\left(\int_{\Omega_\mu}\left[(\nabla_Y\delta\tilde{\boldsymbol{u}}\otimes\boldsymbol{Y})\cdot\boldsymbol{J}^{-1}\right]^S dV\right)\Bigg],\quad\forall\,(\delta\boldsymbol{F},\delta\mathbf{G},\delta\tilde{\boldsymbol{u}},\delta\boldsymbol{L},\delta\mathbf{M})\,.\end{aligned}\tag{5.17}$$

The Lagrange multiplier $\boldsymbol{L}$ is a second-order tensor which enforces the constraint (5.9) and $\mathbf{M}$ is a third-order tensor employed to impose Equation (5.12). Since only the symmetric part of the Lagrange multiplier $\mathbf{M}$ contributes to the virtual work, then we can assume that $\mathbf{M}$ is symmetric in the last two indices, i.e., $\mathrm{M}_{ijk}=\mathrm{M}_{ikj}$.

5.1.3 Micro-scale equilibrium problem

Setting $\delta\boldsymbol{F}=\mathbf{0}$ and $\delta\mathbf{G}=\mathbf{0}$ in Equation (5.17) results in the expression defining the micro-scale weak equilibrium problem. Therefore, the micro-scale equilibrium problem consists in finding the fluctuation field $\tilde{\boldsymbol{u}}$ and the Lagrange multipliers $\boldsymbol{L}$ and $\mathbf{M}$, such that:

$$\begin{aligned}\frac{1}{V_\mu}\Bigg[&\int_{\Omega_\mu}\boldsymbol{P}_\mu:\nabla_Y\delta\tilde{\boldsymbol{u}}dV-\delta\boldsymbol{L}:\left(\int_{\partial\Omega_\mu}\tilde{\boldsymbol{u}}\otimes\boldsymbol{N}dA\right)-\boldsymbol{L}:\left(\int_{\partial\Omega_\mu}\delta\tilde{\boldsymbol{u}}\otimes\boldsymbol{N}dA\right)\\&-\delta\mathbf{M}\vdots\left(\int_{\Omega_\mu}\left[(\nabla_Y\tilde{\boldsymbol{u}}\otimes\boldsymbol{Y})\cdot\boldsymbol{J}^{-1}\right]^S dV\right)\\&-\mathbf{M}\vdots\left(\int_{\Omega_\mu}\left[(\nabla_Y\delta\tilde{\boldsymbol{u}}\otimes\boldsymbol{Y})\cdot\boldsymbol{J}^{-1}\right]^S dV\right)\Bigg]=0.\end{aligned}\tag{5.18}$$

The strong form of this problem is determined in what follows. Due to the symmetries of $\boldsymbol{J}^{-1}$ and $\mathbf{M}$, the term

$$\mathbf{M}\vdots\left(\nabla\delta\tilde{\boldsymbol{u}}\otimes\boldsymbol{Y}\cdot\boldsymbol{J}^{-1}\right)^S=\left[\mathbf{M}\cdot\left(\boldsymbol{J}^{-1}\cdot\boldsymbol{Y}\right)\right]:\nabla\delta\tilde{\boldsymbol{u}}.\tag{5.19}$$

Including this expression in Equation (5.18), recovering Equation (5.8) as equivalent to Equation (5.9) and setting $\delta\boldsymbol{L}=\mathbf{0}$ and $\delta\mathbf{M}=\mathbf{0}$ yields

$$\int_{\Omega_\mu}\left[\boldsymbol{P}_\mu-\boldsymbol{L}-\mathbf{M}\cdot\left(\boldsymbol{J}^{-1}\cdot\boldsymbol{Y}\right)\right]:\nabla_Y\delta\tilde{\boldsymbol{u}}dV=0\tag{5.20}$$

Integrating by parts, the above expression is elaborated to

$$\begin{aligned}&\int_{\partial\Omega_\mu}\left(\left[\boldsymbol{P}_\mu-\boldsymbol{L}-\mathbf{M}\cdot\left(\boldsymbol{J}^{-1}\cdot\boldsymbol{Y}\right)\right]\cdot\boldsymbol{N}\right)\cdot\delta\tilde{\boldsymbol{u}}dA-\int_{\Omega_\mu}\mathrm{div}\left[\boldsymbol{P}_\mu-\boldsymbol{L}-\mathbf{M}\cdot\left(\boldsymbol{J}^{-1}\cdot\boldsymbol{Y}\right)\right]\cdot\delta\tilde{\boldsymbol{u}}dV=\\&\int_{\partial\Omega_\mu}\left(\left[\boldsymbol{P}_\mu-\boldsymbol{L}-\mathbf{M}\cdot\left(\boldsymbol{J}^{-1}\cdot\boldsymbol{Y}\right)\right]\cdot\boldsymbol{N}\right)\cdot\delta\tilde{\boldsymbol{u}}dA-\int_{\Omega_\mu}\left(\mathrm{div}\,\boldsymbol{P}_\mu-\mathbf{M}:\boldsymbol{J}^{-1}\right)\cdot\delta\tilde{\boldsymbol{u}}dV=0\end{aligned}\tag{5.21}$$

Since the above must hold for any $\delta\tilde{\boldsymbol{u}}$, the strong form of the micro-equilibrium is stated by

$$\boldsymbol{P}_\mu \cdot \boldsymbol{N} = \left[\boldsymbol{L} + \mathbf{M} \cdot \left(\boldsymbol{J}^{-1} \cdot \boldsymbol{Y}\right)\right] \cdot \boldsymbol{N}, \quad \text{on } \partial\Omega_\mu, \tag{5.22}$$

$$\operatorname{div} \boldsymbol{P}_\mu = \mathbf{M} : \boldsymbol{J}^{-1}, \quad \text{in } \Omega_\mu. \tag{5.23}$$

This shows that the Lagrange multiplier $\mathbf{M}$ contributes either to a constant body force $\mathbf{M} : \boldsymbol{J}^{-1}$ and a traction force $\left[\mathbf{M} \cdot \left(\boldsymbol{J}^{-1} \cdot \boldsymbol{Y}\right)\right] \cdot \boldsymbol{N}$ field. This is in accordance with the decomposition of the constraint (5.11) into (5.16), where a volume and a boundary integral are found. Moreover, this is coherent with the argument introduced by Luscher (2010), stating that a constant body force field at the micro-scale is required to generate a constant 2^{nd}-order gradient on the RVE.

5.1.4 First Piola-Kirchhoff stress homogenisation

The expression for the homogenised Piola-Kirchhoff stress tensor is obtained from the *Principle of Multi-Scale Virtual Power* by defining $\delta\boldsymbol{L} = \mathbf{0}$, $\delta\mathbf{M} = \mathbf{0}$, $\delta\mathbf{G} = \mathbf{0}$ and $\delta\tilde{\boldsymbol{u}} = \mathbf{0}$ in Equation (5.17), which yields:

$$\boldsymbol{P} : \delta\boldsymbol{F} = \frac{1}{V_\mu}\int_{\Omega_\mu} \boldsymbol{P}_\mu : \delta\boldsymbol{F} dV \Rightarrow \boldsymbol{P} = \frac{1}{V_\mu}\int_{\Omega_\mu} \boldsymbol{P}_\mu dV. \tag{5.24}$$

The above expression is similar to the 1^{st}-order homogenisation counterpart, and may be rewritten as

$$\boldsymbol{P} = \frac{1}{V_\mu}\left[\int_{\partial\Omega_\mu} \boldsymbol{P}_\mu \cdot \boldsymbol{N} \otimes \boldsymbol{Y} dA - \int_{\Omega_\mu} \operatorname{div}_Y \boldsymbol{P}_\mu \otimes \boldsymbol{Y} dV\right]. \tag{5.25}$$

In view of the strong form of the micro-problem, Equation (5.23), and the assumption of Equation (5.4), the second term is null, as shown next:

$$\int_{\Omega_\mu} \operatorname{div}_Y \boldsymbol{P}_\mu \otimes \boldsymbol{Y} dV = \int_{\Omega_\mu} \mathbf{M} : \boldsymbol{J}^{-1} \otimes \boldsymbol{Y} dV = \mathbf{M} : \boldsymbol{J}^{-1} \otimes \int_{\Omega_\mu} \boldsymbol{Y} dV = \mathbf{0}. \tag{5.26}$$

As a consequence, the homogenised stress $\boldsymbol{P}$ can be expressed as a boundary integral only:

$$\boldsymbol{P} = \frac{1}{V_\mu}\int_{\partial\Omega_\mu} \boldsymbol{t}_{\mu 0} \otimes \boldsymbol{Y} dA \tag{5.27}$$

where $\boldsymbol{t}_{\mu 0} = \boldsymbol{P}_\mu \cdot \boldsymbol{N}$ denotes the tractions on the RVE undeformed boundary $\partial\Omega_\mu$. In view of Equation (5.22), the stress homogenisation expression may be further developed as:

$$\begin{aligned}\boldsymbol{P} &= \frac{1}{V_\mu}\int_{\partial\Omega_\mu} \boldsymbol{P}_\mu \cdot \boldsymbol{N} \otimes \boldsymbol{Y} dA = \frac{1}{V_\mu}\int_{\partial\Omega_\mu} \left[\boldsymbol{L} + \mathbf{M} \cdot \left(\boldsymbol{J}^{-1} \cdot \boldsymbol{Y}\right)\right] \cdot \boldsymbol{N} \otimes \boldsymbol{Y} dA \\ &= \frac{1}{V_\mu}\left[\int_{\partial\Omega_\mu} \boldsymbol{L} \cdot \boldsymbol{N} \otimes \boldsymbol{Y} dA + \int_{\partial\Omega_\mu} \mathbf{M} \cdot \left(\boldsymbol{J}^{-1} \cdot \boldsymbol{Y}\right) \cdot \boldsymbol{N} \otimes \boldsymbol{Y} dA\right].\end{aligned} \tag{5.28}$$

It is possible to show that the second term is null, taking into account that $\mathbf{M}$ and $\boldsymbol{J}^{-1}$ are constant in the RVE along with Equation (5.4):

$$\begin{aligned}&\int_{\partial\Omega_\mu} M_{ijk} J^{-1}_{kl} Y_l N_j Y_m dA = M_{ijk} J^{-1}_{kl} \int_{\partial\Omega_\mu} Y_l N_j Y_m dA = \\ &M_{ijk} J^{-1}_{kl} \int_{\Omega_\mu} \frac{\partial (Y_l Y_m)}{\partial Y_j} dV = M_{ijk} J^{-1}_{kl} \int_{\Omega_\mu} \frac{\partial (Y_l Y_m)}{\partial Y_j} dV = \\ &M_{ijk} J^{-1}_{kl} \int_{\Omega_\mu} \left(\delta_{lj} Y_m + \delta_{mj} Y_l\right) dV = 0.\end{aligned} \tag{5.29}$$

Finally, developing the first term as follows:

$$P_{ik} = \frac{1}{V_\mu}\int_{\partial\Omega_\mu} L_{ij}N_j Y_k dA = \frac{1}{V_\mu}L_{ij}\int_{\partial\Omega_\mu} N_j Y_k dA \tag{5.30}$$

$$= \frac{1}{V_\mu}L_{ij}\int_{\Omega_\mu}\frac{\partial Y_k}{\partial Y_j}dV = \frac{1}{V_\mu}L_{ij}\int_{\Omega_\mu}\delta_{kj}dV = L_{ik}, \tag{5.31}$$

it is shown that the Lagrange multiplier $\boldsymbol{L}$ is equal to the homogenised Piola-Kirchhoff stress tensor $\boldsymbol{P}$:

$$\boldsymbol{L} = \boldsymbol{P}. \tag{5.32}$$

5.1.5 Higher-order stress homogenisation

The homogenised higher-order stress tensor $\mathbf{Q}$ is determined by setting $\delta\boldsymbol{L} = \mathbf{0}$, $\delta\mathbf{M} = \mathbf{0}$, $\delta\boldsymbol{F} = \mathbf{0}$ and $\delta\tilde{\boldsymbol{u}} = \mathbf{0}$ in Equation (5.17):

$$\begin{aligned}\mathbf{Q}\vdots\delta\mathbf{G} &= \frac{1}{V_\mu}\int_{\Omega_\mu}\boldsymbol{P}_\mu : (\delta\mathbf{G}\cdot\boldsymbol{Y})\,dV \\ &= \frac{1}{V_\mu}\int_{\Omega_\mu}(\boldsymbol{P}_\mu\otimes\boldsymbol{Y})\vdots\delta\mathbf{G}dV.\end{aligned} \tag{5.33}$$

Due to the right symmetry of $\mathbf{G}$, only the symmetric part of the right-hand side of the above expression contributes to the higher-order stress tensor Blanco et al. (2016b), Luscher (2010), which is expressed as:

$$\mathbf{Q} = \frac{1}{V_\mu}\int_{\Omega_\mu}(\boldsymbol{P}_\mu\otimes\boldsymbol{Y})^S dV. \tag{5.34}$$

The above integrand may be developed as shown below:

$$\begin{aligned}(\boldsymbol{P}\otimes\boldsymbol{Y})^S_{ijk} &= \frac{1}{2}\left(P_{ij}Y_k + P_{ik}Y_j\right) = \frac{1}{2}\left(P_{il}\frac{\partial Y_j}{\partial Y_l}Y_k + P_{il}\frac{\partial Y_k}{\partial Y_l}Y_j\right) = \\ &\frac{1}{2}\left(\frac{\partial\left(P_{il}Y_jY_k\right)}{\partial Y_l} - \frac{\partial P_{il}}{\partial Y_l}Y_jY_k - P_{il}\frac{\partial Y_k}{\partial Y_l}Y_j\right) + \\ &\frac{1}{2}\left(\frac{\partial\left(P_{il}Y_jY_k\right)}{\partial Y_l} - \frac{\partial P_{il}}{\partial Y_l}Y_jY_k - P_{il}\frac{\partial Y_j}{\partial Y_l}Y_k\right) = \\ &\frac{\partial\left(P_{il}Y_jY_k\right)}{\partial Y_l} - \frac{\partial P_{il}}{\partial Y_l}Y_jY_k - \frac{1}{2}\left(P_{ij}Y_k + P_{ik}Y_j\right) \Leftrightarrow \\ (\boldsymbol{P}\otimes\boldsymbol{Y})^S_{ijk} &= \frac{1}{2}\left(\frac{\partial\left(P_{il}Y_jY_k\right)}{\partial Y_l} - \frac{\partial P_{il}}{\partial Y_l}Y_jY_k\right).\end{aligned} \tag{5.35}$$

Applying the volume integral, and as a consequence of the divergence theorem:

$$\begin{aligned}\int_{\Omega_\mu}(\boldsymbol{P}\otimes\boldsymbol{Y})^S_{ijk}\,dV &= \int_{\Omega_\mu}\frac{1}{2}\left(\frac{\partial\left(P_{il}Y_jY_k\right)}{\partial Y_l} - \frac{\partial P_{il}}{\partial Y_l}Y_jY_k\right)dV = \\ &= \frac{1}{2}\left[\int_{\partial\Omega_\mu}P_{il}N_lY_jY_k dA - \int_{\Omega_\mu}\frac{\partial P_{il}}{\partial Y_l}Y_jY_k dV\right].\end{aligned} \tag{5.36}$$

Therefore, Expression (5.34) is rewritten as:

$$\mathbf{Q} = \frac{1}{2V_\mu}\left[\int_{\partial\Omega_\mu}\boldsymbol{P}\cdot\boldsymbol{N}\otimes\boldsymbol{Y}\otimes\boldsymbol{Y}\,dA - \int_{\Omega_\mu}\operatorname{div}\boldsymbol{P}\otimes\boldsymbol{Y}\otimes\boldsymbol{Y}\,dV\right] \tag{5.37}$$

In view of Equations (5.22) and (5.23), including the definition of the 2$^{\text{nd}}$-order moment of volume tensor (Equation (5.2)), this is further elaborated:

$$\begin{aligned}&\mathbf{Q}=\frac{1}{2V_\mu}\left[\int_{\partial\Omega_\mu}\left[\boldsymbol{L}+\mathbf{M}\cdot\left(\boldsymbol{J}^{-1}\cdot\boldsymbol{Y}\right)\right]\cdot\boldsymbol{N}\otimes\boldsymbol{Y}\otimes\boldsymbol{Y}\,dA-\int_{\Omega_\mu}\mathbf{M}:\boldsymbol{J}^{-1}\otimes\boldsymbol{Y}\otimes\boldsymbol{Y}\,dV\right]\Leftrightarrow\\&\mathbf{Q}+\frac{1}{2}\mathbf{M}:\boldsymbol{J}^{-1}\otimes\boldsymbol{J}=\frac{1}{2V_\mu}\int_{\partial\Omega_\mu}\left[\boldsymbol{L}+\mathbf{M}\cdot\left(\boldsymbol{J}^{-1}\cdot\boldsymbol{Y}\right)\right]\cdot\boldsymbol{N}\otimes\boldsymbol{Y}\otimes\boldsymbol{Y}\,dA\end{aligned}\tag{5.38}$$

Taking into account $\mathbf{M}$ symmetry, the above right-hand-side is simplified as shown in what follows, in index notation:

$$\begin{aligned}&\frac{1}{2V_\mu}\left[\int_{\partial\Omega_\mu}\left(L_{il}+\mathsf{M}_{ilm}J^{-1}_{mn}Y_n\right)N_lY_jY_k\,dA\right]=\\&=\frac{1}{2V_\mu}\left[\int_{\partial\Omega_\mu}L_{il}N_lY_jY_k\,dA+\int_{\partial\Omega_\mu}\mathsf{M}_{ilm}J^{-1}_{mn}Y_nN_lY_jY_k\,dA\right]=\\&=\frac{1}{2V_\mu}\left[L_{il}\int_{\partial\Omega_\mu}N_lY_jY_k\,dA+\mathsf{M}_{ilm}J^{-1}_{mn}\int_{\partial\Omega_\mu}Y_nN_lY_jY_k\,dA\right]=\\&=\frac{1}{2V_\mu}\left[L_{il}\int_{\Omega_\mu}\frac{\partial\left(Y_jY_k\right)}{\partial Y_l}\,dV+\mathsf{M}_{ilm}J^{-1}_{mn}\int_{\Omega_\mu}\frac{\partial\left(Y_jY_kY_n\right)}{\partial Y_l}\,dV\right]=\\&=\frac{1}{2V_\mu}\left[L_{il}\int_{\Omega_\mu}\left(\delta_{jl}Y_k+\delta_{kl}Y_j\right)dV+\mathsf{M}_{ilm}J^{-1}_{mn}\int_{\Omega_\mu}\left(\delta_{jl}Y_kY_n+\delta_{kl}Y_jY_n+\delta_{nl}Y_jY_k\right)dV\right]=\\&=\frac{1}{2}\left(\mathsf{M}_{ijm}J^{-1}_{mn}J_{nk}+\mathsf{M}_{ikm}J^{-1}_{mn}J_{nj}+\mathsf{M}_{inm}J^{-1}_{mn}J_{jk}\right)=\\&=\frac{1}{2}\left(\mathsf{M}_{ijk}+\mathsf{M}_{ikj}+\mathsf{M}_{inm}J^{-1}_{nm}J_{jk}\right)\Rightarrow\left[\mathbf{M}+\frac{1}{2}\mathbf{M}:\boldsymbol{J}^{-1}\otimes\boldsymbol{J}\right]_{ijk}.\end{aligned}\tag{5.39}$$

Introducing this simplification into Equation (5.38) leads to:

$$\mathbf{Q}+\frac{1}{2}\mathbf{M}:\boldsymbol{J}^{-1}\otimes\boldsymbol{J}=\mathbf{M}+\frac{1}{2}\mathbf{M}:\boldsymbol{J}^{-1}\otimes\boldsymbol{J}\Leftrightarrow\mathbf{Q}=\mathbf{M}.\tag{5.40}$$

Therefore, the Lagrange multiplier $\mathbf{M}$ is equal to the higher-order stress tensor $\mathbf{Q}$.

5.1.6 Finite element solution of the micro-scale problem

Aiming to solve the equilibrium problem stated by Equation (5.18), it is discretised with the finite element method, leading to

$$\begin{aligned}\delta\tilde{\mathbf{u}}^T\int_{\Omega_\mu}\mathbf{G}^T\mathbf{P}_\mu dV-\delta\mathbf{L}^T\mathbf{C}_L\tilde{\mathbf{u}}-\mathbf{L}^T\mathbf{C}_L\delta\tilde{\mathbf{u}}\\-\delta\mathbf{M}^T\mathbf{C}_M\tilde{\mathbf{u}}-\mathbf{M}^T\mathbf{C}_M\delta\tilde{\mathbf{u}}=0,\quad\forall\left(\delta\tilde{\mathbf{u}},\delta\mathbf{L},\delta\mathbf{M}\right),\end{aligned}\tag{5.41}$$

where $\mathbf{L}$ and $\mathbf{M}$ denote the Lagrange multipliers $\boldsymbol{L}$ and M in vector format, taking into account the right symmetry of M:

$$\mathbf{L}_{2D} = \begin{Bmatrix} L_{11} \\ L_{21} \\ L_{12} \\ L_{22} \end{Bmatrix}, \quad \mathbf{L}_{3D} = \begin{Bmatrix} L_{11} \\ L_{21} \\ L_{31} \\ L_{12} \\ L_{22} \\ L_{32} \\ L_{13} \\ L_{23} \\ L_{33} \end{Bmatrix}, \quad \mathbf{M}_{2D} = \begin{Bmatrix} \mathsf{M}_{111} \\ \mathsf{M}_{211} \\ \mathsf{M}_{122} \\ \mathsf{M}_{222} \\ \mathsf{M}_{112} \\ \mathsf{M}_{212} \end{Bmatrix}, \quad \mathbf{M}_{3D} = \begin{Bmatrix} \mathsf{M}_{111} \\ \mathsf{M}_{211} \\ \mathsf{M}_{311} \\ \mathsf{M}_{122} \\ \mathsf{M}_{222} \\ \mathsf{M}_{322} \\ \mathsf{M}_{133} \\ \mathsf{M}_{233} \\ \mathsf{M}_{333} \\ \mathsf{M}_{112} \\ \mathsf{M}_{212} \\ \mathsf{M}_{312} \\ \mathsf{M}_{123} \\ \mathsf{M}_{223} \\ \mathsf{M}_{323} \\ \mathsf{M}_{113} \\ \mathsf{M}_{213} \\ \mathsf{M}_{313} \end{Bmatrix}, \tag{5.42}$$

and $\mathbf{C}_L$ and $\mathbf{C}_M$ are the constraint matrices related to Equations (5.9) and (5.11), respectively.

Since Equation (5.41) must hold for any displacement fluctuation or Lagrange multiplier, then it can be rewritten in separate equations:

$$\int_{\Omega_\mu} \mathbf{G}^T \mathbf{P}_\mu dV - \mathbf{C}_L^T \mathbf{L} - \mathbf{C}_M^T \mathbf{M} = \mathbf{0} \tag{5.43}$$

$$\mathbf{C}_L \tilde{\mathbf{u}} = \mathbf{0} \tag{5.44}$$

$$\mathbf{C}_M \tilde{\mathbf{u}} = \mathbf{0}. \tag{5.45}$$

Therefore, the residual vector is defined by

$$\mathbf{r} = \begin{Bmatrix} \mathbf{f} - \mathbf{C}_L^T \mathbf{L} - \mathbf{C}_M^T \mathbf{M} \\ \mathbf{C}_L \tilde{\mathbf{u}} \\ \mathbf{C}_M \tilde{\mathbf{u}} \end{Bmatrix}. \tag{5.46}$$

Linearisation of the problem $\mathbf{r} = \mathbf{0}$, yields the following linear system of equations

$$\begin{bmatrix} \mathbf{K} & -\mathbf{C}^T \\ \mathbf{C} & \mathbf{0} \end{bmatrix} \begin{Bmatrix} \Delta\tilde{\mathbf{u}} \\ \boldsymbol{\lambda} \end{Bmatrix} = - \begin{Bmatrix} \mathbf{f} - \mathbf{C}^T \boldsymbol{\lambda} \\ \mathbf{C}\tilde{\mathbf{u}} \end{Bmatrix}, \tag{5.47}$$

where the Lagrange multiplier vector is

$$\boldsymbol{\lambda} = \begin{Bmatrix} \mathbf{L} \\ \mathbf{M} \end{Bmatrix}, \tag{5.48}$$

and the constraint matrix

$$\mathbf{C} = \begin{bmatrix} \mathbf{C}_L \\ \mathbf{C}_M \end{bmatrix}. \tag{5.49}$$

Constraint matrices

The minimal constraint from Equation (5.9) is related to the constraint matrix $\mathbf{C}_L$, which is similar to its definition from Equations (3.40) and (3.41). The structure of the constraint matrix $\mathbf{C}_M$ is easily devised from its underlying constraint, given by Equation (5.12), written in index notation:

$$\text{sym}_{jk}\left[\int_{\Omega_\mu}\frac{\partial H_n}{\partial Y_j}J^{-1}_{kl}Y_l dV\tilde{u}_{in}\right]=\frac{1}{2}\left[\int_{\Omega_\mu}\frac{\partial H_n}{\partial Y_j}Y_l dV J^{-1}_{lk}\tilde{u}_{in}+\int_{\Omega_\mu}\frac{\partial H_n}{\partial Y_k}Y_l dV J^{-1}_{lj}\tilde{u}_{in}\right]. \tag{5.50}$$

Taking into account how Lagrange multiplier vectors are arranged, in Expressions (5.42), the constraint matrix for a 2D RVE must be built as

$$\mathbf{C}_M=\left[\begin{array}{c:c} \left(\int\frac{\partial H_1}{\partial Y_1}Y_1 dV J^{-1}_{11}+\int\frac{\partial H_1}{\partial Y_1}Y_2 dV J^{-1}_{21}\right)\mathbf{I} & \cdots \\ \left(\int\frac{\partial H_1}{\partial Y_2}Y_1 dV J^{-1}_{12}+\int\frac{\partial H_1}{\partial Y_2}Y_2 dV J^{-1}_{22}\right)\mathbf{I} & \cdots \\ \frac{1}{2}\left(\int\frac{\partial H_1}{\partial Y_2}Y_1 dV J^{-1}_{11}+\int\frac{\partial H_1}{\partial Y_2}Y_2 dV J^{-1}_{21}\int\frac{\partial H_1}{\partial Y_1}Y_1 dV J^{-1}_{12}+\int\frac{\partial H_1}{\partial Y_1}Y_2 dV J^{-1}_{22}\right)\mathbf{I} & \cdots \end{array}\right]. \tag{5.51}$$

For the case of a rectangular RVE, the second-order moment of volume is a diagonal tensor, $J^{-1}_{12}=J^{-1}_{21}=0$, therefore the matrix is simplified to

$$\mathbf{C}_M=\left[\begin{array}{c:c} \left(\int\frac{\partial H_1}{\partial Y_1}Y_1 dV J^{-1}_{11}\right)\mathbf{I} & \cdots \\ \left(\int\frac{\partial H_1}{\partial Y_2}Y_2 dV J^{-1}_{22}\right)\mathbf{I} & \cdots \\ \frac{1}{2}\left(\int\frac{\partial H_1}{\partial Y_2}Y_1 dV J^{-1}_{11}+\int\frac{\partial H_1}{\partial Y_1}Y_2 dV J^{-1}_{22}\right)\mathbf{I} & \cdots \end{array}\right]. \tag{5.52}$$

For the case of 3D cubic RVEs it yields

$$\mathbf{C}_M=\left[\begin{array}{c:c} \left(\int\frac{\partial H_1}{\partial Y_1}Y_1 dV J^{-1}_{11}\right)\mathbf{I} & \cdots \\ \left(\int\frac{\partial H_1}{\partial Y_2}Y_2 dV J^{-1}_{22}\right)\mathbf{I} & \cdots \\ \left(\int\frac{\partial H_1}{\partial Y_3}Y_3 dV J^{-1}_{33}\right)\mathbf{I} & \cdots \\ \frac{1}{2}\left(\int\frac{\partial H_1}{\partial Y_2}Y_1 dV J^{-1}_{11}+\int\frac{\partial H_1}{\partial Y_1}Y_2 dV J^{-1}_{22}\right)\mathbf{I} & \cdots \\ \frac{1}{2}\left(\int\frac{\partial H_1}{\partial Y_3}Y_2 dV J^{-1}_{22}+\int\frac{\partial H_1}{\partial Y_2}Y_3 dV J^{-1}_{33}\right)\mathbf{I} & \cdots \\ \frac{1}{2}\left(\int\frac{\partial H_1}{\partial Y_3}Y_1 dV J^{-1}_{11}+\int\frac{\partial H_1}{\partial Y_1}Y_3 dV J^{-1}_{33}\right)\mathbf{I} & \cdots \end{array}\right]. \tag{5.53}$$

5.1.7 Macroscopic tangent operators

In a coupled-scale FE^2 second-order homogenisation framework, the macroscopic consistent tangents must be determined in order to solve the macroscopic equilibrium with the Newton-Raphson method (see Section 4.4.5 and Figure 5.1). For a particular RVE under a given $\boldsymbol{F}$ and $\mathbf{G}$, the micro-scale residual $\mathbf{r}$ is minimised when the RVE equilibrium is found. Therefore, at the RVE equilibrium:

$$\frac{\partial\mathbf{r}}{\partial\mathbf{F}}=\mathbf{0}, \tag{5.54}$$

and

$$\frac{\partial\mathbf{r}}{\partial\mathbf{G}}=\mathbf{0}, \tag{5.55}$$

where $\mathbf{F}$ and $\mathbf{G}$ denote the vector format of the macro-deformation gradient $\boldsymbol{F}$ and the 2$^{\text{nd}}$-order gradient $\mathbf{G}$.

Starting from the derivative with regard to the deformation gradient, it can be written as

$$\begin{bmatrix} \dfrac{\partial \mathbf{f}}{\partial \mathbf{F}} - \mathbf{C}^T \dfrac{\partial \boldsymbol{\lambda}}{\partial \mathbf{F}} \\ \mathbf{C} \dfrac{\partial \tilde{\mathbf{u}}}{\partial \mathbf{F}} \end{bmatrix} = \mathbf{0}. \tag{5.56}$$

The derivative

$$\frac{\partial \mathbf{f}}{\partial \mathbf{F}} = \frac{\partial \mathbf{f}}{\partial \mathbf{u}} \frac{\partial \mathbf{u}}{\partial \mathbf{F}} = \mathbf{K} \left(\mathbf{D}^T + \frac{\partial \tilde{\mathbf{u}}}{\partial \mathbf{F}} \right), \tag{5.57}$$

since the discretised version of Equation (5.3) is given by

$$\mathbf{u} = \mathbf{u}_M + \mathbf{D}^T (\mathbf{F} - \{\mathbf{I}\}) + \mathbf{V}^T \mathbf{G} + \tilde{\mathbf{u}}, \tag{5.58}$$

where the matrices with nodal coordinates are given by:

$$\mathbf{D} = \begin{bmatrix} & Y_1 \mathbf{I} & \\ \ldots & Y_2 \mathbf{I} & \ldots \\ & Y_3 \mathbf{I} & \end{bmatrix}, \tag{5.59}$$

$$\mathbf{V} = \frac{1}{2} \begin{bmatrix} & Y_1 Y_1 \mathbf{I} & \\ & Y_2 Y_2 \mathbf{I} & \\ & Y_3 Y_3 \mathbf{I} & \\ \ldots & Y_1 Y_2 \mathbf{I} & \ldots \\ & Y_1 Y_3 \mathbf{I} & \\ & Y_2 Y_3 \mathbf{I} & \end{bmatrix}. \tag{5.60}$$

Therefore, Equation (5.56) can be rewritten as a linear system of equations with multiple right hand sides:

$$\begin{bmatrix} \mathbf{K} & -\mathbf{C}^T \\ \mathbf{C} & \mathbf{0} \end{bmatrix} \begin{bmatrix} \dfrac{\partial \tilde{\mathbf{u}}}{\partial \mathbf{F}} \\ \dfrac{\partial \boldsymbol{\lambda}}{\partial \mathbf{F}} \end{bmatrix} = - \begin{bmatrix} \mathbf{K} \mathbf{D}^T \\ \mathbf{0} \end{bmatrix}. \tag{5.61}$$

Since the Lagrange multipliers are equal to the homogenised stresses, then the tangents $\frac{\partial \mathbf{P}}{\partial \mathbf{F}}$ and $\frac{\partial \mathbf{Q}}{\partial \mathbf{F}}$ are retrieved from $\frac{\partial \boldsymbol{\lambda}}{\partial \mathbf{F}}$.

Similarly, the derivative with regard to the 2$^{\text{nd}}$-order gradient, from Equation (5.55), yields

$$\begin{bmatrix} \dfrac{\partial \mathbf{f}}{\partial \mathbf{G}} - \mathbf{C}^T \dfrac{\partial \boldsymbol{\lambda}}{\partial \mathbf{G}} \\ \mathbf{C} \dfrac{\partial \tilde{\mathbf{u}}}{\partial \mathbf{G}} \end{bmatrix} = \mathbf{0}, \tag{5.62}$$

with

$$\frac{\partial \mathbf{f}}{\partial \mathbf{G}} = \frac{\partial \mathbf{f}}{\partial \mathbf{u}} \frac{\partial \mathbf{u}}{\partial \mathbf{G}} = \mathbf{K} \left(\mathbf{V}^T + \frac{\partial \tilde{\mathbf{u}}}{\partial \mathbf{G}} \right). \tag{5.63}$$

Expression (5.62) is rearranged in the following system of equations.

$$\begin{bmatrix} \mathbf{K} & -\mathbf{C}^T \\ \mathbf{C} & \mathbf{0} \end{bmatrix} \begin{bmatrix} \dfrac{\partial \tilde{\mathbf{u}}}{\partial \mathbf{G}} \\ \dfrac{\partial \boldsymbol{\lambda}}{\partial \mathbf{G}} \end{bmatrix} = - \begin{bmatrix} \mathbf{K} \mathbf{V}^T \\ \mathbf{0} \end{bmatrix}. \tag{5.64}$$

The tangents $\frac{\partial \mathbf{P}}{\partial \mathbf{G}}$ and $\frac{\partial \mathbf{Q}}{\partial \mathbf{G}}$ are obtained from $\frac{\partial \boldsymbol{\lambda}}{\partial \mathbf{G}}$.

The resulting systems of equations (5.61) and (5.64) are combined in single one, for the sake of compactness and improved computational efficiency, resulting in

$$\begin{bmatrix} \mathbf{K} & -\mathbf{C}^T \\ \mathbf{C} & \mathbf{0} \end{bmatrix} \begin{bmatrix} \dfrac{\partial \tilde{\mathbf{u}}}{\partial \mathbf{F}} & \dfrac{\partial \tilde{\mathbf{u}}}{\partial \mathbf{G}} \\ \dfrac{\partial \boldsymbol{\lambda}}{\partial \mathbf{F}} & \dfrac{\partial \boldsymbol{\lambda}}{\partial \mathbf{G}} \end{bmatrix} = - \begin{bmatrix} \mathbf{K} \mathbf{D}^T & \mathbf{K} \mathbf{V}^T \\ \mathbf{0} & \mathbf{0} \end{bmatrix}. \tag{5.65}$$

5.2 An alternative formulation based on the method of multi-scale virtual power

The formulation presented in Section 5.1 is defined as symmetric due to the symmetry operator in the definition of the homogenised second gradient, Equation (5.6). In fact, the second gradient of the displacements is symmetric by definition (see Equation (4.1)). Nevertheless, in the present multi-scale framework, represented in Figure 5.1, the micro-scale deformations are driven by the macroscopic $\mathbf{G}$, in addition to $\boldsymbol{F}$, which is already symmetric. Therefore, there is no need to define the homogenised second gradient as symmetric, since it is an input in the homogenisation procedure, and not an arbitrary output. In this section, an alternative definition of $\mathbf{G}$ is adopted and the resulting formulation based on the method of multi-scale virtual power is deduced, whose difference relatively to the symmetric formulation lies on the kinematic homogenisation procedure.

5.2.1 Multi-scale kinematics

Kinematic insertion

The kinematic insertion operator is the same defined in Section 5.1, given by Equation (5.3). The assumption that the RVE centroid coincides with the micro-coordinates system is also adopted (see Equation (5.4)).

Kinematic homogenisation

While the macro-deformation gradient definition remains defined by Equation (5.5), the macroscopic second gradient is now expressed as:

$$\mathbf{G} = \frac{1}{V_\mu}\int_{\Omega_\mu} \left(\nabla_Y \boldsymbol{u}_\mu \otimes \boldsymbol{Y}\right)\cdot \boldsymbol{J}^{-1} d\Omega_\mu, \tag{5.66}$$

where the symmetry operator is dropped.

Kinematic admissibility

The constraint arising from the compatibility between the micro-displacement field and the homogenised deformation gradient is given by Equation (5.9). Enforcing the compatibility with the macroscopic second gradient defined by Equation (5.66) results in the following constraint:

$$\int_{\Omega_\mu} (\nabla_Y \tilde{\boldsymbol{u}} \otimes \boldsymbol{Y})\cdot \boldsymbol{J}^{-1} dV = \mathbf{0}. \tag{5.67}$$

It is similar to Equation (5.11), except for the symmetry operator. Moreover, it may also be decomposed into a boundary and a volumetric term, being rewritten as

$$\int_{\partial\Omega_\mu} (\tilde{\boldsymbol{u}} \otimes \boldsymbol{N} \otimes \boldsymbol{Y})\cdot \boldsymbol{J}^{-1} dA - \int_{\Omega_\mu} \tilde{\boldsymbol{u}} dV \otimes \boldsymbol{J}^{-1} = \mathbf{0}. \tag{5.68}$$

5.2.2 Principle of multi-scale virtual power

In the present formulation, the *Principle of Multi-scale Virtual Power* is expressed by:

$$\begin{aligned}\boldsymbol{P}:\delta\boldsymbol{F}+\mathbf{Q}\vdots\delta\mathbf{G}=\frac{1}{V_\mu}\Bigg[&\int_{\Omega_\mu}\boldsymbol{P}_\mu:(\delta\boldsymbol{F}+\delta\mathbf{G}\cdot\boldsymbol{Y}+\nabla_Y\delta\tilde{\boldsymbol{u}})\,dV\\&-\delta\boldsymbol{L}:\left(\int_{\partial\Omega_\mu}\tilde{\boldsymbol{u}}\otimes\boldsymbol{N}dA\right)-\boldsymbol{L}:\left(\int_{\partial\Omega_\mu}\delta\tilde{\boldsymbol{u}}\otimes\boldsymbol{N}dA\right)\\&-\delta\mathbf{M}\vdots\left(\int_{\Omega_\mu}(\nabla_Y\tilde{\boldsymbol{u}}\otimes\boldsymbol{Y})\cdot\boldsymbol{J}^{-1}dV\right)\\&-\mathbf{M}\vdots\left(\int_{\Omega_\mu}(\nabla_Y\delta\tilde{\boldsymbol{u}}\otimes\boldsymbol{Y})\cdot\boldsymbol{J}^{-1}dV\right)\Bigg],\quad\forall\,(\delta\boldsymbol{F},\delta\mathbf{G},\delta\tilde{\boldsymbol{u}},\delta\boldsymbol{L},\delta\mathbf{M}),\end{aligned}\tag{5.69}$$

where the Lagrange multipliers $\boldsymbol{L}$ and $\mathbf{M}$ are included to enforce the constraints (5.9) and (5.67), respectively. It must be remarked that, unlike the formulation from Section 5.1, $\mathbf{M}$ is not symmetric in this case.

5.2.3 Micro-scale equilibrium problem

The weak micro-equilibrium equation is found by setting $\delta\boldsymbol{F}=\mathbf{0}$ and $\delta\mathbf{G}=\mathbf{0}$ in Equation (5.69)), which leads to:

$$\begin{aligned}\frac{1}{V_\mu}\Bigg[&\int_{\Omega_\mu}\boldsymbol{P}_\mu:\nabla_Y\delta\tilde{\boldsymbol{u}}dV-\delta\boldsymbol{L}:\left(\int_{\partial\Omega_\mu}\tilde{\boldsymbol{u}}\otimes\boldsymbol{N}dA\right)-\boldsymbol{L}:\left(\int_{\partial\Omega_\mu}\delta\tilde{\boldsymbol{u}}\otimes\boldsymbol{N}dA\right)\\&-\delta\mathbf{M}\vdots\left(\int_{\Omega_\mu}(\nabla_Y\tilde{\boldsymbol{u}}\otimes\boldsymbol{Y})\cdot\boldsymbol{J}^{-1}dV\right)-\mathbf{M}\vdots\left(\int_{\Omega_\mu}(\nabla_Y\delta\tilde{\boldsymbol{u}}\otimes\boldsymbol{Y})\cdot\boldsymbol{J}^{-1}dV\right)\Bigg]=0.\end{aligned}\tag{5.70}$$

The strong form of this problem is obtained as presented in Section 5.1, and results in the same Expressions (5.22) and (5.23).

5.2.4 Stresses homogenisation

The homogenised first Piola-Kirchhoff stress tensor is obtained with the same procedure of Section 5.1.4, hence Expressions (5.24) and (5.32) remain valid.

Regarding the homogenised higher-order stress tensor, Expressions from (5.6) to (5.38) are also compatible with the present formulation. However, since $\mathbf{M}$ is not symmetric here, the simplification introduced in Expression (5.39) leads to

$$\mathbf{Q}=\mathbf{M}^S.\tag{5.71}$$

As a conclusion, the modification of the kinematic homogenisation procedure introduced here, does not change the relations between the homogenised stresses and the Lagrange multipliers.

5.2.5 Finite element solution of the micro-scale problem

Following the steps described in Section 5.1.6, the finite element discretisation of the equilibrium Equation (5.70) leads to the residual vector expressed by:

$$\mathbf{r}=\begin{Bmatrix}\mathbf{f}-\mathbf{C}_L^T\mathbf{L}-\mathbf{C}_M^T\mathbf{M}\\\mathbf{C}_L\tilde{\mathbf{u}}\\\mathbf{C}_M\tilde{\mathbf{u}}\end{Bmatrix}.\tag{5.72}$$

In this case, since the Lagrange multiplier $\mathbf{M}$ is not symmetric, its vector representation is defined by:

$$\mathbf{M}_{2D} = \begin{Bmatrix} \mathrm{M}_{111} \\ \mathrm{M}_{211} \\ \mathrm{M}_{121} \\ \mathrm{M}_{221} \\ \mathrm{M}_{112} \\ \mathrm{M}_{212} \\ \mathrm{M}_{122} \\ \mathrm{M}_{222} \end{Bmatrix} \quad , \mathbf{M}_{3D} = \begin{Bmatrix} \mathrm{M}_{111} \\ \mathrm{M}_{211} \\ \mathrm{M}_{311} \\ \mathrm{M}_{121} \\ \mathrm{M}_{221} \\ \mathrm{M}_{321} \\ \mathrm{M}_{131} \\ \mathrm{M}_{231} \\ \mathrm{M}_{331} \\ \mathrm{M}_{112} \\ \mathrm{M}_{212} \\ \mathrm{M}_{312} \\ \mathrm{M}_{122} \\ \mathrm{M}_{222} \\ \mathrm{M}_{322} \\ \mathrm{M}_{132} \\ \mathrm{M}_{232} \\ \mathrm{M}_{332} \\ \mathrm{M}_{113} \\ \mathrm{M}_{213} \\ \mathrm{M}_{313} \\ \mathrm{M}_{123} \\ \mathrm{M}_{223} \\ \mathrm{M}_{323} \\ \mathrm{M}_{133} \\ \mathrm{M}_{233} \\ \mathrm{M}_{333} \end{Bmatrix}. \tag{5.73}$$

The constraint matrix $\mathbf{C}_M$, enforcing the constraint defined by Equation (5.67), is expressed by

$$\mathbf{C}_M = \begin{bmatrix} \left(\int \frac{\partial H_1}{\partial Y_1} Y_1 dV J_{11}^{-1}\right)\mathbf{I} & \cdots \\ \left(\int \frac{\partial H_1}{\partial Y_2} Y_1 dV J_{11}^{-1}\right)\mathbf{I} & \cdots \\ \left(\int \frac{\partial H_1}{\partial Y_1} Y_2 dV J_{22}^{-1}\right)\mathbf{I} & \cdots \\ \left(\int \frac{\partial H_1}{\partial Y_2} Y_2 dV J_{22}^{-1}\right)\mathbf{I} & \cdots \end{bmatrix} \tag{5.74}$$

for 2D rectangular RVEs, and for the case of 3D cubic RVEs it yields

$$\mathbf{C}_M = \left[\begin{array}{c|c} \left(\int \frac{\partial H_1}{\partial Y_1} Y_1 dV J_{11}^{-1}\right)\mathbf{I} & \cdots \\ \left(\int \frac{\partial H_1}{\partial Y_2} Y_1 dV J_{11}^{-1}\right)\mathbf{I} & \cdots \\ \left(\int \frac{\partial H_1}{\partial Y_3} Y_1 dV J_{11}^{-1}\right)\mathbf{I} & \cdots \\ \left(\int \frac{\partial H_1}{\partial Y_1} Y_2 dV J_{22}^{-1}\right)\mathbf{I} & \cdots \\ \left(\int \frac{\partial H_1}{\partial Y_2} Y_2 dV J_{22}^{-1}\right)\mathbf{I} & \cdots \\ \left(\int \frac{\partial H_1}{\partial Y_3} Y_2 dV J_{22}^{-1}\right)\mathbf{I} & \cdots \\ \left(\int \frac{\partial H_1}{\partial Y_2} Y_3 dV J_{33}^{-1}\right)\mathbf{I} & \cdots \\ \left(\int \frac{\partial H_1}{\partial Y_1} Y_3 dV J_{33}^{-1}\right)\mathbf{I} & \cdots \\ \left(\int \frac{\partial H_1}{\partial Y_3} Y_3 dV J_{33}^{-1}\right)\mathbf{I} & \cdots \end{array}\right]. \tag{5.75}$$

The vector representation for the Lagrange multiplier $\boldsymbol{L}$, and the corresponding constraint matrix $\mathbf{C}_L$, remain as introduced in Section 5.1.6.

5.2.6 Macrocopic tangent operators

Since the homogenised stresses are still directly related to the Lagrange multipliers, the strategy proposed in Section 5.1.7 is followed in order to obtain the derivatives $\frac{\partial \boldsymbol{\lambda}}{\partial \boldsymbol{F}}$ and $\frac{\partial \boldsymbol{\lambda}}{\partial \mathbf{G}}$. Since the homogenised stresses in this case are defined by

$$\boldsymbol{P} = \boldsymbol{L} \tag{5.76}$$

$$\mathbf{Q} = \mathbf{M}^S = \frac{1}{2}\left(\mathbf{M} + \mathbf{M}^T\right), \tag{5.77}$$

then the tangent operators are readily obtained through

$$\frac{\partial \boldsymbol{P}}{\partial \bullet} = \frac{\partial \boldsymbol{L}}{\partial \bullet} \tag{5.78}$$

$$\frac{\partial \mathbf{Q}}{\partial \bullet} = \frac{1}{2}\left(\frac{\partial \mathbf{M}}{\partial \bullet} + \frac{\partial \mathbf{M}^T}{\partial \bullet}\right), \tag{5.79}$$

where $\bullet$ represents either $\boldsymbol{F}$ or $\mathbf{G}$.

5.2.7 Solution of the micro-scale problem with other constraints

Similarly to the 1$^{\text{st}}$-order homogenisation approach, more restrictive conditions may be prescribed in addition to the minimal kinematic constraint. Although Kouznetsova (2002) has limited her formulation to the periodic case, Kaczmarczyk et al. (2008, 2010) and Luscher (2010) presented results for the three classical constraints: (i) minimal constraint, (ii) periodic fluctuations on the boundary and (iii) the direct constraint (linear condition in 1$^{\text{st}}$-order homogenisation). Since the case of the minimal constraint has already been addressed, the particularisation for the periodic and direct constraints is described below.

Periodic constraint

At this stage, looking at the decomposed version of the minimal constraint in Equation (5.68), it is convenient to assume that the volumetric and boundary terms are satisfied independently, i.e.:

$$\int_{\partial\Omega_\mu} (\tilde{\boldsymbol{u}} \otimes \boldsymbol{N} \otimes \boldsymbol{Y}) \cdot \boldsymbol{J}^{-1} dA = \boldsymbol{0} \Rightarrow \int_{\partial\Omega_\mu} (\tilde{\boldsymbol{u}} \otimes \boldsymbol{N} \otimes \boldsymbol{Y})\, dA = \boldsymbol{0} \tag{5.80}$$

$$\int_{\Omega_\mu} \tilde{\boldsymbol{u}} dV \otimes \boldsymbol{J}^{-1} = \boldsymbol{0} \Rightarrow \int_{\Omega_\mu} \tilde{\boldsymbol{u}} dV = \boldsymbol{0}. \tag{5.81}$$

Enforcing the volumetric constraint separately removes rigid body motion, and avoids the issues related to the prescription of fluctuations on RVE corners, where excessive unphysical deformation arises, as suggested by Luscher (2010).

Fluctuation periodicity is stated by equality of displacement fluctuations on RVE opposite boundaries, i.e., $\tilde{\boldsymbol{u}}^+ = \tilde{\boldsymbol{u}}^-$ with $\boldsymbol{N}^+ = \boldsymbol{N}^-$. Rectangular and cubic RVEs, which are characterised by a constant normal vector on each surface, are considered here. In this particular case, the boundary constraint is rewritten as

$$\int_{\partial\Omega_\mu} \tilde{\boldsymbol{u}} \otimes \boldsymbol{N} \otimes \boldsymbol{Y}\, dA = \boldsymbol{0} \Rightarrow \int_{\partial\Omega_\mu} \tilde{u}_i N_j Y_k dA = \int_{\partial\Omega_\mu^{-,j}} \tilde{u}_i \left(Y_k^+ - Y_k^-\right) dA = 0. \tag{5.82}$$

Moreover, the coordinates of a pair of points Y_k^+ and Y_k^- on a face with normal N_j are equal as long as $j \neq k$, or

$$\left(Y_k^+ - Y_k^-\right)_j = L_k \delta_{jk}, \tag{5.83}$$

where L_k is the undeformed RVE length in the direction k. Thus, Equation (5.82) can be simplified to

$$\int_{\partial\Omega_\mu^{-,j}} \tilde{u}_i\, dA = 0. \tag{5.84}$$

As a conclusion, the periodic constraint for this 2$^{\text{nd}}$-order homogenisation formulation is defined by

$$\int_{\Omega_\mu} \tilde{\boldsymbol{u}} dV = \boldsymbol{0} \tag{5.85}$$

$$\tilde{\boldsymbol{u}}^+ = \tilde{\boldsymbol{u}}^- \tag{5.86}$$

$$\int_{\partial\Omega_\mu^{-,i}} \tilde{\boldsymbol{u}}^-\, dA = \boldsymbol{0}, \text{ for each RVE negative face } i. \tag{5.87}$$

This constraint is similar to the periodic constraint deduced by Luscher (2010).

In the finite element implementation of this constraint, periodicity is enforced by condensation and the integral constraints are imposed with Lagrange multipliers, resulting in the following linear system of equations

$$\left[\begin{array}{c|c|c|c} \mathbf{k}^{ii} & \mathbf{k}^{i+} + \mathbf{k}^{i-} & -\mathbf{C}_V^{i,T} & \mathbf{0} \\ \hline \mathbf{k}^{+i} + \mathbf{k}^{-i} & \mathbf{k}^{++} + \mathbf{k}^{+-} + \mathbf{k}^{-+} + \mathbf{k}^{--} & -\mathbf{C}_V^{+,T} - \mathbf{C}_V^{-,T} & -\mathbf{C}_B^{+,T} \\ \hline \mathbf{C}_V^i & \mathbf{C}_V^+ + \mathbf{C}_V^- & \mathbf{0} & \mathbf{0} \\ \hline \mathbf{0} & \mathbf{C}_B^- & \mathbf{0} & \mathbf{0} \end{array}\right] \left\{\begin{array}{c} \Delta\tilde{\mathbf{u}}^i \\ \Delta\tilde{\mathbf{u}}^- \\ \Delta\boldsymbol{\lambda}_V \\ \Delta\boldsymbol{\lambda}_B \end{array}\right\} = - \left\{\begin{array}{c} \mathbf{f}^i - \mathbf{C}_V^{i,T}\boldsymbol{\lambda}_V \\ \mathbf{f}^+ + \mathbf{f}^- - \mathbf{C}^T\boldsymbol{\lambda} \\ \mathbf{C}_V\tilde{\mathbf{u}} \\ \mathbf{C}_B\tilde{\mathbf{u}}^- \end{array}\right\}. \tag{5.88}$$

The volumetric constraint is enforced by the the Lagrange multiplier $\boldsymbol{\lambda}_V$ and the constraint matrix $\mathbf{C}_V$, defined by

$$\mathbf{C}_V = \left[\begin{array}{c|c|c} \ldots & \int_{\Omega_\mu} H_k dV \cdot \mathbf{I} & \ldots \end{array}\right], \tag{5.89}$$

while the boundary integral constraint is imposed through $\boldsymbol{\lambda}_B$ and $\mathbf{C}_B$. In the case of a rectangular RVE, where the right and top are considered negative, the constraint matrix is built as:

$$\mathbf{C}_B = \begin{bmatrix} \mathbf{C}^{Right} & \mathbf{0} \\ \mathbf{0} & \mathbf{C}^{Top} \end{bmatrix}, \tag{5.90}$$

where the specific constraint matrix for each face s is computed by

$$\mathbf{C}^s = \left[\; \ldots \; \left| \; \int_{\partial\Omega_\mu^s} H_k \, dL \cdot \mathbf{I} \; \right| \; \ldots \; \right], \tag{5.91}$$

with H_k denoting the shape function related to the k-th node of the face s.

In the case of a non-conform mesh, additional Lagrange multipliers are included to enforce fluctuation periodicity, according to the mortar method (see Appendix B).

Direct constraint

The direct constraint is similar to the linear boundary condition in 1st-order models, defining null fluctuation on the RVE boundary. Thus, looking at Equation (5.68), the boundary integral is automatically set to zero, and only the additional volumetric constraint is required. The direct constraint is expressed by

$$\tilde{\boldsymbol{u}} = \mathbf{0}, \quad \text{on } \partial\Omega_\mu \tag{5.92}$$

$$\int_{\Omega_\mu} \tilde{\boldsymbol{u}} \, dV = \mathbf{0}. \tag{5.93}$$

The resulting finite element problem is defined by the following linear system of equations

$$\begin{bmatrix} \mathbf{k}^{ii} & \mathbf{C}_V^T \\ \mathbf{C}_V & \mathbf{0} \end{bmatrix} \begin{Bmatrix} \Delta\tilde{\mathbf{u}}^i \\ \boldsymbol{\lambda} \end{Bmatrix} = - \begin{Bmatrix} \mathbf{f}^i + \mathbf{C}_V^T \boldsymbol{\lambda} \\ \mathbf{C}_V \tilde{\mathbf{u}}^i \end{Bmatrix}, \tag{5.94}$$

where the constraint matrix $\mathbf{C}_V$ is built according to Expression (5.89).

5.3 Kouznetsova's formulation

5.3.1 Micro-scale constraints

Kouznetsova et al. (2002), Kouznetsova (2002) developed the first multi-scale model based on a full gradient 2nd-order homogenisation scheme. The micro-scale minimal kinematic constraints are obtained enforcing the compatibility between macro and micro kinematic quantities. The compatibility between the deformation gradient at both scales leads to the standard uniform traction condition from Equations (3.5) and (5.9), and an additional constraint arises due to the macro-second gradient. The constraint in Expression (5.4) is assumed. Since a 1st-order continuum is deemed at the micro-scale, the macro-second gradient cannot be related to its microscopic counterpart, and this constraint is deduced from an expression defined *apriori* leading to the following constraint:

$$\int_{\partial\Omega_\mu} (\boldsymbol{N} \otimes \tilde{\boldsymbol{u}} \otimes \boldsymbol{Y} + \boldsymbol{Y} \otimes \tilde{\boldsymbol{u}} \otimes \boldsymbol{N}) \, dA = \mathbf{0}. \tag{5.95}$$

Kouznetsova particularises the micro-constraints for the case where fluctuation periodicity is enforced on the boundary of a square RVE, showing that Equation (5.95) reduces to

$$\int_{\partial\Omega_\mu^i} \tilde{\boldsymbol{u}} \, dA = \mathbf{0}, \quad \text{for each RVE surface } i. \tag{5.96}$$

5.3.2 Finite element solution

The solution of the resulting micro-scale problem is performed with the finite element method, where the periodic constraint

$$\tilde{\boldsymbol{u}}^{+} = \tilde{\boldsymbol{u}}^{-} \tag{5.97}$$

is enforced with the condensation method, if the mesh is conform on opposite faces.

Regarding the constraint (5.96), it is imposed with the Lagrange multiplier method, resulting in the following linear system of equations:

$$\begin{bmatrix} \mathbf{k}^{ii} & \mathbf{k}^{i+} + \mathbf{k}^{i-} & \mathbf{0} \\ \mathbf{k}^{+i} & \mathbf{k}^{++} + \mathbf{k}^{+-} + \mathbf{k}^{-+} + \mathbf{k}^{--} & \mathbf{C}^{T} \\ \mathbf{0} & \mathbf{C} & \mathbf{0} \end{bmatrix} \begin{Bmatrix} \Delta\tilde{\mathbf{u}}^{i} \\ \Delta\tilde{\mathbf{u}}^{-} \\ \boldsymbol{\lambda} \end{Bmatrix} = - \begin{Bmatrix} \mathbf{f}^{i} \\ \mathbf{f}^{+} + \mathbf{f}^{-} + \mathbf{C}^{T}\boldsymbol{\lambda} \\ \mathbf{C}\tilde{\mathbf{u}}^{-} \end{Bmatrix}, \tag{5.98}$$

where the constraint matrix $\mathbf{C}$ and the Lagrange multipliers $\boldsymbol{\lambda}$ are used to enforce the constraint (5.96) on negative faces. Due to the periodicity constraint, it will be automatically satisfied on the positive faces. The constraint matrix is similar to the matrix $\mathbf{C}_B$ defined in Equations (5.90) and (5.91). The fluctuation on the RVE corners is prescribed to zero in order to avoid rigid body motion.

If the discretisation does not produce a conform mesh on opposite RVE faces, the mortar method is employed (Reis and Andrade Pires, 2014) using Lagrange multipliers (see Appendix B).

5.3.3 Homogenised stresses

The homogenised 1st Piola-Kirchhoff $\boldsymbol{P}$ and higher-order stress $\mathbf{Q}$ are obtained through Expressions (5.24) and (5.34). While the homogenised $\boldsymbol{P}$ can still be defined as the boundary integral

$$\boldsymbol{P} = \frac{1}{V_\mu}\int_{\partial\Omega_\mu} \boldsymbol{t}_{\mu 0} \otimes \boldsymbol{Y}\, dA, \tag{(5.27)}$$

in this formulation, the higher order stress tensor is expressed by:

$$\mathbf{Q} = \frac{1}{2V_\mu}\int_{\partial\Omega_\mu} \boldsymbol{t}_{\mu 0} \otimes \boldsymbol{Y} \otimes \boldsymbol{Y}\, dA. \tag{5.99}$$

5.3.4 Macroscopic tangent operators

In the discretised problem, due to the homogenised stresses definitions introduced in Section 5.3.3, the homogenised stresses can be computed through the boundary nodal forces as

$$\mathbf{P} = \frac{1}{V_\mu}\mathbf{D}^{b} \cdot \mathbf{f}^{b}, \tag{5.100}$$

$$\mathbf{Q} = \frac{1}{V_\mu}\mathbf{V}^{b} \cdot \mathbf{f}^{b}, \tag{5.101}$$

where the matrices $\mathbf{D}^b$ and $\mathbf{V}^b$ are appropriate boundary nodal coordinate matrices (Expressions (5.59) and (5.60)). Therefore the tangent operators are obtained through

$$\frac{\partial \mathbf{P}}{\partial \mathbf{G}} = \frac{1}{V_\mu}\mathbf{D}^{b} \cdot \frac{\partial \mathbf{f}^{b}}{\partial \mathbf{G}}, \tag{5.102}$$

$$\frac{\partial \mathbf{Q}}{\partial \mathbf{G}} = \frac{1}{V_\mu}\mathbf{V}^{b} \cdot \frac{\partial \mathbf{f}^{b}}{\partial \mathbf{G}}, \tag{5.103}$$

$$\frac{\partial \mathbf{P}}{\partial \mathbf{F}} = \frac{1}{V_\mu}\mathbf{D}^{b} \cdot \frac{\partial \mathbf{f}^{b}}{\partial \mathbf{F}}, \tag{5.104}$$

$$\frac{\partial \mathbf{Q}}{\partial \mathbf{F}} = \frac{1}{V_\mu}\mathbf{V}^{b} \cdot \frac{\partial \mathbf{f}^{b}}{\partial \mathbf{F}}. \tag{5.105}$$

The derivative of the boundary nodal forces with respect to the macroscopic kinematic variables must be determined.

Splitting the boundary nodes (b) in positive (+), negative (-) and prescribed (p) nodes, and employing the chain rule:

$$\frac{\partial \mathbf{f}^b}{\partial \mathbf{F}} = \frac{\partial \mathbf{f}^b}{\partial \mathbf{u}} \frac{\partial \mathbf{u}}{\partial \mathbf{F}} = \begin{bmatrix} \mathbf{k}^{+i} & \mathbf{k}^{++} & \mathbf{k}^{+-} & \mathbf{k}^{+p} \\ \mathbf{k}^{-i} & \mathbf{k}^{-+} & \mathbf{k}^{--} & \mathbf{k}^{-p} \\ \mathbf{k}^{pi} & \mathbf{k}^{p+} & \mathbf{k}^{p-} & \mathbf{k}^{pp} \end{bmatrix} \cdot \begin{bmatrix} \mathbf{D}^{i,T} + \dfrac{\partial \tilde{\mathbf{u}}^i}{\partial \mathbf{F}} \\ \mathbf{D}^{+,T} + \dfrac{\partial \tilde{\mathbf{u}}^+}{\partial \mathbf{F}} \\ \mathbf{D}^{-,T} + \dfrac{\partial \tilde{\mathbf{u}}^-}{\partial \mathbf{F}} \\ \mathbf{D}^{p,T} + \dfrac{\partial \tilde{\mathbf{u}}^p}{\partial \mathbf{F}} \end{bmatrix} =$$

$$= \begin{bmatrix} \mathbf{k}^I \\ \mathbf{k}^- \\ \mathbf{k}^P \end{bmatrix} \cdot \begin{bmatrix} \mathbf{D}^{i,T} \\ \mathbf{D}^{+,T} \\ \mathbf{D}^{-,T} \\ \mathbf{D}^{p,T} \end{bmatrix} + \left[\begin{array}{c|c} \mathbf{k}^{+i} & \mathbf{k}^{++} + \mathbf{k}^{+-} \\ \mathbf{k}^{-i} & \mathbf{k}^{-+} + \mathbf{k}^{--} \\ \mathbf{k}^{pi} & \mathbf{k}^{p+} + \mathbf{k}^{p-} \end{array}\right] \cdot \begin{bmatrix} \dfrac{\partial \tilde{\mathbf{u}}^i}{\partial \mathbf{F}} \\ \dfrac{\partial \tilde{\mathbf{u}}^+}{\partial \mathbf{F}} \end{bmatrix}. \tag{5.106}$$

Similarly

$$\frac{\partial \mathbf{f}^b}{\partial \mathbf{G}} = \frac{\partial \mathbf{f}^b}{\partial \mathbf{u}} \frac{\partial \mathbf{u}}{\partial \mathbf{G}} = \begin{bmatrix} \mathbf{k}^I \\ \mathbf{k}^- \\ \mathbf{k}^P \end{bmatrix} \cdot \begin{bmatrix} \mathbf{V}^{i,T} \\ \mathbf{V}^{+,T} \\ \mathbf{V}^{-,T} \\ \mathbf{V}^{p,T} \end{bmatrix} + \left[\begin{array}{c|c} \mathbf{k}^{+i} & \mathbf{k}^{++} + \mathbf{k}^{+-} \\ \mathbf{k}^{-i} & \mathbf{k}^{-+} + \mathbf{k}^{--} \\ \mathbf{k}^{pi} & \mathbf{k}^{p+} + \mathbf{k}^{p-} \end{array}\right] \cdot \begin{bmatrix} \dfrac{\partial \tilde{\mathbf{u}}^i}{\partial \mathbf{G}} \\ \dfrac{\partial \tilde{\mathbf{u}}^+}{\partial \mathbf{G}} \end{bmatrix}. \tag{5.107}$$

In order to compute the derivatives of the fluctuation with regard to the macro-deformation gradient, the following expression is developed

$$\frac{\partial \mathbf{r}}{\partial \mathbf{F}} = \mathbf{0} \Leftrightarrow \begin{bmatrix} \dfrac{\partial \mathbf{f}^i}{\partial \mathbf{F}} \\ \dfrac{\partial \mathbf{f}^+}{\partial \mathbf{F}} + \dfrac{\partial \mathbf{f}^-}{\partial \mathbf{F}} + \mathbf{C}^T \cdot \dfrac{\partial \boldsymbol{\lambda}}{\partial \mathbf{F}} \\ \mathbf{C} \cdot \dfrac{\partial \tilde{\mathbf{u}}^+}{\partial \mathbf{F}} \end{bmatrix} = \mathbf{0} \Leftrightarrow$$

$$\left[\begin{array}{c|c|c} \mathbf{k}^{ii} & \mathbf{k}^{i+} + \mathbf{k}^{i-} & \mathbf{0} \\ \mathbf{k}^{+i} + \mathbf{k}^{-i} & \mathbf{k}^{++} + \mathbf{k}^{+-} + \mathbf{k}^{-+} + \mathbf{k}^{--} & \mathbf{C}^T \\ \mathbf{0} & \mathbf{C} & \mathbf{0} \end{array}\right] \begin{bmatrix} \dfrac{\partial \tilde{\mathbf{u}}^i}{\partial \mathbf{F}} \\ \dfrac{\partial \tilde{\mathbf{u}}^+}{\partial \mathbf{F}} \\ \dfrac{\partial \boldsymbol{\lambda}}{\partial \mathbf{F}} \end{bmatrix} = - \begin{bmatrix} \mathbf{k}^I \\ \mathbf{k}^+ + \mathbf{k}^- \\ \mathbf{k}^P \end{bmatrix} \cdot \begin{bmatrix} \mathbf{D}^{i,T} \\ \mathbf{D}^{+,T} \\ \mathbf{D}^{-,T} \\ \mathbf{D}^{p,T} \end{bmatrix}. \tag{5.108}$$

The same strategy is followed to obtain the derivatives with regard to the second gradient, leading to the following system of equations

$$\left[\begin{array}{c|c|c} \mathbf{k}^{ii} & \mathbf{k}^{i+} + \mathbf{k}^{i-} & \mathbf{0} \\ \mathbf{k}^{+i} + \mathbf{k}^{-i} & \mathbf{k}^{++} + \mathbf{k}^{+-} + \mathbf{k}^{-+} + \mathbf{k}^{--} & \mathbf{C}^T \\ \mathbf{0} & \mathbf{C} & \mathbf{0} \end{array}\right] \begin{bmatrix} \dfrac{\partial \tilde{\mathbf{u}}^i}{\partial \mathbf{G}} \\ \dfrac{\partial \tilde{\mathbf{u}}^+}{\partial \mathbf{F}} \\ \dfrac{\partial \boldsymbol{\lambda}}{\partial \mathbf{G}} \end{bmatrix} = - \begin{bmatrix} \mathbf{k}^I \\ \mathbf{k}^+ + \mathbf{k}^- \\ \mathbf{k}^P \end{bmatrix} \cdot \begin{bmatrix} \mathbf{V}^{i,T} \\ \mathbf{V}^{+,T} \\ \mathbf{V}^{-,T} \\ \mathbf{V}^{p,T} \end{bmatrix} \tag{5.109}$$

Both systems may be grouped in the following:

$$\left[\begin{array}{c|c|c} \mathbf{k}^{ii} & \mathbf{k}^{i+}+\mathbf{k}^{i-} & \mathbf{0} \\ \mathbf{k}^{+i}+\mathbf{k}^{-i} & \mathbf{k}^{++}+\mathbf{k}^{+-}+\mathbf{k}^{-+}+\mathbf{k}^{--} & \mathbf{C}^T \\ \mathbf{0} & \mathbf{C} & \mathbf{0} \end{array}\right] \left[\begin{array}{cc} \frac{\partial \tilde{\mathbf{u}}^i}{\partial \mathbf{F}} & \frac{\partial \tilde{\mathbf{u}}^i}{\partial \mathbf{G}} \\ \frac{\partial \tilde{\mathbf{u}}^+}{\partial \mathbf{F}} & \frac{\partial \tilde{\mathbf{u}}^+}{\partial \mathbf{G}} \\ \frac{\partial \lambda}{\partial \mathbf{F}} & \frac{\partial \lambda}{\partial \mathbf{G}} \end{array}\right] = - \left[\begin{array}{c} \mathbf{k}^I \\ \mathbf{k}^+ + \mathbf{k}^- \\ \mathbf{k}^P \end{array}\right] \cdot \left[\begin{array}{cc} \mathbf{D}^{i,T} & \mathbf{V}^{i,T} \\ \mathbf{D}^{+,T} & \mathbf{V}^{+,T} \\ \mathbf{D}^{-,T} & \mathbf{V}^{-,T} \\ \mathbf{D}^{p,T} & \mathbf{V}^{p,T} \end{array}\right], \tag{5.110}$$

where the derivatives of the fluctuations with respect to the macro-kinematic variables are readily obtained.

5.4 Luscher's formulation

5.4.1 Micro-scale constraints

Luscher (2010) proposed a model where the micro-scale constraints are obtained by imposing orthogonality between the micro-fields of displacements gradients. The micro-displacement gradient field is expressed by

$$\nabla \boldsymbol{u}_\mu = \boldsymbol{F} - \boldsymbol{I} + \mathbf{G} \cdot \boldsymbol{Y} + \nabla \tilde{\boldsymbol{u}}. \tag{5.111}$$

The orthogonality conditions and resulting micro-constraints are shown next:

$$(\boldsymbol{F}-\boldsymbol{I}) \perp \mathbf{G}\cdot\boldsymbol{Y} \Rightarrow \int_{\Omega_\mu} (\boldsymbol{F}-\boldsymbol{I}) : \mathbf{G}\cdot\boldsymbol{Y}\, dV = 0 \Rightarrow \int_{\Omega_\mu} \boldsymbol{Y}\, dV = \mathbf{0} \tag{5.112}$$

$$(\boldsymbol{F}-\boldsymbol{I}) \perp \nabla\tilde{\boldsymbol{u}} \Rightarrow \int_{\Omega_\mu} (\boldsymbol{F}-\boldsymbol{I}) : \nabla\tilde{\boldsymbol{u}}\, dV = 0 \Rightarrow \int_{\Omega_\mu} \nabla\tilde{\boldsymbol{u}}\, dV = \mathbf{0} \tag{5.113}$$

$$\mathbf{G}\cdot\boldsymbol{Y} \perp \nabla\tilde{\boldsymbol{u}} \Rightarrow \int_{\Omega_\mu} (\mathbf{G}\cdot\boldsymbol{Y}) : \nabla\tilde{\boldsymbol{u}}\, dV = \int_{\Omega_\mu} \mathbf{G} \vdots (\nabla\tilde{\boldsymbol{u}} \otimes \boldsymbol{Y})\, dV = 0 \Rightarrow \int_{\Omega_\mu} \nabla\tilde{\boldsymbol{u}} \otimes \boldsymbol{Y}\, dV = \mathbf{0}. \tag{5.114}$$

While condition (5.112) is also assumed by Kouznetsova (2002) and Equation (5.113) is the well known 1$^{\text{st}}$-order minimal kinematic constraint, the restriction arising from the 2$^{\text{nd}}$-order homogenisation is given by Equation (5.114). This constraint may be developed into a boundary and a volumetric term:

$$\int_{\partial\Omega_\mu} \tilde{\boldsymbol{u}} \otimes \boldsymbol{N} \otimes \boldsymbol{Y}\, dA - \int_{\Omega_\mu} \tilde{\boldsymbol{u}} dV \otimes \boldsymbol{I} = \mathbf{0}. \tag{5.115}$$

This expression is similar to the constraints from Equations and (5.16) (5.68). In fact, Luscher (2010) is the first author to remark the need for a volume constraint, resulting in a constant body force field in the RVE, so that a uniform 2$^{\text{nd}}$-order gradient can be applied.

5.4.2 Finite element solution

Luscher (2010) presents the classical subsets of constraints that still satisfy the 2$^{\text{nd}}$-order related constraint given by Equation (5.115): the minimal constraint itself, periodic boundary fluctuations and null boundary fluctuations. Their implementation is detailed bellow. As proposed by the author, the volumetric term of the constraint

$$\int_{\Omega_\mu} \tilde{\boldsymbol{u}} dV = \mathbf{0}, \tag{5.116}$$

is enforced independently in all cases, in order to remove rigid body motion from the problem solution. The discretised version of Equation (5.116) is given by

$$\mathbf{C}_V \cdot \tilde{\mathbf{u}} = \mathbf{0}, \tag{5.117}$$

where the constraint matrix is obtained as shown in Expression (5.89).

Luscher minimal constraint

Taking into account Equation (5.116), the constraint (5.115) simplifies to

$$\int_{\partial\Omega_\mu} \tilde{\boldsymbol{u}} \otimes \boldsymbol{N} \otimes \boldsymbol{Y}\, dA = \boldsymbol{0}. \tag{5.118}$$

The Lagrange multiplier method is employed to impose the constraints from Equations (5.113), (5.116) and (5.118), leading to the following system of equations:

$$\begin{bmatrix} \mathbf{k}^{ii} & \mathbf{k}^{ib} & \mathbf{C}_V^{i,T} & \mathbf{0} & \mathbf{0} \\ \mathbf{k}^{bi} & \mathbf{k}^{bb} & \mathbf{C}_V^{b,T} & \mathbf{C}_L^T & \mathbf{C}_M^T \\ \mathbf{C}_V^i & \mathbf{C}_V^b & \mathbf{0} & \mathbf{0} & \mathbf{0} \\ \mathbf{0} & \mathbf{C}_L & \mathbf{0} & \mathbf{0} & \mathbf{0} \\ \mathbf{0} & \mathbf{C}_M & \mathbf{0} & \mathbf{0} & \mathbf{0} \end{bmatrix} \begin{Bmatrix} \Delta\tilde{\mathbf{u}}^i \\ \Delta\tilde{\mathbf{u}}^b \\ \boldsymbol{\lambda}_V \\ \boldsymbol{\lambda}_L \\ \boldsymbol{\lambda}_M \end{Bmatrix} = - \begin{Bmatrix} \mathbf{f}^i + \mathbf{C}_V^{i,T}\boldsymbol{\lambda}_V \\ \mathbf{f}^b + \mathbf{C}_V^{b,T}\boldsymbol{\lambda}_V + \mathbf{C}_L^T\boldsymbol{\lambda}_L + \mathbf{C}_M^T\boldsymbol{\lambda}_M \\ \mathbf{C}_V\tilde{\mathbf{u}} \\ \mathbf{C}_L\tilde{\mathbf{u}}^b \\ \mathbf{C}_M\tilde{\mathbf{u}}^b \end{Bmatrix}, \tag{5.119}$$

where the matrix $\mathbf{C}_V$ is given by Equation (5.89), $\mathbf{C}_L$ is related to boundary form of the 1$^{\text{st}}$-order minimal constraint (Equation (5.9)) and $\mathbf{C}_M$ is the constraint matrix enforcing Equation (5.118), defined as

$$\mathbf{C}_B = \begin{bmatrix} & \int_{\partial\Omega_\mu} H_k N_1 Y_1\, dA\boldsymbol{I} & \\ & \int_{\partial\Omega_\mu} H_k N_2 Y_1\, dA\boldsymbol{I} & \\ & \int_{\partial\Omega_\mu} H_k N_3 Y_1\, dA\boldsymbol{I} & \\ & \int_{\partial\Omega_\mu} H_k N_1 Y_2\, dA\boldsymbol{I} & \\ \ldots & \int_{\partial\Omega_\mu} H_k N_2 Y_2\, dA\boldsymbol{I} & \ldots \\ & \int_{\partial\Omega_\mu} H_k N_3 Y_2\, dA\boldsymbol{I} & \\ & \int_{\partial\Omega_\mu} H_k N_1 Y_3\, dA\boldsymbol{I} & \\ & \int_{\partial\Omega_\mu} H_k N_2 Y_3\, dA\boldsymbol{I} & \\ & \int_{\partial\Omega_\mu} H_k N_3 Y_3\, dA\boldsymbol{I} & \end{bmatrix} \tag{5.120}$$

for 3D, and simplified for 2D as:

$$\mathbf{C}_B = \begin{bmatrix} & \int_{\partial\Omega_\mu} H_k N_1 Y_1\, dA\boldsymbol{I} & \\ \ldots & \int_{\partial\Omega_\mu} H_k N_2 Y_1\, dA\boldsymbol{I} & \ldots \\ & \int_{\partial\Omega_\mu} H_k N_1 Y_2\, dA\boldsymbol{I} & \\ & \int_{\partial\Omega_\mu} H_k N_2 Y_2\, dA\boldsymbol{I} & \end{bmatrix}. \tag{5.121}$$

Luscher periodic constraint

Imposing a periodic fluctuation field on the RVE boundaries, within the present formulation, the periodic constraint presented in Section 5.2.7 is recovered. Unlike Kouznetsova's periodic implementation, there is no need to prescribe RVE corners since rigid body motion is obviated with the volumetric constraint (5.116). The equilibrium problem is solved through Equation (5.88), when a conform mesh is employed. In the presence of a non-conform mesh, additional Lagrange multipliers are included according to the mortar method (Appendix B).

Luscher direct constraint

The direct constraint is similar to the linear boundary condition in 1st-order problems, defining that:

$$\tilde{\boldsymbol{u}} = \boldsymbol{0}, \quad \forall \boldsymbol{Y} \in \partial\Omega_{\mu 0}. \tag{5.122}$$

This suffices to satisfy Equation (5.118), and is easily enforced through the condensation method. Therefore, only Equation (5.116) must be enforced separately, which is done with Lagrange multipliers. This coincides with the direct constraint presented in Section 5.2.7.

5.5 A comparison between different formulations

A comparative analysis of the constraints obtained in the formulations presented in this chapter is performed here. A summary of the main equations related to each formulation is provided in Table 5.1.

Starting by the minimal kinematic constraints, all the second-order homogenisation formulations presented above lead to the well known uniform traction condition, also needed in a first-order framework (Equation (3.5)). The differences arise in the constraint related to the macroscopic second gradient. Kouznetsova's constraint (5.95) is similar to the boundary term of Equation (5.16) (symmetric formulation based on Blanco's proposal), apart from the presence of the second-order moment of volume. What distinguishes Kouznetova's formulation is the absence of a volumetric term on the constraint. The difference between the symmetric formulation and the alternative proposed here (Section 5.2) lies on the symmetry operator only, that is dropped on the later (see Equation (5.68)). Despite being a slight difference, it results in a different model, being expected that different responses are obtained. Apart from the second-order moment of volume, the formulation proposed here is similar to Equation (5.115), even though Luscher (2010) employed a completely different approach to obtain the micro-scale constraints. The presence of the inverse of the second-order moment of volume tensor does not play an important role in terms of fluctuations constraints, recovering the cases where it is not taken into account if square or cubic RVEs are deemed, since $\boldsymbol{J}^{-1}$ becomes diagonal and may be written as $\boldsymbol{J}^{-1} = c\boldsymbol{I}$, where c is a constant. Nonetheless, it is extremely important when seeking the meaning of the Lagrange multipliers used to enforce this constraints.

Regarding the particularisation for periodic fluctuations, the Blanco-based symmetric formulation, Luscher's formulation and the formulation proposed in Section 5.2, all result in the same periodic model, introduced in Section 5.2.7. Only Kouznetsova's generalised periodicity is different, due to the absence of the volumetric constraint.

Finally, in what refers to the direct constraint, Luscher's formulation and the formulations based on the method of multi-scale virtual power result in the same model, where the volumetric constraint is enforced along with null fluctuations on the boundary. Kaczmarczyk et al. (2008, 2010) particularised Kouznetsova's formulation to this case, resulting in a model where the volumetric constraint is not considered.

As a conclusion, formulations based on the work of Kouznetsova (2002) result in models where only boundary constraints are enforced on the RVE. However, Luscher (2010) argues that a body force is needed at the micro-scale to impose a constant macroscopic second gradient, as a result of the volumetric constraint. The formulations based on the method of the multi-scale virtual power, that result in variationally consistent multi-scale models, confirm this statement showing that a constant body force field arises (Equation (5.23)), being directly linked to the Lagrange multiplier enforcing the compatibility between the macroscopic second gradient and the micro-scale kinematics.

Table 5.1: Comparison of the main equations defining the different second-order homogenisation formulations introduced in this chapter.

	Blanco-based	**MMVP non-symmetric**	**Luscher**	**Kouznetsova**
Kinematic insertion	$\boldsymbol{u}_\mu = (\boldsymbol{F}-\boldsymbol{I})\,\boldsymbol{Y} + \frac{1}{2}\mathbf{G}:(\boldsymbol{Y}\otimes\boldsymbol{Y}) + \tilde{\boldsymbol{u}}$			
Kinematic homogenisation	$\boldsymbol{F} = \frac{1}{V_\mu}\int_{\Omega_\mu}\boldsymbol{F}_\mu d\Omega_\mu$			
	$\mathbf{G} = \frac{1}{V_\mu}\int_{\Omega_\mu}\left[\left(\nabla_Y \boldsymbol{u}_\mu \otimes \boldsymbol{Y}\right)\cdot\boldsymbol{J}^{-1}\right]^S d\Omega_\mu$	$\mathbf{G} = \frac{1}{V_\mu}\int_{\Omega_\mu}\left(\nabla_Y \boldsymbol{u}_\mu \otimes \boldsymbol{Y}\right)\cdot\boldsymbol{J}^{-1} d\Omega_\mu$	not explicitly defined	not explicitly defined
Minimal constraints	$\int_{\partial\Omega_\mu}\tilde{\boldsymbol{u}}\otimes\boldsymbol{N}dA = \mathbf{0}$			
	$\int_{\Omega_\mu}\left[(\nabla_Y\tilde{\boldsymbol{u}}\otimes\boldsymbol{Y})\cdot\boldsymbol{J}^{-1}\right]^S dV = \mathbf{0}$	$\int_{\Omega_\mu}(\nabla_Y\tilde{\boldsymbol{u}}\otimes\boldsymbol{Y})\cdot\boldsymbol{J}^{-1}dV = \mathbf{0}$	$\int_{\Omega_\mu}(\nabla_Y\tilde{\boldsymbol{u}}\otimes\boldsymbol{Y})\,dV = \mathbf{0}$	$\int_{\partial\Omega_\mu}(\tilde{\boldsymbol{u}}\otimes\boldsymbol{N}\otimes\boldsymbol{Y})^S\,dA = \mathbf{0}$
Periodic constraints	$\tilde{\boldsymbol{u}}^+ = \tilde{\boldsymbol{u}}^-$ $\int_{\partial\Omega_\mu^i}\tilde{\boldsymbol{u}}dA = \mathbf{0}$, for each RVE surface i $\int_{\Omega_\mu}\tilde{\boldsymbol{u}}dV = \mathbf{0}$			$\tilde{\boldsymbol{u}}^+ = \tilde{\boldsymbol{u}}^-$ $\int_{\partial\Omega_\mu^i}\tilde{\boldsymbol{u}}dA = \mathbf{0}$, for each RVE surface i
Direct constraints	$\tilde{\boldsymbol{u}} = \mathbf{0}$ on $\partial\Omega_\mu$ $\int_{\Omega_\mu}\tilde{\boldsymbol{u}}dV = \mathbf{0}$			$\tilde{\boldsymbol{u}} = \mathbf{0}$ on $\partial\Omega_\mu$

Chapter 6

Numerical applications of second-order homogenisation

Aiming to illustrate the features and predictive capability of second-order computational homogenisation based multi-scale models, several numerical examples are analysed in this chapter. The influence of geometrical non-linearities at the micro-scale is evaluated for second-order and first-order homogenisation schemes. Thereafter, the impact of the insertion of the macroscopic second gradient in the response at both scales is examined. The effect of distinct micro-scale constraints, arising from different multi-scale formulations, is evaluated for the case of homogeneous RVEs, by comparison with an analytical solution, for microstructures with voids and for RVEs with fibres, where a measure of the homogenised second gradient is assessed. Size effects due to the RVE length and to the micro-constituents size are analysed separately. Micro-scale simulations accounting for the macroscopic first and second gradient of displacements are conducted over polycrystalline RVEs. In addition, fully coupled FE^2 simulations are also performed. Finally, an adaptive framework for second-order homogenisation is proposed.

6.1 Second-order deformation modes

Before proceeding with the numerical examples, it is important to clarify the importance of the macroscopic second gradient insertion towards an enriched micro-scale analysis, where second-order deformation modes can be taken into account. Therefore, an illustration of the second-order deformation modes is provided in Figure 6.1, where the displacements resulting from insertion of certain $\mathbf{G}$ components are shown, along with the standard first-order modes. In the picture, all the components of $\mathbf{G}$ are zero and $\boldsymbol{F}$ is equal to the identity tensor, except the labelled non-zero component. Basically, besides traction/compression and deformation modes (b) and (c), four additional modes are possible: (d) extensional mode, where the longitudinal transition from a compression to a traction zone is captured, (e) curvature mode, (f) trapezoidal mode and (g) twist mode. A general macroscopic deformation combines all of the six deformation modes.

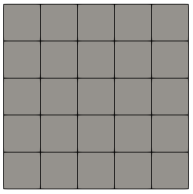

(a) Undeformed RVE

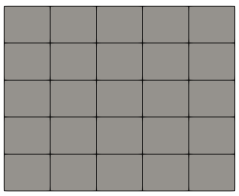

(b) $F_{11} = 1.5$

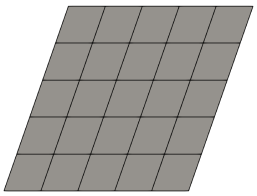

(c) $F_{12} = 0.5$

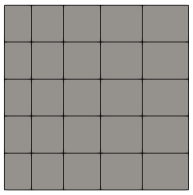

(d) $G_{111} = 0.5$

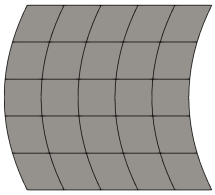

(e) $G_{122} = 0.5$

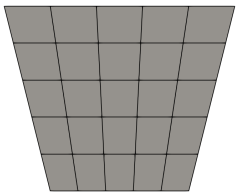

(f) $G_{112} = 0.5$

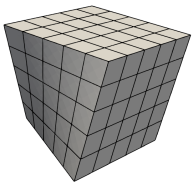

(g) $G_{123} = 0.5$

Figure 6.1: Comparison between 1st-order modes ($\boldsymbol{F}$) and 2nd-order deformation modes ($\mathbf{G}$).

6.2 Influence of geometrical non-linearities

In this section, a square RVE with a circular rigid inclusion is analysed with both 1st and 2nd-order homogenisation models. The constituents are modelled by a linear elastic law, with the properties presented in Table 6.1. Two realisations of this RVE are considered: (i) in the first, the inclusion is placed at the RVE center and (ii) in the second, a skew inclusion is considered. The inclusion occupies 10% of the RVE volume in both cases. The RVEs are discretised with 8-noded quadrilateral elements, with full integration, as shown in Figure 6.2. Although only elastic constituents are considered, quadratic elements are preferably employed in a 2nd-order homogenisation since, due to the possible insertion of a macro-second gradient, RVEs are subjected to a quadratic displacement field, which is better captured by this kind of elements. A macroscopic shear deformation gradient, defined by $F_{12} = 0.5$, is applied to the RVEs, while the macroscopic second gradient is null, $\mathbf{G} = \mathbf{0}$ mm^{-1}.

Table 6.1: Material properties for the constituents of the RVE with a rigid inclusion.

	Matrix	Inclusion
Young modulus (E) [GPa]	70.0	700.0
Poisson ratio (ν)	0.3	0.3

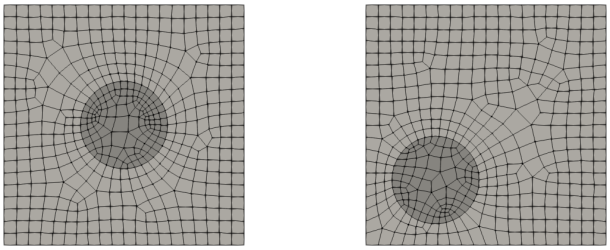

Figure 6.2: Two RVEs with an inclusion ($f = 10\%$).

6.2.1 Results

The microscopic distribution of the equivalent Cauchy stress is plotted over the deformed meshes in Figure 6.3, for several micro-scale constraints, considering the RVE length $l_{RVE} = 1$ mm. In addition, considering the same RVE length, the homogenised first Piola-Kirchhoff stress is presented in Table 6.2 for both RVE configurations, and the homogenised higher-order stress in Table 6.3 for the RVE with a skew inclusion. The homogenised $\mathbf{Q}$ is also shown for a smaller RVE length $l_{RVE} = 0.1$ mm in Table 6.4. The higher-order stress values are presented in vector format, according to the following arrangement:

$$\mathbf{Q} = \left\{ Q_{111} \quad Q_{211} \quad Q_{122} \quad Q_{222} \quad Q_{112} \quad Q_{212} \right\}^T . \tag{6.1}$$

6.2.2 Discussion of the results

Figure 6.3 reveals that, for the case of the RVE with a centred inclusion, the micro-scale results obtained with 1st and 2nd-order homogenisation schemes are similar between the three main groups of constraints: (i) between linear and direct constraints, (ii) the three periodic conditions and (iii) between uniform traction condition and the remaining minimal constraints. This fact is confirmed

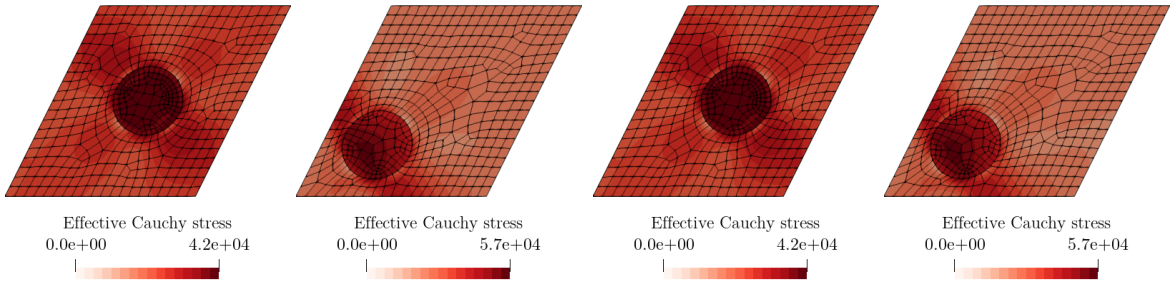

(a) Linear (b) Direct

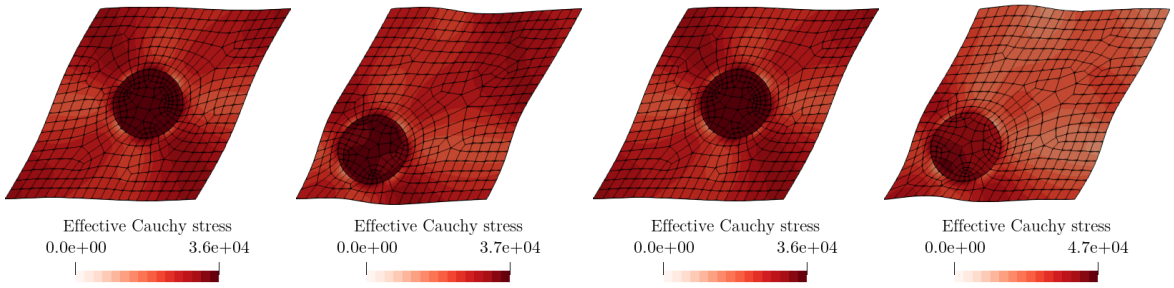

(c) Periodic (d) MMVP Periodic

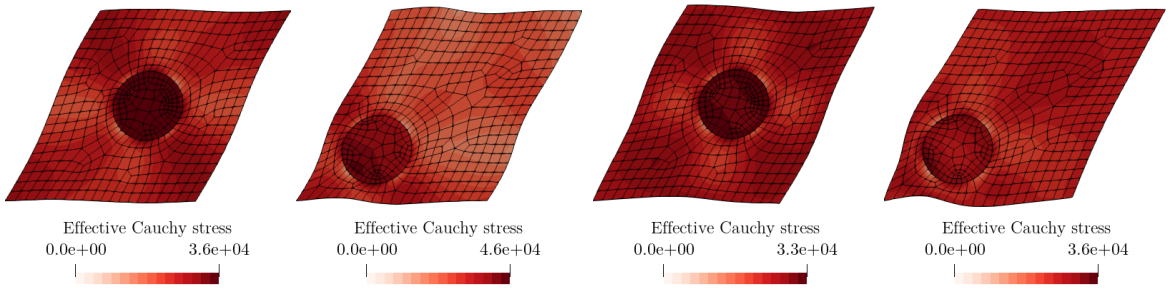

(e) Kouznetsova Periodic (f) Uniform Traction

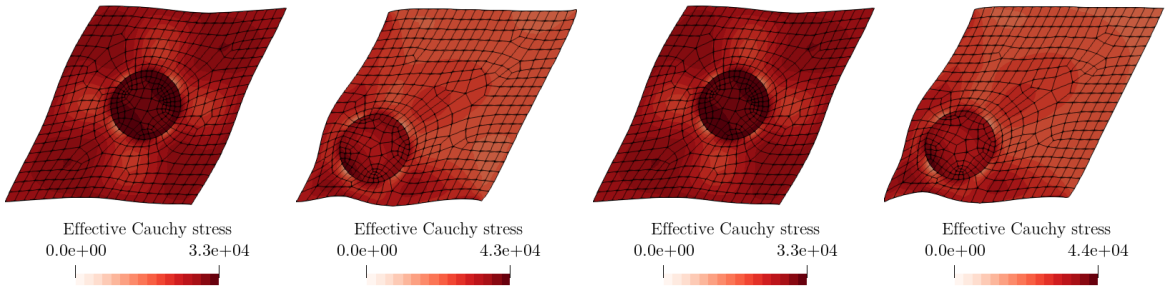

(g) MMVP minimal (h) MMVP Blanco

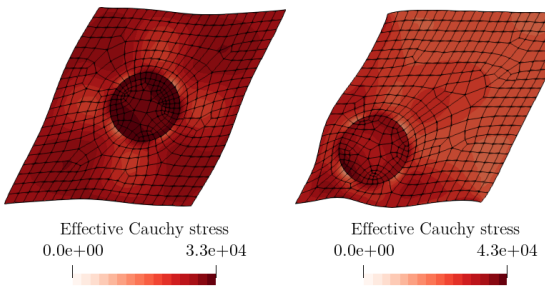

(i) Luscher Minimal

Figure 6.3: Contour plot of the equivalent Cauchy stress [MPa] on the deformed RVEs ($l_{RVE} = 1$ mm, with rigid inclusion) subjected to $F_{12} = 0.5$.

Table 6.2: Homogenised first Piola-Kirchhoff stress tensor [MPa] obtained from RVE with rigid inclusion ($f = 10\%$, $l_{RVE} = 1$ mm) under $F_{12} = 0.5$.

	centred inclusion	skew inclusion
Linear	$\boldsymbol{P} = \begin{bmatrix} -4351.54 & 14928.04 \\ 17080.87 & -4305.65 \end{bmatrix}$	$\boldsymbol{P} = \begin{bmatrix} -4747.78 & 15386.92 \\ 17798.03 & -4822.23 \end{bmatrix}$
Direct	$\boldsymbol{P} = \begin{bmatrix} -4351.54 & 14928.04 \\ 17080.87 & -4305.65 \end{bmatrix}$	$\boldsymbol{P} = \begin{bmatrix} -4727.51 & 15395.17 \\ 17760.78 & -4731.21 \end{bmatrix}$
Periodic	$\boldsymbol{P} = \begin{bmatrix} -4083.50 & 14678.34 \\ 16723.26 & -4089.83 \end{bmatrix}$	$\boldsymbol{P} = \begin{bmatrix} -4083.53 & 14678.40 \\ 16723.32 & -4089.83 \end{bmatrix}$
MMVP Periodic	$\boldsymbol{P} = \begin{bmatrix} -4083.50 & 14678.34 \\ 16723.26 & -4089.83 \end{bmatrix}$	$\boldsymbol{P} = \begin{bmatrix} -4276.76 & 14935.17 \\ 17120.82 & -4371.30 \end{bmatrix}$
Kouznetsova	$\boldsymbol{P} = \begin{bmatrix} -4083.50 & 14678.34 \\ 16723.26 & -4089.83 \end{bmatrix}$	$\boldsymbol{P} = \begin{bmatrix} -4383.67 & 14911.23 \\ 17152.42 & -4482.38 \end{bmatrix}$
U. Traction	$\boldsymbol{P} = \begin{bmatrix} -3752.33 & 14431.51 \\ 16340.52 & -3818.03 \end{bmatrix}$	$\boldsymbol{P} = \begin{bmatrix} -3703.26 & 14347.76 \\ 16208.84 & -3722.14 \end{bmatrix}$
MMVP Min.	$\boldsymbol{P} = \begin{bmatrix} -3752.33 & 14431.51 \\ 16340.52 & -3818.03 \end{bmatrix}$	$\boldsymbol{P} = \begin{bmatrix} -3854.94 & 14608.04 \\ 16561.01 & -3905.91 \end{bmatrix}$
MMVP Min. (Blanco)	$\boldsymbol{P} = \begin{bmatrix} -3752.33 & 14431.51 \\ 16340.52 & -3818.03 \end{bmatrix}$	$\boldsymbol{P} = \begin{bmatrix} -3768.80 & 14565.29 \\ 16522.16 & -3913.73 \end{bmatrix}$
Luscher Min.	$\boldsymbol{P} = \begin{bmatrix} -3752.33 & 14431.51 \\ 16340.52 & -3818.03 \end{bmatrix}$	$\boldsymbol{P} = \begin{bmatrix} -3854.94 & 14608.04 \\ 16561.01 & -3905.91 \end{bmatrix}$

Table 6.3: Homogenised higher-order stress $\mathbf{Q}$ [MPa mm] obtained from the RVE with skew rigid inclusion ($f = 10\%$, $l_{RVE} = 1$ mm) under $F_{12} = 0.5$.

Direct	$\mathbf{Q} =$	{ 347.31	-679.19	-560.11	367.95	-106.14	-219.19 }
MMVP Periodic	$\mathbf{Q} =$	{ 203.48	-524.52	-453.57	223.87	-100.64	-172.83 }
Kouznetsova	$\mathbf{Q} =$	{ 395.35	-522.72	-414.56	526.11	-7.06	-197.31 }
MMVP Min.	$\mathbf{Q} =$	{ 94.24	-417.24	-392.05	136.11	-93.78	-162.13 }
MMVP Blanco	$\mathbf{Q} =$	{ 108.22	-429.50	-411.79	147.77	-122.48	-107.76 }
Luscher Min.	$\mathbf{Q} =$	{ 94.24	-417.24	-392.05	136.11	-93.78	-162.13 }

Table 6.4: Homogenised higher-order stress $\mathbf{Q}$ [MPa mm] obtained from the RVE with skew rigid inclusion ($f = 10\%$, $l_{RVE} = 0.1$ mm) under $F_{12} = 0.5$.

Direct	$\mathbf{Q} =$	{ 34.73	-67.92	-56.01	36.80	-10.61	-21.92 }
MMVP Periodic	$\mathbf{Q} =$	{ 20.34	-52.45	-45.36	22.39	-10.06	-17.28 }
Kouznetsova	$\mathbf{Q} =$	{ 39.54	-52.27	-41.46	52.61	-0.71	-19.73 }
MMVP Min.	$\mathbf{Q} =$	{ 9.42	-41.72	-39.21	13.61	-9.38	-16.21 }
MMVP Blanco	$\mathbf{Q} =$	{ 10.82	-42.95	-41.18	14.78	-12.25	-10.77 }
Luscher Min.	$\mathbf{Q} =$	{ 9.42	-41.72	-39.21	13.61	-9.38	-16.21 }

when looking at Table 6.2, where the homogenised $\boldsymbol{P}$ values are exactly the same. In what refers to the homogenised higher-order stress, its values are negligible for this case (1×10^{-2} MPa mm) and therefore not shown here.

However, differences in the homogenised stresses are observed while analysing the RVE with a skew inclusion, as a consequence of differences on the distribution of the micro-scale stresses. The equivalence between the results obtained with 1st-order and 2nd-order constraints is lost in this case, except for the relation between standard and Kouznetsova's periodicity. Unlike the centred inclusion case, the higher-order stresses assume non-negligible values for the skew inclusion, as shown in Table 6.3. These results indicate that 2nd-order homogenisation schemes capture second-order effects due to geometric non-linearities at the micro-scale, even if a purely 1st-order deformation mode is inserted. In view of the resulting macro-scale constitutive law, this yields a coupling between 1st-order deformations and 2nd-order stresses that is not considered within the Mindlin's elastic model presented in Section 4.5.

Looking at the definition of the homogenised higher-order stress from Equation (5.34) as a measure of the moment of the micro-scale stress field, explains the difference between the values in both RVE configurations. In the case of the centred inclusion, the RVE model is symmetric with regard to the origin, making the moment of the stresses negligible due to its spatial distribution around the centre of the RVE. On the contrary, in the skew inclusion the distribution of the micro-stress field has no symmetries relatively to the origin, leading to non-zero values of the homogenised higher-order stresses.

The results are also strongly dependent on the microscopic constraint. While Kouznetsova's periodic response recovers the standard periodicity, with similar results for both RVE models due to their periodic nature and absence of volumetric constraints, the MMVP periodic constraint yields different results for the skew inclusion. Regarding the minimal constraints, the results obtained with Blanco-based constraint (see Section 5.1) and the MMVP minimal constraint (Section 5.2) are visibly different despite the small change in the formulation. The Luscher-based minimal constraint results similar to the MMVP minimal case. It is interesting to observe that the magnitude of the homogenised stresses tends to be higher for the direct constraint and lower for the minimal constraints.

In the case of a smaller RVE length $l_{RVE} = 0.1$ mm, the micro-scale fields and homogenised first Piola-Kirchhoff stresses obtained are equal to the case where $l_{RVE} = 1.0$ mm. However, the values of the homogenised higher-order stress, shown in Table 6.4, scale with the RVE length. In fact, taking into account Equation (5.34), the position vector $\boldsymbol{Y}$ refers to a lever arm for the stress moment, thus a scaled RVE results in a scaled lever arm, leading to a direct influence on the homogenised higher-order stress.

Finally, from the results obtained in this section, it is concluded that 2nd-order homogenisation-based models capture second-order effects due to geometric non-linearities, resulting in a macro-scale response where the coupling between 1st-order deformation modes and higher-order stresses are naturally coupled. The homogenised response is dependent on the chosen micro-scale constraint.

6.3 Analysis of a heterogeneous RVE under second-order deformation modes

The behaviour of RVEs subjected to different macroscopic second gradient values is analysed in this section, for different RVE lengths and micro-constraints. The macroscopic deformation gradient is kept as $\boldsymbol{F} = \boldsymbol{I}$ so that pure second-order deformation modes are considered. The four second-order deformation modes introduced in Section 6.1 are considered here. The RVE with a centred fibre represented in Figure 6.2 is employed to study the extensional, trapezoidal and curvature modes, while a 3D RVE is required for the twisting mode. The influence of the RVE length is also assessed, using three different values: (i) $l_{RVE} = 0.1$ mm, (ii) $l_{RVE} = 0.5$ mm and (iii) $l_{RVE} = 1.0$ mm.

6.3.1 Extensional mode

Aiming to analyse the RVE behaviour under extensional mode, where transition between a compression to traction zone is captured, the macro-second gradient component $\mathsf{G}_{111} = 0.2$ mm^{-1} is prescribed. The contour plots of the micro-equivalent stress are shown in Figure 6.4. The homogenised stresses are presented in Tables 6.5 and 6.6, in vector format according to Equations (6.1) and (3.51).

Table 6.5: Homogenised first Piola-Kirchhoff stress tensor $\boldsymbol{P}$ [MPa] resulting from the RVE with centred fibre and ($f = 10\%$) under $G_{111} = 0.2$ mm^{-1}.

	$l_{RVE} = 0.1$ mm	$\mathbf{P} =$	{ -5.47	1.4×10^{-4}	1.4×10^{-4}	-0.86 }
Direct	$l_{RVE} = 0.5$ mm	$\mathbf{P} =$	{ -136.78	6.6×10^{-4}	6.6×10^{-4}	-21.46}
	$l_{RVE} = 1.0$ mm	$\mathbf{P} =$	{ -547.77	1.3×10^{-3}	1.3×10^{-3}	-85.95}
	$l_{RVE} = 0.1$ mm	$\mathbf{P} =$	{ -5.45	1.1×10^{-4}	1.1×10^{-4}	-0.92 }
MMVP Periodic	$l_{RVE} = 0.5$ mm	$\mathbf{P} =$	{ -136.18	5.7×10^{-4}	5.7×10^{-4}	-23.12}
	$l_{RVE} = 1.0$ mm	$\mathbf{P} =$	{ -544.80	1.1×10^{-3}	1.1×10^{-3}	-92.63}
	$l_{RVE} = 0.1$ mm	$\mathbf{P} =$	{ -0.74	7.1×10^{-5}	6.7×10^{-5}	-0.36 }
Kouznetsova	$l_{RVE} = 0.5$ mm	$\mathbf{P} =$	{ -18.46	5.5×10^{-4}	4.3×10^{-4}	-8.98 }
	$l_{RVE} = 1.0$ mm	$\mathbf{P} =$	{ -73.75	1.7×10^{-3}	1.0×10^{-3}	-35.90}
	$l_{RVE} = 0.1$ mm	$\mathbf{P} =$	{ -5.46	1.1×10^{-4}	1.1×10^{-4}	-0.87 }
MMVP Minimal	$l_{RVE} = 0.5$ mm	$\mathbf{P} =$	{ -136.50	5.2×10^{-4}	5.2×10^{-4}	-21.86}
	$l_{RVE} = 1.0$ mm	$\mathbf{P} =$	{ -545.99	1.0×10^{-3}	1.0×10^{-3}	-87.46}
	$l_{RVE} = 0.1$ mm	$\mathbf{P} =$	{ -5.44	2.0×10^{-4}	2.0×10^{-4}	-0.70 }
MMVP Blanco	$l_{RVE} = 0.5$ mm	$\mathbf{P} =$	{ -135.67	9.9×10^{-4}	9.9×10^{-4}	-17.17}
	$l_{RVE} = 1.0$ mm	$\mathbf{P} =$	{ -538.32	2.0×10^{-3}	2.0×10^{-3}	-64.83}

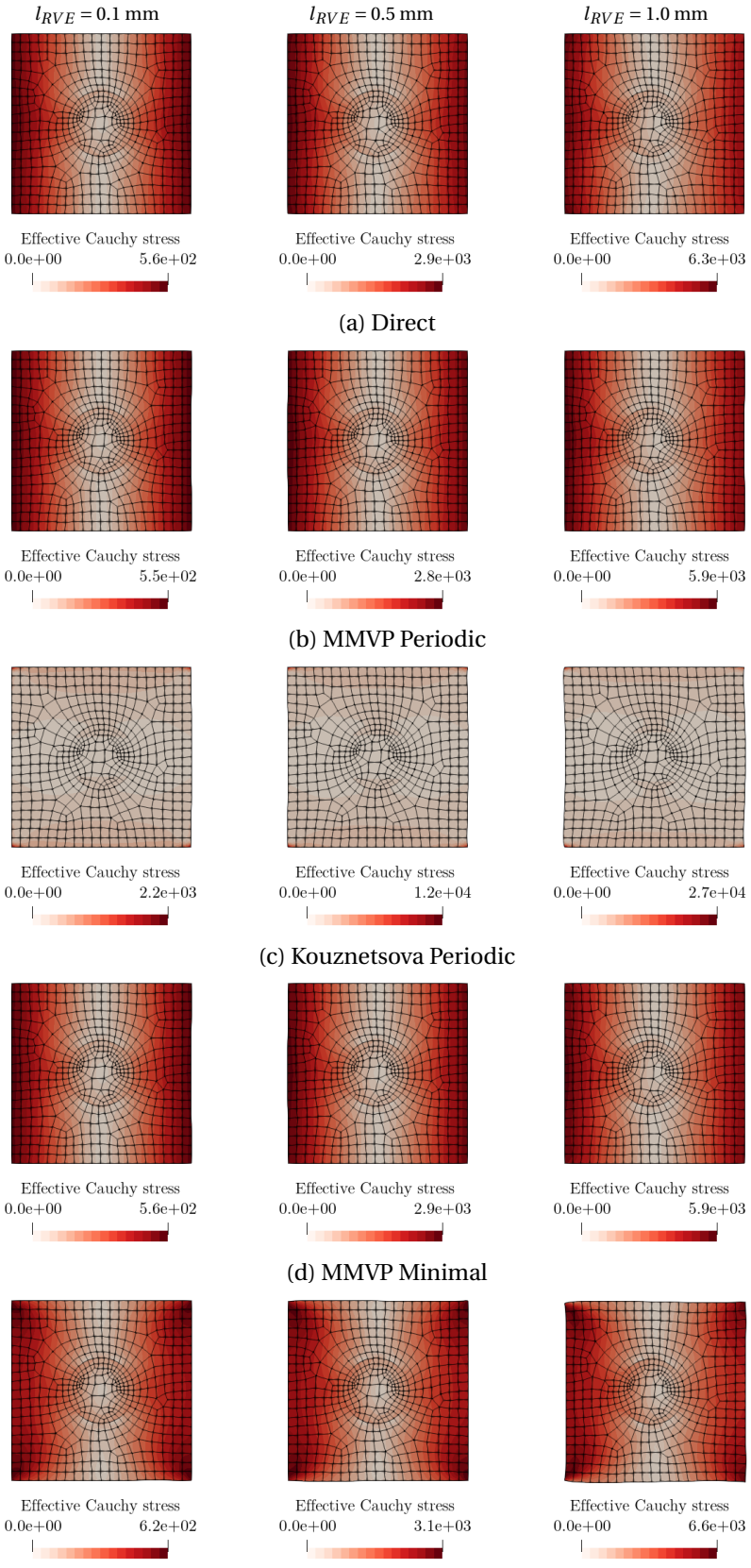

Figure 6.4: Contour plots of the equivalent stress on the deformed RVE with centred fibre subjected to $G_{111} = 0.2$ mm^{-1}, for different RVE lengths and micro-constraints.

Table 6.6: Homogenised higher-order stress tensor $\mathbf{Q}$ [MPa mm] resulting from the RVE with centred fibre and ($f = 10\%$) under $G_{111} = 0.2$ mm^{-1}.

	$l_{RVE} = 0.1$ mm	$\mathbf{Q} =$	{ 15.88	-1.7×10^{-7}	-2.7×10^{-2}	9.7×10^{-8}	1.9×10^{-7}	3.40 }
Direct	$l_{RVE} = 0.5$ mm	$\mathbf{Q} =$	{ 397.27	-6.1×10^{-7}	-0.70	-2.8×10^{-6}	9.1×10^{-6}	84.97 }
	$l_{RVE} = 1.0$ mm	$\mathbf{Q} =$	{ 1592.17	1.7×10^{-5}	-3.20	-3.7×10^{-5}	5.6×10^{-5}	338.87 }
	$l_{RVE} = 0.1$ mm	$\mathbf{Q} =$	{ 15.87	-1.8×10^{-7}	-2.6×10^{-2}	9.9×10^{-8}	1.6×10^{-7}	3.40 }
MMVP Periodic	$l_{RVE} = 0.5$ mm	$\mathbf{Q} =$	{ 397.05	-3.3×10^{-6}	-0.66	-1.1×10^{-6}	3.5×10^{-6}	85.06 }
	$l_{RVE} = 1.0$ mm	$\mathbf{Q} =$	{1589.06	-6.4×10^{-6}	-2.75	-2.3×10^{-5}	3.6×10^{-5}	340.10 }
	$l_{RVE} = 0.1$ mm	$\mathbf{Q} =$	{ 4.19	-1.9×10^{-5}	-3.36	-6.1×10^{-5}	-2.3×10^{-5}	-0.76 }
Kouznetsova	$l_{RVE} = 0.5$ mm	$\mathbf{Q} =$	{ 104.78	-6.1×10^{-4}	-84.00	-1.7×10^{-3}	-6.4×10^{-4}	-19.08 }
	$l_{RVE} = 1.0$ mm	$\mathbf{Q} =$	{ 418.79	-3.2×10^{-3}	-335.71	-7.3×10^{-3}	-2.8×10^{-3}	76.53 }
	$l_{RVE} = 0.1$ mm	$\mathbf{Q} =$	{ 15.87	-1.4×10^{-7}	-2.5×10^{-2}	8.0×10^{-8}	1.9×10^{-7}	3.40 }
MMVP Minimal	$l_{RVE} = 0.5$ mm	$\mathbf{Q} =$	{ 397.00	1.4×10^{-6}	-0.54	-2.2×10^{-6}	8.0×10^{-6}	85.08 }
	$l_{RVE} = 1.0$ mm	$\mathbf{Q} =$	{1588.09	3.5×10^{-5}	-0.99	-2.9×10^{-5}	4.2×10^{-5}	340.12 }
	$l_{RVE} = 0.1$ mm	$\mathbf{Q} =$	{ 15.35	2.1×10^{-7}	0.32	-4.0×10^{-7}	2.2×10^{-7}	2.93 }
MMVP Blanco	$l_{RVE} = 0.5$ mm	$\mathbf{Q} =$	{ 383.59	4.7×10^{-6}	8.31	-1.1×10^{-5}	1.1×10^{-5}	73.08 }
	$l_{RVE} = 1.0$ mm	$\mathbf{Q} =$	{1530.80	1.4×10^{-5}	37.39	-9.0×10^{-6}	6.8×10^{-5}	288.34 }

6.3.2 Trapezoidal mode

The RVE with a centred fibre is subjected to the second gradient component $G_{112} = 0.2$ mm^{-1}. The contour plots of the equivalent stress are shown in Figure 6.5. The resulting homogenised stress tensors are presented in Tables 6.7 and 6.8.

Table 6.7: Homogenised first Piola-Kirchhoff stress tensor $\boldsymbol{P}$ [MPa] resulting from the RVE with centred fibre and ($f = 10\%$) under $G_{112} = 0.2$ mm^{-1}.

	$l_{RVE} = 0.1$ mm	$\mathbf{P} =$	{ -5.50	-3.9×10^{-6}	4.5×10^{-6}	-1.53 }
Direct	$l_{RVE} = 0.5$ mm	$\mathbf{P} =$	{ -137.76	-3.0×10^{-4}	-9.2×10^{-5}	-38.25 }
	$l_{RVE} = 1.0$ mm	$\mathbf{P} =$	{ -553.69	-1.3×10^{-3}	-4.7×10^{-4}	-153.40 }
	$l_{RVE} = 0.1$ mm	$\mathbf{P} =$	{ -5.40	-2.9×10^{-6}	5.5×10^{-6}	-1.53 }
MMVP Periodic	$l_{RVE} = 0.5$ mm	$\mathbf{P} =$	{ -135.05	-3.0×10^{-4}	-8.5×10^{-5}	-38.25 }
	$l_{RVE} = 1.0$ mm	$\mathbf{P} =$	{ -540.52	-1.3×10^{-3}	-4.4×10^{-4}	-152.53 }
	$l_{RVE} = 0.1$ mm	$\mathbf{P} =$	{ -3.08	2.1×10^{-5}	1.4×10^{-5}	-0.53 }
Kouznetsova	$l_{RVE} = 0.5$ mm	$\mathbf{P} =$	{ -77.11	4.9×10^{-4}	2.9×10^{-4}	-13.45 }
	$l_{RVE} = 1.0$ mm	$\mathbf{P} =$	{ -309.18	2.2×10^{-3}	1.3×10^{-3}	-53.93 }
	$l_{RVE} = 0.1$ mm	$\mathbf{P} =$	{ -5.43	-4.0×10^{-6}	4.4×10^{-6}	-1.67 }
MMVP Minimal	$l_{RVE} = 0.5$ mm	$\mathbf{P} =$	{ -135.37	-2.7×10^{-4}	-5.6×10^{-5}	-41.55 }
	$l_{RVE} = 1.0$ mm	$\mathbf{P} =$	{ -535.71	-1.1×10^{-3}	-2.9×10^{-4}	-164.37 }
	$l_{RVE} = 0.1$ mm	$\mathbf{P} =$	{ -4.00	-1.4×10^{-5}	-5.4×10^{-6}	-1.52 }
MMVP Blanco	$l_{RVE} = 0.5$ mm	$\mathbf{P} =$	{ -98.86	-2.9×10^{-4}	-8.6×10^{-5}	-37.44 }
	$l_{RVE} = 1.0$ mm	$\mathbf{P} =$	{ -378.65	-1.2×10^{-3}	-4.0×10^{-4}	-142.35 }

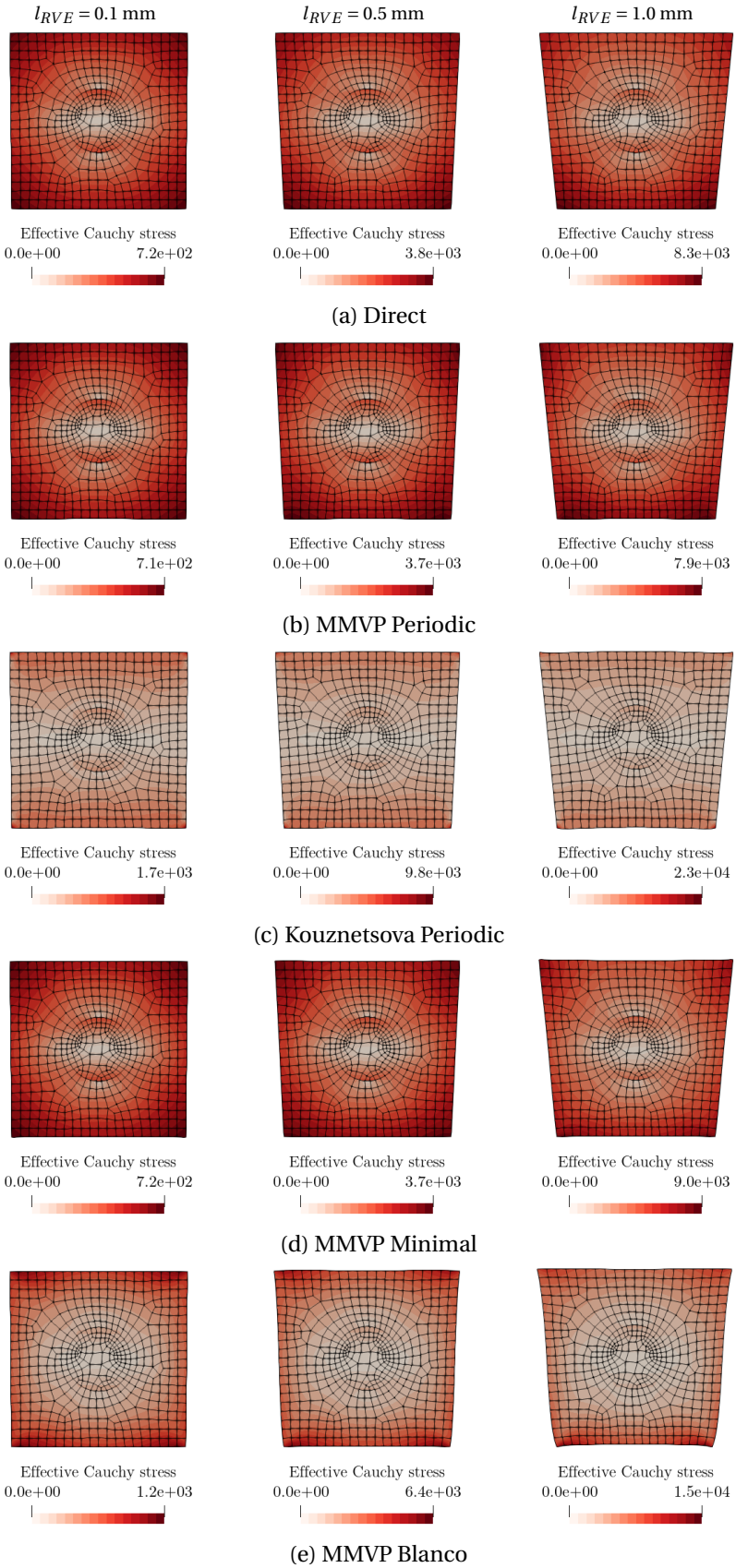

Figure 6.5: Contour plots of the equivalent stress on the deformed RVE with centred fibre subjected to $G_{112} = 0.2\ \text{mm}^{-1}$, for different RVE lengths and micro-constraints.

Table 6.8: Homogenised higher-order stress tensor $\mathbf{Q}$ [MPa mm] resulting from the RVE with centred fibre and ($f = 10\%$) under $G_{112} = 0.2$ mm^{-1}.

Direct	$l_{RVE} = 0.1$ mm	$\mathbf{Q} =$	$\{3.1\times10^{-5}$	4.52	8.0×10^{-6}	6.80	10.25	$1.0\times10^{-5}\}$
	$l_{RVE} = 0.5$ mm	$\mathbf{Q} =$	$\{7.6\times10^{-4}$	113.43	2.0×10^{-4}	170.14	256.62	$2.6\times10^{-4}\}$
	$l_{RVE} = 1.0$ mm	$\mathbf{Q} =$	$\{3.1\times10^{-3}$	459.42	7.7×10^{-4}	680.91	1032.63	$1.1\times10^{-3}\}$
MMVP Periodic	$l_{RVE} = 0.1$ mm	$\mathbf{Q} =$	$\{3.0\times10^{-5}$	4.52	8.0×10^{-6}	6.81	10.24	$1.0\times10^{-5}\}$
	$l_{RVE} = 0.5$ mm	$\mathbf{Q} =$	$\{7.5\times10^{-4}$	113.34	2.0×10^{-4}	169.90	256.27	$2.6\times10^{-4}\}$
	$l_{RVE} = 1.0$ mm	$\mathbf{Q} =$	$\{2.9\times10^{-3}$	458.35	7.7×10^{-4}	676.47	1027.26	$1.0\times10^{-3}\}$
Kouznetsova	$l_{RVE} = 0.1$ mm	$\mathbf{Q} =$	$\{-4.8\times10^{-5}$	2.14	-1.5×10^{-5}	-1.53	7.27	$-1.8\times10^{-5}\}$
	$l_{RVE} = 0.5$ mm	$\mathbf{Q} =$	$\{-1.5\times10^{-3}$	53.67	-4.6×10^{-4}	-38.17	182.04	$-5.1\times10^{-4}\}$
	$l_{RVE} = 1.0$ mm	$\mathbf{Q} =$	$\{-7.4\times10^{-3}$	216.84	-2.3×10^{-3}	-153.22	730.53	$-2.3\times10^{-3}\}$
MMVP Minimal	$l_{RVE} = 0.1$ mm	$\mathbf{Q} =$	$\{3.0\times10^{-5}$	4.52	8.0×10^{-6}	6.81	10.24	$1.0\times10^{-5}\}$
	$l_{RVE} = 0.5$ mm	$\mathbf{Q} =$	$\{7.5\times10^{-4}$	113.09	2.0×10^{-4}	169.44	255.58	$2.6\times10^{-4}\}$
	$l_{RVE} = 1.0$ mm	$\mathbf{Q} =$	$\{3.0\times10^{-3}$	455.08	7.7×10^{-4}	668.17	1016.12	$1.0\times10^{-3}\}$
MMVP Blanco	$l_{RVE} = 0.1$ mm	$\mathbf{Q} =$	$\{3.0\times10^{-5}$	5.13	8.4×10^{-6}	5.87	9.40	$1.0\times10^{-5}\}$
	$l_{RVE} = 0.5$ mm	$\mathbf{Q} =$	$\{7.7\times10^{-4}$	128.60	2.2×10^{-4}	145.10	234.14	$2.5\times10^{-4}\}$
	$l_{RVE} = 1.0$ mm	$\mathbf{Q} =$	$\{3.5\times10^{-3}$	527.74	1.2×10^{-3}	559.84	923.83	$9.2\times10^{-4}\}$

6.3.3 Curvature mode

The curvature mode is enforced to the RVE through the second gradient component G_{122} = 0.2 mm^{-1}. The contour plots of the equivalent stress are shown in Figure 6.6. The homogenised stresses are presented in Tables 6.9 and 6.10.

Table 6.9: Homogenised first Piola-Kirchhoff stress tensor $\boldsymbol{P}$ [MPa] resulting from the RVE with centred fibre and (f = 10%) under G_{122} = 0.2 mm^{-1}.

	l_{RVE} = 0.1 mm	**P** =	{ -0.47	-9.5×10^{-5}	-9.5×10^{-5}	-0.53 }
Direct	l_{RVE} = 0.5 mm	**P** =	{ -11.89	-5.0×10^{-4}	-5.0×10^{-4}	-13.15 }
	l_{RVE} = 1.0 mm	**P** =	{ -47.51	-1.1×10^{-3}	-1.1×10^{-3}	-52.54 }
	l_{RVE} = 0.1 mm	**P** =	{ -0.48	-7.6×10^{-5}	-7.6×10^{-5}	-0.52 }
MMVP Periodic	l_{RVE} = 0.5 mm	**P** =	{ -12.03	-4.0×10^{-4}	-4.0×10^{-4}	-13.11 }
	l_{RVE} = 1.0 mm	**P** =	{ -48.05	-8.8×10^{-4}	-8.7×10^{-4}	-52.40 }
	l_{RVE} = 0.1 mm	**P** =	{ -0.56	-8.7×10^{-5}	-9.1×10^{-5}	-0.34 }
Kouznetsova	l_{RVE} = 0.5 mm	**P** =	{ -13.98	-3.6×10^{-4}	-4.6×10^{-4}	-8.42 }
	l_{RVE} = 1.0 mm	**P** =	{ -55.85	-5.4×10^{-4}	-9.2×10^{-4}	-33.64 }
	l_{RVE} = 0.1 mm	**P** =	{ -0.50	-6.9×10^{-5}	-6.9×10^{-5}	-0.51 }
MMVP Minimal	l_{RVE} = 0.5 mm	**P** =	{ -12.57	-3.7×10^{-4}	-3.7×10^{-4}	-12.68 }
	l_{RVE} = 1.0 mm	**P** =	{ -50.21	-7.9×10^{-4}	-7.9×10^{-4}	-50.68 }
	l_{RVE} = 0.1 mm	**P** =	{ -0.27	-1.3×10^{-4}	-1.3×10^{-4}	-0.39 }
MMVP Blanco	l_{RVE} = 0.5 mm	**P** =	{ -6.70	-6.8×10^{-4}	-6.8×10^{-4}	-9.76 }
	l_{RVE} = 1.0 mm	**P** =	{ -26.73	-1.4×10^{-3}	-1.4×10^{-3}	-38.95 }

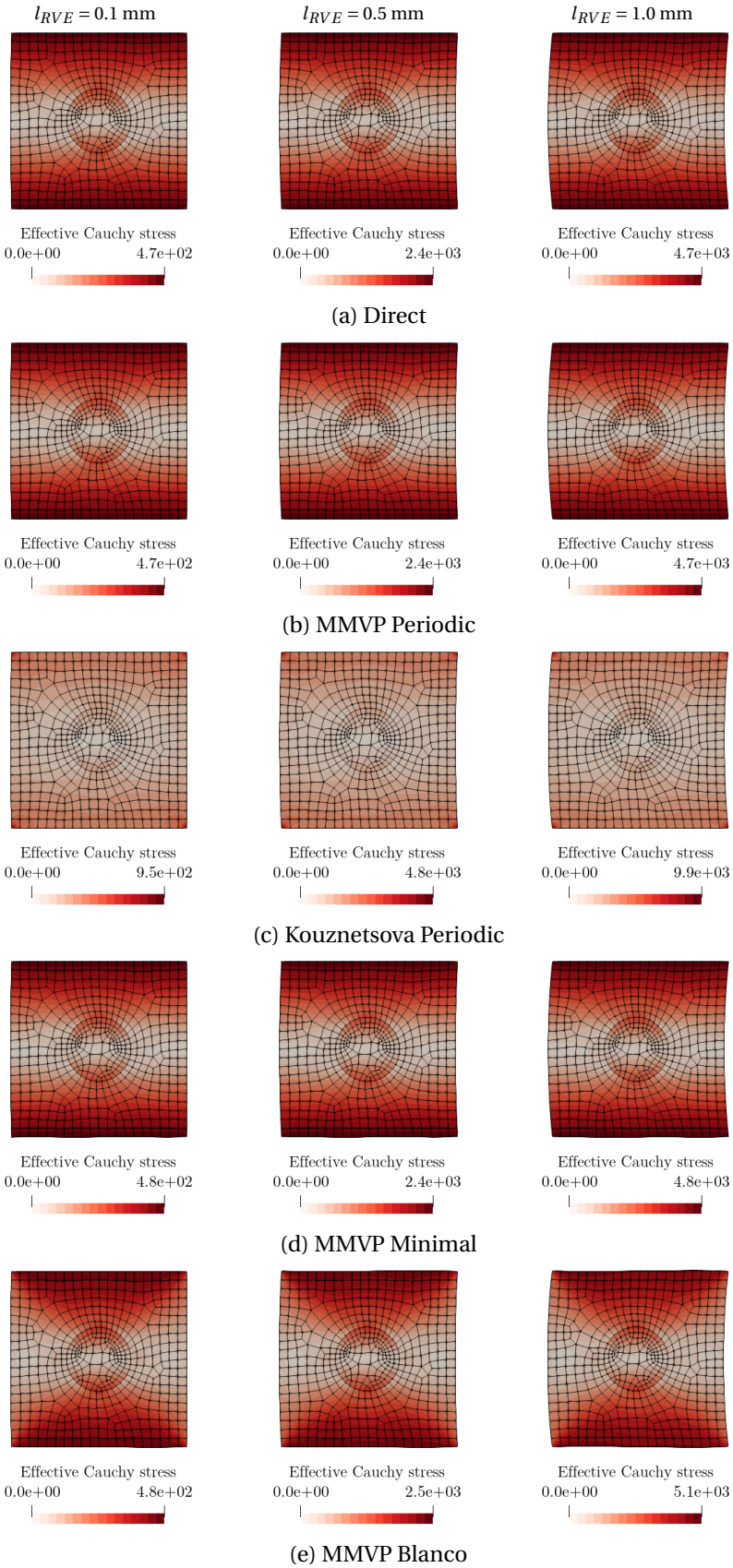

Figure 6.6: Contour plots of the equivalent stress on the deformed RVE with centred fibre subjected to $G_{122} = 0.2$ mm^{-1}, for different RVE lengths and micro-constraints.

Table 6.10: Homogenised higher-order stress tensor **Q** [MPa mm] resulting from the RVE with centred fibre and (f = 10%) under G_{122} = 0.2 mm^{-1}.

	l_{RVE} = 0.1 mm	**Q** =	{-2.7×10^{-2}	1.0×10^{-7}	4.56	3.9×10^{-8}	-4.8×10^{-7}	2.26 }
Direct	l_{RVE} = 0.5 mm	**Q** =	{-0.68	5.5×10^{-6}	113.87	2.3×10^{-6}	-1.2×10^{-5}	56.50 }
	l_{RVE} = 1.0 mm	**Q** =	{-2.88	3.8×10^{-5}	455.02	1.7×10^{-5}	-4.3×10^{-5}	226.07}
	l_{RVE} = 0.1 mm	**Q** =	{-2.6×10^{-2}	6.9×10^{-8}	4.56	5.5×10^{-8}	-5.0×10^{-7}	2.26 }
MMVP Periodic	l_{RVE} = 0.5 mm	**Q** =	{-0.64	2.6×10^{-6}	113.85	2.6×10^{-6}	-1.2×10^{-5}	56.48 }
	l_{RVE} = 1.0 mm	**Q** =	{-2.52	1.5×10^{-5}	454.91	1.8×10^{-5}	-4.8×10^{-5}	226.10}
	l_{RVE} = 0.1 mm	**Q** =	{-3.36	-5.4×10^{-6}	3.60	-1.8×10^{-5}	-7.2×10^{-6}	1.07 }
Kouznetsova	l_{RVE} = 0.5 mm	**Q** =	{-83.99	-1.5×10^{-4}	90.05	-4.7×10^{-4}	-1.9×10^{-4}	26.78 }
	l_{RVE} = 1.0 mm	**Q** =	{-335.59	-7.1×10^{-4}	359.74	-1.9×10^{-3}	-8.0×10^{-4}	107.47}
	l_{RVE} = 0.1 mm	**Q** =	{-2.5×10^{-2}	5.2×10^{-8}	4.55	7.4×10^{-8}	-4.9×10^{-7}	2.26 }
MMVP Minimal	l_{RVE} = 0.5 mm	**Q** =	{-0.61	1.7×10^{-6}	113.83	3.6×10^{-6}	-1.2×10^{-5}	56.47 }
	l_{RVE} = 1.0 mm	**Q** =	{-2.20	8.4×10^{-6}	454.79	2.5×10^{-5}	-4.4×10^{-5}	226.08}
	l_{RVE} = 0.1 mm	**Q** =	{0.32	9.1×10^{-8}	4.33	-7.2×10^{-8}	-9.3×10^{-7}	2.57 }
MMVP Blanco	l_{RVE} = 0.5 mm	**Q** =	{7.95	5.8×10^{-6}	108.15	-4.7×10^{-6}	-2.8×10^{-5}	64.13 }
	l_{RVE} = 1.0 mm	**Q** =	{31.18	4.1×10^{-5}	432.07	-3.4×10^{-5}	-1.3×10^{-4}	256.24}

6.3.4 Twisting mode

The twisting deformation mode can only be imposed to 3D RVE models. Therefore, a cubic RVE with a cylindrical fibre is employed here, as an extension of the 2D RVE used before, where 2410 20-noded hexahedral elements compose the mesh. The macroscopic second gradient component $G_{123} = 0.5$ mm^{-1} is inserted at the micro-scale. The deformed meshes are shown in Figure 6.7 along with the distribution of the equivalent stress. For the sake of brevity, only the significant components of the homogenised stress tensors are presented in Table 6.11.

Table 6.11: Homogenised first Piola-Kirchhoff stresses $\boldsymbol{P}$ [MPa] and higher-order stresses $\mathbf{Q}$ [MPa mm] resulting from the RVE with centred fibre and ($f = 10\%$) under $G_{123} = 0.5$ mm^{-1}.

		P_{11}	P_{22}	P_{33}	Q_{123}	Q_{231}	Q_{312}
Direct	$l_{RVE} = 0.1$ mm	-6.60	-3.89	-3.10	13.73	7.64	5.89
	$l_{RVE} = 0.5$ mm	-164.65	-97.11	-77.40	342.24	191.58	147.97
	$l_{RVE} = 1.0$ mm	-653.51	-385.43	-307.51	1358.04	774.52	599.48
MMVP Periodic	$l_{RVE} = 0.1$ mm	-6.36	-3.57	-2.50	13.37	7.29	5.70
	$l_{RVE} = 0.5$ mm	-158.40	-88.93	-62.20	333.29	182.66	142.94
	$l_{RVE} = 1.0$ mm	-626.01	-351.60	-246.00	1320.05	736.75	577.73
Kouznetsova	$l_{RVE} = 0.1$ mm	-6.36	-3.57	-2.50	13.37	7.29	5.70
	$l_{RVE} = 0.5$ mm	-158.40	-88.93	-62.20	333.29	182.66	142.94
	$l_{RVE} = 1.0$ mm	-626.01	-351.60	-246.00	1320.05	736.75	577.73
MMVP Minimal	$l_{RVE} = 0.1$ mm	-6.61	-3.52	-3.43	12.28	6.34	5.65
	$l_{RVE} = 0.5$ mm	-164.16	-87.54	-85.39	305.16	158.20	141.05
	$l_{RVE} = 1.0$ mm	-644.35	-345.73	-336.14	1199.1 0	630.34	562.60
MMVP Blanco	$l_{RVE} = 0.1$ mm	-2.99	-1.64	-1.12	11.42	7.01	5.94
	$l_{RVE} = 0.5$ mm	-74.03	-40.58	-27.68	283.84	174.37	147.93
	$l_{RVE} = 1.0$ mm	-287.24	-158.10	-107.90	1114.98	687.95	583.92

6.3.5 Discussion of the results

The results presented in Figures 6.4 to 6.7 show that the insertion of a macroscopic second gradient promotes deformation modes at the micro-scale, that cannot be captured by standard first-order homogenisation schemes. The insertion term $\frac{1}{2}\mathbf{G} : (\boldsymbol{Y} \otimes \boldsymbol{Y})$ from Equation (5.3) generates a quadratic displacement field in the RVE, that results in non-typical deformation and stress distributions. The assumption of linear variation of the macro-scale deformation becomes evident in these results, especially for the largest RVE length.

In fact, a larger RVE length promotes a greater magnitude of the quadratic displacement field, that results in larger RVE deformations. As a result, the homogenised stress values increase with the RVE length. Regarding the homogenised higher-order stress, this is accumulated with the effect discussed in Section 6.2.2, where the lever arm also contributes to scale the resulting values. In addition to the coupling between $\mathbf{Q}$ and $\boldsymbol{F}$ found in the same section, here the coupling between $\boldsymbol{P}$ and $\mathbf{G}$ is also found, since the homogenised Piola-Kirchhoff stress is not null even though the first-order macro deformation is not considered ($\boldsymbol{F} = \boldsymbol{I}$). However, while the coupling discussed in Section 6.2.2 is the result of geometric non-linearities in the RVE, the latter coupling is observed

even for the RVE model where the former was not found.

In a general comparison between the results obtained with different micro-scale constraints, the direct constraint tends to provide the stiffer homogenised response while the minimal constraint based on the formulation proposed in Section 5.2 yields the lowest values of the homogenised stresses, with its periodic version in between. Both Kouznetsova's periodicity and Blanco-based minimal constraint result in quite different results, when comparing with the remaining constraints. The exception is found in the case of the twisting deformation, where Kouznetsova's periodic response is equal to the periodic constraint based on the method of multi-scale virtual power. In the remaining examples Kouznetsova's results show a localization on the RVE corners, which is an issue already reported by Luscher (2010). In what refers to Blanco's minimal constraint, an unphysical warping tends to appear near the RVE corners, especially visible for the largest RVE length. It must be remarked that the Luscher's minimal constraint results, not shown here, are similar to the MMVP minimal counterparts, similarly to what has been found in Section 6.2.

In summary, it is found in this section that the RVE length has a strong influence on the deformation undergone by the RVE, due to the quadratic displacement term. Therefore, the deformation modes and the resulting homogenised stresses are more significant for larger RVEs. A coupling between the macroscopic second gradient and the homogenised $\boldsymbol{P}$ is naturally obtained in the present 2^{nd}-order homogenisation schemes. Both Kouznetsova's and Blanco's constraints yields unphysical deformations at the RVE, while the remaining constraints provide quite consistent homogenised stresses.

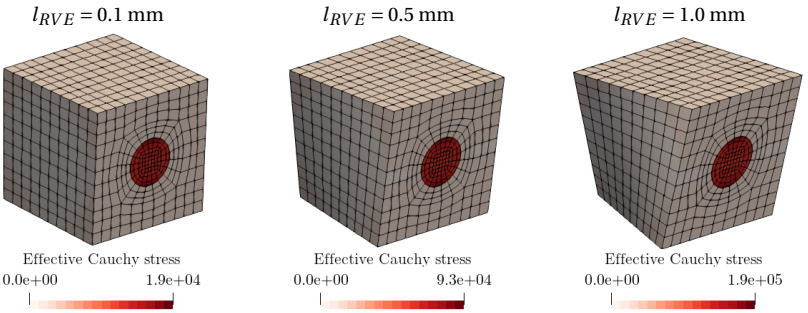

(a) Direct

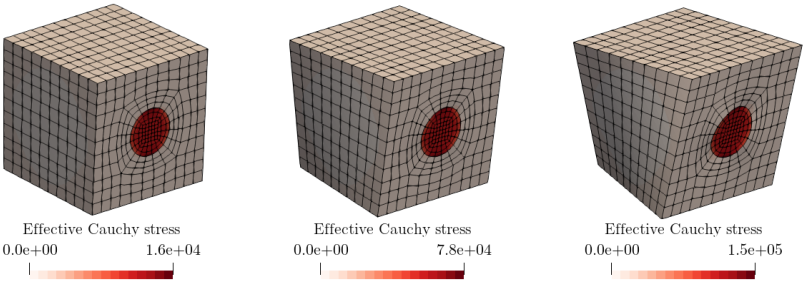

(b) MMVP Periodic

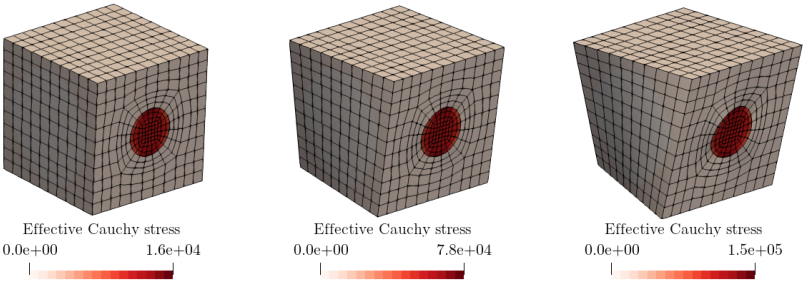

(c) Kouznetsova Periodic

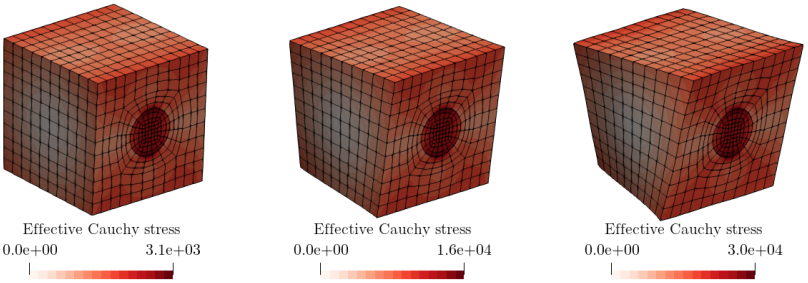

(d) MMVP Minimal

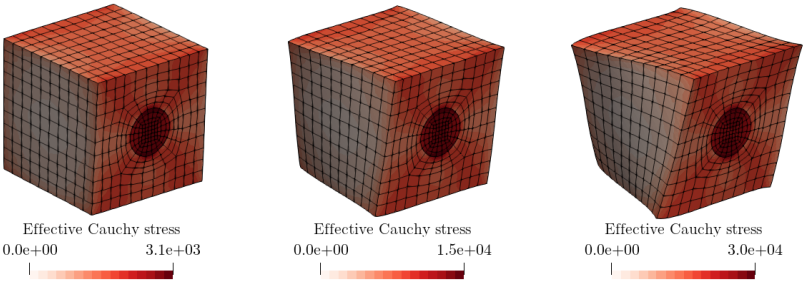

(e) MMVP Blanco

Figure 6.7: Contour plots of the equivalent stress on the deformed RVE with centred fibre subjected to $G_{123} = 0.5$ mm^{-1}, for different RVE lengths and micro-constraints.

6.4 Modelling RVEs with voids

In the second-order homogenisation multi-scale formulations based on the method of the multi-scale virtual power and on Luscher's proposal, a volumetric constraint on the fluctuation field arises, as shown in Equations (5.16), (5.68) and (5.115). This constraint must be enforced over the entire RVE domain Ω_μ, that includes voids domain if they exist. However, voids are usually not meshed in a finite element discretisation, which raises the question about the suitability of these models for the enforcement of the volumetric constraints. The impact of voids discretisation on the results is investigated in the present section.

Two square RVEs with length l_{RVE} = 1.0 mm and a circular void occupying 3% of the total RVE area are subjected to a curvature deformation mode, defined by G_{122} = 0.1 mm^{-1}. The matrix material is modelled by an elastic law with E = 210 MPa and ν = 0.3. Two finite element models with 8-noded quadrilateral elements (full integration) are employed for each RVE, as shown in Figure 6.8, where the voids are not discretised in the first case, but are meshed in the second case, being modelled by an elastic law with very low stiffness (E = 0.001 MPa, ν=0.3).

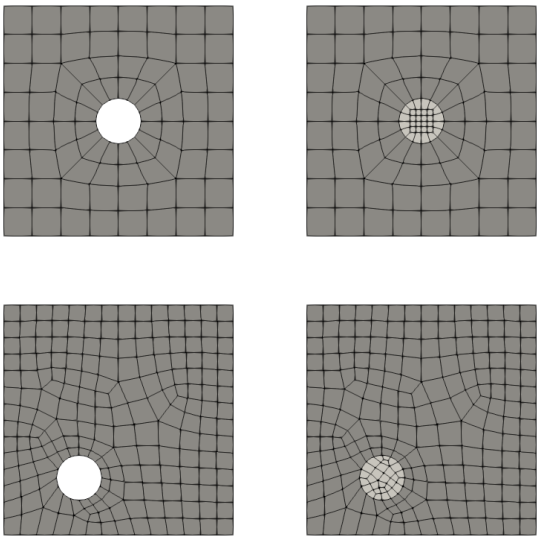

Figure 6.8: Finite element models for the RVEs with a circular void (f = 3%).

6.4.1 Results

The resulting deformed meshes with the representation of the micro-scale distribution of the equivalent stress are presented in Figures 6.9 and 6.10 for different micro-constraints. Some components of the homogenised stress tensors are shown in Table 6.12, for the case of the centred void, and in Table 6.13 for the RVE with the skew void, where the results with and without void discretisation can be compared.

6.4.2 Discussion of the results

In the standard 1st-order micro-scale modelling, it is expected that the voids discretisation has not significant influence on the results obtained. However, in the present framework, it is observed that the resulting micro-scale fields and homogenised stresses are remarkably different between both RVE models. This is true for all micro-constraints, except for the Kouznetsova's generalised periodicity, where no volumetric constraint is enforced. For the remaining constraints, in the case of

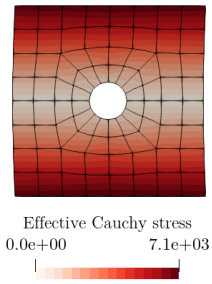

(a) Direct

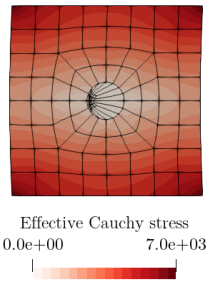

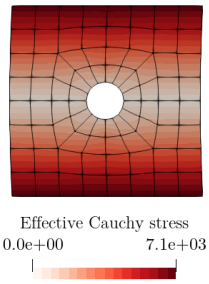

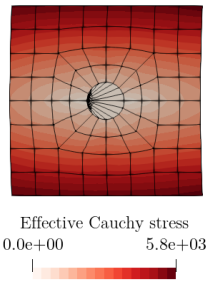

(b) MMVP Periodic

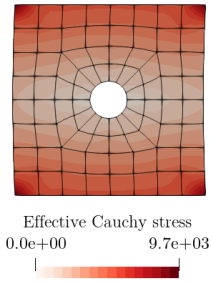

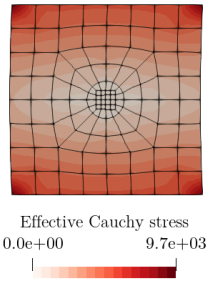

(c) Kouznetsova

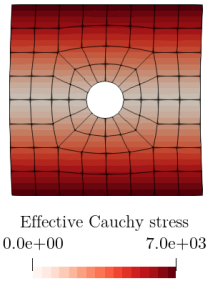

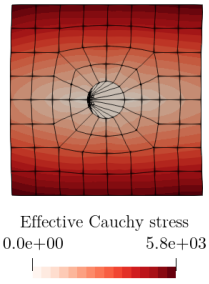

(d) MMVP Minimal

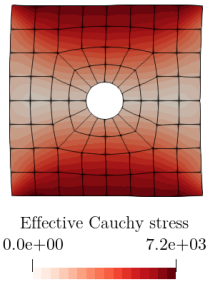

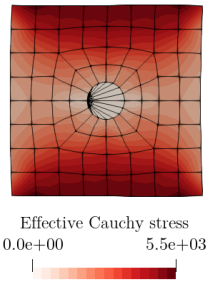

(e) MMVP Blanco

Figure 6.9: Contour plot of the equivalent stress on the deformed RVEs with void, under $G_{122} = 0.1$ mm^{-1}.

the discretised voids, the void elements become extremely deformed. This is caused by the constant body force field that arises at the RVE as a consequence of the volumetric constraint, as referred in Sections 5.1.3 and 5.4.1, acting over a very compliant region.

In the case of the minimal constraints based on the method of multi-scale virtual power, where the Lagrange multipliers are directly related to the homogenised stresses (cf. Equations (5.32), (5.40) and (5.71)), these relations have been verified in both finite element models for the RVE with the centred void. However, when looking at RVE with the skew void, while these equalities are satisfied for the model with the discretised void, the values of the Lagrange multipliers are completely different from the homogenised stress tensors computed from volumetric averaging when the void is not meshed. As a matter of fact, since voids are part of the RVE domain, and the volumetric constraint is enforced over the entire RVE, the contribution of voids must be taken into account so that the multi-scale formulation is correctly employed, even though the concept of displacement fluctuations in voids is questionable.

This fact poses strong limitations in the modelling of RVEs with voids, since the mesh is required and is strongly deformed, causing premature simulation failure due to mesh distortion. In order to overcome this issue, alternative discretisation techniques have to be devised for the void, like adaptive re-meshing or meshless methods. A different approach may be to modify the constraint such that it may be enforced on the voids boundary instead.

Table 6.12: Homogenised stresses ($\boldsymbol{P}$ [MPa] and $\mathbf{Q}$ [MPa mm]) obtained from the RVEs with a centred void ($f = 3\%$) under $G_{122} = 0.1$ mm^{-1}.

		P_{11}	P_{22}	Q_{111}	Q_{122}	Q_{212}
Luscher Direct	void	-32.24	-30.72	-1.79	671.22	335.05
	meshed void	-35.51	-23.19	-461.18	539.78	170.88
MMVP Periodic	void	-32.00	-30.68	-1.75	671.20	335.06
	meshed void	-35.71	-22.14	-522.32	522.32	149.26
Kouznetsova	void	-34.96	-22.79	-484.36	533.07	162.73
	meshed void	-34.96	-22.79	-484.36	533.07	162.73
MMVP Minimal	void	-31.14	-31.13	0.26	672.29	336.37
	meshed void	-32.27	-25.92	-521.92	521.92	149.47
MMVP Blanco	void	-20.64	-16.87	55.03	635.33	382.21
	meshed void	-20.88	-13.17	-475.76	475.77	194.94

Table 6.13: Homogenised stresses ($\boldsymbol{P}$ [MPa] and $\mathbf{Q}$ [MPa mm]) obtained from the RVEs with a skew void ($f = 3\%$) under $G_{122} = 0.1$ mm^{-1}.

		P_{11}	P_{22}	P_{12}	Q_{111}	Q_{122}	Q_{212}
Luscher Direct	void	-29.63	-28.82	138.74	-2.18	636.76	317.59
	meshed void	-112.18	-57.92	117.06	-441.48	512.91	162.16
MMVP Periodic	void	-27.31	-27.83	152.95	3.88	632.72	315.05
	meshed void	-122.54	-63.27	118.60	-496.11	496.12	142.26
Kouznetsova	void	-118.41	-59.62	120.80	-466.01	504.34	152.55
	meshed void	-118.41	-59.62	120.80	-466.01	504.34	152.55
MMVP Minimal	void	-30.60	-30.59	60.40	0.004	657.06	328.66
	meshed void	-123.97	-66.28	133.58	-492.56	492.57	141.57
MMVP Blanco	void	-28.14	-11.17	105.58	61.50	615.57	380.20
	meshed void	-112.38	16.67	149.93	-438.14	438.15	185.02

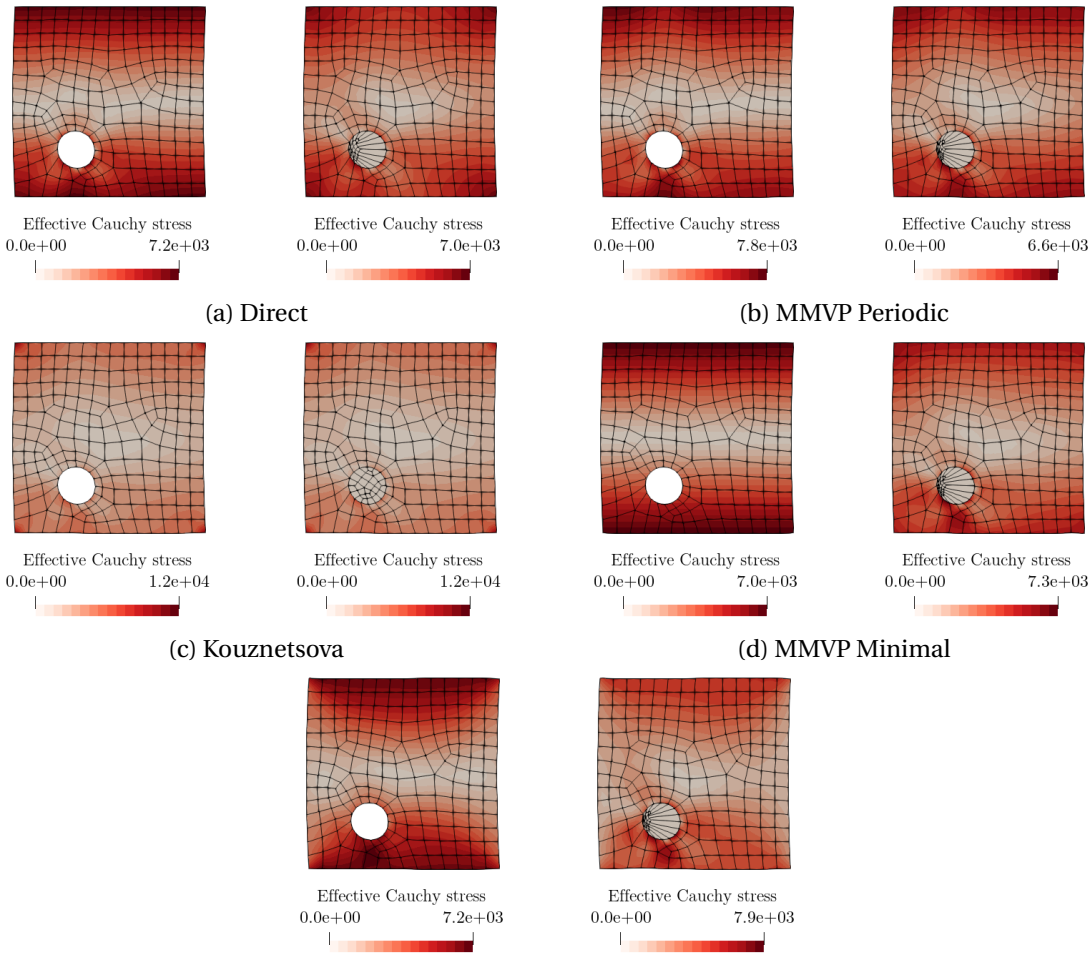

(a) Direct (b) MMVP Periodic

(c) Kouznetsova (d) MMVP Minimal

(e) MMVP Blanco

Figure 6.10: Contour plot of the equivalent stress on the deformed RVEs with a skew void, under $G_{122} = 0.1\ \text{mm}^{-1}$.

6.5 Analysis of the influence of RVE constituents size and RVE length

The influence of the RVE size on the representativeness of the homogenised response is well explored for 1st-order homogenisation schemes. The RVE model must be large enough to be statistically representative, i.e., the model should contain a number of constituents such that the microstructural behaviour is actually represented. Therefore, *the larger the better* philosophy is usually recommended, being the only drawback related to the computational cost of the finite element model. An exception appears when damage localisation is observed at the micro-scale. In that case, a representative model cannot be found and alternative homogenisation schemes must be devised (Gitman et al., 2007).

Obviously, for a physically consistent representation of the micro-structure, the RVE size and RVE length concepts are merged. Unlike 1st-order homogenisation based models, where the physical size of the RVE does not influence the results and only the proportion between the constituents size is important, the RVE length plays a major role in 2nd-order homogenisation models, as shown in the examples from previous sections. Thus, the choice of the RVE model is much more sophisticated, since it must contain an enough number of micro-constituents but with a meaningful RVE length value. Kouznetsova et al. (2004a) recommends the choice of a RVE with the minimum length that allows for the development of the governing micro-scale phenomena, suggesting the use of several realisations to obtain a representative response.

In this section, the isolated influence of the RVE constituents size and the RVE length is analysed numerically. A composite material with randomly distributed fibres is considered. Two distinct RVE lengths (l_{RVE} = 0.207 mm and l_{RVE} = 0.828 mm) are employed, along with two different values of the fibres diameter for each RVE length. The fibres volume fraction is fixed, being equal to 30%. In order to keep this value constant, the number of fibres in each RVE and their diameter must be chosen carefully. Therefore, the fibres diameter is adjusted so that the number of fibres (defining what may be called generalised RVE size) is equal to s_{RVE} = 16 and s_{RVE} = 64 fibres for both RVE lengths (see Figure 6.11). Five realisations are generated for each configuration (Melro et al., 2008), and discretised with 8-noded quadrilateral elements, where the mesh refinement is scaled to the fibres diameter.

Before proceeding, it is important to clarify the concept of generalised RVE size introduced here. The generalised RVE size, s_{RVE}, is a measure of the number of micro-constituent in the RVE model, that is conceptually independent from the RVE length l_{RVE}.

The micro-scale constituents are modelled either with elastic and elasto-plastic laws, as described in the next sections, and different microscopic constraints are employed for both first-order and second-order homogenisation. It must be remarked that, since the meshes employed may not be conform, the mortar method (Appendix B) is used to enforce periodicity constraints (first-order periodic condition, Kouznetsova periodicity and the periodic model based on the method of multi-scale virtual power). The RVEs are subjected to a macro-scale deformation history extracted from a bending beam FE^2 simulation. The macro-scale model is the same introduced in Figure 3.11. In this case, a rotation of 144^o is prescribed in 8 increments. At the micro-scale, the RVE shown in Figure 6.12 is employed, with the elastic properties defined in Table 6.14. The uniform traction boundary condition is enforced. Both the deformation gradient and the second gradient histories are extracted from two macro-scale points, identified in Figure 6.13. Point A is located in the vicinity of the beam centre, where a low deformation level is expected, while point B is located near the bottom surface, where the maximum stretching is achieved. Since a 1st-order continuum is considered at the macro-scale, in this coupled simulation, the second gradient is obtained through the strategy proposed in Appendix D. The resulting macro-scale equivalent strain and second gradient norm are presented in Figure 6.14.

(a) $l_{RVE} = 0.207$ mm
$s_{RVE} = 16$ fibres
$r_f = 0.016$ mm

(b) $l_{RVE} = 0.207$ mm
$s_{RVE} = 64$ fibres
$r_f = 0.008$ mm

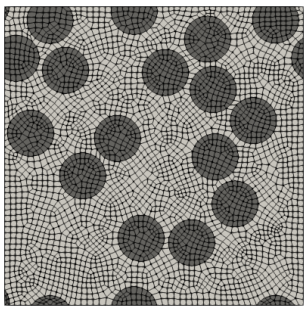

(c) $l_{RVE} = 0.828$ mm
$s_{RVE} = 16$ fibres
$r_f = 0.064$ mm

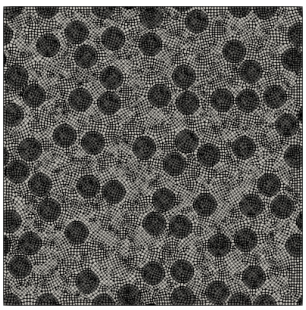

(d) $l_{RVE} = 0.828$ mm
$s_{RVE} = 64$ fibres
$r_f = 0.032$ mm

Figure 6.11: Representation of one realisation of each RVE configuration used in the present size study. All the RVEs have the same fibre volume fraction of 30%.

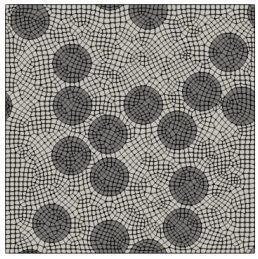

Figure 6.12: RVE employed at the FE^2 simulation for the bending beam.

Table 6.14: Material properties for the constituents of the RVE shown in Figure 6.12.

	Matrix	Inclusions
Young modulus (E) [GPa]	30.0	72.4
Poisson ratio (ν)	0.3	0.2

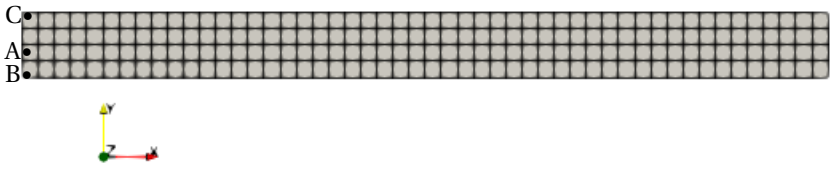

Figure 6.13: Finite element mesh for the beam model. A and B identify the positions of points where both $\boldsymbol{F}$ and $\mathbf{G}$ are extracted from.

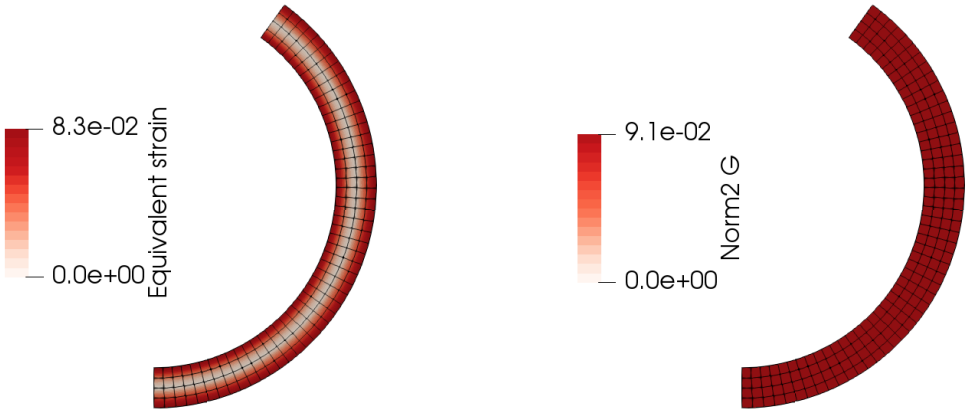

Figure 6.14: Contour plots of the equivalent strain and second gradient norm obtained at the macro-scale, in the FE^2 simulation of the bending beam.

6.5.1 Results with elastic matrix

Here, the results obtained for the RVE size study considering elastic constituents only are presented. The material properties used to model both the matrix and the fibres are presented in Table 6.15.

Table 6.15: Elastic properties for the composite RVEs used in the RVE size study.

	Matrix	Fibres
Young's modulus (E) [GPa]	30	300
Poisson's ratio (ν)	0.3	0.2

The evolution of the equivalent stress, computed with the Cauchy stress obtained from the homogenised first Piola-Kirchhoff (see Equation (2.33)), and the norm of the homogenised higher-order stress is presented in Figures 6.15 and 6.16, for the history at point A, near the beam centre, and Figures 6.17 and 6.18 for point B, located at the bottom of the beam.

6.5.2 Results with elasto-plastic matrix

The simulations are repeated for the same RVE morphologies with different material properties. Non-linear material behaviour is now introduced at the matrix, that is modelled with an elasto-plastic von Mises law. The constitutive properties for both constituents are summarised in Table 6.16.

Table 6.16: Constitutive properties for the composite RVEs with elasto-plastic matrix.

	Matrix	Fibres
Young's modulus (E) [GPa]	72.4	400
Poisson's ratio (ν)	0.3	0.3
Yielding stress (σ_{y0}) [MPa]	352	
Hardening law	see Figure 6.19	

The evolution of the homogenised equivalent stress and the norm of the homogenised higher-order stress tensor, obtained with the history from both macro-scale points, is represented in Figures 6.20 to 6.23.

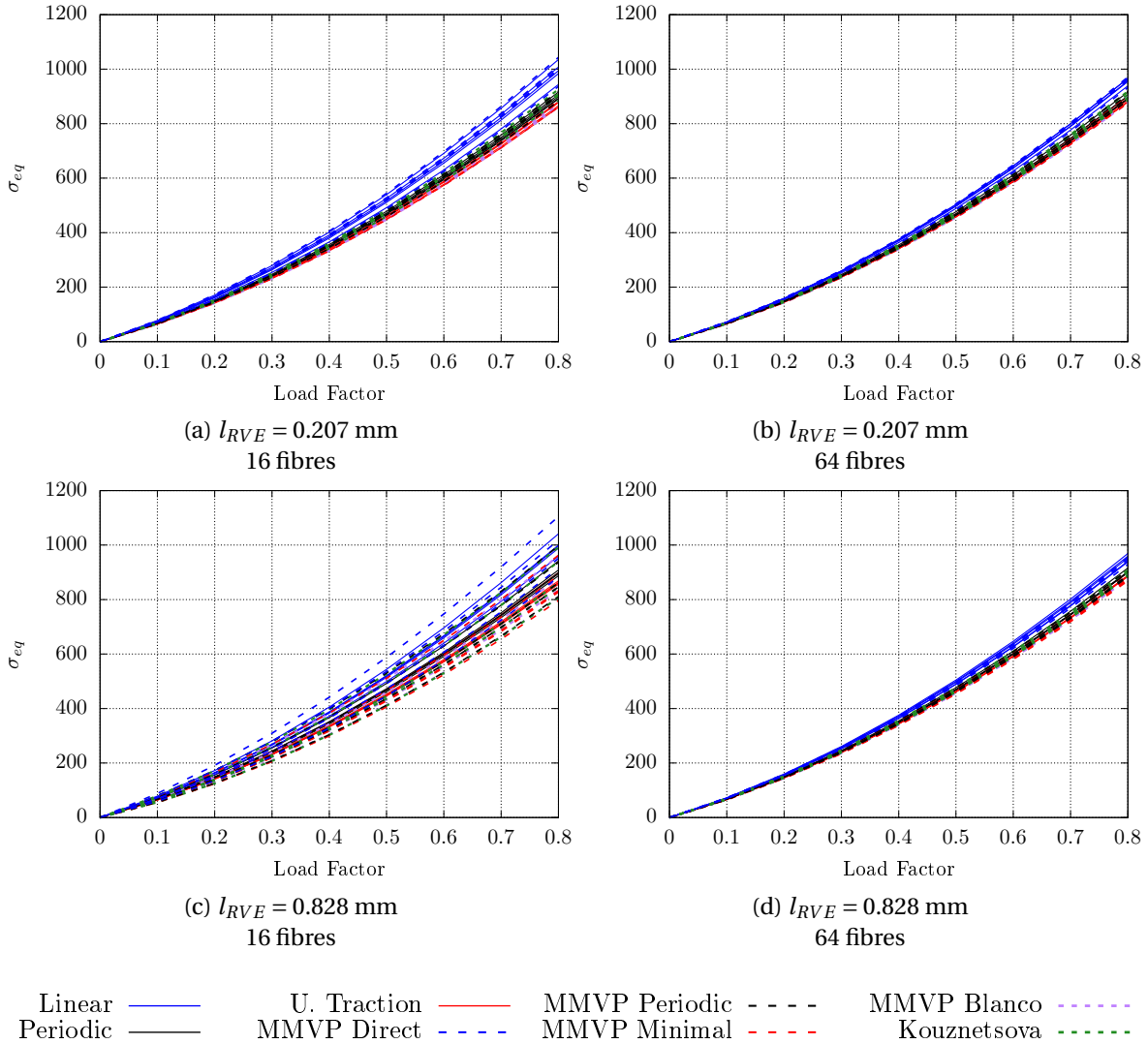

(a) $l_{RVE} = 0.207$ mm
16 fibres

(b) $l_{RVE} = 0.207$ mm
64 fibres

(c) $l_{RVE} = 0.828$ mm
16 fibres

(d) $l_{RVE} = 0.828$ mm
64 fibres

Figure 6.15: Evolution of the homogenised equivalent stress obtained from elastic RVEs under the deformation history from point A.

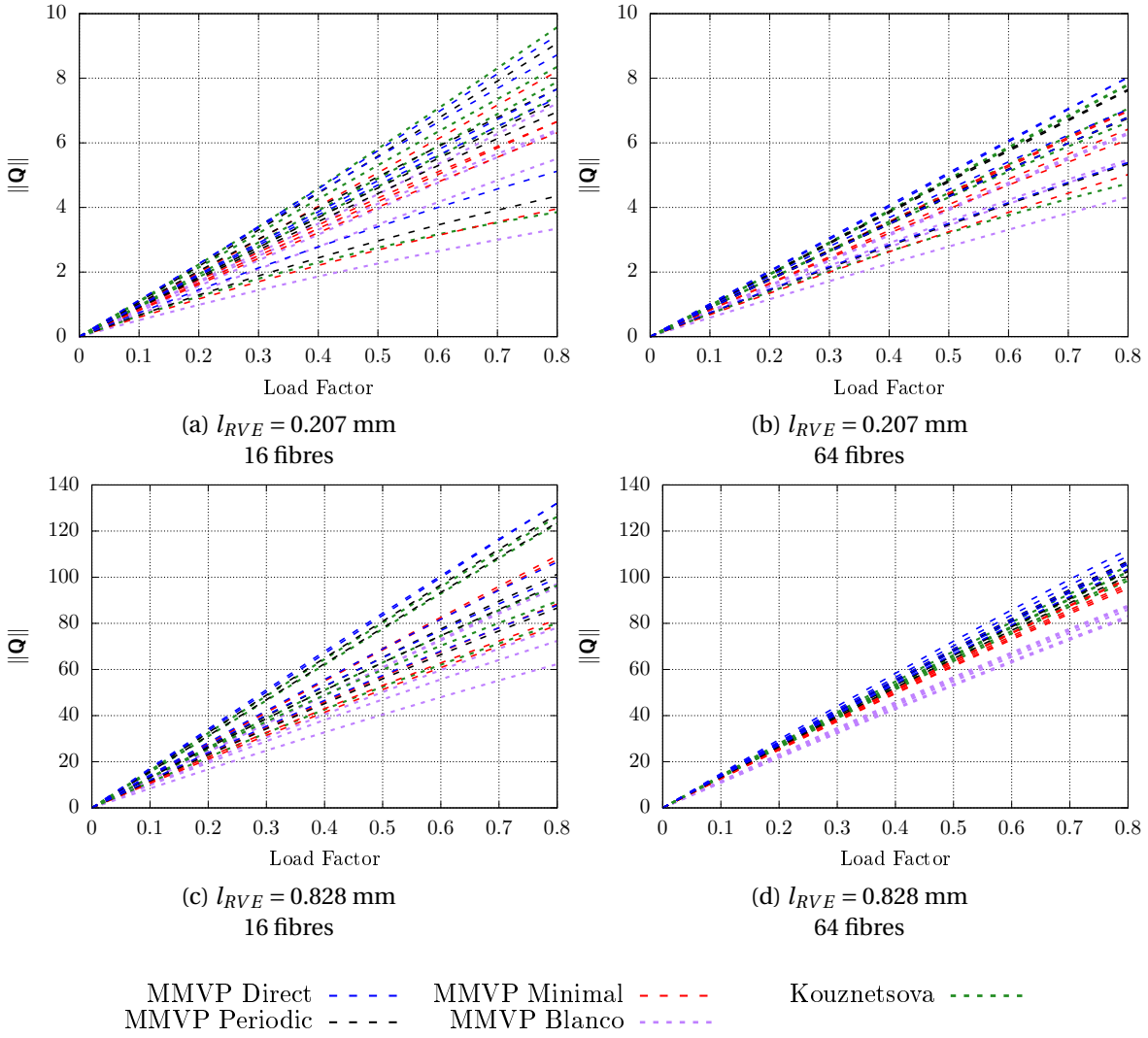

(a) $l_{RVE} = 0.207$ mm
16 fibres

(b) $l_{RVE} = 0.207$ mm
64 fibres

(c) $l_{RVE} = 0.828$ mm
16 fibres

(d) $l_{RVE} = 0.828$ mm
64 fibres

Figure 6.16: Evolution of the norm of the homogenised higher-order stress obtained from elastic RVEs under the deformation history from point A.

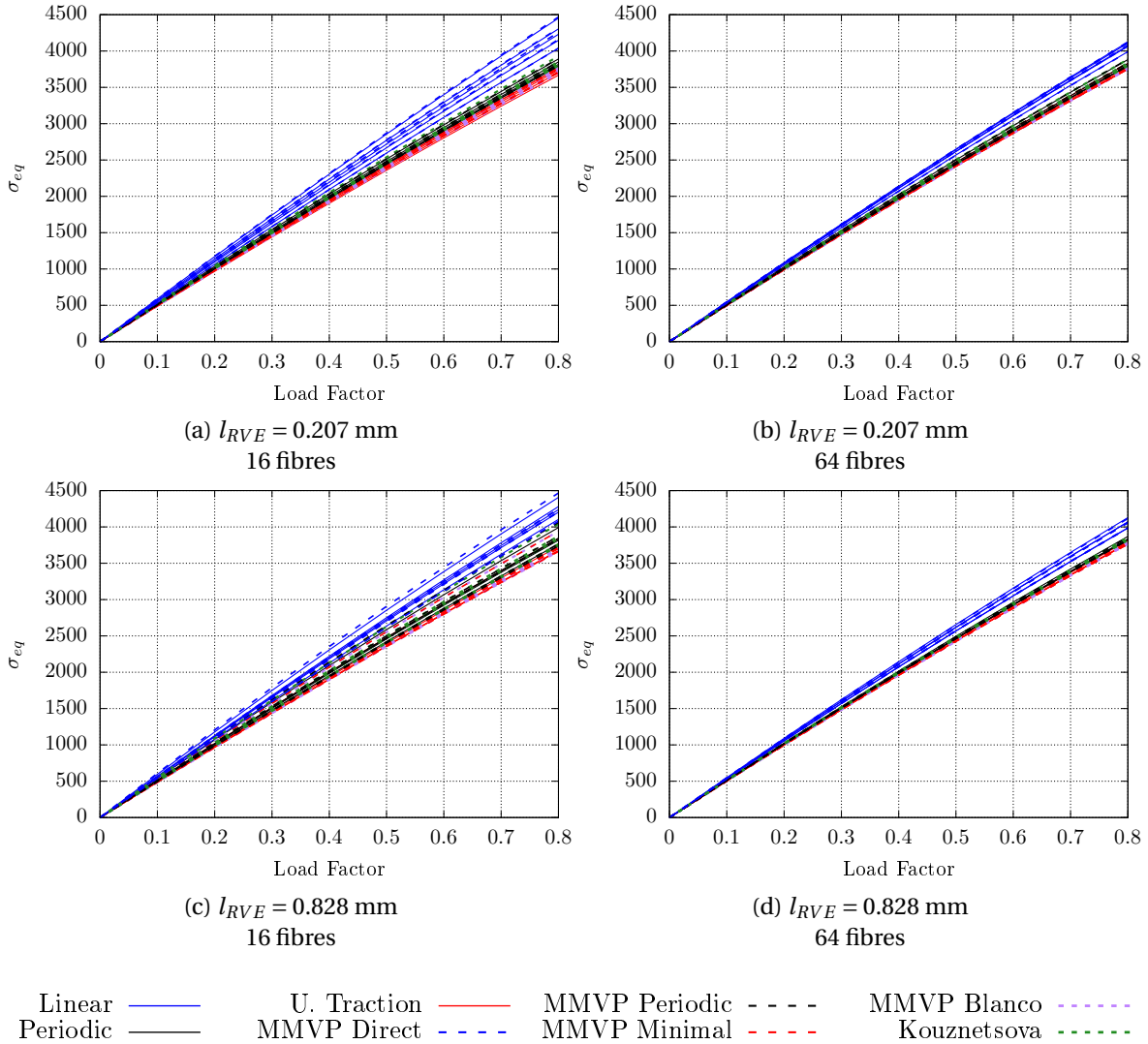

(a) $l_{RVE} = 0.207$ mm
16 fibres

(b) $l_{RVE} = 0.207$ mm
64 fibres

(c) $l_{RVE} = 0.828$ mm
16 fibres

(d) $l_{RVE} = 0.828$ mm
64 fibres

Figure 6.17: Evolution of the homogenised equivalent stress obtained from elastic RVEs under the deformation history from point B.

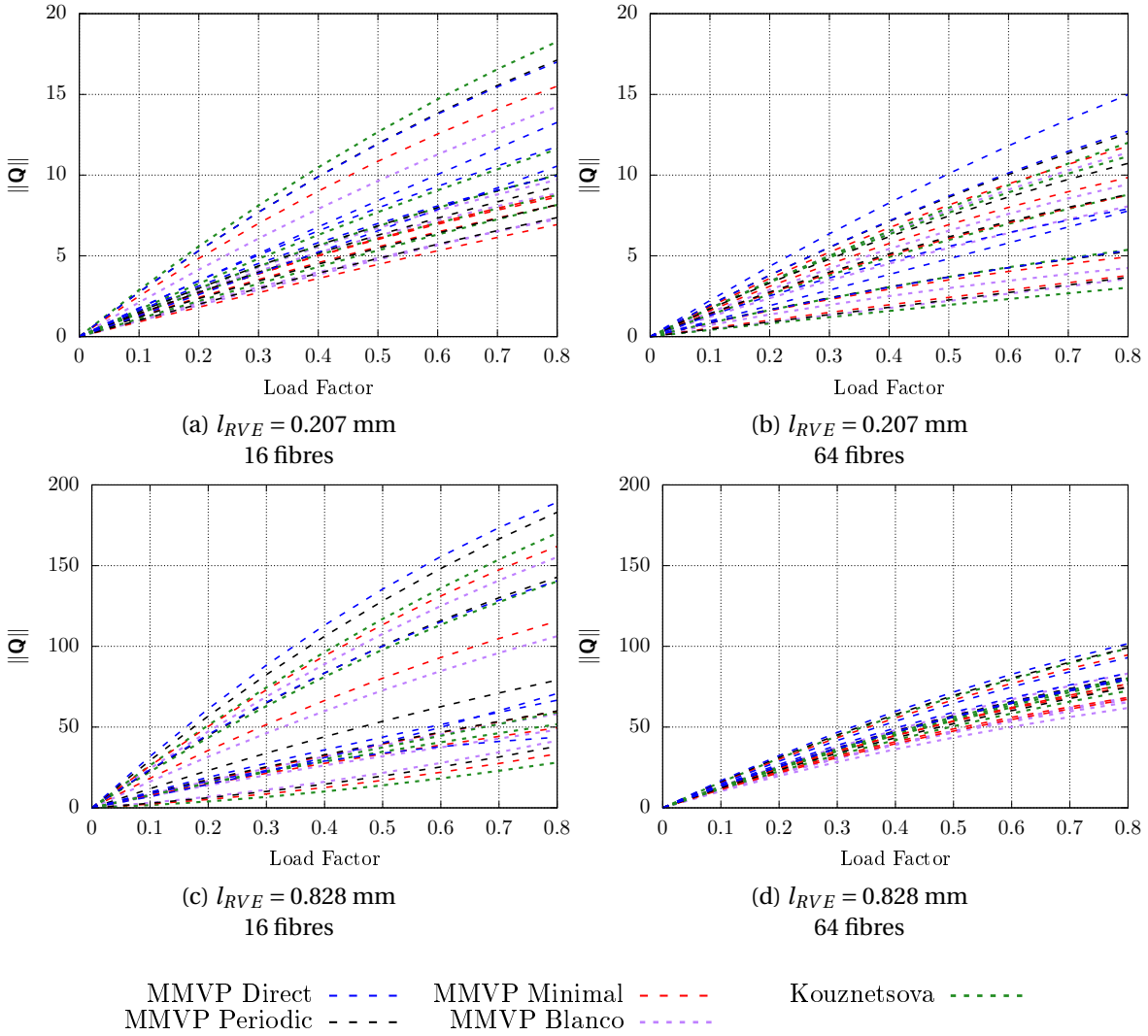

(a) $l_{RVE} = 0.207$ mm
16 fibres

(b) $l_{RVE} = 0.207$ mm
64 fibres

(c) $l_{RVE} = 0.828$ mm
16 fibres

(d) $l_{RVE} = 0.828$ mm
64 fibres

Figure 6.18: Evolution of the norm of the homogenised higher-order stress obtained from elastic RVEs under the deformation history from point B.

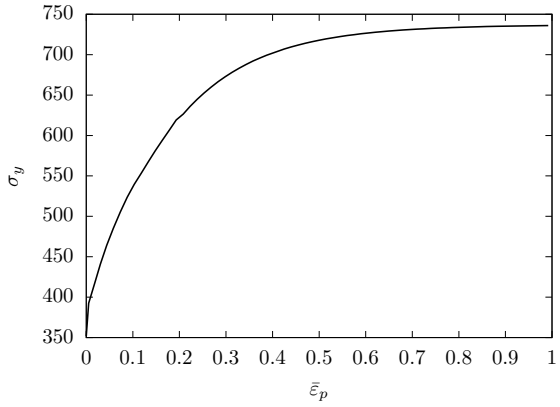

Figure 6.19: Evolution of the yielding stress [MPa] with the accumulated plastic strain, for the elasto-plastic matrix of the composite material.

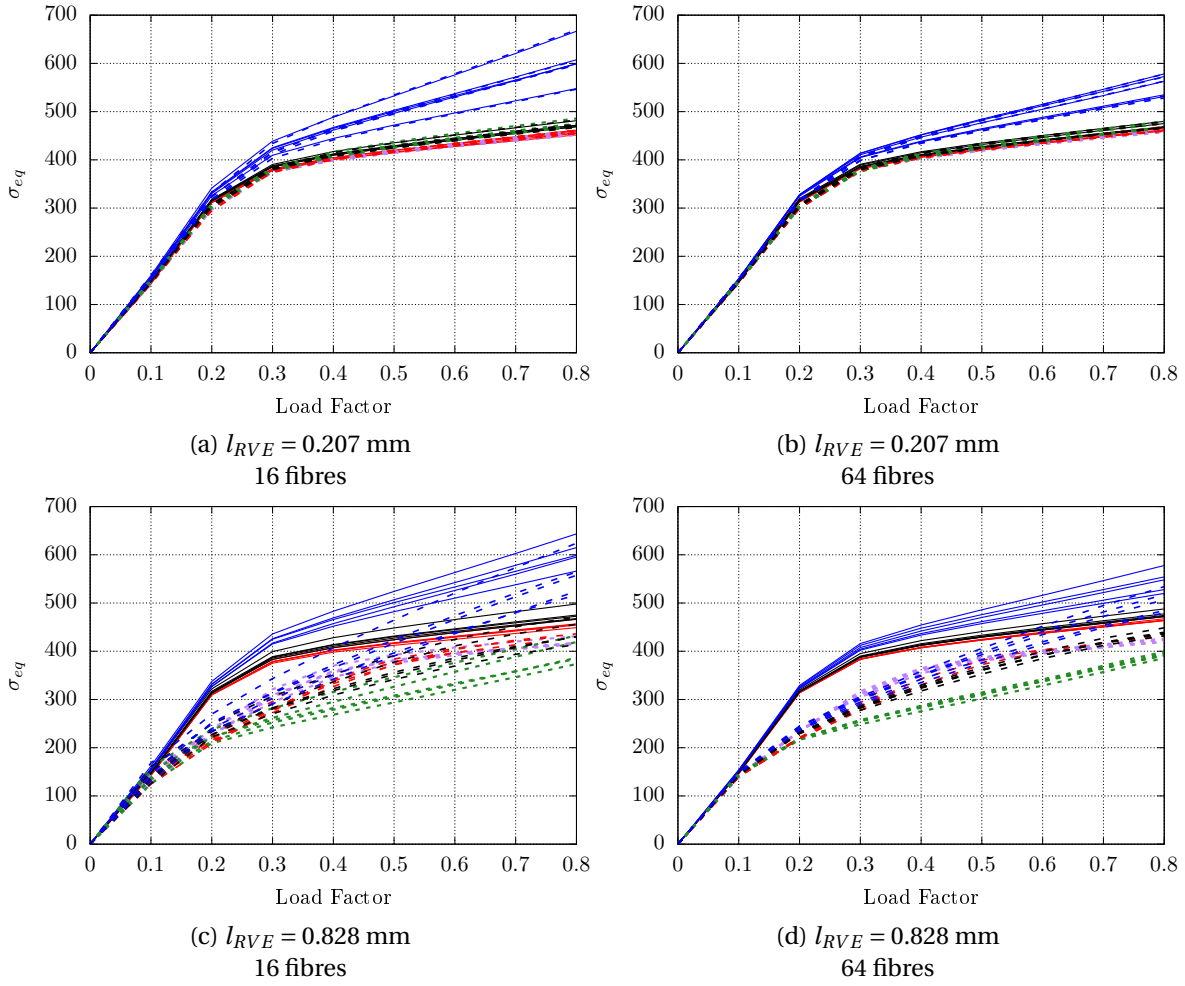

(a) $l_{RVE} = 0.207$ mm
16 fibres

(b) $l_{RVE} = 0.207$ mm
64 fibres

(c) $l_{RVE} = 0.828$ mm
16 fibres

(d) $l_{RVE} = 0.828$ mm
64 fibres

Figure 6.20: Evolution of the homogenised equivalent stress obtained from elasto-plastic RVEs under the deformation history from point A.

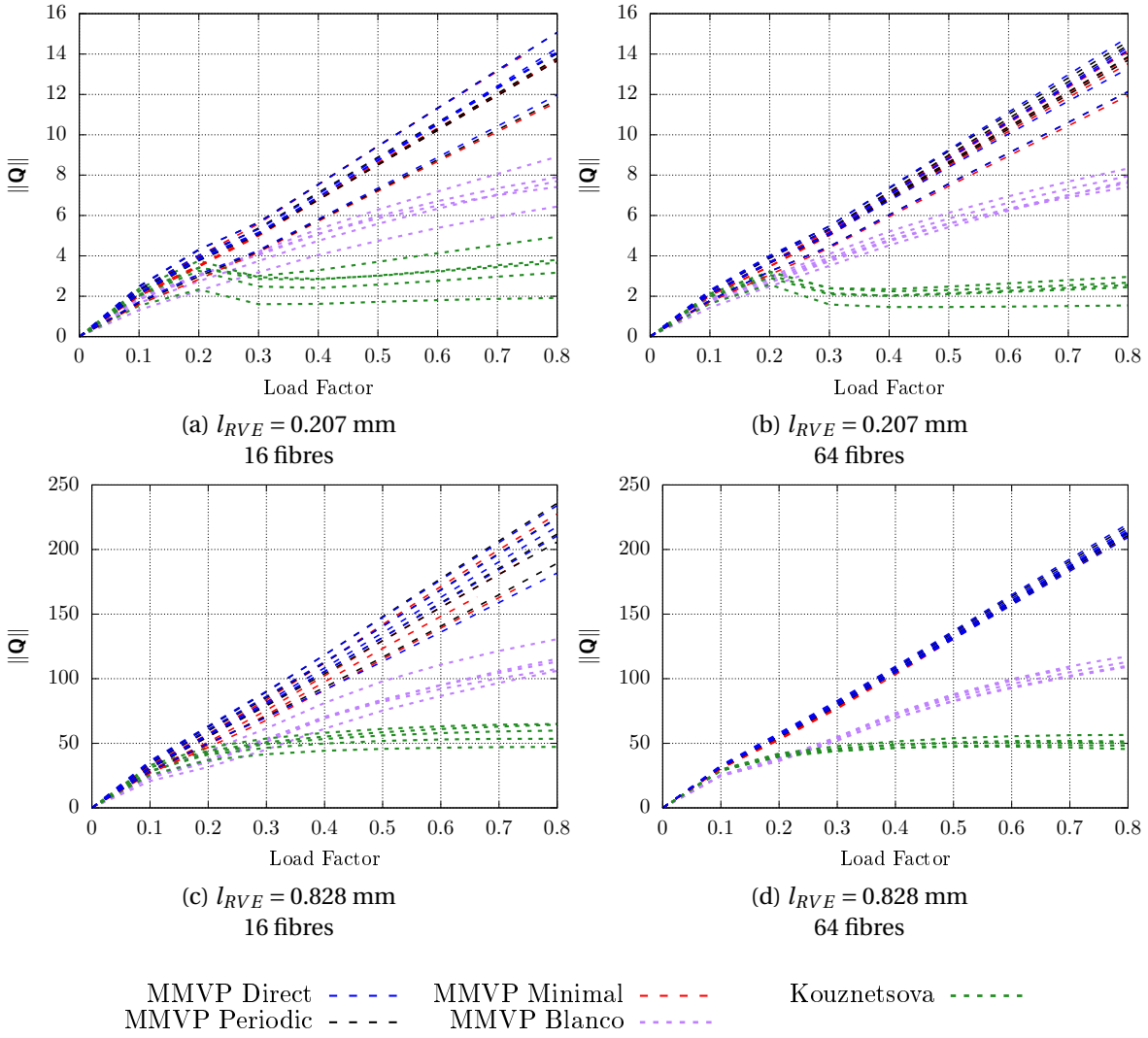

(a) $l_{RVE} = 0.207$ mm
16 fibres

(b) $l_{RVE} = 0.207$ mm
64 fibres

(c) $l_{RVE} = 0.828$ mm
16 fibres

(d) $l_{RVE} = 0.828$ mm
64 fibres

Figure 6.21: Evolution of the norm of the homogenised higher-order stress obtained from elasto-plastic RVEs under the deformation history from point A.

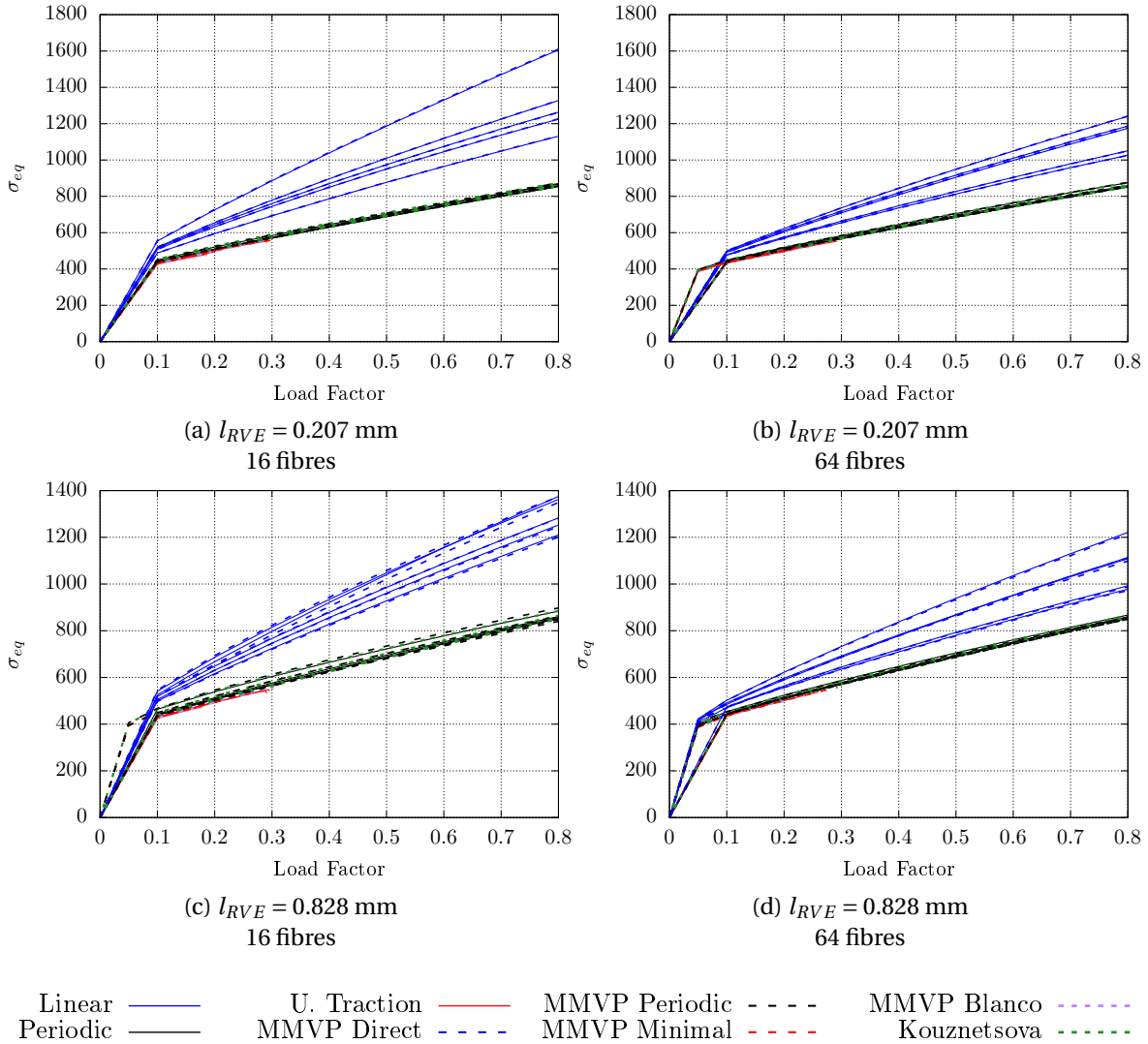

(a) $l_{RVE} = 0.207$ mm
16 fibres

(b) $l_{RVE} = 0.207$ mm
64 fibres

(c) $l_{RVE} = 0.828$ mm
16 fibres

(d) $l_{RVE} = 0.828$ mm
64 fibres

Figure 6.22: Evolution of the homogenised equivalent stress obtained from elasto-plastic RVEs under the deformation history from point B.

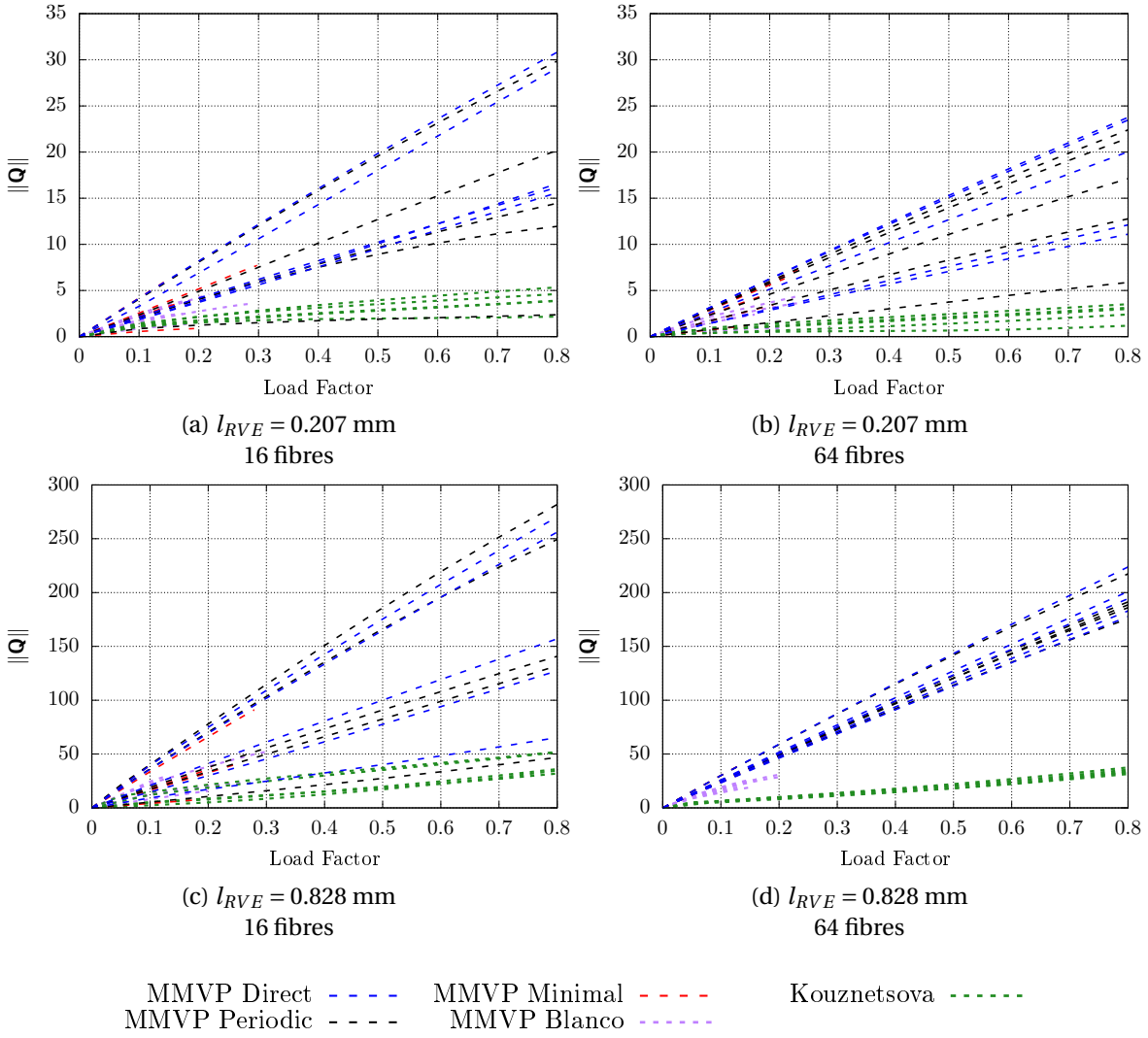

(a) $l_{RVE} = 0.207$ mm
16 fibres

(b) $l_{RVE} = 0.207$ mm
64 fibres

(c) $l_{RVE} = 0.828$ mm
16 fibres

(d) $l_{RVE} = 0.828$ mm
64 fibres

Figure 6.23: Evolution of the norm of the homogenised higher-order stress obtained from elasto-plastic RVEs under the deformation history from point B.

6.5.3 Discussion of the results

The results obtained for the case of the elastic RVEs, presented in Section 6.5.1, reveal that the homogenised response in terms of the equivalent stress (Figures 6.15 and 6.17) is not dependent on the RVE length and the fibres diameter. The dispersion of the results is quite small, being slightly increased when the fibres diameter increases (the generalised RVE size is reduced). It is also remarkable the fact that the homogenised response obtained with 1^{st}-order and 2^{nd}-order multi-scale formulations is coincident.

The effect of the RVE length is observed in the evolution of the homogenised higher-order stresses, Figures 6.16 and 6.18, where the mean value of its norm increases for the largest RVE length. The influence of the generalised RVE size becomes evident when looking at these Figures, where a significant increase of the dispersion is observed when the number of fibres is reduced.

In Figures 6.16 to 6.18, it is possible to identify a trend where the direct constraint provides an upper bound, and the minimal constraints a lower bound, especially in the case of the largest RVE length and largest generalised RVE size. The evolution of the higher-order stress is more compliant with the Blanco-based minimal constraint than with the alternative non-symmetric counterpart.

When comparing the results arising from point A and point B, it is observed that the equivalent stress increases significantly, from 800 MPa to 4000 MPa at the end of the simulation, while the increase of the higher-order stresses norm is almost negligible. In fact, the values of the second gradient are similar at both points and the values of equivalent strain are much higher at point B, since point A is closer to the beam centre (see Figure 6.14).

Regarding the case of the elasto-plastic RVEs, for the deformation history from point A, the evolution of the homogenised equivalent stress obtained from 2^{nd}-order micro-constraints shows a strong dependency on the RVE length, as can be observed in Figure 6.20. While the response coincides with the corresponding standard 1^{st}-order constraints in the case of the smaller RVE length, when $l_{RVE} = 0.828$ mm, the equivalent stress curves diverge showing an earlier onset of the macroscopic yielding. This fact indicates that the *Scale Separation Principle* is not respected by 1^{st}-order homogenisation models at point A with the largest RVE length, despite being verified for a RVE length that is only four times smaller.

In the case of the deformation history from point B, where 1^{st}-order deformation dominates, the RVE length does not influence the homogenised equivalent stress obtained with 2^{nd}-order constraints (see Figure 6.22). Moreover, these curves coincide with the 1^{st}-order counterparts, even for the RVEs with $l_{RVE} = 0.828$ mm. It is noticeable that the simulations involving minimal constraints did not finish.

Looking at the evolution of the norm of the higher-order stress tensor, in Figures 6.21 and 6.23, it is quite consistent for the constraints based on the method of the multi-scale virtual power, depending especially on the realisation. Kouznetsova's periodic response clearly provides a lower bound, with a noticeable yielding-like behaviour in the simulation for point A. Blanco's minimal constraint differs significantly from the remaining MMVP-based constraints.

Like in the elastic case, the generalised RVE size (number of fibres and fibres diameter) only affects the dispersion of the results, not changing remarkably the trend of the homogenised responses.

After the analysis of these results, the main conclusions are summarised in what follows.

- A decoupled analysis of the RVE length l_{RVE} and the micro-constituents size (associated with the generalised RVE size s_{RVE}) effects shows that while the RVE length has an important influence on the 2^{nd}-order homogenisation schemes, the generalised RVE size is related to the dispersion of the results, i.e., to the representativeness of the chosen RVE. Thus, size effects captured by these homogenisation formulations are related to the RVE length only, that drives the non-local character of the macroscopic response, and influence of the size of the micro-constituents is not taken into account. Therefore, an appropriate generalised RVE size must be large enough so that the number of micro-scale constituents included allow to achieve a

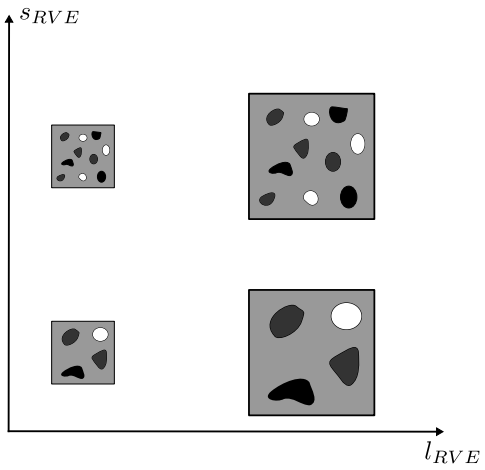

Figure 6.24: Illustration of the framework where the RVE size, s_{RVE}, and RVE length, l_{RVE}, are decoupled.

representative response. Here, it is proposed that the RVE length can be defined regardless its relation to the physical size of the micro-constituents, in order to avoid limitations in the number of constituents included. The RVE length should be calibrated in order to obtain a suitable non-local macroscopic response, where l_{RVE} is intrinsically related to the macroscopic characteristic length. The RVE model is obtained by definition of the generalised RVE size in the first place, and then a scale parameter is employed so that the final RVE model has the appropriate length. This decoupling between RVE length and generalised RVE size is illustrated in Figure 6.24 and is conceptually sound for numerical purposes, since the RVE is a model of the real material.

- Regarding the definition of the scale separation limit, where the response of 1st-order homogenisation models loses its validity, it is concluded that the RVE length and the macroscale deformation wavelength, quantified here by the second gradient of the displacements $\mathbf{G}$, are not the only parameters to be considered when evaluating the *Scale Separation Principle*. The micro-scale constituents local behaviour also plays an important role. It is shown here that for the same RVE configurations, 1st-order constraints yield results coincident with the 2nd-order counterparts if only elasticity is considered, regardless the RVE length, but this is not true if the matrix assumes an elasto-plastic behaviour. In addition to the magnitude of $\mathbf{G}$, the relative magnitude of the strain (based on the first gradient of displacements) must be taken into account. This becomes evident comparing the results between point A and point B, with the elasto-plastic RVE, since the second gradient norm is similar for both points, but only for point A, where the strain level is low, the results differ between 1st and 2nd-order approaches.

6.6 Comparison with small strain analytical solution

The results presented in the previous sections reveal that the choice of the micro-scale constraint leads to very distinct behaviour at both scales. Aiming to understand which constraint leads to the results in closer agreement with physical evidence, a comparison with an analytical solution is performed here.

Kouznetsova et al. (2004a) devised an analytical solution for the homogenised response of 2D homogeneous RVEs under the small strain assumption that recovers the Mindlin elastic model. This solution is compared with numerical results obtained from different micro-constraints, with distinct discretisations. This comparative study is also performed for 3D RVEs.

6.6.1 Two-dimensional RVE

Kouznetsova et al. (2004a) derived an analytical solution for a homogeneous microstructure under small strain, based on the second-order homogenisation scheme proposed by the same authors (Kouznetsova et al., 2004b), by discretising the 2D RVE with a single 8-noded quadrilateral (*quad 8*) element. A Mindlin-like linear elastic model for 2$^{\text{nd}}$-order material is obtained, where the 1$^{\text{st}}$ Piola-Kirchhoff stress tensor is defined by

$$\begin{bmatrix} P_{11} \\ P_{21} \\ P_{12} \\ P_{22} \end{bmatrix} = \begin{bmatrix} \lambda+2\mu & 0 & 0 & \lambda \\ 0 & \lambda & \lambda & 0 \\ 0 & \lambda & \lambda & 0 \\ \lambda & 0 & 0 & \lambda+2\mu \end{bmatrix} \begin{bmatrix} F_{11}-1 \\ F_{21} \\ F_{12} \\ F_{22}-1 \end{bmatrix}, \tag{6.2}$$

and the higher-order stress tensor depends on the second gradient through:

$$\begin{aligned} &\begin{bmatrix} \mathsf{Q}_{111} & \mathsf{Q}_{211} & \mathsf{Q}_{121} & \mathsf{Q}_{221} & \mathsf{Q}_{112} & \mathsf{Q}_{212} & \mathsf{Q}_{122} & \mathsf{Q}_{222} \end{bmatrix}^T = \\ &\begin{bmatrix} \frac{h^2}{6}\left(\frac{\lambda}{2}+\mu\right) & 0 & 0 & \frac{h^2}{24}\lambda & 0 & \frac{h^2}{24}\lambda & 0 & 0 \\ 0 & \frac{h^2}{12}\mu & \frac{h^2}{24}\mu & 0 & \frac{h^2}{24}\mu & 0 & 0 & 0 \\ 0 & \frac{h^2}{24}\mu & \frac{h^2}{16}\left(\frac{\lambda}{3}+\mu\right) & 0 & \frac{h^2}{16}\left(\frac{\lambda}{3}+\mu\right) & 0 & 0 & \frac{h^2}{24}\lambda \\ \frac{h^2}{24}\lambda & 0 & 0 & \frac{h^2}{16}\left(\frac{\lambda}{3}+\mu\right) & 0 & \frac{h^2}{16}\left(\frac{\lambda}{3}+\mu\right) & \frac{h^2}{24}\mu & 0 \\ 0 & \frac{h^2}{24}\mu & \frac{h^2}{16}\left(\frac{\lambda}{3}+\mu\right) & 0 & \frac{h^2}{16}\left(\frac{\lambda}{3}+\mu\right) & 0 & 0 & \frac{h^2}{24}\lambda \\ \frac{h^2}{24}\lambda & 0 & 0 & \frac{h^2}{16}\left(\frac{\lambda}{3}+\mu\right) & 0 & \frac{h^2}{16}\left(\frac{\lambda}{3}+\mu\right) & \frac{h^2}{24}\mu & 0 \\ 0 & 0 & 0 & \frac{h^2}{24}\mu & 0 & \frac{h^2}{24}\mu & \frac{h^2}{12}\mu & 0 \\ 0 & 0 & \frac{h^2}{24}\lambda & 0 & \frac{h^2}{24}\lambda & 0 & 0 & \frac{h^2}{6}\left(\frac{\lambda}{2}+\mu\right) \end{bmatrix} \begin{bmatrix} \mathsf{G}_{111} \\ \mathsf{G}_{211} \\ \mathsf{G}_{121} \\ \mathsf{G}_{221} \\ \mathsf{G}_{112} \\ \mathsf{G}_{212} \\ \mathsf{G}_{122} \\ \mathsf{G}_{222} \end{bmatrix}, \end{aligned} \tag{6.3}$$

where λ and μ denote the Lamé parameters and $h = l_{RVE}$ the RVE length.

A homogeneous RVE with elastic properties $E = 210$ GPa and $\nu = 0.3$, and length $l_{RVE} = 1$ mm, is subjected to a small strain 2$^{\text{nd}}$-order deformation by imposing the macroscopic second gradient $\mathsf{G}_{122} = 0.001$ mm^{-1} (curvature mode), and the results are analysed for distinct discretisations and micro-scale constraints.

In the case where a single *quad 8* element is employed, the results obtained with all the micro-scale constraints (not shown here) are in accordance with the analytical solution, with $\mathsf{Q}_{122} = 6.731$ MPa mm and $\mathsf{Q}_{221} = \mathsf{Q}_{212} = 3.365$ MPa mm. The displacement fluctuation field is null.

The RVE model is also discretised with 4 and 100 elements. The resulting distribution of displacement fluctuation field is presented in Figure 6.25, along with the non-zero components of homogenised **Q**.

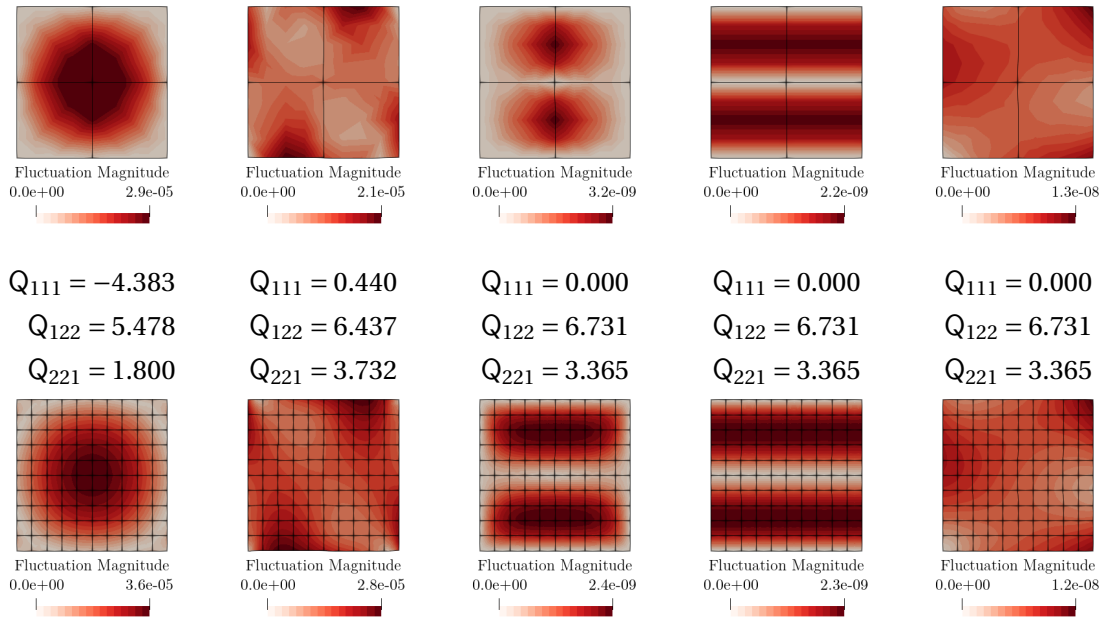

(a) Kouznetsova (b) MMVP Blanco (c) Direct (d) MMVP periodic (e) MMVP minimal

Figure 6.25: Distribution of fluctuation field and components of homogenised $\mathbf{Q}$ [MPa mm] obtained from a homogeneous RVE subjected to $G_{122} = 0.001$ mm^{-1} (curvature mode).

6.6.2 Three-dimensional RVE

The strategy proposed by Kouznetsova et al. (2004a) is extended for 3D RVEs, where a cubic homogeneous RVE with length $l_{RVE} = 1$ mm and the same elastic properties is considered at the micro-scale. In addition to the second gradient component $G_{122} = 0.001$ mm^{-1} (curvature mode), the case where a twisting deformation mode is enforced is also analysed through $G_{123} = 0.001$ mm^{-1}. The RVE is discretised with 20-noded hexahedral elements.

Taking into account the results obtained with Kouznetsova's periodicity from a single element RVE model, the expected 3D homogenised response is given by:

- $Q_{122} = \frac{l_{RVE}^2}{12}\mu G_{122}$ and $Q_{221} = \frac{l_{RVE}^2}{24}\mu G_{122}$ when G_{122} is imposed, which yields $Q_{122} = 6.731$ MPa mm and $Q_{221} = 3.365$ MPa mm when $G_{122} = 0.001$ mm^{-1} (curvature mode);
- $Q_{123} = \frac{l_{RVE}^2}{12}\mu G_{123}$ and $Q_{321} = Q_{231} = \frac{l_{RVE}^2}{24}\mu G_{123}$ when G_{123} is enforced, yielding $Q_{123} = 6.731$ MPa mm and $Q_{321} = Q_{231} = 3.365$ MPa mm when $G_{123} = 0.001$ mm^{-1} (twisting mode).

In addition to the single element discretisation, the RVE is also meshed with 27 and 125 elements. The case with a single element yields the expected results, with null fluctuation field, for all the micro-constraints. The resulting non-zero components of the homogenised higher-order stress $\mathbf{Q}$ and the distribution of fluctuation field obtained with the remaining discretisations are shown in Figures 6.26 and 6.27.

6.6.3 Discussion of the results

It is clearly observed that the results obtained with Kouznetsova's periodicity and the minimal symmetric constraint based on Blanco's formulation depend on the discretisation, and the homogenised $\mathbf{Q}$ deviates from the expected values, especially in the former constraint under a curvature deformation mode (Figures 6.25 and 6.26). On the other hand, the remaining constraints based on the method of multi-scale virtual power, that recover the constraints presented by Luscher, lead to the expected homogenised solution. In addition, null fluctuation fields ($\sim 10^{-9}$ mm) result from the constraints that respect the analytical solution, while relatively significant fluctuations develop in the remaining cases ($\sim 10^{-5}$ mm).

In the case of the twisting deformation (Figure 6.27), the results obtained with the Kouznetsova's periodic constraint are consistent with the analytical solution and do not depend on the discretisation. For the Blanco-based constraint, the homogenised stress components are different but relatively close to the expected.

For such a simple micro-structure, the homogenisation results should not depend on the discretisation so markedly. In the case of the Kouznetsova constraint, this may be explained by the fact that a volumetric constraint is not enforced, which is not a problem when finite element nodes do not exist in the interior of the RVE domain. Nevertheless, when finer discretisations are employed, the differences between the numerical and the analytical solution are remarkable. In what refers to the Blanco-based minimal constraint, since its main particularity is the presence of the symmetry operator (see Equations (5.16) and (5.115)), this is probably the origin of the deviations. In fact, this symmetry operator comes from the definition of the homogenised 2nd gradient, Equation (5.6), which is defined *apriori*, and may be subject of discussion.

Therefore, a comparison between the inserted second gradient and a measure of its homogenised version is performed in the next section.

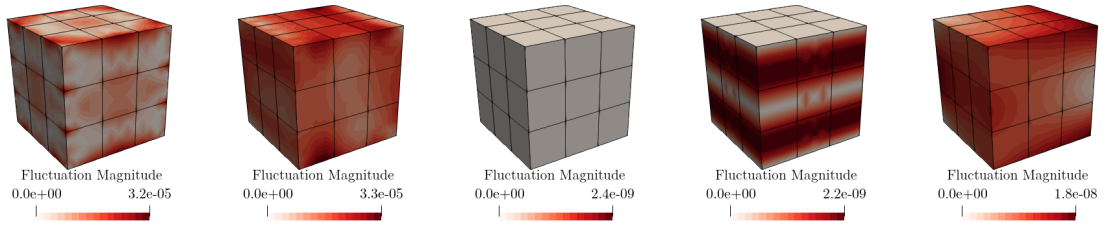

$Q_{111} = -3.807$ $Q_{111} = 0.501$ $Q_{111} = 0.000$ $Q_{111} = 0.000$ $Q_{111} = 0.000$
$Q_{221} = 1.857$ $Q_{221} = 3.810$ $Q_{221} = 3.365$ $Q_{221} = 3.365$ $Q_{221} = 3.365$
$Q_{331} = -1.342$ $Q_{331} = 0.224$ $Q_{331} = 0.000$ $Q_{331} = 0.000$ $Q_{331} = 0.000$
$Q_{122} = 5.345$ $Q_{122} = 6.344$ $Q_{122} = 6.731$ $Q_{122} = 6.731$ $Q_{122} = 6.731$
$Q_{133} = -1.053$ $Q_{133} = 0.053$ $Q_{133} = 0.000$ $Q_{133} = 0.000$ $Q_{133} = 0.000$

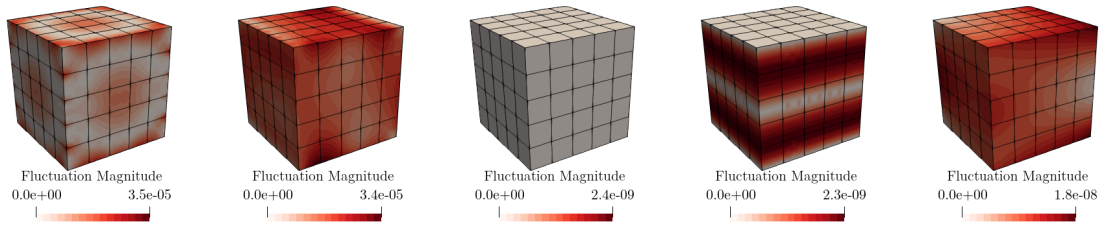

$Q_{111} = -4.068$ $Q_{111} = 0.568$ $Q_{111} = 0.000$ $Q_{111} = 0.000$ $Q_{111} = 0.000$
$Q_{221} = 1.854$ $Q_{221} = 3.815$ $Q_{221} = 3.365$ $Q_{221} = 3.365$ $Q_{221} = 3.365$
$Q_{331} = -1.450$ $Q_{331} = 0.226$ $Q_{331} = 0.000$ $Q_{331} = 0.000$ $Q_{331} = 0.000$
$Q_{122} = 5.451$ $Q_{122} = 6.339$ $Q_{122} = 6.731$ $Q_{122} = 6.731$ $Q_{122} = 6.731$
$Q_{133} = -1.156$ $Q_{133} = 0.054$ $Q_{133} = 0.000$ $Q_{133} = 0.000$ $Q_{133} = 0.000$

(a) Kouznetsova (b) MMVP Blanco (c) Direct (d) MMVP periodic (e) MMVP minimal

Figure 6.26: Distribution of fluctuation field and components of homogenised $\mathbf{Q}$ [MPa mm] obtained from a homogeneous 3D RVE subjected to $G_{122} = 0.001$ mm^{-1} (curvature mode).

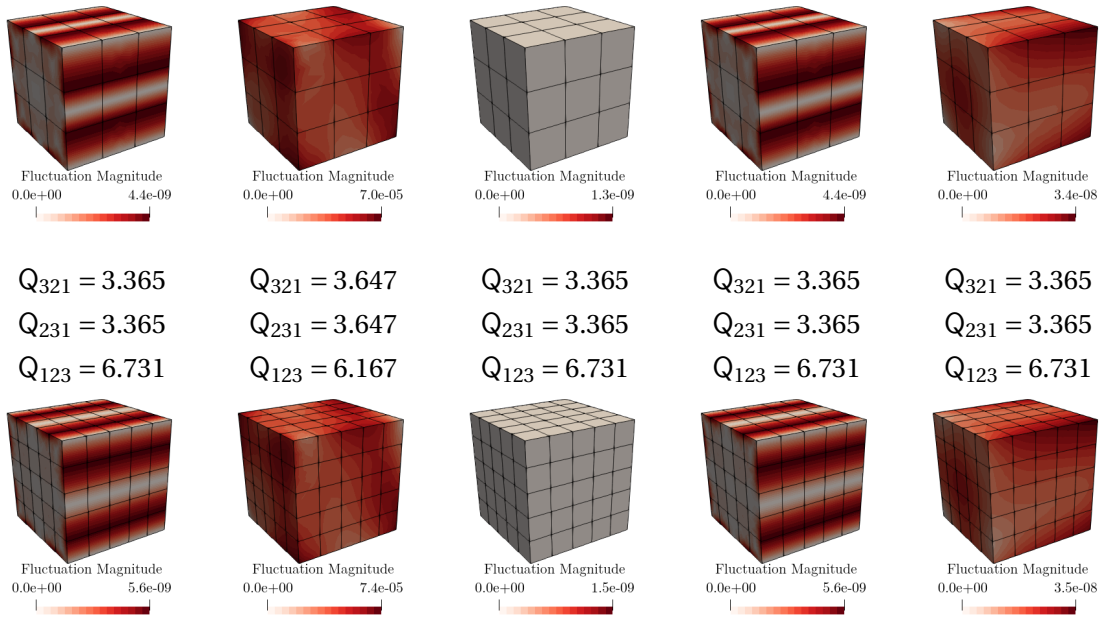

(a) Kouznetsova (b) MMVP Blanco (c) Direct (d) MMVP periodic (e) MMVP minimal

Figure 6.27: Distribution of fluctuation field and components of homogenised $\mathbf{Q}$ [MPa mm] obtained from a homogeneous 3D RVE subjected to $G_{123} = 0.001$ mm^{-1} (twisting mode).

6.7 Assessment of the homogenised second gradient

The suitability of the micro-scale constraints employed in a 2^{nd}-order computational homogenisation scheme is assessed in this section, regarding a correct description of the homogenised second gradient. Since a 1^{st}-order continuum is employed at the micro-scale, the constraints cannot be obtained as a result of the homogenisation concept applied to the 2^{nd}-order gradient directly:

$$\mathbf{G} = \frac{1}{V_\mu}\int_{\Omega\mu} \mathbf{G}_\mu dV. \tag{6.4}$$

The homogenised $\mathbf{G}$ must be defined from 1^{st}-order quantities, as shown in Section 5.1 (Equations (5.6) and (5.66)). While Blanco et al. (2016b) proposed a definition where a symmetry operator is included due to the symmetry of the second gradient, a formulation where is is not imposed *apriori* is developed in Section 5.2. Moreover, Kouznetsova (2002) did not define explicitly the homogenised second gradient. This raises the question of whether or not these models approach a correct characterisation of the second gradient.

Even though the micro-scale 2^{nd}-order gradient $\mathbf{G}_\mu$ is not a kinematic variable in these multi-scale models, it can be evaluated by the 2^{nd}-derivative of the micro-displacement field (see Appendix D), and its homogenised version based on volume averaging, denoted by $\bar{\mathbf{G}}$:

$$\bar{\mathbf{G}} = \frac{1}{V_\mu}\int_{\Omega\mu} \mathbf{G}_\mu dV. \tag{6.5}$$

This homogenised quantity is computed and compared against the inserted counterpart $\mathbf{G}$ for four different RVEs, represented in Figure 6.28. The micro-constituents are modelled by linear elastic laws.

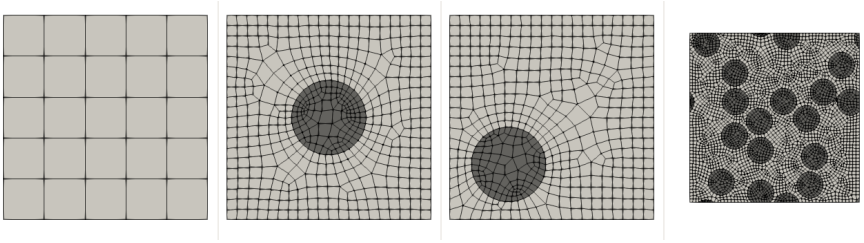

Figure 6.28: RVEs employed in the assessment of the homogenised $\mathbf{G}$. i) homogeneous RVE, l_{RVE} = 1 mm, ii) RVE with centred inclusion, l_{RVE} = 1 mm, iii) RVE with skew inclusion, l_{RVE} = 1 mm, iv) RVE with 16 random inclusions, l_{RVE} = 0.828 mm.

In order to quantify the difference between the imposed $\mathbf{G}$ and the computed $\bar{\mathbf{G}}$, the difference variable is defined as

$$\varepsilon = \frac{\|\bar{\mathbf{G}} - \mathbf{G}\|}{\|\mathbf{G}\|}. \tag{6.6}$$

This difference is computed for six different loading cases. In the first three cases, components of the macroscopic second gradient are inserted separately: i) $G_{112} = G_{121} = 0.2$ mm^{-1}, ii) $G_{122} = 0.2$ mm^{-1} and iii) $G_{222} = 0.2$ mm^{-1}. Thereafter the homogeneous RVE, the RVE with centred inclusion and the RVE with randomly distributed inclusions are subjected to more complex macro-loadings, obtained from the deformation history of a bending beam at three different positions: iv) point A, v) point B and vi) point C, as represented in the FE^2 simulation reported in Section 6.5.1 (see Figure 6.13).

6.7.1 Results

The results are shown in Table 6.17, for the cases where only purely 2nd-order deformations are enforced, and in Table 6.18 for the cases where a bending deformation history has been considered. All the results can be compared graphically in the plots of Figure 6.29.

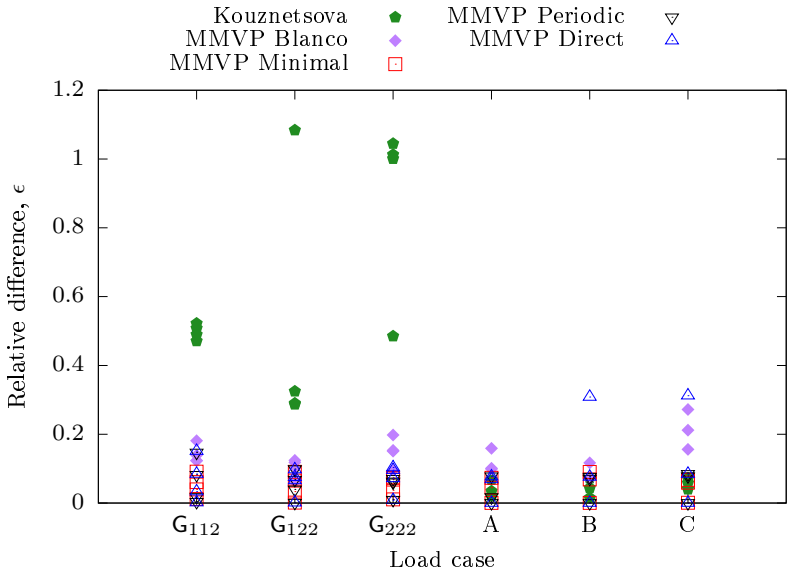

(a)

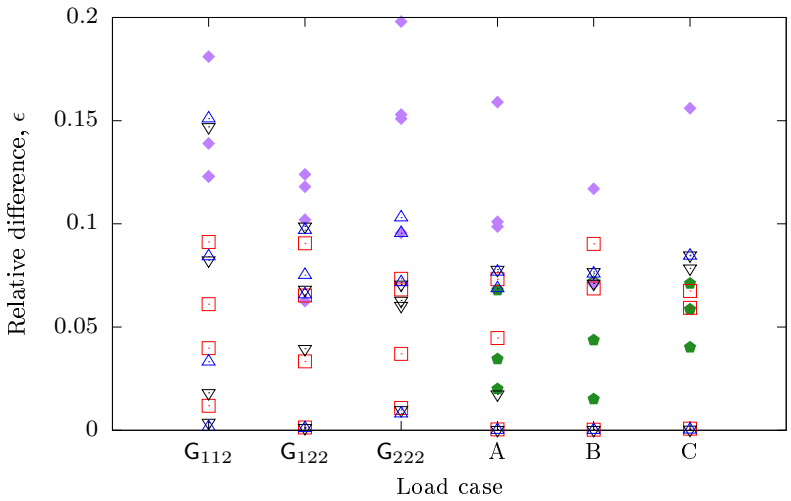

(b)

Figure 6.29: Scatter plots of the relative difference between the imposed 2nd gradient and the averaged counterpart, (a) all results, (b) only relative differences bellow 0.2.

Table 6.17: Measure of the difference between the imposed 2nd gradient and the averaged counterpart (Equation (6.6)), for distinct RVEs and macro-2nd-gradients.

	homogeneous			**centred inclusion**			**skew inclusion**			**composite**		
	G_{112}	G_{122}	G_{222}	G_{112}	G_{122}	G_{222}	G_{112}	G_{122}	G_{222}	G_{112}	G_{122}	G_{222}
Kouznetsova	0.508	0.287	1.001	0.490	0.325	1.013	0.471	0.290	1.045	0.522	1.084	0.485
MMVP Blanco	0.123	0.0626	0.0956	0.123	0.118	0.198	0.139	0.124	0.151	0.181	0.102	0.153
MMVP minimal	0.0119	0.00137	0.0108	0.0611	0.0653	0.0734	0.0912	0.0906	0.0682	0.0398	0.0334	0.0370
MMVP Periodic	0.00377	0.00118	0.00987	0.0824	0.0682	0.0707	0.147	0.0988	0.0604	0.0181	0.0395	0.0629
Direct	0.00148	0.000895	0.00804	0.0842	0.0752	0.0716	0.151	0.0657	0.103	0.0332	0.0970	0.0955

Table 6.18: Measure of the difference between the imposed 2nd gradient and the averaged counterpart (Equation (6.6)), for the random RVE under macro-2nd-gradient and deformation gradient obtained from a beam under bending.

	homogeneous			**centred inclusion**			**composite**		
	A	B	C	A	B	C	A	B	C
Kouznetsova	0.0345	0.0151	0.0402	0.0679	0.0720	0.0711	0.0200	0.0437	0.0586
MMVP Blanco	0.0987	0.0710	0.156	0.101	0.0713	0.212	0.159	0.117	0.272
MMVP minimal	0.0004	0.0003	0.0008	0.0732	0.0687	0.0593	0.0447	0.0903	0.0675
MMVP Periodic	0.0003	0.0003	0.0004	0.0779	0.0767	0.0848	0.0175	0.0711	0.0785
Direct	0.0001	0.0001	0.0002	0.0767	0.0758	0.0845	0.0687	0.308	0.312

6.7.2 Discussion of the results

It is observed in both Tables 6.17 and 6.18 that the difference obtained with the Blanco-based (symmetric) minimal constraint results, in general, in differences above 0.1. In the case of the MMVP minimal constraint (without the symmetric operator) the difference is in general lower than 0.1, which indicates this approach is more appropriate. The models involving boundary periodic and direct constraints, based on the method of multi-scale virtual power, are also appropriate since the differences obtained are lower than 0.1. The exceptions are found for the RVE with a skew inclusion under a G_{112} loading, where the difference for these constraints is around 0.15, and for the composite RVE under the deformation history from points B and C, where the 1st-order deformations dominate, for which the direct constraint yields differences about 0.3.

Regarding the Kouznetsova's periodic constraint, it results in large differences, between 0.3 and 1.1, for pure 2nd-order deformation modes (Table 6.17), even though the corresponding differences are lower than 0.1 when more complex loadings are enforced (Table 6.18).

As a conclusion, it must be stated that the second gradient homogenisation definition with the symmetric operator, as proposed by Blanco et al. (2016a), seems to be less appropriate than the non-symmetric counterpart, proposed in Section 5.2. A deeper analysis and discussion is required in order to fully understand the differences between the models arising from these formulations. Nevertheless, a possible explanation is related to an overconstraint that may arise due to the symmetric insertion operator, since the second gradient coming from the macro-scale is already symmetric by definition. This overconstraint may cause the unphysical warping observed near RVE corners, when Blanco's formulation is employed. The Kouznetsova's periodic constraint does not model pure 2nd-order deformation modes appropriately due to the lack of a volumetric constraint, needed to correctly enforce the macroscopic second gradient at the RVE. The results obtained in this section are coherent with the findings from Section 6.6, confirming that the 2nd-order homogenisation formulation introduced in Section 5.2 yields results that are more admissible.

6.8 Multi-scale analysis of the boundary shear layer problem

Results obtained from FE^2 simulations based on 2nd-order homogenisation, with a 2nd-gradient formulation at the macro-scale and a 1st-order continuum at the micro-scale, are presented in this section. The macro-scale finite element solution is carried out with mixed elements, as presented in Section 4.4. Regarding the micro-scale, the minimal constraints based on the *method of multi-scale virtual power* are employed.

The boundary shear layer example presented in Section 4.6.3 (see also Figure 4.14) is recalled here to be analysed within a multi-scale 2nd-order homogenisation framework. The same dimensions are considered for the boundary shear layer model, where only a strip of width 0.1 mm is discretised along the layer height defined by $h = 1.0$ mm. A horizontal displacement $u = 0.2$ mm is applied on the top surface of the model.

6.8.1 Finite element models

The FE^2 simulation of the boundary shear layer problem is performed with 2D and 3D finite element models.

Three different RVE lengths are analysed, maintaining the RVE models and applying a scale factor: i) $l_{RVE} = 0.1$ mm, which coincides with the width of macro finite element model, being significantly smaller than the layer height, ii) $l_{RVE} = 0.5$ mm, corresponding to a half of the strip height and iii) $l_{RVE} = 1.0$ mm, where the RVE length is equal to the layer height.

The simulations are conducted enforcing the two minimal constraints arising from the method of multi-scale virtual power, both the Blanco-based condition and the non-symmetric constraint, at the micro-scale, separately.

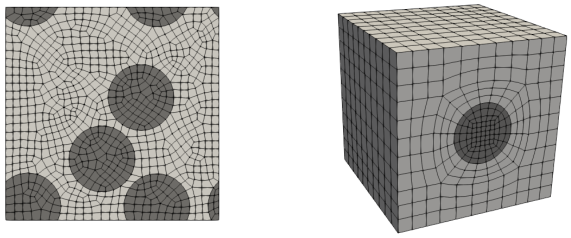

(a) 2D model (b) 3D model

Figure 6.30: RVEs employed to model the microstructure for the boundary shear layer FE^2 simulations.

2D model

Regarding the 2D model, a mesh with 15 Q8F4L1 elements is employed to discretise the macro-scale domain, with appropriate periodicity conditions. At the micro-scale, a RVE with four randomly positioned fibres is used to model the microstructure, as shown in Figure 6.30a. It was generated with the algorithm proposed by Melro et al. (2008). Both the matrix and the fibres are described by elastic laws, with the properties presented in Table 6.19.

3D model

With regard to the 3D model, the hexahedral element H20F8L1 proposed in Section 4.4.2 is used to discretise the macro-scale, where a mesh with 15 elements is employed, with appropriate periodicity conditions. A cubic RVE with a cylindrical rigid fibre, represented in Figure 6.30b, with the material properties also shown in Table 6.19, describes the microstructural behaviour.

Table 6.19: Material properties for the constituents of the RVEs shown in Figure 6.30.

	2D model		**3D model**	
	Matrix	Fibres	Matrix	Fibres
Young modulus (E) [GPa]	30.0	74.0	30.0	300.0
Poisson ratio (ν)	0.3	0.2	0.3	0.3

6.8.2 Results

The distribution of the shear deformation gradient component F_{12} along the layer height is plotted in Figure 6.31 for the 2D model. In addition, the analytical solutions given by Equation (4.77), obtained taking into account the relation between the material characteristic length and the RVE length found by Kouznetsova et al. (2004a) for homogeneous RVEs at small strain:

$$l^2 = \frac{l_{RVE}^2}{12}, \tag{6.7}$$

are included. These results are recovered exactly by the 3D models (not shown in Figure 6.31).

The contour plots of the norm of the higher-order stress tensor at the macro-scale and the equivalent Cauchy stress at the micro-scale, for three RVEs in distinct positions of the layer, are shown in Figure 6.32 for the 2D model, and in Figure 6.33 for the 3D model.

The convergence rates observed in the 2D macro and micro-scale Newton-Raphson iterative schemes is shown in Table 6.20, and similar convergence rates are found for the 3D models.

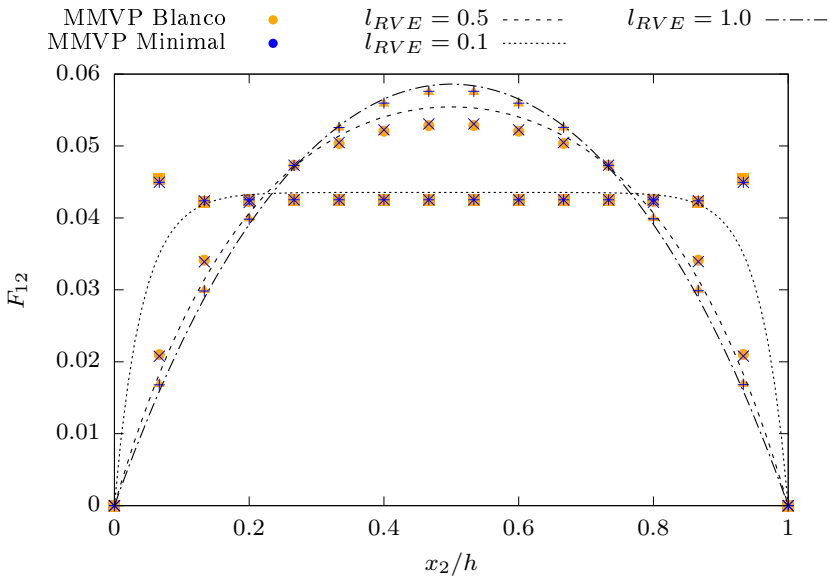

Figure 6.31: Numerical and analytical results for the deformation gradient component F_{12}, in the 2D FE^2 boundary shear layer problem.

Table 6.20: Convergence rates observed at the macro and micro-scale (RVE near the bottom of the layer), in the last incremental step, for the Blanco-based and the non-symmetric minimal constraints.

	Iteration	**Relative residual (%)**	
		Macro	Micro
Blanco Minimal	1	0.549×10^{-2}	759.795
	2	0.704×10^{-6}	1.185
	3	0.171×10^{-11}	0.772×10^{-2}
	4		0.206×10^{-6}
MMVP Minimal	1	0.166×10^{-1}	807.544
	2	0.178×10^{-5}	0.715
	3	0.296×10^{-11}	0.258×10^{-2}
	4		0.387×10^{-7}

6.8.3 Discussion of the results

In the first place, it must be remarked that a quadratic convergence rate is achieved in the Newton-Raphson solution at both scales (Table 6.20), revealing that the tangents deduced in Sections 5.1.7 and 5.2.6 are consistent, and its implementation is correct.

Looking at Figure 6.31, it becomes clear that the RVE length is intrinsically connected to the characteristic length that drives the 2nd-order response at the macro-scale. Moreover, the results from the minimal constraints derived through the method of multi-scale virtual power are very close to the corresponding analytical solutions, indicating that the relation between the RVE length and the characteristic length is well defined by Equation (6.7), even though this relation has been obtained by Kouznetsova et al. (2004a) for small strains. The influence of the micro-scale constraint is negligible. Therefore, this relation is not driven by the multi-scale formulation or the micro-constraints, but is probably related to the insertion operator, which is the common factor between the different formulations analysed. It must be highlighted that the expected distribution of the deformation gradient depends on the characteristic length only (Equation (4.77)), and is independent

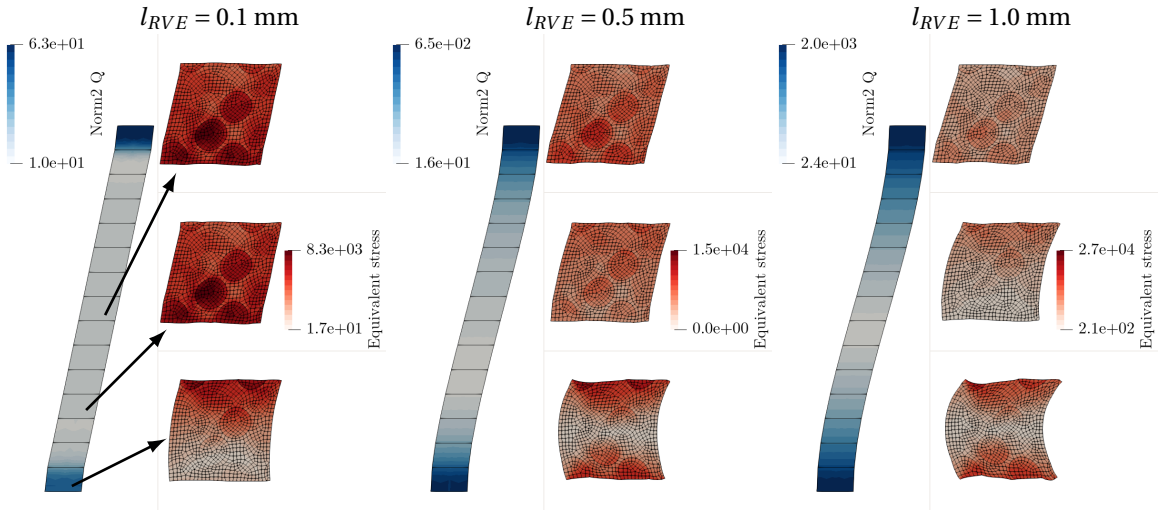

(a) MMVP Blanco

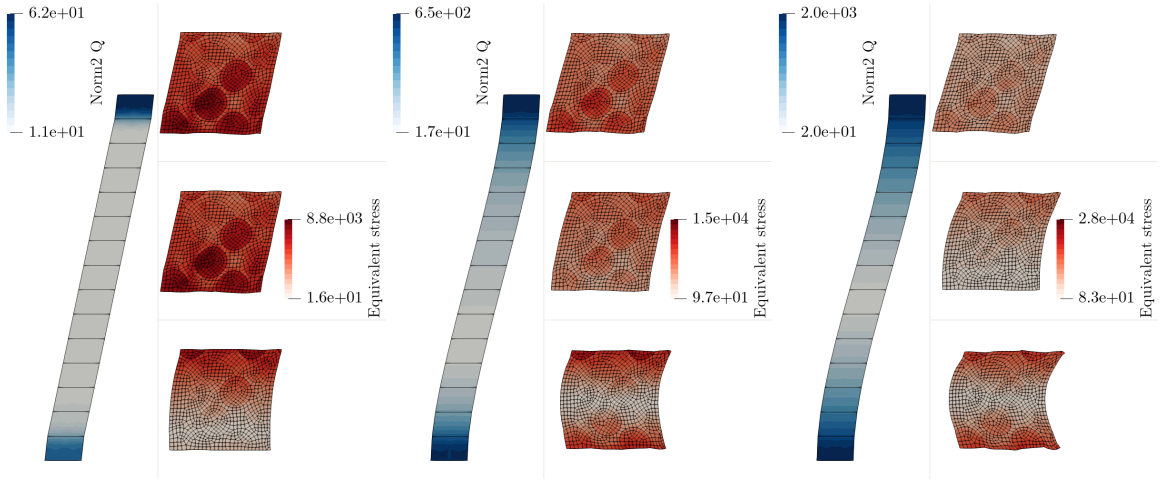

(b) MMVP minimal

Figure 6.32: Contour plot of the equivalent stress on the deformed meshes at the micro-scale, and the norm of the higher-order stress at the macro-scale, for the 2D boundary shear layer FE^2 simulation, with different RVE lengths and micro-constraints.

from the remaining material properties.

In fact, it is observed in Figures 6.32 and 6.33 that the 2^{nd}-order effects increase with the RVE length l_{RVE}, and the deformation of the shear layer approaches the 1^{st}-order case, with constant deformation, as the RVE length decreases. These effects are also noticed at the micro-scale, where the micro-displacements due to the second gradient become increasingly more evident as the RVE length increases. This has an impact on the micro-deformation field, leading to higher values of the stresses at the RVE and, consequently, to greater values of the homogenised higher-order stresses. The second-order effects are especially pronounced in the the regions near the layer boundaries, where the macro-second gradient is dominant, and tend to propagate to inner RVEs as their length increases, revealing the non-local character of this formulation.

A non-physical warping of the RVE near the corners (edges in the 3D model) is observed with the minimal Blanco-based constraint in the regions where second-order deformations are dominant, especially for larger RVE lengths.

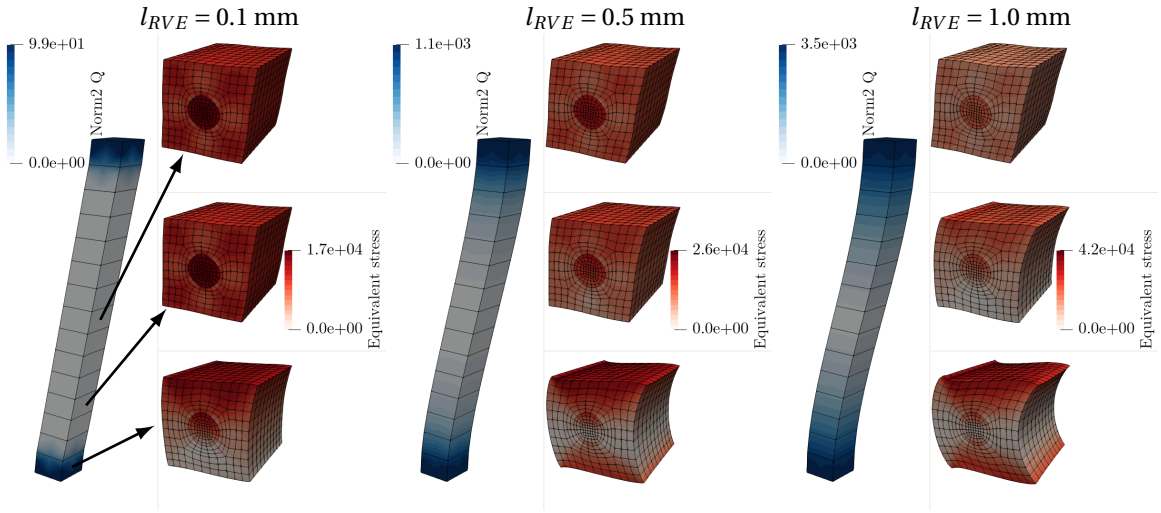

(a) MMVP Blanco

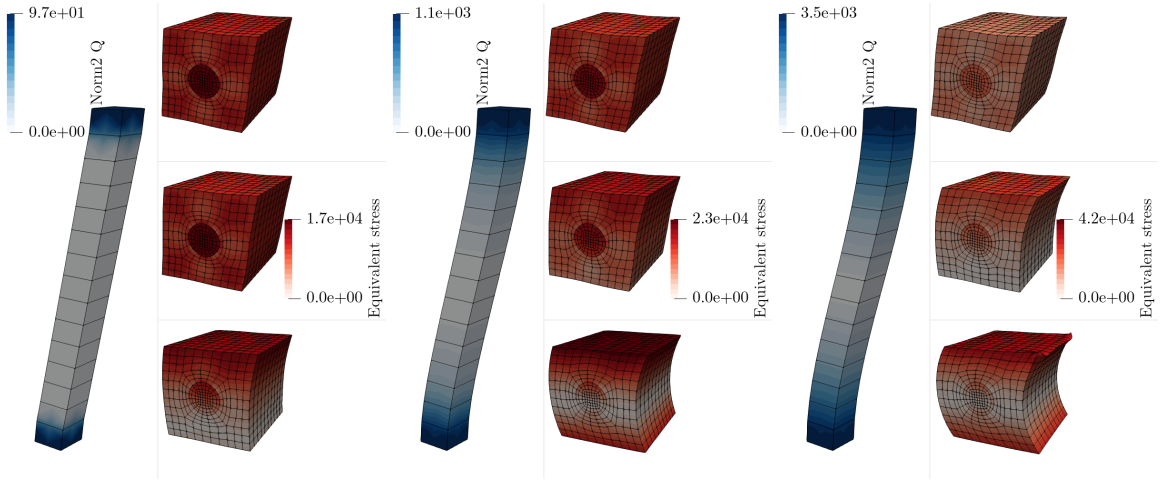

(b) MMVP minimal

Figure 6.33: Contour plot of the equivalent stress on the deformed meshes at the micro-scale, and the norm of the higher-order stress at the macro-scale, for the 3D boundary shear layer FE^2 simulation, with different RVE lengths and micro-constraints.

6.9 Multi-scale analysis of polycrystalline materials

In this section, the multi-scale behaviour of a polycrystalline material is analysed, comparing the response obtained with a 1st-order homogenisation scheme and the responses resulting from 2nd-order approaches obtained with different RVE lengths. The RVE model has been generated with the polycrystal generation and meshing library Neper (Quey et al., 2011), and contains 250 grains discretised with 4913 20-noded hexahedral elements with reduced integration, resulting in a mesh with 22356 nodes, represented in Figure 6.34.

Each crystal is modelled by a single crystal plasticity constitutive model formulated in large strains, where the elastic domain is modelled by an anisotropic hyperelastic law and slip plasticity is considered, with viscoplastic regularisation and sub-stepping techniques used to overcome numerical difficulties (de Carvalho et al.). The material properties are the same for all crystals, being the only difference found in the slip directions. The model parameters are presented in Table 6.21, corresponding to an initial yield stress σ_{y0} = 100 MPa.

In the first place, FE^2 multi-scale simulations involving different macro-scale specimens are performed, employing the Taylor's condition (see Section 3.2.4), in order to obtain the deforma-

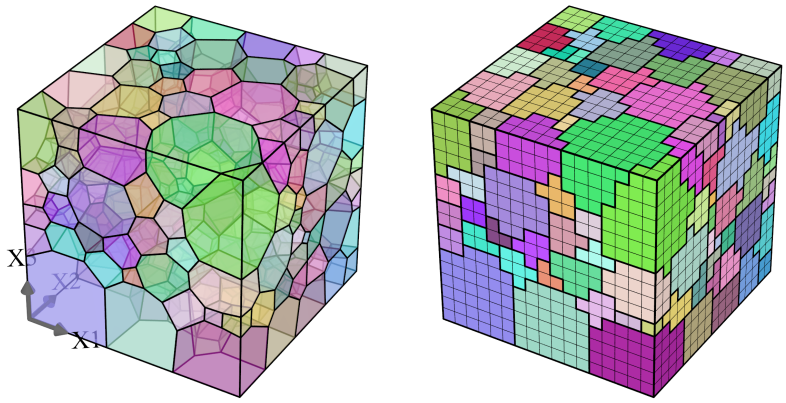

Figure 6.34: RVE employed to model a polycrystalline microstructure, and the corresponding discretisation.

Table 6.21: Material properties for the polycrystalline material.

Elastic properties [GPa]	C_{11}	282.69
	C_{12}	121.15
	C_{44}	80.769
Visco-plastic parameters	ϵ^{pa}	0.01
	ϵ_0^{pa}	10
Algorithmic parameters	n_{visco}	8
	m_{depth}	4
Nadai-Ludwik power law	$\sigma_y(\gamma) = \tilde{\sigma}_y + K(\gamma_0+\gamma)^m$	
	$\tilde{\sigma}_y$ [GPa]	0.088
	K [GPa]	0.195
	γ_0	0.01
	m	0.6

tion gradient and second gradient history at points of interest. Since a 1st-order homogenisation scheme is employed at this stage, the macro-scale second gradient is computed through the technique presented in Appendix D. In order to speedup these computations and reduce memory requirements, since the deformation state is constant in the RVE, the state update procedure only needs to be performed once for each crystal. Thereafter, the collected deformation state histories are enforced to the same RVE, considering either the standard 1st-order homogenisation periodic condition, presented in Section 3.3.3, or the multi-scale virtual power-based periodic constraint for 2nd-order homogenisation, from Section 5.2.7, with three different RVE lengths: i) $l_{RVE} = 0.01$ mm, ii) $l_{RVE} = 0.5$ mm and $l_{RVE} = 1.0$ mm.

6.9.1 Bending beam

The problem of the bending beam presented in Section 3.5.2 is recalled here. The same model dimensions and boundary conditions are assumed. The finite element mesh represented in Figure 6.35, with 250 8-noded elements with reduced integration and 861 nodes, is employed.

Both the deformation gradient and the second gradient history are retrieved from point D represented in Figure 6.35, and enforced in the RVE introduced in Figure 6.34, considering either the standard 1st-order periodic condition and the MMVP periodic constraint for three different RVE lengths: i) $l_{RVE} = 0.01$ mm, ii) $l_{RVE} = 0.5$ mm and $l_{RVE} = 1.0$ mm.

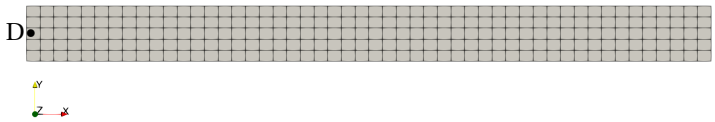

Figure 6.35: Mesh used for the bending beam simulation, with a polycrystalline model.

Results

The macro-scale distribution of the equivalent strain and the norm of the second gradient, at the end of the simulation, are represented in Figure 6.36.

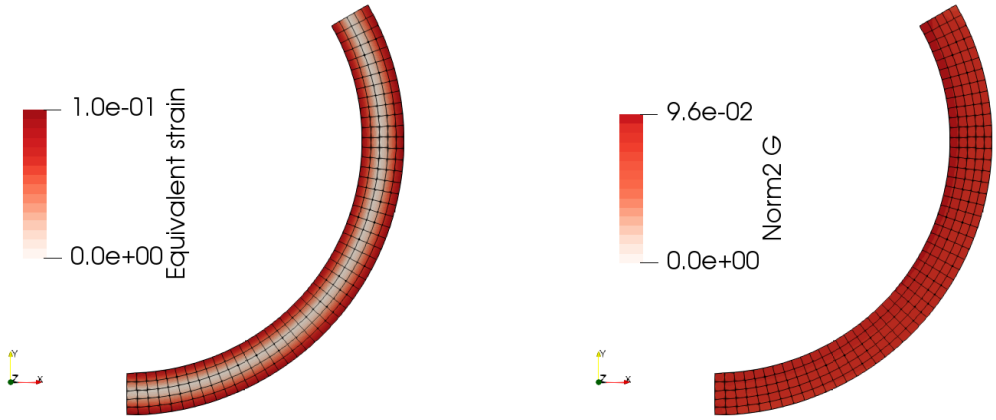

Figure 6.36: Contour plots of the equivalent strain and second gradient norm [mm^{-1}] obtained at the macro-scale, in the bending beam simulation with a polycrystalline material.

The contour plots of the equivalent stress on the RVE deformed meshes are shown in Figure 6.37, for different values of the RVE length. The corresponding evolutions of the homogenised equivalent stress and the norm of the homogenised higher-order stress tensor are presented in Figure 6.38.

6.9.2 Butterfly specimen subjected to shear

A butterfly specimen is subjected to simple shear, by enforcing a horizontal displacement on the top face, while keeping the bottom face fixed. The finite element mesh represented in Figure 6.39, where 5920 20-noded hexahedral elements with reduced integration are employed, resulting in 30061 nodes. The locations at which RVEs are analysed are also identified in this Figure.

A displacement $u_1 = 1.0$ mm is applied to the butterfly top face. The deformation gradient and second gradient histories at both points E and F are stored and thereafter applied to the RVE introduced in Figure 6.34, considering either the standard 1st-order periodic condition and the MMVP periodic constraint for three different RVE lengths: i) $l_{RVE} = 1.0$ mm, ii) $l_{RVE} = 0.5$ mm and $l_{RVE} = 0.1$ mm.

Results

Due to convergence issues in some of the micro-scale simulations, the results are presented for a macro-displacement $u_1 = 0.32$ mm, so that all cases can be compared at the same deformation state. The distribution of the equivalent strain and the norm of the second gradient at the macro-scale is shown in Figure 6.40.

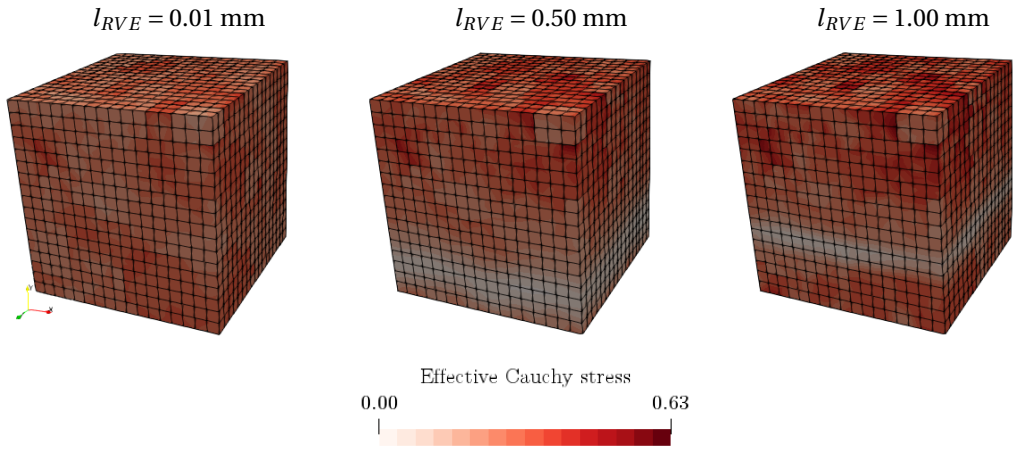

(a) $\alpha = 40^o$

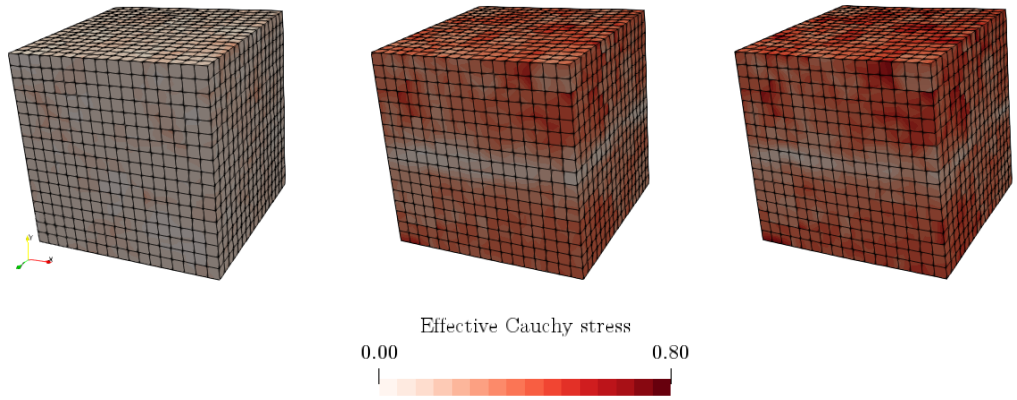

(b) $\alpha = 120^o$

Figure 6.37: Distribution of the equivalent stress [GPa] at the micro-scale deformed meshes, for RVEs with different lengths subjected to the deformation history from point D, when the macro-scale rotation angle is (a) 40^o and (b) 120^o.

The micro-scale distribution of the equivalent stress is presented in Figures 6.41 and 6.42, for the deformation history of points E and F, respectively. The evolution of the homogenised stresses is provided in Figures 6.43 and 6.44, for the same points

6.9.3 Butterfly specimen subjected to traction

A vertical displacement u_2 mm is applied to the top face of the same butterfly specimen model.

Results

All the results presented in what follows are relative to a macro-displacement $u_2 = 0.077$ mm. The distribution of the equivalent strain and the norm of the second gradient in the butterfly specimen is shown in Figure 6.45.

The contour plots of the equivalent stress are presented on the deformed meshes in Figures 6.46 and 6.47, for the deformation history of points E and F, respectively. The evolution of the corresponding homogenised stresses is shown in Figures 6.48 and 6.49.

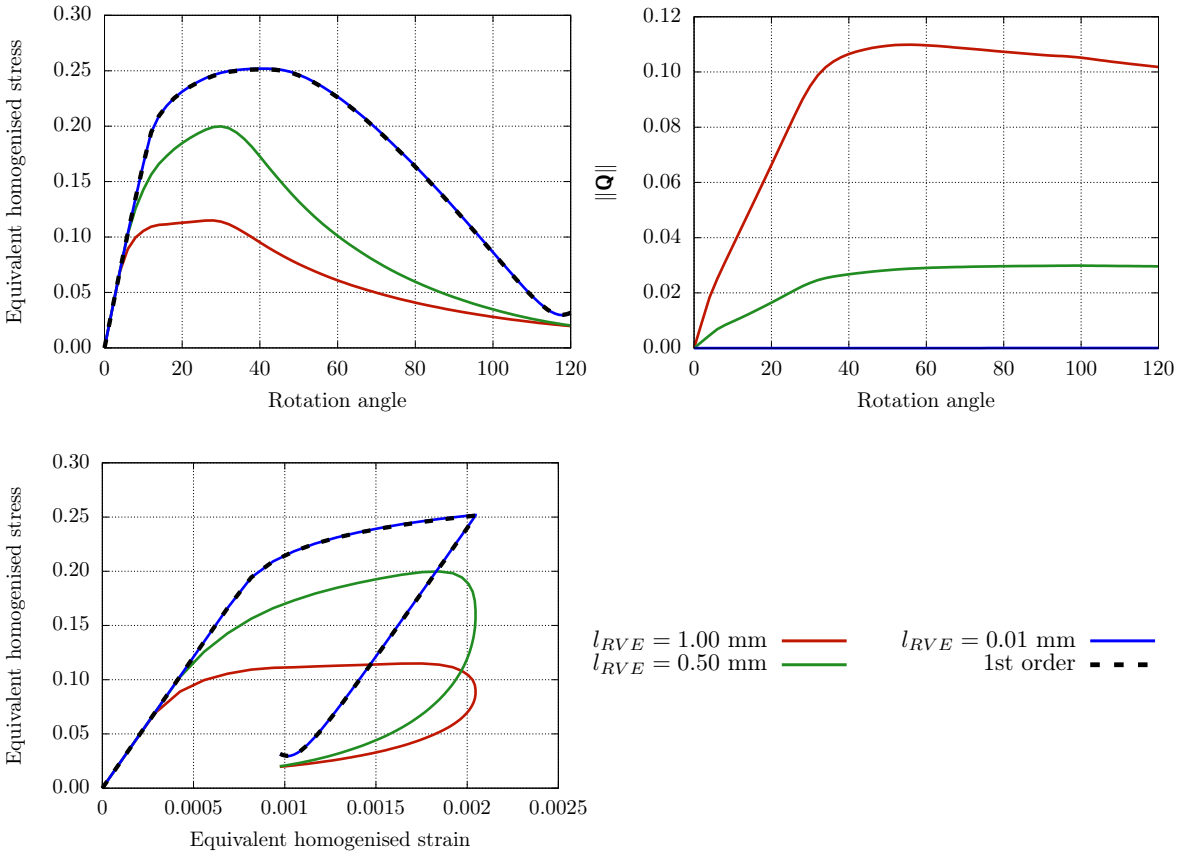

Figure 6.38: Evolution of the equivalent homogenised stress [GPa] and norm of the homogenised higher-order stress [GPa mm], obtained for the RVEs under the deformation history from point D.

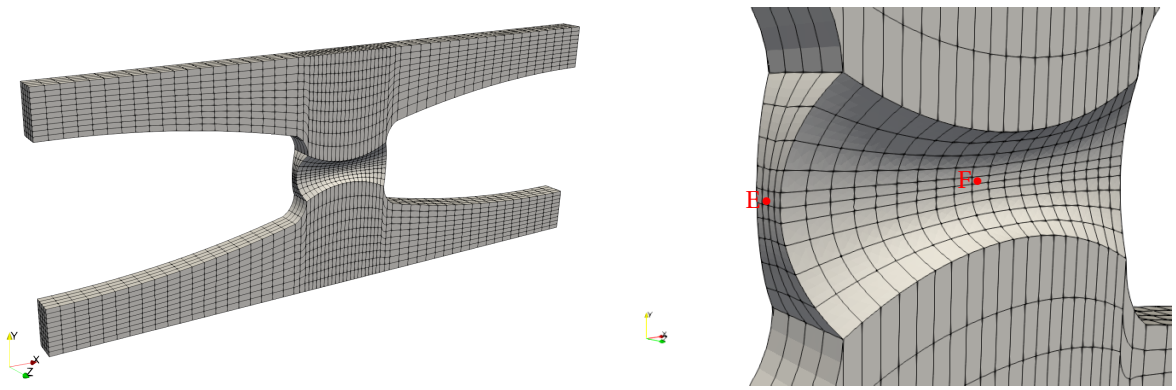

Figure 6.39: Finite element discretisation used for the butterfly specimen, with detail on the necking zone, where points for micro-analyses are identified (E and F).

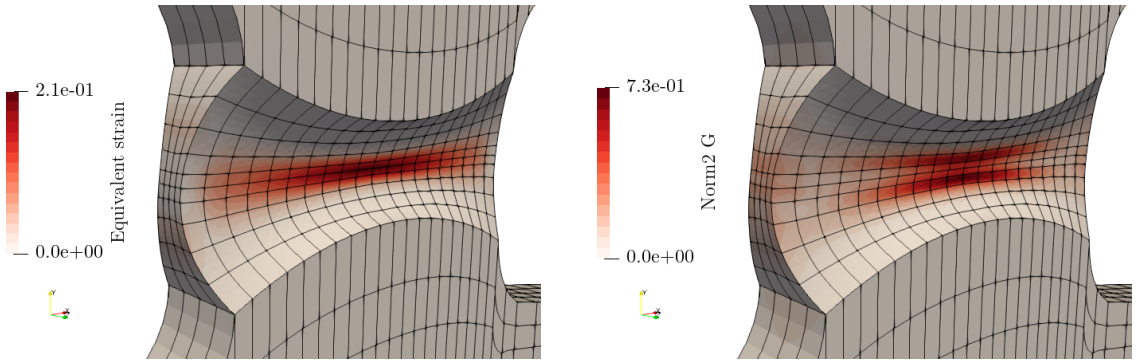

Figure 6.40: Contour plots of the equivalent strain and second gradient norm [mm^{-1}] obtained at the macro-scale, in the butterfly shear simulation with a polycrystalline material.

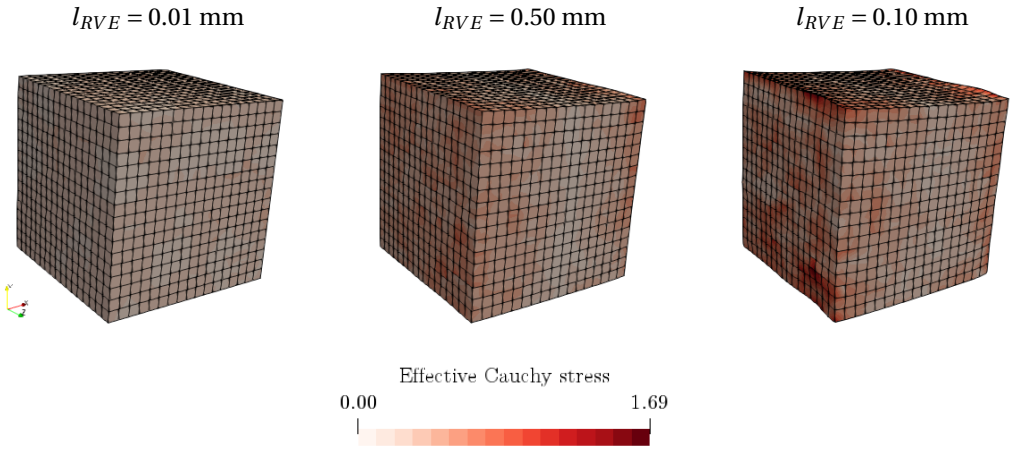

Figure 6.41: Distribution of the equivalent stress [GPa] at the micro-scale deformed meshes, for RVEs with different lengths subjected to the deformation history from point E, when the macro-scale prescribed displacement is 0.32 mm for the butterfly shear simulation.

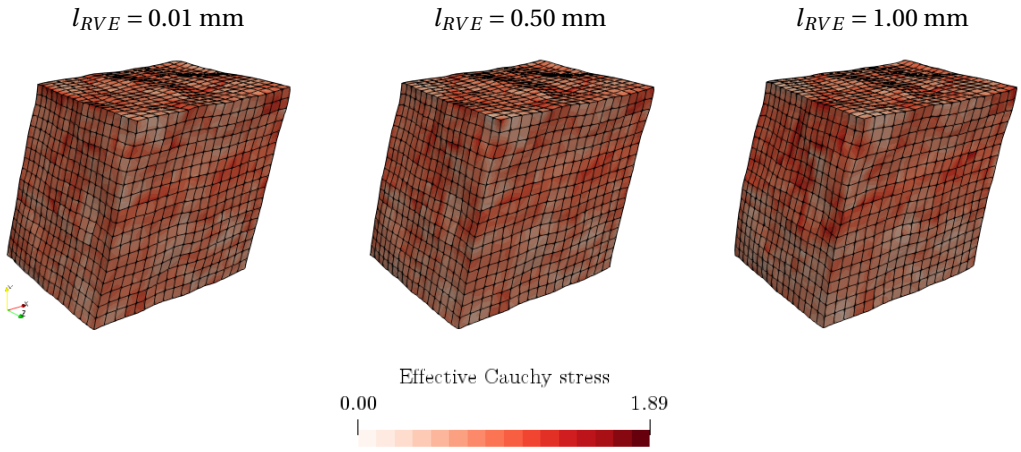

Figure 6.42: Distribution of the equivalent stress [GPa] at the micro-scale deformed meshes, for RVEs with different lengths subjected to the deformation history from point F, when the macro-scale prescribed displacement is 0.32 mm for the butterfly shear simulation.

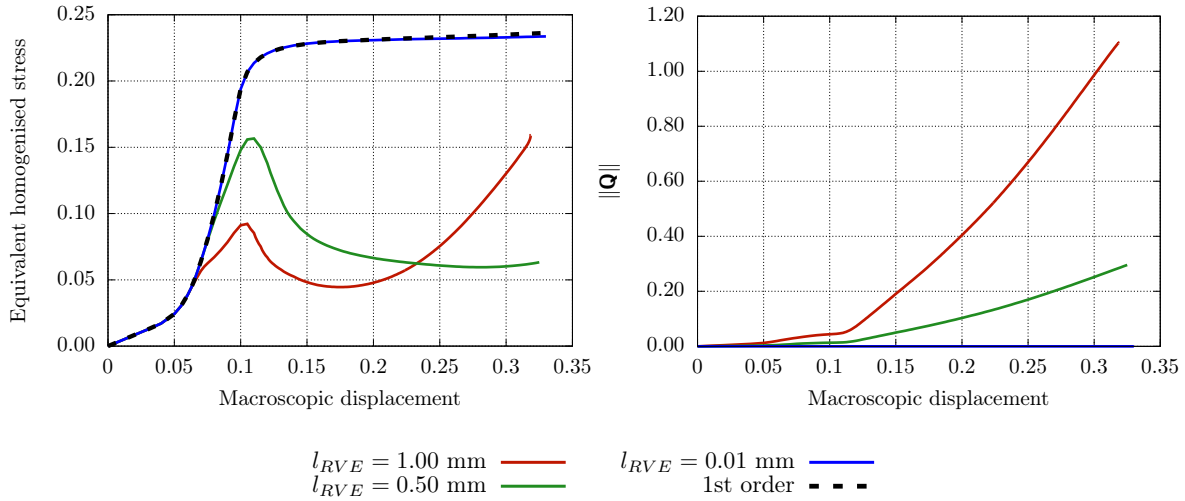

Figure 6.43: Evolution of the equivalent homogenised stress [GPa] and norm of the homogenised higher-order stress [GPa mm], obtained for RVEs under the deformation history at point E, in the butterfly shear simulation.

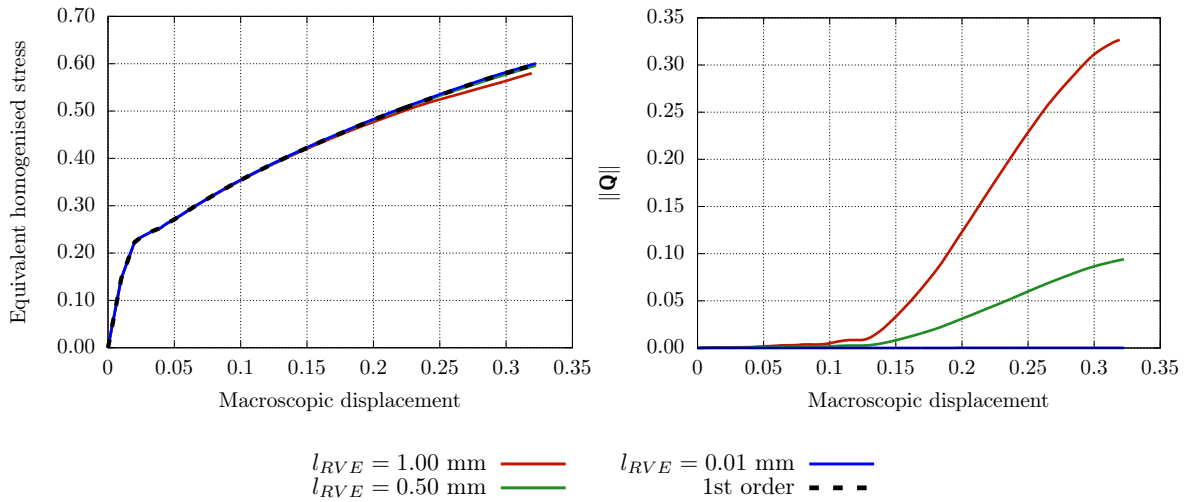

Figure 6.44: Evolution of the equivalent homogenised stress [GPa] and norm of the homogenised higher-order stress [GPa mm], obtained for RVEs under the deformation history at point F, in the butterfly shear simulation.

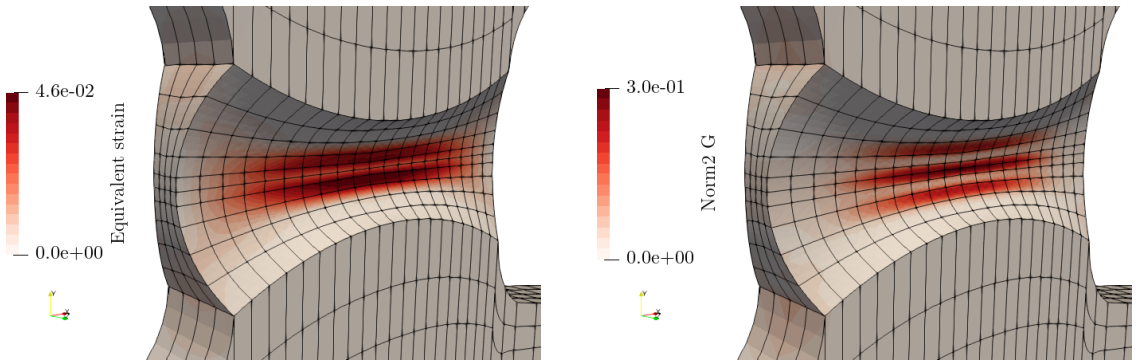

Figure 6.45: Contour plots of the equivalent strain and second gradient norm [mm^{-1}] obtained at the macro-scale, in the butterfly traction simulation with a polycrystalline material.

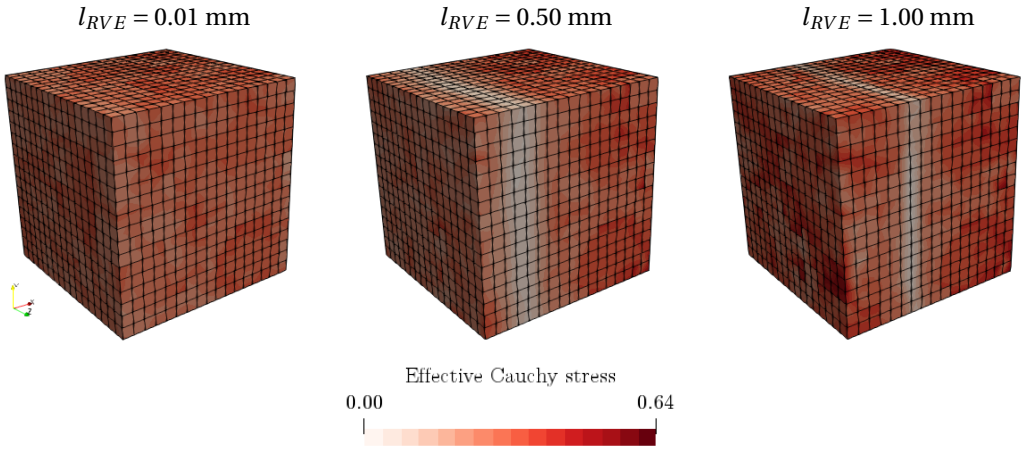

Figure 6.46: Distribution of the equivalent stress [GPa] at the micro-scale deformed meshes, for RVEs with different lengths subjected to the deformation history from point E, when the macro-scale prescribed displacement is 0.077 mm for the butterfly traction simulation.

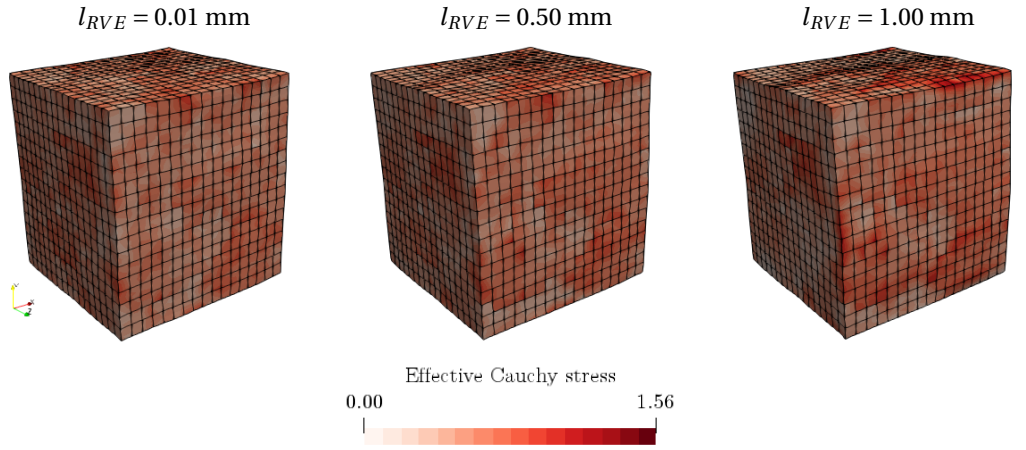

Figure 6.47: Distribution of the equivalent stress [GPa] at the micro-scale deformed meshes, for RVEs with different lengths subjected to the deformation history from point F, when the macro-scale prescribed displacement is 0.077 mm for the butterfly traction simulation.

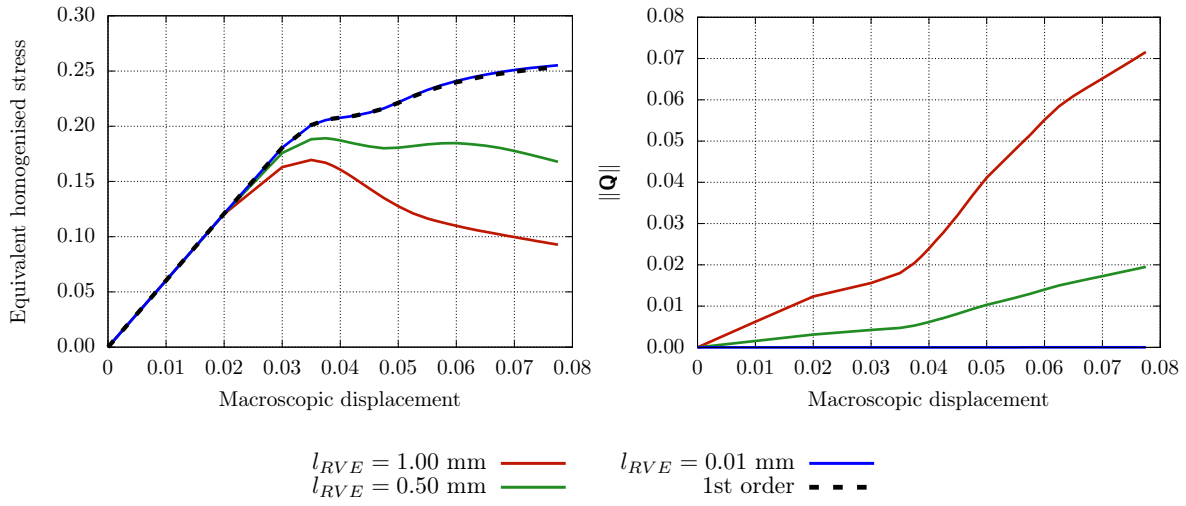

Figure 6.48: Evolution of the equivalent homogenised stress [GPa] and norm of the homogenised higher-order stress [GPa mm], obtained for RVEs under the deformation history at point E, in the butterfly traction simulation.

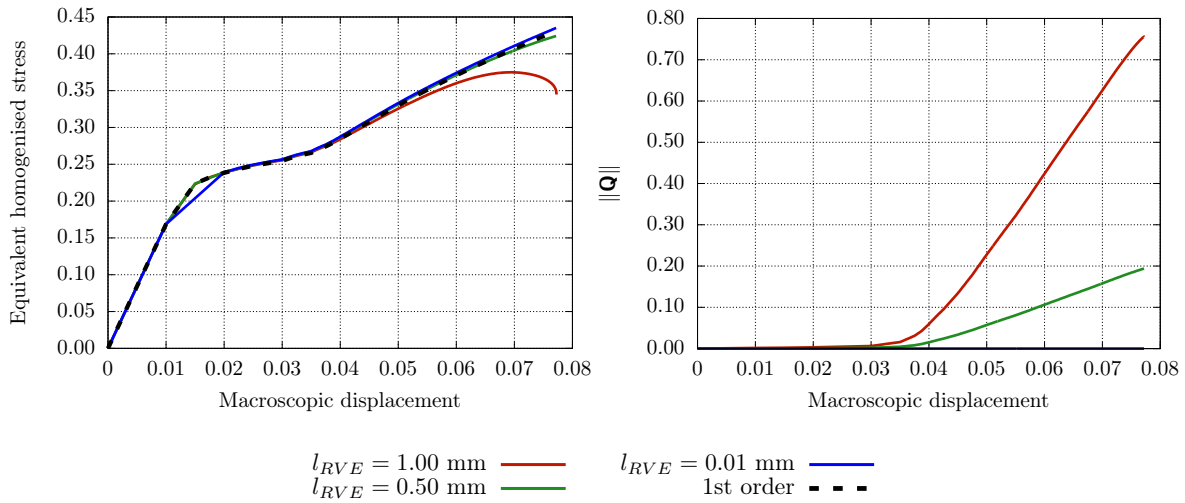

Figure 6.49: Evolution of the equivalent homogenised stress [GPa] and norm of the homogenised higher-order stress [GPa mm], obtained for RVEs under the deformation history at point F, in the butterfly traction simulation.

6.9.4 Discussion of the results

In the bending beam problem, Figures 6.35 and 6.36, point D is located near the initial neutral axis, where the strain values are quite low. On the other hand, the second gradient magnitude is nearly constant on the beam as it deforms. Therefore, the response of RVEs under the deformation history from point D are dominated by the macroscopic second gradient $\mathbf{G}$. As a matter of fact, the homogenised response is strongly dependent on the RVE length, as can be observed in the plots in Figure 6.38. While the RVE with $l_{RVE} = 0.01$ mm captures the response of the 1st-order homogenisation, with negligible values of the higher-order stress tensor, its norm increases with the RVE length and, on the opposite direction, the equivalent homogenised stress decreases when l_{RVE} increases. The evolution of the equivalent homogenised stress is better understood when looking at its dependence with the equivalent homogenised strain, also plotted in Figure 6.38. In the first stage, the typical evolution is observed, with a linear part and the yielding zone, but an unloading-like behaviour is obtained when the equivalent homogenised strain reaches the value 0.002. This transition is sharp for the 1st-order homogenisation response, and the smallest RVE length, being more gradual for both $l_{RVE} = 0.5$ and 1.0 mm. This effect is explained by the position of the neutral axis, which moves upwards, and is captured here due to the finite strain formulation. It is clearly observed when comparing the micro-scale state for a macro-scale rotation of 40^o and 120^o, in Figure 6.37. The smallest RVE length is influenced by the macro-scale deformation gradient only, thus the movement of the neutral axis is captured when the onset of strain unloading reaches point D, resulting in the sharpest transition. For the larger RVE lengths, where the bending deformation mode is captured, the position of the neutral axis is well captured in the RVE, and influences the homogenised response resulting in a moderate transition to the unloading state.

Regarding the butterfly shear example, a very low strain is obtained at point E, on the boundary of the necking, along with a moderate norm of the second gradient (Figure 6.40). When looking at point F, at the specimen center, very strain high strain values (0.21) are observed, with a relatively high norm of the second gradient. In fact, the RVEs linear deformation, i.e., due to the macroscopic deformation gradient, is much more evident for point F than for point E (cf. Figures 6.41 and 6.42). Consequently, the differences between RVEs with different lengths, that result from the macroscopic second gradient, are more visible for the deformation history from point E. Despite the fact that the norm of the second gradient is larger at the location F, the deformation at this point is dominated by the deformation gradient, hence the relative impact of $\mathbf{G}$ is reduced. Nonetheless, a slight curvature is observed for $l_{RVE} = 1.0$ mm, when comparing with the deformed mesh for the smallest RVE length. On the contrary, the effect of the second gradient becomes prominent for the RVEs under the deformation history from point E, since the linear deformation is quite reduced. These observations are also retrieved from the evolution of the homogenised stresses, shown in Figures 6.43 and 6.44. In spite of achieving lower values for the equivalent homogenised stress, the corresponding curves for point E are strongly influenced by the RVE length, in contrast to what is obtained from the RVEs at point F. When comparing the respective evolutions for the norm of the higher-order stress tensor, the values reached for point E (1.1 GPa mm) are greater than the values obtained from point F (0.33 GPa mm), although the larger second gradient is found at the latter. It is noteworthy the fact that the increase of the higher-order stresses is triggered when the macroscopic displacement reaches 0.12 mm, which is probably related to the onset of some strain localisation in the butterfly specimen necking region.

With regard to the butterfly traction simulation, in Figure 6.45, a low level of strain and second gradient is obtained at location E, in contrast with high strain at point F, where the second gradient norm has also high values. An interesting observation is found in the RVEs subjected to the loading history from location E, Figure 6.46, where a neutral zone is obtained for the RVE lengths $l_{RVE} = 0.5$ and 1.0 mm. The initial curvature of the necking boundary in this region causes a bending-like deformation when the specimen is stretched vertically, whose effect at the micro-scale is captured by the largest RVEs, but not by the 1st-order homogenisation formulation (coincident with the results

for the smallest RVE length. Despite the lower macro-scale second gradient norm at this point, its influence on the micro-scale equivalent stress field is more evident than for the RVEs at point F, in Figure 6.47, similarly to what is observed for shear loading. Analysing the curves representing the evolution of the homogenised stresses, in Figures 6.48 and 6.49, a strong influence of the RVE length on the equivalent homogenised stress is observed for the deformation history at point E, being almost negligible for location F, where the curve corresponding to the largest RVE diverges from the remaining only at the final part of the simulation. This divergence is related to a significant increase of the second-order effects, that gain importance relatively to the linear deformation, also explaining the sudden increase of the homogenised higher-order stress norm.

In summary, the results analysed here reinforce the idea that 2^{nd}-order homogenisation-based multi-scale models are able to account for different deformation modes at the micro-scale, which may be important for a detailed characterisation of the microstructural behaviour, and the resulting macro-scale response, when complex phenomena are considered (e.g. phase transformation). For the case of the smallest RVE, $l_{RVE} = 0.01$ mm, the 2^{nd}-order homogenisation results recover the 1^{st}-order counterparts, but in general the results depend on the RVE length, with second-order effects becoming more evident as the RVE length increases. Nonetheless, the influence of the second gradient does not depend on its magnitude and the RVE length only, but the strain magnitude (dependent on the deformation gradient) must also be taken into account, since the importance of the second-order deformation modes may be neglected when the micro-scale deformation is dominated by the macroscopic deformation gradient. This is in agreement with the conclusions presented in Section 6.5.3.

6.10 An adaptive framework for second-order homogenisation

A first-order homogenisation scheme is adequate for the multi-scale characterisation of the mechanical behaviour of deforming solids under the conditions that the underlying RVE length is coherent with the *Scale Separation Principle*, being much smaller than the macro-scale deformation wavelength so that the deformation gradient may be considered constant over the RVE. The qualitative requirements for the introduction of a second-order homogenisation scheme are thoroughly discussed by Kouznetsova (2002). Nonetheless, a quantitative assessment of the conditions where a second-order homogenisation scheme should be adopted to replace the standard first-order approach is lacking, to the author's knowledge.

An interesting strategy is proposed by Temizer and Wriggers (2011) for the determination of critical zones where DNS (Direct Numerical Simulation) should be employed instead of the standard homogenisation approach. The macro-scale second gradient and RVE length are employed as a measure of the relative macroscopic wavelength with regard to the microstructural model. Inspired in this strategy, a framework for an adaptive employment of second-order homogenisation models is introduced in what follows, where the definition of appropriate generalised RVE size and RVE length is addressed along with proposals for the quantitative assessment of the cases where first-order homogenisation is not applicable.

1. In the first place, so that the response obtained is representative, the generalised RVE size s_{RVE} must be determined in such a way that the microstructure model contains a sufficient number of constituents.

2. The RVE model should be scaled to an appropriate RVE length l_{RVE}. This value is intrinsically related to the material characteristic length that drives the non-local effects at the macro-scale. Is is also important to characterise the second-order insertion at the micro-scale in a correct manner. It should be calibrated with experimental results, obtained from specimens carefully designed to capture these size-effects. For instance, Liebold and Müller (2016) use data from ex-

periments on microbeams to calibrate the material length scale for strain gradient macroscopic models.

3. As the RVE model becomes established, the criterion that defines under which conditions a second-order approach must replace the first-order scheme has to be defined. Temizer and Wriggers (2011) employed the non-dimensional quantity $\|\mathbf{G}\| \cdot l_{RVE}$ to define the limit where DNS simulations are required. Taking into account the results obtained throughout this chapter, particularly in Sections 6.5 and 6.9, the amount of strain (based on displacements first gradient) also plays an important role on the resulting second-order effects, that lose importance as the strain level increases. Therefore, a criterion of the type

$$\frac{\|\mathbf{G}\| \cdot l_{RVE}}{\|\boldsymbol{F}-\boldsymbol{I}\|} > tol \tag{6.8}$$

is suggested here. Since the inversely proportional relation may not describe the relative weight between $\|\mathbf{G}\| \cdot l_{RVE}$ and $\|\boldsymbol{F}-\boldsymbol{I}\|$, a more general criterion may be employed, where f_G and f_F denote generic scalar functions:

$$\frac{f_G(\|\mathbf{G}\| \cdot l_{RVE})}{f_F(\|\boldsymbol{F}-\boldsymbol{I}\|)} > tol. \tag{6.9}$$

The value of the tolerance tol, defining when a second-order homogenisation scheme is required, has to be determined. This procedure may be performed with a parametric study where the RVE is subjected to several combinations of $\boldsymbol{F}$ and $\mathbf{G}$. It must be emphasised that the overall behaviour depends not only on the RVE morphology, but also on the description of the constituents. Thus, if a value of tol is determined for the case where a particular constituent is deemed to be elastic, for example, may not be valid any more if it is modelled by an elasto-plastic law. This becomes clear when comparing the results in Sections 6.5.1 and 6.5.2.

4. The problem of interest is analysed under a first-order homogenisation-based FE^2 scheme, where the macro-scale second gradient of the displacements is computed using the strategy described in Appendix D and its norm ($\|\mathbf{G}\|$) is recorded along with the norm of the displacements first gradient ($\|\boldsymbol{F}-\boldsymbol{I}\|$).

5. The results obtained from the first-order FE^2 simulation are analysed in order to determine the critical points where the criterion from Equation (6.9) is satisfied. The results obtained in the analysis 4. will reveal if the simulation conducted is valid at these critical points. Therefore, three alternatives are proposed for the introduction of the second-order homogenisation framework model, depending on the main features of interest to be analysed.

   a) If the micro-scale behaviour and interactions between constituents are the main subject to be assessed, and the coupling with the resulting macro-scale behaviour can be disregarded, then the RVEs located at critical points are re-analysed through micro-scale simulations, where the macroscopic deformation gradient and second gradient history obtained from the first-order simulation are prescribed.

   b) Alternatively, if the macro-scale problem is clearly dominated by second-order effects, or the influence of the micro-scale on the macro-scale results must be rigorously considered, the FE^2 simulation should be repeated considering a second-order homogenisation multi-scale model.

   c) A more complex strategy consists in performing a FE^2 simulation considering a second-order formulation in the elements in which the criterion defined in 3. is verified, while a first-order scheme is maintained in the remaining. This procedure may be adopted as a generalisation of the strategy 5.b), in a post-processing task where the simulation is repeated with this new condition. However, a more interesting idea is to introduce an adaptive switching of the formulation in critical elements during the initial first-order FE^2 simulation. In other words, the

FE^2 simulation 4. starts with a first-order scheme for all elements, the criterion introduced in Equation 6.9 is tested on the fly and when it is verified at any point, the corresponding element switches to a second-order multi-scale formulation.

The framework proposed here is illustrated in Figure 6.50.

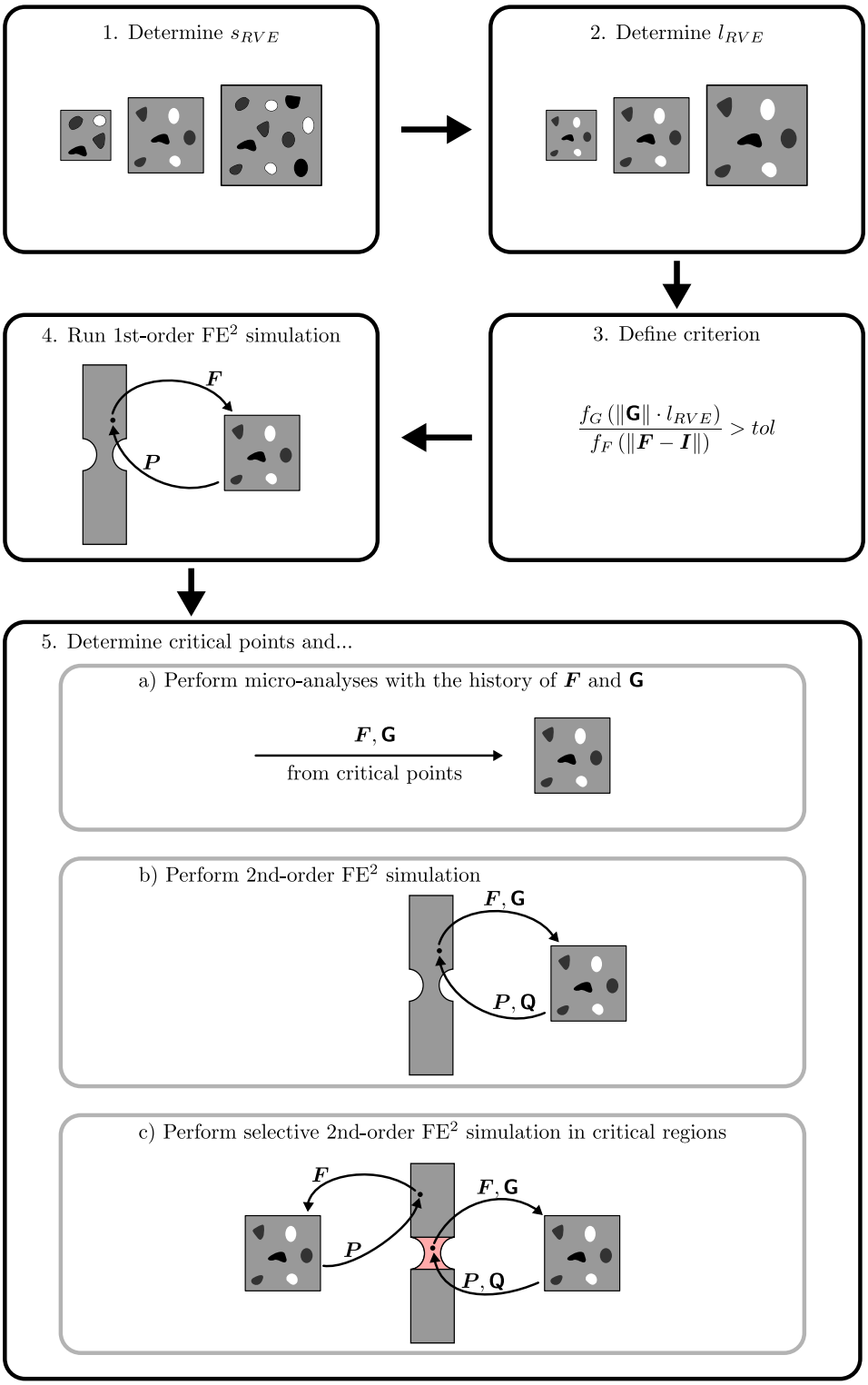

Figure 6.50: Schematic representation of the framework proposed for a critical usage of second-order homogenisation.

6.11 Conclusions

Several numerical examples are analysed in this chapter, aiming to show the characteristics of second-order homogenisation-based multi-scale models, and demonstrate the effectiveness of the finite element implementations described in the previous chapter. A comparison of the results obtained with different micro-scale constraints is performed, at both macro and micro levels. Moreover, a deeper knowledge on some particularities that have not been explored before is pursued, aiming to provide some guidelines for the useful employment of this class of multi-scale models. The main conclusions are summarised here.

It has been observed in Section 6.2 that second-order homogenisation models are sensitive to geometric non-linearities, introduced by the position of constituents in the RVE, resulting in a coupling between between the macroscopic deformation gradient and the homogenised higher-order stress, that is not considered in simple second-gradient constitutive models, where $\boldsymbol{F}$ drives $\boldsymbol{P}$ and $\mathbf{G}$ affects $\mathbf{Q}$ independently. A coupling between the first Piola-Kirchhoff stress tensor and the macroscopic second gradient is also obtained (see Section 6.3), since the insertion of a quadratic displacement field naturally induces stresses at the micro-scale.

The modelling of RVEs with voids has been addressed, and it was possible to conclude that voids must be discretised in order to obtain correct results, when volumetric constraints are enforced at the micro-scale. This limits the analysis of this kind of microstructures since a very compliant mesh subjected to a reactive body force suffers extreme deformation of the elements. Alternative discretisation techniques must be devised to overcome this issue.

The RVE length has a strong impact on the results obtained through second-order homogenisation. The source of this influence is twofold: (i) since the homogenised higher-order stress is a measure of the moment of the micro-scale stresses, the lever arm increases with the RVE length, and so the resulting values of $\mathbf{Q}$; (ii) in addition, the magnitude of the quadratic displacements field due to the insertion of $\mathbf{G}$ depends on the RVE length. In fact, as the homogenised response resulting from these models can be seen as a generalised macroscopic second gradient constitutive law, the RVE length is intrinsically related to the material characteristic length, regardless the selected micro-constraints. This becomes evident when comparing the results with the analytical model from Kouznetsova et al. (2004a), in Section 6.6, and in the boundary shear layer example from Section 6.8. Employing RVEs with different RVE lengths in distinct directions probably results in models where orthotropic material characteristic lengths are obtained at the macro-scale. This subject should be explored in future work.

An appropriate choice of the RVE length, towards a correct characterisation of the resulting material characteristic length, restrains the choice of the microstructural model, in what regards the number of constituents to include, under the assumption that the micro-constituents are modelled with the real physical size. A modelling framework where this assumption is broken, so that the RVE length l_{RVE} and the generalised RVE size s_{RVE} are defined independently, is proposed and assessed in Section 6.5. It is observed that while the RVE length actually influences the material response, the generalised RVE size, related to the micro-constituents number and size in the model, affects only the dispersion of the results when several realisations are analysed. Therefore, effects related to the size of the micro-constituents in the RVE model are not captured by second-order homogenisation models that employ 1^{st}-order at the RVE level. This kind of size effects may be captured if surfaces are accounted for in the homogenisation scheme (Javili et al., 2013), non-local constitutive models are employed at the micro-scale (Nguyen et al., 2019) or second-order continua is employed to model the micro-constituents (a formulation of this type is introduced in Chapter 7). In addition, the results obtained in Section 6.5 highlight the importance of using a RVE model with a sufficient number of constituents, so that a representative response is achieved. In other words, regardless the RVE length, a generalised RVE size large enough must be considered. This conclusion leads to the proposal of a framework where the generalised RVE size is defined so that representativeness is guaranteed, and the RVE length is determined to model the second-order ef-

fects properly. Furthermore, it is observed that the scale separation limit depends not only on the RVE length and the macroscopic deformation wavelength, measured by the second gradient, but the micro-constituents behaviour and the magnitude of the strain, obtained from the deformation gradient, must also be taken into account. This is also confirmed when analysing the results from Section 6.9, where the importance of second-order effects is alleviated with the increase of the first-order strain.

With regard to the distinct micro-constraints, it has been confirmed that the results obtained with the Luscher's minimal constraint recover the minimal constraint developed in Section 5.2. Nevertheless, the Lagrange multipliers employed to enforce the latter assume the values of the homogenised stresses, which is not obtained with the former. The particularisations of this constraint to the direct and periodic constraints provide quite consistent results, being relatively close to the homogenised results obtained with the minimal constraint, with the direct constraint providing the stiffest response and the minimal constraint yielding the most compliant behaviour of this set of constraints. The results obtained with Kouznetsova's and Blanco's constraints lead to homogenised responses that are, in some cases, significantly different from the remaining ones. The already reported (Luscher, 2010) excessive localisation of stresses in the RVE corners has also been observed. In the case of Blanco's minimal constraint, an unphysical warping near the RVE corners is detected when second-order deformation modes are dominant. As a matter of fact, both Kouznetsova's and Blanco's constraints do not provide consistent results for the case of a simple RVE under small strains with different discretisations, contrary to the remaining constraints. Moreover, when assessing a measure of the homogenised second gradient for the several micro-constraints, the difference associated with these two is, in general, larger than for the other constraints. This is related to the lack of volumetric constraint in the Kouznetsova's formulation, and to the overconstraint arising from the symmetry of the macroscopic second gradient.

Nevertheless, the Lagrange multipliers method proves to be an efficient method to enforce all the micro-scale constraints implemented. It allows to obtain the macroscopic tangents easily in the case of the minimal constraints based on the method of multi-scale virtual power, where the relation between Lagrange multipliers and homogenised stresses is confirmed. Quadratic convergence is attained in the Newton-Raphson scheme for the macroscopic problem of the FE^2 simulation in Section 6.8, proving the suitability of the computational framework presented in Sections 5.1.7 and 5.2.6.

Finally, taking into account the observations made throughout the present chapter, a framework for the analysis of multi-scale problems using second-order homogenisation is proposed in Section 6.10.

Chapter 7

A fully second-order multi-scale model at finite strains

A fully second-order homogenisation-based multi-scale model for solids undergoing large strains is developed in this chapter, employing the *Method of Multi-Scale Virtual Power*, where a second gradient continuum is considered at the micro-scale. When comparing to the *standard* second-order homogenisation scheme, presented in Chapter 5, the main differences are related to an enriched constitutive description at the RVE level. Since the second gradient continuum introduces a non-local characterisation, it may be used to reduce the mesh dependence pathology associated with strain localisation as an alternative to the usage of non-local damage models at the micro-scale (Reis et al., 2018). In addition, due to the incorporation of a material characteristic length at the micro-scale, size effects due to micro-constituents size are captured with this formulation, whilst they are not with the standard second-order formulation.

Recently, Lesičar (2015), Lesičar et al. (2017) formulated a model of this type with a small strain description, with the argument that consistency is lost in the scale transition when different descriptions are employed at macro and micro-scales. Despite the fact that standard second-order homogenisation models can provide a consistent approximation regarding the transition of second gradient effects (see the results in Section 6.7), the main goal of the developments introduced in this chapter is to provide a general second-order formulation for the multi-scale description of solids, where more advanced constitutive laws can be employed to describe the micro-scale behaviour. To the author's knowledge, this is the first multi-scale model of this kind formulated at large strains, within a variational consistent framework.

7.1 A general formulation

In the present section, the general formulation of a fully second-order homogenisation-based multi-scale model is developed through the *method of multi-scale virtual power*.

7.1.1 Multi-scale kinematics

Kinematic insertion

Since the macro-scale description is still described by a second gradient continuum, like in the case of the standard second-order homogenisation, the kinematic insertion operator, defining how macro-scale kinematic variables are introduced in the RVE, is similar to the definition proposed in Chapter 5:

$$\boldsymbol{u}_{\mu} = \boldsymbol{u}_{M} + (\boldsymbol{F} - \boldsymbol{I})\,\boldsymbol{Y} + \frac{1}{2}\mathbf{G} : (\boldsymbol{Y} \otimes \boldsymbol{Y}) + \tilde{\boldsymbol{u}}, \tag{5.3}$$

where $\boldsymbol{Y}$ denotes the vector of RVE reference coordinates and $\tilde{\boldsymbol{u}}$ the micro displacement fluctuation field. It is also conveniently assumed that the origin of the micro coordinate system is located at the geometric center of the RVE, such that Equation (5.4) remains valid.

Kinematic homogenisation

In the kinematic homogenisation procedure, the relation between macro and micro-scale kinematic quantities is postulated. As usual, the macro-deformation gradient is obtained through volume averaging of its micro counterpart:

$$\boldsymbol{F} = \frac{1}{V_\mu}\int_{\Omega_\mu} \boldsymbol{F}_\mu d\Omega_\mu. \tag{7.1}$$

In contrast to the formulations presented in Chapter 5, the macroscopic second gradient may be also defined through volumetric homogenisation of its microscopic field, due to the adoption of a second-order continuum at the RVE level:

$$\mathbf{G} = \frac{1}{V_\mu}\int_{\Omega_\mu} \mathbf{G}_\mu d\Omega_\mu. \tag{7.2}$$

Kinematic admissibility

The determination of kinematic admissibility consists in finding the constraints that establish the consistency between kinematic insertion and kinematic homogenisation.

The compatibility between the definition of the homogenised deformation gradient and the deformation gradient microscopic field is found by replacing Equation (5.7) in Equation (7.1), which results in the well known fluctuation constraint

$$\int_{\Omega_\mu} \nabla_Y \tilde{\boldsymbol{u}} dV = \mathbf{0} \Leftrightarrow \int_{\partial\Omega_\mu} \tilde{\boldsymbol{u}} \otimes \boldsymbol{N} dA = \mathbf{0}, \tag{7.3}$$

also found in first and second-order homogenisation schemes.

The micro-scale second gradient of the displacements $\mathbf{G}_\mu$ is defined through double differentiation of Equation (5.3):

$$\mathbf{G}_\mu = \frac{\partial^2 \boldsymbol{u}_\mu}{\partial \boldsymbol{Y}\partial \boldsymbol{Y}} = \mathbf{G} + \nabla_Y\left(\nabla_Y \tilde{\boldsymbol{u}}\right). \tag{7.4}$$

Including this definition in Equation (7.2) leads to the constraint

$$\int_{\Omega_\mu} \nabla_Y\left(\nabla_Y \tilde{\boldsymbol{u}}\right) dV = \mathbf{0}, \tag{7.5}$$

which can be expressed as a boundary integral through

$$\int_{\partial\Omega_\mu} \nabla_Y \tilde{\boldsymbol{u}} \otimes \boldsymbol{N} dA = \mathbf{0}. \tag{7.6}$$

Thus, the additional constraint obtained here due to the transition of the second gradient can be expressed as a boundary condition, which is not possible to achieve within the formulations presented in Sections 5.1 and 5.2, where a volumetric constraint is needed.

7.1.2 Principle of multi-scale virtual power

The conservation of the virtual power is ensured in the scale transition by employing the *principle of multi-scale virtual power*, where the minimal constraints defined by Equations (7.3) and (7.6) are

enforced through Lagrange multipliers $\boldsymbol{L}$ and $\mathbf{M}$, respectively. The resulting variational equation is expressed by:

$$\begin{aligned}\boldsymbol{P}:\delta\boldsymbol{F}+\mathbf{Q}\vdots\delta\mathbf{G}=\frac{1}{V_\mu}\Bigg[&\int_{\Omega_\mu}\boldsymbol{P}_\mu:(\delta\boldsymbol{F}+\delta\mathbf{G}\cdot\boldsymbol{Y}+\nabla_Y\delta\tilde{\boldsymbol{u}})\,dV+\int_{\Omega_\mu}\mathbf{Q}_\mu\vdots(\delta\mathbf{G}+\nabla_Y\nabla_Y\delta\tilde{\boldsymbol{u}})\,dV\\&-\delta\boldsymbol{L}:\left(\int_{\partial\Omega_\mu}\tilde{\boldsymbol{u}}\otimes\boldsymbol{N}dA\right)-\boldsymbol{L}:\left(\int_{\partial\Omega_\mu}\delta\tilde{\boldsymbol{u}}\otimes\boldsymbol{N}dA\right)\\&-\delta\mathbf{M}\vdots\left(\int_{\partial\Omega_\mu}\nabla_Y\tilde{\boldsymbol{u}}\otimes\boldsymbol{N}dA\right)\\&-\mathbf{M}\vdots\left(\int_{\partial\Omega_\mu}\nabla_Y\delta\tilde{\boldsymbol{u}}\otimes\boldsymbol{N}dA\right)\Bigg],\quad\forall\,(\delta\boldsymbol{F},\delta\mathbf{G},\delta\tilde{\boldsymbol{u}},\delta\boldsymbol{L},\delta\mathbf{M})\,.\end{aligned}\tag{7.7}$$

7.1.3 Micro-scale equilibrium problem

The micro-scale equilibrium expression is found by setting $\delta\boldsymbol{F}=\mathbf{0}$ and $\delta\mathbf{G}=\mathbf{0}$ in Equation (7.7). Hence, the micro-equilibrium problem consists in finding the fluctuation field $\tilde{\boldsymbol{u}}$ and the Lagrange multipliers $\boldsymbol{L}$ and $\mathbf{M}$, such that:

$$\begin{aligned}\int_{\Omega_\mu}\left(\boldsymbol{P}_\mu:\nabla_Y\delta\tilde{\boldsymbol{u}}+\mathbf{Q}_\mu\vdots\nabla_Y\nabla_Y\delta\tilde{\boldsymbol{u}}\right)dV-\delta\boldsymbol{L}:\left(\int_{\partial\Omega_\mu}\tilde{\boldsymbol{u}}\otimes\boldsymbol{N}dA\right)-\boldsymbol{L}:\left(\int_{\partial\Omega_\mu}\delta\tilde{\boldsymbol{u}}\otimes\boldsymbol{N}dA\right)\\-\delta\mathbf{M}\vdots\left(\int_{\partial\Omega_\mu}\nabla_Y\tilde{\boldsymbol{u}}\otimes\boldsymbol{N}dA\right)-\mathbf{M}\vdots\left(\int_{\partial\Omega_\mu}\nabla_Y\delta\tilde{\boldsymbol{u}}\otimes\boldsymbol{N}dA\right)=0.\end{aligned}\tag{7.8}$$

The strong form of the equilibrium problem is determined by setting $\delta\boldsymbol{L}=\mathbf{0}$ and $\delta\mathbf{M}=\mathbf{0}$ in Equation (7.8), which leads to

$$\int_{\Omega_\mu}(\boldsymbol{P}_\mu-\boldsymbol{L}):\nabla_Y\delta\tilde{\boldsymbol{u}}dV+\int_{\Omega_\mu}(\mathbf{Q}_\mu-\mathbf{M})\vdots\nabla_Y\nabla_Y\delta\tilde{\boldsymbol{u}}dV=0.\tag{7.9}$$

Integrating by parts, the first term is developed to:

$$\int_{\Omega_\mu}(\boldsymbol{P}_\mu-\boldsymbol{L}):\nabla_Y\delta\tilde{\boldsymbol{u}}dV=\int_{\partial\Omega_\mu}(\boldsymbol{P}_\mu\cdot\boldsymbol{N}-\boldsymbol{L}\cdot\boldsymbol{N})\cdot\delta\tilde{\boldsymbol{u}}dA-\int_{\Omega_\mu}\operatorname{div}\boldsymbol{P}_\mu\cdot\delta\tilde{\boldsymbol{u}}dV.\tag{7.10}$$

Similarly, the second term may be expressed as:

$$\begin{aligned}\int_{\Omega_\mu}(\mathbf{Q}_\mu-\mathbf{M})\vdots\nabla_Y\nabla_Y\delta\tilde{\boldsymbol{u}}dV=\int_{\partial\Omega_\mu}[(\mathbf{Q}_\mu-\mathbf{M})\cdot\boldsymbol{N}]:\nabla_Y\delta\tilde{\boldsymbol{u}}dA-\\\int_{\partial\Omega_\mu}\operatorname{div}(\mathbf{Q}_\mu-\mathbf{M})\cdot\boldsymbol{N}\cdot\delta\tilde{\boldsymbol{u}}dA+\int_{\Omega_\mu}\operatorname{div}[\operatorname{div}(\mathbf{Q}_\mu-\mathbf{M})]\cdot\delta\tilde{\boldsymbol{u}}dV.\end{aligned}\tag{7.11}$$

Following the steps described in Section 4.3, the first term of the above right-hand-side is further developed through integration by parts and decomposition of the the gradient into its normal and surface components (see Section 4.3):

$$\begin{aligned}\int_{\partial\Omega_\mu}[(\mathbf{Q}_\mu-\mathbf{M})\cdot\boldsymbol{N}]:\nabla_Y\delta\tilde{\boldsymbol{u}}dA=&\int_{\partial\Omega_\mu}\operatorname{div}^t\boldsymbol{N}\{[(\mathbf{Q}_\mu-\mathbf{M})\cdot\boldsymbol{N}]\cdot\boldsymbol{N}\}\cdot\delta\tilde{\boldsymbol{u}}dA-\\&\int_{\partial\Omega_\mu}\operatorname{div}^t[(\mathbf{Q}_\mu-\mathbf{M})\cdot\boldsymbol{N}]\cdot\delta\tilde{\boldsymbol{u}}dA+\\&\int_{\partial\Omega_\mu}\{[(\mathbf{Q}_\mu-\mathbf{M})\cdot\boldsymbol{N}]\cdot\boldsymbol{N}\}\cdot D_0\delta\tilde{\boldsymbol{u}}dA+\\&\sum_i^{n_e}\oint_{\Gamma^i}\|[(\mathbf{Q}_\mu-\mathbf{M})\cdot\boldsymbol{N}]\cdot\boldsymbol{m}\|\cdot\delta\tilde{\boldsymbol{u}}dL.\end{aligned}\tag{7.12}$$

Including Equations (7.10)-(7.12) into (7.9), taking into account that $\mathbf{M}$ is constant over the RVE, thus $\operatorname{div}\mathbf{M}=0$, results in

$$\begin{aligned}
&\int_{\Omega_\mu}\left(\operatorname{div}\operatorname{div}\mathbf{Q}_\mu-\operatorname{div}\boldsymbol{P}_\mu\right)\cdot\delta\tilde{\boldsymbol{u}}dV+\\
&\int_{\partial\Omega_\mu}\left\{\boldsymbol{P}_\mu\cdot\boldsymbol{N}-\boldsymbol{L}\cdot\boldsymbol{N}-\operatorname{div}\mathbf{Q}_\mu\cdot\boldsymbol{N}+\operatorname{div}^t\boldsymbol{N}\left\{\left[\left(\mathbf{Q}_\mu-\mathbf{M}\right)\cdot\boldsymbol{N}\right]\cdot\boldsymbol{N}\right\}-\operatorname{div}^t\left[\left(\mathbf{Q}_\mu-\mathbf{M}\right)\cdot\boldsymbol{N}\right]\right\}\cdot\delta\tilde{\boldsymbol{u}}dA+\\
&\int_{\partial\Omega_\mu}\left\{\left[\left(\mathbf{Q}_\mu-\mathbf{M}\right)\cdot\boldsymbol{N}\right]\cdot\boldsymbol{N}\right\}\cdot D_0\delta\tilde{\boldsymbol{u}}dA+\\
&\sum_i^{n_e}\oint_{\Gamma^i}\left\|\left[\left(\mathbf{Q}_\mu-\mathbf{M}\right)\cdot\boldsymbol{N}\right]\cdot\boldsymbol{m}\right\|\cdot\delta\tilde{\boldsymbol{u}}dL=0.
\end{aligned}\tag{7.13}$$

Therefore, the strong form of the micro-scale problem may be expressed as

$$\operatorname{div}\operatorname{div}\mathbf{Q}_\mu-\operatorname{div}\boldsymbol{P}_\mu=\mathbf{0},\quad\text{in }\Omega_\mu\tag{7.14}$$

$$\boldsymbol{P}_\mu\cdot\boldsymbol{N}-\boldsymbol{L}\cdot\boldsymbol{N}-\operatorname{div}\mathbf{Q}_\mu\cdot\boldsymbol{N}+\operatorname{div}^t\boldsymbol{N}\left\{\left[\left(\mathbf{Q}_\mu-\mathbf{M}\right)\cdot\boldsymbol{N}\right]\cdot\boldsymbol{N}\right\}-\operatorname{div}^t\left[\left(\mathbf{Q}_\mu-\mathbf{M}\right)\cdot\boldsymbol{N}\right]=\mathbf{0},\quad\text{on }\partial\Omega_\mu\tag{7.15}$$

$$\left[\left(\mathbf{Q}_\mu-\mathbf{M}\right)\cdot\boldsymbol{N}\right]\cdot\boldsymbol{N}=\mathbf{0},\quad\text{on }\partial\Omega_\mu\tag{7.16}$$

$$\left\|\left[\left(\mathbf{Q}_\mu-\mathbf{M}\right)\cdot\boldsymbol{N}\right]\cdot\boldsymbol{m}\right\|=\mathbf{0},\quad\text{on }\Gamma_\mu.\tag{7.17}$$

7.1.4 Role of the Lagrange multipliers

The physical meaning of the Lagrange multipliers, and its influence on the equilibrium equations is exploited here.

In the first place, introducing Equation (7.16) in (7.15), it is simplified and rewritten as

$$\boldsymbol{L}\cdot\boldsymbol{N}=\boldsymbol{P}_\mu\cdot\boldsymbol{N}-\operatorname{div}\mathbf{Q}_\mu\cdot\boldsymbol{N}-\operatorname{div}^t\left[\left(\mathbf{Q}_\mu-\mathbf{M}\right)\cdot\boldsymbol{N}\right],\quad\text{on }\partial\Omega_\mu.\tag{7.18}$$

The third term of the above right-hand-side may be further simplified, taking into account that $\mathbf{M}$ is constant:

$$\operatorname{div}^t\left[\left(\mathbf{Q}_\mu-\mathbf{M}\right)\cdot\boldsymbol{N}\right]=\operatorname{div}^t\left(\mathbf{Q}_\mu\cdot\boldsymbol{N}\right)-\operatorname{div}^t\left(\mathbf{M}\cdot\boldsymbol{N}\right)=\operatorname{div}^t\left(\mathbf{Q}_\mu\cdot\boldsymbol{N}\right),\tag{7.19}$$

thus:

$$\boldsymbol{L}\cdot\boldsymbol{N}=\boldsymbol{P}_\mu\cdot\boldsymbol{N}-\operatorname{div}\mathbf{Q}_\mu\cdot\boldsymbol{N}-\operatorname{div}^t\left(\mathbf{Q}_\mu\cdot\boldsymbol{N}\right),\quad\text{on }\partial\Omega_\mu.\tag{7.20}$$

Recalling Expression (4.16), the boundary traction may be expressed here by

$$\boldsymbol{t}_\mu=\boldsymbol{P}_\mu\cdot\boldsymbol{N}-\operatorname{div}\mathbf{Q}_\mu\cdot\boldsymbol{N}+\operatorname{div}^t\boldsymbol{N}\left(\mathbf{Q}_\mu\cdot\boldsymbol{N}\right)\cdot\boldsymbol{N}-\operatorname{div}^t\left(\mathbf{Q}_\mu\cdot\boldsymbol{N}\right),\quad\text{on }\partial\Omega_\mu.\tag{7.21}$$

Considering a RVE whose faces are plane, the normal vector is constant in each face and $\operatorname{div}^t\boldsymbol{N}=0$. Then, comparing Equations (7.20) and (7.21), the RVE boundary traction is defined by the Lagrange multiplier $\boldsymbol{L}$ through:

$$\boldsymbol{t}_\mu=\boldsymbol{L}\cdot\boldsymbol{N}.\tag{7.22}$$

Since the $\boldsymbol{L}$ is constant in the RVE, then constraint (7.3) results in a uniform traction on the RVE boundary, similarly to the minimal constraints for both first and second-order formulations presented in Chapters 3 and 5.

In the second place, regarding the reactive nature of the constraint (7.6), Equation (7.16) is rearranged as

$$\left(\mathbf{M}\cdot\boldsymbol{N}\right)\cdot\boldsymbol{N}=\left(\mathbf{Q}_\mu\cdot\boldsymbol{N}\right)\cdot\boldsymbol{N},\quad\text{on }\partial\Omega_\mu.\tag{7.23}$$

Looking at Equation (4.17), it becomes clear that the Lagrange multiplier $\mathbf{M}$ is related to the double traction on the RVE boundary:

$$\boldsymbol{r}_\mu=\left(\mathbf{M}\cdot\boldsymbol{N}\right)\cdot\boldsymbol{N}.\tag{7.24}$$

Moreover, since $\mathbf{M}$ is constant in the RVE, it implies a uniform double traction on the RVE boundary.

7.1.5 First Piola-Kirchhoff stress homogenisation

The homogenised first Piola-Kirchhoff stress tensor is extracted from the *principle of multi-scale virtual power* by defining $\delta \boldsymbol{L} = \boldsymbol{0}$, $\delta \mathbf{M} = \boldsymbol{0}$, $\delta \mathbf{G} = \boldsymbol{0}$ and $\delta \tilde{\boldsymbol{u}} = \boldsymbol{0}$ in Equation (7.7), which leads to:

$$\boldsymbol{P} : \delta \boldsymbol{F} = \frac{1}{V_\mu} \int_{\Omega_\mu} \boldsymbol{P}_\mu : \delta \boldsymbol{F} dV \Rightarrow \boldsymbol{P} = \frac{1}{V_\mu} \int_{\Omega_\mu} \boldsymbol{P}_\mu dV. \tag{7.25}$$

In spite of resulting on the standard expression for the stress homogenisation, it may be developed differently by integrating the above right hand side by parts, and employing the divergence theorem:

$$\int_{\Omega_\mu} \boldsymbol{P}_\mu dV = \int_{\partial\Omega_\mu} \boldsymbol{P}_\mu \cdot \boldsymbol{N} \otimes \boldsymbol{Y} dA - \int_{\Omega_\mu} \operatorname{div} \boldsymbol{P}_\mu \otimes \boldsymbol{Y} dV. \tag{7.26}$$

Introducing the strong form equalities to replace $\boldsymbol{P}_\mu \cdot \boldsymbol{N}$ and $\operatorname{div} \boldsymbol{P}_\mu \otimes \boldsymbol{Y}$ in the above yields:

$$\int_{\Omega_\mu} \boldsymbol{P}_\mu dV = \int_{\partial\Omega_\mu} \left[\boldsymbol{L} \cdot \boldsymbol{N} + \operatorname{div} \mathbf{Q}_\mu \cdot \boldsymbol{N} + \operatorname{div}^t \left(\mathbf{Q}_\mu \cdot \boldsymbol{N} \right) \right] \otimes \boldsymbol{Y} dA - \int_{\Omega_\mu} \operatorname{div} \operatorname{div} \mathbf{Q}_\mu \otimes \boldsymbol{Y} dV. \tag{7.27}$$

The second term of the above right-hand-side is further developed as follows:

$$\begin{aligned} \int_{\partial\Omega_\mu} \operatorname{div} \mathbf{Q}_\mu \cdot \boldsymbol{N} \otimes \boldsymbol{Y} dA \Rightarrow \int_{\partial\Omega_\mu} \frac{\partial \mathrm{Q}_{ijk}}{\partial Y_k} N_j Y_l dA &= \int_{\Omega_\mu} \frac{\partial}{\partial Y_j} \left(\frac{\partial \mathrm{Q}_{ijk}}{\partial Y_k} Y_l \right) dV \\ &= \int_{\Omega_\mu} \frac{\partial \mathrm{Q}_{ijk}}{\partial Y_k \partial Y_j} Y_l dV + \int_{\Omega_\mu} \frac{\partial \mathrm{Q}_{ijk}}{\partial Y_k} \frac{\partial Y_l}{\partial Y_j} dV \\ &\Rightarrow \int_{\Omega_\mu} \operatorname{div} \operatorname{div} \mathbf{Q}_\mu \otimes \boldsymbol{Y} dV + \int_{\Omega_\mu} \operatorname{div} \mathbf{Q}_\mu dV \end{aligned} \tag{7.28}$$

Thus, introducing this expression in Equation (7.27) results in:

$$\begin{aligned} \int_{\Omega_\mu} \boldsymbol{P}_\mu dV &= \int_{\partial\Omega_\mu} \boldsymbol{L} \cdot \boldsymbol{N} \otimes \boldsymbol{Y} dA + \int_{\partial\Omega_\mu} \operatorname{div}^t \left(\mathbf{Q}_\mu \cdot \boldsymbol{N} \right) \otimes \boldsymbol{Y} dA + \int_{\Omega_\mu} \operatorname{div} \mathbf{Q}_\mu dV \\ &= \boldsymbol{L} \cdot V_\mu + \int_{\partial\Omega_\mu} \operatorname{div}^t \left(\mathbf{Q}_\mu \cdot \boldsymbol{N} \right) \otimes \boldsymbol{Y} dA + \int_{\partial\Omega_\mu} \mathbf{Q}_\mu \cdot \boldsymbol{N} dV, \end{aligned} \tag{7.29}$$

where it is demonstrated that the homogenised first Piola-Kirchhoff stress tensor may be computed from boundary integrals only.

7.1.6 Higher-order stress homogenisation

The homogenised higher-order stress tensor $\mathbf{Q}$ is determined by introducing $\delta \boldsymbol{L} = \boldsymbol{0}$, $\mathbf{M} = \boldsymbol{0}$, $\delta \boldsymbol{F} = \boldsymbol{0}$ and $\delta \tilde{\boldsymbol{u}} = \boldsymbol{0}$ in Equation (7.7), leading to:

$$\mathbf{Q} \vdots \delta \mathbf{G} = \frac{1}{V_\mu} \int_{\Omega_\mu} \left[\boldsymbol{P}_\mu : (\delta \mathbf{G} \cdot \boldsymbol{Y}) + \mathbf{Q}_\mu \vdots \delta \mathbf{G} \right] dV \tag{7.30}$$

$$= \frac{1}{V_\mu} \int_{\Omega_\mu} \left(\boldsymbol{P}_\mu \otimes \boldsymbol{Y} + \mathbf{Q}_\mu \right) \vdots \delta \mathbf{G} dV. \tag{7.31}$$

Due to the symmetry of $\mathbf{G}$ and $\mathbf{Q}_\mu$, the homogenised $\mathbf{Q}$ is defined by:

$$\mathbf{Q} = \frac{1}{V_\mu} \int_{\Omega_\mu} \left[\left(\boldsymbol{P}_\mu \otimes \boldsymbol{Y} \right)^S + \mathbf{Q}_\mu \right] dV. \tag{7.32}$$

Aiming to find alternative expressions for Equation (7.32), the following expression and its development is taken as a starting point:

$$\begin{aligned}\frac{\partial^2\left(\mathrm{Q}_{ilm}Y_jY_k\right)}{\partial Y_l\partial Y_m} &= \frac{\partial}{\partial Y_l}\left[\frac{\partial \mathrm{Q}_{ilm}}{\partial Y_m}Y_jY_k+\mathrm{Q}_{ilm}\left(\delta_{mj}Y_k+\delta_{mk}Y_j\right)\right]\\ &= \frac{\partial}{\partial Y_l}\left[\frac{\partial \mathrm{Q}_{ilm}}{\partial Y_m}Y_jY_k+\mathrm{Q}_{ilj}Y_k+\mathrm{Q}_{ilk}Y_j\right]\\ &= \frac{\partial^2\mathrm{Q}_{ilm}}{\partial Y_l\partial Y_m}Y_jY_k+\frac{\partial \mathrm{Q}_{ilm}}{\partial Y_m}\left(\delta_{lj}Y_k+\delta_{lk}Y_j\right)+\frac{\partial \mathrm{Q}_{ilj}}{\partial Y_l}Y_k+\mathrm{Q}_{ilj}\delta_{lk}+\frac{\partial \mathrm{Q}_{ilk}}{\partial Y_l}Y_j+\mathrm{Q}_{ilk}\delta_{lj}\\ &= \frac{\partial^2\mathrm{Q}_{ilm}}{\partial Y_l\partial Y_m}Y_jY_k+\frac{\partial \mathrm{Q}_{ijm}}{\partial Y_m}Y_k+\frac{\partial \mathrm{Q}_{ikm}}{\partial Y_m}Y_j+\frac{\partial \mathrm{Q}_{ijl}}{\partial Y_l}Y_k+\frac{\partial \mathrm{Q}_{ikl}}{\partial Y_l}Y_j+2\mathrm{Q}_{ijk}\\ &= \frac{\partial^2\mathrm{Q}_{ilm}}{\partial Y_l\partial Y_m}Y_jY_k+2\frac{\partial \mathrm{Q}_{ijm}}{\partial Y_m}Y_k+2\frac{\partial \mathrm{Q}_{ikm}}{\partial Y_m}Y_j+2\mathrm{Q}_{ijk}.\end{aligned} \tag{7.33}$$

Integrating the initial expression over the RVE volume yields:

$$\begin{aligned}\int_{\Omega_\mu}\frac{\partial^2\left(\mathrm{Q}_{ilm}Y_jY_k\right)}{\partial Y_l\partial Y_m}dV &= \int_{\partial\Omega_\mu}\frac{\partial\left(\mathrm{Q}_{ilm}Y_jY_k\right)}{\partial Y_m}N_l\,dA\\ &= \int_{\partial\Omega_\mu}\left[\frac{\partial \mathrm{Q}_{ilm}}{\partial Y_m}Y_jY_kN_l+\mathrm{Q}_{ilm}\left(\delta_{mj}Y_k+\delta_{mk}Y_j\right)N_l\right]dA\\ &= \int_{\partial\Omega_\mu}\left[\frac{\partial \mathrm{Q}_{ilm}}{\partial Y_m}Y_jY_kN_l+\mathrm{Q}_{ijl}N_lY_k+\mathrm{Q}_{ikl}N_lY_j\right]dA.\end{aligned} \tag{7.34}$$

Similarly, integration of the first term of the right-hand-side of Equation (7.33), taking into account that the strong form Expression (7.14) states $\mathrm{div}\,\mathrm{div}\,\mathbf{Q}_\mu = \mathrm{div}\,\boldsymbol{P}_\mu$, leads to:

$$\begin{aligned}\int_{\Omega_\mu}\frac{\partial^2\mathrm{Q}_{ilm}}{\partial Y_l\partial Y_m}Y_jY_k\,dV &= \int_{\Omega_\mu}\frac{\partial P_{il}}{\partial Y_l}Y_jY_k\,dV =\\ &= \int_{\Omega_\mu}\frac{\partial\left(P_{il}Y_jY_k\right)}{\partial Y_l}dV-\int_{\Omega_\mu}P_{il}\left(\delta_{lj}Y_k+\delta_{lk}Y_j\right)dV =\\ &= \int_{\partial\Omega_\mu}P_{il}N_lY_jY_k\,dA-\int_{\Omega_\mu}\left(P_{ij}Y_k+P_{ik}Y_j\right)dV.\end{aligned} \tag{7.35}$$

For the second right-hand-side term:

$$\begin{aligned}\int_{\Omega_\mu}\frac{\partial \mathrm{Q}_{ijm}}{\partial Y_m}Y_k\,dV &= \int_{\Omega_\mu}\frac{\partial\left(\mathrm{Q}_{ijm}Y_k\right)}{\partial Y_m}dV-\int_{\Omega_\mu}\mathrm{Q}_{ijm}\delta_{mk}dV\\ &= \int_{\partial\Omega_\mu}\mathrm{Q}_{ijm}N_mY_k\,dA-\int_{\Omega_\mu}\mathrm{Q}_{ijk}dV,\end{aligned} \tag{7.36}$$

and for the third:

$$\begin{aligned}\int_{\Omega_\mu}\frac{\partial \mathrm{Q}_{ikm}}{\partial Y_m}Y_j\,dV &= \int_{\Omega_\mu}\frac{\partial\left(\mathrm{Q}_{ikm}Y_j\right)}{\partial Y_m}dV-\int_{\Omega_\mu}\mathrm{Q}_{ikm}\delta_{mj}dV\\ &= \int_{\partial\Omega_\mu}\mathrm{Q}_{ikm}N_mY_j\,dA-\int_{\Omega_\mu}\mathrm{Q}_{ijk}dV.\end{aligned} \tag{7.37}$$

Therefore, in view of the equality introduced by Expression (7.33), Expression (7.34) is equal to the

sum of Expressions (7.35), (7.36) and (7.37), leading to

$$\begin{aligned}\int_{\partial\Omega_\mu}\left[\frac{\partial \mathrm{Q}_{ilm}}{\partial Y_m}Y_jY_kN_l+\mathrm{Q}_{ijl}N_lY_k+\mathrm{Q}_{ikl}N_lY_j\right]dA=&\int_{\partial\Omega_\mu}P_{il}N_lY_jY_kdA-\\&\int_{\Omega_\mu}\left(P_{ij}Y_k+P_{ik}Y_j\right)dV+\\&2\left(\int_{\partial\Omega_\mu}\mathrm{Q}_{ijm}N_mY_kdA-\int_{\Omega_\mu}\mathrm{Q}_{ijk}dV\right)+\\&2\left(\int_{\partial\Omega_\mu}\mathrm{Q}_{ikm}N_mY_jdA-\int_{\Omega_\mu}\mathrm{Q}_{ijk}dV\right)+\\&2\int_{\Omega_\mu}\mathrm{Q}_{ijk}dV,\end{aligned}\tag{7.38}$$

which may be simplified to

$$\begin{aligned}\int_{\partial\Omega_\mu}\left[\frac{\partial \mathrm{Q}_{ilm}}{\partial Y_m}Y_jY_kN_l\right]dA=&\int_{\partial\Omega_\mu}P_{il}N_lY_jY_kdA-\int_{\Omega_\mu}\left(P_{ij}Y_k+P_{ik}Y_j\right)dV+\\&\int_{\partial\Omega_\mu}\mathrm{Q}_{ijm}N_mY_kdA+\int_{\partial\Omega_\mu}\mathrm{Q}_{ikm}N_mY_jdA-2\int_{\Omega_\mu}\mathrm{Q}_{ijk}dV.\end{aligned}\tag{7.39}$$

Looking at Equation (7.32), it is possible to rewrite the above such that

$$\begin{aligned}\frac{1}{V_\mu}\int_{\Omega_\mu}\left[\mathrm{Q}_{ijk}+\frac{1}{2}\left(P_{ij}Y_k+P_{ik}Y_j\right)\right]dV=&\frac{1}{2V_\mu}\int_{\partial\Omega_\mu}P_{il}N_lY_jY_kdA+\\&+\frac{1}{2V_\mu}\int_{\partial\Omega_\mu}\left(\mathrm{Q}_{ijm}N_mY_k+\mathrm{Q}_{ikm}N_mY_j\right)dA-\\&-\frac{1}{2V_\mu}\int_{\partial\Omega_\mu}\left[\frac{\partial \mathrm{Q}_{ilm}}{\partial Y_m}Y_jY_kN_l\right]dA.\end{aligned}\tag{7.40}$$

Thus, the homogenised higher-order stress tensor may be obtained through boundary integrals only as

$$\begin{aligned}\mathbf{Q}=\frac{1}{V_\mu}\int_{\Omega_\mu}\left[\mathbf{Q}_\mu+(\boldsymbol{P}\otimes\boldsymbol{Y})^S\right]dV=&\frac{1}{2V_\mu}\int_{\partial\Omega_\mu}\boldsymbol{P}_\mu\cdot\boldsymbol{N}\otimes\boldsymbol{Y}\otimes\boldsymbol{Y}dA+\\&+\frac{1}{V_\mu}\int_{\partial\Omega_\mu}\left(\mathbf{Q}_\mu\cdot\boldsymbol{N}\otimes\boldsymbol{Y}\right)^SdA-\\&-\frac{1}{2V_\mu}\int_{\partial\Omega_\mu}\mathrm{div}\,\mathbf{Q}_\mu\cdot\boldsymbol{N}\otimes\boldsymbol{Y}\otimes\boldsymbol{Y}dA.\end{aligned}\tag{7.41}$$

Furthermore, including the equality $\boldsymbol{P}_\mu\cdot\boldsymbol{N}=\boldsymbol{L}\cdot\boldsymbol{N}+\mathrm{div}\,\mathbf{Q}_\mu\cdot\boldsymbol{N}+\mathrm{div}^t\left(\mathbf{Q}_\mu\cdot\boldsymbol{N}\right)$, from Equation (7.20), the above may be rewritten by

$$\begin{aligned}\mathbf{Q}=&\frac{1}{2V_\mu}\int_{\partial\Omega_\mu}\boldsymbol{L}\cdot\boldsymbol{N}\otimes\boldsymbol{Y}\otimes\boldsymbol{Y}dA+\\&+\frac{1}{2V_\mu}\int_{\partial\Omega_\mu}\mathrm{div}^t\left(\mathbf{Q}_\mu\cdot\boldsymbol{N}\right)\otimes\boldsymbol{Y}\otimes\boldsymbol{Y}dA+\\&+\frac{1}{V_\mu}\int_{\partial\Omega_\mu}\left(\mathbf{Q}_\mu\cdot\boldsymbol{N}\otimes\boldsymbol{Y}\right)^SdA.\end{aligned}\tag{7.42}$$

After proving that the first term of the above right-hand-side is null:

$$\int_{\partial\Omega_\mu}\boldsymbol{L}\cdot\boldsymbol{N}\otimes\boldsymbol{Y}\otimes\boldsymbol{Y}dA=\boldsymbol{L}\cdot\int_{\partial\Omega_\mu}\boldsymbol{N}\otimes\boldsymbol{Y}\otimes\boldsymbol{Y}dA=\boldsymbol{L}\cdot\int_{\Omega_\mu}\nabla\left(\boldsymbol{Y}\otimes\boldsymbol{Y}\right)dV=\mathbf{0},\tag{7.43}$$

the homogenised higher-order stress tensor $\mathbf{Q}$ is simply expressed through:

$$\mathbf{Q}=\frac{1}{2V_\mu}\int_{\partial\Omega_\mu}\mathrm{div}^t\left(\mathbf{Q}_\mu\cdot\boldsymbol{N}\right)\otimes\boldsymbol{Y}\otimes\boldsymbol{Y}dA+\frac{1}{V_\mu}\int_{\partial\Omega_\mu}\left(\mathbf{Q}_\mu\cdot\boldsymbol{N}\otimes\boldsymbol{Y}\right)^SdA.\tag{7.44}$$

7.2 A formulation for the solution with mixed finite elements

In view of the finite element solution of the resulting multi-scale problem, a formulation for a fully second-order multi-scale model where the micro-scale equilibrium problem is solved with the mixed finite elements presented in Section 4.4.2 is developed in this section.

The Lagrange multiplier method is employed to enforce the kinematic constraints in Equations (7.3) and (7.6) at the micro-scale. In addition, since the micro-scale is modelled as a second-order continuum, the mixed finite elements presented in Section 4.4.2, that use Lagrange multipliers to guarantee the compatibility between displacements and relaxed deformation gradients, are employed.

7.2.1 Multi-scale kinematics

Kinematic insertion

The insertion operator that dictates the micro-scale displacements field is defined the same way of the general formulation (Section 7.1):

$$\boldsymbol{u}_\mu = \boldsymbol{u}_M + (\boldsymbol{F} - \boldsymbol{I})\,\boldsymbol{Y} + \frac{1}{2}\mathbf{G} : (\boldsymbol{Y} \otimes \boldsymbol{Y}) + \tilde{\boldsymbol{u}}. \tag{5.3}$$

If a mixed formulation is employed at the micro-scale, a relaxed microscopic deformation gradient field, that is conceptually independent from the displacement field (see Section 4.4.2), is introduced. The corresponding insertion operator is expressed by

$$\hat{\boldsymbol{F}}_\mu = \boldsymbol{F} + \mathbf{G} \cdot \boldsymbol{Y} + \hat{\tilde{\boldsymbol{F}}}, \tag{7.45}$$

where $\hat{\tilde{\boldsymbol{F}}}$ is the relaxed fluctuations gradient.

Kinematic homogenisation

The homogenised deformation gradient is obtained as in the general formulation, by volume averaging of the micro-deformation gradient computed from the displacements gradient:

$$\boldsymbol{F} = \frac{1}{V_\mu}\int_{\Omega_\mu} \boldsymbol{F}_\mu \, d\Omega_\mu. \tag{7.46}$$

The macroscopic second gradient is defined through volumetric homogenisation of its microscopic field:

$$\mathbf{G} = \frac{1}{V_\mu}\int_{\Omega_\mu} \mathbf{G}_\mu \, d\Omega_\mu, \tag{7.47}$$

that is, in this particular case, computed as the symmetric gradient of the relaxed micro-deformation gradient, i.e.:

$$\mathbf{G}_\mu = \nabla^s \hat{\boldsymbol{F}}_\mu. \tag{7.48}$$

Kinematic admissibility

The compatibility between the insertion of the displacements field (Equation (5.3)) and the homogenised deformation gradient (Equation (7.46)) leads to the usual minimal constraint:

$$\int_{\Omega_\mu} \nabla_Y \tilde{\boldsymbol{u}} \, dV = \mathbf{0} \Leftrightarrow \int_{\partial\Omega_\mu} \tilde{\boldsymbol{u}} \otimes \boldsymbol{N} \, dA = \mathbf{0}. \tag{7.49}$$

The main difference of the present formulation lies on the minimal constraint arising from the compatibility between the microscopic relaxed deformation gradient field (Equation (7.45)) and the homogenised second gradient (Equation (7.47)), that operates on the relaxed fluctuations gradient:

$$\begin{aligned}\mathbf{G} &= \frac{1}{V_\mu}\int_{\Omega_\mu} \nabla^s \hat{\boldsymbol{F}}_\mu dV \\ &= \frac{1}{V_\mu}\int_{\Omega_\mu} \mathbf{G} + \nabla^s \hat{\tilde{\boldsymbol{F}}}_\mu dV \Rightarrow \int_{\Omega_\mu} \nabla^s \hat{\tilde{\boldsymbol{F}}}_\mu dV = \mathbf{0}.\end{aligned} \tag{7.50}$$

This equation can be expressed as the following boundary integral:

$$\int_{\partial\Omega_\mu} \left(\hat{\tilde{\boldsymbol{F}}} \otimes \boldsymbol{N}\right)^S dA = \mathbf{0}, \tag{7.51}$$

thus, the minimal constraints obtained for this particular formulation can be enforced through boundary conditions only.

7.2.2 Principle of multi-scale virtual power

The expression that states the *principle of multi-scale virtual power* in this case is given by:

$$\begin{aligned}\boldsymbol{P}:\delta\boldsymbol{F} + \mathbf{Q}\vdots\delta\mathbf{G} = \frac{1}{V_\mu}\Bigg[&\int_{\Omega_\mu} \boldsymbol{P}_\mu : (\delta\boldsymbol{F} + \delta\mathbf{G}\cdot\boldsymbol{Y} + \nabla_Y \delta\tilde{\boldsymbol{u}})\, dV + \int_{\Omega_\mu} \mathbf{Q}_\mu \vdots \left(\delta\mathbf{G} + \nabla_Y^s \delta\hat{\tilde{\boldsymbol{F}}}\right) dV \\ &- \int_{\Omega_\mu} \delta\boldsymbol{\lambda} : \left(\nabla_Y \tilde{\boldsymbol{u}} - \hat{\tilde{\boldsymbol{F}}}\right) dV - \int_{\Omega_\mu} \boldsymbol{\lambda} : \left(\nabla_Y \delta\tilde{\boldsymbol{u}} - \delta\hat{\tilde{\boldsymbol{F}}}\right) dV \\ &-\delta\boldsymbol{L} : \left(\int_{\partial\Omega_\mu} \tilde{\boldsymbol{u}} \otimes \boldsymbol{N} dA\right) - \boldsymbol{L} : \left(\int_{\partial\Omega_\mu} \delta\tilde{\boldsymbol{u}} \otimes \boldsymbol{N} dA\right) \\ &-\delta\mathbf{M}\vdots\int_{\partial\Omega_\mu} \left(\hat{\tilde{\boldsymbol{F}}} \otimes \boldsymbol{N}\right)^S dA \\ &- \mathbf{M}\vdots\int_{\partial\Omega_\mu} \left(\delta\hat{\tilde{\boldsymbol{F}}} \otimes \boldsymbol{N}\right)^S dA\Bigg], \quad \forall \left(\delta\boldsymbol{F}, \delta\mathbf{G}, \delta\tilde{\boldsymbol{u}}, \delta\hat{\tilde{\boldsymbol{F}}}, \delta\boldsymbol{\lambda}, \delta\boldsymbol{L}, \delta\mathbf{M}\right),\end{aligned} \tag{7.52}$$

where the Lagrange multiplier $\boldsymbol{\lambda}$ is related to the mixed finite elements concept, enforcing the compatibility between the relaxed deformation gradient and the displacements gradient, and the minimal constraints defined by Equations (7.49) and (7.51) are enforced by the Lagrange multipliers $\boldsymbol{L}$ and $\mathbf{M}$, respectively. The Lagrange multiplier $\mathbf{M}$ is symmetric in the last two indices due to the symmetry of the corresponding constraint.

7.2.3 Micro-scale equilibrium problem

The weak form of the resulting equilibrium equation is obtained by setting $\delta\boldsymbol{F} = \mathbf{0}$ and $\delta\mathbf{G} = \mathbf{0}$ in Equation (7.52):

$$\begin{aligned}\int_{\Omega_\mu} \Bigg[&\boldsymbol{P}_\mu : \nabla_Y \delta\tilde{\boldsymbol{u}} + \mathbf{Q}_\mu \vdots \nabla_Y^s \delta\hat{\tilde{\boldsymbol{F}}}_\mu - \delta\boldsymbol{\lambda} : \left(\nabla_Y \tilde{\boldsymbol{u}} - \hat{\tilde{\boldsymbol{F}}}\right) - \boldsymbol{\lambda} : \left(\nabla_Y \delta\tilde{\boldsymbol{u}} - \delta\hat{\tilde{\boldsymbol{F}}}\right)\Bigg] dV \\ &-\delta\boldsymbol{L} : \left(\int_{\partial\Omega_\mu} \tilde{\boldsymbol{u}} \otimes \boldsymbol{N} dA\right) - \boldsymbol{L} : \left(\int_{\partial\Omega_\mu} \delta\tilde{\boldsymbol{u}} \otimes \boldsymbol{N} dA\right) \\ &-\delta\mathbf{M}\vdots\int_{\partial\Omega_\mu} \left(\hat{\tilde{\boldsymbol{F}}} \otimes \boldsymbol{N}\right)^S dA - \mathbf{M}\vdots\int_{\partial\Omega_\mu} \left(\delta\hat{\tilde{\boldsymbol{F}}} \otimes \boldsymbol{N}\right)^S dA = 0.\end{aligned} \tag{7.53}$$

The strong form of the equilibrium problem is obtained by defining $\delta\boldsymbol{\lambda} = \mathbf{0}$, $\delta\boldsymbol{L} = \mathbf{0}$ and $\delta\mathbf{M} = \mathbf{0}$ in Equation (7.53), and developing the remaining terms as shown next. The standard decomposition of the first term is repeated here:

$$\int_{\Omega_\mu} \boldsymbol{P}_\mu : \nabla_Y \delta\tilde{\boldsymbol{u}} dV = \int_{\partial\Omega_\mu} (\boldsymbol{P}\cdot\boldsymbol{N})\cdot\delta\tilde{\boldsymbol{u}} dA - \int_{\Omega_\mu} \operatorname{div}\boldsymbol{P}\cdot\delta\tilde{\boldsymbol{u}} dV. \tag{7.54}$$

Similarly, the second term is rewritten as:

$$\int_{\Omega_\mu} \mathbf{Q}_\mu \vdots \nabla_Y^s \delta\hat{\tilde{\boldsymbol{F}}} dV = \int_{\partial\Omega_\mu} (\mathbf{Q}\cdot\boldsymbol{N}) : \delta\hat{\tilde{\boldsymbol{F}}} dA - \int_{\Omega_\mu} \operatorname{div}\mathbf{Q} : \delta\hat{\tilde{\boldsymbol{F}}} dV. \tag{7.55}$$

Thereafter:

$$-\int_{\Omega_\mu} \boldsymbol{\lambda} : \nabla_Y \delta\tilde{\boldsymbol{u}} dV = -\int_{\partial\Omega_\mu} (\boldsymbol{\lambda}\cdot\boldsymbol{N})\cdot\delta\tilde{\boldsymbol{u}} dA + \int_{\Omega_\mu} \operatorname{div}\boldsymbol{\lambda}\cdot\delta\tilde{\boldsymbol{u}} dV. \tag{7.56}$$

The terms related to the micro-scale constraints are expressed as

$$-\boldsymbol{L} : \int_{\partial\Omega_\mu} \delta\tilde{\boldsymbol{u}} \otimes \boldsymbol{N} dA = -\int_{\partial\Omega_\mu} (\boldsymbol{L}\cdot\boldsymbol{N})\cdot\delta\tilde{\boldsymbol{u}} dA, \tag{7.57}$$

and

$$-\mathbf{M} \vdots \int_{\partial\Omega_\mu} \delta\hat{\tilde{\boldsymbol{F}}} \otimes \boldsymbol{N} dA = -\int_{\partial\Omega_\mu} (\mathbf{M}\cdot\boldsymbol{N}) : \delta\hat{\tilde{\boldsymbol{F}}} dA. \tag{7.58}$$

Finally, including these decompositions, the following expression arises:

$$\begin{aligned}\int_{\partial\Omega_\mu} (\boldsymbol{P}\cdot\boldsymbol{N} - \boldsymbol{\lambda}\cdot\boldsymbol{N} - \boldsymbol{L}\cdot\boldsymbol{N})\cdot\delta\tilde{\boldsymbol{u}} dA + \int_{\Omega_\mu} (-\operatorname{div}\boldsymbol{P} + \operatorname{div}\boldsymbol{\lambda})\cdot\delta\tilde{\boldsymbol{u}} dV + \\ \int_{\partial\Omega_\mu} (\mathbf{Q}\cdot\boldsymbol{N} - \mathbf{M}\cdot\boldsymbol{N}) : \delta\hat{\tilde{\boldsymbol{F}}} dA + \int_{\Omega_\mu} (-\operatorname{div}\mathbf{Q} + \boldsymbol{\lambda}) : \delta\hat{\tilde{\boldsymbol{F}}} dV = 0.\end{aligned} \tag{7.59}$$

Consequently, the strong equilibrium equations are given by

$$-\operatorname{div}\boldsymbol{P}_\mu + \operatorname{div}\boldsymbol{\lambda} = \mathbf{0}, \quad \text{in } \Omega_\mu \tag{7.60}$$

$$\boldsymbol{P}_\mu\cdot\boldsymbol{N} - \boldsymbol{L}\cdot\boldsymbol{N} - \boldsymbol{\lambda}\cdot\boldsymbol{N} = \mathbf{0}, \quad \text{on } \partial\Omega_\mu \tag{7.61}$$

$$-\operatorname{div}\mathbf{Q}_\mu + \boldsymbol{\lambda} = \mathbf{0}, \quad \text{in } \Omega_\mu \tag{7.62}$$

$$\mathbf{Q}_\mu\cdot\boldsymbol{N} - \mathbf{M}\cdot\boldsymbol{N} = \mathbf{0}, \quad \text{on } \partial\Omega_\mu. \tag{7.63}$$

7.2.4 Finite element solution

Discretisation of Equation (7.53) with mixed finite elements, as introduced in Section 4.4.2, leads to a problem that consists in finding $\tilde{\mathbf{u}}$, $\hat{\tilde{\mathbf{F}}}$, $\boldsymbol{\lambda}$, $\boldsymbol{L}$ and $\mathbf{M}$ such that the residual $\mathbf{r}$ vanishes:

$$\mathbf{r} = \begin{Bmatrix} \mathbf{r}^u \\ \mathbf{r}^F \\ \mathbf{r}^\lambda \\ \mathbf{r}^L \\ \mathbf{r}^M \end{Bmatrix} = \begin{Bmatrix} \mathbf{f}^u + \mathbf{k}^{u\lambda}\boldsymbol{\lambda} - \mathbf{C}_L^T\mathbf{L} \\ \mathbf{f}^F + \mathbf{k}^{F\lambda}\boldsymbol{\lambda} - \mathbf{C}_M^T\mathbf{M} \\ \mathbf{k}^{\lambda u}\tilde{\mathbf{u}} + \mathbf{k}^{\lambda F}\hat{\tilde{\mathbf{F}}} \\ \mathbf{C}_L\tilde{\mathbf{u}} \\ \mathbf{C}_M\hat{\tilde{\mathbf{F}}} \end{Bmatrix} = \mathbf{0}. \tag{7.64}$$

The constraint matrix $\mathbf{C}_L$ refers to the constraint of Equation (7.49), and is built as shown in Equations (3.40) and (3.41). Equation (7.51) is enforced through the constraint matrix $\mathbf{C}_M$, that in this case is defined by

$$\mathbf{C}_M = \left[\begin{array}{ccc:c} \left(\int H_1^F N_1 dA\right)\mathbf{I} & \mathbf{0} & \mathbf{0} & \cdots \\ \mathbf{0} & \left(\int H_1^F N_2 dA\right)\mathbf{I} & \mathbf{0} & \cdots \\ \mathbf{0} & \mathbf{0} & \left(\int H_1^F N_3 dA\right)\mathbf{I} & \cdots \\ \frac{1}{2}\left(\int H_1^F N_2 dA\right)\mathbf{I} & \frac{1}{2}\left(\int H_1^F N_1 dA\right)\mathbf{I} & \mathbf{0} & \cdots \\ \mathbf{0} & \frac{1}{2}\left(\int H_1^F N_3 dA\right)\mathbf{I} & \frac{1}{2}\left(\int H_1^F N_2 dA\right)\mathbf{I} & \cdots \\ \frac{1}{2}\left(\int H_1^F N_3 dA\right)\mathbf{I} & \mathbf{0} & \frac{1}{2}\left(\int H_1^F N_1 dA\right)\mathbf{I} & \cdots \end{array}\right] \tag{7.65}$$

for 3D RVEs and, for 2D problems:

$$\mathbf{C}_M = \left[\begin{array}{cc:c} \left(\int H_1^F N_1 dA\right)\mathbf{I} & \mathbf{0} & \cdots \\ \mathbf{0} & \left(\int H_1^F N_2 dA\right)\mathbf{I} & \cdots \\ \frac{1}{2}\left(\int H_1^F N_2 dA\right)\mathbf{I} & \frac{1}{2}\left(\int H_1^F N_1 dA\right)\mathbf{I} & \cdots \end{array}\right], \tag{7.66}$$

where H_i^F denotes the interpolation functions for the relaxed deformation gradient and N_i represents the components of the outward unit vector in the reference configuration. In the Newton-Raphson framework, the following linear system of equations, obtained through linearisation of the residual vector, must be solved for every iteration:

$$\begin{bmatrix} \mathbf{k}^{uu} & \mathbf{k}^{uF} & \mathbf{k}^{u\lambda} & -\mathbf{C}_L^T & \mathbf{0} \\ \mathbf{k}^{Fu} & \mathbf{k}^{FF} & \mathbf{k}^{F\lambda} & \mathbf{0} & -\mathbf{C}_M^T \\ \mathbf{k}^{\lambda u} & \mathbf{k}^{\lambda F} & \mathbf{0} & \mathbf{0} & \mathbf{0} \\ \mathbf{C}_L & \mathbf{0} & \mathbf{0} & \mathbf{0} & \mathbf{0} \\ \mathbf{0} & \mathbf{C}_M & \mathbf{0} & \mathbf{0} & \mathbf{0} \end{bmatrix}^{(k)} \begin{Bmatrix} \Delta\tilde{\mathbf{u}} \\ \Delta\hat{\tilde{\mathbf{F}}} \\ \Delta\boldsymbol{\lambda} \\ \Delta\mathbf{L} \\ \Delta\mathbf{M} \end{Bmatrix}^{(k+1)} = -\begin{Bmatrix} \mathbf{r}^u \\ \mathbf{r}^F \\ \mathbf{r}^\lambda \\ \mathbf{r}^L \\ \mathbf{r}^M \end{Bmatrix}^{(k)}. \tag{7.67}$$

The algorithm for the solution of the micro-scale problem with mixed finite elements is given in Box 7.1.

7.2.5 First Piola-Kirchhoff stress homogenisation

Expression (7.25) may be particularised for the case where the micro-scale problem is solved with mixed finite elements, taking into account that the strong form is defined by Equations (7.60)-(7.63). Starting from Expression (7.26), it may be rewritten as

$$\int_{\Omega_\mu} \boldsymbol{P}_\mu dV = \int_{\partial\Omega_\mu} (\boldsymbol{L}\cdot\boldsymbol{N} + \boldsymbol{\lambda}\cdot\boldsymbol{N}) \otimes \boldsymbol{Y} dA - \int_{\Omega_\mu} \operatorname{div}\boldsymbol{P}_\mu \otimes \boldsymbol{Y} dV. \tag{7.68}$$

The term related to $\boldsymbol{\lambda}$ is developed as follows:

$$\begin{aligned} \int_{\partial\Omega_\mu} (\boldsymbol{\lambda}\cdot\boldsymbol{N}) \otimes \boldsymbol{Y} dA &= \int_{\Omega_\mu} (\operatorname{div}\boldsymbol{\lambda} \otimes \boldsymbol{Y} + \boldsymbol{\lambda})\, dV = \int_{\Omega_\mu} (\operatorname{div}\boldsymbol{P} \otimes \boldsymbol{Y} + \operatorname{div}\mathbf{Q})\, dV = \\ &= \int_{\Omega_\mu} \operatorname{div}\boldsymbol{P} \otimes \boldsymbol{Y} dV + \int_{\partial\Omega_\mu} \mathbf{Q}\cdot\boldsymbol{N} dA = \int_{\Omega_\mu} \operatorname{div}\boldsymbol{P} \otimes \boldsymbol{Y} dV + \int_{\partial\Omega_\mu} \mathbf{M}\cdot\boldsymbol{N} dA. \end{aligned} \tag{7.69}$$

Considering that

$$\int_{\partial\Omega_\mu} \mathbf{M}\cdot\boldsymbol{N} dA = \mathbf{M}\cdot\int_{\partial\Omega_\mu} \boldsymbol{N} dA = \mathbf{0}, \tag{7.70}$$

and introducing this into Equation (7.68) results in

$$\int_{\Omega_\mu} \boldsymbol{P}_\mu dV = \boldsymbol{L}\cdot\int_{\partial\Omega_\mu} \boldsymbol{N}\otimes\boldsymbol{Y} dA = \boldsymbol{L}\cdot V_\mu, \tag{7.71}$$

thus, the Lagrange multiplier $\boldsymbol{L}$ recovers the homogenised first Piola-Kirchhoff stress tensor:

$$\boldsymbol{P} = \boldsymbol{L}. \tag{7.72}$$

Box 7.1 Algorithm to solve the micro-scale second-order problem with mixed finite elements.

1. Given the macro-scale deformation gradient $\boldsymbol{F}$ and second gradient $\mathbf{G}$, set the initial variables

$$\begin{aligned} k &:= 1 \\ \boldsymbol{u}_\mu^{(k)} &:= (\boldsymbol{F}-\boldsymbol{I})\cdot\boldsymbol{Y} + \frac{1}{2}\mathbf{G}:(\boldsymbol{Y}\otimes\boldsymbol{Y}) \\ \hat{\boldsymbol{F}}_\mu^{(k)} &:= \boldsymbol{F}+\mathbf{G}\cdot\boldsymbol{Y} \\ \tilde{\boldsymbol{u}}^{(k)} &:= \mathbf{0} \\ \hat{\tilde{\boldsymbol{F}}}^{(k)} &:= \mathbf{0} \\ \boldsymbol{\lambda}^{(k)} &:= \mathbf{0} \\ \boldsymbol{L}^{(k)} &:= \mathbf{0} \\ \mathbf{M}^{(k)} &:= \mathbf{0}. \end{aligned}$$

2. Compute the residual $\mathbf{r}^{(k)}$ and check convergence. If converged go to 5), else continue to 3).

3. Solve the linear system of equations (7.67).

4. Update the unknown variables

$$\begin{aligned} \boldsymbol{u}_\mu^{(k+1)} &:= \boldsymbol{u}_\mu^{(k)} + \Delta\tilde{\boldsymbol{u}}^{(k+1)} \\ \hat{\boldsymbol{F}}_\mu^{(k+1)} &:= \hat{\boldsymbol{F}}_\mu^{(k)} + \Delta\hat{\tilde{\boldsymbol{F}}}^{(k+1)} \\ \boldsymbol{\lambda}^{(k+1)} &:= \boldsymbol{\lambda}^{(k)} + \Delta\boldsymbol{\lambda}^{(k+1)} \\ \boldsymbol{L}^{(k+1)} &:= \boldsymbol{L}^{(k)} + \Delta\boldsymbol{L}^{(k+1)} \\ \mathbf{M}^{(k+1)} &:= \mathbf{M}^{(k)} + \Delta\mathbf{M}^{(k+1)} \\ k &:= k+1 \end{aligned}$$

   and go to 2).

5. Compute the homogenised stresses $\boldsymbol{P}$ and $\mathbf{Q}$.

7.2.6 Higher-order stress homogenisation

Regarding the homogenised higher-order stress tensor $\mathbf{Q}$, defined in terms of boundary integral in Equation (7.41), it is developed according to the strong equations for the mixed micro-equilibrium problem as follows:

$$\begin{aligned} \mathbf{Q} = &\frac{1}{2V_\mu}\int_{\partial\Omega_\mu}(\boldsymbol{L}\cdot\boldsymbol{N}+\boldsymbol{\lambda}\cdot\boldsymbol{N})\otimes\boldsymbol{Y}\otimes\boldsymbol{Y}\,dA + \\ &+\frac{1}{V_\mu}\int_{\partial\Omega_\mu}(\mathbf{M}\cdot\boldsymbol{N}\otimes\boldsymbol{Y})^S\,dA - \\ &-\frac{1}{2V_\mu}\int_{\partial\Omega_\mu}\mathrm{div}\,\mathbf{Q}_\mu\cdot\boldsymbol{N}\otimes\boldsymbol{Y}\otimes\boldsymbol{Y}\,dA. \end{aligned} \tag{7.73}$$

While the first term is null, as shown in Equation (7.43), the second term is rewritten as:

$$\frac{1}{2V_\mu}\int_{\partial\Omega_\mu}\lambda_{il}N_lY_jY_k\,dA = \frac{1}{2V_\mu}\int_{\Omega_\mu}\frac{\partial}{\partial Y_l}\left(\lambda_{il}Y_jY_k\right)dA = \frac{1}{2V_\mu}\int_{\Omega_\mu}\frac{\partial}{\partial Y_l}\left(\frac{\partial \mathrm{Q}_{ilm}}{Y_m}Y_jY_k\right)dA, \tag{7.74}$$

that nullifies the last term, as proven next:

$$-\frac{1}{2V_\mu}\int_{\partial\Omega_\mu}\frac{\partial \mathsf{Q}_{ilm}}{\partial Y_m}N_l Y_j Y_k\,dA=-\frac{1}{2V_\mu}\int_{\Omega_\mu}\frac{\partial}{\partial Y_l}\left(\frac{\partial \mathsf{Q}_{ilm}}{\partial Y_m}Y_j Y_k\right)dA. \tag{7.75}$$

Therefore

$$\mathbf{Q}=\frac{1}{V_\mu}\left(\mathbf{M}\cdot\int_{\partial\Omega_\mu}\boldsymbol{N}\otimes\boldsymbol{Y}\,dA\right)^S=\mathbf{M}, \tag{7.76}$$

i.e., the homogenised higher-order stress $\mathbf{Q}$ may be obtained directly from the Lagrange multiplier $\mathbf{M}$.

7.2.7 Macroscopic tangent operators

The homogenised tangent operators, needed in a FE^2 framework, are obtained following the strategy presented in Section 5.1.7, since the Lagrange multipliers recover the homogenised stresses.

Starting by the derivative of the microscopic residual with regard to the macroscopic deformation gradient:

$$\frac{\partial \mathbf{r}}{\partial \mathbf{F}}=\begin{bmatrix}\dfrac{\partial \mathbf{f}^u}{\partial \mathbf{F}}+\mathbf{k}^{u\lambda}\dfrac{\partial \boldsymbol{\lambda}}{\partial \mathbf{F}}-\mathbf{C}_L^T\dfrac{\partial \mathbf{L}}{\partial \mathbf{F}}\\ \dfrac{\partial \mathbf{f}^F}{\partial \mathbf{F}}+\mathbf{k}^{F\lambda}\dfrac{\partial \boldsymbol{\lambda}}{\partial \mathbf{F}}-\mathbf{C}_M^T\dfrac{\partial \mathbf{M}}{\partial \mathbf{F}}\\ \mathbf{k}^{\lambda u}\dfrac{\partial \tilde{\mathbf{u}}}{\partial \mathbf{F}}+\mathbf{k}^{\lambda F}\dfrac{\partial \hat{\tilde{\mathbf{F}}}}{\partial \mathbf{F}}\\ \mathbf{C}_L\dfrac{\partial \tilde{\mathbf{u}}}{\partial \mathbf{F}}\\ \mathbf{C}_M\dfrac{\partial \hat{\tilde{\mathbf{F}}}}{\partial \mathbf{F}}\end{bmatrix}=\mathbf{0}. \tag{7.77}$$

The derivatives of the internal forces may be manipulated as follows:

$$\begin{aligned}\frac{\partial \mathbf{f}^u}{\partial \mathbf{F}}&=\frac{\partial \mathbf{f}^u}{\partial \mathbf{u}}\frac{\partial \mathbf{u}}{\partial \mathbf{F}}+\frac{\partial \mathbf{f}^u}{\partial \hat{\mathbf{F}}_\mu}\frac{\partial \hat{\mathbf{F}}_\mu}{\partial \mathbf{F}}\\ &=\mathbf{k}^{uu}\cdot\left(\mathbf{D}^T+\frac{\partial \tilde{\mathbf{u}}}{\partial \mathbf{F}}\right)+\mathbf{k}^{uF}\cdot\left(\bar{\mathbf{I}}^T+\frac{\partial \hat{\tilde{\mathbf{F}}}}{\partial \mathbf{F}}\right),\end{aligned} \tag{7.78}$$

and

$$\begin{aligned}\frac{\partial \mathbf{f}^F}{\partial \mathbf{F}}&=\frac{\partial \mathbf{f}^F}{\partial \mathbf{u}}\frac{\partial \mathbf{u}}{\partial \mathbf{F}}+\frac{\partial \mathbf{f}^F}{\partial \hat{\mathbf{F}}_\mu}\frac{\partial \hat{\mathbf{F}}_\mu}{\partial \mathbf{F}}\\ &=\mathbf{k}^{Fu}\cdot\left(\mathbf{D}^T+\frac{\partial \tilde{\mathbf{u}}}{\partial \mathbf{F}}\right)+\mathbf{k}^{FF}\cdot\left(\bar{\mathbf{I}}^T+\frac{\partial \hat{\tilde{\mathbf{F}}}}{\partial \mathbf{F}}\right).\end{aligned} \tag{7.79}$$

due to the discretised versions of the insertion operators:

$$\mathbf{u}=\mathbf{u}_M+\mathbf{D}^T(\mathbf{F}-\{\mathbf{I}\})+\mathbf{V}^T\mathbf{G}+\tilde{\mathbf{u}}, \tag{7.80}$$

$$\hat{\mathbf{F}}_\mu=\bar{\mathbf{I}}^T\cdot\mathbf{F}+\mathbf{W}^T\cdot\mathbf{G}+\hat{\tilde{\mathbf{F}}}, \tag{7.81}$$

where the matrices $\mathbf{D}$ and $\mathbf{V}$ are defined in Equations (5.59) and (5.60), and $\bar{\mathbf{I}}$ and $\mathbf{W}$ are expressed

by:

$$\bar{\mathbf{I}} = \left[\begin{array}{cccc:c} 1 & 0 & 0 & 0 & \\ 0 & 1 & 0 & 0 & \cdots \\ 0 & 0 & 1 & 0 & \\ 0 & 0 & 0 & 1 & \end{array}\right], \tag{7.82}$$

$$\mathbf{W} = \left[\begin{array}{cccc:c} Y_1 & 0 & 0 & 0 & \\ 0 & Y_1 & 0 & 0 & \\ 0 & 0 & Y_2 & 0 & \cdots \\ 0 & 0 & 0 & Y_2 & \\ Y_2 & 0 & Y_1 & 0 & \\ 0 & Y_2 & 0 & Y_1 & \end{array}\right], \tag{7.83}$$

for 2D models, and adapted conveniently for 3D analysis. Consequently, Equation (7.77) may be rewritten as a linear system of equations:

$$\left[\begin{array}{ccccc} \mathbf{k}^{uu} & \mathbf{k}^{uF} & \mathbf{k}^{u\lambda} & -\mathbf{C}_L^T & \mathbf{0} \\ \mathbf{k}^{Fu} & \mathbf{k}^{FF} & \mathbf{k}^{F\lambda} & \mathbf{0} & -\mathbf{C}_M^T \\ \mathbf{k}^{\lambda u} & \mathbf{k}^{\lambda F} & \mathbf{k}^{\lambda\lambda} & \mathbf{0} & \mathbf{0} \\ \mathbf{C}_L^T & \mathbf{0} & \mathbf{0} & \mathbf{0} & \mathbf{0} \\ \mathbf{0} & \mathbf{C}_M^T & \mathbf{0} & \mathbf{0} & \mathbf{0} \end{array}\right] \cdot \left[\begin{array}{c} \dfrac{\partial \tilde{\mathbf{u}}}{\partial \mathbf{F}} \\ \dfrac{\partial \hat{\tilde{\mathbf{F}}}}{\partial \mathbf{F}} \\ \dfrac{\partial \boldsymbol{\lambda}}{\partial \mathbf{F}} \\ \dfrac{\partial \mathbf{L}}{\partial \mathbf{F}} \\ \dfrac{\partial \mathbf{M}}{\partial \mathbf{F}} \end{array}\right] = - \left[\begin{array}{cc} \mathbf{k}^{uu} & \mathbf{k}^{uF} \\ \mathbf{k}^{Fu} & \mathbf{k}^{FF} \\ \mathbf{0} & \mathbf{0} \\ \mathbf{0} & \mathbf{0} \\ \mathbf{0} & \mathbf{0} \end{array}\right] \cdot \left[\begin{array}{c} \mathbf{D}^T \\ \bar{\mathbf{I}}^T \end{array}\right]. \tag{7.84}$$

Following the same steps for the development of the derivative with regard to the second gradient:

$$\frac{\partial \mathbf{r}}{\partial \mathbf{G}} = \left[\begin{array}{c} \dfrac{\partial \mathbf{f}^u}{\partial \mathbf{G}} + \mathbf{k}^{u\lambda}\dfrac{\partial \boldsymbol{\lambda}}{\partial \mathbf{G}} - \mathbf{C}_L^T\dfrac{\partial \mathbf{L}}{\partial \mathbf{G}} \\ \dfrac{\partial \mathbf{f}^F}{\partial \mathbf{G}} + \mathbf{k}^{F\lambda}\dfrac{\partial \boldsymbol{\lambda}}{\partial \mathbf{G}} - \mathbf{C}_M^T\dfrac{\partial \mathbf{M}}{\partial \mathbf{G}} \\ \mathbf{k}^{\lambda u}\dfrac{\partial \tilde{\mathbf{u}}}{\partial \mathbf{G}} + \mathbf{k}^{\lambda F}\dfrac{\partial \hat{\tilde{\mathbf{F}}}}{\partial \mathbf{G}} \\ \mathbf{C}_L\dfrac{\partial \tilde{\mathbf{u}}}{\partial \mathbf{G}} \\ \mathbf{C}_M\dfrac{\partial \hat{\tilde{\mathbf{F}}}}{\partial \mathbf{G}} \end{array}\right] = \mathbf{0}, \tag{7.85}$$

it may be written in the form of a similar system of equations:

$$\left[\begin{array}{ccccc} \mathbf{k}^{uu} & \mathbf{k}^{uF} & \mathbf{k}^{u\lambda} & -\mathbf{C}_L^T & \mathbf{0} \\ \mathbf{k}^{Fu} & \mathbf{k}^{FF} & \mathbf{k}^{F\lambda} & \mathbf{0} & -\mathbf{C}_M^T \\ \mathbf{k}^{\lambda u} & \mathbf{k}^{\lambda F} & \mathbf{k}^{\lambda\lambda} & \mathbf{0} & \mathbf{0} \\ \mathbf{C}_L^T & \mathbf{0} & \mathbf{0} & \mathbf{0} & \mathbf{0} \\ \mathbf{0} & \mathbf{C}_M^T & \mathbf{0} & \mathbf{0} & \mathbf{0} \end{array}\right] \cdot \left[\begin{array}{c} \dfrac{\partial \tilde{\mathbf{u}}}{\partial \mathbf{G}} \\ \dfrac{\partial \hat{\tilde{\mathbf{F}}}}{\partial \mathbf{G}} \\ \dfrac{\partial \boldsymbol{\lambda}}{\partial \mathbf{G}} \\ \dfrac{\partial \mathbf{L}}{\partial \mathbf{G}} \\ \dfrac{\partial \mathbf{M}}{\partial \mathbf{G}} \end{array}\right] = - \left[\begin{array}{cc} \mathbf{k}^{uu} & \mathbf{k}^{uF} \\ \mathbf{k}^{Fu} & \mathbf{k}^{FF} \\ \mathbf{0} & \mathbf{0} \\ \mathbf{0} & \mathbf{0} \\ \mathbf{0} & \mathbf{0} \end{array}\right] \cdot \left[\begin{array}{c} \mathbf{V}^T \\ \mathbf{W}^T \end{array}\right]. \tag{7.86}$$

Both systems of equations may be combined, giving rise to the following:

$$\begin{bmatrix} \mathbf{k}^{uu} & \mathbf{k}^{uF} & \mathbf{k}^{u\lambda} & -\mathbf{C}_L^T & \mathbf{0} \\ \mathbf{k}^{Fu} & \mathbf{k}^{FF} & \mathbf{k}^{F\lambda} & \mathbf{0} & -\mathbf{C}_M^T \\ \mathbf{k}^{\lambda u} & \mathbf{k}^{\lambda F} & \mathbf{k}^{\lambda\lambda} & \mathbf{0} & \mathbf{0} \\ \mathbf{C}_L^T & \mathbf{0} & \mathbf{0} & \mathbf{0} & \mathbf{0} \\ \mathbf{0} & \mathbf{C}_M^T & \mathbf{0} & \mathbf{0} & \mathbf{0} \end{bmatrix} \cdot \begin{bmatrix} \frac{\partial \tilde{\mathbf{u}}}{\partial \mathbf{F}} & \frac{\partial \tilde{\mathbf{u}}}{\partial \mathbf{G}} \\ \frac{\partial \hat{\tilde{\mathbf{F}}}}{\partial \mathbf{F}} & \frac{\partial \hat{\tilde{\mathbf{F}}}}{\partial \mathbf{G}} \\ \frac{\partial \boldsymbol{\lambda}}{\partial \mathbf{F}} & \frac{\partial \boldsymbol{\lambda}}{\partial \mathbf{G}} \\ \frac{\partial \mathbf{L}}{\partial \mathbf{F}} & \frac{\partial \mathbf{L}}{\partial \mathbf{G}} \\ \frac{\partial \mathbf{M}}{\partial \mathbf{F}} & \frac{\partial \mathbf{M}}{\partial \mathbf{G}} \end{bmatrix} = - \begin{bmatrix} \mathbf{k}^{uu} & \mathbf{k}^{uF} \\ \mathbf{k}^{Fu} & \mathbf{k}^{FF} \\ \mathbf{0} & \mathbf{0} \\ \mathbf{0} & \mathbf{0} \\ \mathbf{0} & \mathbf{0} \end{bmatrix} \cdot \begin{bmatrix} \mathbf{D}^T & \mathbf{V}^T \\ \bar{\mathbf{I}}^T & \mathbf{W}^T \end{bmatrix}, \tag{7.87}$$

where the four tangents needed for the solution of macroscopic problem are found from the solution:

$$\mathbf{A} = \frac{\partial \mathbf{P}}{\partial \mathbf{F}} = \frac{\partial \mathbf{L}}{\partial \mathbf{F}}, \tag{7.88}$$

$$\mathbf{H}_F = \frac{\partial \mathbf{Q}}{\partial \mathbf{F}} = \frac{\partial \mathbf{M}}{\partial \mathbf{F}}, \tag{7.89}$$

$$\mathbf{A}_F = \frac{\partial \mathbf{P}}{\partial \mathbf{G}} = \frac{\partial \mathbf{L}}{\partial \mathbf{G}}, \tag{7.90}$$

$$\mathbf{H} = \frac{\partial \mathbf{Q}}{\partial \mathbf{G}} = \frac{\partial \mathbf{M}}{\partial \mathbf{G}}. \tag{7.91}$$

7.3 Preliminary numerical results

The fully 2nd-order multi-scale framework proposed in this chapter has been implemented in the finite element program LINKS. Several RVEs, whose constituents are described by the Mindlin's elastic model (see Section 4.5), are analysed in what follows. The macroscopic deformation history in terms of $\boldsymbol{F}$ and $\mathbf{G}$ that is obtained from position A (Figure 6.13) in the macro-scale bending beam problem presented in Section 6.5 is enforced to the RVEs.

7.3.1 Homogeneous RVEs

Two homogeneous RVEs with $l_{RVE} = 1.0$ mm and $l_{RVE} = 0.5$ mm are analysed in this section. Three different discretisations are employed, using 25, 100 and 400 quadrilateral Q8F4L1 mixed elements (see Figure 4.3). The elastic properties are defined by $E = 210$ GPa and $\nu = 0.3$. Two different values for the material characteristic length are considered: $l = 0.5$ mm and $l = 0.1$ mm. The micro-scale distributions of the equivalent stress and the norm of the higher-order stress are presented in Figures 7.1 and 7.2. The homogenised first Piola-Kirchhoff stresses and the most significant components of the homogenised higher-order stress tensor are presented in Tables 7.1 and 7.2.

7.3.2 RVEs with a void

A RVE model with a centred void ($f = 3\%$) is analysed in this section. The same RVE lengths and constitutive parameters employed in the homogeneous RVE example (previous section) are considered here. The resulting micro-scale distributions of the equivalent stress and the norm of the higher-order stress are shown in Figures 7.3 and 7.4. The homogenised first Piola-Kirchhoff stresses and the most significant components of the homogenised higher-order stress tensor are provided in Tables 7.3 and 7.4.

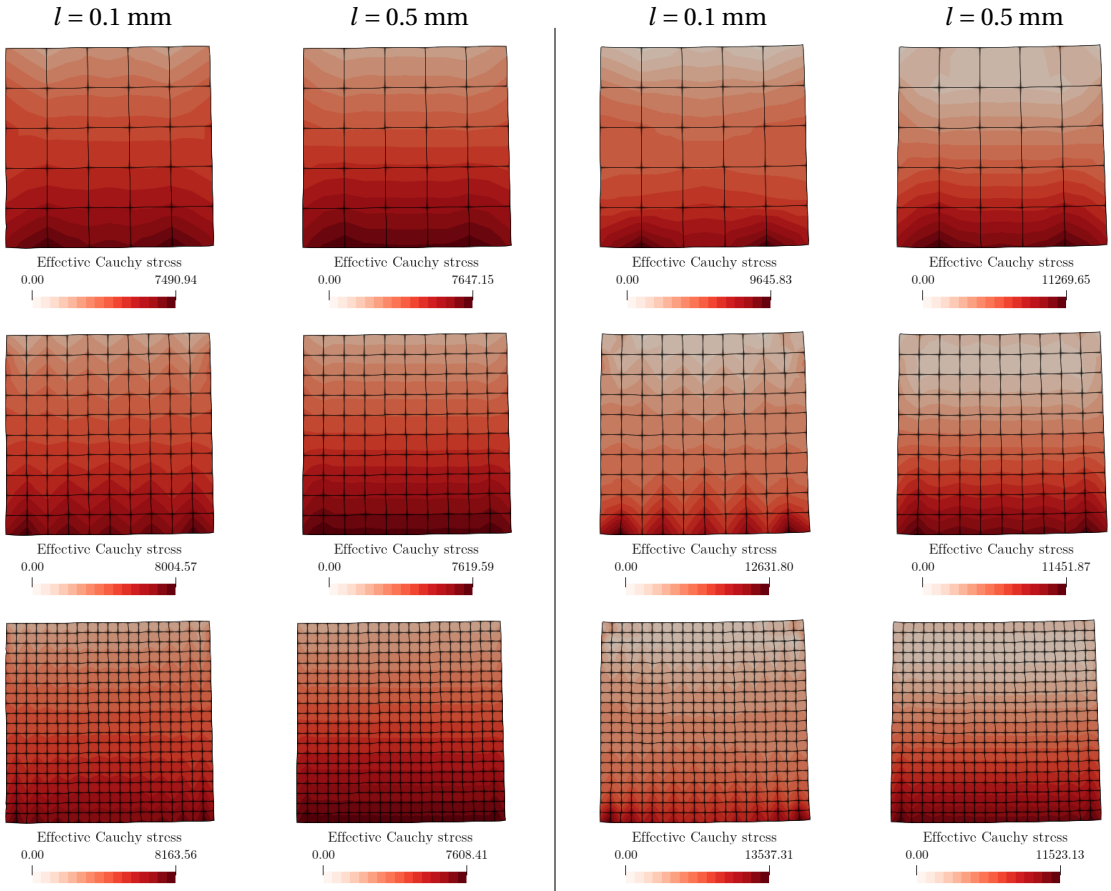

(a) l_{RVE} = 0.5 mm (b) l_{RVE} = 1.0 mm

Figure 7.1: Distribution of the equivalent stress on the deformed RVE meshes for the homogeneous RVE, with different discretisations, RVE lengths and material characteristic lengths.

7.3.3 RVEs with a rigid fibre

A RVE with a rigid fibre is analysed in this section. The elastic properties considered for the matrix and the fibre are presented in Table 6.1. Similarly to the previous examples, two different values are considered for the RVE length (l_{RVE}) and the micro-constituents characteristic length (l). The micro-scale distributions of the equivalent stress and the norm of the higher-order stress obtained in this case are represented in Figures 7.5 and 7.6. Both the homogenised first Piola-Kirchhoff stresses and the most significant components of the homogenised higher-order stress tensor are listed in Tables 7.5 and 7.6.

7.3.4 Discussion of the results

In general, looking at the micro-scale distribution of the equivalent stress (Figures 7.1, 7.3 and 7.5), it is observed that the equivalent stress tends to localise for the smallest value of l, spreading over a larger area when the largest value (l = 0.5 mm) is employed to model the microstructure. This reveals that the non-local nature of second-order continuum models is introduced at the micro-scale in this kind of models. The magnitude of the equivalent stress is not strongly affected by the characteristic material length in the case of the homogeneous RVE and the RVE with a void. However, in the RVE with an inclusion (Figure 7.5), the maximum equivalent stress increases due to the value of l. This is explained by the fact that the increased non-local effect generated by an higher value of l promotes larger deformations in the rigid inclusion, resulting in much larger stresses. When the smallest value of l = 0.1 mm is employed, most of the deformation is found in the matrix. The effect

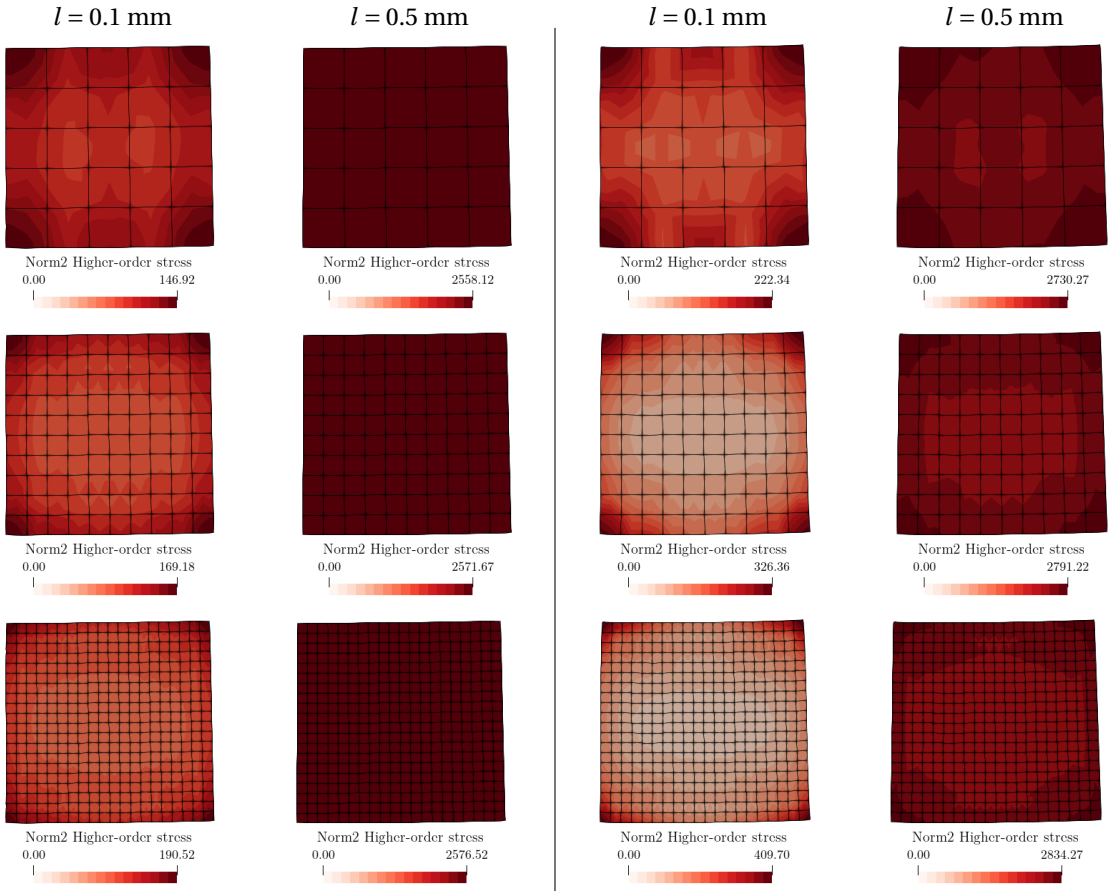

(a) $l_{RVE} = 0.5$ mm (b) $l_{RVE} = 1.0$ mm

Figure 7.2: Distribution of $\|\mathbf{Q}\|$ on the deformed RVE meshes for the homogeneous RVE, with different discretisations, RVE lengths and material characteristic lengths.

of the RVE length in the distribution of the equivalent stress is evident for the homogeneous RVE and the RVE with a void. The increase of the stresses with the RVE length l_{RVE} is due to insertion of the quadratic displacements, that are larger for a larger RVE, as discussed in Section 6.3.

In what refers to the distribution of the magnitude of the higher-order stresses in the RVE (Figures 7.2, 7.4 and 7.6), it tends to localise in the RVE corners when $l = 0.1$ mm is considered, showing a smoother distribution when the largest characteristic length $l = 0.5$ mm is employed. In the case where l coincides with the RVE length l_{RVE} for the homogeneous RVE, the norm of the higher-order stress tensor is constant in the RVE. The maximum value found in the RVE depends mainly on the value of the micro-constituents characteristic length l, as a consequence of the constitutive law employed.

Looking at the homogenised higher-order stress values, in Tables 7.2, 7.4 and 7.6, they increase with the RVE length as observed in the results of Chapter 6, but the most remarkable difference is the strong dependence on the characteristic length l. In fact, since the micro-scale values $\mathbf{Q}_\mu$ depend on the constituents characteristic length through the constitutive law, and $\mathbf{Q}_\mu$ is considered for the higher-order stress homogenisation (see Equation (7.32)), the value of l has an important weight in the resulting macro-scale second-order response.

It must be emphasized that the values of the symmetric Lagrange multiplier $\mathbf{M}$ are quite close to the corresponding values of the homogenised $\mathbf{Q}$, confirming the relation deduced in Equation (7.76). The values of the Lagrange multiplier $\boldsymbol{L}$, not shown here, match almost exactly the homogenised $\boldsymbol{P}$, verifying Equation (7.72).

Finally, it is found that the discretisation has an impact in the results (homogenised and micro-

Table 7.1: Homogenised first Piola-Kirchhoff stresses $\boldsymbol{P}$ [MPa] resulting from the homogeneous RVE subjected to the deformation history from a beam under bending, with different discretisations, RVE lengths and material characteristic lengths.

l_{RVE}	l	Mesh	P_{11}	P_{21}	P_{12}	P_{22}
0.5 mm	0.1 mm	25	3807.13	40.40	9.31	-859.13
		100	3810.03	40.43	9.31	-858.19
		400	3810.96	40.43	9.31	-857.97
	0.5 mm	25	3815.65	40.45	9.33	-856.57
		100	3816.11	40.45	9.34	-857.03
		400	3816.48	40.45	9.34	-857.10
1.0 mm	0.1 mm	25	3835.72	40.51	9.23	-839.19
		100	3864.87	40.82	9.12	-823.55
		400	3867.79	40.85	9.11	-822.57
	0.5 mm	25	3896.85	40.88	9.31	-815.75
		100	3900.81	40.90	9.34	-816.55
		400	3903.49	40.92	9.35	-816.45

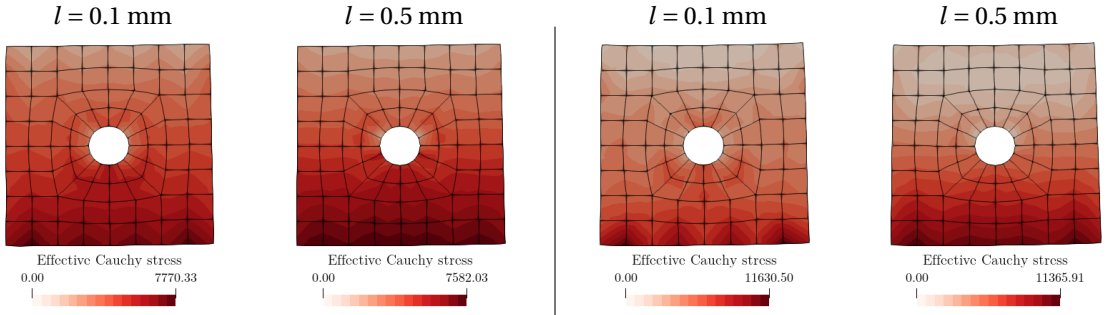

(a) l_{RVE} = 0.5 mm (b) l_{RVE} = 1.0 mm

Figure 7.3: Distribution of the equivalent stress on the deformed RVE meshes for the RVEs with a void, with different RVE lengths and material characteristic lengths.

scale) obtained with a homogeneous RVE, being more critical in the case where the characteristic length is smaller relatively to the RVE length. In fact, for this type of mixed elements, the mesh refinement must take into account the characteristic length, as discussed by Kouznetsova (2002). Moreover, in the present formulation the compatibility between the displacements gradient and the relaxed deformation gradient is not enforced on the boundary, which is an acceptable simplification as long as a sufficiently fine mesh is employed (Kouznetsova, 2002).

Table 7.2: Homogenised higher-order stresses $\mathbf{Q}$ [MPa mm] resulting from the homogeneous RVE subjected to the deformation history from a beam under bending, with different discretisations, RVE lengths and material characteristic lengths.

l_{RVE}	l	Mesh	Q_{211}	Q_{112}	Q_{222}	M_{211}	M_{112}	M_{222}
0.5 mm	0.1 mm	25	50.53	-128.36	67.27	50.39	-130.72	67.84
		100	49.54	-138.60	60.71	49.40	-140.95	61.17
		400	48.74	-142.88	58.12	48.62	-145.26	58.54
	0.5 mm	25	1077.09	-1095.51	1745.28	1077.02	-1098.11	1745.67
		100	1079.15	-1098.71	1741.18	1079.05	-1101.40	1741.53
		400	1079.48	-1100.49	1739.49	1079.37	-1103.21	1739.83
1.0 mm	0.1 mm	25	86.52	-264.92	99.42	85.83	-274.49	102.64
		100	69.75	-353.34	62.26	69.19	-361.84	64.19
		400	66.20	-368.38	55.57	65.67	-376.89	57.37
	0.5 mm	25	1090.20	-1427.02	1702.55	1089.75	-1437.28	1704.10
		100	1095.14	-1446.89	1683.29	1094.59	-1457.47	1684.64
		400	1094.80	-1458.80	1673.96	1094.25	-1469.55	1675.22

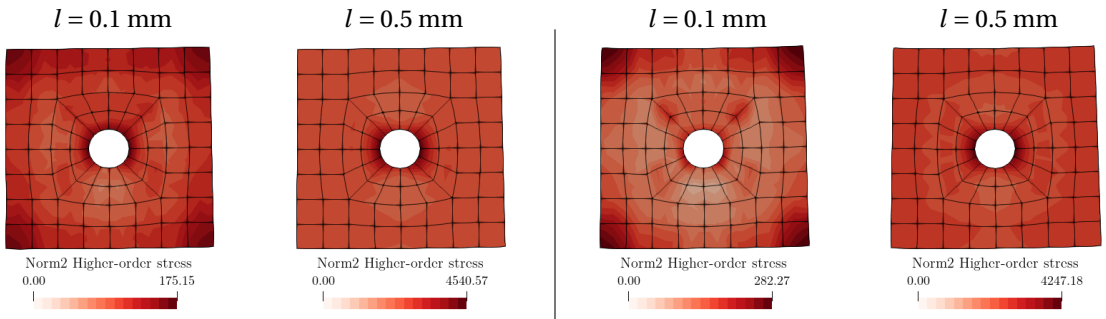

(a) $l_{RVE} = 0.5$ mm (b) $l_{RVE} = 1.0$ mm

Figure 7.4: Distribution of $\|\mathbf{Q}\|$ on the deformed RVE meshes for the RVEs with a void, with different RVE lengths and material characteristic lengths.

Table 7.3: Homogenised first Piola-Kirchhoff stresses $\boldsymbol{P}$ [MPa] resulting from the RVE with a void subjected to the deformation history from a beam under bending, with different RVE lengths and material characteristic lengths.

l_{RVE}	l	P_{11}	P_{21}	P_{12}	P_{22}
0.5 mm	0.1 mm	3652.09	38.75	9.05	-832.33
	0.5 mm	3684.56	39.04	9.10	-832.09
1.0 mm	0.1 mm	3658.23	38.64	8.86	-798.62
	0.5 mm	3763.86	39.40	9.13	-790.01

Table 7.4: Homogenised higher-order stresses $\mathbf{Q}$ [MPa mm] resulting from the RVE with a void subjected to the deformation history from a beam under bending, with different RVE lengths and material characteristic lengths.

l_{RVE}	l	Q_{211}	Q_{112}	Q_{222}	M_{211}	M_{112}	M_{222}
0.5 mm	0.1 mm	47.32	-134.98	59.02	47.20	-137.83	59.55
	0.5 mm	990.91	-1065.08	1567.57	991.89	-1070.24	1567.70
1.0 mm	0.1 mm	73.32	-324.94	73.72	72.66	-335.39	76.16
	0.5 mm	1005.18	-1420.93	1527.16	1005.59	-1434.66	1528.41

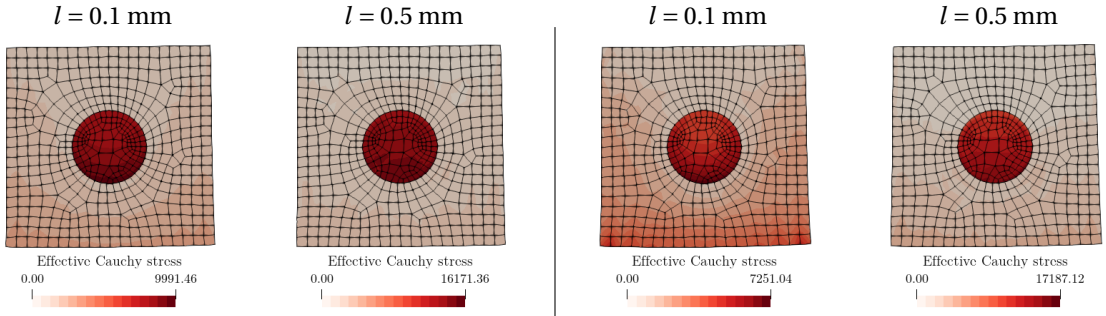

(a) $l_{RVE} = 0.5$ mm (b) $l_{RVE} = 1.0$ mm

Figure 7.5: Distribution of the equivalent stress on the deformed RVE meshes for the RVEs with a rigid fibre, with different RVE lengths and material characteristic lengths.

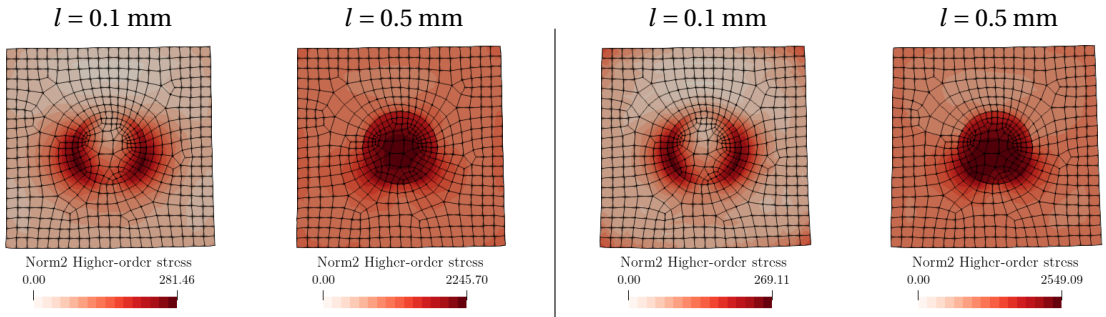

(a) $l_{RVE} = 0.5$ mm (b) $l_{RVE} = 1.0$ mm

Figure 7.6: Distribution of $\|\mathbf{Q}\|$ on the deformed RVE meshes for the RVEs with a rigid fibre, with different RVE lengths and material characteristic lengths.

Table 7.5: Homogenised first Piola-Kirchhoff stresses $\boldsymbol{P}$ [MPa] resulting from the RVE with a rigid fibre subjected to the deformation history from a beam under bending, with different RVE lengths and material characteristic lengths.

l_{RVE}	l	P_{11}	P_{21}	P_{12}	P_{22}
0.5 mm	0.1 mm	1948.97	20.58	4.85	-463.21
	0.5 mm	2403.37	25.04	5.47	-549.72
1.0 mm	0.1 mm	1715.62	18.00	3.92	-373.40
	0.5 mm	2323.49	23.64	4.86	-522.41

Table 7.6: Homogenised higher-order stresses **Q** [MPa mm] resulting from the RVE with a rigid fibre subjected to the deformation history from a beam under bending, with different RVE lengths and material characteristic lengths.

l_{RVE}	l	Q_{211}	Q_{112}	Q_{222}	M_{211}	M_{112}	M_{222}
0.5 mm	0.1 mm	19.16	-53.43	20.33	19.14	-53.53	20.17
	0.5 mm	429.46	-474.79	632.42	429.44	-475.74	632.55
1.0 mm	0.1 mm	24.49	-128.53	18.66	24.46	-129.72	18.76
	0.5 mm	437.43	-613.00	599.27	437.34	-616.39	599.63

7.4 Influence of the constituents size

Aiming to assess the capabilities of the present model to capture the influence of the constituents size on the homogenised response, the RVEs introduced in Section 6.5 are recalled here. The macroscopic deformation history observed at point A in Figure 6.13 is applied to the RVEs. In this case, only the RVEs with length $l_{RVE} = 0.828$ mm are analysed, with two different values of the fibres radius, as shown in Figure 7.7. The results are obtained with five realizations of each RVE configuration. The matrix and fibres are described by the Mindlin's elastic constitutive model, with the properties presented in Table 7.7. The characteristic length is defined to correspond to the fibres radius.

(a) $s_{RVE} = 16$ fibres
$r_f = 0.064$ mm

(b) $s_{RVE} = 64$ fibres
$r_f = 0.032$ mm

Figure 7.7: Representation of one realisation of each RVE configuration employed for the analysis of the fibres size influence.

Table 7.7: Material properties of the microscopic constituents.

	Matrix	Inclusions
Young modulus (E) [GPa]	30.0	72.4
Poisson ratio (ν)	0.3	0.2
Characteristic length (l)	r_f	r_f

The evolution of the homogenised stresses is presented in Figure 7.8.

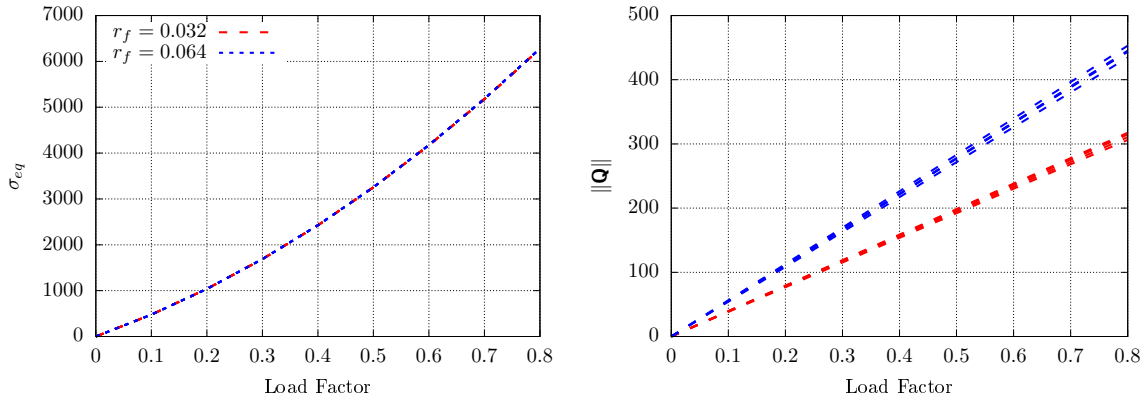

(a) Equivalent homogenised stress σ_{eq}

(b) Magnitude of the homogenised $\mathbf{Q}$

Figure 7.8: Evolution of the homogenised stresses.

7.4.1 Discussion of the results

Even though the equivalent homogenised stress (computed from the homogenised Piola-Kirchhoff) is not influenced by the constituents size, it is clearly demonstrated that the homogenised higher-order stress tensor depends on the fibres radius. The magnitude of the higher-order stress is higher for larger fibres, which is consistent with the fact that for larger constituents the scale separation is weaker, and therefore the second-order effects become more significant. Obviously these results are obtained mainly due to the chosen microscopic characteristic length, that is directly related to the fibres radius. Nevertheless, this is an admissible assumption.

The observations made here are in contrast with the results from Section 6.5. Therefore, whereas standard second-order homogenisation is not able to capture the influence of the constituents size, the fully second-order homogenisation scheme presented in this chapter is able to model this kind of size effects.

7.5 Multi-scale analysis of the boundary shear layer problem

The classical problem of the boundary shear layer, introduced in Section 4.6.3, is analysed here in a multi-scale FE^2 context, with the fully second-order homogenisation formulation. The 15 Q8F4L1 elements mesh is employed to discretise the macro-scale. At the micro-scale, the RVE shown in Figure 6.30a is employed, with the elastic properties presented in Table 6.19. The mixed elements Q8F4L1 are also employed to discretise the microstructure. Two different values of the RVE length are analysed by employing a scale factor to the RVE model (l_{RVE} = 0.5 mm and 1.0 mm), and three different values of the microscopic characteristic length are considered for each case: i) l = 0.05 mm, ii) l = 0.10 mm and iii) l = 0.5 mm.

The distribution of the deformation gradient component F_{12} along the macroscopic layer height is plotted in Figure 7.9, for each RVE length, and for the distinct micro-scale characteristic lengths.

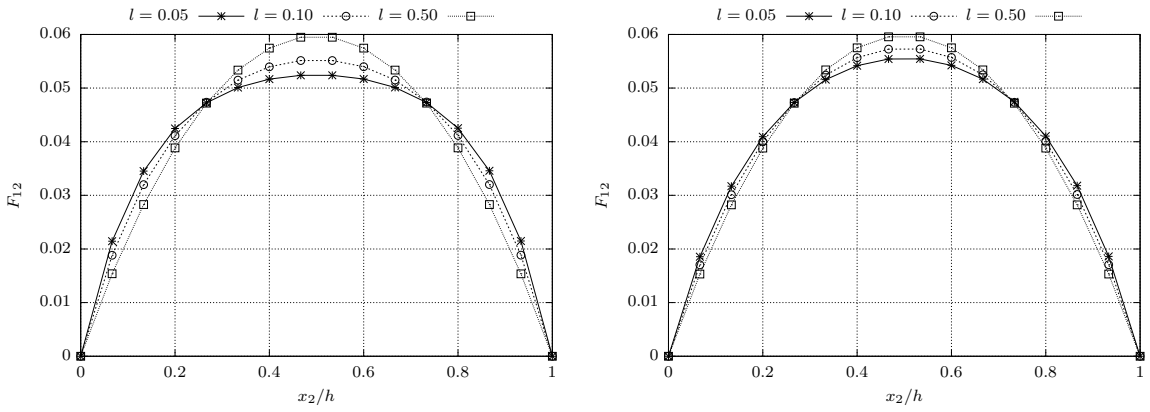

(a) l_{RVE} = 0.5 mm

(b) l_{RVE} = 1.0 mm

Figure 7.9: Distribution of the deformation gradient component F_{12}, along the layer height, in the fully second-order homogenisation FE^2 boundary shear layer problem.

7.5.1 Discussion of the results

As indicated by the preliminary results analysed in Section 7.3, the microscopic characteristic length plays a significant role on the resulting macroscopic second-order response. This is clearly observed when looking at the distribution of the deformation gradient shear component (Figure 7.9), as well as when the values of the higher-order stress magnitude are analysed (Figure 7.10). The influence of the micro-characteristic length is more evident for the smallest RVE length. At the micro-scale, for

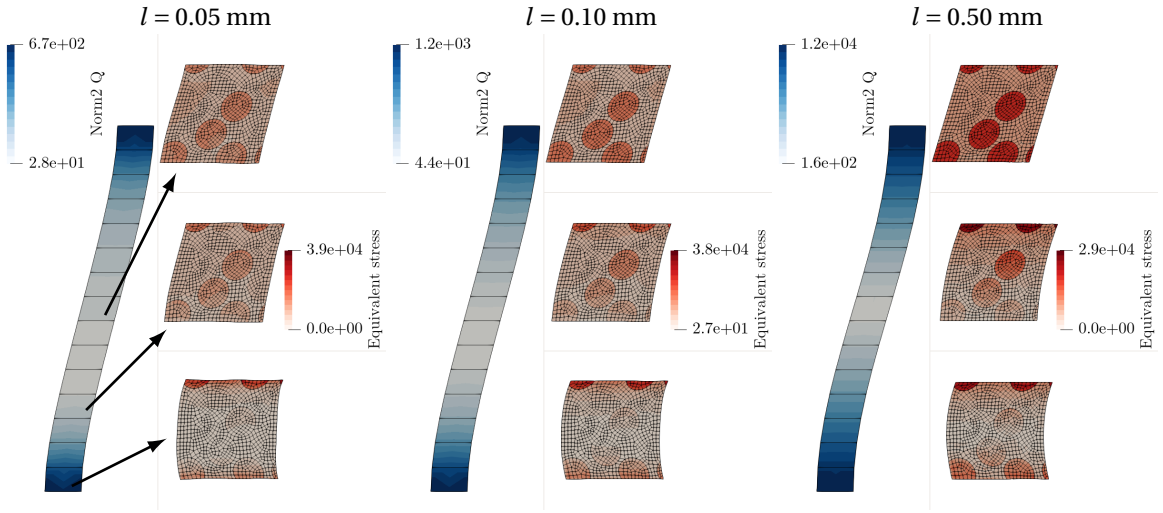

(a) l_{RVE} = 0.5 mm

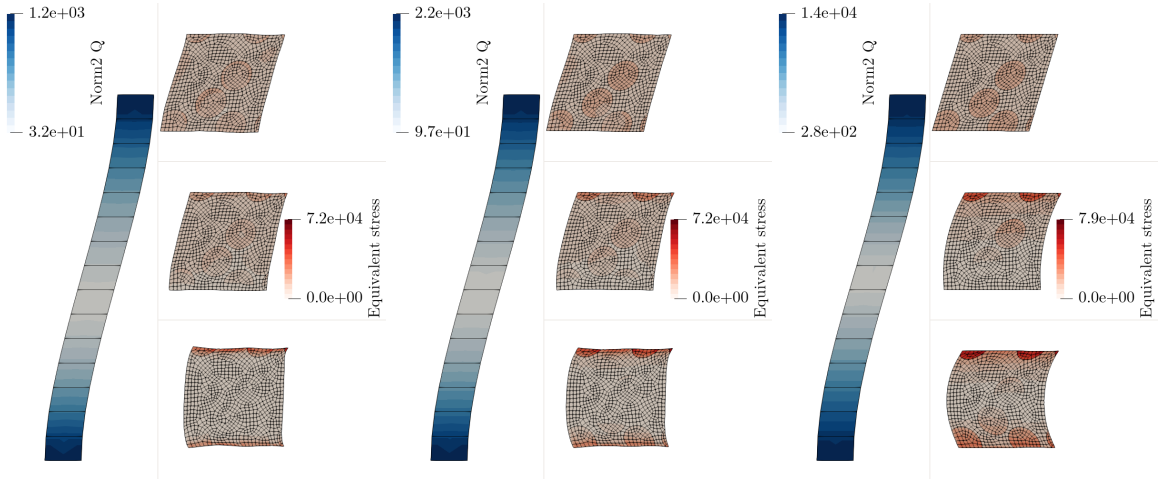

(b) l_{RVE} = 1.0 mm

Figure 7.10: Contour plots of the equivalent stress on the deformed meshes at the micro-scale, and the norm of the higher-order stress at the macro-scale, for the fully second-order homogenisation FE^2 simulation of the boundary shear layer problem, with different RVE lengths and micro-characteristic lengths.

the RVEs located near the bottom of the layer, the deformation tends to localise in narrower regions when the characteristic length decreases, due to the non-local nature of the formulation employed at the RVE level.

7.6 Conclusions

A fully second-order homogenisation formulation for finite strains has been developed in the present chapter, employing the method of multi-scale virtual power, where both the macro and the micro-scale material behaviour is modelled through a second gradient continuum theory. The micro-scale equilibrium problem is solved numerically with mixed finite elements, employing additional Lagrange multipliers to enforce the constraints defining the kinematic admissibility. It is possible to demonstrate that these Lagrange multipliers are directly related to the homogenised stresses $\boldsymbol{P}$ and $\mathbf{Q}$. Since, the resulting micro-scale constraints may be expressed exclusively as boundary conditions, volumetric constraints do not arise, and the issues related to RVEs with voids found for the standard second-order homogenisation (Section 6.4) are not encountered in the present formula-

tion.

The examples analysed in Section 7.3 show the non-local character introduced through the micro-constituents characteristic length, that also plays a major role in the homogenised response. These observations are also made in the FE^2 simulation presented in Section 7.5. The capability of the present model to capture size effects due to micro-constituents size is demonstrated in Section 7.4. Aiming to reduce the error associated with the micro-scale discretisation, mixed finite elements where the boundary compatibility is also enforced should be tested in a future implementation.

Chapter 8

A mixed parallel strategy for the solution of coupled multi-scale problems at finite strains

The computational cost associated with FE^2 multi-scale analysis is directly related to the high number of micro-analyses (Matsui et al., 2004, Smit et al., 1998). In fact, for each Newton-Raphson iteration at the macroscopic problem, the RVE problem attached to each macroscopic integration point must be solved. Parallel computing allows to take advantage of modern computer architectures, and alleviate the burden of the computational cost in multi-scale simulations. A mixed parallel strategy for the solution of FE^2 multi-scale analyses at finite strains, with possibly path dependent constitutive behaviour at the micro-scale, is presented in this chapter. It combines a non-conforming macro-domain decomposition method in the first parallelisation level, with a master-slave approach employed within each subdomain, for the second level.

In the first place, a master-slave scheme is introduced, where the basic task which is performed in parallel is the analysis of a macroscopic element, instead of distributing parallel work by macro-Gauss points. This includes the solution of the micro-scale equilibrium problem together with the homogenisation of the stress and tangent modulus for all Gauss points of the element. In addition, the element contributions for the internal force vector and tangent stiffness matrix are also computed. Therefore, the amount of work done in parallel is increased, and the number of communications is reduced. Dynamic scheduling is adopted for the distribution of macro-elements among available central processing units (CPUs), in order to minimise idling time. The performance of a stand-alone implementation of the proposed master-salve scheme is analysed. Its main drawback is related to memory requirements of the computer running the master process, that may become prohibitive as the multi-scale problem size increases, due to the underlying microscopic data.

The combination of the master-slave scheme with a macroscopic domain decomposition alleviates memory requirements through distribution of data among different machines. The resulting equilibrium problem is solved with an algorithm based on the FETI method (Farhat and Roux, 1991), that does not require iterative solvers as long as there are non-floating subdomains. The mortar method (Wohlmuth, 2001) is employed to deal with non-conforming meshes. Besides allowing an easier mesh generation for complex geometries, the possibility of employing a non-conforming mesh at the macro-scale may be used to reduce the computational cost, decreasing the number of macroscopic elements in certain zones, while maintaining an adequate refinement where it is needed. In order to equilibrate the workload distribution in this mixed parallel strategy, the number of slave CPUs working on each subdomain is adaptively defined according to the computational demand. This parallel strategy, which is implemented through the Message Passing Interface (MPI) standard, allows to run hierarchical multi-scale simulations in computers with either shared or distributed-memory architectures, from a multi-processor workstation to a *Beowulf*

cluster, within a reasonable time, and minimising hardware limitations.

8.1 A master-slave scheme

Since the micro-scale equilibrium problems are independent within each macro-iteration, a master-slave parallel algorithm naturally suits the nested algorithmic structure of coupled multi-scale analysis programs (Kouznetsova, 2002). Within this kind of approach, there is a master processor that deals with the global problem and distributes sub-problems among several slave processors, that can work in parallel. In the context of coupled multi-scale simulations, the master is responsible for the solution of the macro-equilibrium problem and distributes the macro-Gauss points among the slaves, that solve RVE equilibrium problems and perform homogenisation in parallel.

In the implementation of Matsui et al. (2004), the RVEs and the corresponding micro-data are assigned to distributed memory CPUs, with separate input/output devices. With this strategy, only the macroscopic deformation and homogenised stresses have to be transmitted between the master and the slaves. However, it strongly limits the architecture of the machines where the simulation program can be executed, and hampers the process of obtaining good workload balances, especially when elasto-plasticity is considered. In order to overcome this and achieve better speedups, the authors proposed a semi-dynamic assignment, where the RVEs are re-distributed over CPUs according to information from the first macro-increment. However, since non-linearities are more pronounced for large strain formulations and the computational effort related to each RVE evolves, a simple load balancing algorithm might not be able to achieve good workload balances.

Nguyen et al. (2012b) implemented a master-slave parallel algorithm where the RVEs state is stored in the master process. In spite of introducing extra communication, this allows a much more flexible implementation. The parallel distribution is made by cycles, where within each cycle one RVE is sent to each slave, that solves the micro-problem, and returns the results to the master. The master starts a new distribution cycle after all slaves have finished its analysis. The main drawback of this implementation is that a poor workload balance is obtained, due to differences on the RVE solution times on each cycle. When the number of slaves increases, the amount of idling time becomes significant, and poor performances are obtained. This implementation scales up to only 4 parallel processors. Rahul and De (2010) proposed a coarse-grained algorithm, within a matrix-free approach, aiming to minimise communication overheads in a master-slave framework. Scalability results are shown for linear elastic and hyperelastic micro-constituents.

In this section, a MPI (Message Passing Interface) based parallel master-slave implementation is proposed, suitable for either shared memory or distributed memory architectures, where the basic task of the parallel approach is the analysis of a macro-element instead of a macro-Gauss point. With this strategy, the amount of work done in parallel increases, and the number of communications between the master and the slaves is reduced. Aiming at a good workload balance, dynamic scheduling is adopted for the macro-elements parallel distribution among the processors, reducing the slaves idling time, even when machines with different specifications (CPU clock) are employed.

For each macroscopic iteration, the master starts by distributing one element to each of the available slaves, along with the needed data concerning the element displacements and underlying RVEs data (nodal coordinates, internal variables and stress state), as represented in the first block of Figure 8.1. When any of the slaves finishes its work, the master receives its output (element internal force vector and stiffness matrix), processes this data by assembling it to the global counterparts, and sends a new element to be analysed by this slave. Then it is ready to receive the output from the next slave, and repeats this process until all elements are analysed (second block of Figure 8.1). Since the master can receive the output of any slave, the slaves do not have to wait for each other to proceed with the analysis of a new element, resulting in higher parallel efficiencies.

The elements sorting is defined in each iteration by the corresponding analysis time. Then the elements requiring more computational effort are sent in the first place to the slaves. Since these

elements are more prone to cause an increment cutting, it is better to analyse them sooner rather than later in order to minimise unnecessary analysis time.

It is important to remark that with a parallel distribution by macro-elements (instead of macro-Gauss points), the granularity of the problem increases. The element-level routines to compute the deformation gradient at the macro-Gauss points, the element internal force vector and stiffness matrix are also done in parallel at the slaves, in addition to the solution of the microscopic RVE analysis. This notably reduces the work that has to be performed by the master sequentially, hence increasing the expected speedup.

The main disadvantage of this implementation is related to the storage of all RVE data, that is centralised in the master process. In spite of allowing a dynamic scheduling, memory requirements for the master process may be prohibitive when large FEM models are employed.

8.2 Numerical examples with the master-slave scheme

In the present section, scalability studies are presented to assess the parallel efficiency of the proposed master-slave algorithm. In the first example, the microstructure is modelled considering a linear elastic behaviour of the constituents at the local level. The second example illustrates a problem, which has a small number of elements at the macro-scale, but inelastic behaviour is considered at the micro-scale. The objective is to change the amount of computational work that needs to be done at each scale. The multi-scale simulations are performed with both linear and periodic boundary conditions, in a first-order homogenisation framework. All the results presented here, involving computing time measures, were analysed on our computing machine *Atlanticus*, which has two Intel Xeon E5-2650 v4 (2.20 GHz) processors, with a total of 24 physical cores, 128 GB of RAM DDR4, and operates the Ubuntu 16.04 64-bit operating system. The program was compiled with the GNU Fortran compiler, linked with *MPICH* MPI library.

In order to keep this contribution self-contained, some concepts related to scalability analysis are described here. The speedup obtained with n parallel processors, S_n, is obtained as the ratio between the sequential, t_1, and parallel, t_n, computing times:

$$S_n = \frac{t_1}{t_n}. \tag{8.1}$$

The ideal situation is achieved when the speedup value is equal to the number of processors, i.e.,

$$S_n = n \Rightarrow t_n = \frac{t_1}{n}. \tag{8.2}$$

Then, the parallel efficiency is computed as

$$E_n = \frac{S_n}{n}. \tag{8.3}$$

It is noteworthy to mention that Amdahl's law states that the speedup that can be achieved is limited by the share of computing time that can be done in parallel, p:

$$t_1 = p \times t_1 + (1-p)\, t_1. \tag{8.4}$$

In this case, the expected wallclock time with n parallel processors is

$$t_n = \frac{p \times t_1}{n} + (1-p)\, t_1, \tag{8.5}$$

therefore the speedup is limited to

$$S_n = \frac{1}{p/n + 1 - p}. \tag{8.6}$$

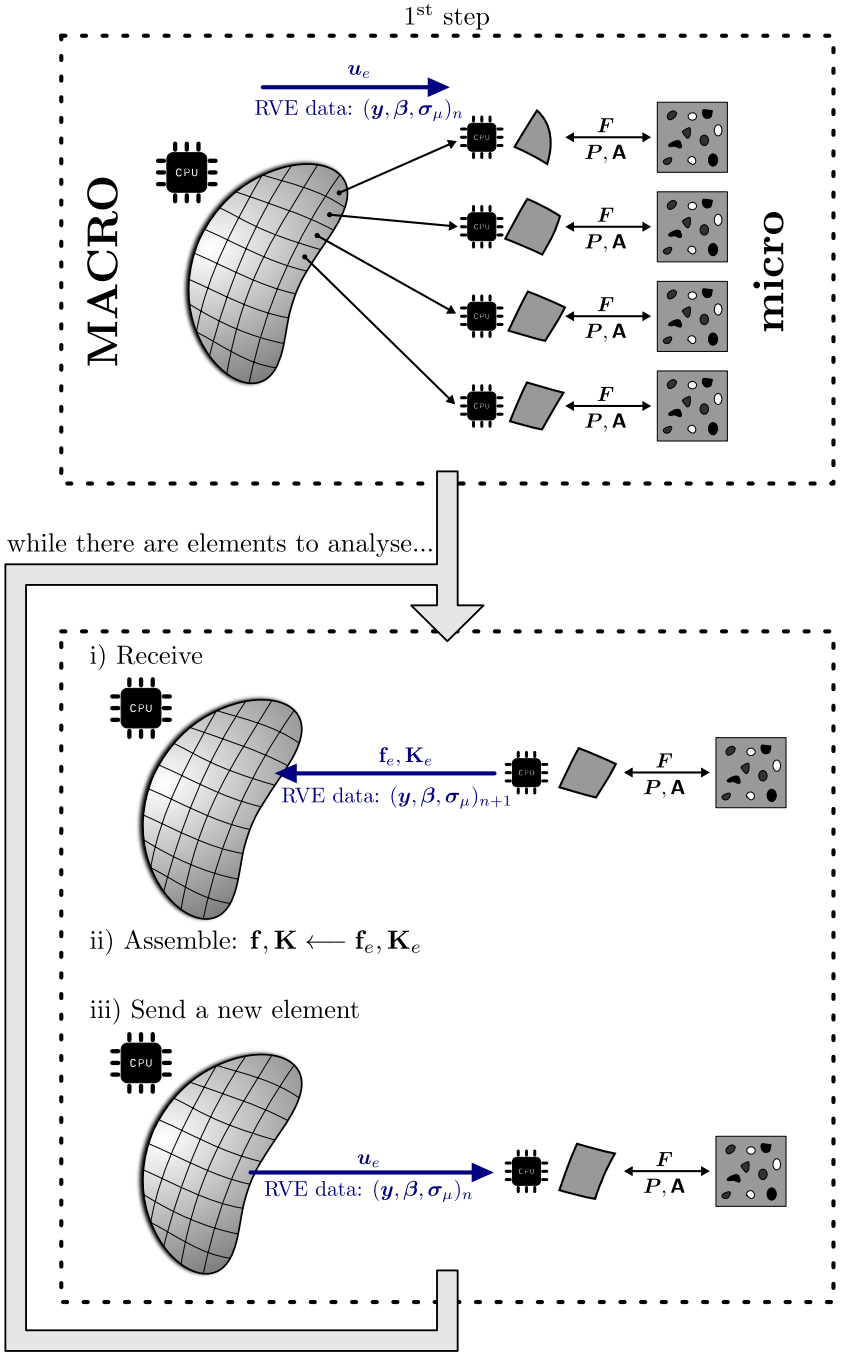

Figure 8.1: Schematic representation of master-slave algorithm with dynamic scheduling. Firstly, the elements are sent to available slaves. Then, when a slave finishes, i) the master receives the results and updates data, ii) assembles to the global macro-problem variables and iii) sends a new element to that slave.

Table 8.1: Elastic material properties for the matrix of the butterfly specimen microstructure.

material	von Mises
E (GPa)	210
ν	0.3

8.2.1 Butterfly specimen

In this example, the three-dimensional (3D) butterfly specimen represented in Figure 8.2a is analysed with the parallel strategy presented in Section 8.1. Due to the symmetry relatively to the xy plane, the finite element model considers only one half of the specimen. The discretisation is shown in Figure 8.2b, where 576 20-noded hexahedral elements with reduced integration have been used, yielding a mesh with 3,589 nodes. A vertical displacement $u = 0.54$ mm is imposed to the nodes on the top surface of the specimen, in 20 equally spaced increments. For this problem, there are $576 \times 8 = 4,608$ micro-scale boundary value problems to solve at each macroscopic Newton-Raphson iteration. The microstructure is modelled through a cubic RVE of size $d = 10$ μm, with a spherical void occupying 0.1% of the volume. It is discretised with 1,504 elements of the same type employed at the macro-scale, resulting in a mesh with 7,020 nodes (see Figure 8.3). Therefore, this multi-scale model generates more than 97×10^6 degrees of freedom. The matrix material behaviour is modelled with a linear elastic law extended to finite strains through the well-known hyperelastic-based multiplicative framework (de Souza Neto et al., 2008, Perić et al., 1992, Simo and Hughes, 1998, Simo et al., 1985, Weber and Anand, 1990), with the properties presented in Table 8.1.

It is important to emphasize that even though the physical size of the RVE is assumed to be much smaller than the size of the structure, as stated in Section 3.2, within a 1$^{\text{st}}$-order homogenisation scheme the homogenised results are independent of the absolut size of the RVE finite element model, but depend on the relative proportions of the micro-constituents.

The evolution of the reaction force in y-direction is plotted in Figure 8.4. In Figure 8.5, the distribution of the macroscopic equivalent von Mises stress is shown. The microscopic equivalent von Mises stress distribution in a RVE on element G, defined in Figure 8.2b, is presented in Figure 8.6.

The wallclock time obtained in the solution of the 1$^{\text{st}}$ incremental step with different number of slaves is plotted in Figure 8.7, along with the speedup and parallel efficiency. The evolution of the time with the number of CPUs is similar in both linear and periodic boundary conditions. Significant time reductions are observed when parallel computing is employed, in comparison with the sequential case, which is recovered when only 1 slave is employed. The speedup evolves almost linearly up to 16 slaves, with a slope slightly lower than the ideal case. The speedup values are marginally higher for the linear boundary condition, but the scalability trend is similar. With 16 slaves a speedup of 13.7 and 14.6 times is obtained for each boundary condition, which corresponds to efficiencies of ~ 85% and ~ 91%. A small drop is observed in the parallel efficiency when the number of slaves increases. A tracing tool was employed to investigate this fact. It was observed that the source of parallel inefficiency lies mainly on the synchronisation that inevitably occurs at the end of each macroscopic iteration. Since some slaves finish their last analysed element faster than others, the master (and finished slaves) have to wait for the slowest slave to finish before the master can solve the macroscopic boundary problem. However, the fact that macro-element analyses are sorted according to decreasing computation time, results in reduced waiting times at the end of the macroscopic iteration.

This drop in the parallel efficiency is more evident when using 24 slaves, which is when the computer is at full charge. This additional loss of performance is caused by the operating system background processes that consume resources. In spite of this, interesting speedup values are obtained, between 18 and 19.7 times, with a parallel efficiency around ~ 75% to ~ 82%.

The potential of the current implementation is highlighted by the significant time savings that

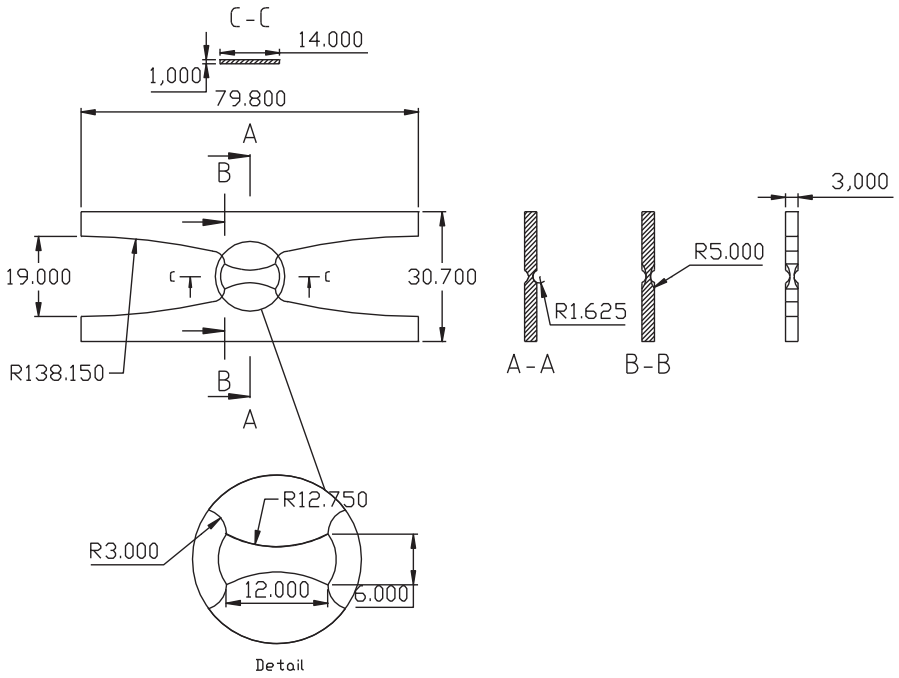

(a)

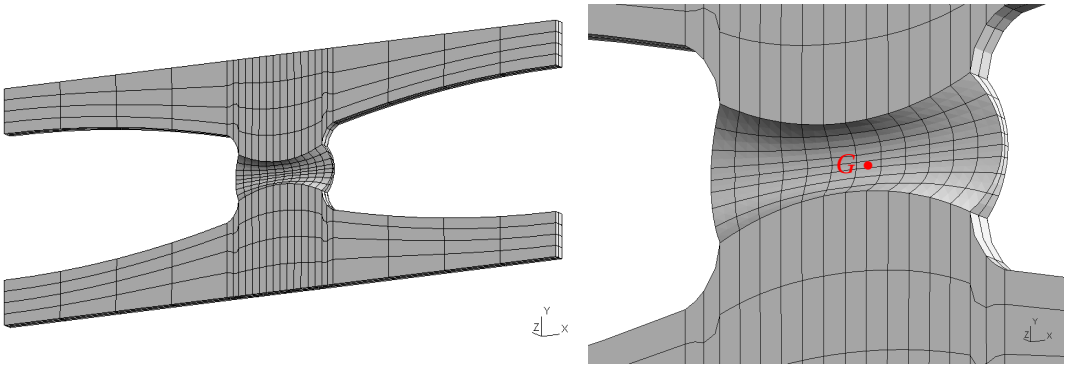

(b)

Figure 8.2: (a) Geometry and dimensions (Bai, 2008, Malcher, 2012) and (b) discretisation of the butterfly specimen, with detail of the necking region.

are achieved within the present multi-scale simulation. In the following example, dissipative constitutive behaviour is introduced at the micro-scale.

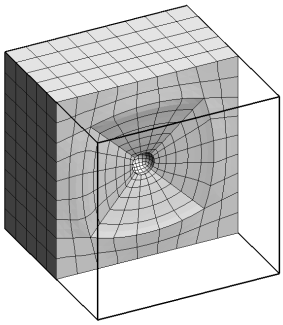

Figure 8.3: Section of the mesh used in the cubic RVE with a spherical void ($f = 0.1\%$).

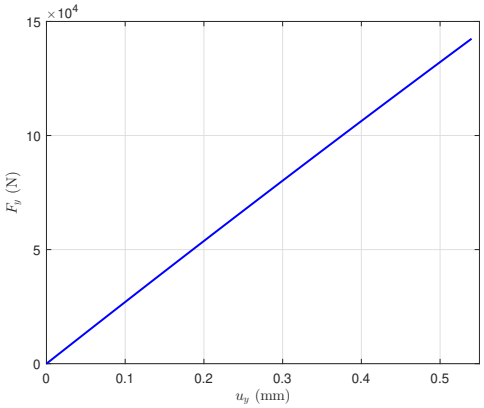

Figure 8.4: Vertical reactions in the 3D Butterfly specimen, subjected to a traction load, obtained from the multi-scale simulation.

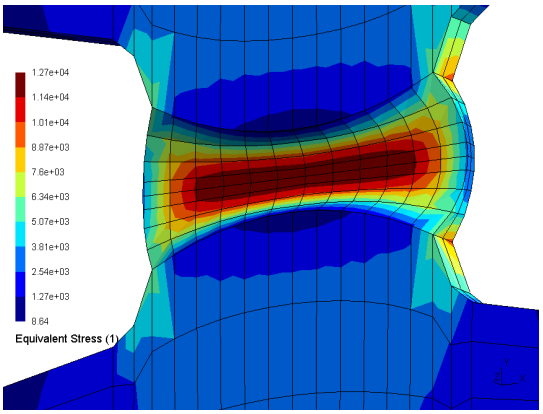

Figure 8.5: Contour plot of the von Mises equivalent stress in the deformed mesh of the 3D Butterfly specimen, when $u = 0.54$ mm.

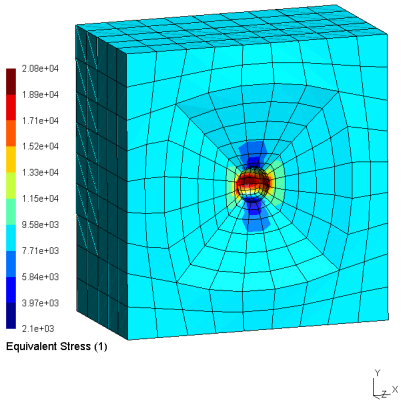

Figure 8.6: Contour plot of the von Mises equivalent stress in a RVE on the element G, defined in Figure 8.2b, when $u = 0.54$ mm.

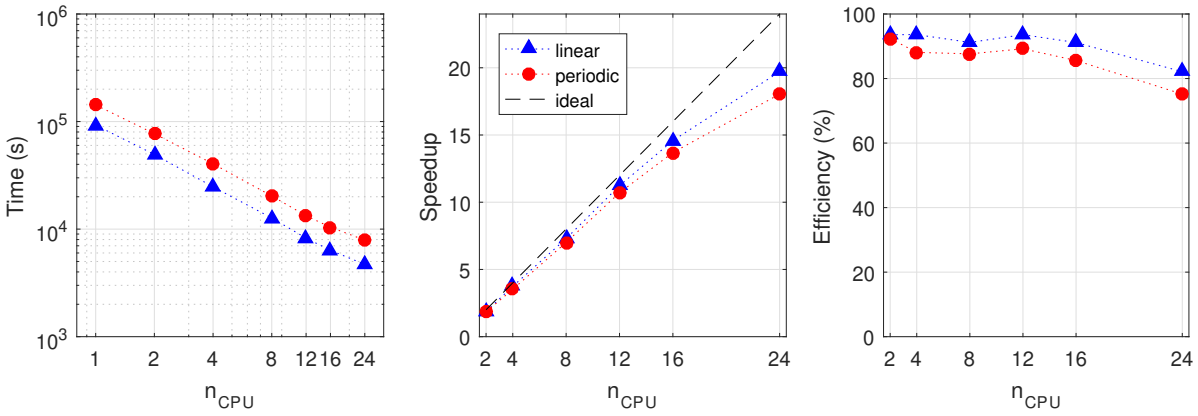

Figure 8.7: Time to solve one increment of the multi-scale 3D butterfly specimen problem, using a different number of slave CPUs with the master-slave parallel scheme (left), along with the corresponding speedup (middle) and parallel efficiency (right).

8.2.2 3D Uniaxial specimen

In this example, the multi-scale simulation of the traction of a 3D cylindrical uniaxial specimen with a notch of radius $R = 4$ mm is performed. The geometry of the macro-domain is shown in Figure 8.8a. Due to symmetry, only one eighth of the domain has to be modelled, as presented in Figure 8.8b. A total of 352 20-noded hexahedral elements (with reduced integration - 8 Gauss points) are employed, resulting in a mesh with 1,877 nodes. Therefore, $352 \times 8 = 2{,}816$ micro-scale boundary value problems have to be solved at each macroscopic Newton-Raphson iteration. A displacement of 1.1 mm is applied to the top surface of the specimen in 20 equally spaced incremental loads. The micro-scale geometric model is the same used in the previous example. Hence, almost 60×10^6 multi-scale degrees of freedom exist in this problem. However, non-linear material behaviour is considered at the micro-scale in this example. The matrix constitutive response is described by the elasto-plastic von Mises model, with the properties of the Aluminium 2024-T351 presented in Table 8.2 and the hardening curve plotted in Figure 8.9 (Bao and Wierzbicki, 2004, Malcher, 2012).

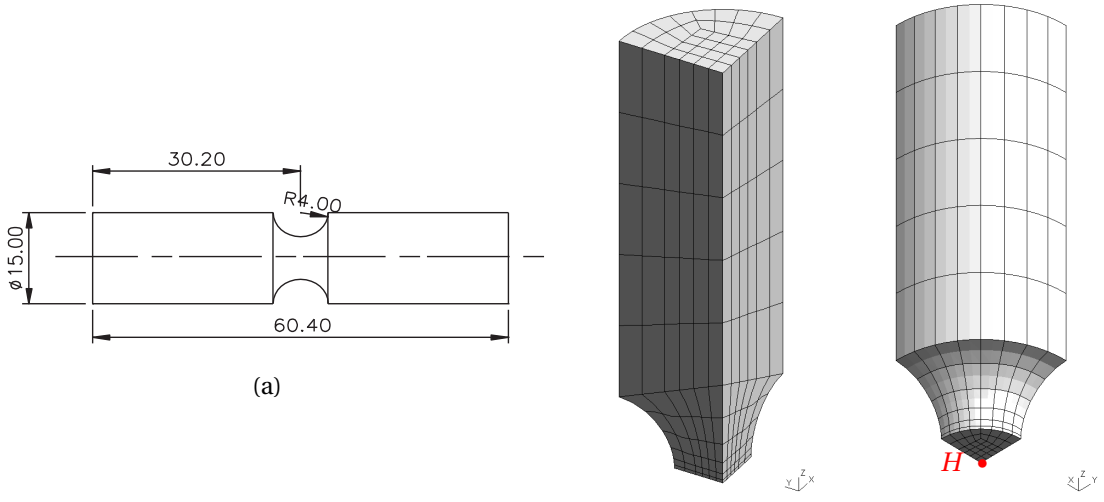

(a) (b)

Figure 8.8: (a) Geometry and dimensions (in mm) and (b) discretisation of the notched cylindrical uniaxial specimen.

The reaction force in the load direction is plotted against the applied displacement in Figure 8.10. The macroscopic distribution of equivalent von Mises stress is shown in Figure 8.11, when $u = 0.66$ mm. The deformed RVE corresponding to a RVE in element H represented in Figure 8.8b, at the same instant, is shown in Figure 8.12, where the microscopic fields of the equivalent stress and accumulated plastic strain are plotted.

For this example, the timing is also analysed with different number of slave processes. Since the trend observed with either linear or periodic boundary condition is similar to the previous example, only the latter is presented in the analyses that follow. In order to assess the influence of the extra degree of non-linearity introduced by the microstructure dissipative behaviour, the wallclock

Table 8.2: Material properties of the aluminium 2024-T351 (Bao and Wierzbicki, 2004, Malcher, 2012).

material	von Mises
E (GPa)	72.4
ν	0.3
σ_{y0} (MPa)	352

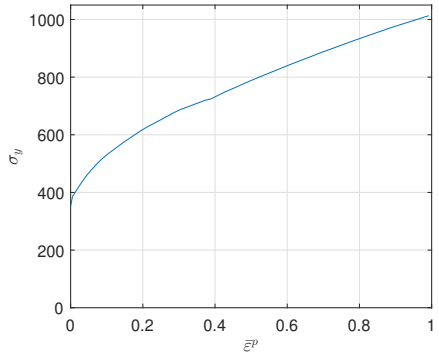

Figure 8.9: Hardening curve of the aluminium 2024-T351 - stress in MPa (Bao and Wierzbicki, 2004, Malcher, 2012).

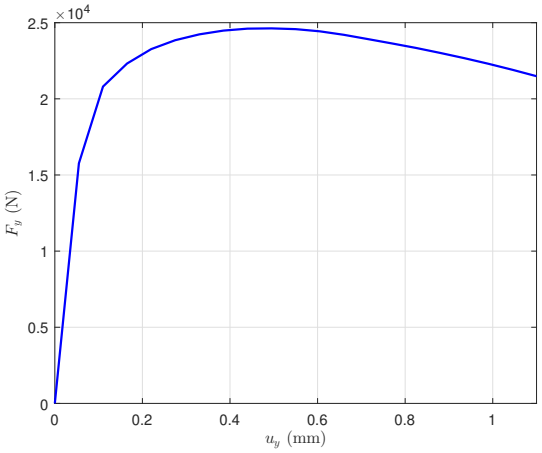

Figure 8.10: Vertical reactions in the 3D cylindrical notched specimen obtained from the multi-scale simulation.

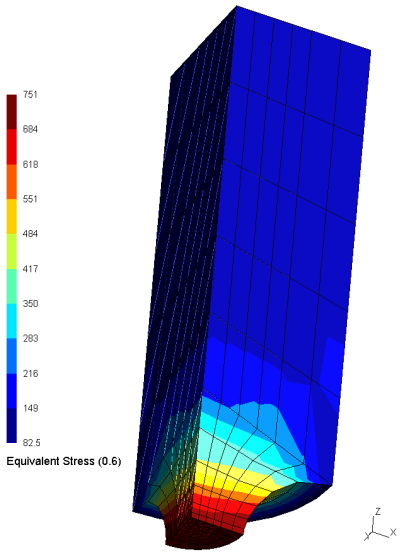

Figure 8.11: Contour plot of the von Mises equivalent stress, in the deformed mesh of the 3D uniaxial specimen, for $u = 0.66$ mm.

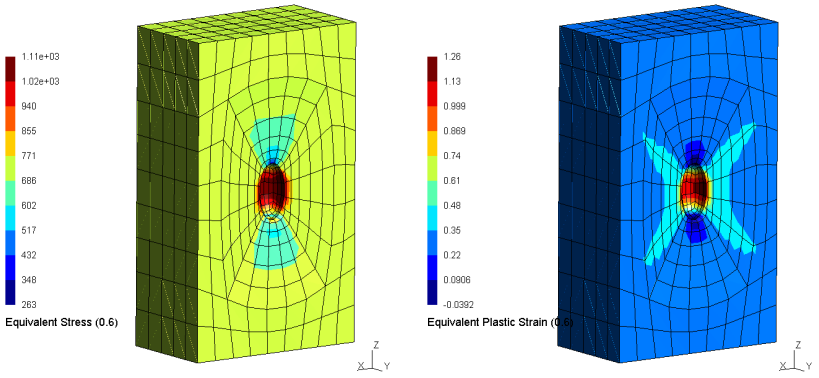

(a) (b)

Figure 8.12: Contour plot of (a) the von Mises equivalent stress and (b) accumulated plastic strain in the deformed mesh of a RVE on element H, defined in Figure 8.8b, for $u = 0.66$ mm.

time is plotted, along with the corresponding speedup and parallel efficiency, for the 1st and the 5th increment in Figure 8.13.

The timing evolution with an increasing number of slaves follows a trend similar to the observed in the butterfly specimen example. However, the speedup is much closer to the ideal case, which is reflected by parallel efficiencies close to 100%, especially in the 1st increment. Even for the 5th increment, where non-linearities are more pronounced, efficiencies above 92% are obtained up to 16 slaves. A drop is observed when using 24 slaves, by the same reasons presented in Section 8.2.1.

The higher speedups obtained in this simulation are explained by the higher ratio between micro and macro-analysis computational cost. Here, since the number of macro elements is lower, less communications are required between master and slaves, minimising communication and synchronisation overheads. Moreover, since the computational effort for RVE simulations is heavier, the amount of parallel computing time increases, and higher speedups are possible according to Amdahl's law. By employing a tracing tool, it was possible to observe that dynamic scheduling for the distribution of work among slaves returns a very good workload balance. It was also observed that the main source of parallel inefficiency is related to synchronisation overheads at the end of macroscopic iterations which, in this simulation, have a more reduced impact in the overall performance.

8.3 A non-conforming domain decomposition method

In order to overcome the main disadvantage of a single master-slave scheme for FE² simulations, a non-conforming macro-domain decomposition method is introduced in this section, to split the computational effort and memory requirements of multi-scale analysis among different processors/computers.

Feyel and Chaboche (2000) employed the FETI domain decomposition method to perform parallel computing on multi-scale simulations. The standard FETI method deals with conforming discretisations on the interface (Farhat and Roux, 1991, Rheinbach, 2009). Nevertheless, it may be interesting to allow for discretisations with non-matching meshes at the interface. For example, when dealing with macro-structures with complex geometries, an independent meshing of different structural parts, that is likely to result in non-conforming interfaces, facilitates the discretisation process. In addition, the modelling of multi-physics problems, like fluid-solid interaction, usually generates non-conforming discretisations at the interfaces.

Furthermore, even for relatively simple macro-models, whenever mesh refinement is needed on a specific part of the domain, a standard conforming discretisation leads to an increasing number

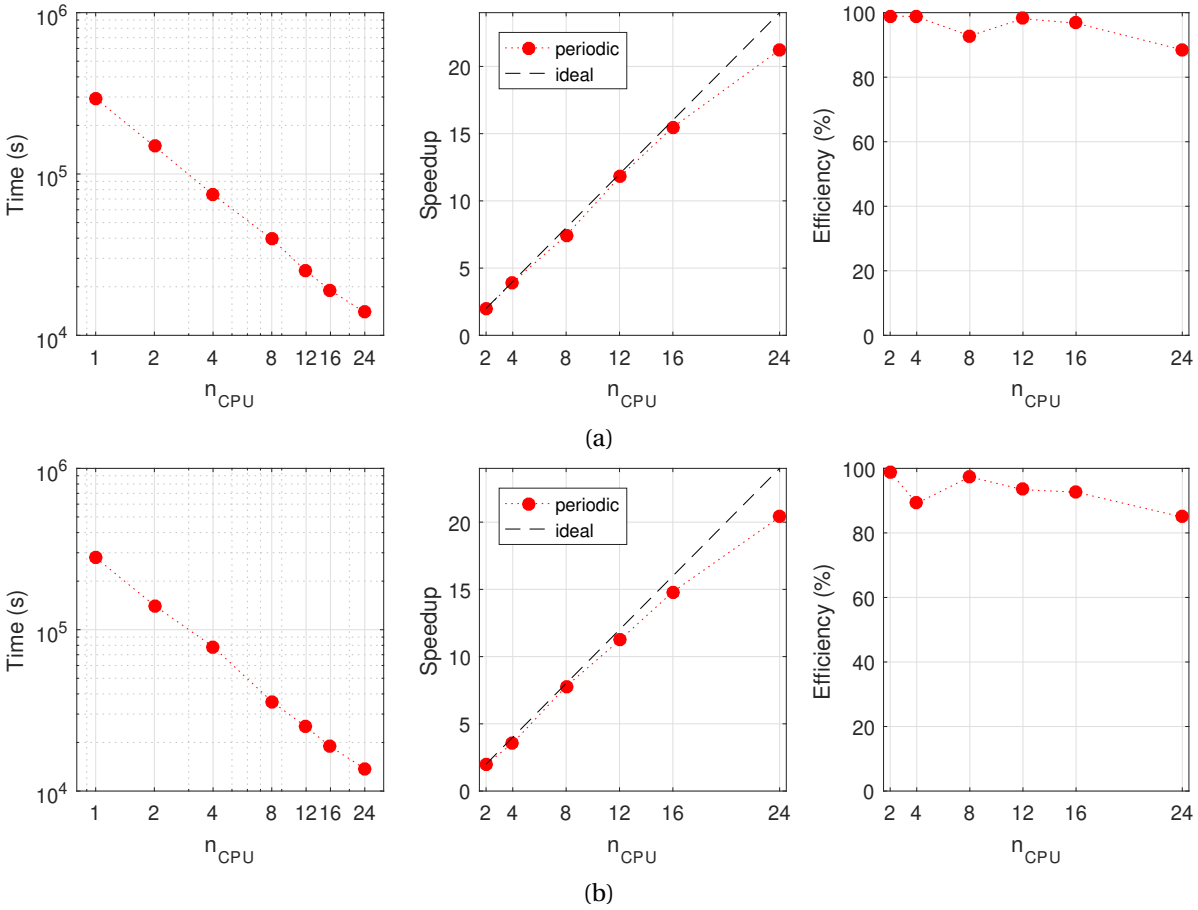

Figure 8.13: Time to solve (a) the 1st ($u = 0.055$ mm) and (b) the 5th increment ($u = 0.275$ mm) of the multi-scale 3D uniaxial traction problem, using a different number of slave CPUs with the master-slave parallel scheme (left), along with the corresponding speedup (middle) and parallel efficiency (right).

of elements over the entire domain to cope with this refinement, especially in structured meshes. Non-conforming discretisations allow to generate meshes where the number of elements is minimised outside critical zones, while keeping an adequate refinement level inside. Since the number of macro-elements has a direct impact on the total number of macro-integration points, and consequently on the amount of micro-analyses needed in a multi-scale framework, non-conforming meshes can help to reduce the computational cost of FE^2 simulations.

The mortar method allows to deal with non-conforming discretisations within a variationally consistent formulation (Popp et al., 2012, Wohlmuth, 2001). Lacour and Maday (1997) compared the suitability of the mortar element method and the polynomial FETI method for matching non-conforming discretisations on a domain decomposition problem. The mortar method showed to be more appropriate, leading to well conditioned algebraic systems of equations and satisfying conditions that demonstrate the optimality of the approximation.

In what refers to the application of the mortar method in the context of multi-scale modelling, Lloberas-Valls et al. (2012a,b) proposed an adaptive concurrent multi-scale framework to model strain localisation of brittle materials, where the macro-structure is divided into subdomains whose mesh may be selectively refined to accomplish a discretisation of the meso-scale material model. The FETI method is employed to deal with the domain decomposition problem, and the mortar method is used to cope with non-conforming meshes. Reis and Andrade Pires (2013) developed a mortar formulation to enforce periodic displacement fluctuations on the boundary of RVE models with non-conforming meshes on opposite sides.

In this section, a solution based on the FETI method (Farhat and Roux, 1991), which is very general and well established in the literature, is employed for the domain decomposition problem in conjunction with the mortar method, so that non-conforming discretisations between subdomains may be considered. Here, for the sake of simplicity, it will be adopted for the decomposition of the macroscopic domain into two subdomains, which are non-floating, i.e., they have enough Dirichlet boundary conditions so that their stiffness matrices are non-singular. However, this may be extended for general case, requiring the use iterative solvers or a dual-primal FETI formulation (Farhat and Roux, 1991, Farhat et al., 2001). Stefanica (2001) performed a comparison of preconditioners for the FETI solution with the mortar method. The formulation of the mortar domain decomposition problem and the strategies employed to deal with it are presented in Appendix B.

8.3.1 A FETI-based solution for domain decomposition with non-floating subdomains

Let us consider a body that is divided into n_Ω subdomains, that may have either non-mortar and mortar interface dofs. After linearisation of the discretised version of Equations (B.4) and (B.5), with a reorganisation of the dofs according to their nodal positions, the equilibrium problem is solved through the iterative system of equations:

$$\left[\begin{array}{ccc:c} \mathbf{K}^{(1)} & & \mathbf{0} & \mathbf{W}^{(1),T} \\ & \ddots & & \vdots \\ \mathbf{0} & & \mathbf{K}^{(n_\Omega)} & \mathbf{W}^{(n_\Omega),T} \\ \hdashline \mathbf{W}^{(1)} & \cdots & \mathbf{W}^{(n_\Omega)} & \mathbf{0} \end{array}\right] \left\{\begin{array}{c} \Delta\mathbf{u}^{(1)} \\ \vdots \\ \Delta\mathbf{u}^{(n_\Omega)} \\ \boldsymbol{\lambda} \end{array}\right\} = - \left\{\begin{array}{c} \mathbf{r}^{(1)} \\ \vdots \\ \mathbf{r}^{(n_\Omega)} \\ \mathbf{0} \end{array}\right\}, \tag{8.7}$$

where the interface relation matrices $\mathbf{W}^{(k)}$ are suitably defined as

$$\mathbf{W}^{(k)} = \left[\mathbf{0} \;\; \mathbf{D}^{nm} \;\; -\mathbf{A}^{m}\right]^{(k)}. \tag{8.8}$$

In the case of conforming meshes, these matrices are boolean matrices.

The Lagrange multiplier vector $\boldsymbol{\lambda}$ can be eliminated from the unknown vector, so that the equilibrium problem may be set independently in each subdomain k as:

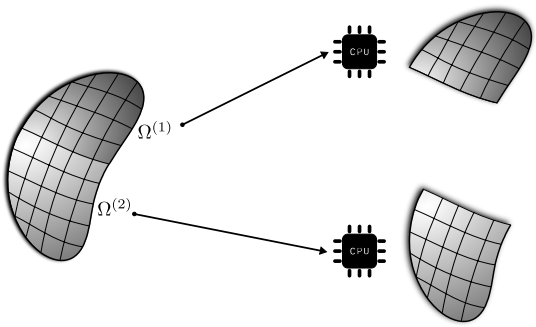

Figure 8.14: Scheme for the parallel implementation of a macroscale domain decomposition method.

$$\left[\mathbf{K}^{(k)}\right]\left\{\Delta\mathbf{u}^{(k)}\right\} = -\left\{\mathbf{r}^{(k)} + \mathbf{W}^{(k),T}\boldsymbol{\lambda}\right\}. \tag{8.9}$$

Since only non-floating subdomains are considered here, all subdomain stiffness matrices are non-singular, and the expression for the corresponding displacement field may be given by:

$$\Delta\mathbf{u}^{(k)} = -\left[\mathbf{K}^{(k)}\right]^{-1}\left(\mathbf{r}^{(k)} + \mathbf{W}^{(k),T}\boldsymbol{\lambda}\right). \tag{8.10}$$

The continuity constraint, which is stated by the last row of Equation (8.7), can be expressed as:

$$\sum_{k=1}^{n_\Omega} \mathbf{W}^{(k)}\Delta\mathbf{u}^{(k)} = \mathbf{0}. \tag{8.11}$$

Introducing the definition of the local displacement (Equation (8.10)) into Equation (8.11), it may be rewritten in terms of the Lagrange multiplier vector:

$$\sum_{k=1}^{n_\Omega} \mathbf{W}^{(k)}\left[\mathbf{K}^{(k)}\right]^{-1}\mathbf{W}^{(k),T}\cdot\boldsymbol{\lambda} = -\sum_{k=1}^{n_\Omega} \mathbf{W}^{(k)}\left[\mathbf{K}^{(k)}\right]^{-1}\mathbf{r}^{(k)} \tag{8.12}$$

The Lagrange multiplier vector is determined through this equation and, thereafter, the solution of the subdomain displacements is easily obtained from Equation (8.10).

8.3.2 Parallel implementation

In the present contribution, this domain decomposition method is implemented at the macroscale. The macroscopic domain is divided into smaller subdomains, that can be analysed in parallel by different computers, in order to alleviate memory requirements. This idea is depicted in Figure 8.14. Since only non-floating subdomains are considered here, there is no need to solve the linear system of equations with an iterative solver. Moreover, as memory requirements and computational cost are mainly related to the underlying micro-scale analyses and not to the size of the macroscopic linear system of equations, direct solvers can be employed. Nevertheless, this approach can be extended to the general case (see Farhat and Roux (1991) for more details). A study on preconditioners for the FETI algorithm in non-matching meshes tied with the mortar method is provided by Stefanica (2001). The same author has proposed a preconditioner well suited for parallel implementations (Stefanica, 2005).

The core of the present parallel implementation takes place at the Newton-Raphson scheme for the solution of the macroscopic equilibrium problem. Therefore, at each macro-iteration, the domain decomposition strategy is defined according to the steps defined in Box 8.1.

It is important to remark that the subdomain tying matrices $\mathbf{W}^{(k)}$ only need to be determined once, at the problem initialisation, even in the case of non-conforming meshes. Furthermore, the

Box 8.1 Framework for the parallel domain decomposition strategy.

1. Compute the subdomains flexibility matrix

$$\mathbf{F}^{(k)} = \mathbf{W}^{(k)} \left[\mathbf{K}^{(k)}\right]^{-1} \mathbf{W}^{(k),T} \tag{8.13}$$

and gap vector

$$\mathbf{g}^{(k)} = -\mathbf{W}^{(k)} \left[\mathbf{K}^{(k)}\right]^{-1} \mathbf{r}^{(k)}. \tag{8.14}$$

This task may be performed independently on each subdomain, thus in parallel. This stage involves the multi-scale analysis to obtain the constitutive response, allowing to compute the residual $\mathbf{r}^{(\mathbf{k})}$ and the tangent stiffness $\mathbf{K}^{(k)}$;

2. Assemble the flexibility and gap measures in one processor:

$$\mathbf{F} = \sum_{k=1}^{n_\Omega} \mathbf{F}^{(k)} \tag{8.15}$$

$$\mathbf{g} = \sum_{k=1}^{n_\Omega} \mathbf{g}^{(k)}. \tag{8.16}$$

This is essentially a communication task;

3. Solve the system of equations (8.12), rewritten here as

$$\mathbf{F}\boldsymbol{\lambda} = \mathbf{g}, \tag{8.17}$$

to determine the Lagrange multiplier vector. This is done in the processor where the information was assembled, and the result $\boldsymbol{\lambda}$ is broadcast to all the subdomains;

4. Solve the constrained problem in Equation (8.10) to determine the iterative displacement, which is done in parallel for each subdomain.

inverse of the subdomain stiffness matrix does not need to be explicitly computed to solve Expressions (8.10), (8.13) and (8.14). The right multiplications are obtained more efficiently as the solution of linear systems of equations.

8.4 A mixed parallel strategy

The domain decomposition method presented in Section 8.3 allows the reduction of memory requirements for the solution of hierarchical multi-scale simulations, distributing the macro-domain analysis among different computers so that the underlying microscopic data may be stored separately. In fact, this is the main drawback of the master-slave approach introduced in Section 8.1, where all RVEs data must be stored in the machine running the master processor, which may limit the size of multi-scale problems to be solved with this strategy.

In the context of the domain decomposition method, an increasing number of processors working in parallel can be achieved by either increasing the number of subdomains or by using multiple processors working on each subdomain. The former solution may be used at the expense of an increasing size of the interface problem. Moreover, in the present context, the choice of the number of subdomains should be made taking into account hardware resources (RAM in different machines) or the morphology of the macro-scale model. Since most of the computational cost is related to

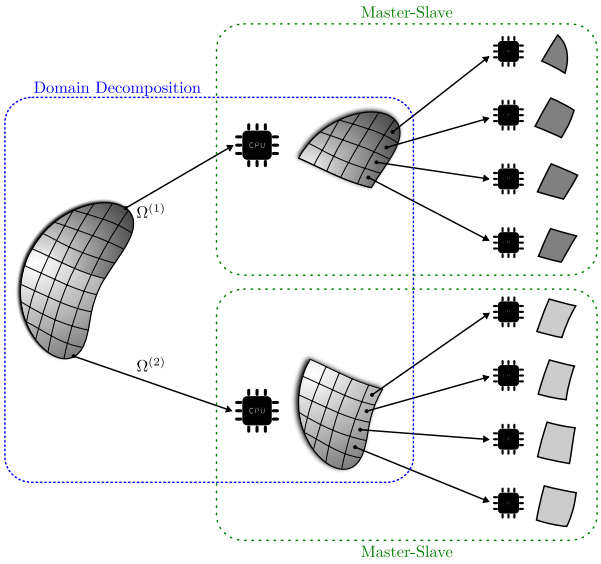

Figure 8.15: Schematic illustration of the mixed parallel strategy.

the underlying micro-scale analyses, which obtain the residual and the stiffness in each subdomain (step 1 in Box 8.1), the latter approach becomes more interesting in the context of multi-scale simulations.

In this section, a mixed parallel strategy that combines the domain decomposition method presented in Section 8.3 with the master-slave approach introduced in Section 8.1 is proposed. The non-conforming domain decomposition method is used in the first parallelisation level, and the master-slave strategy, which has proven to achieve interesting speedups, is employed within each subdomain, in the second level of parallel computing. An overall scheme of this strategy is illustrated in Figure 8.15.

In practice, the parallel processors working on the domain decomposition problem become masters in the corresponding subdomains, and a set of slave CPUs is attached to each master in order to add parallelism to the local multi-scale analysis. Memory requirements in each master are related to the size of the underlying subdomain. Hence, the microscopic information of each RVE is stored only in the master of the corresponding subdomain. One of the masters, the so-called *main master*, is responsible for the data input and results output, and for the solution of the interface problem.

The parallel work is distributed by the masters to their slaves with a dynamic scheduling, according to the technique presented in Section 8.1, so that the workload balance is guaranteed within each subdomain analysis.

It is important to highlight that, in addition to the distribution of memory requirements, the computational cost can be reduced with this mixed strategy due to the possibility of using non-conforming meshes. The macroscopic mesh may be coarsened in regions where low levels of deformation occur, while maintaining an adequate refinement level in critical regions, which results in a reduced total number of macroscopic elements, and therefore in less micro-scale analysis to perform.

Obviously, the computational load associated with each subdomain depends on the number of macro-elements and on the evolution of deformation. Zones undergoing higher deformations require additional computational effort at both scales.

In order to balance the global computational load, a strategy to obtain a similar computing time on different subdomains has been developed. The main idea is to distribute the available slaves among the subdomains dynamically, according to the expected computational effort, such that the global workload is balanced among all slaves.

In the first macro-scale iteration, the slaves are distributed to the subdomains according to the corresponding number of macro elements. Then, in the subsequent macro-iterations, the master-slave groups are updated according to the estimated sequential time for the multi-scale analysis in each subdomain. Taking subdomain 1 as reference, the ratio of slave CPUs can be defined for all subdomains:

$$\frac{n_{slaves_i}}{n_{slaves_1}}. \tag{8.18}$$

In order to achieve an equilibrated wallclock time among subdomains, the slaves ratio should be similar to the estimated sequential time ratio, i.e.:

$$\frac{n_{slaves_i}}{n_{slaves_1}} \approx r_i = \frac{\bar{t}_i}{\bar{t}_1}. \tag{8.19}$$

The estimated sequential time in a subdomain i, $\bar{t}_i$, is determined from the wallclock time for the multi-scale analysis t_i measured on the previous macro-iteration, according to the number of slaves that were used:

$$\bar{t}_i = n_{slaves_i}^{previous} \times t_i. \tag{8.20}$$

With the timing ratios r_i and the total number of available slaves n_{slaves} at hand, and assuming that the number of slaves on subdomain i may be expressed as

$$n_{slaves_i} = r_i n_{slaves_1}, \tag{8.21}$$

the number of slaves attached to subdomain 1 is obtained through the solution of the following equation:

$$\sum_{i=1}^{n_\Omega} r_i n_{slaves_1} = n_{slaves}. \tag{8.22}$$

The number of slaves on the remaining subdomains is recovered through Expression (8.21), under the condition $n_{slaves_i} \geq 1$.

For the first macro-iteration, the ratio r_i is obtained from the number of macroscopic elements in the subdomain i:

$$r_i = \frac{n_{elems\ i}}{n_{elems\ 1}}. \tag{8.23}$$

This strategy is summarised in Algorithm 1.

Algorithm 1: Algorithm for adaptive distribution of slaves between subdomains

if *1st macro-iteration* **then**
  get the number of elements $n_{elems\ i}$ on each subdomain
  $r_i = \frac{n_{elems_i}}{n_{elems_1}}$
else
  get multi-scale analysis time t_i on each subdomain
  $\bar{t}_i = t_i \times n_{slaves_i}$
  $r_i = \frac{\bar{t}_i}{\bar{t}_1}$
end
Solve Equation (8.22) to obtain n_{slaves_1}
$n_{slaves_i} = r_i \times n_{slaves_1}$

Table 8.3: Comparison of RAM allocated to the master processors in the master-slave and mixed implementations, for the 3D butterfly specimen.

		Memory (MB)
master-slave	Master	14196
mixed	Master 1	7124
	Master 2	7119

8.5 Numerical examples with the mixed parallel strategy

The examples presented in Section 8.2 are analysed again here, with the mixed parallel strategy, using an increasing number of slave processors. The standard domain decomposition algorithm is recovered when 2 slaves are used.

8.5.1 Butterfly specimen

The butterfly specimen traction problem, presented in Section 8.2.1, is solved here with the mixed parallel strategy. The macroscopic domain is split into two similar subdomains, as illustrated in Figure 8.16. The light gray and dark gray subdomains have each 288 elements.

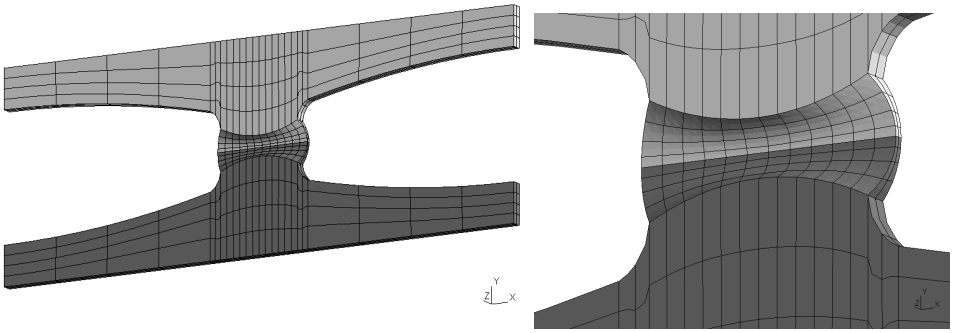

Figure 8.16: Domain decomposition of the butterfly specimen and corresponding discretisation.

With regard to the amount of RAM that is allocated to each master in both the master-slave and the mixed implementations, which is presented in Table 8.3, a significant reduction was observed with the mixed strategy, as expected. For the mixed approach, the amount of RAM is almost equally distributed between the two masters, being slightly higher in master 1 (the main master) due to the memory allocated for output variables and the solution of the interface problem.

The computation time to solve one macro-increment with different number of slaves is plotted in Figure 8.17, along with the corresponding speedup and parallel efficiency. The sequential time, which is obtained with only one processor, is included in the left figure for comparison.

The speedup evolution obtained with the mixed implementation is similar to the values observed for the master-slave approach, presented in Figure 8.7. This is explained by the fact that the computational work is equally distributed between the two masters, since both subdomains are similar (see Figure 8.16).

Therefore, when employing the mixed strategy to multi-scale problems where the macroscopic domain is split into two similar subdomains, it is possible to observe that the memory requirements for each master are reduced in roughly 50%, and the time gains are close to the ones obtained with

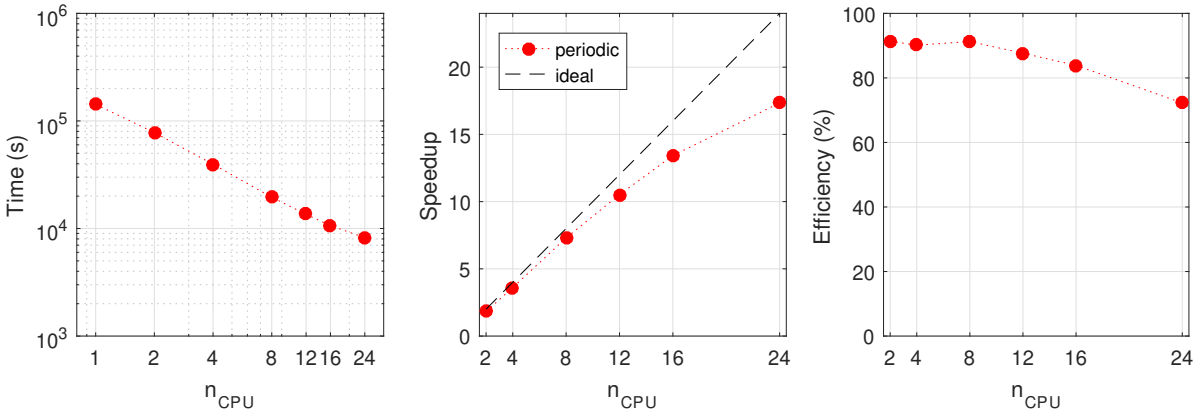

Figure 8.17: Time to solve the multi-scale butterfly traction problem, using a different number of slave CPUs with the mixed parallel strategy (left), along with the corresponding speedup (middle) and parallel efficiency (right).

the master-slave implementation. Neverthless, the master-slave approach is always slightly faster. This can be justified since there is not need to solve the interface problem.

8.5.2 3D uniaxial specimen

Here, the multi-scale simulation of the 3D cylindrical notched specimen is carried out with the mixed implementation, considering two distinct meshes: i) a conforming discretisation and ii) a non-conforming discretisation, where the ability of the mortar method embedded in this implementation is shown.

Conforming discretisation

The multi-scale problem presented in Section 8.2.2 is solved here with the proposed mixed parallel framework. The discretisation is slightly modified in order to accomplish the chosen domain decomposition, as presented in Figure 8.18. Nonetheless, the total number of macro-elements remains the same, as well as the discretisation in the critical region. The light gray domain has 128 elements and the dark gray domain 224 elements. It must be mentioned that in addition to having an higher number of elements, the elements in the dark gray subdomain are expected to undergo larger deformations. Therefore, the computational load on this subdomain is expected to be significantly higher.

The reaction force evolution obtained is coincident to what is observed in Figure 8.10, as expected. A comparison between the memory requirements of the master processes with the standard master-slave approach and the mixed strategy is presented in Table 8.4. They are not equally distributed between the 2 masters with the mixed parallel strategy, since the number of elements on each subdomain is not the same. Therefore, the amount of RVEs data is greater in the dark gray subdomain (master 1). Nonetheless, it is possible to observe a significant reduction in the memory necessary for each master (master 1 and master 2) even when the subdomains are not similar.

Table 8.4: Comparison of RAM allocated to the master processors in the master-slave and mixed implementations, for the 3D uniaxial simulation.

		Memory (MB)
master-slave	Master	8842
mixed	Master 1	5625
	Master 2	3227

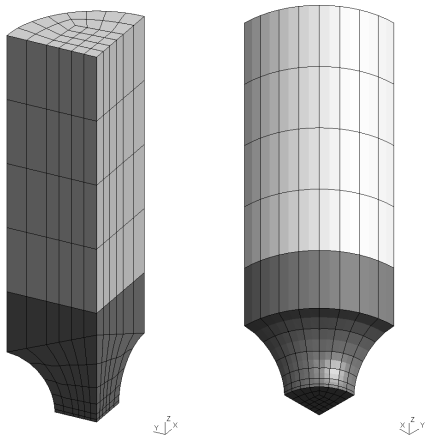

Figure 8.18: Domain decomposition of the notched cylindrical uniaxial specimen and corresponding discretisation.

The evolution of the computing time to solve the 1st and the 5th increment of this multi-scale problem with an increasing number of slaves is plotted in Figure 8.19. Unlike the butterfly specimen example, here the evolution of the computational time with the number of CPUs is quite different when compared with the master-slave implementation results (see Figure 8.13). In fact, when using only 2 slaves, one per subdomain, the parallel efficiency is about 70% and 60%, for the 1st and 5th increment respectively, which is much lower than what is achieved with the master-slave approach, where this value is very close to 100%. However, the efficiency recovers when more slaves are employed, and gets closer to the values observed with the master-slave implementation, except for some timing fluctuations. This is especially true for the 1st increment, while for the 5th increment the parallel efficiency recovers to stabilize around the value of 70%.

This behaviour is due to the imbalance of the computational effort between the subdomains, which results from an higher number of elements in the dark gray subdomain, along with the additional effort coming from larger deformations in this subdomain. With only two slaves there is no possibility to perform their adaptive distribution over the subdomains, since at least one slave per subdomain is required. However, when the number increases it becomes possible to do so and a good workload balance is achieved. For this case, the parallel efficiency gets closer to the values observed with the master-slave approach.

This situation is illustrated in Figure 8.20, where the evolution of the number of slaves working on each subdomain is plotted (left plot). In the first iteration, 15 slaves work on the notch subdomain (dark gray) and 9 on the top one (light gray) due to the difference on the number of macro-elements. As the solution of the problem evolves, the elements on the notch subdomain require higher computational effort, as shown in the middle plot, with a large difference between the estimated sequential time in the two subdomains, that would cause a strong workload imbalance. Moreover, the estimated sequential time in the dark gray subdomain varies significantly (red curve). However, due to the adaptive re-distribution of slaves described in Algorithm 1, the number of slaves assigned to this subdomain is dynamically changed to values between 17 and 20, and the wallclock time becomes more equilibrated, as shown in the right plot.

As the finite strain problem evolves, the computational effort gets even more unbalanced between subdomains, and the workload balancing task becomes more difficult. This is the reason why the efficiency is significantly lower for the 5th increment. Nonetheless, a parallel efficiency of 70% is achieved, which reflects a speedup close to 17 times, with important memory requirements savings.

It is possible to conclude that the mixed parallel strategy is applicable to problems where the macro-domain decomposition creates very different subdomains. Obviously, the reduction in mem-

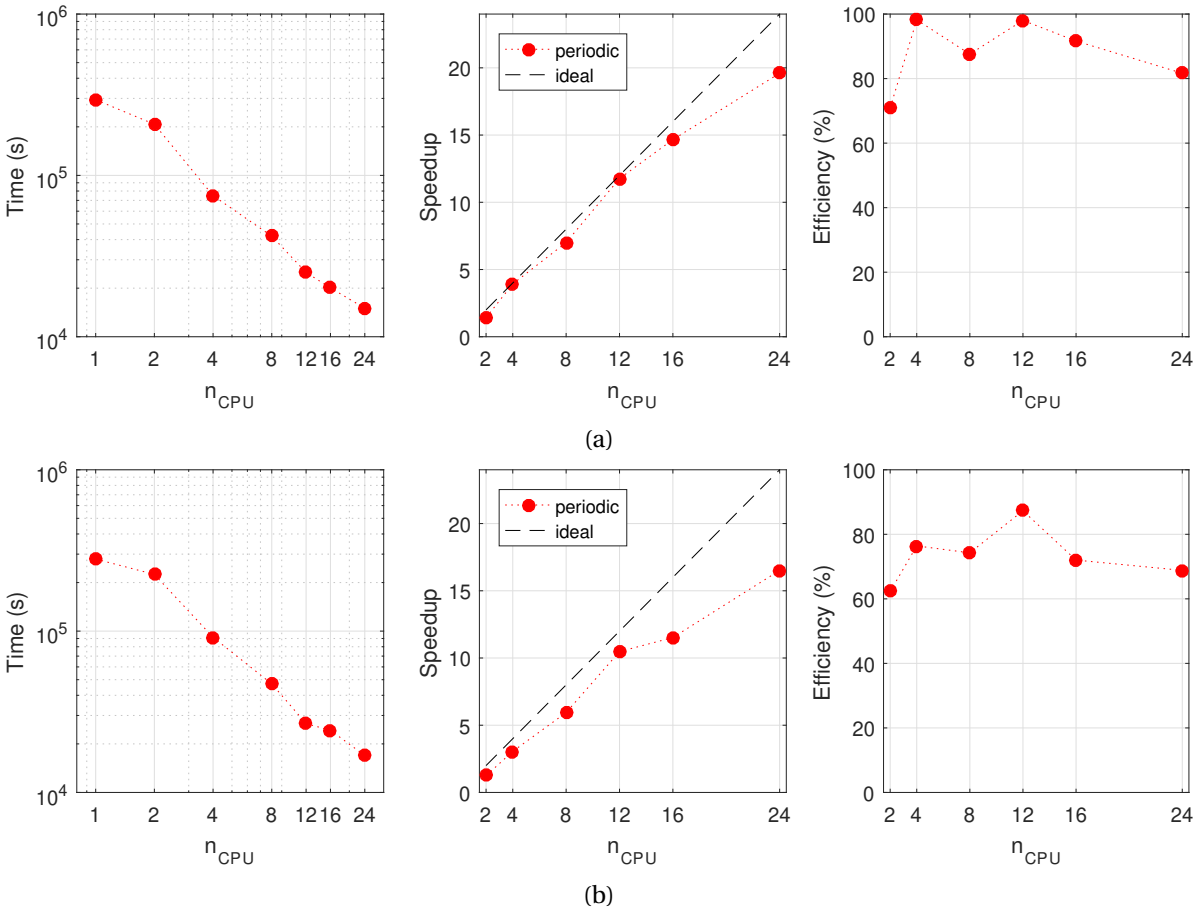

Figure 8.19: Time to solve (a) the 1st and (b) the 5th increment of the multi-scale 3D uniaxial traction problem, using a different number of slave CPUs with the mixed parallel strategy (left), along with the corresponding speedup (middle) and parallel efficiency (right).

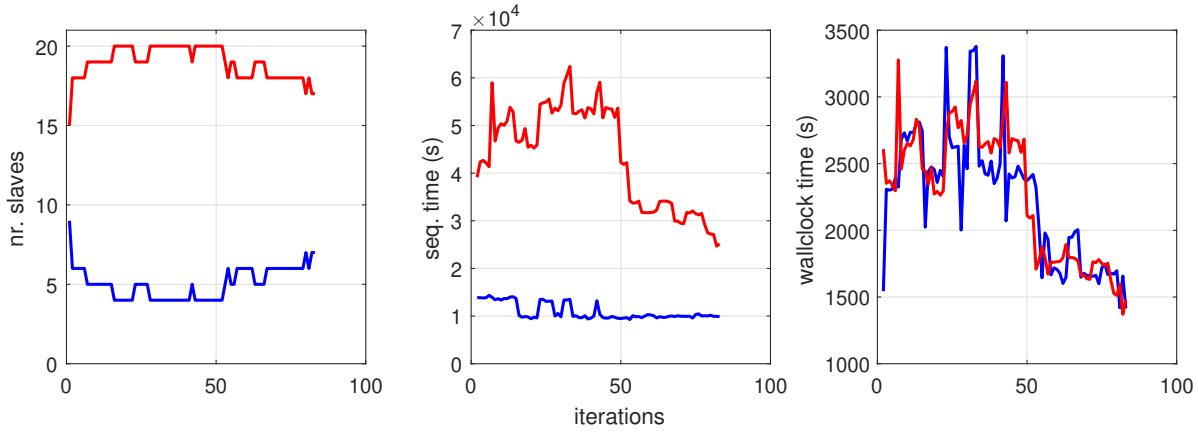

Figure 8.20: Evolution of the number of slaves working on each subdomain of the 3D cylindrical notched specimen (left), estimated sequential time (middle) and observed wallclock time (right). Blue curves refer to the top subdomain (light gray) and the red ones to the notch subdomain (dark gray).

Table 8.5: Comparison of RAM allocated to the master processors in the mixed implementation, for the non-conforming 3D uniaxial simulation.

		Memory (MB)
mixed	Master 1	5625
	Master 2	2121

ory requirements depends on the number of macro-elements in each subdomain. Nevertheless, even when the subdomain requires a distinct computational effort, the proposed adaptive strategy for the distribution of slaves is able to balance the workload, as long as the number of available slaves is high enough. For this case, the speedups are similar to the values obtained with the master-slave approach. As a future improvement, this algorithm can be enhanced with a work-stealing approach, where the slaves working on a subdomain migrate to work on another subdomain when the first one finishes. This would provide a further reduction in the workload imbalance, especially when large deformations occur.

Non-conforming discretisation

In order to show the suitability of the current implementation to deal with 3D non-conforming discretisations, the cylindrical notched specimen is meshed according to the representation in Figure 8.21. The number of elements in the light gray domain is reduced to 84, while the dark gray domain remains with 224 elements.

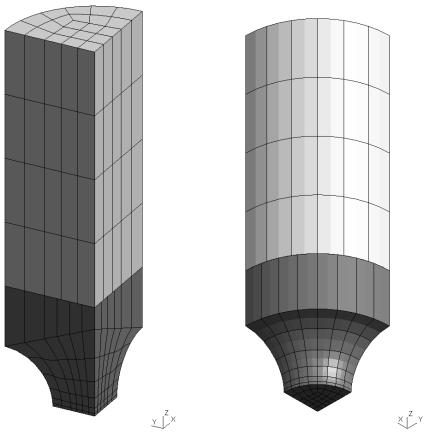

Figure 8.21: Non-conforming discretisation and domain decomposition of the notched cylindrical uniaxial specimen.

Contour plots of the displacements magnitude and the macroscopic von Mises equivalent stress, when $u = 0.22$ mm, are presented in Figure 8.22. The continuity of both fields is verified across the non-conforming interface.

The amount of RAM allocated in each of the master processes is shown in Table 8.5. When comparing with the values of Table 8.4, it is verified that the memory requirements in master 1, where the dark gray subdomain is solved, remains equal, while in master 2 it has decreased, since a coarser mesh is now being employed in the light gray subdomain.

Therefore, the mortar method employed within the domain decomposition method in the mixed parallel strategy, allows the use of meshes with distinct refinements on each of the subdomains.

In addition, the quadratic rate convergence of the Newton-Raphson scheme for the solution of the macro-scale problem is preserved. The evolution of the relative error in a typical incremental

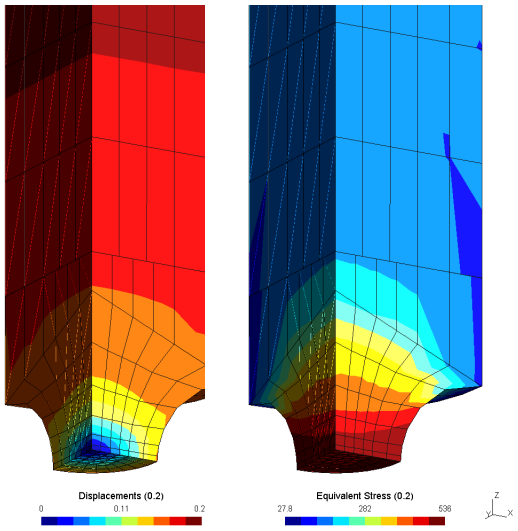

(a) (b)

Figure 8.22: Contour plot of (a) the displacements magnitude and (b) the macroscopic von Mises equivalent stress in the deformed mesh of the non-conforming domain decomposition of the cylindrical notched specimen, when $u = 0.22$ mm.

Table 8.6: Convergence rate for an incremental step of the non-conforming cylindrical notched specimen multi-scale problem (macro-problem).

iteration	**relative error** (%)
1	7.90612
2	0.432200
3	0.103933×10^{-2}
4	0.310922×10^{-7}

step is shown in Table 8.6.

8.6 Conclusions

In the present chapter a mixed parallel strategy for the solution of homogenisation-based multi-scale constitutive problems undergoing finite strains is proposed. It combines a non-conforming macro-domain decomposition method in the first parallelisation level, with a master-slave approach employed within each subdomain, for the second level. Firstly, a master-slave parallel algorithm is presented, where the distribution of parallel work is done by macro-elements with dynamic scheduling, in order to reduce the number of communications and increase the amount of work done in parallel by the slaves, while maintaining a good workload balance. Application examples show that good speedups are achieved even when strong non-linearities are present at both scales. The main disadvantage of this approach is related to memory requirements of the master process, where all RVEs data is centralised. For large size problems, the amount of memory required may become prohibitive.

The combination of this master-slave scheme with a macroscopic domain decomposition alleviates this issue. In the proposed mixed implementation, the domain decomposition is implemented with the mortar method, so that subdomains with non-conforming meshes can be used. This allows a greater flexibility on the generation of the finite element discretisation and a possible reduction of the number of macroscopic elements and, consequently, of the overall computational

effort. The resulting macroscopic problem is undertaken with a FETI-based solution. An adaptive distribution of slave processes working in the subdomains is proposed, in order to minimise the computational workload imbalance. The presented results have demonstrated that this approach is able to reduce the memory requirements of the master process, by splitting the problem into smaller subdomains. Moreover, if the number of available slaves is large enough, a good workload distribution can be obtained, even when subdomains requiring quite distinct computational effort are employed. The macroscopic fields continuity is ensured across the non-conforming interface, and quadratic convergence rate is achieved in the Newton-Raphson scheme.

In spite of being applied to FE^2 simulations in a 1^{st}-order homogenisation scheme only, it is important to mention that the master-slave scheme may be employed in simulations where a second-order continuum is used at the macro-scale without additional considerations. In fact, it has been applied in the simulations presented in Section 6.8. In what refers to the mixed parallel strategy, since the mortar formulation has been developed for a first-order continuum, it cannot be used in second-order homogenisation problems. Nevertheless, in a mixed finite element formulation where relaxed deformation gradients are included, in addition to displacements, as nodal unknown variables, a mortar formulation that enforces displacements and deformation gradient continuity across the subdomains interface can be developed.

Chapter 9

Conclusions

Multi-scale models based on computational homogenisation constitute a valuable tool to model materials with possibly complex microstructures, providing a link between the macroscopic behaviour and the underlying microstructural phenomena, accounting for finite strains and dissipative mechanisms. Nevertheless, the solution of FE^2 simulations is computationally expensive due to the large number micro-scale problems to analyse. In addition, standard first-order homogenisation schemes assume the uniformity of the macroscopic deformation gradient in the RVE and therefore only linear macroscopic deformation modes are passed to the micro-scale, disregarding more complex deformations that may appear in regions with high strain gradients and for loadings like bending or torsion.

Second-order homogenisation-based multi-scale models, where quadratic deformation modes are enforced on the micro-scale, are explored in this thesis, along with computational strategies that enable a more efficient solution of multi-scale simulations. Three different types of multi-scale formulations are addressed: (i) the standard first-order homogenisation scheme, (ii) second-order homogenisation-based models where the macro-scale is modelled as a second-order continuum, while the micro-scale is described by the classical first-order continuum mechanics and (iii) a fully second-order homogenisation multi-scale formulation, where the material behaviour is modelled with a second-order continuum at both scales. The *method of multi-scale virtual power* is employed to derive the formulations introduced, guaranteeing a variationally consistent scale transition.

The first-order homogenisation framework is introduced in Chapter 3, where two distinct strategies to enforce the micro-scale boundary conditions (uniform traction and mortar periodic) in the resulting finite element equilibrium problem are analysed: (i) the condensation method and (ii) the Lagrange multiplier method. The Lagrange multiplier method, in spite of increasing the size of the resulting linear system of equations, performs better with regard to computing time and memory requirements. The computation of the homogenised consistent tangents, needed in a FE^2 framework, is also more efficient with the Lagrange multiplier implementation. In addition, aiming to enable a faster solution of this kind of formulations taking advantage of modern computer architectures, parallel strategies are proposed in Chapter 8. In the first place, a master-slave parallel algorithm is presented, where the distribution of parallel work is done by macro-elements with dynamic scheduling, in order to reduce the number of communications and increase the amount of work done in parallel by the slaves, while maintaining a good workload balance. Application examples show that good speedups are achieved even when strong non-linearities are present at both scales. The main disadvantage of this approach is related to memory requirements of the master process, where all RVEs data is centralised. For large size problems, the amount of memory required may become prohibitive. Therefore, a mixed parallel strategy where a non-conforming macro-domain decomposition method is combined with the master-slave approach employed within each subdomain is proposed. The domain decomposition is implemented with the mortar method, so that subdomains with non-conforming meshes can be used. This allows a greater flexibility on the gen-

eration of the macro-scale finite element discretisation. The resulting macroscopic problem is undertaken with a FETI-based solution. An adaptive distribution of slave processes working in the subdomains allows to achieve good workload distributions between subdomains. In spite of being introduced for a 1^{st}-order homogenisation scheme, it is important to mention that the master-slave scheme has been employed in simulations where a second-order continuum is used at the macro-scale without additional considerations.

In the quest to capture second-order deformation modes at the micro-scale through second-order homogenisation schemes, the macro-scale must be properly modelled by a second-order continuum model. A full gradient formulation for 2^{nd}-order continuum at large strains, presented in Chapter 4, is considered throughout this thesis. A three-dimensional hexahedral finite element is proposed to deal with the solution of the resulting equilibrium equation, that requires C^1 continuity of the displacement field. Numerical examples show that the results obtained with this element are in agreement with analytical solutions and the corresponding 2D results obtained with well established quadrilateral elements.

Several formulations for second-order homogenisation-based models, where the micro-scale behaviour is described by the classical first-order continuum theory, are presented in Chapter 5, along with the corresponding implementation details. Due to the good performance obtained with first-order homogenisation models, the Lagrange multiplier method is also employed to enforce the micro-constraints in these second-order homogenisation schemes. Firstly, the formulation proposed by Blanco et al. (2016b) is particularised for the quasi-static case, in the absence of external body forces. Thereafter, an alternative formulation is developed, also using the *method of multi-scale virtual power*, but modifying the definition of the homogenised second gradient. For the minimally constrained models arising from these formulations, it is possible to relate the Lagrange multipliers directly with the homogenised stresses, facilitating the computation of the homogenised consistent tangents. Finally, in order to clarify the impact of the assumptions made by other formulations available in the literature, Kouznetsova and Luscher's models are also introduced. Whereas formulations based on the work of Kouznetsova (2002) result in models where only boundary constraints are enforced on the RVE, the remaining formulations analysed here require volumetric constraints to be imposed at the micro-scale.

In fact, Kouznetsova's periodic constraint does not provide consistent results for the case of a simple RVE under small strains with different discretisations, due to the lack of the volumetric constraint. The minimal constraint of Blanco's-based formulation suffers from the same pathology but, in this case, it is related to an overconstraint caused by the symmetric definition of the macroscopic second gradient. In contrast, the constraints based on the alternative formulation presented in Section 5.2 result in consistent responses. In the assessment of a measure of the homogenised second gradient for different micro-constraints, in Section 6.7, the difference associated with these two formulations is, in general, larger than for the remaining constraints.

It is observed that the response obtained with Luscher's minimal constraint recovers the response of the RVE under the minimal constraint of the alternative formulation developed in Section 5.2. Moreover, it is confirmed that the relation between the Lagrange multipliers and the homogenised stresses is valid, along with the computational framework presented in Sections 5.1.7 and 5.2.6 to obtain the consistent tangents in a FE^2 simulation (Section 6.8).

Second-order homogenisation models are sensitive to geometric non-linearities, introduced by the position of constituents in the RVE, resulting in a coupling between between the macroscopic deformation gradient and the homogenised higher-order stress, that is not considered in the Mindlin's elastic model. A coupling between the first Piola-Kirchhoff stress tensor and the macroscopic second gradient is also obtained.

For RVEs with voids in the microstructure, voids domain must be discretised to obtain the correct results for the formulations where volumetric constraints are enforced at the micro-scale. This poses limitations in the analysis of this kind of microstructures, since a very compliant mesh subjected to a reactive body force suffers extreme deformation causing numerical problems.

In a first-order homogenisation scheme, the RVE length (the physical length of the model) does not influence the response obtained, that depends mainly on the proportion of the micro-constituents and their interactions. Moreover, the larger RVE size (number of constituents) is considered to model the microstructure, the larger is the representativeness of the RVE, yielding a response that is closer to the *real* behaviour. In contrast, the length of the RVE model plays a major role in the multi-scale behaviour obtained with models based on second-order homogenisation. As a matter of fact, since the homogenised response establishes the constitutive law at the macro-scale, the RVE length defines the characteristic length that drives the non-local and second-order effects. The relation between the RVE length and the resulting characteristic length found by Kouznetsova et al. (2004a) remains valid for the minimal constraints of the formulations based on the *method of multi-scale virtual power*, when a non-dissipative behaviour is considered at the micro-scale. Therefore, the choice of an appropriate RVE for second-order homogenisation schemes is hampered by the need to select a representative model with the length that properly defines the macroscopic non-local behaviour. In the limit, it may happen that the RVE with an appropriate length does not contain a representative number of constituents and the RVE length needed to provide a representative response overestimates the physical material characteristic length, leading to results that do not describe the real behaviour.

In order to gain a better understanding of the isolated effect of the RVE length and the RVE constituents size in the macroscopic response obtained with second-order homogenisation models, several realisations of four different kinds of RVE models are considered to model a composite material with a fixed fibre volume fraction in Section 6.5. Two different values of the RVE length (the physical size of the model) are analysed. For a fixed value of the RVE length, two different values are employed for the fibres size, adjusting the number of fibres to maintain the fibre volume fraction in the RVE. Hence, since the number of constituents may vary for the same RVE length, it can be seen as the definition of a generalised RVE size.

When comparing the results obtained with second-order and first-order homogenisation models, it is observed that the scale separation limit, that is defined here by the divergence of the homogenised responses between the two approaches, does not depend exclusively on the RVE length and the magnitude of the macroscopic second gradient, but is also affected by the micro-constituents constitutive behaviour and by the magnitude of the first-order strain. This is also perceived for the case of RVEs with a polycrystalline microstructure (Section 6.9)

Moreover, whereas the RVE length actually influences the homogenised response, the generalised RVE size, defined by the number of micro-constituents in the RVE model, also related to the fibres size, affects only the dispersion of the results obtained with different realisations of the same RVE kind. The conclusions extracted from this observation are twofold. In the first place, it is shown numerically that size effects related to the size of the micro-constituents are not captured by second-order homogenisation models that employ a first-order description at the RVE level. In the second place, the convergence of the macroscopic response obtained with the increasing of the number of constituents in the RVE model observed in first-order homogenisation schemes can be replicated for second-order homogenisation models, as long as the generalised RVE size increases maintaining the length of the RVE model.

In fact, within the framework of computational homogenisation, the RVE can be seen as a numerical model of the real microstructure, whose dimensions may be decoupled from the real constituents dimensions. Therefore, for a given RVE length, the representativeness of the RVE model may be enhanced by adjusting the size of the constituents in the model by a scale factor in order to include a larger number of micro-constituents.

These observations motivated the proposal of an adaptive framework for the multi-scale analysis through second-order homogenisation, presented in Section 6.10, where guidelines are proposed for the choice of the RVE length and the generalised RVE size, and the RVE length, the magnitude of the macroscopic second gradient and the first-order strain are employed to define a criterion for the determination of critical macroscopic regions where second-order homogenisation should

be used.

A fully second-order homogenisation formulation for solids undergoing large strains is developed in Chapter 7. Unlike the second-order homogenisation schemes discussed before, in this case a second gradient continuum theory is considered at the micro-scale. With this, a characteristic length is incorporated at the micro-scale. To the author's knowledge, this is the first multi-scale model of this kind formulated at large strains. The numerical implementation is described in detail, employing Lagrange multipliers to enforce the micro-scale constraints. The relation between the Lagrange multipliers and the homogenised stresses is demonstrated. Several numerical examples have been introduced to verify the implementation and understand the main features of this approach, either in a micro-scale and a FE^2 context. In addition to the RVE length, the non-local character introduced through the micro-constituents characteristic length plays a major role in the multi-scale response. With this formulation, size effects due to micro-constituents size are captured. The issue reported for RVEs with voids, modelled with second-order homogenisation models with a first-order description at the micro-scale, does not arise in this fully second-order homogenisation scheme, since all the micro-constraints can be expressed on the RVE boundary.

9.1 Future work

The domain decomposition method included in the mixed parallel strategy is valid for a first-order description only. Therefore, only the master-scale scheme can be employed in a second-order homogenisation framework. Nonetheless, it is possible to develop a mortar formulation for mixed finite elements where both C^0 and C^1 continuity is enforced across subdomain's interfaces.

With regard to the second-order homogenisation models, alternative discretisation techniques must be devised to enable the modelling of RVEs with voids without discretising voids domain. In addition, methodologies for the determination of an appropriate RVE length must be explored. The calibration of the RVE length value through the analysis of experimental results is a subject that must be further investigated. It must be remarked that it is possible to employ RVEs with different RVE lengths in distinct directions, which is expected to yield macroscopic responses where orthotropic material characteristic lengths are obtained. This subject should be explored in future work.

Finally, since only relatively simple numerical examples have been analysed with a fully second-order homogenisation model, additional studies involving more complex macro and microstructures should be performed in order to achieve a deeper insight in the multi-scale response obtained with this kind of model. The effect of disregarding the boundary compatibility term for mixed finite elements in the error associated with the micro-scale discretisation must be critically analysed.

Appendix A

Linearisation of the virtual work equation

The weak formulation of the equilibrium equation is linearised in this Appendix. In the first place, the general procedure for the linearisation of non-linear problems is summarized. Thereafter, the virtual work equations for finite strain problems, defined in either material and spatial configurations, are linearised.

A.1 Linearisation of non-linear problems

Consider a non-linear problem defined by the function $\mathscr{Y} : \mathscr{D} \subset \mathscr{X} \rightarrow \mathscr{Y}$, where the goal is to find $\mathscr{X} \in \mathscr{D}$ such that:

$$\mathscr{Y}(\mathscr{X}) = \mathbf{0}. \tag{A.1}$$

The linearisation of this problem about a point $\mathscr{X}_0$ consists in finding $\mathscr{U} \in \mathscr{X}$ that satisfies:

$$L(\mathscr{U}) = \mathscr{Y}(\mathscr{X}_0) + D\mathscr{Y}(\mathscr{X}_0)[\mathscr{U}] = \mathbf{0}, \tag{A.2}$$

where

$$D\mathscr{Y}(\mathscr{X}_0)[\mathscr{U}] = \frac{d}{d\epsilon}\mathscr{Y}(\mathscr{X}_0 + \epsilon\mathscr{U})\bigg|_{\epsilon=0}. \tag{A.3}$$

A.2 Finite Strain Virtual Work Linearisation

A.2.1 Material Description

The material version of the virtual work functional is given by:

$$G(\boldsymbol{u}, \delta\boldsymbol{u}) = \int_\Omega [\boldsymbol{P}(\boldsymbol{u}) : \nabla_X \delta\boldsymbol{u} - \boldsymbol{b}_0 \cdot \delta\boldsymbol{u}]\, dV - \int_{\partial\Omega} \boldsymbol{t}_0 \cdot \delta\boldsymbol{u} dA = 0, \quad \forall \delta\boldsymbol{u} \in \mathscr{V}. \tag{A.4}$$

The Piola-Kirchhoff stress tensor can be represented as a function of the deformation gradient:

$$\boldsymbol{P}(\boldsymbol{u}) = \boldsymbol{P}(\boldsymbol{F}(\boldsymbol{u})), \tag{A.5}$$

whose material definition is given by Expression (2.14).

The linearisation of the weak equilibrium equation about $\boldsymbol{u}^*$ with respect to the iterative displacement $\Delta\boldsymbol{u}$ is given by:

$$L(\Delta\boldsymbol{u}, \delta\boldsymbol{u}) = G(\boldsymbol{u}^*, \delta\boldsymbol{u}) + DG(\boldsymbol{u}^*, \delta\boldsymbol{u})[\Delta\boldsymbol{u}] = 0. \tag{A.6}$$

In this case, the directional derivative yields:

$$\begin{aligned} DG(\boldsymbol{u}^*, \delta\boldsymbol{u})[\Delta\boldsymbol{u}] &= \frac{d}{d\epsilon} G(\boldsymbol{u}^* + \epsilon\Delta\boldsymbol{u}, \delta\boldsymbol{u})\bigg|_{\epsilon=0} \\ &= \frac{d}{d\epsilon}\bigg|_{\epsilon=0} \int_\Omega \boldsymbol{P}(\boldsymbol{F}(\boldsymbol{u}^* + \epsilon\Delta\boldsymbol{u})) : \nabla_X \delta\boldsymbol{u} dV. \end{aligned} \tag{A.7}$$

Since the deformation gradient depends on the perturbation ϵ through

$$\boldsymbol{F}(\boldsymbol{u}^* + \epsilon\Delta\boldsymbol{u}) = \boldsymbol{I} + \nabla_X(\boldsymbol{u}^* + \epsilon\Delta\boldsymbol{u}) = \boldsymbol{F}^* + \epsilon\nabla_X\Delta\boldsymbol{u}, \tag{A.8}$$

the final expression of the directional derivative is given by:

$$DG(\boldsymbol{u}^*, \delta\boldsymbol{u})[\Delta\boldsymbol{u}] = \int_\Omega \mathbf{A} : \nabla_X\Delta\boldsymbol{u} : \nabla_X\delta\boldsymbol{u}\, dV, \tag{A.9}$$

where the material tangent modulus is defined as:

$$\mathbf{A} = \left.\frac{\partial \boldsymbol{P}}{\partial \boldsymbol{F}}\right|_{\boldsymbol{F}=\boldsymbol{F}^*}. \tag{A.10}$$

Finally, recovering the linearisation concept introduced by Expression (A.6), the linearised virtual work equation for large deformation in the material description is expressed by:

$$\int_\Omega \mathbf{A} : \nabla_X\Delta\boldsymbol{u} : \nabla_X\delta\boldsymbol{u}\, dV = -\int_\Omega \left[\boldsymbol{P} : \nabla_X\delta\boldsymbol{u} - \boldsymbol{b}_0 \cdot \delta\boldsymbol{u}\right] dV + \int_{\partial\Omega} \boldsymbol{t}_0 \cdot \delta\boldsymbol{u}\, dA, \quad \forall\delta\boldsymbol{u} \in \mathcal{V}. \tag{A.11}$$

A.2.2 Spatial Description

The virtual work functional considering a spatial description of motion is expressed as:

$$G(\boldsymbol{u}, \delta\boldsymbol{u}) = \int_{\varphi(\Omega)} \left[\boldsymbol{\sigma}(\boldsymbol{u}) : \nabla_x\delta\boldsymbol{u} - \boldsymbol{b} \cdot \delta\boldsymbol{u}\right] dV - \int_{\varphi(\partial\Omega)} \boldsymbol{t} \cdot \delta\boldsymbol{u}\, dA = 0, \quad \forall\delta\boldsymbol{u} \in \mathcal{V}, \tag{A.12}$$

where the Cauchy stress tensor is a function of the deformation gradient:

$$\boldsymbol{\sigma} = \boldsymbol{\sigma}(\boldsymbol{F}(\boldsymbol{u})) = \boldsymbol{\sigma}(\boldsymbol{I} + \nabla_X\boldsymbol{u}). \tag{A.13}$$

The spatial and the material virtual work functional are equivalent, but expressed according to distinct descriptions. The following expressions relate the spatial and material gradient of a generic tensor field $\boldsymbol{a}$, and the integral of a scalar a computed in the reference and in the deformed configuration:

$$\nabla_X\boldsymbol{a} = \nabla_x\boldsymbol{a} \cdot \boldsymbol{F}, \tag{A.14a}$$

$$\int_{\varphi(\Omega)} a(\boldsymbol{x})\, dV = \int_\Omega J(\boldsymbol{X})\, a(\varphi(\boldsymbol{X}))\, dV, \quad J = \det\boldsymbol{F}. \tag{A.14b}$$

Therefore, the directional derivative obtained in the material description (Expression (A.9)) can be rewritten in the spatial form as:

$$\begin{aligned} DG(\boldsymbol{u}^*, \delta\boldsymbol{u})[\Delta\boldsymbol{u}] &= \int_{\varphi(\Omega)} \frac{1}{J}\mathbf{A} : (\nabla_x\Delta\boldsymbol{u} \cdot \boldsymbol{F}) : (\nabla_x\delta\boldsymbol{u} \cdot \boldsymbol{F})\, dV \\ &= \int_\Omega \mathbf{a} : (\nabla_x\Delta\boldsymbol{u}) : (\nabla_x\delta\boldsymbol{u})\, dV, \end{aligned} \tag{A.15}$$

where the spatial tangent modulus components is defined by:

$$\mathsf{a}_{ijkl} = \frac{1}{J}\mathsf{A}_{imkn}F_{jm}F_{ln}. \tag{A.16}$$

With the relation between the first Piola-Kirchhoff tensor and the Kirchhoff tensor, the material tangent modulus may be expressed by:

$$\begin{aligned} \mathsf{A}_{imkn} &= \frac{\partial P_{im}}{\partial F_{kn}} = \frac{\partial(\tau_{ip}F^{-1}_{mp})}{\partial F_{kn}} \\ &= \frac{\partial\tau_{ip}}{\partial F_{kn}}F^{-1}_{mp} + \tau_{ip}\frac{\partial F^{-1}_{mp}}{\partial F_{kn}} \\ &= \frac{\partial\tau_{ip}}{\partial F_{kn}}F^{-1}_{mp} - \tau_{ip}F^{-1}_{mk}F^{-1}_{np}, \end{aligned} \tag{A.17}$$

which allows to express the spatial tangent modulus as:

$$\mathsf{a}_{ijkl} = \frac{1}{J}\frac{\partial \tau_{ij}}{\partial F_{kn}} F_{ln} - \sigma_{il}\delta_{jk}. \tag{A.18}$$

Finally, the linearised version of the spatial virtual work equation is given by:

$$\int_{\varphi(\Omega)} \mathbf{a} : \nabla_x \Delta \boldsymbol{u} : \nabla_x \delta \boldsymbol{u} dV = -\int_{\varphi(\Omega)} [\boldsymbol{\sigma} : \nabla_x \delta \boldsymbol{u} - \boldsymbol{b} \cdot \delta \boldsymbol{u}]\, dV + \int_{\varphi(\partial\Omega)} \boldsymbol{t} \cdot \delta \boldsymbol{u} dA, \quad \forall \delta \boldsymbol{u} \in \mathcal{V}. \tag{A.19}$$

Appendix B

The mortar method in solid mechanics

The mortar method has been originally developed in the context of the domain decomposition techniques (see e.g. Bernardi et al. (1993)), aiming to overcome restrictions in the decomposition of sub-domains. Nevertheless, it has been successfully applied in coupling domains with distinct discretisations, such as spectral methods with finite elements, and also coupling finite element sub-domains with non-conform discretisation. The latter is the focus of the present work. Furthermore, it has been also applied in the context of computational contact mechanics, in order to impose contact conditions between different solids (Popp, 2012, Puso, 2004, Puso and Laursen, 2003). The mathematical background as well as the proofs regarding the method optimality are detailed by Wohlmuth (2001).

The basic idea is to impose tying or contact between two discretised solids in a weak form, introducing Lagrange multipliers that act as interface tractions to guarantee suitable contact conditions between solids. The formulation in the context of continuum mechanics is presented here. Moreover, the application of the method to enforce periodic boundary conditions on RVEs discretised with meshes that are not conform on opposite faces is addressed.

B.1 Problem Definition

B.1.1 Strong Formulation

Before proceeding, it is important to recall the strong formulation of the general equilibrium problem in a solid:

$$\begin{cases} \mathrm{div}_x\,\boldsymbol{\sigma} + \boldsymbol{b} = \rho\,\ddot{\boldsymbol{u}} & \text{in } \varphi(\Omega) \\ \boldsymbol{t} = \boldsymbol{\sigma}\cdot\boldsymbol{n} & \text{on } \varphi(\partial\Omega) \end{cases}. \tag{2.37}$$

Consider now that the solid domain Ω is divided into two disjoint subdomains, i.e. $\Omega = \Omega^{(1)} \bigcup \Omega^{(2)}$, as shown in Figure B.1. An interface surface arises in each of the subdomains. Let us consider $\Gamma^{(1)}$ the non-mortar interface, and $\Gamma^{(2)}$ the mortar counterpart. Displacement continuity is required over the interface. Therefore, in addition to the momentum balance within each subdomain, a continuity condition must be stated:

$$\begin{cases} \mathrm{div}_x\,\boldsymbol{\sigma} + \boldsymbol{b} = \rho^{(i)}\,\ddot{\boldsymbol{u}}^{(i)} & \text{in } \varphi(\Omega^{(k)}) \\ \boldsymbol{t} = \boldsymbol{\sigma}\cdot\boldsymbol{n} & \text{on } \varphi(\partial\Omega^{(k)}), \quad k = 1,2, \\ \boldsymbol{g} = \boldsymbol{u}^{(1)} - \boldsymbol{u}^{(2)} = \boldsymbol{0} & \text{on } \varphi(\Gamma^{(1)}) \end{cases} \tag{B.1}$$

where the gap function $\boldsymbol{g}$, defined on the non-mortar interface $\Gamma^{(1)}$, measures the displacement *jump* between subdomains.

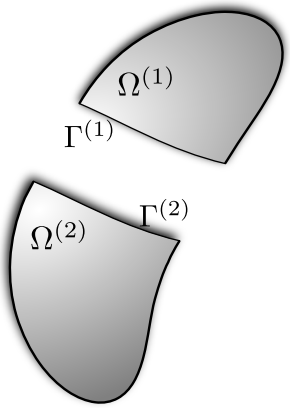

Figure B.1: A body decomposed into two subdomains Ω_1 and Ω_2, and the corresponding interfaces Γ_1 and Γ_2.

B.1.2 Weak formulation

The weak formulation for this problem, considering a quasi-static deformation ($\ddot{\boldsymbol{u}} = \boldsymbol{0}$), is defined from an augmented functional, where the continuity constraint is enforced by a Lagrange multiplier representing the traction forces that enforce $\boldsymbol{g} = \boldsymbol{0}$, i.e., $\boldsymbol{\lambda} = -\boldsymbol{t}^{(1)} = \boldsymbol{t}^{(2)}$

$$\int_{\varphi(\Omega)} (\boldsymbol{\sigma} : \nabla_x \boldsymbol{u} - \boldsymbol{b} \cdot \boldsymbol{u})\, dV - \int_{\varphi(\partial\Omega)} \boldsymbol{t} \cdot \boldsymbol{u} dA + \int_{\varphi(\Gamma_c^{(1)})} \boldsymbol{\lambda} \cdot \boldsymbol{g} dA. \tag{B.2}$$

The weak equilibrium equation is obtained with the application of the *Virtual Work Principle*:

$$\int_{\varphi(\Omega)} (\boldsymbol{\sigma} : \nabla_x \delta\boldsymbol{u} - \boldsymbol{b} \cdot \delta\boldsymbol{u})\, dV - \int_{\varphi(\partial\Omega)} \boldsymbol{t} \cdot \delta\boldsymbol{u} dA + \int_{\varphi(\Gamma^{(1)})} \left(\delta\boldsymbol{\lambda} \cdot \boldsymbol{g} + \boldsymbol{\lambda} \cdot \delta\boldsymbol{g}\right) dA = 0. \tag{B.3}$$

Since this equality must hold for any variation $\delta\boldsymbol{u}$ or $\delta\boldsymbol{\lambda}$, it can be rewritten as:

$$\int_{\varphi(\Omega)} (\boldsymbol{\sigma} : \nabla_x \delta\boldsymbol{u} - \boldsymbol{b} \cdot \delta\boldsymbol{u})\, dV - \int_{\varphi(\partial\Omega)} \boldsymbol{t} \cdot \delta\boldsymbol{u} dA + \int_{\varphi(\Gamma^{(1)})} \boldsymbol{\lambda} \cdot \delta\boldsymbol{g} dA = 0, \quad \forall \delta\boldsymbol{u} \in \mathcal{V}, \tag{B.4}$$

$$\int_{\varphi(\Gamma^{(1)})} \delta\boldsymbol{\lambda} \cdot \boldsymbol{g} dA = 0, \quad \forall \delta\boldsymbol{\lambda} \in \mathcal{M}. \tag{B.5}$$

B.1.3 Discretisation

The finite element method, presented in Section 2.5, is employed to discretise and solve the current equilibrium problem. In the context of a finite element discretisation, the mortar method allows to deal with meshes generated independently for each subdomain resulting in non-coincident interface elements.

Interface elements are inherited from the corresponding subdomain meshes, as represented in Figure B.2. The discretised non-mortar interface is denoted by $\Gamma^{(s)}$ while $\Gamma^{(m)}$ defines the mortar counterpart. The nodes on the non-mortar side $\Gamma^{(s)}$ are considered slaves, whereas the nodes on the mortar interface $\Gamma^{(m)}$ are master nodes. The nodal displacements vector is split as follows:

$$\mathbf{u} = \begin{Bmatrix} \mathbf{u}^{(n)} \\ \mathbf{u}^{(s)} \\ \mathbf{u}^{(m)} \end{Bmatrix}, \tag{B.6}$$

where the superscript s refers to the slave nodes, m to the master nodes and n to the nodes that do not belong to any of the interfaces.

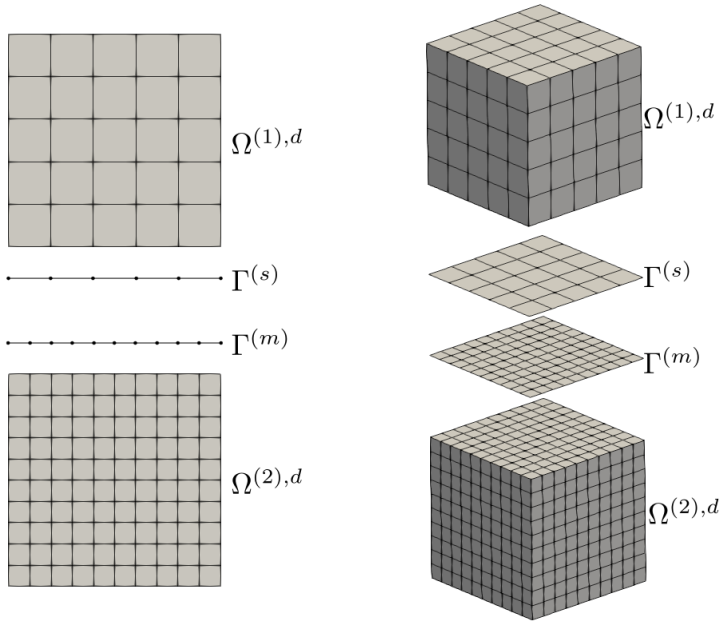

Figure B.2: Example of discretised interfaces on 2D and 3D problems.

A standard finite element discretisation is employed to interpolate the displacements inside each subdomain. The displacements on the interface are interpolated by the shape functions corresponding to the interface mesh, which is inherited from the corresponding subdomain discretisation, i.e., the shape functions $N_k^{(s)}$ are the trace of the corresponding bulk discretisation:

$$\boldsymbol{u}^{(s)}(\boldsymbol{\xi}) = \sum_{k=1}^{n_n^{(s)}} N_k^{(s)}(\boldsymbol{\xi})\,\mathbf{u}_k^{(s)}, \tag{B.7}$$

$$\boldsymbol{u}^{(m)}(\boldsymbol{\zeta}) = \sum_{k=1}^{n_n^{(m)}} N_k^{(m)}(\boldsymbol{\zeta})\,\mathbf{u}_k^{(m)}. \tag{B.8}$$

where $\boldsymbol{\xi}$ and $\boldsymbol{\zeta}$ are the coordinates in the natural space of non-mortar and mortar elements, respectively, N_k corresponds to the shape function value related to k-th node, $\mathbf{u}_k$ is the nodal displacement vector, and $n_n^{(s)}$ and $n_n^{(m)}$ the number of nodes on the non-mortar and the mortar side, respectively.

Lagrange multipliers are interpolated on the slave interface $\Gamma^{(s)}$ using functions M_k that must be suitably chosen to guarantee the optimality properties of the mortar method:

$$\boldsymbol{\lambda}(\boldsymbol{\xi}) = \sum_{k=1}^{n_n^{(s)}} M_k(\boldsymbol{\xi})\,\boldsymbol{\lambda}_k. \tag{B.9}$$

The choice of interpolation functions for the Lagrange multipliers is discussed in Section B.3.

Discretisation of the first two terms of Equation (B.4) is standard (see Section 2.5.2). The discretised coupling interface terms may be conveniently written in matrix format:

$$\int_{\Gamma^{(1)}} \boldsymbol{\lambda}\cdot\delta\boldsymbol{g}\,dA \Rightarrow \boldsymbol{\lambda}^T\mathbf{A}^{nm}\delta\mathbf{u}^{(s)} - \boldsymbol{\lambda}^T\mathbf{A}^{m}\delta\mathbf{u}^{(m)} = \delta\mathbf{u}^T\mathbf{W}^T\boldsymbol{\lambda} \quad , \tag{B.10}$$

$$\int_{\Gamma^{(1)}} \delta\boldsymbol{\lambda}\cdot\boldsymbol{g}\,dA \Rightarrow \delta\boldsymbol{\lambda}^T\mathbf{A}^{nm}\mathbf{u}^{(s)} - \delta\boldsymbol{\lambda}^T\mathbf{A}^{m}\mathbf{u}^{(m)} = \delta\boldsymbol{\lambda}^T\mathbf{W}\mathbf{u} \quad , \tag{B.11}$$

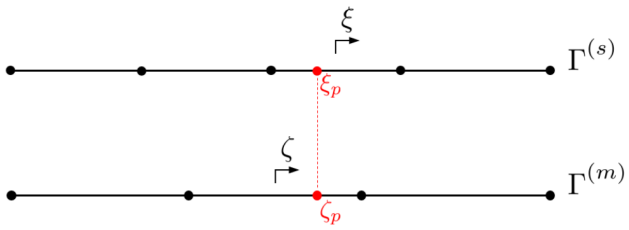

Figure B.3: Mapping procedure from non-mortar to mortar side.

where the so-called non-mortar matrix $\mathbf{A}^{nm}$ and mortar matrix $\mathbf{A}^{m}$ are defined by:

$$\mathbf{A}^{nm} = \begin{bmatrix} \mathbf{A}^{nm}_{11} & \cdots & \mathbf{A}^{nm}_{1n^{(s)}_n} \\ \vdots & \mathbf{A}^{nm}_{kl} & \vdots \\ \mathbf{A}^{nm}_{n^{(s)}_n 1} & \cdots & \mathbf{A}^{nm}_{n^{(s)}_n n^{(s)}_n} \end{bmatrix}, \tag{B.12}$$

$$\mathbf{A}^{m} = \begin{bmatrix} \mathbf{A}^{m}_{11} & \cdots & \mathbf{A}^{m}_{1n^{(m)}_n} \\ \vdots & \mathbf{A}^{m}_{kl} & \vdots \\ \mathbf{A}^{m}_{n^{(s)}_n 1} & \cdots & \mathbf{A}^{m}_{n^{(s)}_n n^{(m)}_n} \end{bmatrix}, \tag{B.13}$$

with the sub-matrices

$$\mathbf{A}^{nm}_{kl} = \int_{\Gamma^{(s),d}} M_k N^{(s)}_l \, dA \cdot \mathbf{I}, \tag{B.14}$$

$$\mathbf{A}^{m}_{kl} = \int_{\Gamma^{(s),d}} M_k N^{(m)}_l \, dA \cdot \mathbf{I}, \tag{B.15}$$

where $\mathbf{I}$ denotes the identity matrix with the spatial dimension of the underlying problem (2 or 3), and

$$\mathbf{W} = \begin{bmatrix} \mathbf{0} & \mathbf{A}^{nm} & -\mathbf{A}^{m} \end{bmatrix}. \tag{B.16}$$

Numerical integration is employed to determine the integrals in Equations (B.15) and (B.14), which are carried out over the non-mortar side $\Gamma^{(s)}$. While for the non-mortar matrix all functions are defined on the non-mortar side, the mortar shape functions $N^{(m)}_l$ must be determined on the mortar side $\Gamma^{(m)}$. Therefore, the integration points defined on the natural coordinates of the non-mortar side $\boldsymbol{\xi}$ must be projected on the mortar discretised interface to determine the corresponding coordinate $\boldsymbol{\zeta}$. This procedure is schematically shown in Figure B.3. More details regarding the determination of mortar integrals are presented in Section B.2.

Finally, the discretised version of Expressions (B.4) and (B.5) yields

$$\begin{cases} \delta\mathbf{u}^T \left\{ \mathbf{f}^{int} - \mathbf{f}^{ext} + \mathbf{W}^T \boldsymbol{\lambda} \right\} = 0 & \forall \delta\mathbf{u} \in \mathcal{V}^d \\ \delta\boldsymbol{\lambda}^T \left\{ \mathbf{W}\mathbf{u} \right\} = 0 & \forall \delta\boldsymbol{\lambda} \in \mathcal{M}^d \end{cases}, \tag{B.17}$$

where the force vectors $\mathbf{f}^*$ are compatible with the definition introduced in Expression (B.6). Since this must hold for any set $\delta\mathbf{u}$ and $\delta\boldsymbol{\lambda}$, the resulting equilibrium problem is defined by the following equation:

$$\begin{cases} \mathbf{f}^{int} - \mathbf{f}^{ext} + \mathbf{W}^T \boldsymbol{\lambda} = \mathbf{0} \\ \mathbf{W}\mathbf{u} = \mathbf{0} \end{cases}. \tag{B.18}$$

B.1.4 Linearisation

The above system of equations is linear on $\boldsymbol{\lambda}$, but the term $\mathbf{r} = \mathbf{f}^{int} - \mathbf{f}^{ext}$ is non-linear on the displacement field $\bar{\mathbf{u}}$. Hence, the iterative Newton-Raphson scheme is applied to solve Equation (B.18), which requires proper linearisation regarding the displacement field $\bar{\mathbf{u}}$. This is quite similar to the linearisation of a standard finite element problem, where the stiffness matrix concept is presented (see Section 2.5). The only difference is that the discretised degrees of freedom are re-sorted according to the corresponding group, and extra terms related to tying constraints appear. The resulting linearised system of equations is given by:

$$\begin{bmatrix} \mathbf{K} & \mathbf{W}^T \\ \mathbf{W} & \mathbf{0} \end{bmatrix} \begin{Bmatrix} \Delta\mathbf{u} \\ \boldsymbol{\lambda} \end{Bmatrix} = - \begin{Bmatrix} \mathbf{r} \\ \mathbf{0} \end{Bmatrix}, \tag{B.19}$$

which, for the sake of clarity, can be expressed in its extended form:

$$\begin{bmatrix} \mathbf{k}^{nn} & \mathbf{k}^{ns} & \mathbf{k}^{nm} & \mathbf{0} \\ \mathbf{k}^{sn} & \mathbf{k}^{ss} & \mathbf{0} & \mathbf{A}^{nm,T} \\ \mathbf{k}^{mn} & \mathbf{0} & \mathbf{k}^{mm} & -\mathbf{A}^{m,T} \\ \mathbf{0} & \mathbf{A}^{nm} & -\mathbf{A}^{m} & \mathbf{0} \end{bmatrix} \begin{Bmatrix} \Delta\mathbf{u}^{(n)} \\ \Delta\mathbf{u}^{(s)} \\ \Delta\mathbf{u}^{(m)} \\ \boldsymbol{\lambda} \end{Bmatrix} = - \begin{Bmatrix} \mathbf{r}^{(n)} \\ \mathbf{r}^{(s)} \\ \mathbf{r}^{(m)} \\ \mathbf{0} \end{Bmatrix}. \tag{B.20}$$

The matrices $\mathbf{k}^{\bullet\bullet}$ represent the stiffness submatrices relating degrees of freedom of distinct groups. Note that no stiffness matrix relating master and slave degrees of freedom exist, since they belong to distinct subdomains, and are related by mortar constraints.

This system of equations explicitly shows the main disadvantage of this approach: the number of unknowns increases with the size of the nodal Lagrange multiplier vector $\boldsymbol{\lambda}$. Nevertheless, this can be easily overcome, since it can be eliminated from the unknown vector. Looking at the second equation of Expression (B.20), the Lagrange multiplier vector can be expressed by:

$$\boldsymbol{\lambda} = \left[\mathbf{A}^{nm,T}\right]^{-1} \left(-\mathbf{r}^{(s)} - \mathbf{k}^{sn}\Delta\mathbf{u}^{(n)} - \mathbf{k}^{ss}\Delta\mathbf{u}^{(s)}\right). \tag{B.21}$$

Replacing the above expression in the remaining equations of the system of equations (B.20), and defining the matrix $\boldsymbol{\alpha} = [\mathbf{A}^{nm}]^{-1}\mathbf{A}^{m}$, results in the following:

$$\begin{bmatrix} \mathbf{k}^{nn} & \mathbf{k}^{ns} & \mathbf{k}^{nm} \\ \mathbf{k}^{mn} + \boldsymbol{\alpha}^T\mathbf{k}^{sn} & \boldsymbol{\alpha}^T\mathbf{k}^{ss} & \mathbf{k}^{mm} \\ \mathbf{0} & \mathbf{A}^{nm} & -\mathbf{A}^{m} \end{bmatrix} \begin{Bmatrix} \Delta\mathbf{u}^{(n)} \\ \Delta\mathbf{u}^{(s)} \\ \Delta\mathbf{u}^{(m)} \end{Bmatrix} = - \begin{Bmatrix} \mathbf{r}^{(n)} \\ \mathbf{r}^{(m)} + \boldsymbol{\alpha}^T\mathbf{r}^{(s)} \\ \mathbf{0} \end{Bmatrix}. \tag{B.22}$$

In addition, from the last equation it is possible to retrieve the following linear relation between slave and master iterative displacements:

$$\Delta\mathbf{u}^{(s)} = \boldsymbol{\alpha}\Delta\mathbf{u}^{(m)}. \tag{B.23}$$

This enables a reduction of the size of the system of equations, which is finally stated as:

$$\begin{bmatrix} \mathbf{k}^{nn} & \mathbf{k}^{nm} + \mathbf{k}^{ns}\boldsymbol{\alpha} \\ \mathbf{k}^{mn} + \boldsymbol{\alpha}^T\mathbf{k}^{sn} & \mathbf{k}^{mm} + \boldsymbol{\alpha}^T\mathbf{k}^{ss}\boldsymbol{\alpha} \end{bmatrix} \begin{Bmatrix} \Delta\mathbf{u}^{(n)} \\ \Delta\mathbf{u}^{(m)} \end{Bmatrix} = - \begin{Bmatrix} \mathbf{r}^{(n)} \\ \mathbf{r}^{(m)} + \boldsymbol{\alpha}^T\mathbf{r}^{(s)} \end{Bmatrix}. \tag{B.24}$$

B.2 Determination of Mortar Integrals

In order to solve the linear system of equations of Expression (B.20), besides stiffness submatrices, mortar matrices $\mathbf{A}^{nm}$ and $\mathbf{A}^{m}$ must be determined, which involves the computation of mortar integrals over the slave interface. In the present numerical framework, Gaussian quadrature is applied to compute the integrals. However, since mortar and non-mortar shape functions are defined on non-conform meshes, integrands may not be C^1-continuous in slave elements. Hence, special attention is required so that this numerical technique does not lose its accuracy. It is important to remark that in the context of mesh tying problems, these integrals only need to be evaluated once, during the problem initialisation, since the relative positions between mortar and non-mortar interfaces will not change.

B.2.1 Two-dimensional problems

Regarding the computation of non-mortar integrals, straightforward application of Gaussian quadrature (see Section 2.5.5) on slave interface elements is possible:

$$A_{e,ij}^{nm} = \sum_{p=1}^{n_{gp}} w_p M_i\left(\xi_p\right) N_j^{(s)}\left(\xi_p\right) J_p. \tag{B.25}$$

The global non-mortar matrix (Expression (B.12)) is obtained by assemblage of elemental counterparts:

$$\mathbf{A}^{nm} = \bigwedge_{e=1}^{n_e} \mathbf{A}_e^{nm}. \tag{B.26}$$

More complicated procedures arise for determining the mortar matrix $\mathbf{A}^{m}$ (Expression (B.13)), since it involves the integration of quantities that are not defined on the slave elements. A mapping between master and slave interfaces is needed to overcome this difficulty. Furthermore, integration cannot be performed directly on slave elements, since it does not guarantee that the integrand is C^1-continuous (continuous first derivative) in the integration domain, and Gaussian quadrature may lose its accuracy. This motivates the definition of mortar segments, in which both M_i and $N_j^{(m)}$ derivatives are continuous.

In practice, these segments are defined by exterior nodes of both master and slave elements. Therefore, it is necessary to introduce discrete projection methods to obtain the definition of mortar segments on the slave interface. The special case of parallel straight interfaces is treated in a straightforward fashion, whereas in the general case a normal vector field must be defined on the slave side, in order to obtain projections of either non-mortar and mortar nodes on the opposite side. The procedure to determine mortar segments in a general framework is well described by Popp (2012).

In the context of the present work, only straight parallel interfaces are analysed, as represented in Figure B.4. Since only one coordinate suffices to define positions on both interfaces (let one consider x), projections of nodes on the opposite side are direct. Hence, the definition of mortar segments, as well as the mapping of integration points between master and slave sides, becomes quite simple when comparing with the general case.

A parametrized space $\omega \in [-1,1]$, where integration points ω_p are defined, is associated to a given mortar segment, limited by x_a and x_b. The corresponding x_p coordinates are easily retrieved by:

$$x_p = \frac{1}{2}\left[\omega_p\left(x_b - x_a\right) + x_a + x_b\right]. \tag{B.27}$$

With the global coordinate at hand, the coordinates in the elements natural space, on both non-

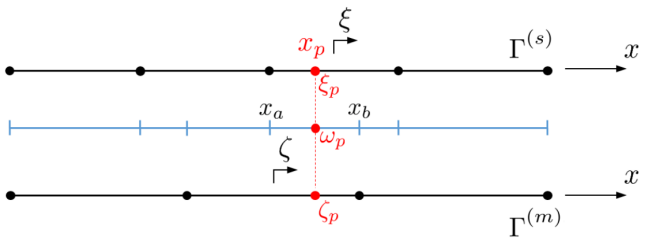

Figure B.4: Definition of mortar segments (in blue), limited by end nodes of either non-mortar and mortar elements.

mortar and mortar sides, are obtained with the solution of the following equations, for ξ_p and ζ_p:

$$\begin{aligned} x_p &= \sum_{k=1}^{n_n^{(s)}} N_i^{(s)}(\xi_p) x_i \\ x_p &= \sum_{l=1}^{n_n^{(m)}} N_i^{(m)}(\zeta_p) x_i \end{aligned} . \tag{B.28}$$

In the case of 2-noded elements, the solution is explicit. However, for higher order elements, non-linear equations must be solved, thus, a local Newton-Raphson scheme is introduced.

The contribution of each mortar segment d integral to the mortar matrix is computed by:

$$A_{d,ij}^m = \sum_{p=1}^{n_{gp}} w_p M_i\left(\xi(\omega_p)\right) N_j^{(m)}\left(\zeta(\omega_p)\right) J_p, \tag{B.29}$$

where

$$J_p = \frac{\partial \boldsymbol{x}_p}{\partial \omega_p} = \frac{\partial \boldsymbol{x}_p}{\partial \xi} \frac{\partial \xi}{\partial \omega_p}. \tag{B.30}$$

Finally, the global mortar matrix is obtained by assemblage of all n_d mortar segments contributions:

$$\mathbf{A}^m = \bigwedge_{d=1}^{n_d} \mathbf{A}_d^m. \tag{B.31}$$

B.2.2 Three-dimensional problems

Although the concepts introduced in the previous section, related to the 2D case, are extensible to 3D problems, the actual implementation is much more difficult due to geometric issues. In the present document, only the case of plane parallel surfaces is considered. The generic situation is treated by Puso and Laursen (2003) and Puso (2004).

The most cumbersome task is the definition of mortar segments for 3D problems, which consists in finding the intersections between mortar and non-mortar elements, as shown in Figure B.5. In the present work, a clipping algorithm from the *Polypack* package (Kennison, 2000), which returns the intersection of two polygons defined in a bi-dimensional space, is used to obtain the intersection polygon between a mortar and a non-mortar element. This is possible since, in this particular case, both master and slave discretisations can be defined in the same plane, i.e., using a system of two coordinates. In the general case, an auxiliary plane associated to each slave element is created, where all nodes are projected, and then the clipping algorithm is employed. Obviously, it is not known *a priori* which elements from both sides will generate a non-empty intersection, thus all possibilities must be tested.

Similarly to the 2D situation, mortar integrals are computed over mortar segments, in order to guarantee functions continuity. A numerical integration scheme must be defined to determine

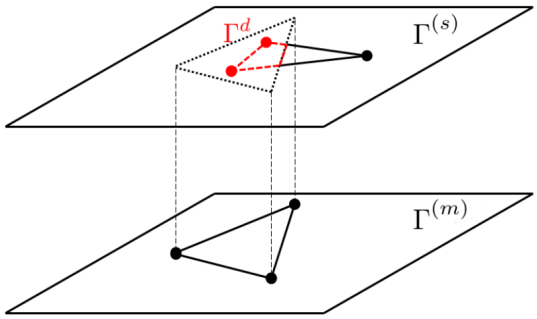

(a) Clipping

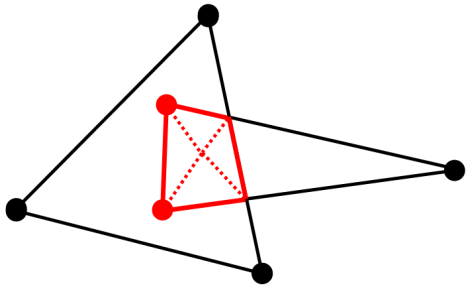

(b) Subdivide polygon in triangles

Figure B.5: Definition of mortar segments for 3D problems.

$\int_{\Gamma^d} M_k(\boldsymbol{\xi}) N_l(\boldsymbol{\zeta}) dA$, which is not so direct, since the resulting polygon has an arbitrary shape. Therefore, the intersection polygon is subdivided into n_p triangles, where n_p is the number of polygon sides. This is performed defining the polygon geometric center as a common vertex, which is linked to each of the polygon vertices, as shown in Figure B.5b. Integration is performed over these triangles according to the Gauss-Radau rule (Cowper, 1973). The contributions from the triangles are assembled into the global mortar matrix:

$$\mathbf{A}^m = \mathop{\mathsf{A}}_{d=1}^{n_d} \sum_{t=1}^{n_p} \mathbf{A}^m_{d,t}. \tag{B.32}$$

The strategy employed in the present case is summarized in Box B.1.

B.3 Lagrange Multipliers Interpolation

While standard finite element shape functions are used to interpolate the displacement field on the subdomains and their interfaces, different interpolation functions M_i can be used for the Lagrange multipliers. These interpolation functions must satisfy a set of approximation properties, as discussed by Wohlmuth (2001), that introduces the mathematical theory behind the mortar method. Two different sets of interpolation functions for the Lagrange multipliers are presented in this section.

B.3.1 Standard basis

The most obvious choice for the interpolation of Lagrange multipliers is to use the standard element shape functions on the interface, which are also used to interpolate geometry and displacement field. Thus, since $M_k \equiv N^{(s)}_k$, the discrete Lagrange multiplier field yields:

$$\boldsymbol{\lambda}(\boldsymbol{\xi}) = \sum_{k=1}^{n^{(s)}_n} N^{(s)}_k(\boldsymbol{\xi}) \boldsymbol{\lambda}_k. \tag{B.33}$$

With this approach, slave and master displacements are globally related, which is perceptible by the existence of a dense dependency matrix $\boldsymbol{\alpha}$. Besides this fact, inverting the mortar matrix $\mathbf{A}^{nm}$ involves more complicated algorithms (LU-decomposition based algorithms, e.g.), increasing the computation time. An alternative, which is able to overcome these inconvenient situations, is introduced with a dual basis for the Lagrange multipliers interpolation functions.

Box B.1 Algorithm for computing mortar integrals in 3D problems, with plane parallel interfaces.

I. Loop over non-mortar elements: $i = 1, n_{el}^{(s)}$

1. Compute the element non-mortar matrix

$$A_{i,kl}^{nm} = \int_{\Gamma^i} M_k(\boldsymbol{\xi}) N_l^{(s)}(\boldsymbol{\xi}) \, dA;$$

2. Assemble into the global non-mortar matrix $\mathbf{A}^{nm}$;
3. Loop over mortar elements: $j = 1, n_{el}^{(m)}$
   i) Determine the polygon intersection: $\Gamma^d \equiv \Gamma^i \cap \Gamma^j$;
   ii) If the polygon intersection exists ($n_p \geq 3$):
      a) Obtain the polygon geometric center, and subdivide in n_p triangles;
      b) For each triangle, apply Gauss-Radau integration rule to compute

$$A_{t,kl}^{m} = \int_{\Gamma^d} M_k(\boldsymbol{\xi}) N_l^{(m)}(\boldsymbol{\zeta}) \, dA;$$

      c) Compute the mortar segment contribution

$$\mathbf{A}_d^m = \sum_{t=1}^{n_p} \mathbf{A}_t^m;$$

      d) Assemble into the global mortar matrix $\mathbf{A}^m$.

B.3.2 Dual basis

Dual basis interpolation functions for Lagrange multipliers are based on the assumption that they satisfy the bi-orthogonality condition with the displacement shape functions, i.e.:

$$\int_{\Gamma^{(s)}} M_k N_l^{(s)} \, dA = \delta_{kl} \int_{\Gamma^{(s)}} N_l^{(s)} \, dA. \tag{B.34}$$

For practical reasons, this condition is applied in an element-wise framework:

$$\int_{\Gamma_e^{(s)}} M_k N_l^{(s)} \, dA_e = \delta_{kl} \int_{\Gamma_e^{(s)}} N_l^{(s)} \, dA_e. \tag{B.35}$$

Under this condition, the non-mortar matrix $\mathbf{A}^{nm}$ becomes diagonal:

$$\mathbf{A}^{nm} \rightarrow \mathbf{D}^{nm} : \; D_{ii}^{nm} = \int_{\Gamma^{(s)}} N_i \, dA, \tag{B.36}$$

which reflects the fact that, unlike standard basis, with a dual basis the coupling between mortar and slave is localized, therefore, the dependency matrix $\boldsymbol{\alpha}$ becomes a sparse matrix instead of a dense matrix. Furthermore, the inversion of $\mathbf{A}^{nm} \equiv \mathbf{D}^{nm}$ becomes trivial.

Considering all these benefits, this approach is especially suitable to employ within the solution of the discretised problem, through the reduced system on Expression (B.24). As pointed by Popp (2012), condensation of the linear system of equations could also be performed in the framework of standard basis. However, it is not desirable since it involves the inversion of a mass matrix, and the global coupling between slave and master nodes leads to a more complex system of equations to solve.

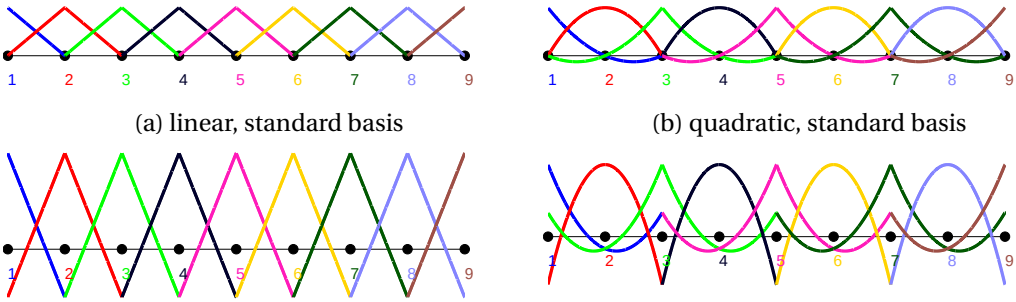

(a) linear, standard basis

(b) quadratic, standard basis

(c) linear, dual basis

(d) quadratic, dual basis

Figure B.6: Representation of Lagrange multiplier interpolation functions for 1D interface elements, in both standard and dual basis.

For some types of elements, the definition of dual basis shape functions by means of explicit expressions is possible, namely, when interface elements are characterised by constant Jacobian. Expressions for these cases are presented next.

In the case of linear 2D elements, non-mortar discretized interface results in **linear 1D elements** (*line 2*). Dual basis interpolation functions are defined by:

$$M_1(\xi) = \frac{1}{2}(1-3\xi), \quad M_2(\xi) = \frac{1}{2}(1+3\xi). \tag{B.37}$$

A different situation arises when quadratic elements are used, which results in **1D quadratic elements** (*line 3*). If these elements are undistorted, it is possible to define the following dual basis expressions:

$$M_1(\xi) = \frac{1}{4}\left(5\xi^2 - 2\xi - 1\right), \quad M_2(\xi) = \frac{1}{2}\left(3 - 5\xi^2\right), \quad M_3(\xi) = \frac{1}{4}\left(5\xi^2 + 2\xi - 1\right). \tag{B.38}$$

For the general case, a method which is presented below must be applied. However, note that for applications like mesh tying, as mortar relations are defined only once at problem initialisation, the above expressions may be used.

Functions in standard and dual basis are plotted for both linear and quadratic 1D elements in Figure B.6.

When **linear 3D elements** are considered, two distinct interface types of element may appear: linear triangular (3 nodes) or linear quadrilateral (4 nodes). While for the latter it is not possible to define general expressions, for **linear triangular elements** (*tri 3*) the determinant of the Jacobian is constant, thus, the explicit expressions for this case yield:

$$M_1(\xi,\eta) = 3 - 4\xi - 4\eta, \quad M_2(\xi,\eta) = 4\xi - 1, \quad M_3(\xi,\eta) = 4\eta - 1. \tag{B.39}$$

Whenever the definition of *apriori* expressions is not possible, the method described in the following paragraphs may be applied (Hartmann et al., 2007).

Consider that the interpolation function functions M_k may be obtained as a linear combination of $N_j^{(s)}$:

$$M_k(\boldsymbol{\xi}) = \sum_{j=1}^{n_n^{(s)}} a_{kj} N_j^{(s)}(\boldsymbol{\xi}). \tag{B.40}$$

Introducing this definition in the bi-orthogonality condition (B.35), and representing the result in matrix form, the following relation is obtained:

$$\mathbf{A}^e\mathbf{M} = \mathbf{D}^e, \tag{B.41}$$

where the matrix $\mathbf{A}^e$ stores the linear mapping coefficients ($A^e_{kj} = a_{kj}$), $\mathbf{M}$ is a mass matrix-like:

$$\mathbf{M} = \int_{\Gamma^{(s)}_e} N^{(s)}_j N^{(s)}_l \, dA, \tag{B.42}$$

and $\mathbf{D}^e$ is a local diagonal matrix:

$$D^e_{ll} = \int_{\Gamma^{(s)}_e} N^{(s)}_l \, dA. \tag{B.43}$$

Finally, the linear coefficients are obtained with

$$\mathbf{A}^e = \mathbf{D}^e \mathbf{M}^{-1}. \tag{B.44}$$

Although the above procedure for obtaining dual basis functions can be extended for **quadratic 2D interface elements**, some computational problems and inconsistencies may arise. In the specific case of mesh tying problems, when considering *tri 6* interface elements, some diagonal components will assume zero value, thus $\mathbf{D}^{nm}$ becomes singular, and the condensation method introduced in Expression (B.24) is no longer feasible, since it is not possible to obtain the relation mapping matrix $\boldsymbol{\alpha}$. This is due to the fact that integration of shape functions related to corner nodes on this kind of elements results in a null value.

This question is even more restrictive for contact problems, where the mortar method is used to impose contact conditions, since an integral positivity condition

$$\int_{\Gamma^{(s)}} M_k \, dA > 0 \tag{B.45}$$

must be satisfied, in order to avoid unphysical gaps and penetrations (Popp et al., 2012), which is not in the case of *Tri 6* and *Quad 8* interface elements.

Motivated by this shortcoming, Popp (Popp et al., 2012, Popp, 2012) proposed two alternative strategies to define dual Lagrange multiplier interpolation functions. One is based on quadratic and the second on linear dual Lagrange multipliers. Only the former is presented and implemented in the context of the present work, since the latter assumes that only nodes at element corners carry Lagrange multipliers.

A modification of shape functions on non-mortar side is proposed, which, for *Tri 6* elements, is defined by

$$\begin{Bmatrix} \tilde{N}_1 \\ \tilde{N}_2 \\ \tilde{N}_3 \\ \tilde{N}_4 \\ \tilde{N}_5 \\ \tilde{N}_6 \end{Bmatrix} = \begin{bmatrix} 1 & 0 & 0 & 0 & 0 & 0 \\ \alpha & 1-2\alpha & \alpha & 0 & 0 & 0 \\ 0 & 0 & 1 & 0 & 0 & 0 \\ 0 & 0 & \alpha & 1-2\alpha & \alpha & 0 \\ 0 & 0 & 0 & 0 & 1 & 0 \\ \alpha & 0 & 0 & 0 & \alpha & 1-2\alpha \end{bmatrix}^T \begin{Bmatrix} N_1 \\ N_2 \\ N_3 \\ N_4 \\ N_5 \\ N_6 \end{Bmatrix}. \tag{B.46}$$

The authors state that for $\alpha = 1/5$ integral positivity is guaranteed for the modified shape functions, and feasible dual Lagrange interpolation functions can be obtained by the enforcement of the biorthogonality condition between M_k and $\tilde{N}^{(s)}_j$, following the procedure defined by Expressions (B.40) to (B.44).

With regard to the mortar matrices, $\mathbf{A}^m$ is computed as in the usual case,

$$A_{m,kl} = \int_{\Gamma^{(s)}} M_k N^{(m)}_l \, dA, \tag{B.47}$$

where the only difference is the definition of functions M_k, whereas the non-mortar matrix yields

$$\mathbf{A}^{nm} = \tilde{\mathbf{D}}\mathbf{T}^{-1}, \tag{B.48}$$

where $\tilde{\boldsymbol{D}}$ denotes the diagonal matrix that results from the biorthogonality condition, which is given by

$$\tilde{D}_{kk} = \int_{\Gamma^{(s)}} \tilde{N}_k^{(s)} \, dA. \tag{B.49}$$

Once this matrix is computed with basis on the transformed shape functions, it is mapped by Expression (B.48) to $\mathbf{A}^{nm}$ through the global transformation matrix $\mathbf{T}$. Although it is not diagonal anymore, its inverse is obtained in a simple fashion:

$$\left[\mathbf{A}^{nm}\right]^{-1} = \mathbf{T}\tilde{\mathbf{D}}^{-1}. \tag{B.50}$$

Since $\tilde{\mathbf{D}}$ is diagonal, its inversion becomes trivial, and the global transformation matrix is obtained by assemblage of the element transformation matrices, defined by:

$$\mathbf{T}_{el} = \begin{bmatrix} 1 & 0 & 0 & 0 & 0 & 0 \\ \alpha & 1-2\alpha & \alpha & 0 & 0 & 0 \\ 0 & 0 & 1 & 0 & 0 & 0 \\ 0 & 0 & \alpha & 1-2\alpha & \alpha & 0 \\ 0 & 0 & 0 & 0 & 1 & 0 \\ \alpha & 0 & 0 & 0 & \alpha & 1-2\alpha \end{bmatrix}. \tag{B.51}$$

Therefore, besides overcoming the referred problems, the computational convenience introduced by the usage of dual basis Lagrange interpolation functions is maintained with this procedure.

B.3.3 Modifications to avoid over-constraint

In the context of the mortar method, special situations exist where over-constraint issues may arise, and suitable approaches must be introduced.

If a node to which an essential (Dirichlet) boundary condition is applied lies in a non-mortar interface, it does not make sense that this node carries a Lagrange multiplier component, since its solution is already defined.

In these cases, the Lagrange multiplier association is conceptually removed from the node, and a modification of the interpolation functions M_k is established on its vicinity, for the sake of consistency and stability and so that important interpolation characteristics, such as the partition of unity property ($\sum_k M_k = 1$), are maintained. Detailed information about the procedures to modify interpolation functions is presented by Wohlmuth (2001).

This approach is also applied whenever more than two subdomains meet at a crosspoint (1D interfaces) or an edge (*wirebaskets* on 2D interfaces), as represented in Figure B.7. In this situation, more than one mortar constraint is applied to a node that is in the intersection between two discretized slave interfaces, leading to over-constraint problems. Note that in a crosspoint n_s nodes exist, that arise from the discretisation of n_s intersecting subdomains.

In the available literature, it is stated that this issue is solved with the introduction of modifications on Lagrange multiplier interpolation functions in the vicinity of crosspoints, similarly to the case of nodes constrained by essential boundary conditions (c.f. Popp (2012), Puso and Laursen (2003)). Although this procedure is widely presented for crosspoints, a detailed explanation for its implementation has not been found, namely concerning the choice of the mortar side that actually constrains the possibly over-constrained nodes. In what refers to 3D problems, the *wirebaskets* definition is presented by Wohlmuth (2001), but no computational strategy is introduced to deal with them. Moreover, Puso and Laursen (2003), besides proposing a method to deal with mesh tying for general 3D problems, only present the case of crosspoints in a 2D framework.

The modifications on the interpolation functions in the vicinity of over-constrained nodes are presented below, with special focus on dual basis functions. In the case of 1D linear interface elements, the element adjacent to the constrained node carries only one interpolation function, which is constant through the entire element: $M_k = 1$. This is valid for both standard and dual basis.

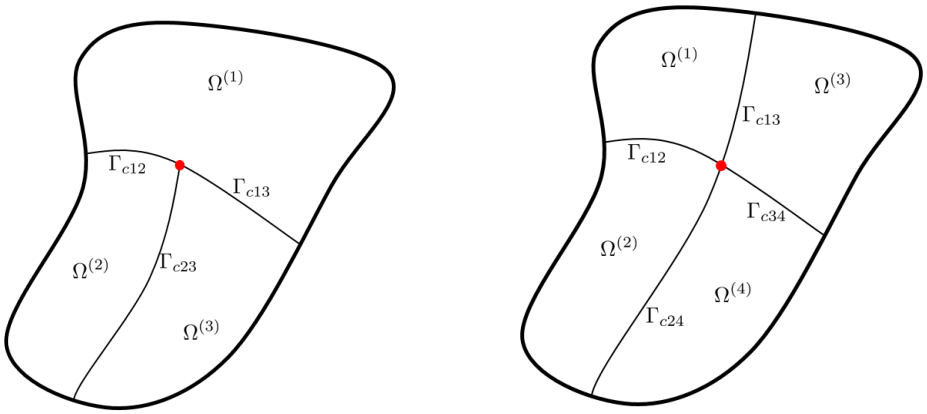

Figure B.7: Body divided in more than two subdomains, that meet at a crosspoint(in red).

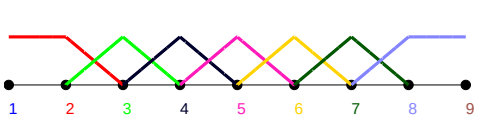

(a) linear, standard basis

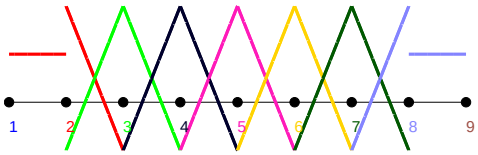

(b) linear, dual basis

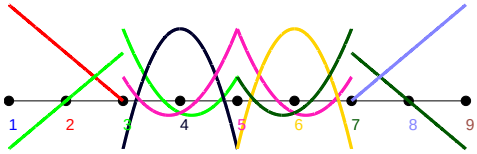

(c) quadratic, dual basis

Figure B.8: Representation of Lagrange multiplier interpolation functions for 1D interface elements, with suitable modifications on extreme nodes, in order to take into account imposed boundary conditions.

In what refers to 1D quadratic elements, if the left node is prescribed, then modified shape functions on the adjacent element yield:

$$M_1(\xi) = 0, \quad M_2(\xi) = 1 - \xi, \quad M_3(\xi) = \xi. \tag{B.52}$$

On the other hand, if an essential boundary condition is applied to the right side node, then:

$$M_1(\xi) = -\xi, \quad M_2(\xi) = 1 + \xi, \quad M_3(\xi) = 0. \tag{B.53}$$

Representations of interpolation functions M_k with suitable modifications on the limit nodes, considering that they are subjected to essential boundary conditions, are shown in Figure B.8. These plots may be directly compared with the corresponding on Figure B.6.

With regard to the 3D case, Wohlmuth (2001) proposes a technique to modify dual basis interpolation functions in the vicinity of a prescribed boundary, that is suitable for linear quadrilateral and triangular interface meshes. Despite the fact that these modifications have the same theoretical explanation presented above, its application to 3D examples becomes cumbersome due to a larger number of geometric possibilities. In the cited reference, the modifications for 3D case are stated as follows, where some comments have been introduced for the sake of clarity:

- Divide interface nodes on:

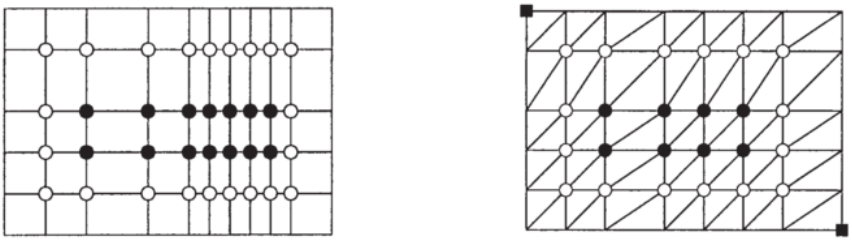

Figure B.9: Possible non-mortar interfaces on 3D problems, with representation of node subgroups to modify interpolation functions (Wohlmuth, 2001).

(i) interior nodes $\boldsymbol{X}_i$, which are not connected to any boundary node through element connectivities, i.e. $\partial(\text{supp}M_i)\bigcap\partial\Gamma^{(s)}=\emptyset$, and

(ii) boundary nodes, which share element connections with nodes on the boundary of the interface;

- Interior nodes (filled circles on Figure B.9) assume interpolation functions as defined, without any modifications;
- Nodes in group (ii) are split into three subgroups:

  (a) nodes $\boldsymbol{X}_l \notin \partial\Gamma^{(s)}$ that do not belong to the interface boundary (represented by empty circles),

  (b) nodes on the boundary, which are connected to nodes of subgroup (a), i.e., $\mathscr{X}_l=\left\{\boldsymbol{X}_j : \boldsymbol{X}_j \in \partial\Gamma^{(s)}\bigcap\partial(\text{supp}M_l)\right\}$, and

  (c) nodes in the subgroup defined by $\mathscr{M}=\left\{\boldsymbol{X}_j : \boldsymbol{X}_j \in \partial\Gamma^{(s)}\right\}\setminus\bigcup_{\boldsymbol{X}_l\in\Gamma^{(s)}}\mathscr{X}_l$, which are the nodes that belong to the boundary of the interface but are not connected to any node of subgroup (a) (filled squares);

- Modify interpolation functions of nodes on subgroup (a) according to:

$$\bar{M}_l = M_l + \sum_{\boldsymbol{X}_j\in\mathscr{X}_l}\frac{1}{n_j}M_j + \sum_{\boldsymbol{X}_j\in\mathscr{X}}\alpha_{lj}M_j, \tag{B.54}$$

where n_j is the number of sets $\mathscr{X}_k$ such that $\boldsymbol{X}_j\in\mathscr{X}_k$, which reflects the number of nodes of subgroup (a) to which a node j of subgroup (b) is connected; and

$$\alpha_{lj} = 1 \text{ if } \partial(\text{supp}M_l)\bigcap\partial(\text{supp}M_j) \text{ contains an edge,} \tag{B.55}$$

$$\alpha_{lj} = 0 \text{ elsewhere.} \tag{B.56}$$

This means that the interpolation function associated with each node j in subgroup (c) is transferred to the node of subgroup (a) that belongs to an element sharing an edge with the element to which node j belongs.

It must be remarked that, with these modifications, not only function values are modified, but also the support of Lagrange multiplier interpolation functions, since contributions from distinct nodes are added to node l, extending the spatial domain where M_l is originally defined.

This strategy has been implemented in the context of the present work. The developed algorithm is presented in Box B.2. In first place, nodes which are subjected to modifications on its interpolation function are identified, as well as the corresponding boundary nodes that are responsible for that modification, and the corresponding parameter n_j. This step is followed by a standard procedure for the determination of mortar matrices, and, in a final step, suitable assemblage

is preformed, adding modification terms to the corresponding mortar matrix $\mathbf{A}^m$ positions. An explanation of the validity of this procedure is given next. Looking at the modified Expression (B.54), mortar integrals yield:

$$\int_{\Gamma^{(s)}} \bar{M}_l N_k^{(m)} dA = \int_{\Gamma^{(s)}} M_l N_k^{(m)} dA + \sum_{\boldsymbol{X}_j \in \mathscr{X}_l} \frac{1}{n_j} \int_{\Gamma^{(s)}} M_j N_k^{(m)} dA + \sum_{\boldsymbol{X}_j \in \mathscr{X}} \alpha_{kj} \int_{\Gamma^{(s)}} M_j N_k^{(m)} dA. \quad \text{(B.57)}$$

Therefore, it is possible to compute these integrals in a first stage, without introducing any modifications, adding contributions of nodes j, that modify nodes l, to the corresponding rows, during the assemblage procedure.

Box B.2 Pseudo-algorithm for the modification of Lagrange multiplier interpolation functions on 3D mortar problems.

I. Determine nodes l belonging to subgroup (a), and corresponding nodes j in subgroups (b) and (c) that will modify each node l, as well as the associated parameter n_j;

II. Loop over non-mortar elements: $i = 1, n_{el}^{(s)}$

1. Compute elemental non-mortar diagonal matrix

$$D_{i,kk}^{nm} = \int_{\Gamma^i} N_k^{(s)}(\boldsymbol{\xi}) dA;$$

2. Assemble into the global non-mortar matrix $\mathbf{D}^{nm}$;
3. Loop over mortar elements: $j = 1, n_{el}^{(m)}$
   i) Determine the polygon intersection: $\Gamma^d \equiv \Gamma^i \cap \Gamma^j$;
   ii) If polygon intersection exists ($n_p \geq 3$):
      a) Obtain the polygon geometric center, and subdivide in n_p triangles;
      b) Determine interpolation functions M_k on dual basis;
      c) For each triangle, apply Gauss-Radau integration rule to compute

$$A_{t,kl}^m = \int_{\Gamma^d} M_k(\boldsymbol{\xi}) N_l^{(m)}(\boldsymbol{\zeta}) dA;$$

      d) Compute $\mathbf{a} = \sum_{t=1}^{n_p} \mathbf{a}_t^m$;
      e) Standard assemblage to global mortar matrix $\mathbf{A}^m$ (except boundary nodes);
      f) Add modification contributions to $\mathbf{A}^m$. If j modifies k:

$$\int_{\Gamma^d} M_j(\boldsymbol{\xi}) N_l^{(m)}(\boldsymbol{\zeta}) dA n_j \rightarrow A_{kl}^m,$$

      or

$$\int_{\Gamma^d} M_j(\boldsymbol{\xi}) N_l^{(m)}(\boldsymbol{\zeta}) dA \rightarrow A_{kl}^m.$$

B.4 Mortar Periodic Boundary Condition

The periodic boundary condition is the most widely used in RVE analysis. This is due to the fact that the homogenised properties obtained with periodic boundary condition lie between the counterparts obtained with linear displacement and uniform traction on the boundary, and, furthermore, that results converge faster to a stable response as the RVE size increases (Terada et al., 2000).

However, implementation of standard perdiodic boundary condition (see Section 3.3.3) introduces strong limitations on the RVE finite element model, since it requires the mesh to be periodic, i.e., nodes on the positive side must have direct correspondence with nodes on the negative side. Although for simple models this requirement is easily satisfied, it may become cumbersome when complex microstructures are modelled.

A very interesting proposal to deal with RVEs whose discretisation is not conform on opposite sides is presented by Reis and Andrade Pires (2014). The basic idea is to introduce the mortar method at the RVE level, in order to impose that the displacement fluctuation field is equal on opposite faces (Expression (3.20)). Actually, this strategy may be seen as a mesh tying problem between opposite faces, since the periodic boundary condition assumes that the microstructure is periodic itself, thus, it may be seen as a spatial repetition of the RVE, as shown in Figure B.10.

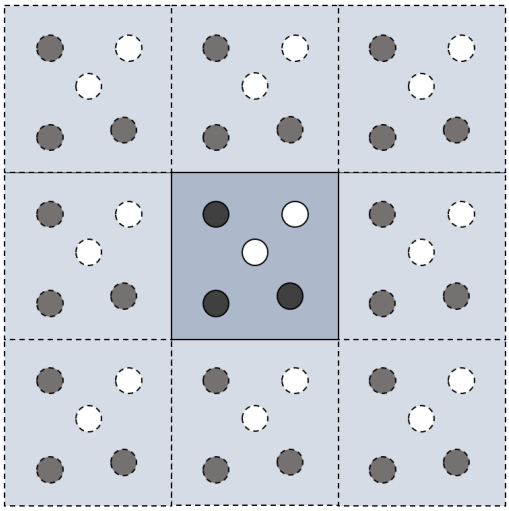

Figure B.10: Representation of a periodic microstructure as a spatial repetition of similar RVEs.

B.4.1 Problem Formulation

Taking into account the RVE equilibrium strong equations, an additional constraint is added by the following equation:

$$\boldsymbol{g} = \tilde{\boldsymbol{u}}^{+} - \tilde{\boldsymbol{u}}^{-} = \boldsymbol{0}. \tag{B.58}$$

It is remarked that, unlike traditional mesh tying problems, here the gap $\boldsymbol{g}$ is defined by the difference between displacement fluctuations and not between total displacements.

Similarly to what is presented in Section B.1.2, Lagrange multipliers are introduced in the functional in order to impose the above condition, and, applying the *Virtual Work Principle*, the constrained counterpart of Expression (3.11) yields:

$$\int_{\varphi(\Omega_\mu)} \boldsymbol{\sigma}(\boldsymbol{y},t) : \nabla_x \delta\tilde{\mathbf{u}} dV + \int_{\varphi(\Gamma^+)} \boldsymbol{\lambda} \cdot \delta\boldsymbol{g} dA = 0, \quad \forall\, \delta\tilde{\mathbf{u}} \in \tilde{\mathcal{V}} \tag{B.59}$$

$$\int_{\varphi(\Gamma^+)} \delta\boldsymbol{\lambda} \cdot \boldsymbol{g} dA = 0, \quad \forall \delta\boldsymbol{\lambda} \in \mathcal{M}. \tag{B.60}$$

In this case, the positive side is defined as the non-mortar side, and the Lagrange multiplier vector coincides with the traction vector field on this side that is responsible for satisfying the boundary condition.

B.4.2 Numerical solution

Considering a finite element discretisation, and following the steps presented in Section B.1.3, the constrained equilibrium equation is defined by

$$\begin{Bmatrix} \mathbf{f}^{i} \\ \mathbf{f}^{-} - \mathbf{A}^{m,T}\boldsymbol{\lambda} \\ \mathbf{f}^{+} + \mathbf{A}^{nm,T}\boldsymbol{\lambda} \\ \mathbf{A}^{nm}\tilde{\mathbf{u}}^{+} - \mathbf{A}^{m}\tilde{\mathbf{u}}^{-} \end{Bmatrix} = \mathbf{0}. \tag{B.61}$$

Linearisation with regard to the displacement fluctuations results in the following system of equations:

$$\begin{bmatrix} \mathbf{k}^{ii} & \mathbf{k}^{i-} & \mathbf{k}^{i+} & \mathbf{0} \\ \mathbf{k}^{-i} & \mathbf{k}^{--} & \mathbf{k}^{-+} & -\mathbf{A}^{m,T} \\ \mathbf{k}^{+i} & \mathbf{k}^{+-} & \mathbf{k}^{++} & \mathbf{A}^{nm,T} \\ \mathbf{0} & -\mathbf{A}^{m} & \mathbf{A}^{nm} & \mathbf{0} \end{bmatrix} \begin{Bmatrix} \Delta\tilde{\mathbf{u}}^{i} \\ \Delta\tilde{\mathbf{u}}^{-} \\ \Delta\tilde{\mathbf{u}}^{+} \\ \boldsymbol{\lambda} \end{Bmatrix} = - \begin{Bmatrix} \mathbf{f}^{i} \\ \mathbf{f}^{-} \\ \mathbf{f}^{+} \\ \mathbf{0} \end{Bmatrix}. \tag{B.62}$$

This represents the linear system of equation for the Lagrange multiplier solution of the equilibrium problem.

Reis and Andrade Pires (2014) implemented this micro-constraint with the condensation method, aiming to reduce the number of unknowns on the linear system of equations. A suitable condensation procedure (see Section B.1.4) is performed. The resulting system of equations (B.63) recovers the general condensed system of equations for a RVE problem, expressed by (3.35), where non-mortar degrees of freedom (+) are dependent, and mortar (−) are free:

$$\left[\begin{array}{c|c} \mathbf{k}^{ii} & \mathbf{k}^{i-} + \mathbf{k}^{i+}\boldsymbol{\alpha} \\ \hline \mathbf{k}^{-i} + \boldsymbol{\alpha}^{T}\mathbf{k}^{+i} & \mathbf{k}^{--} + \mathbf{k}^{-+}\boldsymbol{\alpha} + \boldsymbol{\alpha}^{T}\mathbf{k}^{+-} + \boldsymbol{\alpha}^{T}\mathbf{k}^{++}\boldsymbol{\alpha} \end{array}\right] \begin{Bmatrix} \Delta\tilde{\mathbf{u}}^{i} \\ \Delta\tilde{\mathbf{u}}^{-} \end{Bmatrix} = - \begin{Bmatrix} \mathbf{f}^{i} \\ \mathbf{f}^{-} + \boldsymbol{\alpha}^{T}\mathbf{f}^{+} \end{Bmatrix}. \tag{B.63}$$

The dependency relation is given by

$$\tilde{\mathbf{u}}^{+} = \left[\mathbf{A}^{nm}\right]^{-1}\mathbf{A}^{m}\tilde{\mathbf{u}}^{-} = \boldsymbol{\alpha}\tilde{\mathbf{u}}^{-}, \tag{B.64}$$

where $\boldsymbol{\alpha} = [\mathbf{A}^{nm}]^{-1}\mathbf{A}^{m}$ denotes the dependency matrix.

B.4.3 Homogenised consistent tangent modulus

The homogenised material tangent modulus for the condensed problem is computed with the procedure presented in Section 3.3.5. However, if the problem is solved through the mixed approach presented in Equation (B.62), a slightly different procedure is required.

The same starting point is employed. The homogenised stress vector can still be obtained through Equation (3.47), hence the material tangent modulus matrix is determined by Expression (3.53). Developing this expression for this particular case yields:

$$\begin{aligned} \mathbf{A} &= \frac{1}{V_{\mu}}\mathbf{D}_{b}\left[\frac{\partial\mathbf{f}^{b}}{\partial\mathbf{u}^{i}}\frac{\partial\mathbf{u}^{i}}{\partial\mathbf{F}} + \frac{\partial\mathbf{f}^{b}}{\partial\mathbf{u}^{-}}\frac{\partial\mathbf{u}^{-}}{\partial\mathbf{F}} + \frac{\partial\mathbf{f}^{b}}{\partial\mathbf{u}^{+}}\frac{\partial\mathbf{u}^{+}}{\partial\mathbf{F}} + \frac{\partial\mathbf{f}^{b}}{\partial\mathbf{u}^{p}}\frac{\partial\mathbf{u}^{p}}{\partial\mathbf{F}}\right] \\ &= \frac{1}{V_{\mu}}\mathbf{D}_{b}\left[\mathbf{k}^{bi}\frac{\partial\mathbf{u}^{i}}{\partial\mathbf{F}} + \mathbf{k}^{b-}\frac{\partial\mathbf{u}^{-}}{\partial\mathbf{F}} + \mathbf{k}^{b+}\frac{\partial\mathbf{u}^{+}}{\partial\mathbf{F}} + \mathbf{k}^{bp}\frac{\partial\mathbf{u}^{p}}{\partial\mathbf{F}}\right] \\ &= \frac{1}{V_{\mu}}\mathbf{D}^{b}\left(\begin{bmatrix}\mathbf{k}^{bi} & \mathbf{k}^{b-} & \mathbf{k}^{b+}\end{bmatrix}\begin{bmatrix}\frac{\partial\tilde{\mathbf{u}}^{i}}{\partial\mathbf{F}} \\ \frac{\partial\tilde{\mathbf{u}}^{-}}{\partial\mathbf{F}} \\ \frac{\partial\tilde{\mathbf{u}}^{+}}{\partial\mathbf{F}}\end{bmatrix} + \left[\mathbf{K}^{B}\right]\left[\mathbf{D}^{total}\right]^{T}\right). \end{aligned} \tag{B.65}$$

In order to compute the derivatives of the fluctuations with regard to the macro-deformation gradient, the derivative of the residual in Equation (B.61) is set to zero, which is true when RVE equilibrium is achieved:

$$\frac{\partial}{\partial \mathbf{F}} \begin{Bmatrix} \mathbf{f}^{i} \\ \mathbf{f}^{-} - \mathbf{A}^{m,T}\boldsymbol{\lambda} \\ \mathbf{f}^{+} + \mathbf{A}^{nm,T}\boldsymbol{\lambda} \\ \mathbf{A}^{nm}\tilde{\mathbf{u}}^{+} - \mathbf{A}^{m}\tilde{\mathbf{u}}^{-} \end{Bmatrix} = \mathbf{0}. \tag{B.66}$$

Developing this expression leads to the following linear system of equations with multiple right-hand-sides:

$$\begin{bmatrix} \mathbf{k}^{ii} & \mathbf{k}^{i-} & \mathbf{k}^{i+} & \mathbf{0} \\ \mathbf{k}^{-i} & \mathbf{k}^{--} & \mathbf{k}^{-+} & -\mathbf{A}^{m,T} \\ \mathbf{k}^{+i} & \mathbf{k}^{+-} & \mathbf{k}^{++} & \mathbf{A}^{nm,T} \\ \mathbf{0} & -\mathbf{A}^{m} & \mathbf{A}^{nm} & \mathbf{0} \end{bmatrix} \cdot \begin{bmatrix} \frac{\partial \tilde{\mathbf{u}}^{i}}{\partial \mathbf{F}} \\ \frac{\partial \tilde{\mathbf{u}}^{-}}{\partial \mathbf{F}} \\ \frac{\partial \tilde{\mathbf{u}}^{+}}{\partial \mathbf{F}} \\ \frac{\partial \boldsymbol{\lambda}}{\partial \mathbf{F}} \end{bmatrix} = \begin{bmatrix} \mathbf{k}^{ii} & \mathbf{k}^{i-} & \mathbf{k}^{i+} & \mathbf{k}^{ip} \\ \mathbf{k}^{-i} & \mathbf{k}^{--} & \mathbf{k}^{-+} & \mathbf{k}^{-p} \\ \mathbf{k}^{+i} & \mathbf{k}^{+-} & \mathbf{k}^{++} & \mathbf{k}^{+p} \\ \mathbf{0} & \mathbf{0} & \mathbf{0} & \mathbf{0} \end{bmatrix} [\mathbf{D}_{total}]^{T}, \tag{B.67}$$

which allows to obtain the unknown derivatives required to compute the material tangent modulus.

Appendix C

Integration of quadratic triangular element shape functions

In the implementation of both uniform traction and mortar periodic boundary conditions, it is necessary to compute the integrals of the shape functions over RVE boundaries, which means that the shape functions of three-dimensional elements must be integrated over some of their interfaces. In practice, each 3D element interface yields a corresponding 2D element, and this procedure may be reduced to the integration of shape functions of the interface element, over its domain.

Due to numerical reasons, it is not desirable that the resulting value yields zero. However, when considering quadratic triangular interface elements (*tri 6*), the integration of shape functions related to element corners leads to this undesirable result. This fact is shown in the present Appendix.

The *tri 6* element shape functions are expressed in the parametric space (ξ, η) as:

$$\begin{cases} N_1 = (1-\xi-\eta)(2(1-\xi-\eta)-1) \\ N_2 = 2\xi^2 - \xi \\ N_3 = 2\eta^2 - \eta \\ N_4 = 4\xi(1-\xi-\eta) \\ N_5 = 4\xi\eta \\ N_6 = 4\eta(1-\xi-\eta) \end{cases}, \tag{C.1}$$

where 1, 2 and 3 refer to corner nodes, and 4, 5 and 6 correspond to edge nodes, as illustrated in Figure C.1.

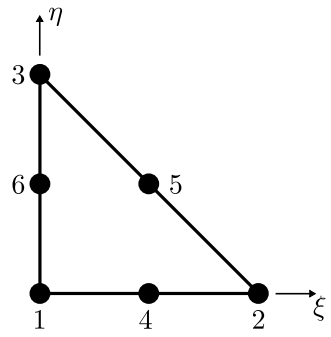

Figure C.1: Representation of the quadratic triangular element (*tri 6*).

Integration of corners related shape functions, over the element domain, is performed in what follows, aiming to show that zero is obtained for all three corners:

$$\begin{aligned}
\int_{\Omega^{(e)}} N_1 dA_e &= \int_0^1 \int_0^{1-\xi} \left[1-\xi-\eta\right]\left[2\left(1-\xi-\eta\right)-1\right] d\eta d\xi \\
&= \int_0^1 \int_0^{1-\xi} \left(2\xi^2+2\eta^2-3\xi-3\eta+4\xi\eta+1\right) d\eta d\xi \\
&= \int_0^1 \left[(2\xi^2-3\xi+1)(1-\xi)+\frac{2}{3}(1-\xi)^3+\frac{1}{2}(4\xi-3)(1-\xi)^2\right] d\xi \\
&= \int_0^1 \left[\left(-2\xi^3+5\xi^2-4\xi+1\right)+\frac{2}{3}\left(-\xi^3+3\xi^2-3\xi+1\right)+\frac{1}{2}\left((4\xi^3-11\xi^2+10\xi-3\right)\right] d\xi \\
&= \left(-\frac{2}{4}+\frac{5}{3}-2+1\right)+\frac{2}{3}\left(-\frac{1}{4}+1-\frac{3}{2}+1\right)+\frac{1}{2}\left(1-\frac{11}{3}+5-3\right) \\
&= \frac{1}{6}+\frac{1}{6}-\frac{1}{3}=0, \qquad \text{(C.2)}
\end{aligned}$$

$$\begin{aligned}
\int_{\Omega^{(e)}} N_2 dA_e &= \int_0^1 \int_0^{1-\xi} \left(2\xi^2-\xi\right) d\eta d\xi \\
&= \int_0^1 \left(2\xi^2-\xi\right)(1-\xi)\, d\xi \\
&= \int_0^1 \left(-2\xi^3+3\xi^2-\xi\right) d\xi \\
&= -\frac{2}{4}+1-\frac{1}{2}=0, \qquad \text{(C.3)}
\end{aligned}$$

$$\begin{aligned}
\int_{\Omega^{(e)}} N_3 dA_e &= \int_0^1 \left(\int_0^{1-\xi} 2\eta^2-\eta\right) d\eta d\xi \\
&= \int_0^1 \left[\frac{2}{3}(1-\xi)^3-\frac{1}{2}(1-\xi)^2\right] d\xi \\
&= \int_0^1 \left[\frac{2}{3}\left(-\xi^3+3\xi^2-3\xi+1\right)-\frac{1}{2}\left(\xi^2-2\xi+1\right)\right] d\xi \\
&= \frac{1}{6}-\frac{1}{6}=0. \qquad \text{(C.4)}
\end{aligned}$$

Appendix D

Computing second-order displacement derivatives from quadratic elements

The second gradient of the displacements may be expressed in index notation by:

$$\mathbf{G} = \frac{\partial^2 \boldsymbol{u}}{\partial \boldsymbol{X}^2} \Rightarrow G_{ijk} = \frac{\partial^2 u_i}{\partial X_j \partial X_k}. \tag{D.1}$$

In the framework of the finite element method, the displacement at a given point in an element is obtained from nodal displacements through the shape functions:

$$u_i = \bar{u}_{ij} N_j, \tag{D.2}$$

where N_j denotes the shape function value related to the j-th node of the element, and $\bar{u}_{ij}$ is the nodal displacement in direction i and related to the j-th node.

The second gradient can be computed as

$$\frac{\partial^2 u_i}{\partial X_j \partial X_k} = \bar{u}_{il} \frac{\partial^2 N_l}{\partial X_j \partial X_k}. \tag{D.3}$$

Therefore, in addition to the nodal displacements $\bar{\boldsymbol{u}}$, it is necessary to determine a third-order array $\mathbf{H}^x$ with the second derivatives of the shape functions:

$$\mathsf{H}^x_{ijk} = \frac{\partial^2 N_i}{\partial X_j \partial X_k}, \tag{D.4}$$

such that the second gradient

$$\mathbf{G} = \bar{\boldsymbol{u}} \cdot \mathbf{H}^x. \tag{D.5}$$

Obviously, this is only possible for elements with quadratic shape functions. A similar approach is followed by Nguyen et al. (2013) and Otero Gruer (2015).

The shape functions are defined in the natural coordinates space $\boldsymbol{\xi}$, thus it is straightforward to obtain the second derivatives in this space:

$$\mathsf{H}_{ijk} = \frac{\partial^2 N_i}{\partial \xi_j \partial \xi_k}. \tag{D.6}$$

The matrix with the first derivatives of the shape functions with regard to the Cartesian coordinates, $\boldsymbol{B}$, and the parametric coordinates, $\boldsymbol{B}^\xi$, along with the Jacobian matrix $\boldsymbol{J}$ and its inverse $\boldsymbol{J}^{-1}$

are denoted respectively as

$$
\begin{aligned}
B_{ij} &= \frac{\partial N_j}{\partial x_i}, \\
B^{\xi}_{ij} &= \frac{\partial N_j}{\partial \xi_i}, \\
J_{ij} &= \frac{\partial x_j}{\partial \xi_i}, \\
J^{-1}_{ij} &= \frac{\partial \xi_j}{\partial x_i}.
\end{aligned} \tag{D.7}
$$

The second derivatives of the shape functions with regard to the Cartesian coordinates are given by:

$$
\begin{aligned}
\mathsf{H}_{ijk} &= \frac{\partial}{\partial x_k}\left(\frac{\partial N_i}{\partial x_j}\right) \\
&= J^{-1}_{km} \cdot \frac{\partial}{\partial \xi_m}\left(\frac{\partial N_i}{\partial x_j}\right) \\
&= J^{-1}_{km} \cdot \frac{\partial}{\partial \xi_m}\left(J^{-1}_{jl} \cdot B^{\xi}_{li}\right) \\
&= J^{-1}_{km} \cdot \frac{\partial J^{-1}_{jl}}{\partial \xi_m} \cdot B^{\xi}_{li} + J^{-1}_{km} \cdot J^{-1}_{jl} \cdot \frac{\partial B^{\xi}_{li}}{\partial \xi_m}.
\end{aligned} \tag{D.8}
$$

In the second term of Expression (D.8),

$$
\frac{\partial B^{\xi}_{li}}{\partial \xi_m} = \mathsf{H}^{\xi}_{ilm}. \tag{D.9}
$$

In the first term, it is necessary to determine the derivative of the inverse of the Jacobian:

$$
\mathsf{A}_{jlm} = \frac{\partial J^{-1}_{jl}}{\partial \xi_m}. \tag{D.10}
$$

Departing from the definition of the inverse:

$$
\boldsymbol{J}^{-1} \cdot \boldsymbol{J} = \boldsymbol{I} \Rightarrow J^{-1}_{jl} \cdot J_{lp} = \delta_{jp}, \tag{D.11}
$$

and differentiating with regard to ξ_m, we obtain

$$
\frac{\partial J^{-1}_{jl}}{\partial \xi_m} \cdot J_{lp} + J^{-1}_{jl} \cdot \frac{\partial J_{lp}}{\partial \xi_m} = 0. \tag{D.12}
$$

From this equation, it results that

$$
\frac{\partial J^{-1}_{jl}}{\partial \xi_m} = \mathsf{A}_{jlm} = -J^{-1}_{jq} \cdot \frac{\partial J_{qp}}{\partial \xi_m} \cdot J^{-1}_{pl}. \tag{D.13}
$$

The derivative of the Jacobian matrix is expressed by

$$
\mathsf{B}_{qpm} = \frac{\partial J_{qp}}{\partial \xi_m} = \frac{\partial}{\partial \xi_m}\left(\frac{\partial x_p}{\partial \xi_q}\right). \tag{D.14}
$$

The coordinate x_p may be obtained from element nodal coordinates $\bar{X}_{pn}$ and shape function values N_n:

$$
x_p = \bar{X}_{pn} \cdot N_n, \tag{D.15}
$$

therefore, the derivative yields:

$$\mathsf{B}_{qpm} = \bar{X}_{pn} \cdot \frac{\partial^2 N_n}{\partial \xi_m \partial \xi_q} = \bar{X}_{pn} \cdot \mathsf{H}^{\xi}_{nqm} \tag{D.16}$$

Finally, the second derivatives of the shape functions with regard to the Cartesian coordinates are expressed as:

$$\begin{aligned} \mathsf{H}_{ijk} &= J^{-1}_{km} \cdot \left(J^{-1}_{jl} \cdot \mathsf{H}^{\xi}_{ilm} - J^{-1}_{jq} \cdot \mathsf{B}_{qpm} \cdot J^{-1}_{pl} \cdot B^{\xi}_{li} \right) \\ &= J^{-1}_{km} \cdot \left(J^{-1}_{jl} \cdot \mathsf{H}^{\xi}_{ilm} - J^{-1}_{jq} \cdot \mathsf{B}_{qpm} \cdot B_{pi} \right). \end{aligned} \tag{D.17}$$

Bibliography

M.M. Ameen, R.H.J. Peerlings, and M.G.D. Geers. A quantitative assessment of the scale separation limits of classical and higher-order asymptotic homogenization. *European Journal of Mechanics - A/Solids*, 71:89–100, sep 2018. ISSN 09977538. doi: 10.1016/j.euromechsol.2018.02.011. URL https://www.sciencedirect.com/science/article/pii/S0997753817303303.

S. Amstutz, S. M. Giusti, A. A. Novotny, and E. A. de Souza Neto. Topological derivative for multi-scale linear elasticity models applied to the synthesis of microstructures. *International Journal for Numerical Methods in Engineering*, 84(6):733–756, 2010.

F.X.C. Andrade, F.M. Andrade Pires, J.M.A. César de Sá, and L. Malcher. Nonlocal Integral Formulation for a Plasticity-Induced Damage Model. *Computer Methods in Material Science*, 9(1):49–54, 2009.

F.X.C. Andrade, J.M.A. Cesar de Sa, and F.M. Andrade Pires. A ductile damage nonlocal model of integral-type at finite strains: formulation and numerical issues. *International Journal of Damage Mechanics*, 20:515–557, 2011.

F.X.C. Andrade, F.M. Andrade Pires, and J.M.A. César de Sá. Consistent tangent operators for implicit non-local models of integral type. *Computers and Structures*, 141(Supplement C):59 – 73, 2014.

Yuanli Bai. *Effect of Loading History on Necking and Fracture*. PhD thesis, Massachusetts Institute of Technology, 2008.

Daniel Balzani, Ashutosh Gandhi, Axel Klawonn, Martin Lanser, Oliver Rheinbach, and Jörg Schröder. One-Way and Fully-Coupled FE2 Methods for Heterogeneous Elasticity and Plasticity Problems: Parallel Scalability and an Application to Thermo-Elastoplasticity of Dual-Phase Steels. volume 113 of *Lecture Notes in Computational Science and Engineering*, pages 91–112. Springer International Publishing, Cham, 2016. URL http://link.springer.com/10.1007/978-3-319-40528-5.

Yingbin Bao and Tomasz Wierzbicki. On fracture locus in the equivalent strain and stress triaxiality space. *International Journal of Mechanical Sciences*, 46(1):81 – 98, 2004.

Z.P. Bažant and F.-B. Lin. Nonlocal yield-limit degradation. *International Journal for Numerical Methods in Engineering*, 26:1805–1823, 1988.

Z.P. Bažant and G. Pijaudier-Cabot. Nonlocal Continuum Damage, Localization Instability and Convergence. *Journal of Applied Mechanics*, 55:287–290, 1988.

Z.P. Bazant and M. Jirásek. Nonlocal integral formulations of plasticity and damage: Survey of progress. *Jornal of Engineering Mechanics*, 128(11):4133–4145, 2002.

Ted Belytschko and Jeong-Hoon Song. Coarse-graining of multiscale crack propagation. *International Journal for Numerical Methods in Engineering*, 81(5):537–563, 2010.

C. Bernardi, Y. Maday, and A. T. Patera. Domain decomposition by the mortar element method. *Asymptotic and Numerical Methods for Partial Differential Equations with Critical Parameters*, 384:269–286, 1993.

Albrecht Bertram. Compendium on gradient materials, 2017. URL http://www.redaktion.tu-berlin.de/fileadmin/fg49/publikationen/bertram/Compendium_on_Gradient_Materials_Dec_2017.pdf.

M.A. Bessa, R. Bostanabad, Z. Liu, A. Hu, Daniel W. Apley, C. Brinson, W. Chen, and Wing Kam Liu. A framework for data-driven analysis of materials under uncertainty: Countering the curse of dimensionality. *Computer Methods in Applied Mechanics and Engineering*, 320:633–667, 2017. doi: 10.1016/j.cma.2017.03.037. URL https://linkinghub.elsevier.com/retrieve/pii/S0045782516314803.

Pablo J. Blanco, Pablo J. Sánchez, Eduardo A. de Souza Neto, and Raúl A. Feijóo. Variational Foundations and Generalized Unified Theory of RVE-Based Multiscale Models. *Archives of Computational Methods in Engineering*, 23(2):191–253, 2016a. URL http://link.springer.com/10.1007/s11831-014-9137-5.

P.J. Blanco, P.J. Sánchez, E.A. de Souza Neto, and R.A. Feijóo. The method of multiscale virtual power for the derivation of a second order mechanical model. *Mechanics of Materials*, 99: 53 – 67, 2016b. ISSN 0167-6636. doi: http://dx.doi.org/10.1016/j.mechmat.2016.05.003. URL http://www.sciencedirect.com/science/article/pii/S0167663616300400.

E. Bosco, V. G. Kouznetsova, E. W. C. Coenen, M. G. D. Geers, and A. Salvadori. A multi-scale framework for localizing microstructures towards the onset of macroscopic discontinuity. *Computational Mechanics*, 54(2):299–319, 2014. URL http://dx.doi.org/10.1007/s00466-014-0986-4.

E. Bosco, V. G. Kouznetsova, and M. G. D. Geers. Multi-scale computational homogenization-localization for propagating discontinuities using x-fem. *International Journal for Numerical Methods in Engineering*, 102(3-4):496–527, 2015. ISSN 1097-0207. URL http://dx.doi.org/10.1002/nme.4838.

L. Brand. *Vector and Tensor Analysis*. John Wiley and Sons, London: Chapman and Hall, 1947.

Michael Brünig, Steffen Gerke, and Vanessa Hagenbrock. Micro-mechanical studies on the effect of the stress triaxiality and the Lode parameter on ductile damage. *International Journal of Plasticity*, 50:49–65, 2013.

Pedro G. Coelho, João B. Cardoso, Paulo R. Fernandes, and Hélder C. Rodrigues. Parallel computing techniques applied to the simultaneous design of structure and material. *Advances in Engineering Software*, 42(5):219–227, 2011. doi: 10.1016/j.advengsoft.2010.10.003. URL http://dx.doi.org/10.1016/j.advengsoft.2010.10.003.

E. W C Coenen, V. G. Kouznetsova, E. Bosco, and M. G D Geers. A multi-scale approach to bridge microscale damage and macroscale failure: A nested computational homogenization-localization framework. *International Journal of Fracture*, 178(1-2):157–178, 2012a. ISSN 03769429. doi: 10.1007/s10704-012-9765-4.

E.W.C. Coenen, V.G. Kouznetsova, and M.G.D. Geers. Multi-scale continuous-discontinuous framework for computational-homogenization-localization. *Journal of the Mechanics and Physics of Solids*, 60(8):1486–1507, 2012b. ISSN 00225096. doi: 10.1016/j.jmps.2012.04.002. URL http://www.sciencedirect.com/science/article/pii/S0022509612000749.

E. Cosserat and F. Cosserat. *Théorie des Corps Déformables*. Hermann and Fils, 1909.

G. R. Cowper. Gaussian quadrature formulas for triangles. *International Journal for Numerical Methods in Engineering*, 7:405–408, 1973.

R. De Borst and H. Mühlhaus. Gradient-dependent plasticity: formulation and algorithmic aspects. *International Journal for Numerical Methods in Engineering*, 35:521–539, 1992.

M. Vieira de Carvalho, D. de Bortoli, and F.M. Andrade Pires. On the computational treatment of fully coupled crystal plasticity slip and martensitic transformation constitutive models at finite strains. *In preparation*.

E.A. de Souza Neto and R.A. Feijóo. Variational foundations of multi-scale constitutive models of solid:: Small and large strain kinematical formulation. LNCC R&D Report 16/2006, LNCC, 2006.

E.A. de Souza Neto and R.A. Feijóo. Variational foundations of large strain multiscale solid constitutive models: Kinematical formulation. In M. V. Júnior, E.A. de Souza Neto, and P. A. Muñoz Rojas, editors, *Advanced Computational Materials Modeling: from Classical to Multiscale Techniques*. Wiley-VCH, 2010.

E.A. de Souza Neto, D. Peric, and D.R.J. Owen. *Computational Methods for Plasticity: Theory and Applications*. Wiley, 2008.

E.A. de Souza Neto, S. Amstutz, S.M. Giusti, and A. A. Novotny. Topological derivative-based optimization of micro-structures considering different multi-scale models. 62(1):23–56, 2010.

E.A. de Souza Neto, P.J. Blanco, P.J. Sánchez, and R.a. Feijóo. An RVE-based multiscale theory of solids with micro-scale inertia and body force effects. *Mechanics of Materials*, 80:136–144, 2015.

J.D. Eshelby. The determination of the elastic field of an ellipsoidal inclusion and related problems. *Proceedings of the Royal Society of London A*, 241:376–396, 1957.

European Space Agency. Smooth deployment for second MARSIS antenna boom, 2005. URL https://www.esa.int/Our_Activities/Operations/Smooth_deployment_for_second_MARSIS_antenna_boom.

C. Farhat and F.-X. Roux. A method of finite element tearing and interconnecting and its parallel solution algorithm. *Int. J. Numer. Methods Engrg.*, 32:1205–1227, 1991.

Charbel Farhat, Michel Lesoinne, Patrick Letallec, Kendall Pierson, and Daniel Rixen. FETI-DP: A dual-primal unified FETI method part I: A faster alternative to the two-level FETI method. *International Journal for Numerical Methods in Engineering*, 50(7):1523–1544, 2001.

A Ferrer, J Oliver, J. C. Cante, and O Lloberas-Valls. Vademecum-based approach to multi-scale topological material design. *Advanced Modeling and Simulation in Engineering Sciences*, 3(1):23, 2016.

Frédéric Feyel and Jean-Louis Chaboche. FE2 multiscale approach for modelling the elastovisco plastic behaviour of long fibre SiC/Ti composite materials. *Computer Methods in Applied Mechanics and Engineering*, 183:309–330, 2000.

Jacob Fish, Tao Jiang, and Zheng Yuan. A staggered nonlocal multiscale model for a heterogeneous medium. *International Journal for Numerical Methods in Engineering*, 91:142–157, 2012.

N. A. Fleck, G. M. Muller, M. F. Ashby, and J. W. Hutchinson. Strain gradient plasticity: Theory and experiment. *Acta Metallurgica Et Materialia*, 42(2):475–487, 1994. doi: 10.1016/0956-7151(94)90502-9.

Felix Fritzen and Matthias Leuschner. Nonlinear reduced order homogenization of materials including cohesive interfaces. *Computational Mechanics*, 56(1):131–151, 2015.

Felix Fritzen, Samuel Forest, Thomas Böhlke, Djimedo Kondo, and Toufik Kanit. Computational homogenization of elasto-plastic porous metals. *International Journal of Plasticity*, 29:102–119, 2012.

Felix Fritzen, Max Hodapp, and Matthias Leuschner. GPU accelerated computational homogenization based on a variational approach in a reduced basis framework. *Computer Methods in Applied Mechanics and Engineering*, 278:186–217, 2014.

M.G.D. Geers, V.G. Kouznetsova, and W.A.M. Brekelmans. Multi-scale computational homogenization: Trends and challenges. *Journal of Computational and Applied Mathematics*, 234(7):2175–2182, 2010. URL http://www.sciencedirect.com/science/article/pii/S0377042709005536.

Somnath Ghosh, Kyunghoon Lee, and Suresh Moorthy. Multiple scale analysis of heterogeneous elastic structures using homogenization theory and Voronoi cell finite element method. *International Journal of Solids and Structures*, 32(1):27–62, 1995.

Somnath Ghosh, Kyunghoon Lee, and Prasanna Raghavan. A multi-level computational model for multi-scale damage analysis in composite and porous materials. *International Journal of Solids and Structures*, 38(14):2335–2385, 2001.

I.M. Gitman, H. Askes, and L.J. Sluys. Representative volume: Existence and size determination. *Engineering Fracture Mechanics*, 74(16):2518–2534, 2007.

I.M. Gitman, H. Askes, and L.J. Sluys. Coupled-volume multi-scale modelling of quasi-brittle material. *European Journal of Mechanics - A/Solids*, 27:302–327, 2008.

Sebatián Miguel Giusti. *Análise de sensibilidade topológica em modelos constitutivos multi-escalas*. PhD thesis, Laboratório Nacional de Computação Científica, 2009.

S.M. Giusti, P.J. Blanco, E.A. de Souza Neto, and R.A. Feijóo. An assessment of the Gurson yield criterion by a computational multi-scale approach. *Engineering Computations*, 26(3):281–301, 2009.

Governo da República Portuguesa. Arrancou a segunda fase do programa para lançamento de satélites nos Açores, 2019. URL https://www.portugal.gov.pt/pt/gc21/comunicacao/noticia?i=arrancou-a-segunda-fase-do-programa-para-lancamento-de-satelites-nos-acores.

Governo dos Açores. Azores International Research Center should be formally established in 2017, says Brito e Abreu, 2016. URL http://www.azores.gov.pt/Portal/en/entidades/srmct/noticias/Azores_International_Research_Center_should_be_formally_established_in_2017_says_Brito_e_Abreu.htm.

J. Miranda Guedes and Noboru Kikuchi. Preprocessing and postprocessing for materials based on the homogenization method with adaptive finite element methods. *Computer Methods in Applied Mechanics and Engineering*, 83(2):143–198, 1990.

A. L. Gurson. Continuum theory of ductile rupture by void nucleation and growth: Part I - Yield criteria and flow rules for porous ductile media. *Journal of Engineering Materials and Technology*, 99:2–15, 1977.

S. Hartmann, S. Brunssen, E. Ramm, and B. Wohlmuth. Unilateral non-linear dynamic contact of thin-walled structures using a primal-dual active set strategy. *International Journal for Numerical Methods in Engineering*, 70:883–912, 2007.

Z. Hashin. Analysis of Composite Materials - A Survey. *Journal of Applied Mechanics*, 50:481–505, 1983.

J.A. Hernández, J. Oliver, A.E. Huespe, M.A. Caicedo, and J.C. Cante. High-performance model reduction techniques in computational multiscale homogenization. *Computer Methods in Applied Mechanics and Engineering*, 276:149–189, 2014.

R. Hill. A self-consistent mechanics of composite materials. *Journal of the Mechanics and Physics of Solids*, 4:213–222, 1965.

HSL. MA41 Sparse unsymmetric system: unsymmetric multifrontal method. http://www.hsl.rl.ac.uk/catalogue/ma41.html, 2013.

Intel. Intel MKL PARDISO - Parallel Direct Sparse Solver Interface. https://software.intel.com/en-us/mkl-developer-reference-fortran-intel-mkl-pardiso-parallel-direct-sparse-solver-interface, 2018.

A. Javili, A. Mcbride, J. Mergheim, P. Steinmann, and U. Schmidt. Micro-to-macro transitions for continua with surface structure at the microscale. *International Journal of Solids and Structures*, 50(16-17):2561–2572, 2013. ISSN 00207683. doi: 10.1016/j.ijsolstr.2013.03.022. URL http://dx.doi.org/10.1016/j.ijsolstr.2013.03.022.

Ju Won Jeong, Young Ik Yoo, Dong Kil Shin, Jae Hyuk Lim, Kyung Won Kim, and Jung Ju Lee. A novel tape spring hinge mechanism for quasi-static deployment of a satellite deployable using shape memory alloy. *Review of Scientific Instruments*, 85(2):025001, 2014. doi: 10.1063/1.4862470. URL http://aip.scitation.org/doi/10.1063/1.4862470.

M. Jirásek. Nonlocal models for damage and fracture: comparison of approaches. *International Journal of Solids and Structures*, 35:4133–4145, 1998.

M. Jirásek and B. Patzák. Consistent tangent stiffness for nonlocal damage models. *Computers and Structures*, 80:1279–1293, 2002.

M. Jirásek and S. Rolshoven. Comparison of integral-type nonlocal plasticity models for strain-softening materials. *International Journal of Engineering Science*, 41:1553–1602, 2003.

Łukasz Kaczmarczyk, Chris J. Pearce, and Nenad Bićanić. Scale transition and enforcement of RVE boundary conditions in second-order computational homogenization. *International Journal for Numerical Methods in Engineering*, 74(3):506–522, 2008. doi: 10.1002/nme.2188. URL http://doi.wiley.com/10.1002/nme.2188.

Łukasz Kaczmarczyk, Chris J. Pearce, and Nenad Bićanić. Studies of microstructural size effect and higher-order deformation in second-order computational homogenization. *Computers & Structures*, 88(23-24):1383–1390, 2010. doi: 10.1016/j.compstruc.2008.08.004. URL http://linkinghub.elsevier.com/retrieve/pii/S0045794908001922.

T. Kanit, S. Forest, I. Galliet, V. Mounoury, and D. Jeulin. Determination of the size of the representative volume element for random composites: statistical and numerical approach. *International Journal of Solids and Structures*, 40(13-14):3647–3679, 2003. ISSN 00207683.

P. Kanouté, D. P. Boso, J. L. Chaboche, and B. A. Schrefler. Multiscale Methods for Composites: A Review. *Archives of Computational Methods in Engineering*, 16(1):31–75, 2009.

Junji Kato, Daishun Yachi, Kenjiro Terada, and Takashi Kyoya. Topology optimization of microstructure for composites applying a decoupling multi-scale analysis. *Structural and Multidisciplinary Optimization*, 49(4):595–608, 2014.

David J. Kennison. Polypack, a package of routines to manipulate polygons. http://ngwww.ucar.edu/supplements/polypack/index.html, 2000. Accessed: 21-09-2015.

V. Kouznetsova, W.A.M. Brekelmans, and F.P.T. Baaijens. Approach to micro-macro modeling of heterogeneous materials. *Computational Mechanics*, 27:37–48, 2001.

V. Kouznetsova, M.G.D. Geers, and W.A.M. Brekelmans. Multi-scale constitutive modelling of heterogeneous materials with a gradient-enhanced computational homogenization scheme. *International Journal for Numerical Methods in Engineering*, 54:1235–1260, 2002.

V. G. Kouznetsova, Marc G. D. Geers, Professor, and W. A. M. Brekelmans. Size of a Representative Volume Element in a Second-Order Computational Homogenization Framework. *International Journal for Multiscale Computational Engineering*, 2(4):575–598, 2004a. ISSN 1543-1649. doi: 10.1615/IntJMultCompEng.v2.i4.50. URL http://www.dl.begellhouse.com/journals/61fd1b191cf7e96f,3eec4b24232ba10b,636e8ffa63ed38af.html.

V.G. Kouznetsova. *Computational homogenization for the multi-scale analysis of multi-phase materials*. PhD thesis, Technische Universiteit Eindhoven, 2002.

V.G. Kouznetsova, M.G.D. Geers, and W.a.M. Brekelmans. Multi-scale second-order computational homogenization of multi-phase materials: a nested finite element solution strategy. *Computer Methods in Applied Mechanics and Engineering*, 193(48-51):5525–5550, 2004b.

Hiroyuki Kuramae, Yuki Ikeya, Hidetoshi Sakamoto, Hideo Morimoto, and Eiji Nakamachi. Multiscale parallel finite element analyses of LDH sheet formability tests based on crystallographic homogenization method. *International Journal of Mechanical Sciences*, 52(2):183–197, 2010. URL http://linkinghub.elsevier.com/retrieve/pii/S0020740309001568.

Young-Rok Kwon and Byung-Chai Lee. Three dimensional elements with lagrange multipliers for the modified couple stress theory. *Computational Mechanics*, 2017. ISSN 1432-0924. doi: 10.1007/s00466-017-1487-z. URL https://doi.org/10.1007/s00466-017-1487-z.

C. Lacour and Y. Maday. Two different approaches for matching nonconforming grids: The Mortar Element method and the Feti Method. *BIT Numerical Mathematics*, 37(3):720–738, 1997. ISSN 00063835.

Tomislav Lesičar. *Multiscale Modeling of Heterogeneous Materials Using Second-Order Homogenization*. PhD thesis, University of Zagreb, 2015.

Tomislav Lesičar, Jurica Sorić, and Zdenko Tonković. Large strain, two-scale computational approach using C1 continuity finite element employing a second gradient theory. *Computer Methods in Applied Mechanics and Engineering*, 298:303–324, 2016. ISSN 00457825. doi: 10.1016/j.cma.2015.09.017.

Tomislav Lesičar, Zdenko Tonković, and Jurica Sorić. Two-scale computational approach using strain gradient theory at microlevel. *International Journal of Mechanical Sciences*, 126:67 – 78, 2017. doi: https://doi.org/10.1016/j.ijmecsci.2017.02.017. URL http://www.sciencedirect.com/science/article/pii/S0020740316304258.

Christian Liebold and Wolfgang H. Müller. Comparison of gradient elasticity models for the bending of micromaterials. *Computational Materials Science*, 116:52–61, 2016. ISSN 09270256. doi: 10.

1016/j.commatsci.2015.10.031. URL http://dx.doi.org/10.1016/j.commatsci.2015.10.031.

O. Lloberas-Valls, D. J. Rixen, a. Simone, and L. J. Sluys. On micro-to-macro connections in domain decomposition multiscale methods. *Computer Methods in Applied Mechanics and Engineering*, 225-228:177–196, 2012a. URL http://dx.doi.org/10.1016/j.cma.2012.03.022.

O. Lloberas-Valls, D.J. Rixen, A. Simone, and L.J. Sluys. Multiscale domain decomposition analysis of quasi-brittle heterogeneous materials. *International Journal for Numerical Methods in Engineering*, 89(11):1337–1366, 2012b. URL http://doi.wiley.com/10.1002/nme.3286.

D. J. Luscher. A hierarchical framework for the multiscale modeling of microstructure evolution in heterogeneous materials, 2010.

Lucival Malcher. *Continuum Modelling and Numerical Simulation of Damage for Ductile Materials*. PhD thesis, Faculdade de Engenharia da Universidade do Porto, 2012.

H. M. Y. C. Mallikarachchi. *Thin-Walled Composite Deployable Booms with Tape-Spring Hinges*. PhD thesis, University of Cambridge, 2011.

J. Marty, J. Réthoré, and A. Combescure. Experimental investigation of higher-order homogenization schemes under large strain. *International Journal of Solids and Structures*, 88-89: 263–273, jun 2016. ISSN 00207683. doi: 10.1016/j.ijsolstr.2016.03.001. URL https://www.sciencedirect.com/science/article/pii/S0020768316001128.

T. J. Massart. *Multi-scale modeling of damage in masonry structures*. PhD thesis, Technische Universiteit Eindhoven, 2003.

Karel Matouš, Marc G.D. Geers, Varvara G. Kouznetsova, and Andrew Gillman. A review of predictive nonlinear theories for multiscale modeling of heterogeneous materials. *Journal of Computational Physics*, 330:192–220, 2017. ISSN 00219991. doi: 10.1016/j.jcp.2016.10.070. URL http://dx.doi.org/10.1016/j.jcp.2016.10.070.

Kazumi Matsui, Kenjiro Terada, and Kohei Yuge. Two-scale finite element analysis of heterogeneous solids with periodic microstructures. *Computers & Structures*, 82:593–606, 2004.

Takashi Matsushima, René Chambon, and Denis Caillerie. Large strain finite element analysis of a local second gradient model: application to localization. *International Journal for Numerical Methods in Engineering*, 54(4):499–521, 2002. ISSN 0029-5981. URL http://doi.wiley.com/10.1002/nme.433.

A.R. Melro, P.P. Camanho, and S.T. Pinho. Generation of random distribution of fibres in long-fibre reinforced composites. *Composites Science and Technology*, 68(9):2092–2102, jul 2008. ISSN 0266-3538. doi: 10.1016/J.COMPSCITECH.2008.03.013. URL https://www.sciencedirect.com/science/article/pii/S0266353808001048.

C. Miehe and C. G. Bayreuther. On multiscale fe analyses of heterogeneous structures: from homogenization to multigrid solvers. *International Journal for Numerical Methods in Engineering*, 71(10):1135–1180, 2007. ISSN 1097-0207. URL http://dx.doi.org/10.1002/nme.1972.

C. Miehe and A. Koch. Computational micro-to-macro transitions of discretized microstructures undergoing small strains. *Archive of Applied Mechanics*, 72:300–317, 2002.

Christian Miehe, Jan Schotte, and Jörg Schröder. Computational micro-macro transitions and overall moduli in the analysis of polycrystals at large strains. *Computational Materials Science*, 16: 372–382, 1999a.

Christian Miehe, Jörg Schröder, and Jan Schotte. Computational homogenization analysis in finite plasticity Simulation of texture development in polycrystalline materials. *Computer Methods in Applied Mechanics and Engineering*, 171:387–418, 1999b.

R. D. Mindlin. Micro-structure in linear elasticity. *Arch. Ration. Mech. Anal.*, 16:51–78, 1964.

R.D. Mindlin and N.N. Eshel. On first strain-gradient theories in linear elasticity. *International Journal of Solids and Structures*, 4(1):109–124, 1968. doi: 10.1016/0020-7683(68)90036-X. URL http://linkinghub.elsevier.com/retrieve/pii/002076836890036X.

Matthew Mosby and Karel Matouš. Hierarchically parallel coupled finite strain multiscale solver for modeling heterogeneous layers. *International Journal for Numerical Methods in Engineering*, 102 (3-4):748–765, 2015.

Matthew Mosby and Karel Matouš. Computational homogenization at extreme scales. *Extreme Mechanics Letters*, 6:68–74, 2016.

V.-D. Nguyen and L. Noels. Computational homogenization of cellular materials. *International Journal of Solids and Structures*, 51(11-12):2183–2203, 2014. ISSN 00207683. doi: 10.1016/j.ijsolstr.2014.02.029. URL http://dx.doi.org/10.1016/j.ijsolstr.2014.02.029.

V. D. Nguyen, G. Becker, and L. Noels. Multiscale computational homogenization methods with a gradient enhanced scheme based on the discontinuous Galerkin formulation. *Computer Methods in Applied Mechanics and Engineering*, 260:63–77, 2013. ISSN 00457825. doi: 10.1016/j.cma.2013.03.024.

V. P. Nguyen, O. Lloberas-Valls, M. Stroeven, and L. J. Sluys. Computational homogenization for multiscale crack modeling. Implementation and computational aspects. *International Journal for Numerical Methods in Engineering*, 89:192–226, 2012a.

Van Dung Nguyen, Ling Wu, and Ludovic Noels. Unified treatment of microscopic boundary conditions and efficient algorithms for estimating tangent operators of the homogenized behavior in the computational homogenization method. *Computational Mechanics*, 59(3):1–23, 2016. ISSN 01787675. doi: 10.1007/s00466-016-1358-z.

Van-Dung Nguyen, Ling Wu, and Ludovic Noels. A micro-mechanical model of reinforced polymer failure with length scale effects and predictive capabilities. Validation on carbon fiber reinforced high-crosslinked RTM6 epoxy resin. *Mechanics of Materials*, 2019. ISSN 01676636. doi: 10.1016/j.mechmat.2019.02.017. URL https://doi.org/10.1016/j.mechmat.2019.02.017.

Vinh Phu Nguyen, Oriol Lloberas-Valls, Martijn Stroeven, and Lambertus Johannes Sluys. On the existence of representative volumes for softening quasi-brittle materials: A failure zone averaging scheme. *Computer Methods in Applied Mechanics and Engineering*, 199:3028–3038, 2010.

Vinh Phu Nguyen, Martijn Stroeven, and Lambertus Johannes Sluys. Multiscale failure modeling of concrete: Micromechanical modeling, discontinuous homogenization and parallel computations. *Computer Methods in Applied Mechanics and Engineering*, 201-204:139–156, 2012b.

J. Oliver, M. Caicedo, E. Roubin, A.E. Huespe, and J.A. Hernández. Continuum approach to computational multiscale modeling of propagating fracture. *Computer Methods in Applied Mechanics and Engineering*, 294:384–427, 2015. URL http://linkinghub.elsevier.com/retrieve/pii/S0045782515001851.

Fermin Otero Gruer. *Multiscale numerical modelling of microstructured reinforced composites*. PhD thesis, Universitat Polit'ecnica de Catalunya, 2015.

S.-A. Papanicolopulos, A. Zervos, and I. Vardoulakis. A three-dimensional C 1 finite element for gradient elasticity. *International Journal for Numerical Methods in Engineering*, 77(10):1396–1415, 2009. ISSN 00295981. doi: 10.1002/nme.2449. URL http://doi.wiley.com/10.1002/nme.2449.

R.H.J. Peerlings, R. De Borst, W.A.M. Brekelmans, and J.H.P. De Vree. Gradient-enhanced damage for quasi-brittle materials. *International Journal for Numerical Methods in Engineering*, 39:1512–1533, 1996.

R.H.J. Peerlings, M.G.D. Geers, R. De Borst, and W.A.M. Brekelmans. A critical comparison of nonlocal and gradient-enhanced softening continua. *International Journal of Solids and Structures*, 38(44–45):7723–7746, 2001.

C. Pellegrino, U. Galvanetto, and B. A. Schrefler. Numerical homogenization of periodic composite materials with non-linear material components. *International Journal for Numerical Methods in Engineering*, 46:1609–1637, 1999.

D. Perić, D.R.J. Owen, and M.E. Honnor. A model for finite strain elasto-plasticity based on logarithmic strain: computational issues. *Computer Methods in Applied Mechanics and Engineering*, 94: 35–61, 1992.

J. Petera and J. F. T. Pittman. Isoparametric Hermite elements. *International Journal for Numerical Methods in Engineering*, 37(20):3489–3519, 1994. ISSN 0029-5981. doi: 10.1002/nme.1620372006. URL http://doi.wiley.com/10.1002/nme.1620372006.

G. Pijaudier-Cabot and Z.P Bazant. Nonlocal damage theory. *Jornal of Engineering Mechanics*, 113 (10):1512–1533, 1987.

J.A. Plews and C.A. Duarte. Bridging multiple structural scales with a generalized finite element method. *International Journal for Numerical Methods in Engineering*, 102(3-4):180–201, 2015. ISSN 1097-0207.

Castrenze Polizzoto. A note on the higher order strain and stress tensors within deformation gradient elasticity theories: Physical interpretations and comparisons. *International Journal of Solids and Structures*, 90:116–121, 2016. ISSN 00207683. doi: 10.1016/j.ijsolstr.2016.04.001. URL https://linkinghub.elsevier.com/retrieve/pii/S0020768316300191.

A. Popp, B. Wohlmuth, M. Gee, and W. Wall. Dual quadratic mortar finite element methods for 3D finite deformation contact. *SIAM Journal on Scientific Computing*, 34(4):421–446, 2012.

Alexander Popp. *Mortar Methods for Computational Contact Mechanics and General Interface Problems*. PhD thesis, Technische Universität München, 2012.

Michael A. Puso. A 3D mortar method for solid mechanics. *International Journal for Numerical Methods in Engineering*, 59(3):315–336, 2004.

Michael A. Puso and Tod A. Laursen. Mesh tying on curved interfaces in 3D. *Engineering Computations*, 20(3):305–319, 2003.

R. Quey, P.R. Dawson, and F. Barbe. Large-scale 3D random polycrystals for the finite element method: Generation, meshing and remeshing. *Computer Methods in Applied Mechanics and Engineering*, 200(17-20):1729–1745, 2011. ISSN 0045-7825. doi: 10.1016/J.CMA.2011.01.002. URL https://www.sciencedirect.com/science/article/pii/S004578251100003X.

Rahul and Suvranu De. An efficient coarse-grained parallel algorithm for global-local multiscale computations on massively parallel systems. *International Journal for Numerical Methods in Engineering*, 82(3):379–402, 2010.

F.J.P. Reis. *Multi-Scale Modelling and Analysis of Heterogeneous Solids at Finite Strains*. PhD thesis, Faculdade de Engenharia da Universidade do Porto, 2014.

F.J.P Reis and F. M. Andrade Pires. An adaptive sub-incremental strategy for the solution of homogenization-based multi-scale problems. *Computer Methods in Applied Mechanics and Engineering*, 257:164–182, 2013.

F.J.P. Reis and F.M. Andrade Pires. A mortar based approach for the enforcement of periodic boundary conditions on arbitrarily generated meshes. *Computer Methods in Applied Mechanics and Engineering*, 274:168–191, 2014.

F.J.P. Reis, I.A. Rodrigues Lopes, F.M. Andrade Pires, and F.X.C. Andrade. Microscale analysis of heterogeneous ductile materials with nonlocal damage models of integral type. *Computers & Structures*, 201:37–57, 2018. ISSN 00457949. doi: 10.1016/j.compstruc.2018.02.013. URL https://www.sciencedirect.com/science/article/pii/S0045794917309847.

Oliver Rheinbach. Parallel Iterative Substructuring in Structural Mechanics. *Archives of Computational Methods in Engineering*, 16(4):425–463, 2009.

D. Roca, O. Lloberas-Valls, J. Cante, and J. Oliver. A computational multiscale homogenization framework accounting for inertial effects: Application to acoustic metamaterials modelling. *Computer Methods in Applied Mechanics and Engineering*, 330:415–446, 2018. ISSN 00457825. doi: 10.1016/j.cma.2017.10.025. URL https://www.sciencedirect.com/science/article/pii/S0045782517306989.

H. Rodrigues, J. M. Guedes, and M. P. Bendsoe. Hierarchical optimization of material and structure. *Structural and Multidisciplinary Optimization*, 24(1):1–10, 2002. doi: 10.1007/s00158-002-0209-z.

I. A. Rodrigues Lopes, F. M. Andrade Pires, and F. J. P. Reis. A mixed parallel strategy for the solution of coupled multi-scale problems at finite strains. *Computational Mechanics*, 61(1-2):157–180, 2018. doi: 10.1007/s00466-017-1472-6. URL http://link.springer.com/10.1007/s00466-017-1472-6.

E.I. Saavedra Flores, E.A. de Souza Neto, and C. Pearce. A large strain computational multi-scale model for the dissipative behaviour of wood cell-wall. *Computational Materials Science*, 50(3):1202–1211, 2011.

P. J. Sánchez, P. J. Blanco, A. E. Huespe, and R. A. Feijóo. Failure-Oriented Multi-scale Variational Formulation: Micro-structures with nucleation and evolution of softening bands. *Computer Methods in Applied Mechanics and Engineering*, 257:221–247, 2013.

John Y. Shu, Wayne E. King, and Norman A. Fleck. Finite elements for materials with strain gradient effects. *International Journal for Numerical Methods in Engineering*, 44(3):373–391, 1999. ISSN 0029-5981.

J. C. Simo and T. J. R Hughes. *Computational Inelasticity*. 1998.

J. C. Simo, R. L. Taylor, and P. Wriggers. A perturbed lagrangian formulation for the finite element solution of contact problems. *Computer Methods in Applied Mechanics and Engineering*, 50:163–180, 1985.

R.J.M. Smit, W.A.M. Brekelmans, and H.E.H. Meijer. Prediction of the mechanical behavior of nonlinear heterogeneous systems by multi-level finite element modeling. *Computer Methods in Applied Mechanics and Engineering*, 155(1-2):181–192, 1998.

D. D. Somer, E. a. de Souza Neto, W. G. Dettmer, and D. Perić. A sub-stepping scheme for multi-scale analysis of solids. *Computer Methods in Applied Mechanics and Engineering*, 198:1006–1016, 2009.

A. Sridhar, V. G. Kouznetsova, and M. G. D. Geers. Homogenization of locally resonant acoustic metamaterials towards an emergent enriched continuum. *Computational Mechanics*, 57(3):423–435, mar 2016. ISSN 0178-7675. doi: 10.1007/s00466-015-1254-y. URL http://link.springer.com/10.1007/s00466-015-1254-y.

Dan Stefanica. A numerical study of FETI algorithms for mortar finite element methods. *SIAM Journal on Scientific Computing*, 23(4):1135–1160, 2001.

Dan Stefanica. Parallel FETI algorithms for mortars. *Applied Numerical Mathematics*, 54(2):266–279, 2005.

İ. Temizer and P. Wriggers. An adaptive multiscale resolution strategy for the finite deformation analysis of microheterogeneous structures. *Computer Methods in Applied Mechanics and Engineering*, 200(37-40):2639–2661, sep 2011. ISSN 00457825. doi: 10.1016/j.cma.2010.06.013. URL http://dx.doi.org/10.1016/j.cma.2010.06.013.

Kenjiro Terada, Muneo Hori, Takashi Kyoya, and Noboru Kikuchi. Simulation of the multi-scale convergence in computational homogenization approaches. *International Journal of Solids and Structures*, 37(16):2285–2311, 2000.

S. Toro, P.J. Sánchez, A.E. Huespe, S.M. Giusti, P.J. Blanco, and R.A. Feijóo. A two-scale failure model for heterogeneous materials: numerical implementation based on the finite element method. *International Journal for Numerical Methods in Engineering*, 97(5):313–351, 2014.

S. Toro, P. J. Sánchez, J. M. Podestá, P. J. Blanco, A. E. Huespe, and R. A. Feijóo. Cohesive surface model for fracture based on a two-scale formulation: computational implementation aspects. *Computational Mechanics*, 58(4):549–585, 2016a. ISSN 0178-7675. URL http://link.springer.com/10.1007/s00466-016-1306-y.

S. Toro, P.J. Sánchez, P.J. Blanco, E.A. de Souza Neto, A.E. Huespe, and R.A. Feijóo. Multiscale formulation for material failure accounting for cohesive cracks at the macro and micro scales. *International Journal of Plasticity*, 76:75–110, 2016b. ISSN 07496419. URL http://linkinghub.elsevier.com/retrieve/pii/S0749641915001199.

R. A. Toupin. Theories of elasticity with couple-stress. *Archive for Rational Mechanics and Analysis*, 17(2):85–112, 1964. doi: 10.1007/BF00253050.

V. Tvergaard and A. Needleman. Analysis of the cup-cone fracture in a round tensile bar. *Acta Metallurgica*, 32:157–169, 1984.

G. Weber and L. Anand. Finite deformation constitutive equations and a time integration procedure for isotropic, hyperelastic-viscoplastic solids. *Computer Methods in Applied Mechanics and Engineering*, 79:173–202, 1990.

Barbara I. Wohlmuth. *Discretization Methods and Iterative Solvers Based on Domain Decomposition*. Springer Verlag, Berlin, Heidelberg, New York, 2001.

Liang Xia and Piotr Breitkopf. Concurrent topology optimization design of material and structure within FE2 nonlinear multiscale analysis framework. *Computer Methods in Applied Mechanics and Engineering*, 278:524–542, 2014. doi: 10.1016/j.cma.2014.05.022. URL http://dx.doi.org/10.1016/j.cma.2014.05.022.

J. C. Yee and S. Pellegrino. Composite Tube Hinges. *Journal of Aerospace Engineering*, 18(4):224–231, 2005. doi: 10.1061/(asce)0893-1321(2005)18:4(224).

A. Zervos. Finite elements for elasticity with microstructure and gradient elasticity. *International Journal for Numerical Methods in Engineering*, 73(4):564–595, 2008. ISSN 1097-0207. doi: 10.1002/nme.2093. URL http://dx.doi.org/10.1002/nme.2093.

A Zervos, S.-A. Papanicolopulos, and I Vardoulakis. Two Finite-Element Discretizations for Gradient Elasticity. *Journal of Engineering Mechanics*, 135(3):203–213, 2009. ISSN 0733-9399. doi: 10.1061/(ASCE)0733-9399(2009)135:3(203). URL http://doi.wiley.com/10.1002/nme.2449.

L Zybell, Uwe Muehlich, Meinhard Kuna, and Z L. Zhang. A three-dimensional finite element for gradient elasticity based on a mixed-type formulation. 52:268–273, 02 2012.